

**The development of bite force resistance and cranial  
form in Neanderthals and modern humans**

Candidate: **Lisa Genochio**

Supervisor: **Prof. Paul O'Higgins**

Submission for the degree of PhD in Human Sciences

Hull York Medical School

Submission data: December 2022

*A mes parents, grand-parents et mon frère,*

*A Tom,*

## Abstract

The general aim of the thesis is to understand how biting mechanics interact with cranial form to impact post-natal craniofacial ontogeny in modern humans and Neanderthals. To this end, CT scans of ontogenetic samples of 12 Neanderthal and 63 modern human crania were collected and a series of reconstructions of Neanderthal crania were carried out. Geometric morphometric and multivariate regression approaches were used to create a craniofacial growth model for each species. Using these two models, 3D virtual crania representing the mean adult, juvenile, and infant were extracted in each species. These 6 mean crania were then converted into finite element models and used to conduct two biting simulations: at the right second premolar or second deciduous molar (RP<sup>2</sup>/RdM<sup>2</sup>) and right first incisor (RI<sup>1</sup>), applying the same muscle forces for all models because these are unknown especially for Neanderthals. This study compared modes and magnitudes of deformation, and the distribution and magnitude of tensile and compressive strains between the mean infant, juvenile, and adult models within each species and between the two species at each age stage.

The morphometric analyses indicate that cranial ontogenetic trajectories differ between modern humans and Neanderthals. The finite element analyses (FEA) in both biting simulations indicate that, within each species, the mean infant juvenile and adult models deform differently. Further, in both biting simulations, the highest strains are localised over similar regions of the cranium; over the anterior maxilla, orbits, and anterior subnasal surface. Modern humans and Neanderthals deform differently and show differences in the development of biting forces during RI<sup>1</sup> and RP<sup>2</sup>/RdM<sup>2</sup> biting simulations at each stage. These findings confirm that modern human and Neanderthal crania have divergent postnatal developmental trajectories and manifest differences in the resistance of masticatory system loadings throughout life. Differences in modes of deformation and so, strain distributions are considered in light of known differences in craniofacial bone growth remodeling between Neanderthals and modern humans. The findings show some correspondence with the remodeling maps for both species, particularly during RP<sup>2</sup>/RdM<sup>2</sup> biting simulations. They do not falsify the hypothesis that facial remodeling differences arise because of differences in load resistance, and so, in the strain environment during post-natal development. As such, how differences among adult crania arise through post-natal interactions between form and functional loadings merits further investigation through more detailed analyses of a wider range of loading scenarios.

# List of contents

## Table of Contents

Abstract.....	3
List of contents.....	4
Table of Contents.....	4
List of Figures.....	8
List of Tables.....	18
Acknowledgements.....	20
Author’s declaration.....	21
1.0 Introduction.....	22
1.1 Skull growth.....	24
1.1.1 Modern human craniofacial anatomy, development and function.....	25
1.1.2 Neanderthal craniofacial anatomy, development and function.....	36
1.2 Cranial form and function in modern human and Neanderthal.....	42
1.2.1 Cranial form, function, modularity and integration.....	42
1.2.2 Production of bite force.....	43
1.2.3 Resisting bite force.....	45
1.3 Bone biomechanical function and adaptation.....	48
1.3.1 Bone structure and morphology.....	48
1.3.2 Bone mechanical properties.....	50
1.3.3 Bone mechanical adaptation.....	52
1.4 Objectives and hypotheses.....	57
2.0 Modern human and Neanderthal post-natal craniofacial allometry and the extraction of infant, juvenile and adult models.....	60
2.1 Samples.....	60
2.1.1 Modern human.....	60
2.1.2 Neanderthal.....	64

2.2 Geometric morphometrics.....	68
2.2.1 Landmarks and semi-landmarks .....	69
2.2.2 Sliding semi-landmarks .....	71
2.3 Multivariate statistical methods .....	73
2.3.1 Generalised Procrustes Analysis .....	73
2.3.2 Principal Component Analysis.....	74
2.3.3 Multivariate regression analysis .....	74
2.4 Results .....	75
2.4.1 Comparison of ontogenetic allometries .....	75
2.4.2 Modern humans.....	76
2.4.3 Neanderthals.....	80
2.4.4 The models and their validity .....	81
2.5 Discussion.....	84
3.0 Biting simulations in modern humans .....	88
3.1 Introduction .....	88
3.2 Materials and methods .....	88
3.2.1 Finite element models .....	88
3.2.2 Mechanical advantages and peak bite forces.....	96
3.3 Model solution and data analysis .....	98
3.3.1 Mechanical advantages .....	99
3.3.2 Deformations .....	101
3.3.3 Tensile and compressive strains .....	105
3.4 Discussion.....	115
3.4.1 Mechanical advantages, peak bite forces and force production efficiencies.....	115
3.4.2 Craniofacial skeletal performance during right first incisor and second premolar/deciduous molar biting.....	117
3.4.3 Significance of apparent differences between the mean modern human infant, juvenile and adult models.....	121

4.0 Biting simulations in Neanderthals .....	127
4.1 Introduction .....	127
4.2 Material and Methods .....	127
4.2.1 Finite element models .....	127
4.2.2 Mechanical advantages and peak bite forces.....	131
4.3 Model solution and data analysis .....	132
4.3.1 Mechanical advantages .....	133
4.3.2 Deformations .....	135
4.3.3 Tensile and compressive strains .....	138
4.4 Discussion.....	150
4.4.1 Mechanical advantages, peak bite forces and force production efficiencies.....	150
4.4.2 Craniofacial skeletal performance during right first incisor and second premolar/deciduous molar biting.....	152
4.4.3 Significance of apparent differences between the mean Neanderthal infant, juvenile and adult models .....	154
5.0 Comparison of modern human and Neanderthal biting performance.....	157
5.1 Craniofacial deformations, strains and bone growth remodeling.....	158
5.1.1 Mechanical advantages .....	158
5.1.2 Deformations .....	165
5.1.3 Tensile and compressive strains .....	173
5.1.4 Peak strains over both biting simulations.....	186
5.2 Discussion.....	188
5.2.1 Mechanical advantages, peak bite forces and force production efficiencies.....	188
5.2.2 Craniofacial skeletal performance during right first incisor and second premolar/deciduous molar biting.....	191
5.2.3 Significance of apparent differences between the mean Neanderthal and modern human infant, juvenile and adult models .....	192
6.0 General discussion and conclusions.....	195
6.1 Synthesis of key findings and discussion .....	195

6.2 Limitations of the present study and implications .....	215
Supplementary materials.....	222
Literature cited .....	225
Appendix 1: Neanderthal reconstructions.....	293
Appendix 2: Sensitivity test of the effect of filling in of frontal and maxillary sinuses.....	311
Appendix 3: Sensitivity test on the effects of different teeth .....	319

## List of Figures

Figure 1. Neurocranium. (2022, December 4). In Wikipedia. <a href="https://en.wikipedia.org/wiki/Neurocranium">https://en.wikipedia.org/wiki/Neurocranium</a> .....	24
Figure 2. Facial skeleton. (2022, December 22). In Wikipedia. <a href="https://en.wikipedia.org/wiki/Facial_skeleton">https://en.wikipedia.org/wiki/Facial_skeleton</a> .....	25
Figure 3. The epithelial-mesenchymal transformation process (Kalluri and Weinberg, 2009)..	27
Figure 4. Schematic superior (A, B) and lateral views (a, b) of the fetal skull. A and a show the stage of development where the cranial vault is largely membranous and the intramembranous ossification centres (yellow) have begun to form. B and b, show the skull at birth, when the intramembranous ossification centres expand and the sutures and fontanelles develop (modified from Stern, 2003). .....	28
Figure 5. Newborn skull with fontanelles (Sadler, 2010). .....	29
Figure 6. Bone structures (modified from Hart et al, 2017 and Rauch and Schonau, 2005). ....	49
Figure 7. Relationship between force and displacement in an elastic material. At the yield point the deformation becomes plastic until the point of fracture (Hart et al, 2017; Lieberman, 2011; Cole and Van der Meulen, 2011; Burstein et al, 1972). .....	50
Figure 8. Gibraltar 1 skull before reconstruction. ....	66
Figure 9. Gibraltar 1 skull after reflected relabelling. ....	66
Figure 10. La Chapelle-aux-Saints reconstructed. ....	67
Figure 11. La Ferrassie 1 cranium before reconstruction .....	67
Figure 12. Gibraltar 1 after reflected relabelling and reconstruction with parts from La Chapelle-aux-Saints and Saccopastore 1, added using warping approaches. ....	68
Figure 13. Reconstructed Gibraltar 1 specimen used as a reference surface to mesh the mean infant, juvenile and adult landmarks and semi-landmark coordinates. ....	68
Figure 14. Final template with 57 fixed landmarks used to build the ontogenetic growth model. ....	71
Figure 15. Final template with 57 fixed landmarks, 246 semi-landmarks and 5 curves (orbits, zygomatic arches and nasal aperture) used to build the ontogenetic growth model. ....	71
Figure 16. PC1 vs PC2 of shape of the full modern human sample with the infants in blue, juveniles in green and adults in red. ....	76
Figure 17. PC1 vs PC3 of shape of the full modern human sample with the infants in blue, juveniles in green and adults in red. ....	76
Figure 18. PC1 vs PC2 of form including the full modern human sample with the infants in blue, juveniles in green and adults in red. ....	77

Figure 19. PC1 vs PC3 of form including the full modern human sample with the infants in blue, juveniles in green and adults in red. ....	77
Figure 20. Adult specimen used as a reference surface to estimate the mean infant, juvenile and adult models. ....	77
Figure 21. PC1 vs PC2/PC3 in shape space including the full Neanderthal sample with the infants in blue, juveniles in green and adults in red. ....	80
Figure 22. The modern human adult, infant (around 2-3 years old) and juvenile (8-10 years old) models.....	82
Figure 23. The Neanderthal adult, infant (around 2-3 years old) and juvenile (8-10 years old) models.....	82
Figure 24. PC1 vs PC2/PC3 in form space including the full modern human sample with the infants in dark blue, juveniles in green and adults in red; the full Neanderthal sample with the infants in skyblue, juveniles in yellow and adults in brown. The models are represented with black symbols: modern human infant (circle); modern human juvenile (triangle); modern human adult (cross); Neanderthal infant (purple star); Neanderthal juvenile (purple square); Neanderthal adult (purple diamond).....	83
Figure 25. Adult, juvenile and infant mean models with the corresponding teeth.....	90
Figure 26. Strains experienced by FE model 1 (0.35) and model 2 (0.70) at the 69 sampling points over the face during the LI <sup>1</sup> biting simulations. The tensile (red and pink) and compressive (light blue and dark blue) strains in each model are unscaled and at each landmark the ratio between them is exactly the ratio of squared centroid sizes of each model ( $1^2:2^2 = 1:4$ ). From an unpublished validation study conducted by Ricardo Godinho and Paul O'Higgins.....	95
Figure 27. To calculate the mechanical advantage for the mean infant, juvenile and adult in both species, the landmarks defined to guide the placement of muscle vectors for FEA were used to calculate the muscle in-lever arms (temporalis, masseter and medial pterygoid lines of action shown by black solid lines). The in-lever arms were calculated as the perpendicular distances from the fulcrum (TMJ/glenoid fossa) to the respective muscle line of action (examples indicated by grey lines). The out-lever arms were calculated as the perpendicular distance from the fulcrum to the vector of the peak bite force applied (red dotted line). The open triangle indicates the fulcrum and the constraint at the glenoid fossa. The solid triangles represent the constraints at the bite points.....	97
Figure 28. 126 points used to extract the surface strain magnitudes from the solved Finite Element models. ....	98
Figure 29. Landmark and semi-landmark configurations used to calculate the deformation of the cranium in each model after loading at the right first incisor (RI <sup>1</sup> ) and right premolar 2 (RP <sup>2</sup> ) or	

deciduous molar 2 (RdM<sup>2</sup>). Note: The teeth were added to the cranium after warping to estimate age means, so are not perfectly aligned with the landmarks..... 98

Figure 30. Size and shape analysis of modes and magnitudes of deformation of the modern human infant, juvenile and adult models from the RP<sup>2</sup>/RdM<sup>2</sup> biting simulations. A) Size and shape PCA plot. Below are warped surfaces from the PC plots with colourmaps illustrating the expansions and contractions of local surface areas between the unloaded and loaded models: B) unscaled, C) scaled by size and D) scaled by peak bite force. The deformations were magnified x1000. Colour scale bars indicate ratios of areas between unloaded and loaded models. .... 103

Figure 31. Size and shape analysis of modes and magnitudes of deformation of the modern human infant, juvenile and adult models from the RI<sup>1</sup> biting simulations. A) Size and shape PCA plot. Below are warped surfaces from the PC plots with colourmaps illustrating the expansions and contractions of local surface areas between the unloaded and loaded models: B) unscaled, C) scaled by size and D) scaled by peak bite force. The deformations were magnified x500. Colour scale bars indicate ratios of areas between unloaded and loaded models..... 104

Figure 32. Strain contour plots of the solved modern human infant juvenile and adult FE models (from left to right) under RP<sup>2</sup>/RdM<sup>2</sup> biting simulation in front and lateral views. Tensile (top) and compressive strains (bottom) are unscaled (A, D), scaled for size (B, E) and scaled for peak bite force (C, F). ..... 106

Figure 33. Strain contour plots of the solved modern human infant juvenile and adult FE models (from left to right) under RI<sup>1</sup> biting simulation in front and lateral views. Tensile (top) and compressive strains (bottom) are unscaled (A, D), scaled for size (B, E), scaled for peak bite force (C, F). ..... 107

Figure 34. Strains experienced by the modern human (MH) infant (red), juvenile (brown) and adult (yellow) FE models at the 126 sampling points over the face during the RP<sup>2</sup>/RdM<sup>2</sup> biting simulations. The tensile (solid) and compressive (dashed) strains are unscaled. See landmark details in supplementary material Figure 1. .... 108

Figure 35. Unscaled and scaled by size strains experienced by the modern human (MH) infant (red), juvenile (brown) and adult (yellow) FE models at the 126 sampling points over the face during the RP<sup>2</sup>/RdM<sup>2</sup> biting simulation. The juvenile (black) and adult (grey) models were scaled according to the infant centroid size (cs). See landmark details in supplementary material Figure 1. .... 110

Figure 36. Unscaled and scaled by peak bite force strains experienced by the modern human (MH) infant (red), juvenile (brown) and adult (yellow) FE models at the 126 sampling points over the face during the RP<sup>2</sup>/RdM<sup>2</sup> biting simulation. The juvenile (black) and adult (grey) models

were scaled according to the infant peak bite force. See landmark details in supplementary material Figure 1. ....	111
Figure 37. Strains experienced by the modern human (MH) infant (red), juvenile (brown) and adult (yellow) FE models at the 126 sampling points over the face during the RI <sup>1</sup> biting simulation. The tensile (solid) and compressive (dashed) strains are unscaled. See landmark details in supplementary material Figure 1. ....	112
Figure 38. Unscaled and scaled by size strains experienced by the modern human (MH) infant (red), juvenile (brown) and adult (yellow) FE models at the 126 sampling points over the face during the RI <sup>1</sup> biting simulation. The juvenile (black) and adult (grey) models were scaled according to the infant centroid size (cs). See landmark details in supplementary material Figure 1. ....	113
Figure 39. Unscaled and scaled by peak bite force strains experienced by the modern human (MH) infant (red), juvenile (brown) and adult (yellow) FE models at the 126 sampling points over the face during the RI <sup>1</sup> biting simulation. The juvenile (black) and adult (grey) models were scaled according to the infant peak bite force. See landmark details in supplementary material Figure 1. ....	114
Figure 40. Neanderthal adult, juvenile and infant models with the corresponding human teeth. ....	128
Figure 41. Landmark and semi-landmark configuration used to calculate the deformation of the cranium in each model after loading at the right first incisor (RI <sup>1</sup> ) and right premolar 2 (RP <sup>2</sup> ) or deciduous molar 2 (RdM <sup>2</sup> ). Note: The teeth were added to the cranium after warping to estimate age means, so are not perfectly aligned with the landmarks. ....	132
Figure 42. 126 points used to extract the surface strain magnitudes from the solved Finite Element models. ....	132
Figure 43. Size and shape analysis of modes and magnitudes of deformation of the Neanderthal infant, juvenile and adult models from the RP <sup>2</sup> /RdM <sup>2</sup> biting simulations. A) Size and shape PC 1-3 plot. B-D, warped surfaces between unloaded and loaded models with colourmaps illustrating regions of surface contraction and expansion under RP <sup>2</sup> /RdM <sup>2</sup> biting: B) unscaled, C) scaled by size and D) scaled by peak bite force. The deformations were magnified x1000. Colour scale bars indicate ratios of areas between unloaded and loaded models. ....	135
Figure 44. Size and shape analysis of modes and magnitudes of deformation of the Neanderthal infant, juvenile and adult models from the RI <sup>1</sup> biting simulations. A) Size and shape PC1-3 plot. B-D, warped surfaces between unloaded and loaded models with colourmaps illustrating regions of surface contraction and expansion in each Neanderthal relative to the mean unloaded model under RI <sup>1</sup> biting simulations: B) unscaled, C) scaled by size and D) scaled by peak bite force. The	

deformations were magnified x500. Colour scale bars indicate ratios of areas between unloaded and loaded models.....	136
Figure 45. Strain contour plots of the solved Neanderthal infant juvenile and adult FE models (from left to right) under RP <sup>2</sup> /RdM <sup>2</sup> biting simulation in frontal and lateral views. Tensile (top) and compressive strains (bottom) are unscaled (A, D), scaled by size (B, E) and scaled by bite force (C, F).....	140
Figure 46. Strain contour plots of the solved Neanderthal infant juvenile and adult FE models (from left to right) under RI <sup>1</sup> biting simulation in frontal and lateral views. Tensile (top) and compressive strains (bottom) are unscaled (A, D), scaled by size (B, E) and scaled by bite force (C, F).....	141
Figure 47. Strains experienced by the Neanderthal (NEA) infant (blue), juvenile (green) and adult (sky blue) FE models at the 126 sampling points distributed over the maxilla and supraorbital ridge during the RP <sup>2</sup> /RdM <sup>2</sup> biting simulations. The tensile (solid) and compressive (dashed) strains are unscaled. See landmark details in supplementary material Figure 1. ....	142
Figure 48. Strains, unscaled and scaled by size, experienced by the Neanderthal (NEA) infant (blue), juvenile (green) and adult (sky blue) FE models at the 126 sampling points distributed over the face during the RP <sup>2</sup> /RdM <sup>2</sup> biting simulation. The juvenile (black) and adult (grey) models were scaled according to the infant centroid size (cs). See landmark details in supplementary material Figure 1. ....	143
Figure 49. Unscaled and scaled by bite force strains experienced by the Neanderthal (NEA) infant (blue), juvenile (green) and adult (sky blue) FE models at the 126 sampling points distributed over the face during the RP <sup>2</sup> /RdM <sup>2</sup> biting simulation. The juvenile (black) and adult (grey) models were scaled according to the infant bite force. See landmark details in supplementary material Figure 1. ....	145
Figure 50. Strains experienced by the Neanderthal (NEA) infant (blue), juvenile (green) and adult (sky blue) FE models at the 126 sampling points distributed over the maxilla and supraorbital ridge during the RI <sup>1</sup> biting simulations. The tensile (solid) and compressive (dashed) strains are unscaled. See landmark details in supplementary material Figure 1. ....	147
Figure 51. Unscaled and scaled by size strains experienced by the Neanderthal (NEA) infant (blue), juvenile (green) and adult (sky blue) FE models at the 126 sampling points distributed over the face during the RI <sup>1</sup> biting simulation. The juvenile (black) and adult (grey) models were scaled according to the infant centroid size (cs). See landmark details in supplementary material Figure 1. ....	148
Figure 52. Unscaled and scaled by bite force strains experienced by the Neanderthal (NEA) infant (blue), juvenile (green) and adult (sky blue) FE models at the 126 sampling points distributed	

over the face during the RI<sup>1</sup> biting simulation. The juvenile (black) and adult (grey) models were scaled according to the infant bite force. See landmark details in supplementary material Figure 1. .... 149

Figure 53. Graphs of mechanical advantages of each muscle in Neanderthals (orange) and modern human (blue) infant, juvenile and adult models at the RI<sup>1</sup> bite point. .... 159

Figure 54. Graphs of mechanical advantages of each muscle in Neanderthals (orange) and modern human (blue) infant, juvenile and adult models at the RP<sup>2</sup>/RdM<sup>2</sup> bite point. .... 160

Figure 55. Right first incisor (RI<sup>1</sup>) and right second premolar and second deciduous molar (RP<sup>2</sup>/RdM<sup>2</sup>) peak bite forces for the modern human (orange) and Neanderthal (blue) infant, juvenile and adult models. .... 162

Figure 56. Plots of force production efficiencies in the RI<sup>1</sup> and RP<sup>2</sup>/RdM<sup>2</sup> biting simulations comparing the mean modern (blue) human and Neanderthal (orange) infant, juvenile and adult models. F<sub>b</sub>, peak bite force; F<sub>m</sub>, net applied muscle force, F<sub>c</sub>, joint (at the glenoid fossa) reaction force. .... 164

Figure 57. Size and shape analysis of modes and magnitudes of deformation (changes in size and shape) of the modern human (black diamond) and Neanderthal (grey diamond) infant models for the RP<sup>2</sup>/RdM<sup>2</sup> biting simulation. Surface colourmaps A and B illustrate the deformations between the mean unloaded model (Black circle) and loaded modern human and Neanderthal infant models, respectively. The deformation of the modern human (insets A) is visualised at the same distance (degree of overall deformation) from the unloaded mean as the loaded Neanderthal (Inset B), indicated by the intersection of the dashed grey line with the modern human loading vector. The difference in deformation between these models (Neanderthal as reference, modern human as target) is visualised with the unloaded mean as reference, along the (grey arrow) vector parallel to and the same length as the (dashed grey line) vector between the deformed Neanderthal and modern human (see text). The deformations were magnified x1000. .... 165

Figure 58. Size and shape analysis of modes and magnitudes of deformation of the modern human (black diamond) and Neanderthal (grey diamond) juvenile models for the RP<sup>2</sup>/RdM<sup>2</sup> biting simulation. Surface colourmaps A and B illustrate the deformations between the mean unloaded model (Black circle) and loaded Neanderthal and modern human juvenile models, respectively. The deformation of the modern human (insets A) is visualised at the same distance (degree of overall deformation) from the unloaded mean as the loaded Neanderthal (Inset B), indicated by the intersection of the dashed grey line with the modern human loading vector. The difference in deformation between these models (Neanderthal as reference, modern human as target) is visualised with the unloaded mean as reference, along the (grey arrow)

vector parallel to and the same length as the (dashed grey line) vector between the deformed Neanderthal and modern human (see text). The deformations were magnified x1000. .... 168

Figure 59. Size and shape analysis of modes and magnitudes of deformation of the modern human (black diamond) and Neanderthal (grey diamond) adult models for the  $RP^2/RdM^2$  biting simulation. Surface colourmaps A and B illustrate the deformations between the mean unloaded model (Black circle) and loaded modern human and Neanderthal adult models, respectively. The deformation of the modern human (insets A) is visualised at the same distance (degree of overall deformation) from the unloaded mean as the loaded Neanderthal (Inset B), indicated by the intersection of the dashed grey line with the modern human loading vector. The difference in deformation between these models (Neanderthal as reference, modern human as target) is visualised with the unloaded mean as reference, along the (grey arrow) vector parallel to and the same length as the (dashed grey line) vector between the deformed Neanderthal and modern human (see text). The deformations were magnified x1000..... 169

Figure 60. Size and shape analysis of modes and magnitudes of deformation of the modern human (black diamond) and Neanderthal (grey diamond) infant models for the  $RI^1$  biting simulation. Surface colourmaps A and B illustrate the deformations between the mean unloaded model (Black circle) and loaded modern human and Neanderthal infant models, respectively. The deformation of the modern human (insets A) is visualised at the same distance (degree of overall deformation) from the unloaded mean as the loaded Neanderthal (Inset B), indicated by the intersection of the dashed grey line with the modern human loading vector. The difference in deformation between these models (Neanderthal as reference, modern human as target) is visualised with the unloaded mean as reference, along the (grey arrow) vector parallel to and the same length as the (dashed grey line) vector between the deformed Neanderthal and modern human (see text). The deformations were magnified x500..... 170

Figure 61. Size and shape analysis of modes and magnitudes of deformation of the modern human (black diamond) and Neanderthal (grey diamond) juvenile models for the  $RI^1$  biting simulation. Surface colourmaps A and B illustrate the deformations between the mean unloaded model (Black circle) and loaded modern human and Neanderthal juvenile models, respectively. The deformation of the modern human (insets A) is visualised at the same distance (degree of overall deformation) from the unloaded mean as the loaded Neanderthal (Inset B), indicated by the intersection of the dashed grey line with the modern human loading vector. The difference in deformation between these models (Neanderthal as reference, modern human as target) is visualised with the unloaded mean as reference, along the (grey arrow) vector parallel to and the same length as the (dashed grey line) vector between the deformed Neanderthal and modern human (see text). The deformations were magnified x500..... 171

Figure 62. Size and shape analysis of modes and magnitudes of deformation of the modern human (black diamond) and Neanderthal (grey diamond) adult models for the  $RI^1$  biting simulation. Surface colourmaps A and B illustrate the deformations between the mean unloaded model (Black circle) and loaded modern human and Neanderthal adult models, respectively. The deformation of the modern human (insets A) is visualised at the same distance (degree of overall deformation) from the unloaded mean as the loaded Neanderthal (Inset B), indicated by the intersection of the dashed grey line with the modern human loading vector. The difference in deformation between these models (Neanderthal as reference, modern human as target) is visualised with the unloaded mean as reference, along the (grey arrow) vector parallel to and the same length as the (dashed grey line) vector between the deformed Neanderthal and modern human (see text). The deformations were magnified x500..... 172

Figure 63. Tensile ( $\epsilon_1$ ) strain contour plots, in frontal and lateral views, of the solved modern human (A) and Neanderthal (B, C, D) infant juvenile and adult FE models (from left to right) under  $RP^2/RdM^2$  biting simulations. Tensile strains are unscaled (A, B), scaled in Neanderthals by size (C) and scaled by peak bite force (D) relative to modern humans per age stage. .... 174

Figure 64. Compressive ( $\epsilon_3$ ) strain contour plots, in frontal and lateral views, of the solved modern human (A) and Neanderthal (B, C, D) infant juvenile and adult FE models (from left to right) under  $RP^2/RdM^2$  biting simulations. Tensile strains are unscaled (A, B), scaled in Neanderthals by size (C) and scaled by peak bite force (D) relative to modern humans per age stage..... 175

Figure 65. Tensile ( $\epsilon_1$ ) strain contour plots, in frontal and lateral views, of the solved modern human (A) and Neanderthal (B, C, D) infant juvenile and adult FE models (from left to right) under  $RI^1$  biting simulations. Tensile strains are unscaled (A, B), scaled in Neanderthals by size (C) and scaled by peak bite force (D) relative to modern humans per age stage. .... 176

Figure 66. Compressive ( $\epsilon_3$ ) strain contour plots, in frontal and lateral views, of the solved modern human (A) and Neanderthal (B, C, D) infant juvenile and adult FE models (from left to right) under  $RI^1$  biting simulations. Tensile strains are unscaled (A, B), scaled in Neanderthals by size (C) and scaled by peak bite force (D) relative to modern humans per age stage. .... 177

Figure 67. Strains experienced by the Neanderthal (NEA) and modern human (MH) infant, juvenile and adult FE models at the 126 sampling points over the face during the  $RP^2/RdM^2$  biting simulation. The tensile (solid) and compressive (dashed) strains are unscaled. See landmark details in supplementary material Figure 1. .... 179

Figure 68. Strains experienced by the Neanderthal (NEA) and modern human (MH) infant, juvenile and adult FE models at the 126 sampling points over the face during the  $RP^2/RdM^2$  biting simulation. The tensile (solid) and compressive (dashed) strains are scaled in Neanderthals by

size relative to humans, per age stage. See landmark details in supplementary material Figure 1. .....	180
Figure 69. Strains experienced by the Neanderthal (NEA) and modern human (MH) infant, juvenile and adult FE models at the 126 sampling points over the face during the RP <sup>2</sup> /RdM <sup>2</sup> biting simulation. The tensile (solid) and compressive (dashed) strains are scaled in Neanderthals by peak bite force relative to modern humans per age stage. See landmark details in supplementary material Figure 1. ....	181
Figure 70. Strains experienced by the Neanderthal (NEA) and modern human (MH) infant, juvenile and adult FE models at the 126 sampling points over the face during the RI <sup>1</sup> biting simulation. The tensile (solid) and compressive (dashed) strains are unscaled. See landmark details in supplementary material Figure 1. ....	183
Figure 71. Strains experienced by the Neanderthal (NEA) and modern human (MH) infant, juvenile and adult FE models at the 126 sampling points over the face during the RI <sup>1</sup> biting simulation. The tensile (solid) and compressive (dashed) strains are scaled in Neanderthals by size relative to modern humans per age stage. See landmark details in supplementary material Figure 1. ....	184
Figure 72. Strains experienced by the Neanderthal (NEA) and modern human (MH) infant, juvenile and adult FE models at the 126 sampling points over the face during the RI <sup>1</sup> biting simulation. The tensile (solid) and compressive (dashed) strains are scaled in Neanderthals by peak bite force relative to modern humans per age stage. See landmark details in supplementary material Figure 1. ....	185
Figure 73. Combined maximum strain contour plots of both RI <sup>1</sup> and RP <sup>2</sup> /RdM <sup>2</sup> biting simulations. Tensile (right) and compressive strains (left) are unscaled (A, modern humans; B, Neanderthals), in Neanderthals these are scaled relative to humans by size per age stage (C) and scaled by peak bite force per age stage (D). ....	187
Figure 74. Schematic representation of a male chimpanzee (A), a female Sinantropus (B) and male modern human skull representing phylogenetic changes leading to the reduction of the neural-orbital disjunction in hominid crania according to the spatial model (Fiscella and Smith, 2006, adaptation from Weidenreich 1941). ....	197
Figure 75. Bending of the supraorbital region in the frontal plane in the Neanderthal adult model. The forces causing bending in the frontal plane are the bite force (FB) pushing upward and the masseter and temporalis muscles (FM) pulling downward. Adaptation of Hylander et al, 1991. ....	198
Figure 76. A) Original Neanderthal mean adult model, B) altered supraorbital Neanderthal model. ....	200

Figure 77. Tensile and compressive strains experienced by the Neanderthal with altered supraorbital (blue) and mean Neanderthal adult FE models at 60 sampling points over the supraorbital during the RI<sup>1</sup> biting simulation. The tensile (solid) and compressive (dashed) strains are unscaled. See landmark details in supplementary material Figure 3. .... 201

Figure 78. RP<sup>2</sup> biting simulation in the modern human juvenile model. A) Surface colourmap (from Figure 27, Chapter 3) illustrating the surface deformation between the mean unloaded model and the loaded modern human juvenile. B) Tensile ( $\epsilon_1$ ) strain contour plot. C) Compressive ( $\epsilon_3$ ) strain contour plot (both strain maps from Figure 32, Chapter 3). .... 207

Figure 79. RP<sup>2</sup> biting A), D) Tensile ( $\epsilon_1$ ) strains in the modern human and Neanderthal juveniles, respectively. B), E) Compressive ( $\epsilon_3$ ) strains in the modern human and Neanderthal juveniles, respectively. From Figure 54: C), F) Colourmaps of surface area change (deformation) in the modern human and Neanderthal, respectively and G) colour map of difference in deformation between the Neanderthal (reference) and modern human (target). .... 208

Figure 80. Registration-free colourmaps of local surface area expansion or contraction showing differences in mode and magnitude of deformation between the Neanderthal and modern human infant models during the RdM<sup>2</sup> biting simulations. A) original, B) reflected working to balancing sides, C) reflected working to balancing to working sides with black rectangle indicating that the expansion of area at that location is consistent irrespective of biting side, D) Mean bone growth remodeling maps representing the average distribution of remodeling activity for modern humans aged 3 to 6 years old (red= non or low resorption, blue = usually resorptive; Schuh et al, 2019). .... 210

Figure 81. Colourmaps of local surface area expansion or contraction showing differences in mode and magnitude of deformation between the Neanderthal and modern human juvenile models during the RP<sup>2</sup> biting simulations. A) original, B) reflected working to balancing side, C) reflected balancing to working side D) Generalized bone growth remodeling patterns for modern humans aged 7 to 17 years and E) for adults (Martinez-Maza et al, 2013), F) Bone growth surface remodeling map representing the average pattern for modern humans aged 7 to 12 years old (Schuh et al, 2019). .... 211

Figure 82. Colourmaps of local surface area expansion or contraction showing differences in mode and magnitude of deformation between the Neanderthal and modern human infant (A:top row) and juvenile (B: bottom row) models during the RP<sup>2</sup>/RdM<sup>2</sup> biting simulations. Rows A, B Left column, reflected working to balancing sides and rows A,B right column, reflected balancing to working side. Remodeling maps showing bone deposition (in purple) and resorption (in blue) for a 5-year-old Neanderthal (C), 5 year old modern human (D) and a (E) 12 year old modern human (Lacruz et al., 2015b). .... 212

## List of Tables

Table 1. Human sample with specimen ID, sex, age category, a description of the stage of dental development, age in years and centroid sizes for a total of 63 specimens. When the age was not known, it was estimated, up to a maximum of 23.5 years, when full dental maturity is reached indicating adulthood (AlQahtani, Hector and Liversidge, 2010).....	63
Table 2. Neanderthal sample with specimen ID, sex, age category, age in years, repository and centroid sizes. ....	65
Table 3. Template landmarks.....	70
Table 4. Human subsample: 34 infant and juvenile specimens with specimen ID, sex, age category, a description of the stage of dental development, age in years and centroid sizes. .	78
Table 5. Applied muscle forces (in Newtons, N). The muscle forces were estimated for all the masticatory muscles in a previous study (Toro-Ibacache et al., 2016a) from muscle cross-sectional areas using the CT scans of a fully preserved <i>H. sapiens</i> cadaveric head. ....	92
Table 6. Centroid sizes of the modern human infant, juvenile and adult models. Maximum bite reaction forces (Peak bite force) generated by the infant, juvenile and adult models and calculated for the right first incisor ( $RI^1$ ) and right second premolar and second deciduous molar bite points ( $RP^2/RdM^2$ ) in Newton (N). ....	96
Table 7. Mechanical advantages of the main masticatory muscles for the mean modern human infant, juvenile and adult. ....	99
Table 8. Ratios of the Mechanical advantages of the main masticatory muscles for the mean modern human infant, juvenile and adult. ....	100
Table 9. Force Production efficiencies in the $RI^1$ and $RP^2/RdM^2$ biting simulations, calculated from the finite element models of the modern human infant, juvenile and adult. $F_b$ , peak bite force; $F_m$ , net applied muscle force, $F_c$ , joint reaction force. ....	101
Table 10. Centroid sizes (cs) for the Neanderthal infant, juvenile and adult models. Bite reaction forces (Peak bite force) generated by the infant, juvenile and adult models and calculated for the right first incisor ( $RI^1$ ) and right second premolar or second deciduous molar ( $RP^2/RdM^2$ ) bite points. ....	131
Table 11. Mechanical advantages of the main masticatory muscles for the mean Neanderthal infant, juvenile and adult. ....	133
Table 12. Ratios of the Mechanical advantages of the main masticatory muscles for the mean modern human infant, juvenile and adult. ....	133

Table 13. Force Production efficiencies in the RI<sup>1</sup> and RP<sup>2</sup>/RdM<sup>2</sup> biting simulations, calculated from the Finite Element models of a mean Neanderthal infant, juvenile and adult. Fb, peak bite force; Fm, net applied muscle force, Fc, glenoid fossa reaction force. .... 134

Table 14. Centroid sizes (cs) and peak bite forces from previous FEAs, for the right first incisor (RI<sup>1</sup>) and right second premolar and second deciduous molar (RP<sup>2</sup>/RdM<sup>2</sup>) bite points in the modern human and Neanderthal infant, juvenile and adult models. .... 162

Table 15. Peak bite forces estimated from the mechanical advantages for the right first incisor (RI<sup>1</sup>) and right second premolar and second deciduous molar (RP<sup>2</sup>/RdM<sup>2</sup>) bite points in the modern human and Neanderthal infant, juvenile and adult models. Peak bite force estimation= (in-lever arms for each masticatory muscle part\*(muscle forces/number of masticatory muscle parts))/out-lever arms; Mechanical advantages in modern humans are presented in Table 8 and for Neanderthals in Table 13; muscle forces presented in Table 6. .... 163

Table 16. Force Production efficiencies at the RI<sup>1</sup> and RP<sup>2</sup>/RdM<sup>2</sup> biting simulations, calculated from the Finite Element models of the mean modern human Neanderthal infant, juvenile and adult models. Fb, peak bite force; Fm, net applied muscle force, Fc, joint (at the glenoid fossa) reaction force..... 163

## Acknowledgements

I would like to thank in particular Prof. Paul O’Higgins for offering me the opportunity to carry out this work and being my mentor and supervisor. Then, I thank the Palaeohub team and especially Dr. Laura Fitton, Dr. Phil Cox, Dr. Cobb for their help and precious advice. Thanks to Dr. Eloy Galvez-Lopez, Dr. António Profico, Dr. Federica Landi, Dr. Emily Hunter and Dr. Edwin Dickinson for their technical support, suggestions and feedback as well as Dr. Louison Boule for her help in the virtual reconstruction of the Neanderthal fossils and virtual segmentation of modern human skulls. Finally, I thank Master student Ben Mapplebeck for his work on the supraorbital of the adult Neanderthal mean model.

I thank D. Shapiro, Joan T. Richtsmeier, G. Holoborow, S. Black and L. Scheuer for information on, and access to, the Bosma and Dundee-Scheuer human skeletal collections. For permission to access fossil materials, I would like to thank the following institutes and their collaborators: Musée National d’Histoire Naturelle, Musée de l’Homme (Paris, France), Musée national de la Préhistoire and his director J.J. Cleyet Merle, Museum of Natural History (London, UK), Patrick Semal and the Institut Royal des Sciences Naturelles de Belgique (Bruxelles, Belgique), Jean Jacques Hublin and Philipp Gunz from the Max Planck Institute for Evolutionary Anthropology (Leipzig, Germany), Luca Bondioli and the Pigorini Museum (Università di Sapienza, Rome, Italy), Giggio Manzi and the Department of Environmental Biology, University La Sapienza (Rome, Italy); Laboratory of Paleoanthropology and Bioarchaeology (Sapienza University of Rome, Rome, Italy); Liubov Golovanova and Vladimir Doronichev from the Laboratory of Prehistory (Saint-Petersburg, Russia), and the Dan David Center of Human Evolution and Biohistory Research, Shmunis family anthropological institute, Sackler Faculty of Medicine, Tel Aviv University (Tel Aviv, Israel) for granting access to Amud 1. Finally, we thank the Nespos archive for access to modern and fossil materials (CT-scans of the Roc de Marsal specimen).

## Author's declaration

I confirm that this work is original and that if any passage(s) or diagram(s) have been copied from academic papers, books, the internet or any other sources these are clearly identified by the use of quotation marks and the references are fully cited. I certify that, other than where indicated, this is my own work and does not breach the regulations of HYMS, the University of Hull or the University of York regarding plagiarism or academic conduct in examinations. I have read the HYMS Code of Practice on Academic Misconduct, and state that this piece of work is my own and does not contain any unacknowledged work from any other sources.

## 1.0 Introduction

Studies of hominin cranial development have consistently found species-typical morphologies to already be present at early juvenile stages, suggesting that some aspects of species differences in cranial form are the product of variation in prenatal morphogenesis (Ponce De León et al., 2008; Bastir, O'Higgins and Rosas, 2007; Bastir and Rosas, 2004; Cobb and O'Higgins, 2004; Gonzalez, Perez and Bernal, 2010; Mitteroecker et al., 2004). However, how differences in postnatal- growth and development generate differences in skull morphology has also been addressed among hominins. From an evolutionary perspective, post-natal craniofacial ontogeny is modulated by environmental factors (e.g. biomechanical function, diet; Bastir et al., 2007; Bastir and Rosas, 2004; Cobb and O'Higgins, 2004; Mitteroecker, Gunz, and Bookstein, 2005; Christoph P.E. Zollikofer, 2012; Christoph Peter Eduard Zollikofer and Ponce De León, 2004). Biomechanical loads induced by feeding have been hypothesized as one of the major influences shaping the skull elements during post-natal ontogeny (Aiello and Dean, 1990). This thesis addresses this hypothesis by investigating associations between differences in how biomechanical loads due to biting are borne by the growing cranium and how they relate to differences in post-natal growth and development between modern humans and Neanderthals. After birth, the skull and especially the face and masticatory apparatus radically change in size and shape. With the emergence of permanent teeth, the consequent changes in the dental row likely impact loading (Smith, 1991; Smith et al., 2007b; Krovitz, Thompson and Nelson, 2009). Diet, and so the demands on the masticatory apparatus also change, particularly from neonatal to juvenile stages, with the shift to solid food. Little is known about the relationships and interactions between these dietary changes and the changes in form of the cranium. A diet typical of adults is presumed to be facilitated by functional increases in maximum bite force during postnatal ontogeny, however, how the modern human cranium adapts to changes in loading through changes in the form, modulated in part by changes in bony remodeling is unclear. Further if and how this differs in Neanderthals remains unknown.

There is strong evidence that skeletal structures adapt to loads to minimise strains (Hart et al., 2017; Toro-Ibacache and O'Higgins, 2016; Sugiyama et al., 2012; Frost, 1987; Lanyon, 1987; Rubin and Lanyon, 1985; O'Connor, Lanyon and MacFie, 1982; Sugiyama, Price and Lanyon, 2010; Gross et al., 1997), therefore a promising approach to address these topics is through Finite Element Analysis (FEA), to predict the strains

arising from masticatory system loading. This thesis adopts this approach to compare predicted strain maps between different ontogenetic stages in modern humans and Neanderthals as well as between these species in an attempt to assess the extent to which differences relate to known differences in facial remodeling maps. Post-natal cranial growth models are estimated in modern humans and Neanderthals using geometric morphometric methods (Bookstein, 1982, 1991, 1996b; O'Higgins and Dryden, 1992; Marcus and Corti, 1996; Cobb and O'Higgins, 2004; Mitteroecker et al., 2004; Gunz, Mitteroecker and Bookstein, 2005; Mitteroecker et al., 2013) and this is followed by FEA on mean infants, juveniles and adults which are in turn compared with published maps of facial remodeling.

The dissertation is presented in five sections. This introduction provides a literature review of previous research relevant to the study. Chapter two explains the methods used to create the post-natal skull growth models in modern humans and Neanderthals. It also describes how the fossil specimens were reconstructed to create the growth model in Neanderthals. Chapter three explains how the Finite Element (FE) models were designed in modern humans and how the biting simulations were conducted. Chapter four describes the FE models and biting simulations for the same ontogenetic stages in Neanderthals and, as in the previous chapter, presents and compares the predicted deformations and strains between ontogenetic stages in this species. Finally, chapter five addresses the main topic of this thesis by comparing the results between species and assessing the extent to which they may relate to differences in facial remodeling.

In this chapter previous relevant studies of skull growth in modern humans and Neanderthals are reviewed. Key aspects of craniofacial growth and bone remodeling in modern humans and Neanderthals are reviewed, as are studies that have addressed potential links between cranial form, function and the ability of the cranium to generate and resist bite forces. To resist strains/stresses from anterior and posterior biting, the skull deforms and these deformations lead to straining of its bony elements, potentially triggering bone adaptation, which in turn impacts subsequent bone deformation and strains. Therefore, previous studies of bone mechanics and mechanical adaptation are reviewed in the last section.

## 1.1 Skull growth

Aspects of human craniofacial form are determined prenatally. Thus, population-specific morphologies of craniofacial traits in *Homo sapiens* are evident at birth and are accentuated and modified to variable degrees during postnatal ontogeny through divergent shape trajectories (Gonzalez, Perez and Bernal, 2010; Vidarsdóttir and Cobb, 2004; Vidarsdóttir, O’Higgins and Stringer, 2002; Liversidge, 1994; Smith et al., 2010a). Further, craniofacial shape differences between *Homo sapiens* and related species have been identified early in ontogeny with divergence of postnatal ontogenetic trajectories also contributing to species differentiation in non-hominid and hominid primates (Ackermann and Krovitz, 2002; Cobb and O’Higgins, 2004; Mitteroecker et al., 2004; Curtis et al., 2011). However, other studies have disagreed, finding similar patterns of post-natal shape change, i.e. parallel trajectories, that do not alter the basic species-specific facial shape already established during earlier ontogeny (Ackermann and Krovitz, 2002; Neubauer, Gunz and Hublin, 2009; Gunz et al., 2012, 2010; Mitteroecker et al., 2001; Smith et al., 2007b). The different conclusions arising from these studies may be attributable in part to methodological differences and limited availability of samples, but also to differences in opinion about the relative importance of the degree of divergence between these two species. However, the question of whether the mid and upper faces of Neanderthals and modern humans share a common postnatal pattern of ontogeny remains open. Similarities and differences in the ontogeny of the facial complex have not been assessed in detail. Despite

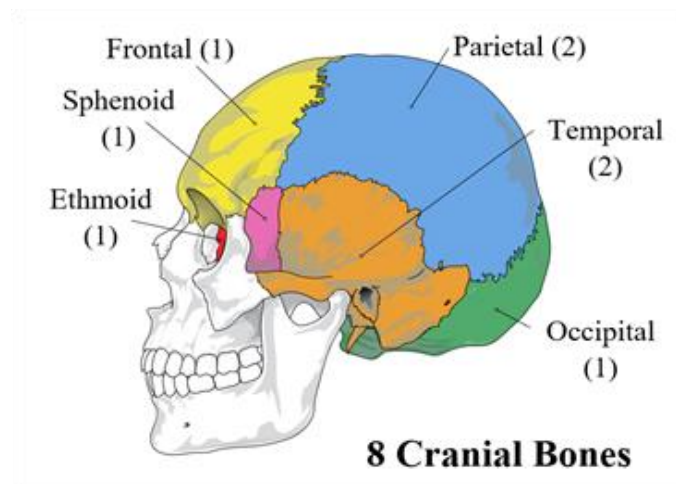
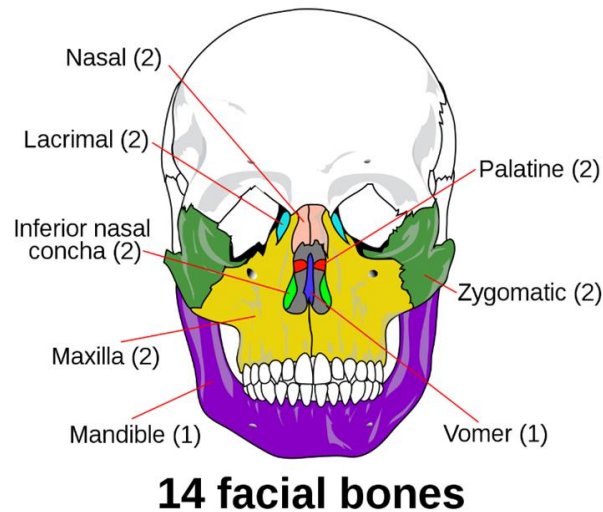


Figure 1. Neurocranium. (2022, December 4). In Wikipedia. <https://en.wikipedia.org/wiki/Neurocranium>

the morphological differences between adult individuals of the two species being well described (Rak, 1986; Franciscus and Churchill, 2002; Stringer, 2002; Weaver, Roseman and Stringer, 2007), we have incomplete knowledge of how they arise.

### 1.1.1.1 Modern human craniofacial anatomy, development and function

The cranium is commonly described as being composed of at least two semi-independent modules: the neurocranium (Figure 1) which surrounds and protects the brain; and the viscerocranium or facial skeleton (Figure 2) which supports the face and its organs (Cheverud, 1982; Cheverud and Routman, 1995).



**14 facial bones**  
*Figure 2.* Facial skeleton. (2022, December 22). In Wikipedia. [https://en.wikipedia.org/wiki/Facial\\_skeleton](https://en.wikipedia.org/wiki/Facial_skeleton).

Ontogenetically, neurocranium and viscerocranium differ by their embryological origins which are described below. Moreover, they also present different functional and developmental constraints (Sadler, 2003). The neurocranium can be sub-divided into the cranial vault and basicranium. The cranial vault is composed of the following bones: paired parietal bones; the squamous part of the paired temporal bones and the interparietal part of the occipital bone (Figure 2). These bones form through intramembranous ossification with bone expansion occurring at the sutures (see below). The basicranium is said to form a stable platform upon which the rest of the skull grows and attaches (Biegert, 1957, 1963; Lieberman, Pearson and Mowbray, 2000). It also provides and protects the skull foramina (openings allowing the passage of blood vessels, cranial nerves, etc) through which the brain connects to the face and the rest of the body. In contrast with the vault, the basicranium grows through the process of endochondral ossification.

The facial skeleton or viscerocranium (Figure 2) is mostly composed of dermal bone (arising from intramembranous ossification) and derives in large part from ectodermal cells of the neural crest (see below) (Couly, Creuzet, Bennaceur, Vincent, and Le Douarin, 2002; Dixon, Hoyte, and Ronning, 2017). Cartilaginous elements are found in

the nasal lateral walls (the conchae), septum and between the orbits (trochlea). It is made up of 14 individual bones (Figure 2) many of which fuse during development: paired conchae, paired lacrimal bones, paired maxillary bones, paired palatine bones, paired zygomatic bones, paired nasal bones, the mandible, vomer, paired frontal bones and the sphenoid. From embryological and anatomical perspectives, the facial skeleton can be divided into the upper, middle and lower face. The upper face is the region comprising the supraorbital and the eye sockets. The lower face hosts the mandible and teeth, and finally, the middle face (or midface) denotes the portion of the face comprising the nasal bones and walls, lacrimal maxillary, zygomatic and bones as well as the upper dentition (Brooker, 2012).

Prenatal growth and development can be divided into three phases: the preimplantation phase (the first 7 days), the embryonic phase (first 8 weeks) and the fetal phase (from 8 weeks to birth) (Stool, 2001; Moore, Persaud and Torchia, 2018; Sadler, 2018). Postnatally facial growth and development continue, modifying the form of the facial skeleton to a considerable degree (White and Folkens, 2011; Enlow, 1996; Moss and Young, 1960; O'Higgins et al., 2011; McCollum, 2008; Lieberman, 2011). This section focuses on the development of the cranial vault, sutures, maxillae and masticatory system during prenatal and postnatal growth development because these are most relevant to the studies presented in this thesis.

#### *1.1.1.1 Ontogeny of the cranial vault and sutures*

During the embryonic phase, most of the skull primordia pass through a parenchymatous phase (or condensation) where epithelial cells become mesenchymal cells through a process of epithelial-mesenchymal transformation (EMT; Figure 3). In the third week, mesenchymal cells migrate and proliferate along the neural tube to form a longitudinal column of paraxial mesoderm (Dixon, Hoyte and Rönning, 2017; Sadler, 2018; Moore, Persaud and Torchia, 2018). This paraxial mesoderm then gives rise to the somites which later differentiate to become sclerotomic somites and first appear in the future occipital region of the embryo (Ross, 2005). The head mesoderm then forms seven cranial somitomers that do not condense into somites. The neurocranium develops from the paraxial mesoderm, the first five somites, and the somitomers rostral to the first somites (Dixon, Hoyte and Rönning, 2017; Rodeck and Whittle, 2019). At the end of the embryonic phase, the head mesenchyme is supplemented with cranial neural crest cells. Neural crest cells are specialized, multipotential migratory cells which are also generated by

EMT. The neural crest also contributes to the development of the neurocranium by forming the frontal, sphenoid and squamous bones (Sperber, Sperber and Guttman, 2010; Sadler, 2018). It is also important in the formation of the sutures in which some neural crest-derived cells remain between the two parietal bones and contribute to the signalling system that governs the growth of the cranial vault (Rodeck and Whittle, 2019). The development of the cranial bones begins with the condensation of mesenchymal cells that surround the developing brain. During the 5<sup>th</sup> week, the condensed mesenchyme gives

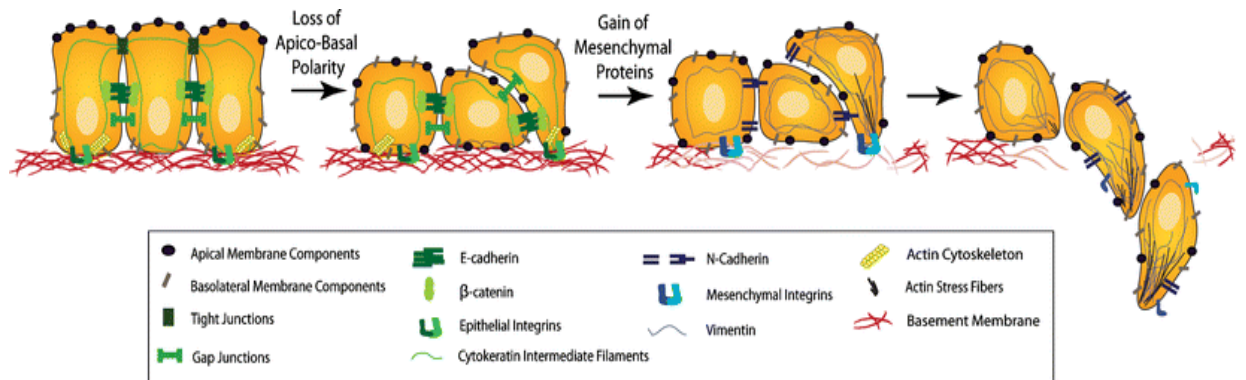


Figure 3. The epithelial-mesenchymal transformation process (Kalluri and Weinberg, 2009).

rise to the membranous neurocranium which is arranged as a capsular membrane around the developing brain (Jin, Sim and Kim, 2016; Sadler, 2018; Sperber, Sperber and Guttman, 2010). This is the first sign of the cranial vault. Towards the end of the embryonic period, the brain expands dramatically and the capsule responds to this demand (Sperber, Sperber and Guttman, 2010; Adeeb et al., 2012). Growth of the brain and the capsular membrane occurs simultaneously in all three dimensions. During this last part of the embryonic phase, the mesenchymal condensation extends and forms the floor for the brain, the primordium of the cranial base (basicranium) (Sperber et al, 2010; Tubbs et al, 2012).

During the fetal phase, the ossification process of the future cranial vault begins. Its bones are formed through intramembranous (IM) ossification, which directly converts the primary meninx into bone tissue (Dixon, Hoyte and Rønning, 2017; Hay, 2005). IM ossification starts with the formation of ossification centres that eventually form individual bones. The development of cranial vault bones follows the order shown in Figure 4: two frontal and parietal bones formed from a primary ossification at the 8<sup>th</sup> week form and remain separated at birth by the frontal (metopic), coronal and sagittal sutures (Sadler, 2018; Glorieux, 2003). A single and four ossification centres appears at the 8th week and

the 3rd month, respectively, to form the squamous portion and the tympanic ring of the temporal bone by an intramembranous ossification from a single and four centres appearing in (Jin et al, 2016; Sperber, Sperber and Guttman, 2010; Tubbs, Bosmia and Cohen-Gadol, 2012). Endochondral ossification begins of the floor of the neurocranium begins, from a cartilaginous precursor, in the 12<sup>th</sup> week, and forms part of the occipital bone (Sadler, 2018; Glorieux, 2003).

Sutures are formed during embryonic and fetal development (Opperman, 2000; Sadler, 2018; Glorieux, 2003; Cohen, 1993). They are filled with flexible fibrous tissues that act as intramembranous growth sites. They remain unossified and allow new bone formation at the edges of the bone formation fronts. Sutures allow rapid expansion of the cranial vault during prenatal growth and development and accommodate strains due to the growth of the brain, by allowing expansion of the vault through deposition of bone and recruitment of mesenchymal tissue into their advancing edges (Opperman, 2000; Sadler, 2018; Glorieux, 2003). The sutures also play a role at birth allowing the bones to move and adapt to the birth canal. At birth, the infant presents fontanelles (spaces between the skull bones where the sutures intersect; Figure 5), spanned by a membrane and enclosing underlying soft tissue and the brain (Opperman, 2000; Sadler, 2018; Glorieux, 2003). The fontanelles include the anterior fontanelle, at the junction of the 2 frontal and

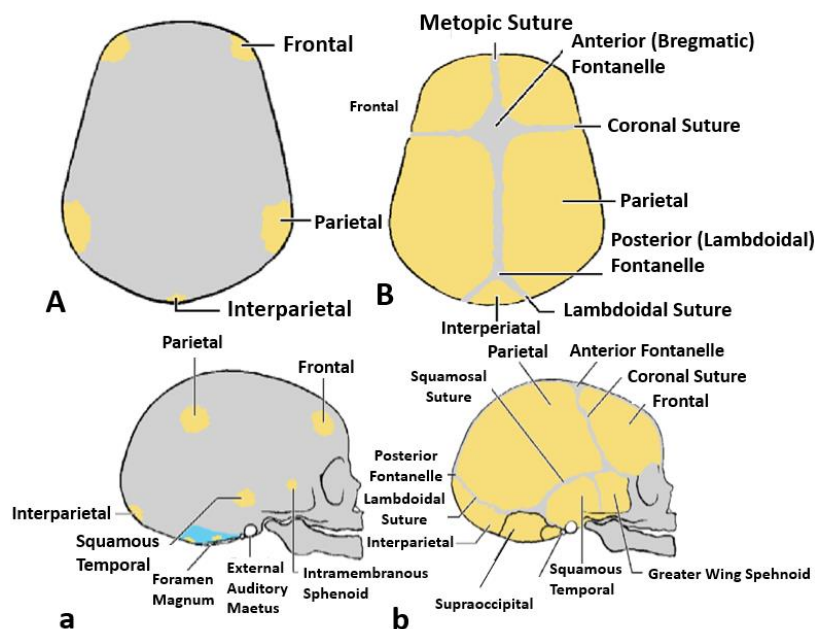


*Figure 4.* Schematic superior (A, B) and lateral views (a, b) of the fetal skull. A and a show the stage of development where the cranial vault is largely membranous and the intramembranous ossification centres (yellow) have begun to form. B and b, show the skull at birth, when the intramembranous ossification centres expand and the sutures and fontanelles develop (modified from Stern, 2003).

parietal bones, that closes at 2 years post nately (Figure 4). The posterior fontanelle, at the junction of the 2 parietal and occipital bones, closes during the first few months after-birth (White and Folkens, 2011; Sadler, 2018). The cranial sutures persist while the fontanelles are closing and play a major role during postnatal growth. Indeed, they respond to and accommodate brain expansion (Tubbs, Bosmia and Cohen-Gadol, 2012; Opperman, 2000). As the cranial vault bones are drawn apart by their displacement due to the expanding brain, the sutures lay down bony tissue by intramembranous ossification

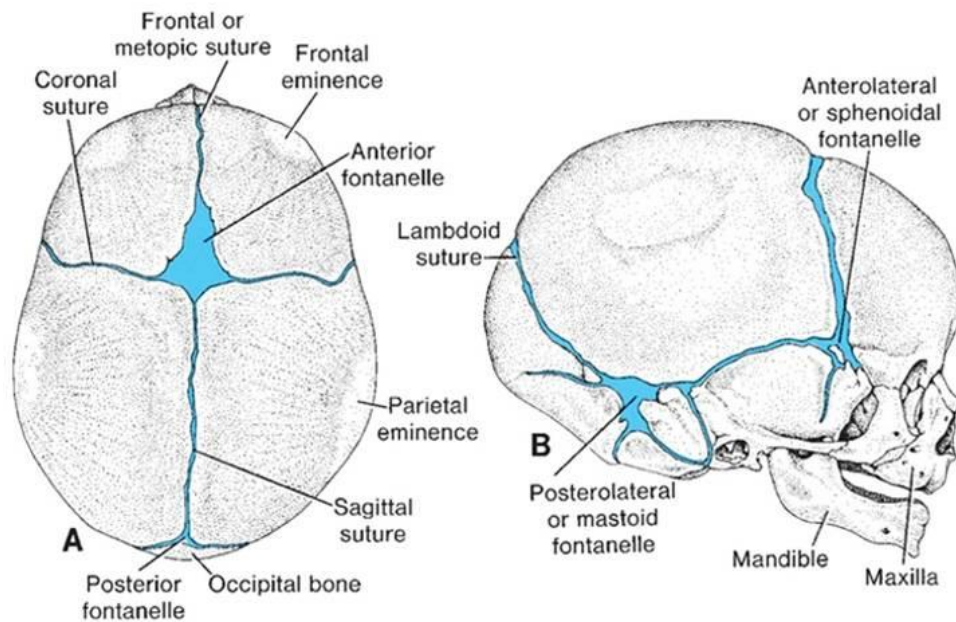


Figure 5. Newborn skull with fontanelles (Sadler, 2010).

at a rate that accommodates the displacements thereby enlarging the circumference of each bone (Tubbs, Bosmia and Cohen-Gadol, 2012; Opperman, 2000). This membranous bone is then converted into more structured bone tissue. The rate of growth at the skull sutures keeps pace with brain growth, being fast during the first years of life and gradually decreases through puberty. An increase in width primarily of the bones that meet at the interparietal, lambdoidal and parietotemporal sutures is observed; then, an increase in length occurs due to growth of the cranial base that stimulates growth, primarily at the coronal suture; an increase in height due to brain expansion is accommodated mainly by growth at the temporoparietal sutures (Opperman, 2000; Adeeb et al., 2012).

#### 1.1.1.2 Ontogeny of the maxilla

The maxillae (Figure 2) are the largest bones of the midface and provide structural support to the viscerocranium or facial skeleton. By their union, they form the whole of the upper jaw. Each bone contains a maxillary sinus and forms the roof of the mouth, the

floor and outer walls of the nasal cavity and the floors of the orbits (Dalgorf and Higgins, 2008; Sperber, Sperber and Guttman, 2010; Wilderman et al., 2018). Each maxilla presents a body with a cuboid form and connects with the rest of the facial structures through the alveolar, frontal, zygomatic and palatine processes. On the anterior aspect, the maxillae form the inferior and lateral borders of the pyriform aperture. They also articulate with the nasal bones medially at the anterior border of the frontal process (Okay et al., 2001; Saffar, Lasfargues and Cherruau, 1997) and the zygomatic bone laterally. Finally, inferiorly and posteriorly, they articulate with the upper teeth through the alveolar process and the palatine respectively.

The development of the maxillary complex starts at the fourth week of gestation right after the development of the somites (see above). During that period, the first evidence arises of a brain and of the early head, with the beginning of the formation of the face and “neck” by pharyngeal arches. During the post-somitic period (after the formation of the somites), the maxillary body’s external features start to be formed and the head as a whole undergoes significant development. At 5 months *in utero*, facial morphology becomes identifiable (Radlanski and Renz, 2006).

The most important part of the formation of the facial complex takes place between four- and eight weeks post-conception. Indeed, during that period arise a prominent forebrain and the stomodeum: the primordial mouth and the topographical centre of the face (Baxter and Shroff, 2011). Around it, the five facial prominences are formed. Three of these prominences (or facial primordia) are derived from the migration of neural crest cells: paired maxillary and frontonasal prominences. The last two, the mandibular prominences, are derived from the first pair of the five pharyngeal arches (Trevizan and Consolaro, 2017; Sperber, Sperber and Guttman, 2010). The paired frontonasal, maxillary and mandibular prominences fuse and the first two merge to create the upper jaw and palate (which separates the nasal pits from the future mouth) and the mandible (Trevizan and Consolaro, 2017; Sperber, Sperber and Guttman, 2010).

Maxillary ossification begins around the 6<sup>th</sup> week by intramembranous ossification through two ossification centres. One of these centres gives rise to the maxilla and the other to the premaxilla. In the third month, these fuse around the alveolar process and the premaxilla becomes part of the maxilla. However, the suture between the two portions persists in the palate until midlife but is not seen on the facial surface. In newborns, the

maxilla is longer horizontally than vertically, compared to an adult. The maxillary sinus develops and grows in concert with the development of the maxilla and related bones (O'Higgins, Bastir and Kupczik, 2006; Rae and Koppe, 2004, 2008; Butaric and Maddux, 2016).

During post-natal development, the midface is mostly influenced by the growth of other structures. First, the development of the orbits occurs throughout the first 18 months (Krimmel et al., 2015; Landi et al., 2021). The initial rapid growth of the orbits contributes to the vertical expansion of the face and the separation of the neuro- and viscerocranium. It has been hypothesised that the growth and demands of the respiratory apparatus also shape the maxilla (Rosas and Bastir, 2002; Trinkaus, 2003; Weaver, 2009; Bastir, Godoy and Rosas, 2011; Bastir and Rosas, 2013), as does the development of the teeth (Sperber, Sperber and Guttman, 2010; Alfaqeeh, Gaete, and Tucker, 2013). The maxilla has a central position in the craniofacial complex and the biological functions it supports (respiration, mastication, vision etc), therefore, the growth of the maxilla is likely to be influenced by the growth of the surrounding bones and soft tissues (Bastir et al, 2008; Moss and Young, 1960; Smith et al., 2014; Goergen, Holton and Grünheid, 2017; Landi et al., 2021; Schuh et al, 2019).

Growth remodeling (bone formation and bone resorption), during the post-natal period, is a significant process by which bones change in size and in shape. It is an integral process in craniofacial growth and sculpts the form of the face during post-natal development, accommodating bone displacements (Lacruz et al., 2019; Bromage, 1989; Enlow, 1979). At the cellular level, the cells responsible for bone formation are osteoblasts and osteoclasts. The coordinated activities of osteoblasts and osteoclasts form and resorb bone surfaces, respectively. In the human maxilla, several studies have been conducted over the last 60 years, to describe the pattern of bone remodeling in adult specimens. Enlow and Bang in 1965, found bone formation on the posterior and superior parts of the bone, whereas the anterior-inferior region was predominantly resorptive from the age of 4-7 years (Enlow and Bang, 1965). These findings have been confirmed in recent decades using microscopic techniques (Martinez-Maza et al., 2011, 2016) and are said to be characteristic of *H. sapiens*, contributing to the development of an orthognathic face, in contrast to other hominins. It is said that. in our species, resorption over the anterior maxilla to the zygomatic bone compensates for forward displacements of the maxilla. However, in younger specimens (4-5 years), resorptive fields vary over time in their extent over the

anterior and subnasal maxilla. Bone resorption of variable extent is observed over the anterior maxilla and zygomatic regions from an early age to later stages (between 4 to 12 years); the resorptive region over the frontal process seems to decrease over time, while the resorptive region over the maxilla enlarges with it. The proportion of the total maxillary surface area that undergoes bone resorption stabilizes after 3 years (Schuh et al., 2019). In subadults, bone formation is observed over the external aspects of the frontal process; canine fossa and zygomatic process, and, bone resorption is seen over variable small regions of the maxilla and at the alveolar process (Brachetta-Aporta, Gonzalez and Bernal, 2019). Therefore, the spatial distribution and sizes of bone remodeling fields change throughout post-natal ontogeny and appear to be associated with changes in maxillary form which comprise a greater increase in height than anteroposterior length, projection of the anterior-inferior maxilla above the incisors and canines, and an increase in nasal aperture dimensions (Brachetta-Aporta, Gonzalez and Bernal, 2019; Barbeito-Andrés et al., 2016; Gonzalez, Perez and Bernal, 2010).

Most recent studies agree that the maxilla displays large degrees of variation in remodeling among individuals in the distribution of bone formation and resorption, particularly along with the anterior teeth and in the zygomatic and alveolar process (Freidline et al., 2017; Martinez-Maza, Rosas and Nieto-Díaz, 2013; McCollum, 2008; Brachetta-Aporta, Gonzalez and Bernal, 2019) and so, it is difficult to directly link these fields with the development of the orthognathic maxilla of modern humans. Their regulation is unknown, but they appear to be species-specific and so may be heritable and genetically regulated. Thus, Ealba et al., (2015) in a study of jaw (beak) length in duck and quail found spatially patterned differences between these species in resorptive field locations, mediated by neural crest mesenchyme cells and their derivatives (which exert precise control over the expression levels of key transcription factors as well as the timing of skeletal cell differentiation) and concluded that these are important in mediating differences in jaw length.

However, the high degree of variability of growth remodeling fields could indicate that the mechanism whereby these fields arise and change is not under tight genetic control. Alternatively, it is plausible that, like other bones in the body, the characteristic remodeling features of the anterior face in modern humans could be a response to alterations in loadings and therefore local strains, relating the interaction of preexisting cranial form

(from the stage of development before they appear) to the functional demands of mastication. Indeed, bone tissues are very responsive to mechanical stimuli, especially during childhood and puberty (Brachetta-Aporta, Gonzalez and Bernal, 2019; Schuh et al., 2019; Gosman et al., 2013). Such a mechanical hypothesis might explain the dramatic variations observed in the sizes and locations of bone facial remodeling observed in prior studies. However, more work needs to be done to directly link bone formation and resorption activities and strains due to mastication during post-natal ontogeny.

#### *1.1.1.3 Ontogeny of the masticatory system*

The masticatory system is a sophisticated three-dimensional structure comprising skeletal and soft tissue elements that carry out the complex action of mastication (chewing, crushing, etc), rendering food suitable for swallowing and digestion. In turn, it responds developmentally to feeding behaviour and so adult form is affected by loading history (Sella-Tunis et al., 2018; Toro-Ibacache, Zapata Muñoz and O'Higgins, 2015; Toro-Ibacache, Zapata Muñoz and O'Higgins, 2016). Its configuration is constrained by the need to generate adequate biting forces while dissipating forces due to masticatory loadings within the cranium. The masticatory apparatus is composed of 3 major bones, the maxilla, the mandible and the temporal bone which is connected to the maxilla and forms the temporomandibular joint (TMJ) with the mandible (White and Folkens, 2011). Two other minor bones are associated with this complex: the sphenoid which is fixed between the maxilla and the temporal bone and, the hyoid, a floating bone beneath the mandible that links the mandible to other structures, serving as an attachment point for muscles and ligaments. The muscles of the masticatory system are organized into five groups according to their functions and they exist as pairs (Sadrameli and Mupparapu, 2018; Soboļeva, Lauriņa and Slaidiņa, 2005). The first group includes the primary muscles of mastication, composed of four muscles (on each side) responsible for TMJ function and mandibular movements (van der Bilt et al., 2006; Alomar et al., 2007; Standing, 2021). This includes the masseter and temporalis muscles which are responsible for closing the jaw, the medial pterygoid, also involved in closing the jaw and lateral movements of the mandible; and, finally, the lateral pterygoids which open the mouth and contribute to lateral deviation and anterior movement of the jaw (Alomar et al., 2007; Mazza et al., 2009). The second and third groups of muscles are accessory muscles of mastication directly or indirectly associated with mandibular function. The second group functions assist jaw opening and coordinate mandibular movement during biting (Netter and Scott,

2019; Alomar et al., 2007; Mazza et al., 2009). The muscles of this group are, in the main, attached to the hyoid and mandible (digastric, geniohyoid, mylohyoid, omohyoid, sternohyoid, sternothyroid, stylohyoid, and thyrohyoid muscles). The muscles of the third group (sternocleidomastoid, scalenus anterior, scalenus medius, and scalenus posterior muscles) are associated with stabilisation of the skull and neck during mastication and allow the mandible to move relative to the skull (Netter and Scott, 2019; Alomar et al., 2007; Mazza et al., 2009). They are cervical muscles and are attached to the sternum, temporal bone, clavicle, cervical vertebrae 1-7 and ribs 1-2 (Netter and Scott, 2019; Standring, 2021). The last two groups of muscles are extrinsic and intrinsic muscles of the tongue that help to elevate, depress, withdraw or protrude the tongue as well as modify its form and move it from cheek to cheek (Netter and Scott, 2019; Standring, 2021). Finally, the temporomandibular joints (TMJ) comprising the mandibular condyles, and the glenoid fossae permit movements of the mandible relative to the cranium during mastication. They also provide lateral stability and absorb loads due to the movements during mastication and distribute a portion of the forces arising from loading into the cranium (Alomar et al., 2007; Standring, 2021).

The masticatory system undergoes dramatic changes throughout post-natal ontogeny, the teeth are shed and replaced and the dental row changes in form to adapt to the development and eruption of teeth. In primates, including humans, the emergence of the adult dentition is marked by the appearance of the first molar (Smith, 1986; Kelley and Schwartz, 2010). The timing of this event varies among primates (Machanda et al., 2015) but is a consistent signal preceding weaning. A recent study of masticatory system ontogeny in papionins has shown that biomechanical constraints during post-natal development determine the location of molar eruption (Singleton, 2015). Indeed, the distalmost molar maintains a consistent position relative to the temporomandibular joint (TMJ) while the anterior dentition migrates anteriorly. This maintains the relative functional capacity of the masticatory system throughout ontogeny. This has also been demonstrated and supported by studies from Kelley and Schwartz in 2010 and Schwartz in 2012 in *Pan* and modern humans where newly erupted deciduous and permanent molars maintain a species-specific position anterior to the TMJ. These findings led to the hypothesis that there is a “biomechanically optimal location for a molar eruption” anterior to the muscle resultant force vector and that successive molars erupt only when this position is vacated as a result of anteriorward facial growth (Schwartz, 2012).

Muscle architecture also undergoes significant changes. Indeed, throughout ontogeny muscles change in size and shape with alterations to the lengths, orientations and cross-sectional areas of their muscle fibres (Lieberman, Mcbratney and Krovitz, 2002; Pearson, 1997; Stewart and German, 1999). Numerous studies have been conducted on this subject in primates in order to better understand the relationships between masticatory muscle architecture and allometry (Anapol, Shahnoor and Ross, 2008; Perry, Hartstone-Rose and Logan, 2011; Hartstone-Rose et al., 2018; Dickinson, Fitton and Kupczik, 2018), biomechanical properties (Antón, 1999, 2000; Gokhin et al., 2009; Lieberman, McBratney and Krovitz, 2002; Lieberman et al., 2004) and, dietary processing and acquisition (Eng et al., 2009; Taylor and Vinyard, 2009; Perry et al., 2014; Hartstone-Rose et al., 2018). Analyses of the masseter muscle in *Macaca mulatta* have shown that the number of sarcomeres (basic contractile unit of muscle fibre) increases throughout ontogeny, leading to elongation of the muscle (Carlson, 1983; Carlson and Schneiderman, 1983). Another study on dry masticatory muscle weight determined that the mass of these muscles scales isometrically with body mass during development in primates (Cachel, 1984). More recently, Dickinson et al (2018) conducted an ontogenetic study of the adductor musculature of *Macaca fascicularis* and observed that muscle mass and fascicle lengths scale with positive allometry relative to both jaw lengths and condyle-molar length across the life span.

Therefore, all the ontogenetic changes observed in primates and modern humans suggest that aspects of chewing performance, such as bite force and gape potential, change throughout growth and development, responding to changes in diet and feeding behaviours. In *Macaca fascicularis*, the larger individuals seem to demonstrate adaptations during development towards maximizing gape potential and bite force potential at both anterior and posterior bite points (Dickinson, Fitton and Kupczik, 2018). In the same way, modern humans exhibit increasing maximum bite force throughout ontogeny and changes in bite force along the tooth row, with the highest forces occurring at the posterior dentition (Edmonds and Glowacka, 2020). Moreover, the masseter provides the greatest leverage compared to other jaw adductors at each bite point. Jaw adductor muscle leverage changes in concert with the portions of the tooth row where bite force is also the highest, and this pattern remains consistent throughout ontogeny (Edmonds and Glowacka, 2020). Indeed, at each emergence stage, the highest leverage values for all adductor muscles occur at the most posterior bite point present, which follows the prediction under a classic lever model, in that moving the load closer to the fulcrum (i.e. temporomandibular joint) reduces the amount of muscular effort needed to power a given bite. Edmonds and

Glowacka., (2020) show that relative increases in adductor muscle leverage mirror the increase in maximum bite forces, increasing during ontogeny, at the posterior dentition.

### 1.1.2 Neanderthal craniofacial anatomy, development and function

#### 1.1.2.1 Craniofacial post-natal development

Throughout the last decades, Neanderthals have been extensively studied and described as presenting unique craniofacial features that are distinct from other hominin fossils and extant humans. Neanderthals are very large-brained with large and prognathic faces: they lack a chin; have relatively wide and squared piriform apertures; a broad, projecting nasal bridge; depressed internal nasal floors; swept-back zygomatic arches; inflated infraorbital areas; the mental foramen is located below the first molar; and they present a retromolar space (a space behind the third molar commonly considered a Neanderthal autapomorphy, but see (Franciscus, and Trinkaus, 1995; A Rosas, and Bastir, 2004; Trinkaus, 2003).

It is unclear how the observed differences in craniofacial shape between adult *Homo sapiens* and Neanderthal arise during ontogeny. Changes in facial morphology arise during ontogeny through a complex series of interactions between genetic and environmental factors. Over the last decades, morphometric studies have arrived at different conclusions about the extent to which these differences are established pre-natally (Ackerman and Krovitz, 2002; De Leon and Zollikofer, 2001) and the contributions of such differences to those among adults relative to the differences that arise post-natally (Bastir, O'Higgins, and Rosas, 2007; Krovitz, and Thompson, 2003). By calculating ontogenetic allometries, differences between species can be identified; these consist of differences in how shape changes with size, and the extent and rates of size-related shape changes (Cobb and O'Higgins, 2004). Several studies on facial ontogenetic allometric trajectories have compared modern humans with Neanderthals. Ponce De León and Zollikofer (2001), using geometric morphometric analyses, claimed that differences between modern human and Neanderthal faces are already established in early pre-natal ontogeny and that post-natal ontogenetic shape changes in Neanderthals did not differ from those of modern humans in their mode, but simply in their extent, that, during post-natal ontogeny, both species change in shape in the same ways but to different degrees. Further studies on several juvenile fossil Neanderthal mandibles and dentitions have indicated that the development of this species was fast relative to modern humans (Dean, Stringer and Bromage, 1986;

Krovitz, Thompson and Nelson, 2009; Stringer, 1990; Smith et al., 2007a, 2010a; Ramirez Rozzi and Bermudez De Castro, 2004). Indeed, the formation of the crown for the third molar seems to be completed 2 to 4 years earlier than in *Homo sapiens* (Guatelli-Steinberg, Reid, Bishop, and Spencer Larsen, 2005 but see Tanya M. Smith et al., 2010). Similarly, Neanderthal brain growth has been shown to be fast relative to *H. sapiens* (Ponce De León et al., 2008) with modern humans showing a globularisation phase during the first year of life in which the endocast transforms from an elongated to a more globular shape. This phase doesn't exist in Neanderthals and most of the differences observed in endocasts, between the two species seem to already be present at birth (Gunz et al., 2010; Ponce de León and Zollikofer, 2001a). These studies concur in concluding (or not excluding that) parallel ontogenetic shape trajectories exist between Neanderthals and *Homo sapiens*. However, other authors have demonstrated, using different methodological approaches, divergent ontogenetic shape trajectories. Using Euclidean distance matrix analysis, Krovitz (2003) noted that the morphological differences observed between the two species became further accentuated during post-natal ontogeny, implying divergent post-natal trajectories. Bastir et al., (2007) used Geometric Morphometric analyses on several Neanderthal and modern human faces and mandibles to study their ontogeny. They have shown that, despite a higher rate of facial growth and shape transformation at an early developmental stage in Neanderthals, facial ontogeny is consistently different between these species and that this contributes to the observed differences in adult form (Bastir et al, 2007). Therefore, there still exists a debate among researchers about whether or not Neanderthals and modern humans have divergent or common ontogenetic shape trajectories.

More recently, an unpublished thesis (Landi, 2020) on the modes and magnitudes of craniofacial growth and development in Neanderthals and modern humans has shown that differences are accentuated postnatally and are located mostly in the zygomaticomaxillary region and the supraorbital region. This study also investigated the magnitudes of integration among facial regions of the two species, using PLS analyses, showing that while some patterns of covariation are similar between the two species (nose, orbits and palate), notable differences exist with respect to the integration of changes in the nasal region with those in the brain and maxilla. It was suggested by in Landi, 2020 that these differences may relate to known differences in the expansion of the brain, thermoregula-

tion and air conditioning (Wolpoff, 1968a; Franciscus and Trinkaus, 1988), pre-processing of food (Carlson and Van Gerven, 1977) and reduction in dental size (Brace and Mahler, 1971; Brace, Rosenberg and Hunt, 1987).

Over the last few decades, numerous studies have investigated differences in the distributions of facial bone surface growth remodeling features in living (Brachetta-Aporta, Gonzalez, and Bernal, 2018; Brachetta Aporta, Martinez-Maza, Gonzalez, and Bernal, 2014; Kranioti et al., 2009; Kurihara and Enlow, 1980; Martinez-Maza et al., 2016; Martinez-Maza, Rosas, and Nieto-Díaz, 2013; Mowbray, 2005; O'Higgins and Jones, 1998) and extinct primates, especially hominins (Bromage and Dean, 1985; Bromage, 1989; McCollum, 2008, 1999; Martinez-Maza et al., 2011; Lacruz et al., 2013, 2015b). Understanding the dynamics of facial bone surface growth remodeling contributes to the understanding of how aspects of craniofacial morphology arise. The location, distribution and timing of such activity appears to be consistent within species and to differ between related ones, such as extinct and extant hominins (Bromage, 1989; Lieberman and McCarthy, 1999; Ponce de León and Zollikofer, 2001b). It has been shown that extant species with prognathic faces (such as great apes, the gracile australopiths and *Homo ergaster*) manifest bone deposition over the external aspect of the maxilla while orthognathic ones such as *Paranthropus* (Bromage, 1989; Bromage and Boyde, 1996, McCollum, 2008), *Homo antecessor* (Bromage, 1989) and *Homo sapiens* (Schuh et al., 2019) develop variable resorptive regions over the subnasal and anterior aspects of the maxilla. Studies conducted on Neanderthal specimens have shown that adult and sub-adult specimens manifest bone deposition over the same regions (Lacruz et al., 2013, 2015b). The differences in the nature and distribution of surface remodeling features in the midface between modern humans and Neanderthals indicate that these species do not share postnatal facial ontogenetic growth remodeling processes and so are unlikely to share common ontogenetic allometries (Lacruz et al., 2013, 2015b). While differences in facial growth remodeling have been shown to be species-specific and to associated with differences in facial morphology, the causes of such differences are unknown. On the one hand, the species specificity implies heritability and so genetic regulation (direct or indirect, see below), yet bone is known to adapt by surface and internal remodeling to applied loads (Wolff, 1986; Sugiyama et al, 2012; Currey, 2003; Mosley and Lanyon, 1998; Ruff et al, 2006; Enlow and Bang, 1965). It may be that heritable aspects of facial form lead to differences in mechanical loading and so indirectly affect remodeling. However, little

is known about the influence of different masticatory system loading histories in related hominins in influencing the development of interspecific differences in facial growth remodeling. This topic is addressed in this thesis.

#### 1.1.2.2 *The supraorbital ridge*

The supraorbital torus arises from differential growth of the inner and outer tables of the frontal bone as the face projects forwards (Lieberman, Ross and Ravosa, 2000; Ravosa, 1991b). Indeed, the inner table of the frontal bone follows the growth trajectory of the cranial vault, growing along with the brain. The outer table, which includes the interior supraorbital region, grows along with the upper face, independently of the inner table (Lieberman, Ross and Ravosa, 2000; Sirianni and Swindler, 1985). The structural significance of the supraorbital ridge in hominins and among modern human populations and its morphological variations have always been a controversial topic for biological anthropologists. The browridge is considered by many researchers to be an important anatomical area for the study of human evolution because of its location, the variability of its expression among the genus *Homo*, including modern human populations and because its reduction is seen as a marker of gracilization in human evolution (Fiscella and Smith, 2006; Shea and Russell, 1986).

Several hypotheses have been explored in trying to explain this particular structure. One of these hypotheses is the craniofacial size model (Ravosa, 1991c, 1991a); this model posits that variation in the supraorbital ridge is directly related to overall craniofacial size (Vinyard and Smith, 2001, 1997). Indeed, ontogenetic and allometric studies have indicated that this structure is related to craniofacial size and the neural-orbital disjunction (Fiscella, 2004; Fiscella and Smith, 2006; Ravosa, 1988; Ravosa, Noble, Hylander, Johnson, and Kowalski, 2000a). Moreover, an association between the metric traits of modern human browridges and craniofacial size was demonstrated by Vinyard and Smith (2001) however other studies have demonstrated that human populations with larger skulls are not always more robust (Hawks et al., 2000; Baab et al., 2010).

Moss and Young (1960) hypothesized that the development of the marked separation between the orbital and cerebral components of the frontal bone during either ontogeny or phylogeny is associated with the development of a browridge (Moss and Young, 1960; Shea, 1985a; Shea and Russell, 1986; Lieberman, Ross and Ravosa, 2000;

Vinyard and Smith, 1997, 2001; Lieberman, Mcbratney and Krovitz, 2002). This is the “spatial hypothesis”, it argues that the supraorbital ridge ‘fills’ the disjunction between the frontals and anterior-superior orbital rim. Therefore, variation in the morphology of the browridge could be predicted by variations in neural-orbital disjunction (Russell et al., 1985). A study examining changes in anterior-posterior dimensions of the frontal sinus at the glabellar region in modern humans during ontogeny validated the hypothesis and showed that in modern humans, because of the anterior expansion of the cerebral component, the supraorbital ridge is reduced (Fiscella and Smith, 2006; Moss and Young, 1960). However, studies on the Kabwe 1 cranium, a specimen that presents a huge browridge but a similar facial size to Neanderthals, have shown that the browridge is much larger than the minimum size required to accommodate the disjunction between the orbits and frontal bone. Thus, spatial requirements do not fully explain the browridge in this specimen and alternative, social signalling functions have been suggested as an additional explanation (Godinho, Spikins and O’Higgins, 2018; see below).

Alternatively, the size of the supraorbital torus occurring in many extant and extinct primates has been hypothesized to be determined by the need to resist loading of the masticatory system and is an adaptation to resist facial torsion (Bookstein et al., 1999; Banri Endo and Adachi, 1988; Russell et al., 1985) arising from post-canine biting as well as food-pre-processing (Carlson and Van Gerven, 1977; Russell et al., 1985; Zink, Lieberman and Lucas, 2014; Zink and Lieberman, 2016). Indeed, early studies of the supraorbital region suggested that this area develops as a buttress against the forces generated by biting and mastication (Ravosa, 1988, 1991). Endo (1966, 1970) suggested that during mastication, the lateral supraorbital region is pulled downward by the action of the masseter and temporalis while the “glabellar” region is pushed upward by the bite force. Some studies on fossil hominins (Oyen, Rice, and Cannon, 1979), extant humans (Endo, 1970; Hilloowala and Trent, 1988) and other non-primates (Hylander, Johnson and Picq, 1991; Kupczik et al., 2007; Ravosa et al., 2000) have supported this hypothesis. However, this topic is a regular source of debate because studies on non-human primates have failed to record elevated strains in the browridge (Hylander, Picq and Johnson, 1991; Kupczik et al., 2007; Ravosa et al., 2000) during biting on any tooth and mastication.

Counter to these findings it has been argued that the low supraorbital strains found in primates reflect ontogenetic adaptations (Kupczik et al., 2007); that low strains occur in adults because brow morphology is already optimized for resisting masticatory loading.

In relation to this, Kupzick et al 2007 conducted an FEA in *Macaca fascicularis* subadults and showed that predicted strains are low in the supraorbital torus throughout ontogeny. This was attributed either to there being no mechanical role for the torus in relation to masticatory system loading or to a process of continual adaptation during ontogeny. Finally, the possibility remains (and is untested) that the browridge reflects a lower site-specific bone deposition threshold, and that it grows despite experiencing low strains.

More recently, a Finite Element Analysis (FEA) of the supraorbital and facial structures of an archaic hominin (Kabwe 1) has shown, by removal in a virtual model, that the supraorbital ridge in this specimen has little impact on mechanical performance during biting (Godinho, Spikins, and O'Higgins, 2018). Thus, this thesis aims to further investigate the possible role of the supraorbital in resisting masticatory loading in Neanderthals, by assessing strains in this region during growth and development.

Several other possible explanations have been presented for the presence of the large browridge in hominins such as Neanderthals. These hypotheses are related to adaptations to environmental conditions (protection from a blow to the head, Tappen, 1973, 1978), to hunting (protection of the eyes in aquatic environments, provision of sunshade, Verhaegen, 2013) and prevention of hair from obscuring vision (Krantz, 1973). However, these hypotheses lack supporting evidence and are largely untestable.

In the last decade, another hypothesis has arisen from archaeological studies of recent human societies. The absence of a large browridge in recent *Homo sapiens* and modern humans has been posited to reflect changes in mechanisms of facial expression important for social interaction (Godinho, Spikins, et al., 2018). The loss of large browridges, due to a reduced face and larger frontal brain, enhanced the capacity of the frontalis muscle to move eyebrows over the frontal (Parr, Waller and Vick, 2007). The facial reduction observed in *Homo sapiens* is accompanied by a reduction of the brows and a more vertical forehead that may have impacted the action of the occipitofrontalis muscle. These particular movements are essential in subtle non-verbal communication, and signalling behaviours; but also, to allow us to express more complex emotions (surprise, indignation...) a key aspect of our complex social interactions (Godinho et al., 2018). This model posits that reduced browridges led to enhanced social signalling, rather than that social signalling drove this reduction in the brows. As such, the enhanced action

of occipitofrontalis is more akin to a spandrel (Gould and Lewontin, 1979) than an adaptation, and the reduced browridges (for whatever reason) precede and lead to this hypothesized enhancement of frontalis function in social signalling.

## 1.2 Cranial form and function in modern human and Neanderthal

The skull houses and protects the brain and the sensory organs as well as providing skeletal support for the teeth and muscles that enable biting and chewing (Lieberman, Mcbratney and Krovitz, 2002). Thus, there exists an association between cranial form and masticatory function. This has two components, the generation of masticatory system forces (Antón, 1990; Godinho et al., 2018; O'Connor, Franciscus and Holton, 2005) and resistance to them (Demes, 1987; Rak, 1983, 1986).

### 1.2.1 Cranial form, function, modularity and integration

The hominin skull, like that of every mammal, is a complex and a highly integrated structure. By definition, integration is referring to the connectedness or interdependence among skull components during evolution, development and throughout mature life (Lieberman, 2011; Lacruz et al., 2019). Concerning the evolution of the human skull, it has been proposed that integration may contribute to the form of cranial components such that evolutionary changes in specific cranial structures impact adjacent structures. Integration, or co-variation, among morphological units, has been studied extensively using morphometric and mathematical models to understand and predict how changes in individual units may occur in response to changes in other units (Cheverud et al., 1999). However, the extent to which patterns of cranial integration and changes in these patterns reflect selection, and genetic drift (Lieberman, 2011), or are evolutionary by-products, 'spandrels' (Gould and Lewontin, 1979) is unknown.

The changes in craniofacial morphology observed in hominin evolution have been suggested to be related to multiple factors, including expansion of the brain, and changes in cranial base angle (Enlow, and Hans, 1996; Lieberman, 2011; Lieberman et al., 2008; Lieberman, McBratney, and Krovitz, 2002b), thermoregulation and air conditioning (Baab et al., 2010; Wolpoff, 1968b; Carey and Steegmann, 1981; Franciscus and Trinkaus, 1988), preprocessing of food (Carlson, 1976; Carlson and Van Gerven, 1977; Zink and Lieberman, 2016; Zink, Lieberman and Lucas, 2014), stabilization of the head during running (Lieberman, 2011; Lieberman et al., 2008), and reduction in the size of the dentition (Brace and Mahler, 1971; Brace, Rosenberg and Hunt, 1987; Brace, 1967). In *Homo sapiens*, the shortening of the human face has been explained by three major

changes: increased flexion of the cranial base, a relatively longer anterior cranial base (Bastir and Rosas, 2016; Bastir, Rosas and Sheets, 2006; Lieberman, Mcbratney and Krovitz, 2002; Lieberman, Pearson and Mowbray, 2000) and a shorter and retracted upper face. Moreover, it has been proposed that the greater muscle mechanical advantages and bite force production efficiency in *Homo sapiens* could be a spandrel (Gould and Lewontin, 1979), primarily driven by midfacial reduction, which itself may be driven by other factors such as food pre-processing, changes in thermoregulatory and ventilatory requirements, and gracilisation due changes in social interactions ( Eng, Lieberman, Zink, and Peters, 2013; Fitton, et al., 2018; Ledogar et al., 2016; Lieberman, 2011). In Neanderthals, air conditioning has been hypothesized to be one of the main drivers in craniofacial form allowing them to survive extremely cold environments (Coon, 1962; Franciscus and Trinkaus, 1988). Additionally, masticatory (Demes, 1987; Antón, 1990; Spencer and Demes, 1993; Antón, 1996; Clement, Hillson and Aiello, 2012; O'Connor, Franciscus and Holton, 2005) and non-masticatory activities and associated loadings have been implicated as influencing Neanderthal cranial morphology (the anterior dental loading hypothesis; Demes and Creel, 1988; Rak, 1986).

#### 1.2.2 Production of bite force

Bite force is used to generate pressure between the occlusal surfaces of the teeth. Bite force is one indicator of the functional state and performance of the masticatory system. It results from the action of jaw elevator muscles interacting with craniomandibular biomechanical form (e.g lever arm lengths and orientations; Bakke, 2006). Bite force measurements can be made directly using a suitable transducer between the teeth while biting. This approach to force assessment is a convenient way of assessing submaximal force, however, it can be used only in extant species. In living humans, this method has been widely applied with variable results (Paphangkorakit, and Osborn, 1997; Sinn, De Assis, and Throckmorton, 1996). In extinct species, this approach is not possible and retrodictions of bite force have been made based on estimates of physiological variables known to be related to force production (Ferrario et al., 2004). Thus, researchers have used bony proxies to estimate muscle cross-sectional areas (Antón, 1990; Demes and Creel, 1988; O'Connor, Franciscus and Holton, 2005; Eng et al., 2013), used as proxies for physiological cross-sectional areas which are related to the maximal force a muscle can produce. During biting, the force generated by masticatory muscles is transferred to the teeth. This is converted into bite force by the masticatory lever system which is dependent on skull

morphology (i.e the relative positions of fulcrum, bite point, muscle origins and insertions). Measurement of mechanical advantage (ratio of in-lever to out-lever lengths) has been used by researchers to assess the efficiency of the masticatory lever system (Demes and Creel, 1988; Antón, 1990; O'Connor, Franciscus and Holton, 2005; Eng et al., 2013; Godinho et al., 2018). However, this technique presents some limitations. Indeed, differences are found between estimates of cross-sectional area from bony proxies and actual physiological muscle cross-sectional areas. Despite these limitations, this methodology remains the only available approach (Eng et al., 2013; Toro-Ibacache, Zapata Muñoz and O'higgins, 2015), to estimate muscle forces in extinct species and especially hominins.

In recent decades, estimated bite force has been compared between *Homo sapiens* and Neanderthals as well as with other hominins by several workers. The results of these studies show some variability. *Homo sapiens* is thought to possess masticatory muscles that are generally smaller or comparable in cross-sectional area to Pleistocene and recent robust specimens (Eng et al., 2013; O'Connor et al., 2005). However, our more retracted and shorter face results in more anteriorly positioned masticatory muscles, increasing their mechanical advantages. Using these approaches, bite forces for modern humans have been estimated to be comparable to, or higher than, those calculated for Neanderthals and some recent robust specimens from the middle Pleistocene (Eng et al., 2013; O'Connor et al., 2005) as well as chimpanzees (Ledogar et al., 2016). A recent study on the *Homo heidelbergensis* specimen from Kabwe (also known as Broken Hill I) comparing biting performance with a modern human specimen, has shown that the modern human masticatory system is more efficient at converting muscle forces into bite forces (Godinho, Fitton, et al., 2018). Many studies have investigated masticatory biomechanics in Neanderthals (Rak, 1986; Demes, 1987; Trinkaus, 1987a; Demes and Creel, 1988; Antón, 1990, 1996; Spencer and Demes, 1993; O'Connor, Franciscus and Holton, 2005; Clement, Hillson and Aiello, 2012). From these, Neanderthals appear to be adapted to generate high and/or repetitive occlusal loads, especially at the anterior dentition, consistent with the hypothesis that they used their incisors as a “third hand”, as a tool to manufacture objects (Rak, 1986; Demes and Creel, 1988; Volpato et al., 2012). However, further studies of force-production capability and efficiency have contradicted these findings, reaching the conclusion that Neanderthals are quite similar to modern humans in maximal anterior bite force production (Antón, 1990; Antón and Howell, 1994; O'Connor, Franciscus and Holton, 2005).

In terms of ontogeny, how bite force production and efficiency develop has received relatively little attention in modern humans and Neanderthals (Thompson, Biknevicius and German, 2003; Erickson, Lappin and Vliet, 2003; Herrel and O'Reilly, 2006; Edmonds and Glowacka, 2020). The masticatory system undergoes significant changes during ontogeny with the appearance of the permanent dentition, the development of the masticatory muscles and changes in the shape of the dental row (Smith, 1994; Holly Smith, Crummett and Brandt, 1994; Kelley and Schwartz, 2010). The timing of eruption of the first permanent molar (M1), is considered to be important because it is thought to indicate a change in diet when juvenile primates are weaned and begin to consume solid and more adult food. These changes have contributed to the presumption that bite forces increase during ontogeny (Bakke, 2006; Bakke, Holm, Jensen, Michler, and Möller, 1990; Ingervall and Minder, 1997; Kamegai et al., 2005; Usui, Uematsu, Morimoto, Kurihara, and Kanegae, 2007). That this is the case is confirmed by a recent study in modern humans using constrained lever models to predict bite force at different bite points and live bite force data in an ontogenetic context. This study has shown that maximal bite forces increase throughout ontogeny and change along the tooth row, with the highest forces occurring at the posterior dentition (Edmonds and Glowacka, 2020). However, the relationship between differences in craniofacial morphology between modern humans and extinct hominins and differences in bite force performance between species during ontogeny remains unclear. This is a topic that will be addressed in this thesis.

### 1.2.3 Resisting bite force

During mastication, forces are transmitted to food items and are resisted by the skull. Thus, the craniofacial complex needs to develop to withstand masticatory forces.

Several studies based on simple engineering analyses have attempted to assess cranial deformations and resulting strains to determine the extent to which craniofacial form is adapted to resist deformations. Early research on primate craniofacial biomechanics commonly conceptualized the skull as a simple geometric structure or system of structures (e.g., beams and cylinders) in efforts to predict stresses and strains in the face (Endo, 1966; Endo, 1965; Görke, 1904). Several vertical and horizontal structures within the cranium were described as pillars made of thick cortical bone (or buttresses) allowing dissipation of occlusal forces that are channelled throughout the face (Benninghoff, 1925; Bluntschli, 1926; Couly and Hureau, 1976; Cryer, 1916; Banri Endo, 1966; Görke, 1904;

Richter, 1920; Roberts and Tattersall, 1974; Sicher and Tandler, 1928). These studies led to the “axial compression” hypothesis; that the craniofacial skeleton is axially compressed during mastication. Masticatory stresses were suggested to be transmitted from the molar region to the frontal bone via three important structures, the interorbital “pillar” medially, the postorbital bar laterally, and the pterygoid processes of the sphenoid posteriorly (Görke, 1904; Benninghoff, 1925; Roberts and Tattersall, 1974). However, this approach is unlikely to fully predict deformation regimes, especially in other primates, which present a more curved and irregular skull. Similarly, the relative orientation of muscle forces was not taken into account in these early studies which focused only on the vertical components and so lacked the ability to fully model deformations in other structures of the skull.

In the 1960-70s, Endo conducted several *in vivo* strain gauge experiments in human and gorilla skulls, with similar results in these two species (Endo, 1965; Endo, 1966). In these analyses, the physical skull was loaded with simulated bilateral temporalis and masseter muscle forces, and developed reaction forces at the temporomandibular joints (TMJ) with bite forces applied singly to each tooth, excluding the third upper molar (Endo, 1966a). He found that during incisor biting, the midline nasal element experienced axial compression in the sagittal plane while the lateral orbital elements experienced bending moments and tension. He also found a similar pattern during posterior biting with tensions and compressions in a small region of the contralateral inter-orbital skeleton and in the ipsilateral orbital skeleton, respectively. These results were explained as the consequences of the downward pull of temporalis and masseter muscles and upwardly directed bite forces. Furthermore, high strains were also found in the browridge during incisor biting which led Endo (1965, 1966) to propose that the browridge acts as a stabilizing structure for the craniofacial skeleton during biting (Endo, 1965). From this work, other debates emerged regarding how forces acting on the craniofacial skeleton deform it during biting and how best to describe these deformations. These include 1) bending in the frontal plane (Endo, 1966a, 1973; Russell et al., 1985; Picq and Hylander, 1989; Hylander, Johnson and Picq, 1991), 2) bending in the sagittal plane (Cartmill, 1974; Hylander, 1977; Demes, 1982; Preuschoft et al., 1986), 3) dorsoventral shear of the face relative to the braincase (Hylander, 1977; Demes, 1982; Preuschoft et al., 1986). Finally, Greaves (1985) proposed a cylindrical model of the craniofacial skeleton to characterize how facial strains develop and are resisted. He observed asymmetric bilateral activation

of the muscles during masticatory function. Indeed, during unilateral mastication the working muscles exert a greater force than the balancing ones resulting in twisting the skull towards the working side. At the same time, a reaction force is generated at the biting point that twists the skull towards the opposite side. In this loading regime, the face is twisted on the braincase about the anteroposterior axis of the skull (Greaves, 1985, 1995). Therefore, tensile and compressive strain orientations are predicted to be 45° to the twisting axis, resulting in the post-orbital bar being compressed on the working side and tensioned on the balancing side (Greaves, 1985; Hylander, Picq and Johnson, 1991; Greaves, 1995; Ross, 2001, 2008). The anterior dental loading hypothesis is considered further in the conclusion chapter (Chapter 6.1) of this thesis, in the context of the findings of finite element analyses that examined the effects of alterations of the frontal incisor biting load resistance.

The spatial distribution of strains and stresses predicted by this simplified engineering model are similar to those found in vitro experiments (Banri Endo, 1966, 1973; Rak, 1983 but see Picq and Hylander, 1989). However, such simplified models do not allow detailed prediction of the deformations, and therefore strains, that crania undergo during biting. Thus several *in vivo* studies have been conducted on non-human species and especially primates such as strepsirrhines *Otolemur* (Ravosa et al., 2000; Ross, 2001) and *Aotus* (Ross and Hylander, 1996; Ross, 2001), *Macaca fascicularis* and *Papio Anubis* (Hylander, Picq and Johnson, 1991).

The facial skeleton is a complex structure with heterogeneous material properties and variations in form within and between species. In consequence, these studies present some variation in findings according to the individuals and species under analysis (Ross, 2001). Thus, some researchers have shown that cranial deformations and resulting Von Mises strain patterns do not conform to the predictions of a single loading regime but rather to what might be expected of more complex loadings acting on complex morphologies (Ross, 2001, 2008; Lieberman, 2011).

Studies of ontogenetic changes in loadings and resulting strains that take account of changes in form are lacking. Indeed, the crania of young individuals prior to their sexual maturity may well be particularly affected by changes in the mechanical environment (e.g masticatory loadings) because they need to adapt to experienced loads, whereas in adults the expectation is that the craniofacial skeleton is optimized to resist their masticatory

loading regime. A strong possibility exists that the cranium undergoes continuous adaptation during postnatal growth and development (Bouvier and Hylander, 1996; Pearson and Lieberman, 2004; Ruff, Holt and Trinkaus, 2006; Kupczik et al., 2009). Thus, the examination of ontogenetic changes in cranial load resistance in modern humans and Neanderthals is a further aim of this thesis.

### 1.3 Bone biomechanical function and adaptation

#### 1.3.1 Bone structure and morphology

Bone is a composite material made of 40% inorganic component (hydroxyapatite), 25% water and 35% of organic components such as proteins and collagen (Ethier and Simmons, 2007). Like all connective tissues, the osseous tissue contains few cells and a large amount of extracellular matrix. There are four types of cells that take part in growing, maintaining and adapting bone: osteoblasts, osteogenic cells, osteocytes and osteoclasts. The bone cells responsible for forming new bone are the osteoblasts. These specialised cells are found in the endosteum and cellular layer of the periosteum, the two-growing portions of the bone (Lindsay, 1996; Hart et al., 2017). They derive from progenitors, osteogenic cells, which show mitotic activity and are the only bone cells that do not divide. Osteoblasts secrete the collagen matrix and the other proteins needed to create new bone tissue. As the secreted matrix surrounds the osteoblasts, these become trapped within it and become osteocytes. The osteocytes are the primary cell of mature bone and the most common type of bone cell (Biga et al., 2020). In the bone tissue, each osteocyte is located in a small cavity called a lacuna. These specialised cells maintain the mineral concentration of the matrix via the secretion of enzymes. The osteoclasts are involved in bone resorption by breaking down the bone. These cells are multinucleated and originate from monocytes and macrophages. Finally, bone is a dynamic tissue with balanced formation and resorption (see below). To do this, the osteoclasts and osteoblast are acting together by continually breaking down bone and forming new bone, respectively (Biga et al., 2020).

Throughout development, the process of bone formation and ossification gives rise to two macrostructurally different types of bone, cortical (also called compact bone or the cortex) and trabecular (or cancellous) (see Figure 5; Biga et al., 2020; Lindsay, 1996; White and Folkens, 2005). Cortical bone is the stronger portion of the bone tissue with an average a level of porosity below 10% (Ethier and Simmons, 2007). It makes up

the external surface of most bones and is in immediate contact with the periosteum. Cortical bone is highly organized and comprises tube-like structures, the osteons (Haversian system). Each osteon is made of concentric tubes of collagen and a calcified matrix making up lamellae. In the centre of each osteon is a Haversian (or central) canal, which contains blood and lymphatic vessels as well as nerves. These vessels and nerves branch off at right angles through Volkmann's canals, to extend to the periosteum and endosteum. Moreover, the osteons are populated by osteocytes, in their lacunae, found at the junctions between adjacent lamellae. Osteocytes are interconnected with other osteocytes and progenitor cells by processes that extend through canaliculi that form a network throughout the bone (Cowin, 2007; Biga et al., 2020). The essential nutrients are transported to the osteocytes through this system.

The cancellous bone, less dense than the cortical bone, provides structural support and flexibility to the bones. It is found in the extremities (epiphyses) of the long bones (Figure 6) and vertebral bodies such as the ribs, shoulder blades and in a variety of flat bones of the skeleton (Parkinson and Fazzalari, 2013). Like cortical bone, cancellous bone contains osteocytes housed in lacunae. However, the cells are arranged in a lattice-like

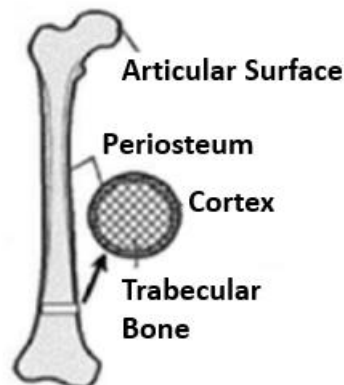


*Figure 6.* Bone structures (modified from Hart et al, 2017 and Rauch and Schonau, 2005).

network of matrix, the trabeculae (singular=trabecula) comprising rods and plate-like structures (Guo, 2001; Keaveny et al., 2001; Biga et al., 2020).

### 1.3.2 Bone mechanical properties

The mechanical properties of bone are fundamental to the ability of the skeleton to respond to the various demands placed on it by functional loading and to provide protection to the organs it supports. Bone is defined as a linearly elastic, inhomogeneous, anisotropic, ductile material (Cowin, 2001; Currey, 2006; Humphrey and Delange, 2004). It is a complex material due to its organisation at the micro-and macrostructural levels. Its complexity at the microstructural level concerns the arrangement of collagen and hydroxyapatite while organisation at the macrostructural level is concerned with the whole bone and its material properties (Katz et al., 2008). At both levels, bone is highly adaptable to accommodate habitual loading, regulating its structure according to aspects of its loading regime and mechanical environment that include loading magnitude, rate, and frequency, and the distribution and magnitude of strains consequent upon deformations arising from loading.

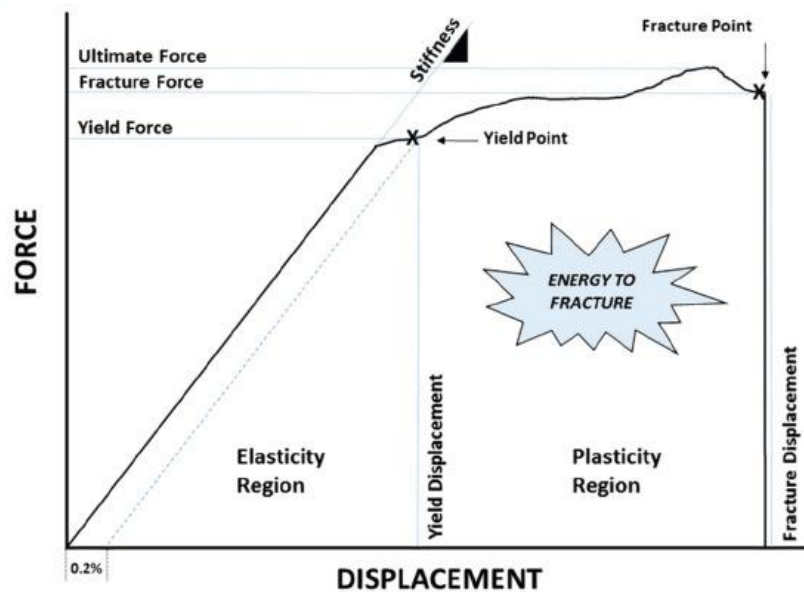


*Figure 7.* Relationship between force and displacement in an elastic material. At the yield point the deformation becomes plastic until the point of fracture (Hart et al, 2017; Lieberman, 2011; Cole and Van der Meulen, 2011; Burstein et al, 1972).

External forces applied to a bone produce internal stresses that lead to deformation, which can be described in terms of strains (structural deformation). Stress ( $\sigma$ ) is a measure of load per unit area (in Newtons per square meter ( $\text{N/m}^2$ ) or Pascals (Pa)). It can be defined as the ratio of force (F) to the cross-sectional area (A) of the bone to which it is applied ( $\sigma = F/A$ ). It has been shown that normal stresses develop when loading

occurs perpendicularly to a given plane (tensile when the structure is stretched, and compressive when compressed) while shear stresses develop if these loadings are parallel to a same plane (Bird and Ross, 2014). Between these loading directions, both normal and shear stresses develop. Strain is a measure of linear and shear deformation expressed as microstrains ( $\mu\epsilon$ ) or a percentage (%) of change in the dimension of the bone due to loading. It can be expressed as well as  $\epsilon = \Delta L/L$ , where  $\Delta L$  represents length after deformation  $L$  equals the original length. Strains can also be compressive, tensile or shearing. Under pure compressive and tensile strains, the bone changes form with no angular displacement of its material. With shearing strains, there are also changes in form and a change in the angle between two adjacent sides (Bird and Ross, 2014; Hart et al., 2017; Godinho, 2016). The degree of stiffness and elasticity of bone is expressed by the Elastic Modulus or *Young's modulus* ( $E$ ). Bone under load behaves as a linearly elastic material and exhibits two distinct behavioural characteristics due to its microscopic architecture that determines its properties. At lower-level strains, bone elastically stores and returns applied stress, thus escaping permanent deformation and micro-damages. Conversely, if the strain exceeds the elastic limit, plastic deformation occurs generating permanent damage and deformation. The point at the limit between elastic and plastic regions is called the yield point (Figure 7). Before this point, the stress-strain curve (Bird and Ross, 2014) is linear. *Young's modulus* is calculated as its slope in this linear region and is expressed in Pascals (Pa). The maximum strength of a material can be defined by the highest point on the stress-strain curve; however, it does not necessarily coincide with the yield point.

Bone is a highly complex structure, especially at the microstructural level due to its particular composition which can vary in terms of density, mineralisation, cortical and trabecular bone distribution and organisation. Thus, it has been shown that regional variations in material properties exist within bone tissue (Rho et al., 1999), both within a single bone and between bones (Dechow, Chung and Bolouri, 2008; Dechow et al., 1993). Past studies have debated the association between these differences in material properties (within and between bones) and functional differences (Dechow et al., 1993; Dechow, Chung and Bolouri, 2008). Indeed, due to its microstructure and the three-dimensional orientation of its osteons (Currey, 2006; Dechow, Chung and Bolouri, 2008), bone is an anisotropic material. Therefore, bone responds and behaves in relation to the loading specificities (such as magnitude, direction, rate and frequency) applied to it and responds differently, in terms of strength according to the direction of applied force (Bouxsein and

Karasik, 2006; Friedman, 2006; Ammann and Rizzoli, 2003). Rho et al., (1999) examined the material properties of cortical bone, using nanoindentation to measure the modulus of elasticity and found a value of 22.4 GPa in longitudinal loading of cortical bone tissue (average of osteons and interstitial lamellae) and 16.6 GPa in transverse loading. Thus, while the relationship between mechanical load and mechanical behaviour is multifactorial; a bone's strength and stiffness are greatest in the direction in which it is most commonly loaded (Martin and Correa, 2010; Currey, 2003).

### 1.3.3 Bone mechanical adaptation

The adaptation of bone to specific functions has been widely studied, especially in medicine, palaeontology and bioarchaeology. Indeed, the assumption that bone morphology reflects its loading history has been deeply investigated in living specimens and fossil remains (Demes, 1987; Enlow and Bang, 1965; Kupczik et al., 2009; Lacruz, Bromage, O'Higgins, Toro-Ibacache, et al., 2015; Lieberman, Pearson, Polk, Demes, and Crompton, 2003; Martinez-Maza et al., 2011; O'Higgins et al., 2007; Rosas and Martinez-Maza, 2010; Ruff et al., 2006; Spencer and Demes, 1993). Bone growth and development is influenced by factors such as mechanical loading experienced during ontogeny (Moss, 1997a, 1997b; Carlson, 2005). This loading causes deformation, which triggers electrical and/or biochemical signals (Bonucci, 2009; Ethier and Simmons, 2007; Klein-Nulend and Bonewald, 2019) in a process called mechanotransduction that results in bone formation and mechanical adaptation (Currey, 2006; Ruff, Holt and Trinkaus, 2006; Klein-Nulend and Bonewald, 2019). The mechanical adaptation of bone arises through bone modelling and remodeling. During these processes, we observed bone deposition and resorption via the action of specialized cells, the osteoclasts and osteoblasts. In bone modelling, resorption and deposition occur independently at distinct skeletal sites to bring about changes in bone architecture and changes in size or/and shape. Adaptation is less marked with skeletal maturation (Robling, Castillo and Turner, 2006). Bone remodeling occurs simultaneously (through the coordinated action of osteoblasts and osteoclasts) but asynchronously at multiple different locations within the skeleton (Hall, 2005). It is involved in repairing the skeleton when damaged and maintaining mineral homeostasis by liberating stores of calcium and phosphorus (Kenkre and Bassett, 2018; Manolagas and Almeida, 2018). This dynamic process of bone deposition and resorption takes place in temporary anatomical structures known as basic multicellular units (BMU,

Frost, 1973). These structures are composed of osteoblasts for bone deposition, and osteoclasts involved in resorption. They also contain a capillary blood supply and connective tissue. The BMU has a longer lifespan than individual osteoblasts and osteoclasts and so, requires constant replacement of these cells, a process controlled by the osteocytes.

The term ‘bone growth remodeling’ is commonly used (Bromage and Boyde, 2008; Lacruz et al., 2015b) to refer to the action of osteoblasts and osteoclasts in shaping the craniofacial skeleton, although strictly this bone growth modelling. The term ‘bone growth remodeling’ is used to describe the action of osteoblasts and osteoclasts in shaping the developing skull in this thesis, for consistency with prior work

Bone cell activities vary depending on the loading regime and include the proliferation of osteoblasts and osteoclasts, their reorientation within tissue and the production of DNA, collagen and glycosaminoglycans (hyaluronan and chondroitin-6-sulphate; Hall, 2005; Kular, Tickner, Chim, and Xu, 2012). Over the last decades, several mechanisms have been hypothesised and tested in order to detect deformation at the osteocytes level. These mechanisms include measurement of direct deformation of the bones and their cells using electric and magnetic transduction measurements, oxygen tension and osteocyte hypoxia measurements and hydrostatic pressure (measurement of pressure exerted by a fluid at a given point in a defined space) with recording of bulk and shear strains (Robling et al., 2006; Klein-Nulend and Bonewald, 2008; Bonucci, 2009). Bone responds to deformation through dedifferentiation of bone lining cells into osteoblasts which results in bone remodeling and bone mechanical adaptation (Klein-Nulend and Bonewald, 2008; Bonucci, 2009). Bone adaptation occurs via a change in mass and morphology to enable it to withstand habitually applied loads without reaching the failure point (Ortner, 2003; Robling, Castillo and Turner, 2006; Nordström et al., 1996; Goodship et al., 1998). During loading, applied forces generating strain can act in isolation (uniaxial) or in combination (biaxial or triaxial); at any given time, the bone will experience different modes (tensile vs compressive) of strain at various locations and of varying magnitudes. These are translated to the tissue level, where bone cells sense the mechanical signal and react via coordinated deposition and resorption. This study compares strains between species over the maxilla, and, as previously found in a study comparing biting performances in adult Neanderthal and *Homo heidelbergensis* (Godinho et al., 2018) it is expected that strains will be greater in modern humans for the same loadings. Since bone is weaker under tension and shear than under compression (Currey, 2002), the presence of resorption over the maxilla in modern humans with bone deposition in the same regions in Neanderthals

may reflect differences in straining, plausibly with greater tension developing in modern humans. However, the bone resorption found over the maxilla in modern humans might also be explained by smaller strains (because of habitually lower biting forces), during masticatory system loading which also could lead to resorption of relatively unloaded bone.

However, the causes of the differences in surface growth remodeling over the maxilla between modern humans, non-human primates and other hominins are still debated. To predict skeletal responses to loads various parameters have been used. In ‘synthesising’ crania based on FEA, Witzel (2011) and Witzel and Preuschoft (2005) used a deductive technique of structural analysis reliant on Finite Element Analysis (Finite Element structure analysis, FESS) to assess the relationship between skull function and skull shape in Neanderthal and *Diplodocus* crania. This method is applied to a non-specific homogenous body that offers the stresses ample volume for spreading between points of force application and constraints. The form of the body is then iteratively modified according to stress or strain modes, distributions and magnitudes until it is adapted to the applied loading regimen(s). In these applications to crania, the loading regime typical of masticatory forces in each species was applied to a volume, with pre-existing cavities representing those encasing organs in the skull (i.e., brain, eyes). Through repeated loadings, regions of low stress were iteratively removed. The form of the resulting ‘crania’ was then compared with those of actual crania (Witzel and Preuschoft, 2005, 2002; Witzel, 2011). The authors obtained at the end of this process, structures that closely resemble Neanderthal and *Diplodocus* crania (Witzel and Preuschoft, 2005; Witzel, 2011). Thus, this study suggests that skull form in Neanderthals is adapted to optimally bear loads from biting, chewing and protecting the sense organs. The similarity of the eventual cranial model to the real crania led the authors to conclude that the form of the cranium is strongly dependent on applied loads and resulting mechanical stresses. Moreover, in both studies, ‘bone’ was removed throughout the cranium based on the same stress or strain level without taking into account site-specific mechanosensitivity. Therefore, the results seem to support a generalized threshold model and show that compressive strains are effective in predicting skeletal form.

Alternative approaches to predicting the relationship between load resistance and bone adaptation have been employed. Thus, Oxnard et al., (1995), showed a close relationship between regions that are under net tension in the incus and surface remodeling

features that develop with age. This approach is based on extensive observations of musculoskeletal systems where it is noted that bone exists where net compression is found, and where there is net tension it is replaced by ligament or fibrous tissue (Oxnard, 1993, 2004). This is also an effective approach in predicting adapted skeletal form, but is likely a gross approximation. Many other parameters from FEA have been used in an attempt to more closely predict bone adaptation. Thus Lipphaus and Witzel (2019) use a more nuanced set of parameters, based mainly on compressive stress but also paying attention to tension as a signal to convert cartilage to bone. This echoes Oxnard's (1993, 2004) use of compression to predict bone, and tension, bone replacement with fibrous/ligamentous tissue. Likewise, Gröning et al., (2013) show a correlation between strains and bone distribution in the mandible, with high strains, due to masticatory loadings, located in regions with thicker cortical bone and dense trabecular network. An alternative is to use strain energy density to predict bone architecture (e.g. Tarala, et al., (2011)). Other approaches include that of Reina et al., (2007) who applied an internal bone remodeling algorithm based on tensors computed from FEA, to a filled FE model of a human mandible and found a good match between the resulting density maps and the distribution of bone in the real specimen. All of these approaches are doubtless considerable simplifications, but empirically they have utility.

The physical loads experienced over time by an individual during 'normal activity' will result in a balance of bone formation/resorption. However, if the loads rise above the range normally encountered, bone formation rate is increased. This adaptive phenomenon is encapsulated in the "mechanostat" hypothesis (Frost, 1987; 2003). It predicts that bone is remodelled in areas submitted to physiological loadings with the resulting strain magnitude playing an important role in the formation, resorption and maintenance of the bone tissue. The idea is that bone tissue will be formed if bone strains during loading are above a certain magnitude but resorbed if the strains are below another threshold. In most skeletal sites, a threshold ranging between 1500-2500  $\mu\text{E}$  (Frost, 1987) to 3000  $\mu\text{E}$  (Skerry, 2000) is hypothesized to trigger bone deposition. Conversely, if strains are lower than these values, bone resorption occurs. Other factors have been shown to induce bone formation/resorption including dynamic vs static loading (Lanyon and Rubin, 1984; Turner et al., 1998), strain rate (Mosley and Lanyon, 1998) and strain frequency (Judex et al., 2007). To regulate bone adaptation, it has been suggested that site-specific pattern-

ing information exists throughout the skeleton with different sites having different thresholds, allowing them to respond to site-specific changes in loads (Currey, 2006; Himeno-Ando, Izumi, Yamaguchi, and Iimura, 2012; Skerry, 2000; Vatsa et al., 2008 but see Cooke et al., 2021).

It has been hypothesised that diet and masticatory loadings could shape the mid-face in *Homo sapiens* but also in other hominins (Daegling et al., 2013) such as our own species and Neanderthals. Indeed, during contraction, muscles directly strain the bone where they insert. The resulting strains derived from loadings induce or reduce the amount and direction of bone formation and resorption, changing bone morphology in such a way that the new form is functionally optimised (Kranioti et al., 2009). Thus, loading histories in modern humans and Neanderthals might well be reflected in temporal and spatial differences in the distributions of regions of surface deposition and resorption. Differences in bone growth remodeling exist between these two species (Lacruz et al., 2015b, 2019; Schuh et al., 2019). Indeed, analyses of bone remodeling of the developing craniofacial complex provide insights into the growth process that the craniofacial complex undergoes during development and inform us about ontogenetic processes that lead to differences in final adult form (Lacruz et al., 2015b; Schuh et al., 2019). In modern humans, maxillary growth is characterised by bone resorption on the anterior subnasal surface, whereas in Neanderthals extensive bone deposition is found in this region (Lacruz et al., 2015b, 2019; Schuh et al., 2019). Such differences in the pattern of bone remodeling between Neanderthals and modern humans have been hypothesized to be related to genetic signals that differ between these species, or to differences in force resistance arising from food processing during post-natal development. Additionally, within each species, the forces experienced by the cranium develop over time as diet and paramasticatory behaviour change (O'Connor, Franciscus and Holton, 2005; Edmonds and Glowacka, 2020; Holly Smith, Crummett and Brandt, 1994). In Neanderthals, paramasticatory behaviour is hypothesized to include “anterior dental loading” or the use of “teeth-as-tools” (ADLH) hypotheses (Clement et al., 2012, Smith and Paquette, 1989; Trinkaus, 1983). It is argued that Neanderthals heavily used their anterior teeth both for food preparation/mastication and for cultural practices such as the processing of materials for the production of different artefacts (Brace, 1995; Demes, 1987; Rak, 1986; Smith, 1983; Spencer and Demes, 1993; Trinkaus, 1987). Therefore, it has been proposed that the unique craniofacial anatomy in Neanderthal could be an adaptive response to high magnitude forces at the anterior dentition during such activities (Clement et al., 2012;

Estalrich and Marín-Arroyo, 2021; Fiorenza et al., 2019; Krueger et al., 2019; Spencer and Demes, 1993).

While the hypothesis that differences in growth remodeling are driven by differences in genetic regulation of craniofacial growth cannot be tested in the current work, the hypothesis that remodeling differences arise from differences in how biting forces are generated and borne by the cranium can be tested. Thus, if changes in mechanical forces interact with changes in cranial form during development to drive differences in growth re-modelling, we expect differences in strain magnitudes and distributions to reflect the anatomical locations of differences in growth remodeling.

#### 1.4 Objectives and hypotheses

The general aim of the thesis is to understand how biting mechanics interact with cranial form to impact post-natal craniofacial ontogeny in modern humans and Neanderthals. Based on the foregoing review, several specific research questions have been identified for this thesis:

1 - Facial ontogenetic trajectories do not diverge significantly among Neanderthals and modern humans:

Differences in results have been reported concerning postnatal facial ontogenetic trajectories between modern humans and Neanderthals (Ponce de León and Zollikofer, 2001b; Ackermann and Krovitz, 2002; Bastir, O'Higgins and Rosas, 2007). It is clear that differences exist between modern human and Neanderthal craniofacial morphology at all age stages, it is unclear how these differences arise and if similar morphological changes occur in the two species. This hypothesis will be tested by comparing and visualising differences in ontogenetic trajectories between the two species.

To test these hypotheses, detailed craniofacial ontogenetic 3D models are compared among modern humans and Neanderthals using an approach based on landmarks and semi-landmarks analysed using geometric morphometrics to build and compare post-natal growth models in modern humans and Neanderthals.

2 - There are no ontogenetic changes in cranial load resistance in modern humans

Studies of ontogenetic changes in loadings and resulting strains that take account of changes in form are lacking in modern humans. However, a strong possibility exists that

the cranium undergoes continuous adaptation during postnatal growth and development (Bouvier and Hylander, 1996; Pearson and Lieberman, 2004; Ruff, Holt and Trinkaus, 2006; Kupczik et al., 2009). This hypothesis will be tested by qualitatively and quantitatively comparing load resistance (deformations and resulting strains) at different age stages. Mean infant, juvenile and adult models are extracted from the post-natal growth models built previously. Then, biting simulations are conducted on these models using Finite Element Analyses (FEA) to estimate and compare deformations and resulting strains.

3 - There are no ontogenetic changes in cranial load resistance in Neanderthals.

As for modern humans, little is known about ontogenetic changes in loadings and resulting strains in the Neanderthal craniofacial complex. As with modern humans, this hypothesis will be tested by qualitatively and quantitatively comparing load resistance (deformations and resulting strains) at different age stages.

4 - There are no differences in cranial load resistance between modern humans and Neanderthals.

Analyses of bone modelling of the developing craniofacial complex provide insights into craniofacial growth and development and so inform us about ontogenetic processes that lead to differences in final adult form. In modern humans, maxillary growth is characterised by bone resorption on the anterior subnasal surface, whereas in Neanderthals extensive bone deposition is found in this region.

Such differences in the pattern of bone remodeling between Neanderthals and modern humans have been hypothesized to be related to genetic signals that differ between these species, or to differences in force resistance arising from food processing during post-natal development. Additionally, within each species, the forces experienced by the cranium develop over time as diet and paramasticatory behaviour change. While the hypothesis that differences in growth remodeling are driven by differences in genetic regulation of craniofacial growth cannot be directly tested (because Neanderthals are fossils and candidate genetic mechanisms to regulate the spatial distribution and activity of remodeling fields in living humans are lacking in the literature), we can test the hypothesis that remodeling differences arise from differences in how biting forces are generated and borne by the cranium. Thus, if changes in mechanical forces interact with changes in

cranial form during development to drive differences in growth re-modelling, we expect differences in strain magnitudes and distributions to reflect the anatomical locations of differences in growth remodeling.

To test this hypothesis, the deformations and strains arising from FEA biting simulations are compared between modern humans and Neanderthals. To assess if these might underlie differences in remodeling, they are compared to the distributions and activities of craniofacial bone remodeling fields in modern humans and Neanderthals.

## 2.0 Modern human and Neanderthal post-natal craniofacial allometry and the extraction of infant, juvenile and adult models

This chapter presents the test of the first hypothesis, that facial ontogenetic trajectories do not diverge significantly among Neanderthals and modern humans. This comprised segmentation and 3D cranial reconstruction, with the repair of damaged and incomplete material, followed by landmarking and semi-landmarking of the cranial surfaces of both species and statistical analyses of variation and allometry to describe and compare these between species. Finally, average individuals representing the broad age categories of infant, juvenile and adult were extracted for the finite element analyses of biting performance presented in subsequent chapters.

### 2.1 Samples

#### 2.1.1 Modern human

The sample used in this study is composed of 63 segmented skulls reconstructed in 3D from CT data from individuals with ages ranging from early newborn to adulthood (Table 1). The sample was collated from various collections and resources: The Bosma collection of the University of Maryland (Baltimore, USA), the Scheuer collection of the University of Dundee (UK) and collections from Hull York Medical School (UK), the online database Nespos, courtesy of the University of Leeds (UK) and University College London (UK), information on chronological age is only available for material in the Scheuer-Dundee collection, for the other collections, the age of the specimens was estimated based on molar eruption (Carr, 1962; Schaefer et al., 2009) to a maximum of 23.5 years old when full dental maturity is reached and specimens are considered fully adult (AlQahtani, Hector and Liversidge, 2010). Age class was defined for all the specimens as follows: infants from newborn to 4 years, juveniles from 5 to 17 years, and adults from 18 years onward. Here, the modelling of ontogenetic changes focuses on allometry, which relates changes in shape with size. Thus, chronological age is not used in these analyses. It was estimated simply to ensure that sampling of the post-natal period is as even as possible, given the constraints of available specimens and to identify broad age categories: infant, juvenile and adult. The specimens from the Scheuer collection, the Hull York Medical School and the University of College London were reconstructed in 3D from a

stack of 2D images used in a previous PhD thesis by Federica Landi in 2020. The specimens from the Bosma collection were reconstructed in the same way during this thesis. The 3D reconstruction involved segmentation, where the structures of interest are labeled as particular materials by either automatically or manually delineating their physical boundaries in contiguous slices (Mansoor et al., 2015). In this thesis, the CT scans of the modern human sample were segmented semi-automatically using the software Avizo 9.0 (FEI Visualization) (FEI Visualization). Because these CT scans are of dry bones and good resolution, the contrast between the cranium and the air was good and therefore, the initial segmentation was able to be performed using a single global threshold that maximized the inclusion of bone material in the resulting virtual reconstruction of the skulls. This threshold was estimated using the grey-level histogram (bimodal) method where the threshold was placed in the valley between the two peaks, representing the skull and the background (Pun, 1980). Because some bones in this anatomical region are extremely thin, especially in young specimens (zygomatic arches, orbits, sinuses...), this method often resulted in errors in reconstruction. Therefore, some manual corrections were locally necessary to virtually fill the cracks. In addition, when present, the mandibles of the specimens were virtually removed from the rest of the cranium. Finally, small holes in the surfaces were corrected using the Mesh Doctor automatic polygon improvement tool (Carlson et al., 2016) of the software Geomagic® (Studio 2018).

In two infant specimens, one zygomatic arch was damaged. These were virtually repaired after the segmentation process, replacing them with their reflected intact anti-mere. This was done using the reflected relabelling method (Gunz and Mitteroecker, 2013) and R 3.6.1 (Development Core Team, 2019) with the package Arothron (Profico et al., 2021). This method first required the specification of paired (bilateral) and unpaired (“midsagittal”) points. Then, the surface was symmetrized based on the paired landmarks. Landmark labels from the right-side landmarks were interchanged and used to create a mirrored version of the symmetrized surface, aligned with the symmetrized surface. The last step was to superimpose the mirrored surface on the original surface using a Procrustes fit based on the available landmarks. Then, the parts of interest were extracted from the mirrored surface and merged with the original cranial surface using Geomagic® (Studio 2018) tools.

The last step was to extract the external surface mesh of each specimen for landmarking. We used R 3.6.1 with Morpho v.2.9 (Schlager, 2017) and Arothron packages (Profico et al., 2021) to isolate the external surfaces. The extraction process can create small holes and inequities in the final meshes; these were cleaned and the holes were filled using Geomagic® (Studio 2018).

Table 1. Human sample with specimen ID, sex, age category, a description of the stage of dental development, age in years and centroid sizes for a total of 63 specimens. When the age was not known, it was estimated, up to a maximum of 23.5 years, when full dental maturity is reached indicating adulthood (AlQahtani, Hector and Liversidge, 2010).

specimen	sex	age category	Teeth	age	Centroid sizes
SCH6-18	Unknown	Adult	M3_erupting	> 18	1390.62
Anat800	Male	Adult	M3_erupted	23.5	1358.72
UCLAC_60	Unknown	Adult	M3_erupted	23.5	1439.52
UCLAC_66	Unknown	Adult	M3_erupted	23.5	1445.69
VA001	Female	Adult	M3_erupted	23.5	1375.24
VA002	Male	Adult	M3_erupted	23.5	1450.1
VA003	Male	Adult	M3_erupted	23.5	1443.2
VA004	Female	Adult	M3_erupting	23.5	1347.91
VA007	Male	Adult	M2_erupted	≤20	1497.73
VA012	Male	Adult	M3_erupted	23.5	1417.79
VA019	Female	Adult	M3_erupting	≤20	1338.47
VA021	Male	Adult	M3_erupted	23.5	1425.32
VA024	Female	Adult	M3_erupting	≤20	1460.77
VA025	Unknown	Adult	M3_erupted	23.5	1446.48
VA030	Female	Adult	M3_erupted	23.5	1379.35
VA050	Unknown	Adult	M3_erupted	23.5	1453.84
VA051	Female	Adult	M3_erupted	23.5	1421.06
VA052	Unknown	Adult	M3_erupted	23.5	1426.97
VA053	Male	Adult	M3_erupting	23.5	1400.27
BOSMA07	Unknown	Infant	No_teeth_erupted	≤1	843.39
HPN_005	Unknown	Infant	No_teeth_erupted	≤1	793.859
HPN_002	Unknown	Infant	No_teeth_erupted	≤1	854.429
HPN_004	Unknown	Infant	No_teeth_erupted	≤1	799.73
HPN_006	Unknown	Infant	No_teeth_erupted	≤1	853.964
Hum1175	Unknown	Infant	No_teeth_erupted	≤1	817.84
SCH2_	Unknown	Infant	No_teeth_erupted	≤1	789.674
SCH13	Unknown	Infant	M1_in_crypt	≤4	1183.26
UCL_3_	Unknown	Infant	No_teeth_erupted	≤1	840.996
UCL_A23	Unknown	Infant	M1_in_crypt	≤4	1174.57
UCL_C34	Unknown	Infant	No_teeth_erupted	≤1	878.114
UCLA23D	Unknown	Infant	No_teeth_erupted	≤1	1108.29
BOSMA08	Unknown	Infant	deciduous teeth	≤3	1112.84
BOSMA09	Unknown	Juvenile	M1_in_Crypt	≤4	1169.35
H-I001_	Unknown	Juvenile	M1_in_Crypt	≤5	1332.51
BOSMA11	Unknown	Juvenile	M1_in_crypt	≤5	1226.13
BOSMA14	Unknown	Juvenile	M1_in_crypt	≤5	1185.34
BOSMA16	Unknown	Juvenile	M1_erupting	≤8	1221.87
BOSMA17	Unknown	Juvenile	M1_in_crypt	≤5	1210.21
BOSMA18	Unknown	Juvenile	M1_almost_erupting	≤8	1291.24
BOSMA19	Unknown	Juvenile	M1_in_crypt	≤5	1259.99
BOSMA20	Unknown	Juvenile	M1_in_crypt	≤5	1150.74
BOSMA21	Unknown	Juvenile	M1_in_crypt	≤5	1170.46
BOSMA22	Unknown	Juvenile	M1_in_crypt	≤5	1231.32
BOSMA23	Unknown	Juvenile	M1_erupted	≤8	1294.12
BOSMA24	Unknown	Juvenile	M1_erupting	≤9	1356.77
BOSMA28	Unknown	Juvenile	C_erupting	≤12	1307.95
BOSMA29	Unknown	Juvenile	M2_erupting	≤17	1329.77
BOSMA30	Unknown	Juvenile	M2_erupting	≤17	1344.54
SCH1-12	Unknown	Juvenile	M2_erupting	≤12	1343.38
SCH4_8y	Unknown	Juvenile	lateral_incisor_and_M2_in_crypt	≤8	1278.11
SCH7_8y	Unknown	Juvenile	M2_erupting	≤10	1319.94
SCH7fex	Unknown	Juvenile	C_erupted	≤12	1314.69
SCH13bm	Unknown	Juvenile	M2_erupting	≤11	1317.93
SCH13ri	Unknown	Juvenile	M1_erupting	≤10	1304.96
SCH36-10	Unknown	Juvenile	M1_erupting	≤10	1323.88
SCH39fl	Male	Juvenile	premolars_in_crypt	≤8	1351.63
SCH156y	Unknown	Juvenile	I1_in_Crypt	≤7	1289.59
SCH258y	Female	Juvenile	M2_in_crypt	≤10	1311.93
UCL-A06	Unknown	Juvenile	M1_erupting	≤8	1206.32
UCLA23M	Unknown	Juvenile	M1_erupting	≤8	1309.48
UCLCDJu	Unknown	Juvenile	M2_erupting	≤12	1373.2
UCLF279	Unknown	Juvenile	C_erupting	≤12	1318.49
UCLH102	Unknown	Juvenile	M2_in_crypt	≤12	1340.74

### 2.1.1.2 Neanderthal

The sample used in this study is composed of CT scans, reconstructed 3D virtual models or pre-existing 3D surfaces of 12 Neanderthal fossils aged from early newborn to adult (Table 2). The sample was collated with appropriate permissions from the curators of fossils or creators of digital reconstructions. Material was obtained from: the Max Planck Institute (Leipzig, Germany); University of Bordeaux (Bordeaux, France), Muséum national d'Histoire Naturelle (MHHM, Paris, France); Natural History Museum (NHM, London, UK); Dan David Center of Human Evolution and Biohistory Research, Schmunis family anthropological institute, Sackler Faculty of Medicine, Tel Aviv University (Tel Aviv, Israel); Museo Nazionale Preistorico Etnografico "L. Pigorini" (Rome, Italy); Università di Sapienza; the Laboratory of Palaeoanthropology and bioarchaeology of Sapienza University of Rome; the Laboratory of Prehistory (Saint-Petersburg, Russia) and the online database Nespos. As for the modern human sample, we carried out a 3D reconstruction using the same segmentation approach on the CT scans collected for some specimens (see Table 2). In addition, in processing the record of these fossil specimens, thresholding of these crania was then reviewed, slice by slice, to correct any errors in segmentation (small holes, unwanted material, etc.) by using the brush tool available in Avizo 9.0 (FEI Visualization).

Table 2. Neanderthal sample with specimen ID, sex, age category, age in years, repository and centroid sizes.

Specimen	sex	age category	age	Collection	Datation	Data type	Centroid sizes
Le Moustier 2/Mezmaiskaja	unknown	Infant	unknown	Max Planck institute, Leipzig, Germany University of Bordeaux, Bordeaux, France Laboratory of Prehistory, St Petersburg, Russia	50-40 ka	3D reconstructed virtual model	901.828
Gibraltar 2	Male	Juvenile	unknown	London NHM, UK	120-60 ka	CT scans	1335.67
La Quina H18	unknown	juvenile	unknown	Laboratory of Paleoanthropology and bioarcheology of Sapienza University of Rome, Italy	60-50 ka	3D virtual surface	1319.9
Pech de l'Aze Engis 2	unknown unknown	Infant juvenile	2-3 years old unknown	MHNN, Paris, France Université de Liège, Belgium	90-60 ka 34.5-36 ka	CT scans CT scans	1251.57 1342.84
Roc de Marsal	unknown	Juvenile	5-6 years old	Nespos Archive	50 ka	CT scans	1389.57
Amud 1	unknown	Adult	unknown	Dan David Center of Human Evolution and Biohistory Research, Shmunis family anthropological institute, Sackler Faculty of Medicine, Tel Aviv University, Tel Aviv, Israel	70 ka	3D virtual surface	1603.32
Gibraltar 1	Female	Adult	unknown	London NHM, UK	120-60 ka	CT scans	1435.53
Guattari 1	unknown	Adult	unknown	Museo Nazionale Preistorico Etnografico "L. Pigorini", Rome, Italy	60-50 ka	CT scans	1549.24
La Chapelle aux Saints 1	unknown	Adult	unknown	MHNN, Paris, France	60-50 ka	CT scans	1581.92
La Ferrassie 1	unknown	Adult	unknown	MHNN, Paris, France	70-50 ka	CT scans	1620.25
Saccopastore 1	unknown	Adult	unknown	Universita Sapienza di Roma, Italy	130-100 ka	CT scans	1443.48

The CT-scans of mandible of the Roc de Marsal 1 were used separately and the landmark configuration of La Chapelle aux Saints 1, was obtained from the repository of the archaeology department of the University of York (unpublished).

#### 2.1.2.1 Gibraltar 1 reconstruction

As noted above, reconstructions of several Neanderthal crania were required in order to create a craniofacial growth model for this species. The reconstruction of the Gibraltar 1 fossil (Figure 8) is described here in detail below because its surface was used in combination with the landmark and semi-landmark dataset to create the mean Neanderthal infant, juvenile and adult models. The reconstructions of other remaining crania are described in Appendix 1: Neanderthal reconstructions.

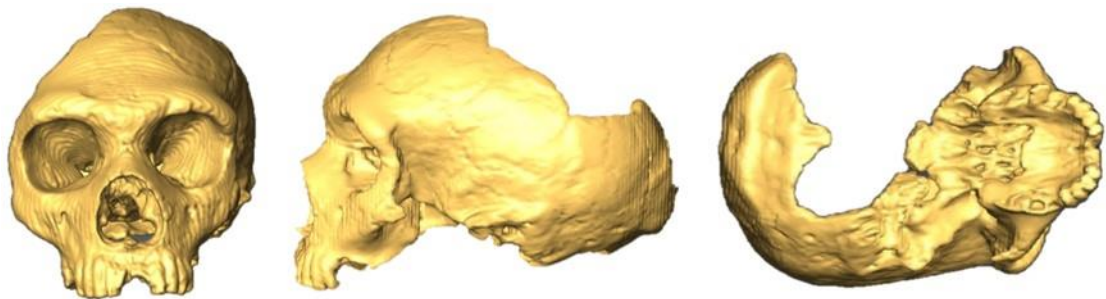


Figure 8. Gibraltar 1 skull before reconstruction.

The Gibraltar 1 skull presents well-preserved facial and palatal regions. However, it presents several missing parts that are important for this project: the zygomatic arches, the basicranium and the right temporal and sphenoid bones, part of the right parietal bone and the nasal septum. These were reconstructed using parts of other adult Neanderthal fossils.

A reflected relabelling (see section 2.1.1) was first conducted on the entire skull to symmetrise the cranium and reconstruct the left side of the cranial vault including the right parietal, sphenoid and temporal bones (Figure 9).

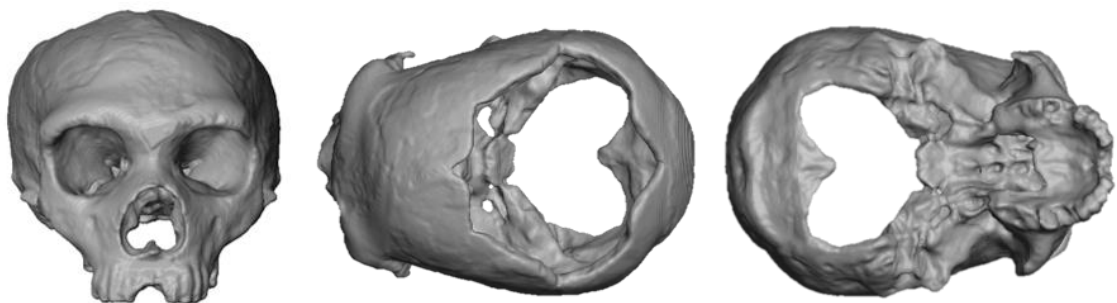
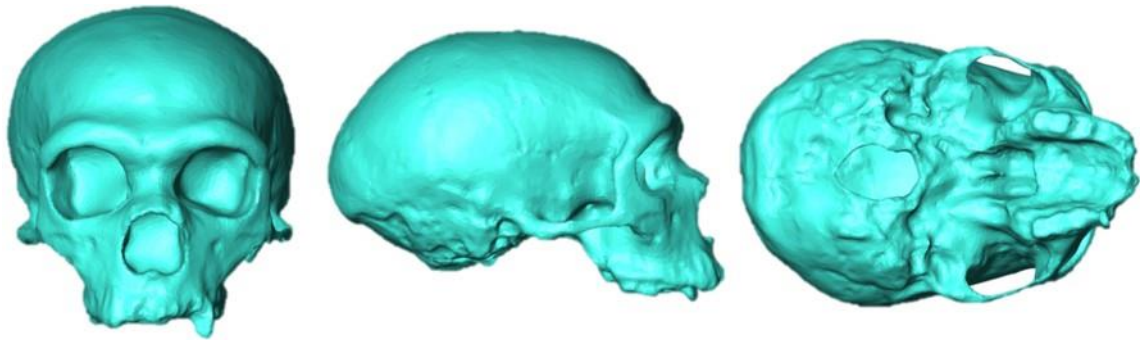


Figure 9. Gibraltar 1 skull after reflected relabelling.

To reconstruct the superior part of the cranial vault (part of the left and right parietal and temporal bones), the Neanderthal adult skull Saccopastore 1 was scaled and warped onto Gibraltar 1. This used two different sets of landmarks and semi-landmarks (31 landmarks and 55 landmarks and semi-landmarks) and Avizo v. 9.0. The warped Saccopastore 1 specimen was then imported into Geomagic® (Studio 2018) and the relevant parts of the cranial vault were extracted and merged into Gibraltar 1.



*Figure 10.* La Chapelle-aux-Saints reconstructed.

The basicranium was reconstructed using the reconstructed cranium of La Chapelle aux Saints 1 (see Appendix 1 and Figure 10). The reconstructed La Chapelle aux Saints 1 version was first scaled to Gibraltar 1 using 25 landmarks. Then, La Chapelle aux Saints 1 was warped to the partially reconstructed Gibraltar 1 specimen using 128 landmarks and semilandarks. The basicranium of the warped La Chapelle aux Saints cranium was extracted in Geomagic® (Studio 2018) and merged into Gibraltar 1. Then, the partially reconstructed Gibraltar 1 was remeshed and finalised by filling small holes and smoothing irregularities using Geomagic® (Studio 2018).



*Figure 11.* La Ferrassie 1 cranium before reconstruction

The zygomatic arches were reconstructed using the reconstruction of the La Ferrassie 1 adult specimen (see Supplementary data 1). This specimen has well-preserved zygomatic arches (Figure 11). The reconstructed version of this cranium rather than the original was used because it allowed the placement of an adequate number of landmarks and semi-landmarks to control the warping. The La Ferrassie 1 cranium was scaled and

warped to the Gibraltar 1 cranium. For this, a new set of 263 landmarks and semi-landmarks was created on the reconstructed version of Gibraltar 1 and La Chapelle aux Saints to ensure more precise warping. The zygomatic arches were then extracted from the warped cranium and merged into Gibraltar 1 (Figure 12). Finally, the right side of the Gibraltar 1 was mirrored to create the left side in order to have a clean surface for Finite Element Analyses.

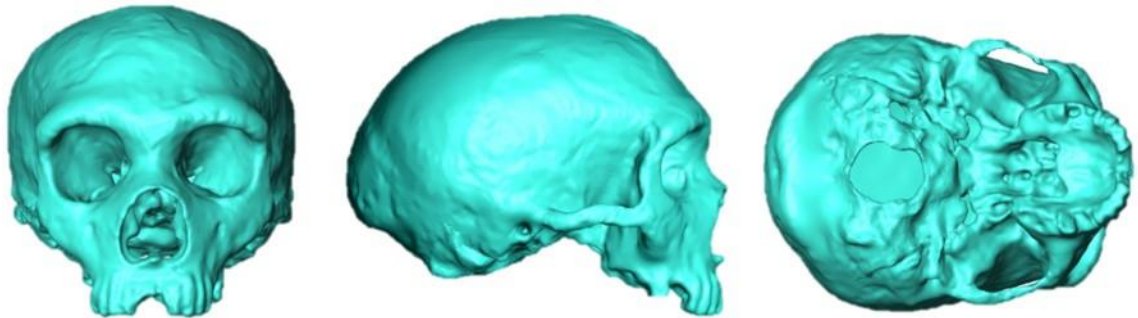


*Figure 12.* Gibraltar 1 after reflected relabelling and reconstruction with parts from La Chapelle-aux-Saints and Saccopastore 1, added using warping approaches.

The last step of the reconstruction was to repair the nasal septum. This anatomical structure is important for subsequent Finite Element Analyses (FEA) since it may bear loadings and influence the propagation, and thus the distribution, of strains between the inferior part of the maxilla and the upper face. Because none of the adult Neanderthal fossil crania collected for this project presents a preserved nasal septum, a modern human adult specimen was used as the source model. The adult specimen (SCH6-18), was scaled and warped to Gibraltar 1 using 57 landmarks. The nasal septum was extracted and merged to create the final reconstructed version of Gibraltar 1 (Figure 13).

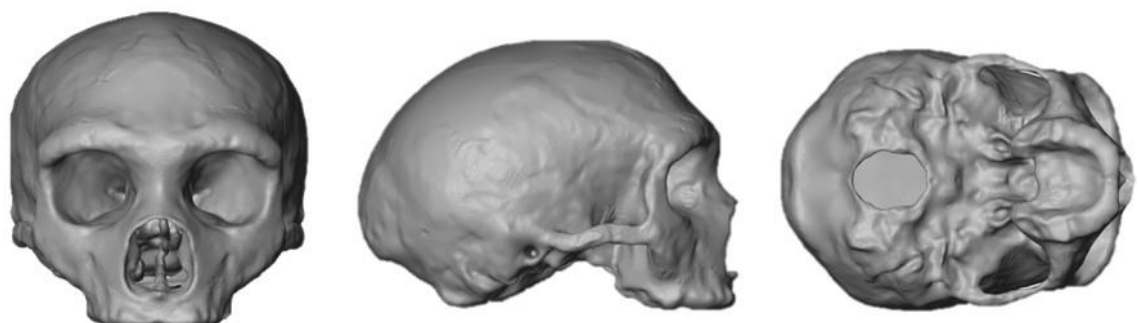


*Figure 13.* Reconstructed Gibraltar 1 specimen used as a reference surface to mesh the mean infant, juvenile and adult landmarks and semi-landmark coordinates.

## 2.2 Geometric morphometrics

Geometric morphometric (GM) methods allow statistical analysis of variation and covariation among configurations of landmarks or between a configuration and other var-

iables of interest. Registration-based geometric morphometric methods convert the coordinates of a configuration of landmarks into variables representing size and shape that are amenable to subsequent multivariate analysis (Bookstein, 1984; Dryden and Mardia, 1993; Goodall, 1991; Kendall, 1977, 1984; Kent, Tyler, and Vardi, 1994; Sneath, 1967).

### 2.2.1 Landmarks and semi-landmarks

Landmarking and semi-landmarking employed the semiautomated approach embedded in the Evan Toolbox v.1.75 (Figure 14 and Figure 15). This uses a template to guide landmarking and to carry out semi-landmarking of surfaces and curves between landmarks. The template comprises a surface that was made using the best-preserved adult human specimen. This surface was symmetrised by mirroring and the teeth were removed. A configuration of 57 fixed landmarks (Figure 14) was then marked up on the template surface (landmarks used in this study are indicated in Table 3). The fixed landmarks are located over the facial skeleton (including the orbits and nasal aperture), zygomatic arches, cranial base, vault and alveolar process. The landmarks at the posterior limits of the maxillary tuberosity (Table 3 landmark 22:30) were least identifiable and so positions were estimated and projected 7 times (see section 2.2.2) and averaged, using the Evan toolbox 1.75. The template also includes 246 surface semi-landmarks over the cranial vault, basicranium, supraorbital ridges, maxilla, right and left orbits and zygomatic arches. The semi-landmarks on the cranial vault were placed in a regular pattern on the right side of the cranium and then mirrored and projected onto the left using R and the package Arothron (Profico et al., 2021). The semi-landmark configuration was then added to the template in the Evan toolbox (v.1.75). Finally, additional semi-landmarks were recorded to represent 5 curves on the cranial surface (shown in red in Figures 14 and 15):

the superior border of the right and left zygomatic arches, the orbital rim and the edge of the nasal aperture.

Table 3. Template landmarks.

1	Alveolare
2	Alveolare incisor
3	Basion
4	Bregma
5	Glabella
6	Inion
7:52	end-zygomatic arch
8:56	posterior occipital condyle
9:53	Mastoidale
10:54	Zygion
11:55	Zygomaxillare
12	Hormion
13	Staphylion
14:15	Junction palatine/sphenoid bone
16:17	Anterior occipital condyle
18:26	1rst-2nd incisor
19:27	Anterior M1
20:28	Posterior M1
21:29	Anterior M2
22:30	Maxillary tuberosity
23:33	Foreman lacerum
24:34	Top nasal aperture
25:35	Junction vomer/sphenoid bone
31:32	Frontomalare orbital
36:37	Supraorbital foramen
38:39	Edge bottom orbital
40:45	Frontomalare temporale
41:44	Jugale
42:43	Auriculare
46	Rhinion
47	Lambda
48	Nasion
49	Nasospinale
50	Opisthion
51	Orale
57	Alveolon

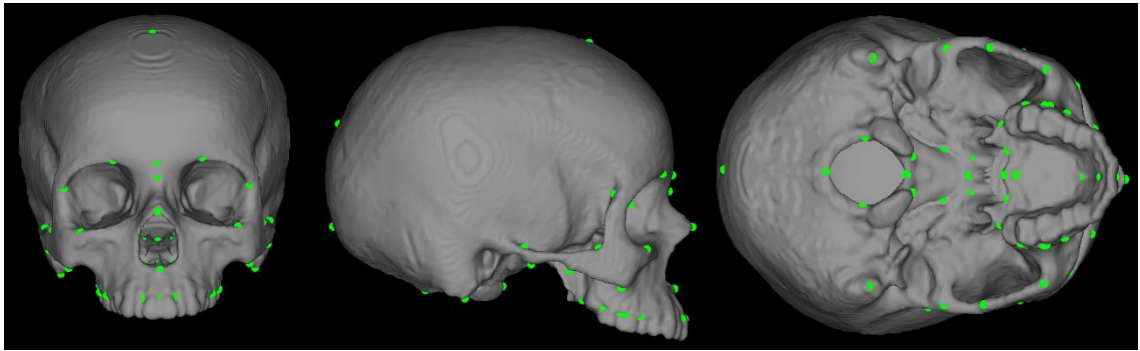


Figure 14. Final template with 57 fixed landmarks used to build the ontogenetic growth model.

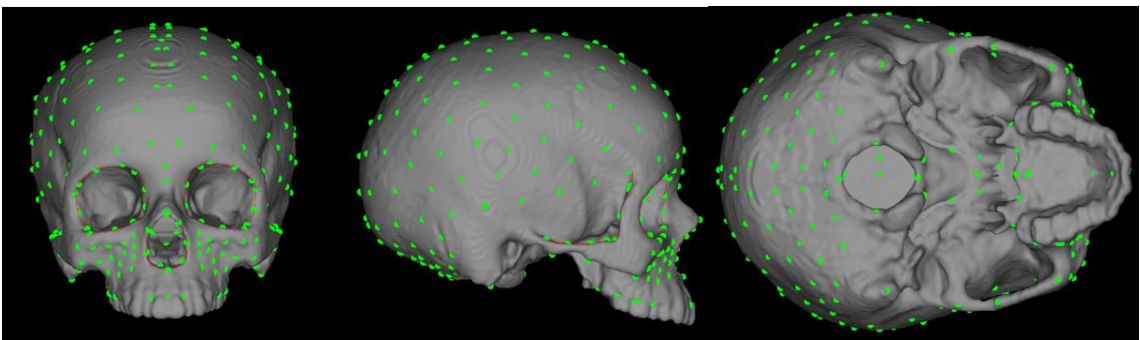


Figure 15. Final template with 57 fixed landmarks, 246 semi-landmarks and 5 curves (orbits, zygomatic arches and nasal aperture) used to build the ontogenetic growth model.

### 2.2.2 Sliding semi-landmarks

Having built the template, the next task was to landmark and semi-landmark each (target) specimen. While landmarks can be identified using homologous features of the cranium, semi-landmarks describe surfaces and curves. While they lie on each surface or curve, the homology of their locations is unknowable. To deal with this issue, Bookstein, (1996a, b) proposed that semi-landmarks should be located on specimens in such a way that the increase in sample variance due to the addition of semi-landmarks to a configuration of landmarks is minimised in some way. The aim is to minimise variance due to errors in location of semi-landmarks while retaining variance due to differences in shape (of the surfaces or curves). Bookstein's solution (Bookstein, 1996a, 1996c) is to minimise the bending energy of a triplet of thin plate. To achieve this, semi-landmarks are projected to, and iteratively slid over surfaces or curves until a minimum is achieved. An alternative, not applied here, is Rohlf's (Rohlf., 1990) suggestion of minimising Procrustes distance by sliding. It has been argued (Bookstein, 1997; Mitteroecker and Gunz, 2009; Gunz and Mitteroecker, 2013) that minimising bending energy is a more sensible ap-

proach because it gives weight to local differences in landmark location in guiding sliding, while Procrustes minimisation gives all landmarks equal weight, even if very distant from the semi-landmarks being slid. These alternatives lead to different solutions but similar estimates of e.g. mean surface shape, allometry etc (Gunz, Mitteroecker and Bookstein, 2005; Perez, Bernal and Gonzalez, 2006). While the choice of algorithm for sliding semi-landmarks is still actively being researched, in this study, the currently most commonly used approach, through the minimisation of bending energy, was applied.

The Evan toolbox (v1.75) was used for landmarking and semi-landmarking. For most specimens landmarking was accomplished semiautomatically, using the warping feature of the toolbox to estimate an initial position for each landmark based on the positions of a small number of hand-digitised landmarks on the target specimen. After warping the full set of landmarks from the template (reference) specimen to the target, manual adjustment was carried out to ensure good placement. The next step was to semi-landmark each target specimen. This was achieved by first warping all semi-landmarks from the template to the space of the target specimen. This was followed by projecting them to the nearest point on the surface of each target specimen. This initial positioning of semi-landmarks was then adjusted by sliding, based on minimisation of bending energy (Bookstein, 1996b, 1996a, 1996c) against the template.

The sliding algorithm is iterative, the semi-landmarks on all specimens are slid with respect to the initial template. Next, the sample mean landmarks and semi-landmarks are used to create a new template which is the mean form of the current iteration of the landmark and semi-landmark configuration for the sample, and against which sliding is repeated. This was repeated for 7 iterations, after which the mean varied little between iterations; unlike that for GPA, the algorithm for sliding semi-landmarks does not always reach a minimum and so sliding is stopped after the first few iterations, when the mean changes little between iterations.

In the present study, sliding was performed in the Evan toolbox v 1.75 with all the modern human and Neanderthal specimens semi-landmarked together against the common template. This ensures comparability of landmark and semi-landmark sets between species and so, permits joint statistical analysis of these species. After sliding, landmarks and semi-landmarks each were given the same weight in subsequent statistical analyses (Gunz, Mitteroecker and Bookstein, 2005; Gunz and Mitteroecker, 2013).

## 2.3 Multivariate statistical methods

### 2.3.1 Generalised Procrustes Analysis

Once the specimens were landmarked and semi-landmarked, statistical analyses were carried out to model and compare growth allometry in each species. Landmarks and semi-landmarks were treated identically, and so, for simplicity, the configuration as a whole is referred to here as the ‘landmark configuration’.

Statistical analyses used the methods of geometric morphometrics which facilitate analyses of shape and size variation among landmark configurations. The size and shape of each configuration was computed using Generalized Procrustes Analysis (GPA) (Dryden and Mardia, 1993; Goodall, 1991; Gower, 1975; David G. Kendall, 1984; Rohlf and Slice, 1990). The purpose of GPA is simply to estimate the shape variables which are the landmark coordinates after GPA. GPA is an iterative fitting of the landmark configuration of each specimen to the mean landmark configuration. An arbitrary configuration is chosen as the initial estimate of the mean and this and each configuration in the sample are scaled to centroid size =1, translated to the same centroid and the specimen configuration is rotated against the current estimate of the mean to minimise the sum of squared differences between the equivalent landmarks in each configuration. The sample mean is then re-estimated based on the scaled translated and rotated landmark coordinates and the process is repeated until the sum of squared distances reduces little (less than the threshold value for termination) between iterations. The square root of this sum between each specimen and the mean or between two specimens is the Procrustes distance.

After GPA, the shape of each configuration is represented by a point on the surface of Kendall’s shape space (Kendall, 1984; Rohlf and Slice, 1990; Dryden and Mardia, 1993; Weber and Bookstein, 2011; Goodall, 1991), which, for triangles, has the form of a sphere with unit radius (reflecting the scaling to unit size in GPA). Differences in shape result in differences in location of points representing landmark configurations. The scatter of concentrated points over the surface, which occurs when variations are small, as in this study, can be visualised via a tangent projection (Dryden and Mardia, 1993). This linearises the local space and provides variables (the tangent projected shape coordinates) suitable for subsequent statistical analysis. It is also possible to analyse size and shape jointly using GPA. Either by giving size its full weight, by rescaling GPA coordinates or omitting the scaling step of GPA (size and shape analyses). These methods produce almost identical results when variations are small but all result in larger variances among

larger configurations (O'Higgins and Milne, 2013; O'Higgins, Fitton and Godinho, 2019), or by including the natural logarithm ( $\ln$ ) of centroid size (form analyses) as a column appended to the matrix of shape variables, to account for the effects of size on the covariance matrix (Mitteroecker and Gunz, 2009). The size and shape analysis is suited to the analysis of deformations from FEA and the form analysis (Milne and O'Higgins, 2012), to the statistical analysis of size and shape variation and covariations among and between the samples of human and Neanderthal crania.

### 2.3.2 Principal Component Analysis

To visualise groupings and modes of variation among specimens, ordination methods were used. Principal Component Analysis (PCA) is commonly used as an ordination method in GM studies (Landi and O'Higgins, 2019). PCA is a data reduction method that can summarise, in a few dimensions, the distribution of data that exists in high dimensional space. It extracts principal components (PCs) that successively represent decreasing proportions of overall variance (Zelditch and Moscarella, 2004). PCs are, by convention, sorted according to the percentage of total variance each explains. The morphological features of variation they explain can be visualized by warping the mean along each PC (O'Higgins, 2000; Mitteroecker, Gunz, Windhager, and Schaefer, 2013)

Full GPAs (with scaling), followed by Principal Component analyses, were conducted on the modern human and Neanderthal samples separately using the Evan toolbox (ver. 1.75). These analyses allowed shape variations within each sample to be assessed and visualised. The PCAs were used to determine groupings of specimens to estimate the mean sizes and shapes of crania in each species. In this thesis, the term "infant" was used for the specimens showing no signs of eruption of the first permanent molar (normally appearing around 6 years old, (Sadler, 2003)) which correspond, in this sample, to the specimens strictly below 5 years old (Table 1). In the same way, the term "juvenile" was used to define the specimens between 5 and 17 years old (Table 1). Finally, the adults, in this thesis, correspond to the specimens strictly above 17 years old in Table 1.

### 2.3.3 Multivariate regression analysis

Multivariate regression allows the prediction of specimen shape (dependent variables) for a given value of the independent variable and allows computation of the proportion of total shape variance explained by the independent variable (Drake and

Klingenberg, 2008; Klingenberg, 2013; Klingenberg and Marugán-Lobón, 2013; Landi and O'Higgins, 2019). It was applied here to both the modern human and Neanderthal samples to estimate growth allometry and mean infant and juvenile cranial form as a basis for building the finite element models used in subsequent chapters.

## 2.4 Results

### 2.4.1 Comparison of ontogenetic allometries

In both species, a multivariate regression of craniofacial shape on size was performed using the full samples from infant to adult. The regression vectors for the two species were extracted and the angle between them was computed using R and the packages: “Morpho”, “geomorph” and “stringr” (Schlager, 2017; Baken et al. 2021; Adams et al., 2022; Wickham, 2022). In the shape space, an angle of  $41.3^\circ$  was found between the modern human and Neanderthal ontogenetic allometric vectors. Its significance was calculated using a permutation test, in which species membership was randomly permuted and the angle recalculated. Indeed, one thousand permutations were carried out and the estimated angle between the species was compared with the distribution of permuted angles to assess its significance. The final results confirm an angle of  $41.3^\circ$  between ontogenetic allometric vectors between the samples of modern humans and Neanderthals with a p-value less than 0.01 ( $<0.01$ ).

## 2.4.2 Modern humans

Two PCAs were carried out on the modern human sample, one using the shape coordinates after GPA and the other, the shape coordinates plus the ln of centroid size (form space). The first three PCs are plotted from each analysis in Figures 16 to 19.

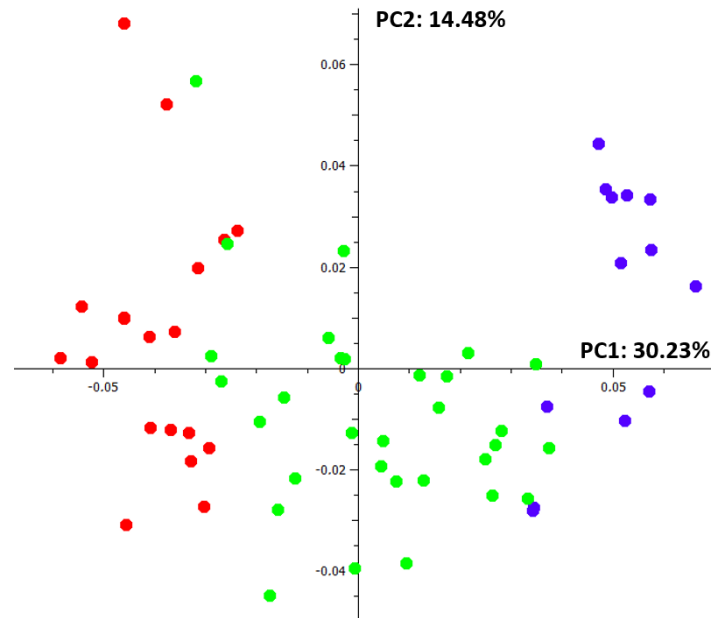


Figure 16. PC1 vs PC2 of shape of the full modern human sample with the infants in blue, juveniles in green and adults in red.

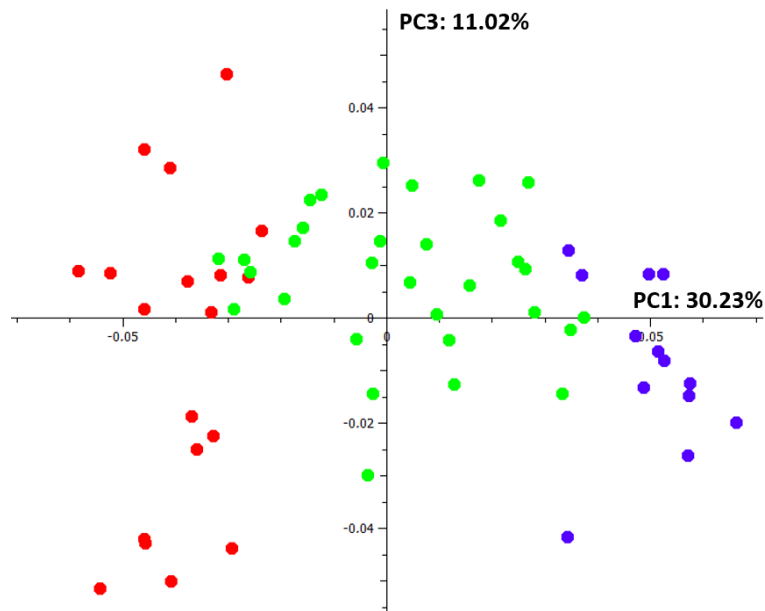


Figure 17. PC1 vs PC3 of shape of the full modern human sample with the infants in blue, juveniles in green and adults in red.

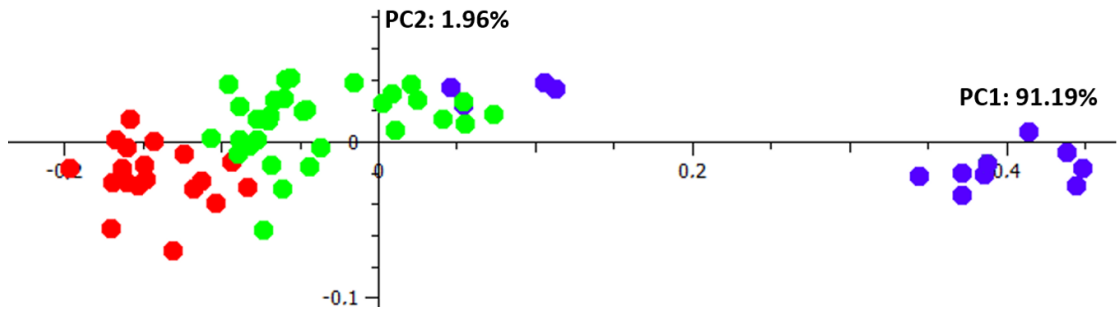


Figure 18. PC1 vs PC2 of form including the full modern human sample with the infants in blue, juveniles in green and adults in red.

In both PC plots, infant, juvenile and adult groups are distributed approximately according to age (known or estimated from dental eruption charts), from left to right on PC1. In the shape analysis PC1 and PC2 together explain 44.71% of the total variance and in form space, they explain 93.15% of the total variance. In the form space analysis

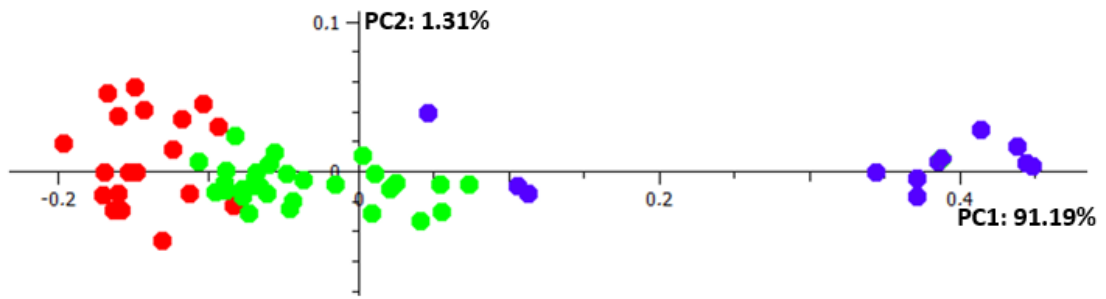


Figure 19. PC1 vs PC3 of form including the full modern human sample with the infants in blue, juveniles in green and adults in red.

differences in ln centroid size and allometric shape changes are represented by PC1. A large discontinuity is evident on PC1 in the infant sample, which lacks infants between the ages of 1 and 3 years, during which period a considerable (~30%) change in cranial centroid size occurs. The centroid sizes of each specimen are presented in Table 4.

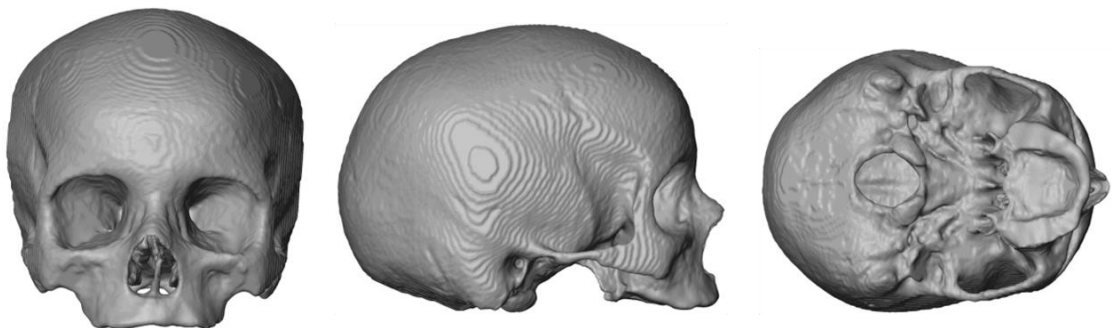


Figure 20. Adult specimen used as a reference surface to estimate the mean infant, juvenile and adult models.

In the PCA of shape (Figures 18 and 19), the distribution of specimens from infant to adult stages is curvilinear, reflecting the shift from predominantly neurocranial to predominantly facial growth in the juvenile stage (Figure 18). Because of this, it was decided to derive representative juvenile and infant surfaces for subsequent FEA from a regression of the (approximately linearly distributed) juvenile and infants alone (see Table 4 for details of this subsample) and to estimate adult size and shape directly through GPA, omitting scaling of adults alone. Alternative approaches to estimating this mean, such as rescaling mean adult shape coordinates or via form space analysis are also possible, but all approaches yield very similar results because variations are small. A modern human adult surface was selected to warp to the mean adult landmark configuration (Figure 20) based on the quality and detail (preservation of thin structures such as the orbits, internal

*Table 4.* Human subsample: 34 infant and juvenile specimens with specimen ID, sex, age category, a description of the stage of dental development, age in years and centroid sizes.

specimen	sex	age_category	Teeth	age	Centroid sizes
BOSMA07	Unknown	Infant	No_teeth_erupted	≤1	843.39
HPN_005	Unknown	Infant	No_teeth_erupted	≤1	793.859
HPN_002	Unknown	Infant	No_teeth_erupted	≤1	854.429
HPN_004	Unknown	Infant	No_teeth_erupted	≤1	799.73
HPN_006	Unknown	Infant	No_teeth_erupted	≤1	853.964
Hum1175	Unknown	Infant	No_teeth_erupted	≤1	817.84
SCH2__	Unknown	Infant	No_teeth_erupted	≤1	789.674
SCH13	Unknown	Infant	M1_in_crypt	≤4	1183.26
UCL_3__	Unknown	Infant	No_teeth_erupted	≤1	840.996
UCL_A23	Unknown	Infant	M1_in_crypt	≤4	1174.57
UCL_C34	Unknown	Infant	No_teeth_erupted	≤1	878.114
UCLA23D	Unknown	Infant	No_teeth_erupt	≤1	1108.29
BOSMA08	Unknown	Infant	deciduous teeth	≤4	1112.84
BOSMA09	Unknown	Juvenile	M1_in_crypt	≤4	1169.35
H-I001_	Unknown	Juvenile	M1_in_Crypt	≤5	1332.51
BOSMA11	Unknown	Juvenile	M1_in_crypt	≤5	1226.13
BOSMA14	Unknown	Juvenile	M1_in_crypt	≤5	1185.34
BOSMA16	Unknown	Juvenile	M1_erupting	≤5	1221.87
BOSMA17	Unknown	Juvenile	M1_in_crypt	≤8	1210.21
BOSMA18	Unknown	Juvenile	M1_almost_erupting	≤5	1291.24
BOSMA19	Unknown	Juvenile	M1_in_crypt	≤8	1259.99
BOSMA20	Unknown	Juvenile	M1_in_crypt	≤5	1150.74
BOSMA21	Unknown	Juvenile	M1_in_crypt	≤5	1170.46
BOSMA22	Unknown	Juvenile	M1_in_crypt	≤5	1231.32
BOSMA23	Unknown	Juvenile	M1_erupted	≤5	1294.12
BOSMA24	Unknown	Juvenile	M1_erupting	≤8	1356.77
SCH4_8y	Unknown	Juvenile	M1_erupting	≤9	1278.11
SCH7_8y	Unknown	Juvenile	M2_in_crypt	≤10	1319.94
SCH7fex	Unknown	Juvenile	C_erupting	≤12	1314.69
SCH39fl	Male	Juvenile	premolars_in_crypt	≤8	1351.63
SCH156y	Unknown	Juvenile	I1_in_Crypt	≤7	1289.59
SCH258y	Female	Juvenile	M2_in_crypt	≤10	1311.93
UCL-A06	Unknown	Juvenile	M1_erupting	≤8	1206.32
UCLA23M	Unknown	Juvenile	M1_erupting	≤8	1309.48

nasal structures and zygomatic arches as well as the completeness of dentition) of the 3D reconstruction (see section 2.1.1).

#### *2.4.2.1 Multivariate regression*

Multivariate regression was used to estimate an infant and a juvenile cranial surface to build finite element models. The eventual aim is to compare the performance of FE models between comparable modern humans and Neanderthals. However, the sampling of modern human infants is biased towards younger ages (Figure 18) and that of Neanderthals is limited to two infants and four juveniles, with a different age distribution to that of modern humans. For this reason, in both species, multivariate regression of shape on centroid size of the infant and juvenile sample described in Table 4 was used to estimate the mean shape coordinates. Centroid size was used rather than age for the regression because shape does not covary linearly with age. Thus, for modern humans, after the regression, the estimated juvenile and infant cranial shapes were scaled to the mean centroid sizes corresponding to an age of 2 to 3 years for the infant model and 8 to 10 years for the juvenile (Table 4). Finally, the adult surface (Figure 20) was warped using Evan Toolbox (v.1.75) to each of these sets of mean coordinates to estimate infant and juvenile human mean surfaces.

## 2.4.3 Neanderthals

### 2.4.3.1 Principal Component Analysis

The Neanderthal sample is much smaller than the modern human and so estimation of infant and juvenile surfaces comparable to those extracted above, for modern humans, involves a greater degree of approximation. As for the modern human sample, principal component analysis of shape all of the Neanderthals was carried out to visualise patterns of variation among specimens and age categories. Figure 21 presents plots of PC1 vs PC2 and PC1 vs PC3. In both, infant, juvenile and adult groups are arranged according to estimated age estimates (from the literature or estimated here using dental eruption charts). PC1 and PC2 together explain 63.75% of the total variance. As with modern humans, there is evidence of curvilinearity in the distribution of specimens from infant to adult.

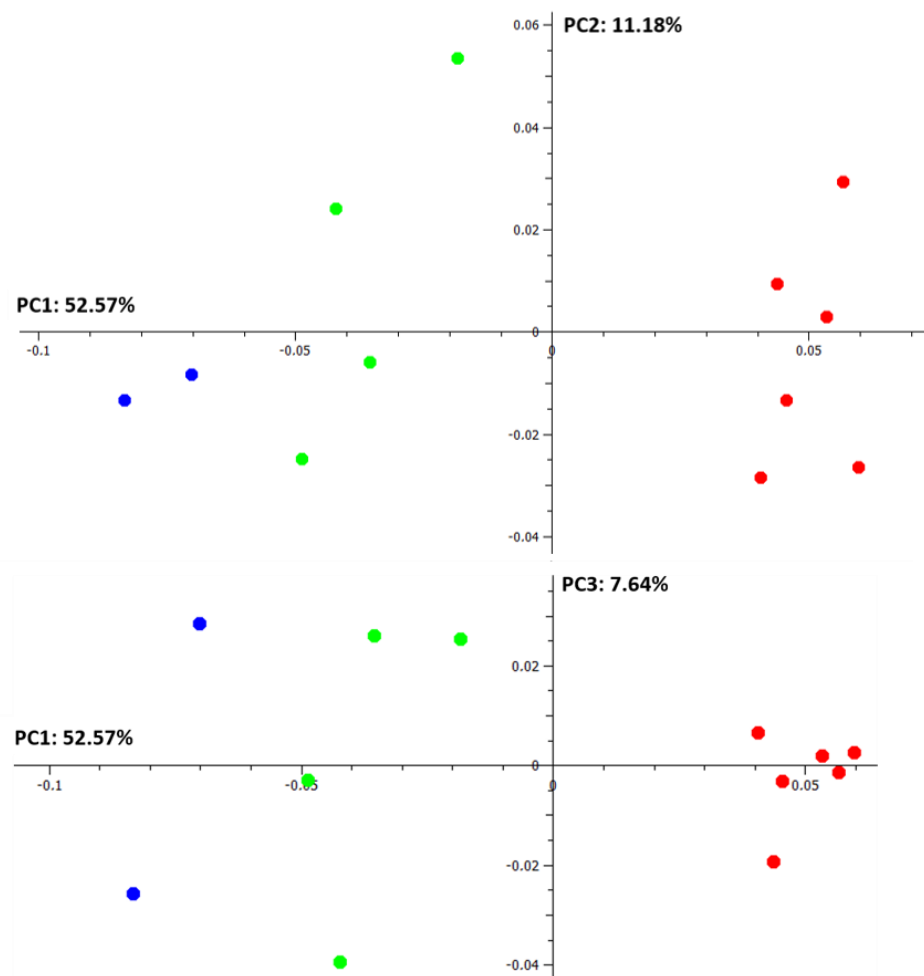


Figure 21. PC1 vs PC2/PC3 in shape space including the full Neanderthal sample with the infants in blue, juveniles in green and adults in red.

The centroid sizes of each specimen are presented in Table 2. The mean adult size and shape was estimated as the mean of the adult sample after a separate GPA omitting scaling. The Gibraltar 1 reconstruction (adult) surface was warped to this mean landmark configuration to estimate the mean adult cranial surface mesh.

Because the distribution of the whole sample appears curvilinear (Figure 21), as was the case with modern humans, and because sampling of subadults is limited, representative juvenile and infant surfaces for subsequent FEA were derived from a multivariate regression of shape on centroid size of the (approximately linearly distributed) juvenile and infants alone. This is the same as was done with modern humans.

#### *2.4.3.2 Multivariate regression analysis*

A multivariate regression of shape on centroid size was conducted on the infant and juvenile sub-sample (Table 2). Via the regression, the mean landmark configurations were estimated at similar infant and juvenile stages to those from the modern human sample based on assessment of dental development/eruption and centroid sizes. The centroid size at which the shape of the Neanderthal infant cranium was extracted was 1145.22 which is close to that of Pech de l'Aze (estimated to be 2-3 years old) and similar to that of the infant modern human model. To extract the juvenile surface the mean centroid size of all the juvenile Neanderthals in the sample was used. The infant and juvenile landmark and semi-landmark configuration shapes were then scaled to the centroid sizes used to extract them (see above). The surface of the reconstructed Gibraltar 1 specimen was then warped to these landmark configurations using Evan Toolbox (v.1.75) to create estimates of the mean cranial surface in Neanderthal infants and juveniles.

#### *2.4.4 The models and their validity*

The Neanderthal and modern human infant, juvenile and adult surfaces were extracted as described above. After warping of surfaces small holes and irregularities were removed using Geomagic® (Studio 2018). This was followed by reflected relabelling and symmetrisation of each of them using the Evan Toolbox v.1.75 (Dryden and Mardia, 1993; Mardia, Bookstein and Moreton, 2005). Finally, the models were converted into volumes and resampled using Avizo 9.0 (FEI Visualization) to create Finite Element models with medium resolution. These are presented in Figures 22 and 23.

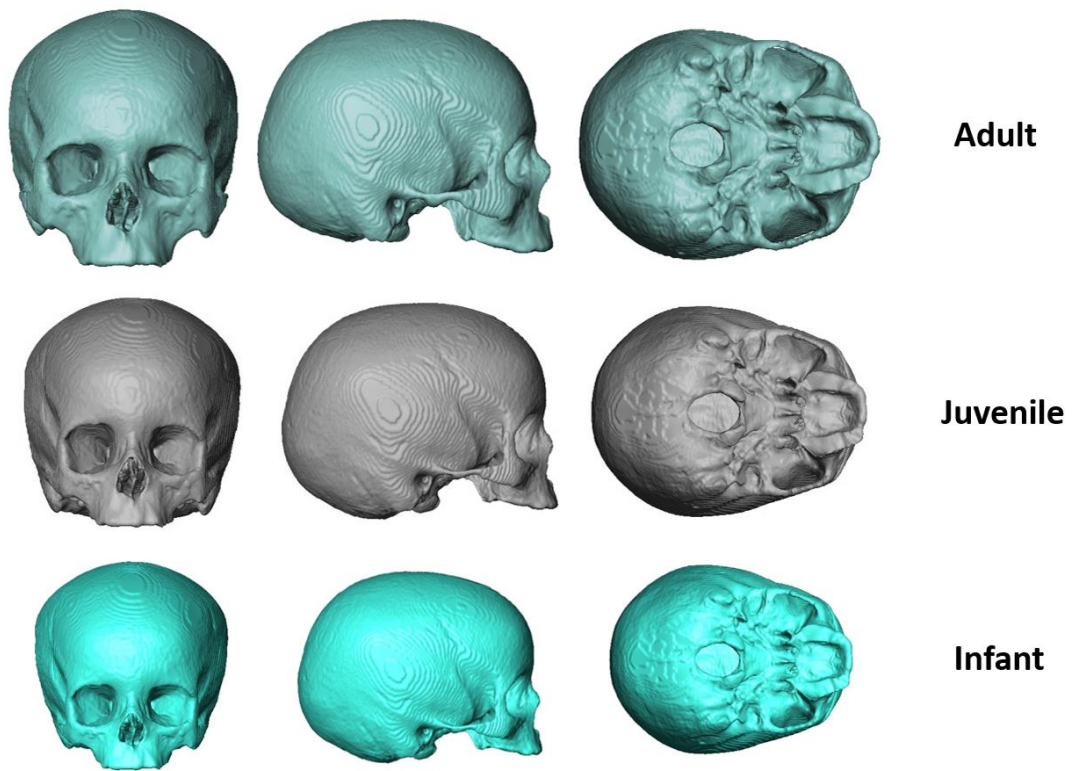


Figure 22. The modern human adult, infant (around 2-3 years old) and juvenile (8-10 years old) models.

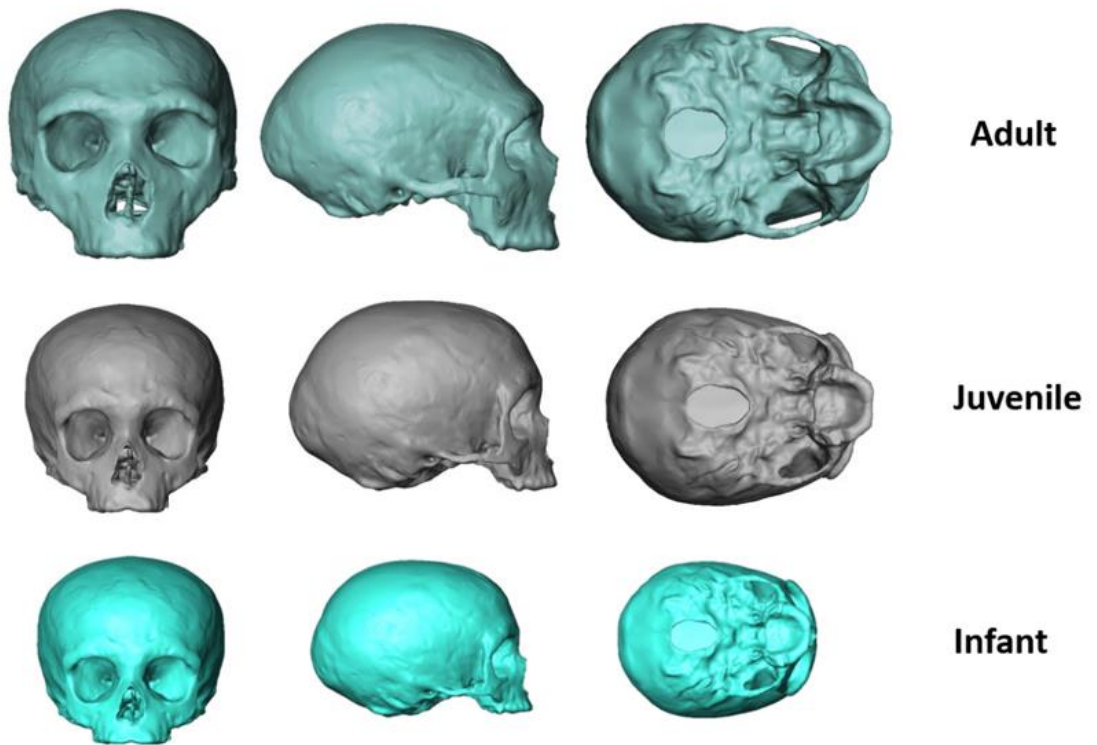
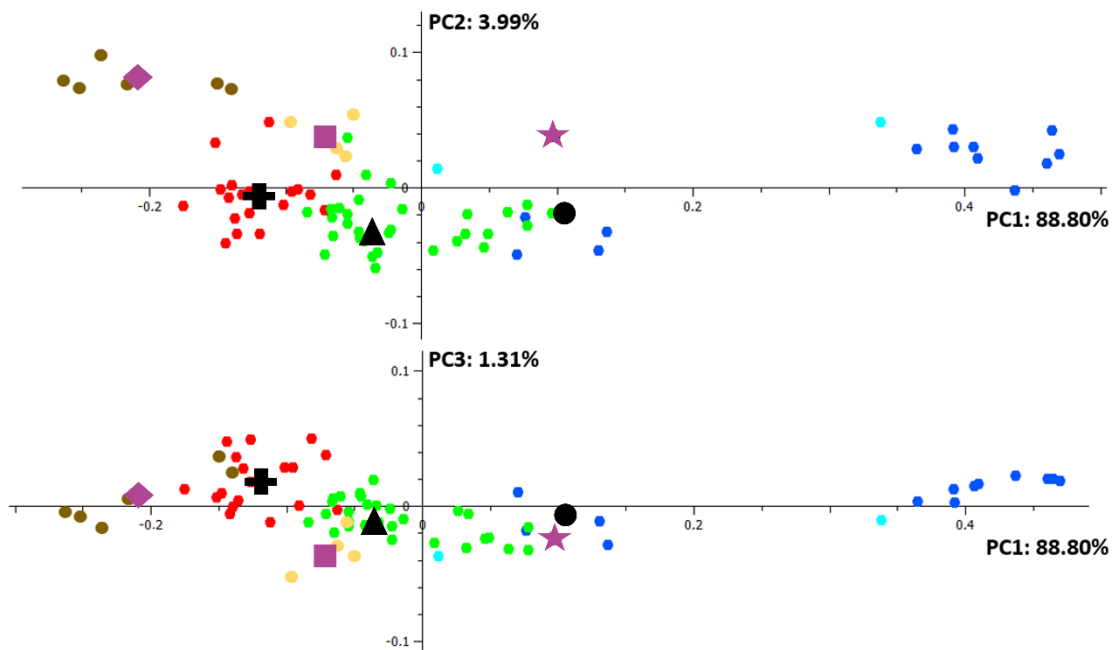


Figure 23. The Neanderthal adult, infant (around 2-3 years old) and juvenile (8-10 years old) models.

To validate these models, in the sense of ensuring that they are reasonable estimates of infant, juvenile and adult cranial form in each species, and comparable, a PCA of form (shape plus ln centroid size) was conducted using the landmarks and semi-landmarks of the Neanderthal and modern human samples and those estimated for infant, juvenile and adult models extracted as described above. Figure 23 presents plots of the first three PCs. The first PC strongly reflects size and allometric shape differences in both species. The infant and juvenile models are similar to each other and each lies within the distribution of the infants and juveniles of their respective species. The modern human mean infant lies towards the negative end of the distribution of modern human infants on PC1 because most of the infants sampled in this study are ~1 year old or less, while the infant model was extracted to represent an individual around 2-3 years old. Similarly, for Neanderthals, only two infant specimens were available, and the extracted infant model lies nearer the older specimen (Pech de l’Aze ~2-3 years old). Both adult models lie centrally within their respective species distributions.



*Figure 24.* PC1 vs PC2/PC3 in form space including the full modern human sample with the infants in dark blue, juveniles in green and adults in red; the full Neanderthal sample with the infants in skyblue, juveniles in yellow and adults in brown. The models are represented with black symbols: modern human infant (circle); modern human juvenile (triangle); modern human adult (cross); Neanderthal infant (purple star); Neanderthal juvenile (purple square); Neanderthal adult (purple diamond).

## 2.5 Discussion

The aim of this study was to use three-dimensional geometric morphometric methods and virtual reconstruction to compare post-natal craniofacial ontogenies by examining Neanderthal and modern human crania ranging from infant to adult and to extract suitable representative models of infants, juveniles and adults for subsequent functional analysis.

The extraction of models as described above required a degree of estimation because of the lack of Neanderthal material that was available for study and because the human sample unevenly represents the post-natal growth period. The models were estimated with the aim of representing infants approximately of 2-3 years of age, juveniles, 8-10 years and adults. The validation PCA demonstrates that these are reasonable estimates, although it is always possible to achieve slightly different estimates using different assumptions and criteria, these models were accepted as appropriate estimates for subsequent comparative functional analyses (see following chapters).

How and to what degree postnatal ontogeny contributes to the generation of differences among adults of mammalian species, including species of *Homo*, is highly debated. Until recently, a common view has been that morphological diversification is principally grounded in pre-natal ontogenetic modification, whereas post-natal ontogenies are rather similar among mammals except for heterochronic modifications (Klingenberg, McIntyre and Zaklan, 1998; Klingenberg and McIntyre, 1998). With the emergence of novel geometric morphometric and multivariate analyses, more detailed analyses of the ontogeny of differences have been conducted, providing new insights (O'Higgins and Jones, 1998; Cobb and O'Higgins, 2004; O'Higgins, Chadfield and Jones, 2001).

Modern humans and Neanderthals present clear differences in skull architecture and these are present at an early stage in these two species (Trinkaus, 2005; Franciscus, 1999). However, it is still unclear if postnatal ontogeny further accentuates the differences between adults, and if so, to what degree. Numerous studies have argued that most of the morphological differences between *Homo sapiens* and Neanderthals are established prenatally and carried into adulthood along parallel trajectories of shape transformation (Ponce de León and Zollikofer, 2001a). Nonetheless, whether ontogenetic trajectories are parallel or not, and if post-natal facial ontogeny in Neanderthals is also characterized by higher rates of growth and shape transformation at an early stage are still debated (Ponce

de León and Zollikofer, 2001a; Ramirez Rozzi and Bermudez De Castro, 2004). One hypothesis is that *H. sapiens* and Neanderthals share the same spatio-temporal pattern of growth and development among cranial components, with the latter being simply “overgrown” (hypermorphic) with respect to modern humans. In this scenario, an extension of allometry in Neanderthals relative to modern humans is hypothesised (hypermorphosis; Zollikofer and de León, 2001; Ramirez Rozzi and Bermudez De Castro, 2004; Smith et al., 2007a; Gunz et al., 2010; Tallman, 2016), with differences between these two species being established in the prenatal and early postnatal period with postnatal growth (changes in size) being associated with similar or identical allometric development of shape, but to varying degrees. The PCA of Figure 21 clearly shows that adult Neanderthals lie beyond adult modern humans on PC1, which largely reflects aspects of ontogenetic allometry, and so supports the view that Neanderthals are hypermorphic with respect to modern humans. Additionally, on these first two PCs the allometric trajectories of these species appear parallel.

However, all these studies were conducted with limited samples and examined limited craniofacial regions, and the studies claiming parallel postnatal ontogenies have been criticised for not taking account of the entire dimensionality of the shape space (Bastir, O’Higgins and Rosas, 2007).

Thus, in this study, despite the appearance of parallel ontogenetic trajectories, a multivariate regression analyses comparing ontogenetic allometric vectors between the two species, using the full dimensionality of the data (Table 4) indicates that these are significantly divergent between the modern human and Neanderthal samples. Therefore, the hypothesis of a parallel ontogenetic trajectory is rejected, but a note of caution is required. The infant Neanderthal sample is very small and better sampling of Neanderthals in general and of this age group in particular might change this result. It contrasts with previous findings that suggested the two species follow identical patterns of allometric development (Ponce de León and Zollikofer, 2001b; Ackermann and Krovitz, 2002). However, it agrees with that of Bastir et al (2007) who by using geometric morphometric regression and principal component analyses, found a significant divergence of 44 degrees in the trajectories of growth and development of the mandible of *H. sapiens* and Neanderthals. These studies suggest that post-natal, as much as prenatal transformations, are responsible for differences between these two species. In the same way, they agree with other studies that have analysed patterns of tooth eruption in both species, showing

that Neanderthals do not simply have a more prolonged period of growth and development but that they also show accelerated dental eruption, potentially accompanied by more rapid size and shape changes in the cranium when compared to individuals of *H. sapiens* that are presumed to be of a similar age (Macchiarelli et al., 2013; Smith et al., 2007a).

Additionally, within modern humans, differences in postnatal craniofacial allometries have been identified among different human populations (Vioarsdóttir, O'Higgins and Stringer, 2002). Such differences likely arise because of differences in the growth of localised regions and structures and the interactions between them. Indeed, many studies have addressed interactions among the cranial base, neurocranium and mandible and the influence of these on human craniofacial development (Barbeito-Andrés et al., 2015; Bastir, Rosas and O'higgins, 2006; Enlow, 1979; Lieberman, McBratney and Krovitz, 2002; Richtsmeier and DeLeon, 2009; Singh et al., 2012; Zollikofer, Bienvenu and Ponce de León, 2017). These studies suggest a hierarchy of interactions among craniofacial components in driving the post-natal growth and development of the human face. Variations in these interactions could explain differences in ontogenetic trajectories among species and age classes.

A recent study using path analysis on craniofacial skeletal components has shown that from 0 to 6 years of age, the anterior septal and subnasal height have the greatest and most consistent interactions with facial height (Landi et al., 2021). These results support the hypothesis that the nasal septum has a significant influence on early post-natal human facial growth (Al Dayeh et al., 2013; Goergen, Holton and Grünheid, 2017; Hall and Precious, 2013; Holton et al., 2011; Verwoerd and Verwoerd-Verhoef, 2007; Wong, Filatov and Kibblewhite, 2010; Holton, Yokley and Figueroa, 2012). When looking at the soft tissues, the same study found that the tongue and masseter tend to affect skeletal components associated with masticatory system loading such as the subnasal region (Landi et al., 2021). Therefore, spatially and throughout ontogeny, the balance between cartilaginous and soft tissue influences on facial growth appears to change.

It would be of interest to investigate if the interactions among cranial and facial components change significantly and show differences between modern humans and Neanderthals during post-natal ontogeny, but very large and well-preserved samples are needed to tease out statistical interactions. However, divergence of ontogenetic allometric

trajectories between Neanderthals and modern humans could reflect differences in patterns and magnitudes of integration among the facial regions of these two species. Such differences in interactions might underlie the differences in morphology and, potentially, differences in function (e.g., masticatory system loading and load resistance) during ontogeny.

Ontogenetic differences in patterns of facial bone remodeling are known to exist between Neanderthals and modern humans (Lacruz et al., 2015b; Martinez-Maza et al., 2011; Martinez-Maza, Rosas and Nieto-Díaz, 2013). Thus, Neanderthals present extensive bone deposition over the maxilla at all ages while bone resorption is mainly found at the anterior maxilla in modern humans between 1 to 4 years old (Schuh et al., 2019). These differences between the two species are said to reflect and possibly underlie, differences in their craniofacial growth trajectories (O'Higgins et al., 2012).

It is of interest to understand if such remodeling differences are the result of differences in how masticatory system loads are generated and resisted in these species or arise because of other factors. To these ends, the representative infant, juvenile and adult models of these two species produced in this chapter are used in subsequent chapters to simulate and compare biting and peak bite force resistance in modern humans and Neanderthals at different stages of postnatal ontogeny.

## 3.0 Biting simulations in modern humans

### 3.1 Introduction

In this chapter the 3D models representing a human infant, juvenile and adult from Chapter 2 are used to estimate the action and mechanical advantages of masticatory muscles acting to generate biting forces at the incisors and last premolar (infants) or first molar (juveniles and adults). They are then used as the basis for construction of finite element models simulating these bites (using Vox-FE). The results of these analyses and biting simulations (biting forces, cranial deformations and resulting strains) are reported and compared between age stages.

The aim of these analyses is to test the second hypothesis of this thesis: that there are no ontogenetic changes in cranial load resistance in modern humans. This hypothesis will be tested by qualitatively and quantitatively comparing load resistance (deformations and resulting strains) in finite element models representing different post-natal stages based on the surfaces of infant, juvenile and adult human crania derived in the previous chapter. The results of these analyses will later be compared with the results of similar analyses in Neanderthals and related to differences in craniofacial growth, development and remodeling

### 3.2 Materials and methods

#### 3.2.1 Finite element models

Finite element analysis (FEA) is a widely used numerical tool for solving complex engineering and mathematical problems (Logan, 2016). FEA has increasingly been applied in biology to study skeletal biomechanics. In palaeoanthropology, this tool has been used in studies of craniofacial biomechanics and biting performance among hominins (Smith et al., 2015a; Wood et al., 2011; Strait et al., 2007, 2009, 2010; Godinho et al., 2018; Ledogar et al., 2016). FEA of the craniofacial complex, including simulation of biting, involves three major steps. First, is the creation of the 3D models with the allocation of bone material properties (Toro-Ibacache et al., 2016). Then, these models are loaded to simulate muscle attachments, lines of action and forces. Constraints are applied at biting points and joints to fix the cranium in space (O'Higgins et al., 2012, 2011; Godinho et al., 2018). Finally, the post-processing step consists of the interpretation of the results. This section presents the different steps related to this study.

### 3.2.1.1 Model creation

Three FE models were created in Vox-FE, a custom FEA pre- and postprocessing voxel-based software tool (Fagan et al., 2007; Liu et al., 2012), from the three representative surfaces extracted from the human growth model. These represent modern humans at different age stages (infant, juvenile and adult) but lack teeth. The first step in the process of FE model creation was to allocate one tooth set to each mean surface. Previous FE studies conducted on another modern human cranium (Godinho et al., 2018) have shown that differences in tooth type affect the magnitude of strains on a loaded model but not the general location of regions of high and low strain. A similar sensitivity test was conducted in the present study with the Neanderthal adult model to assess the effects of using human teeth (see Appendix 3 and Chapter 4, for details of sensitivity tests on tooth choice). Dentition was chosen from adult and infant individuals: adult teeth excluding the third molar ( $M^3$ ); adult teeth from the central incisor to the first permanent molar 1 ( $M^1$ ) for the juvenile (due to the lack of high-resolution CT images of juvenile teeth) and, finally; deciduous teeth from the central incisor ( $RI^1$ ) to the deciduous molar 2 ( $RdM^2$ ). For each model, the teeth placed on the mean surfaces were segmented and isolated from the rest of the ‘donor’ skull. Only the right upper dentition was segmented and Geomagic® (Studio 2018) was used to mirror the teeth to create a left side. This ensured symmetry for biting simulations. These virtual teeth were warped onto the three surfaces using Avizo 9.0 (FEI Visualization) using 6 landmarks on the alveolar process (Figure 25) and then merged and cleaned using the “mesh” doctor” tool from Geomagic® (Studio 2018). The models were segmented as a single material (eventually allocated the material properties of bone, see below) and the frontal and maxillary sinuses were filled with the same material, because in fossils the sinus is not easily segmented and prior studies have indicated that filling of the sinuses has little effect on how the cranium resists strains (Toro-Ibacache, Zapata Muñoz and O’Higgins, 2016; see Appendix 2). Points of contact between the teeth were removed by manual segmentation to ensure that the cranium is not stiffened by these and that loads applied to any tooth are not distributed to adjacent ones. The final three surfaces were converted into a volume stack using Avizo 9.0 (FEI Visualization) resampled an isometric voxel size of 0.30 mm for the infant, 0.40 mm for the juvenile and 0.40 mm for the adult. Then, these were converted into a mesh for FEA (voxel-based model-cubic mesh as used by Vox-FE) using the vox3mat software tool.

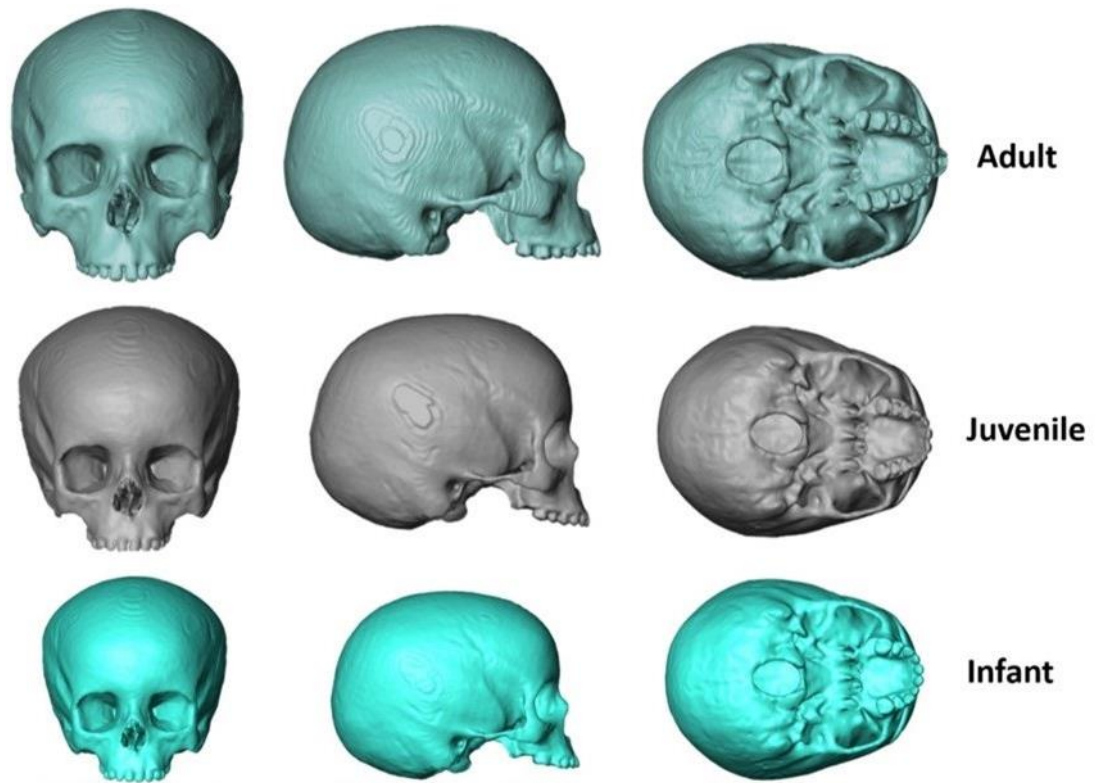


Figure 25. Adult, juvenile and infant mean models with the corresponding teeth.

### 3.2.1.2 Finite element parameters

#### 3.2.1.2.1 Muscle loads

The loads were applied in the same way for each of the three models. They were applied directly to the nodes of the voxel elements representing the regions of attachment of muscles included in the FE model for all biting simulations (see Supplementary materials Figure 2). The nodes representing the muscle attachments were ‘painted’ (allocated) over the relevant surfaces of the models using the Node Selection Tool in Vox-FE. The muscles used in these experiments and the applied forces used here are the same as those used in previous FEA studies of modern humans and hominins, using the same software (Toro-Ibacache and O’Higgins, 2016; Godinho et al., 2018). The maximum muscle forces were estimated from a CT scan (not by bone proxies) of a fully preserved head adult modern human (with all the masticatory muscles present) by estimating the muscle cross-sectional areas (Toro-Ibacache et al, 2016a). The details are given in Table 5. Muscle forces were applied to the models in Vox-FE using the Force Property Editor tool which allows the user to define the origins and end points of the muscle forces. The origins are the mean coordinates of all the nodes selected for each muscle and the end points of the

muscle force vectors (the muscle insertions on the mandible), were defined using landmarks defined in Avizo 9.0 (FEI Visualization) and imported into Vox-FE. Muscle forces were applied as parallel muscle forces in Vox-FE and the forces were evenly distributed over all the nodes using the Area option of the software. (see Supplementary materials, Figure 2). These directions of muscle force vectors were estimated based on the insertions of muscles on a modern human mandible which was warped to each mean cranium (adult, juvenile and infant). They were applied as parallel muscle forces in Vox-FE and the forces were evenly distributed over all the nodes using the Area option of the software (see Supplemental Material Figure 2). These forces are not physiological because muscle activations and forces change throughout life, from one bite point to another (chewing cycles are different) and between modern humans and Neanderthals (Toro-Ibacache and O’Higgins, 2016; Kamegai et al., 2005; Usui et al., 2007; Edmonds and Glowacka, 2020; O’Connor, Franciscus and Holton, 2005; Eng et al., 2013). However, by keeping the forces constant among the models and bites, comparability between models and bites is maintained. Because applied muscle forces are the same in all models, differences in deformations and principal strains are due to differences in the sizes and shapes of the crania and differences in muscle vectors. Size differences are marked between infant and adult crania, and these were accounted for by scaling principal strains according to the ratio of squares of centroid sizes (see section 3.4.1, Dumont, Grosse and Slater; 2009). Additionally, differences in biting forces between infant and adult were accounted for by post-analysis scaling of strains (see later) by the ratio of biting forces experienced by each model (Godinho et al., 2018). For each biting simulation, similar lines of muscle action to those used by Godinho et al., (2018) in their study of *Homo sapiens* and Broken Hill were allocated. Previous studies (Ross, 2005; Bright and Rayfield, 2011; Fitton et al., 2012; Toro-Ibacache et al., 2016; Godinho et al., 2018) have shown that varying muscle vectors by a few degrees (as occurs between models in this study) or varying relative forces among muscles within reasonable limits (which affect net vectors) have a limited impact on the results of FEA (Bright, and Rayfield, 2011; Godinho et al., 2018; Ross, 2005; Toro-Ibacache, Fitton, Fagan, and O’Higgins, 2016; Toro-Ibacache, Zapata Muñoz, and O’Higgins, 2016).

*Table 5.* Applied muscle forces (in Newtons, N). The muscle forces were estimated for all the masticatory muscles in a previous study (Toro-Ibacache et al., 2016a) from muscle cross-sectional areas using the CT scans of a fully preserved *H. sapiens* cadaveric head.

	<b>Left</b>	<b>Right</b>
<b>Temporalis</b>	168.02	170.67
<b>Masseter</b>	134.06	124.01
<b>Medial pterygoid</b>	124.01	117.49

#### 3.2.1.2.2 Constraints

Constraints were applied at both temporomandibular joints (TMJ) in the x, y and z-axes of each model. These constraints are necessary to prevent models from rotating when loaded (Godinho et al., 2018). Other constraints, comprising 30 nodes, constrained in the vertical z direction, were applied at the teeth to simulate biting (RP<sup>2</sup>/RdM<sup>2</sup> and RI<sup>1</sup>).

#### 3.2.1.2.3 Material properties

In all models, the cranial bones and teeth were allocated material properties, typical of bone, with a Young's modulus of 17 GPa and Poisson's ratio of 0.3. This was because the models were simplified, making the bone entirely solid (no diploe/no paranasal sinuses) to allow comparability with Neanderthals where details of sinus and internal bone structure are lacking (see Appendix 2 for sensitivity study). This also facilitates the repair of dentition and the addition of the dentition to warped models because the teeth have the same material properties as bone and so the roots do not need to be considered. Prior validation and sensitivity studies have investigated the effects of building models in this way (Dechow, Nail, Schwartz-Dabney, and Ashman, 1993; Fitton, Prôa, Rowland, Toro-Ibacache, and O'Higgins, 2015; Godinho, Toro-Ibacache, Fitton, and O'Higgins, 2017; Schwartz-Dabney and Dechow, 2003; Toro-Ibacache, Fitton, et al., 2016). These studies have shown that these models allow comparison of the distributions of strains among similarly simplified models but they underestimate the degree of deformation and the magnitude of strains. Moreover, by using the same conditions (material properties, constraints and muscle loads) for each model (infant, juvenile and adult), it is possible to directly compare deformations and strains with those from prior studies using similar parameters (Godinho et al., 2018, 2017).

#### 3.2.1.2.4 Scalings

The FEA results from these analyses do not take into account of differences in applied forces. The results indicate how identical muscle forces translate into bite and

joint reaction forces, strains and cranial deformations. However, in reality, the skulls experience different muscle forces and so, achieve peak bite forces that differ because of differences in these and in form (size and shape). To compare performance, it is, therefore, necessary to take differences in forces into account. Further, if forces do not differ between crania, but the size of the cranium is bigger, strains will be lower and vice versa. Thus, the strains experienced by the crania, were scaled according to i) peak bite forces (Table 6), because applied muscle forces are unknown, especially in Neanderthals; see Table 6 and ii) size differences (Dumont, Grosse and Slater, 2009).

Differences in size between models (Table 6) were taken into account by scaling principal strain magnitudes (see below section 3.4.3) according to the recommendation of Dumont, Grosse and Slater (2009). They showed that when comparing two Finite Element models presenting the same shape but different size, strains are inversely proportional to surface area. This was confirmed in a validation study conducted at York by Ricardo Godinho and Paul O'Higgins (unpublished). Two skull models were built from one adult modern human specimen with the same number of voxels but with different voxel sizes. The first model has voxel size of 0.35 mm and the second model a voxel size of 0.70 mm (double the size of the first). Both models were loaded in a similar way to the models in this thesis with the same material properties and muscle loads. These were applied directly to the nodes of the voxel elements representing the regions of attachment of muscles (temporalis, masseter and medial pterygoid) included in the FE models and a left first incisor biting simulation was conducted. Principal strains 1 and 3 were extracted from the two loaded models using 69 landmarks located around both craniofacial complexes. The study showed that model 1 (0.35 mm voxel size) experienced higher strains than model 2 (with double the voxel size; 0.7mm =side length) of model 1. The resulting principal strains were exactly inversely proportional to the square of centroid size (Figure 26).

When models have the same shape (geometry ignoring scaling), the effects of scaling on stresses can be corrected for by scaling to surface area or,  $\text{length}^2$  or  $\text{volume}^{2/3}$ . Strains can also be scaled in this way in the FE models in this thesis because they have homogeneous material properties. Dumont, Grosse and Slater (2009) observed that when two models present different shapes, they do not necessarily have the same surface area to volume ratios and thus stresses are no longer proportional to the load. Therefore, they

recommend that the surface area should be used to scale stresses and strains (in models with homogenous material properties as in this thesis).

However, when shape/geometry differs between models their mechanical behaviour will also be different, irrespective of differences in size. The extent to which their behaviour differs will depend on the degree to which and how they differ in shape. It is quite possible for surface area to decrease between otherwise identical models (e.g., by filling sinuses or replacing cancellous bone with a homogenous material) while locally decreasing strains (Fitton et al., 2015 and see Appendix 2). In this example, while area decreases, centroid size is unaltered and volume increases. Similarly, surface area can differ between models, with little or no effect on strains as was the case in a recent study of the impact of reducing the size of the large brow ridges of *Homo heidelbergensis* (Godinho, Spikins and O'Higgins). In this case, with smaller browridges, centroid size and volume also decrease. In these examples surface area, length and volume differ in different ways between models. Scaling by surface area does not exactly correct for size because not all surface regions contribute to the same degree to load resistance and likewise, scaling by centroid size<sup>2</sup> or volume<sup>2/3</sup> is inexact.

While these are extreme examples, the same applies to more subtle differences in geometry. Estimates of model size based on surface area or, length<sup>2</sup> or volume<sup>2/3</sup> will deviate from each other depending on the extent of differences in shape. Different choices of variables as the basis of scaling will give different results. Using area to scale stresses in models with filled-in sinuses (area is smaller) to the same 'size' (=area) as models with unfilled sinuses would result in all stresses becoming smaller in the filled model after scaling (increasing its area to match that of the unfilled model), while using length<sup>2</sup> (unchanged) would leave them unaltered and volume<sup>2/3</sup> (increased in the filled model) would result in larger scaled stresses. These differences are because all measures of size (area, length, volume) interact with shape and so all are affected by shape change. Further, mechanical performance may be affected by shape.

In this thesis, contour plots and principal strains 1 and 3 were scaled using the ratio of squared centroid sizes between models rather than surface area or volume<sup>2/3</sup> because measurement of surface areas and volumes can be difficult to obtain reliably on complex structures such as skulls because results may vary depending on the methods used to image, segment and reconstruct models. Centroid size is arguably less sensitive

to errors due to differences in image resolution, segmentation and reconstruction because differences in finer details of structure will likely impact estimates of area more than landmark coordinates. Further, centroid size is derived from many landmarks and so is much less sensitive to localised shape differences than any single length. The same landmark (57) and semilandmark (246) configuration (Figure 14 and Figure 15) was used in all models. This configuration was designed to capture craniofacial shape differences among the models (indeed it was used to warp and create the models, see section 2.4.4). Thus, scaling by centroid size is based on a consistent set of landmarks and semi-landmarks for all models. For easier reading of this thesis, we will call this scaling, scaling by size (square centroid size, square cs).

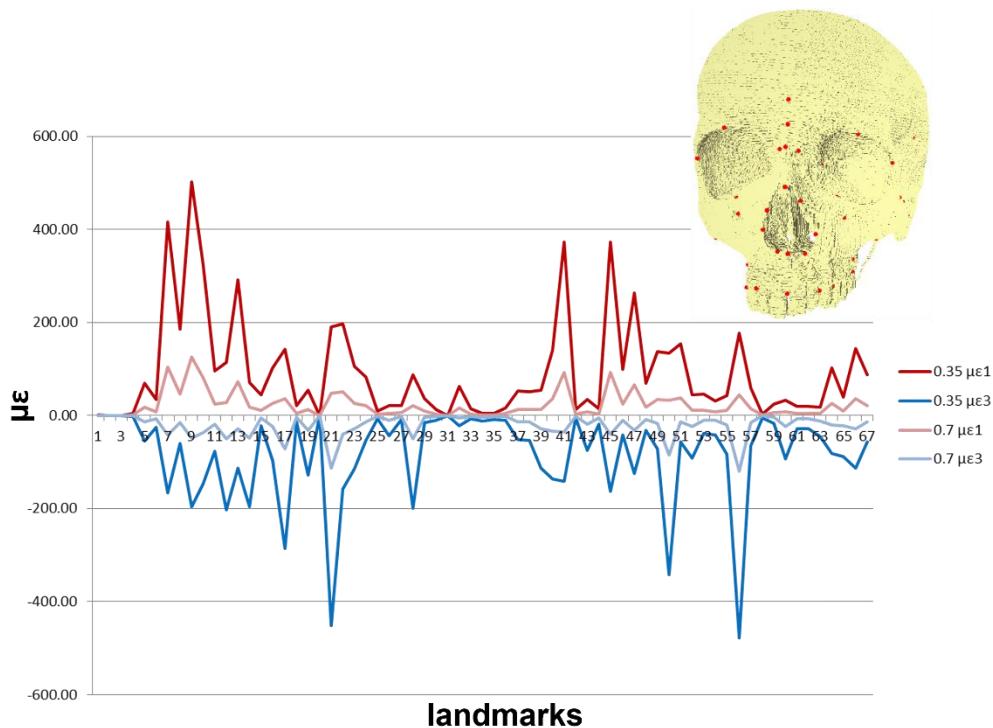


*Figure 26.* Strains experienced by FE model 1 (0.35) and model 2 (0.70) at the 69 sampling points over the face during the LI<sup>1</sup> biting simulations. The tensile (red and pink) and compressive (light blue and dark blue) strains in each model are unscaled and at each landmark the ratio between them is exactly the ratio of squared centroid sizes of each model ( $1^2 : 2^2 = 1:4$ ). From an unpublished validation study conducted by Ricardo Godinho and Paul O’Higgins.

In the same way, it is important to determine how differences in size and force impact the magnitude of overall deformation as assessed by size and shape distances calculated using GMM approaches. As previous studies show (Godinho, Spikins and

O’Higgins, 2018; O’Higgins and Milne, 2013), Procrustes size and shape distances between identically shaped unloaded and loaded models of different size scales inversely with lengths (such as centroid size) and directly with force. Thus, ratios of centroid sizes or forces were used to scale the size and shape distances (and so, the resulting PCAs) of loaded and unloaded models. The above studies also showed that Procrustes shape distances scale with the ratio of squared centroid sizes but this scaling was not applied in the present study because deformations due to loading comprise both size and shape changes and there is no justification for ignoring the size changes.

*Table 6.* Centroid sizes of the modern human infant, juvenile and adult models. Maximum bite reaction forces (Peak bite force) generated by the infant, juvenile and adult models and calculated for the right first incisor (RI<sup>1</sup>) and right second premolar and second deciduous molar bite points (RP<sup>2</sup>/RdM<sup>2</sup>) in Newton (N).

	<b>Modern human</b>		
	<b>Centroid size</b>	<b>Peak bite force (RI<sup>1</sup>)</b>	<b>Peak bite force (RP<sup>2</sup>/RdM<sup>2</sup>)</b>
<b>Infant</b>	1139.63	262	399
<b>Juvenile</b>	1311.38	271	379
<b>Adult</b>	1414.24	256	354

### 3.2.2 Mechanical advantages and peak bite forces

Mechanical advantages (MA: ratio of force out, to force in) were calculated for the jaw adductor muscles (temporalis, masseter and medial pterygoid) based on 3D landmarks on the mean modern human infant, juvenile and adult models (Figure 27). Landmarking of these models was based on their surfaces using Avizo 9.0 (FEI Visualization). To estimate the insertion of the temporalis, masseter and pterygoid in modern human models, an age-appropriate modern human mandible was scaled on each model. In order to estimate and bracket the mechanical advantages of the temporalis and masseter muscles, these were calculated for their most anterior and posterior points of origin. For temporalis, the methodology of a previous study was followed, and so, a third (intermediate) line of action was also defined, approximately in the centre line of the muscle, where it bulges and reaches its most superior point (Godinho et al., 2018). The in-lever arms were calculated as the perpendicular distance from the fulcrum to the respective muscle line of

action (Figure 27). The out-lever arms for the right incisor and second premolar or deciduous molar bite were calculated as the perpendicular distance from the fulcrum to the vector of the peak bite force applied as according to O'Connor et al., (2005).

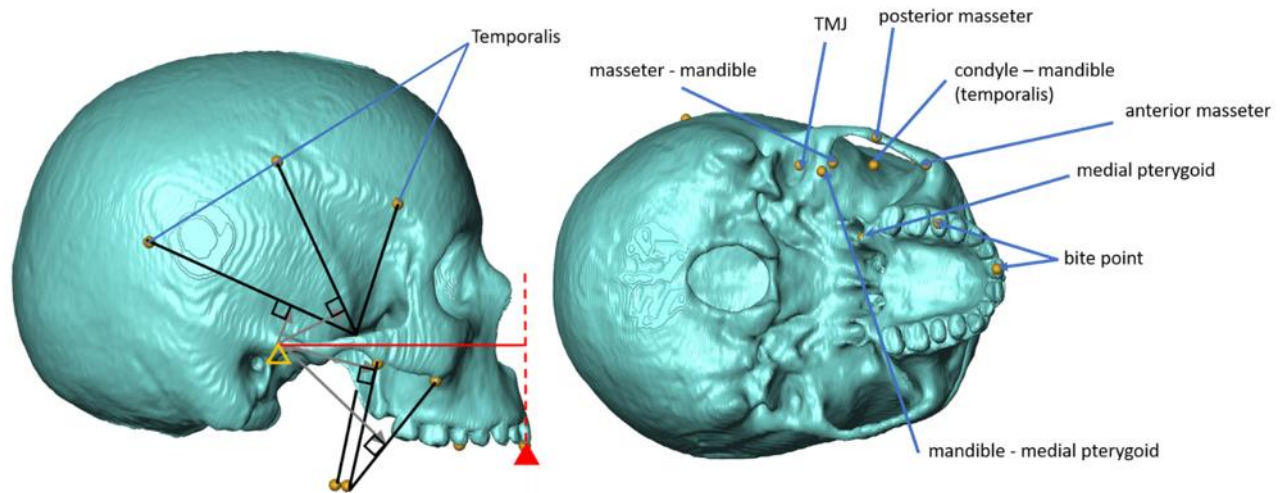


*Figure 27.* To calculate the mechanical advantage for the mean infant, juvenile and adult in both species, the landmarks defined to guide the placement of muscle vectors for FEA were used to calculate the muscle in-lever arms (temporalis, masseter and medial pterygoid lines of action shown by black solid lines). The in-lever arms were calculated as the perpendicular distances from the fulcrum (TMJ/glenoid fossa) to the respective muscle line of action (examples indicated by grey lines). The out-lever arms were calculated as the perpendicular distance from the fulcrum to the vector of the peak bite force applied (red dotted line). The open triangle indicates the fulcrum and the constraint at the glenoid fossa. The solid triangles represent the constraints at the bite points.

Peak bite forces ( $F_b$ ) were calculated from the reaction forces at the bite points of the finite element models in the mean modern human infant, juvenile and adult. Force production efficiency was assessed for each model in terms of two ratios: the proportion of net applied muscle force converted into peak bite force (peak bite force production efficiency) and the proportion that contributes to reaction forces at the fulcrum of the glenoid fossa (Figure 27). These are calculated following the definition given by Godinho et al., (2018) as the ratio of the peak bite force and net muscle force applied ( $F_b/F_m$ ) and the ratio of the summed reaction forces at the glenoid fossae and net muscle force applied ( $F_c/F_m$ ; Antón, 1990; O'Connor, Franciscus and Holton, 2005). The reaction force at the glenoid fossa was calculated in Vox-FE in each model ( $F_c$ ). In the same way, following Godinho et al., (2018), the term “net muscle force” is applied here to the sum of all reaction forces at the constrained nodes on the teeth and glenoid fossa ( $F_m$ ). It differs from the total muscle force due to the orientation of the muscle force vectors. It should be noted

that the maximal bite forces estimated by the FEA are referred to as ‘peak bite forces’ throughout for consistency.

### 3.3 Model solution and data analysis

Simulated bites in the three FE models representing infant, juvenile and adult modern humans were solved using Vox-FE. Over surfaces there are three strains reported by vox FE,  $\epsilon_1$ -3, the first is normally tensile, and the third is normally compressive. The second is indeterminate because the surface only has two dimensions. The resulting tensile ( $\epsilon_1$ ) and compressive ( $\epsilon_3$ ) strain contour maps were visually compared. Additionally, the surface strain (tensile and compressive) magnitudes at 126 matched points distributed along the midface and supraorbital (Figure 28) were plotted and quantitatively compared. These points were symmetrically sited on each model using reflected relabelling carried out using the R package “Morpho” (Schlager, 2017).

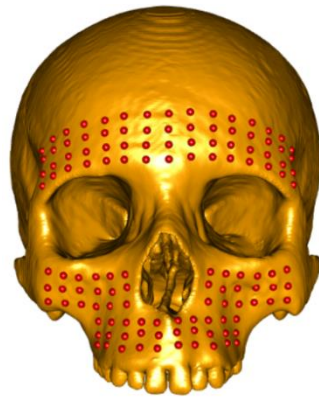


Figure 28. 126 points used to extract the surface strain magnitudes from the solved Finite Element models.

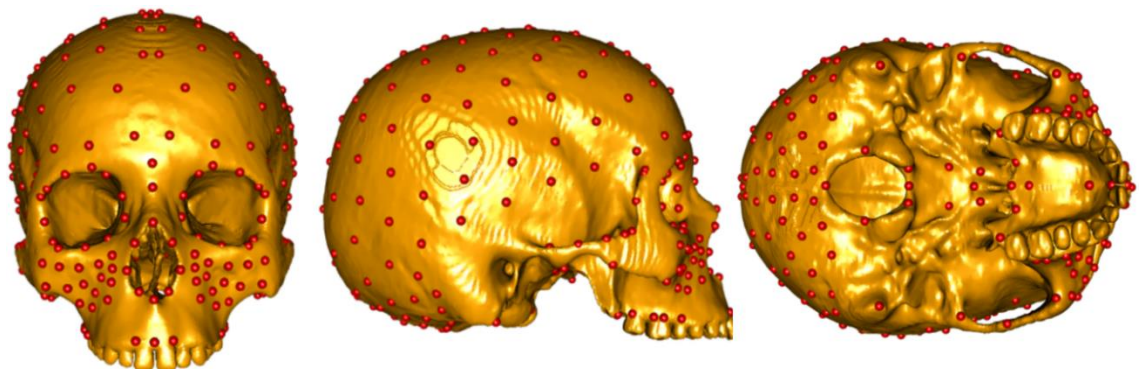


Figure 29. Landmark and semi-landmark configurations used to calculate the deformation of the cranium in each model after loading at the right first incisor ( $RI^1$ ) and right premolar 2 ( $RP^2$ ) or deciduous molar 2 ( $RdM^2$ ). Note: The teeth were added to the cranium after warping to estimate age means, so are not perfectly aligned with the landmarks.

Finally, the modes of global deformation (changes in size and shape due to loading) relative to the unloaded mean (of the infant, juvenile and adult models) were compared among the models. This was achieved through geometric morphometric (GM) analyses of 303 landmarks and semi-landmarks (from the post-natal growth model) located

over the cranium (see Figure 29 for the landmark and semi-landmark configuration). The approach is the same as was used in previous similar studies (O’Higgins et al., 2011, 2012; Milne and O’Higgins, 2012; O’Higgins and Milne, 2013; Godinho et al., 2018). First, a GPA of the landmarks and semi-landmarks from all unloaded and loaded crania is carried out to remove differences in size, location and rotation. Next, size is reintroduced by multiplying the shape coordinates of each loaded and unloaded model by its centroid size. The displacement vectors of each landmark between loaded and unloaded models were then calculated by subtracting the coordinates of the unscaled, unloaded model from the scaled, loaded model. To compare deformations among the three models, while ignoring differences in unloaded model size and shape, the displacement vectors for each model were added to the grand mean unloaded specimen (e.g. mean size and shape of the mean unloaded specimens), resulting in three deformed grand means, one for each age group mean. These were then submitted to a PCA together with the landmarks of the unloaded grand mean. These calculations refer (centre) all displacements and so, deformations to the grand mean, allowing vectors of deformation to be compared directly based on the angle between them (O’Higgins, Fitton and Godinho, 2019).

### 3.3.1 Mechanical advantages

For the mean modern human infant, juvenile and adult models, mechanical advantages (MAs) were calculated for the jaw adductor muscles (anterior, middle and posterior temporalis, anterior and posterior masseter and medial pterygoid) using the methods described in section 3.2.2 (Figure 27). The ratios of the mechanical advantages of the main masticatory muscles were also been calculated between the three models. We are expected to see a difference in MAs between the modern human models (Table 7 and Table 8).

*Table 7.* Mechanical advantages of the main masticatory muscles for the mean modern human infant, juvenile and adult.

			Temporalis (anterior)	Temporalis (middle)	Temporalis (posterior)	Masseter (anterior)	Masseter (posterior)	Medial pterygoid
<b>Modern human</b>	<b>Infant</b>	<b>RI<sup>1</sup></b>	0.30	0.23	0.11	0.44	0.30	0.38
		<b>RdM<sup>2</sup></b>	0.47	0.36	0.17	0.70	0.47	0.60
	<b>Juvenile</b>	<b>RI<sup>1</sup></b>	0.28	0.25	0.17	0.44	0.29	0.38
		<b>RP<sup>2</sup></b>	0.40	0.36	0.25	0.63	0.41	0.55
	<b>Adult</b>	<b>RI<sup>1</sup></b>	0.27	0.25	0.13	0.47	0.31	0.37
		<b>RP<sup>2</sup></b>	0.38	0.36	0.19	0.66	0.44	0.52

*Table 8.* Ratios of the Mechanical advantages of the main masticatory muscles for the mean modern human infant, juvenile and adult.

			Temporalis (anterior)	Temporalis (middle)	Temporalis (posterior)	Masseter (anterior)	Masseter (posterior)	Medial pterygoid
Modern human	Juvenile/ Infant	RI <sup>1</sup>	0.92	1.09	1.59	0.99	0.96	1.00
		RdM <sup>2</sup> / RP <sup>2</sup>	0.84	1.00	1.45	0.90	0.88	0.92
	Adult/ Infant	RI <sup>1</sup>	0.91	1.11	1.23	1.06	1.06	0.99
		RdM <sup>2</sup> / RP <sup>2</sup>	0.95	0.99	0.75	1.05	1.06	0.95
	Adult/ Juvenile	RI <sup>1</sup>	0.98	1.02	0.78	1.08	1.10	0.98
		RdM <sup>2</sup> / RP <sup>2</sup>	0.95	0.99	0.75	1.05	1.06	0.95

At the RI<sup>1</sup> bite point, the mechanical advantages (MAs) show different age-related trends for the main muscles of mastication (Tables 7 and 8). Thus, the MA of anterior masseter increases from infant to adult, middle temporalis from infant to juvenile with the adult having a similar MA to the juvenile (Table 7). The posterior temporalis has the smallest MAs, which peak in the juvenile model and then decrease in the adult. The anterior temporalis MAs are maximal in the infant model (Table 7) and the posterior masseter and medial pterygoid have MAs that vary little with age (Table 7).

At the RP<sup>2</sup>/RdM<sup>2</sup> bite point, the mechanical advantages (MAs) for all the models are, as expected, greater than those for the RI<sup>1</sup> bite (Tables 7 and 8). For the anterior and posterior masseter muscles, the MAs decrease from infant to juvenile and increase from juvenile to adult with the infant showing the maximum value. For the anterior part of the temporalis, the MAs decrease from infant to adult (Table 7 and Table 8). For the middle part of the temporalis muscle and the medial pterygoid, the models present similar values (Table 7 and Table 8). Finally, for the posterior part of the temporalis, MA increases from the infant to reach its maximal value for the juvenile and then decreases in the adult (Table 7 and Table 8).

*Table 9.* Force Production efficiencies in the RI<sup>1</sup> and RP<sup>2</sup>/RdM<sup>2</sup> biting simulations, calculated from the finite element models of the modern human infant, juvenile and adult. Fb, peak bite force; Fm, net applied muscle force, Fc, joint reaction force.

bite point	Force production efficiencies					
	Fb/Fm			Fc/Fm		
	Infant	Juvenile	Adult	Infant	Juvenile	Adult
RI <sup>1</sup>	0.33	0.35	0.35	0.67	0.65	0.65
RP <sup>2</sup> /RdM <sup>2</sup>	0.50	0.48	0.48	0.50	0.52	0.52

The ratios of peak bite force (Fb) and of the condylar constraint (Fc) reaction forces and the net muscle forces (the sum of all reaction forces at the constrained nodes on the teeth and glenoid fossa - Fm) predicted for the modern human models, are presented in Table 9. The values differ much more between bite points than between age stages. For the right first incisor (RI<sup>1</sup>) biting simulation, the infant model presents the lowest peak bite force production efficiency and the juvenile and adult models the highest. In consequence, the ratio of the joint (at the glenoid fossa) reaction forces to net applied muscle forces is larger in the infant model than in the juvenile and adult models. For the right second premolar or deciduous molar biting simulations (RP<sup>2</sup>/RdM<sup>2</sup>), the infant model presents the highest peak bite force efficiency and lowest reaction forces at the glenoid fossa. The juvenile and adult models present the same lower peak bite force efficiency than the infant model and larger reaction forces at the glenoid fossa.

### 3.3.2 Deformations

Size and shape analyses of global deformation of the three models were conducted for both biting simulations (Figure 30 and Figure 31). To aid visualisation, deformations were magnified 500x for RI<sup>1</sup> biting and 1000x for RP<sup>2</sup>/RdM<sup>2</sup> biting using the Evan toolbox v.1.75. Then, using the R package “Arothron” (Profico et al, 2019), the mean unloaded cranium mesh triangle areas were compared with those of the loaded specimens to create registration-free colourmaps showing regions of the cranial surface where the triangles in the cranial mesh are reduced in area (in purple) or increased (yellow/orange) as a consequence of the biting simulation (Profico et al., 2019; Figure 30B; 30C; 30D and Figure 31B; 31C; 31D). Raw deformations, as well as deformations scaled for centroid size and peak bite force with the infant model as a reference, were compared among models and biting simulations. To do so, the juvenile and adult loaded surfaces were extracted

from their vectors between the unloaded and the loaded surfaces, and adjusted by increasing or decreasing them in proportion to their ratios of size (cs) and/or peak bite force with respect to the infant modern human model.

In both biting simulations, the infant, juvenile and adult models present different magnitudes and modes of deformation. As indicated by the lengths of vectors between the unloaded and each of the loaded models. The infant deforms most, followed by the juvenile and finally the adult (Figure 30A and Figure 31A). In the PCA plots, PC1 accounts for 88.87% of the total variance in the RP<sup>2</sup>/RdM<sup>2</sup> biting simulation and 93.70% in the RI<sup>1</sup> biting simulation, indicating greater heterogeneity of deformation in the former (greater proportion of variance explained in higher order PCs).

Warping the grand mean surface model from the point representing the unloaded cranium in Figure 30 to that representing each of the loaded crania shows that loading on the RP<sup>2</sup>/RdM<sup>2</sup> causes, in all models, downward deflection of the zygomatic arches and upwards rotation of the palate, together with the midface, toward the working side (right). This results in asymmetry between the working and balancing sides of the cranium. The colourmaps in Figure 30 show that under RP<sup>2</sup>/RdM<sup>2</sup> biting simulations, the maxilla and zygomatic arches present large surface area expansions, decreasing in degree from infant to adult. Contractions of surface area are seen over the cranial vault and particularly the infra-temporal region, in the supraorbital region, between the orbits, and around the nasal aperture in all the models

The RI<sup>1</sup> biting simulation (Figure 31) causes an upward displacement of the anterior maxilla and palate and a large inferior deflection of the zygomatic arches, especially on the working side, most marked in infant and juvenile models. The colourmaps indicate that the central supraorbital region experiences marked, symmetrical contraction of surface area (Figure 31B).

Scaling deformations by centroid size (cs) and peak bite force (Table 6) only slightly impacts the degree of deformation in each of the three models and both biting simulations, because these varies little (Figure 30C; 30D and Figure 31C; 31D). For the RP<sup>2</sup>/RdM<sup>2</sup> biting simulation, scaling by cs and by peak bite force, slightly increases the magnitude of deformation in the juvenile and adult models (Figure 30C; 30D). For the RI<sup>1</sup> biting simulation (Figure 31C; 31D) scaling by cs moderately increases the magnitude of deformation of juvenile and adult models. Scaling for differences in peak bite force

has a very small effect because these differ little (see Table 6), Scaling strains for RI<sup>1</sup> peak bite force (relative to infants) decreases their magnitudes in the juvenile but increases them in the adult model (see Table 6).

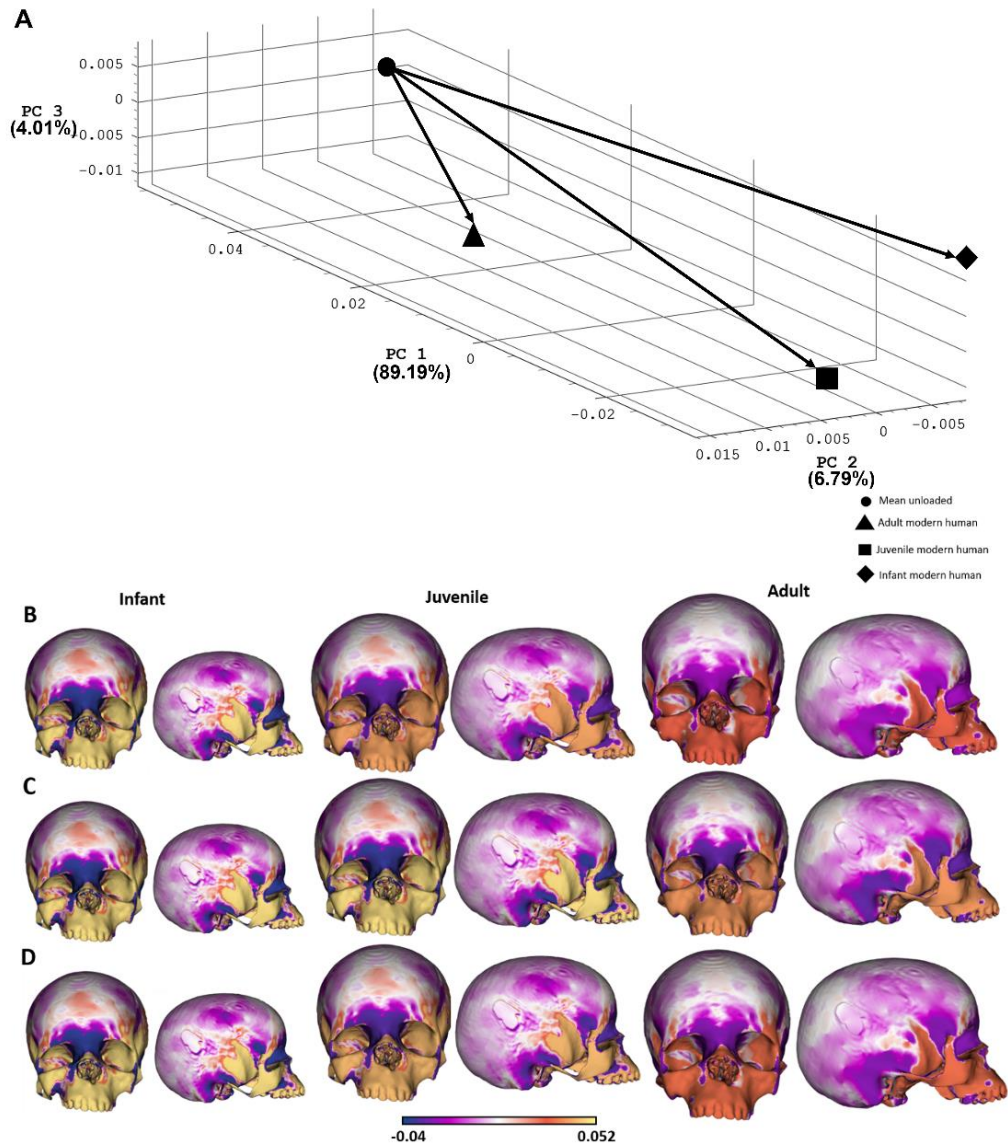


*Figure 30.* Size and shape analysis of modes and magnitudes of deformation of the modern human infant, juvenile and adult models from the RP<sup>2</sup>/RdM<sup>2</sup> biting simulations. A) Size and shape PCA plot. Below are warped surfaces from the PC plots with colourmaps illustrating the expansions and contractions of local surface areas between the unloaded and loaded models: B) unscaled, C) scaled by size and D) scaled by peak bite force. The deformations were magnified x1000. Colour scale bars indicate ratios of areas between unloaded and loaded models.

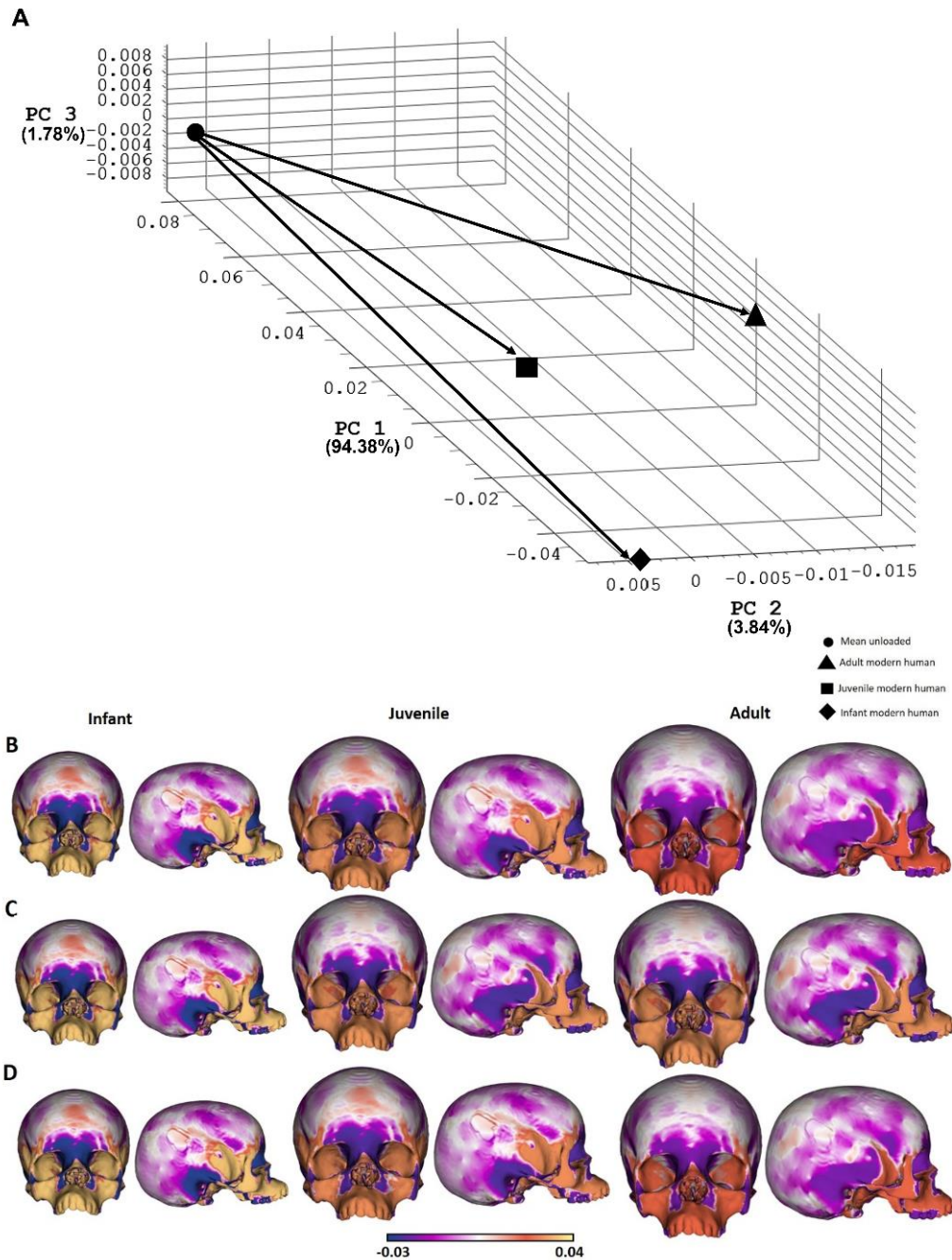


*Figure 31.* Size and shape analysis of modes and magnitudes of deformation of the modern human infant, juvenile and adult models from the R1 biting simulations. A) Size and shape PCA plot. Below are warped surfaces from the PC plots with colourmaps illustrating the expansions and contractions of local surface areas between the unloaded and loaded models: B) unscaled, C) scaled by size and D) scaled by peak bite force. The deformations were magnified x500. Colour scale bars indicate ratios of areas between unloaded and loaded models.

### 3.3.3 Tensile and compressive strains

This section describes the results obtained from the right second premolar (RP<sup>2</sup>) or right deciduous molar 2 (RdM<sup>2</sup>) and right first incisor 1 (RI<sup>1</sup>) biting simulations in modern human (MH) infant, juvenile and adult models. It aims to assess and compare the performance of each model in resisting biting loads, based on the resulting strains. It is expected that differences will be found in; i) ability to resist masticatory loading, ii) magnitude and mode of deformation experienced by the cranium. The study proceeds by testing the null hypothesis that these do not differ between age stages.

Figures 32 and 33 show the principal strain contour plots for each model during RP<sup>2</sup>/RdM<sup>2</sup> and RI<sup>1</sup> biting simulations. The data were also scaled by size (centroid size) and by peak bite force, using the infant model as a reference in each case (note: in this thesis we refer to strains as being greater or smaller throughout the thesis, as a way of describing their differences in absolute magnitudes, i.e., ignoring the sign of tensile vs compressive strains).

During RP<sup>2</sup>/RdM<sup>2</sup> biting simulations, the modern human infant model presents overall greater tensile ( $\epsilon_1$ ) and compressive principal strains ( $\epsilon_3$ ) and the adult the smallest even after scaling for size (square of centroid size, squared cs) and peak bite force. In the three models, strains are generally comparable, with the largest strains being found on the working side (right) and in similar anatomical areas, such as directly above the bite point, the zygoma, the right part of the anterior maxilla, around the orbitals, and nasal bone. Similarly, during RI<sup>1</sup> biting simulation, strains decrease from infant to adult stages irrespective of scaling. In all models, the maximum tensile and compressive strains are found just above the bite point, the inferior part of the maxilla (from the alveolar process to the nasal aperture) and at the zygomatic arches. The strains are broadly symmetric between the working and balancing (left) sides in each model, except near the bite point where the strains are greater on the working side. Scaling strains for peak bite force (relative to infants) decreases their magnitudes in the juvenile and adult models for RP<sup>2</sup>/RdM<sup>2</sup> but increases them for the RI<sup>1</sup> biting for the juvenile model (see Table 6). Likewise scaling for size increases them in the juvenile and adult models. Scaling by peak bite forces has little overall effect because peak bite forces do not vary to great degree (Table 6) and it has no effect on the distribution and relative differences in strain magnitudes over the cranium. However, scaling by the square of centroid size has a bigger impact, especially during the RP<sup>2</sup>/RdM<sup>2</sup> biting simulation where the juvenile model presents equivalent or

higher tensile and compressive strains for the anterior maxilla and around the nasal aperture (Figure 32).

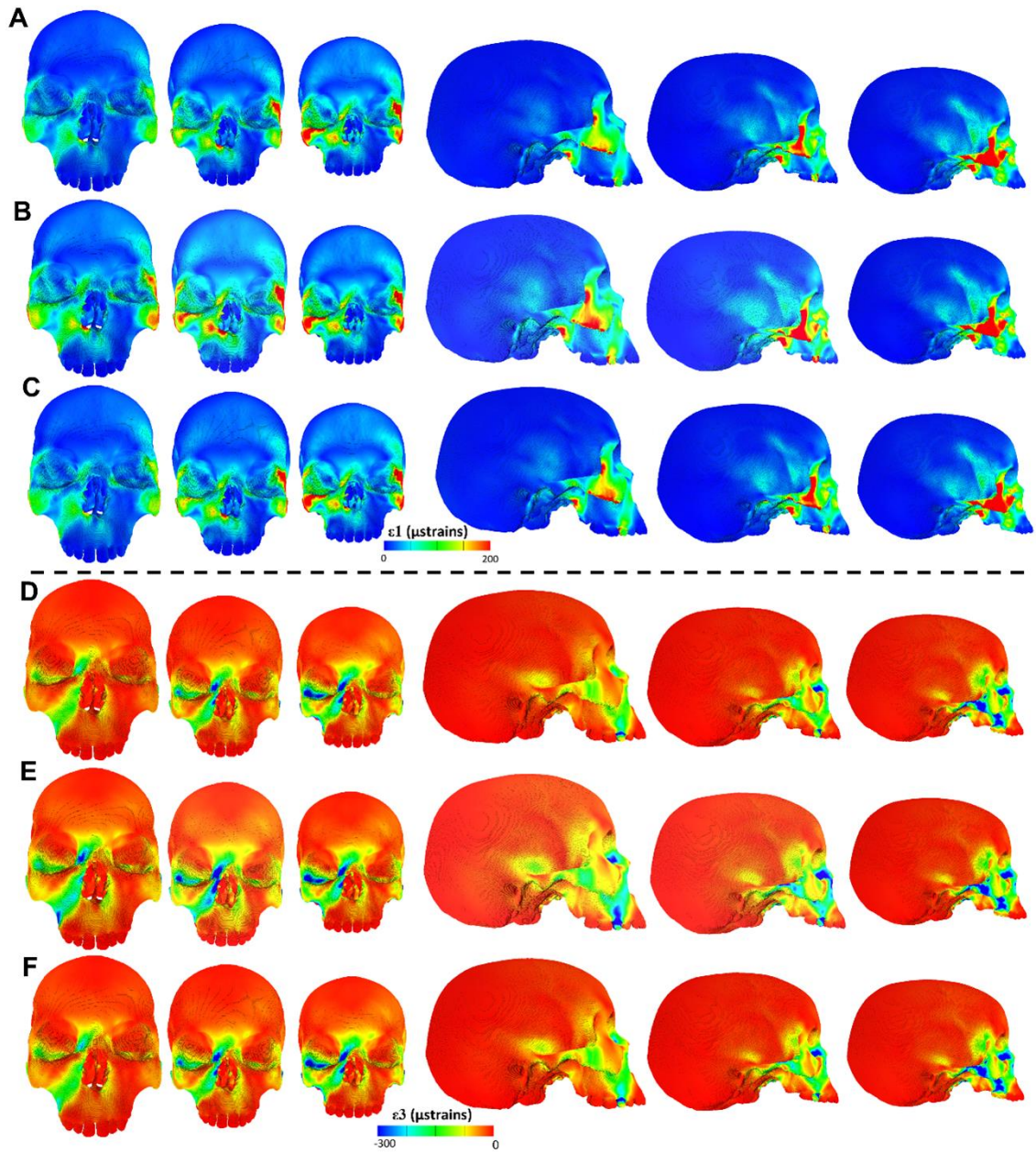


Figure 32. Strain contour plots of the solved modern human infant juvenile and adult FE models (from left to right) under  $RP^2/RdM^2$  biting simulation in front and lateral views. Tensile (top) and compressive strains (bottom) are unscaled (A, D), scaled for size (B, E) and scaled for peak bite force (C, F).

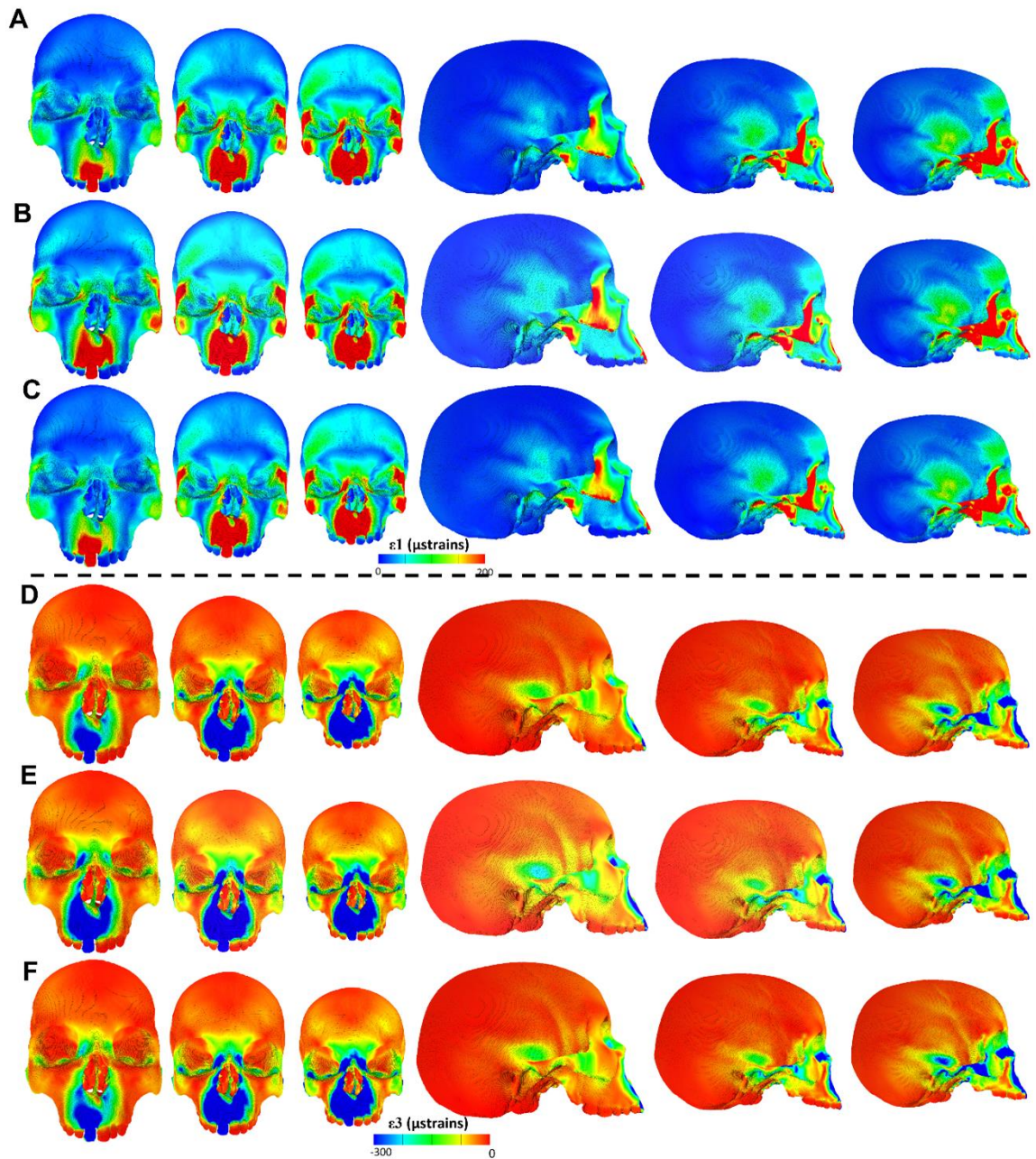


Figure 33. Strain contour plots of the solved modern human infant juvenile and adult FE models (from left to right) under  $R1^1$  biting simulation in front and lateral views. Tensile (top) and compressive strains (bottom) are unscaled (A, D), scaled for size (B, E), scaled for peak bite force (C, F).

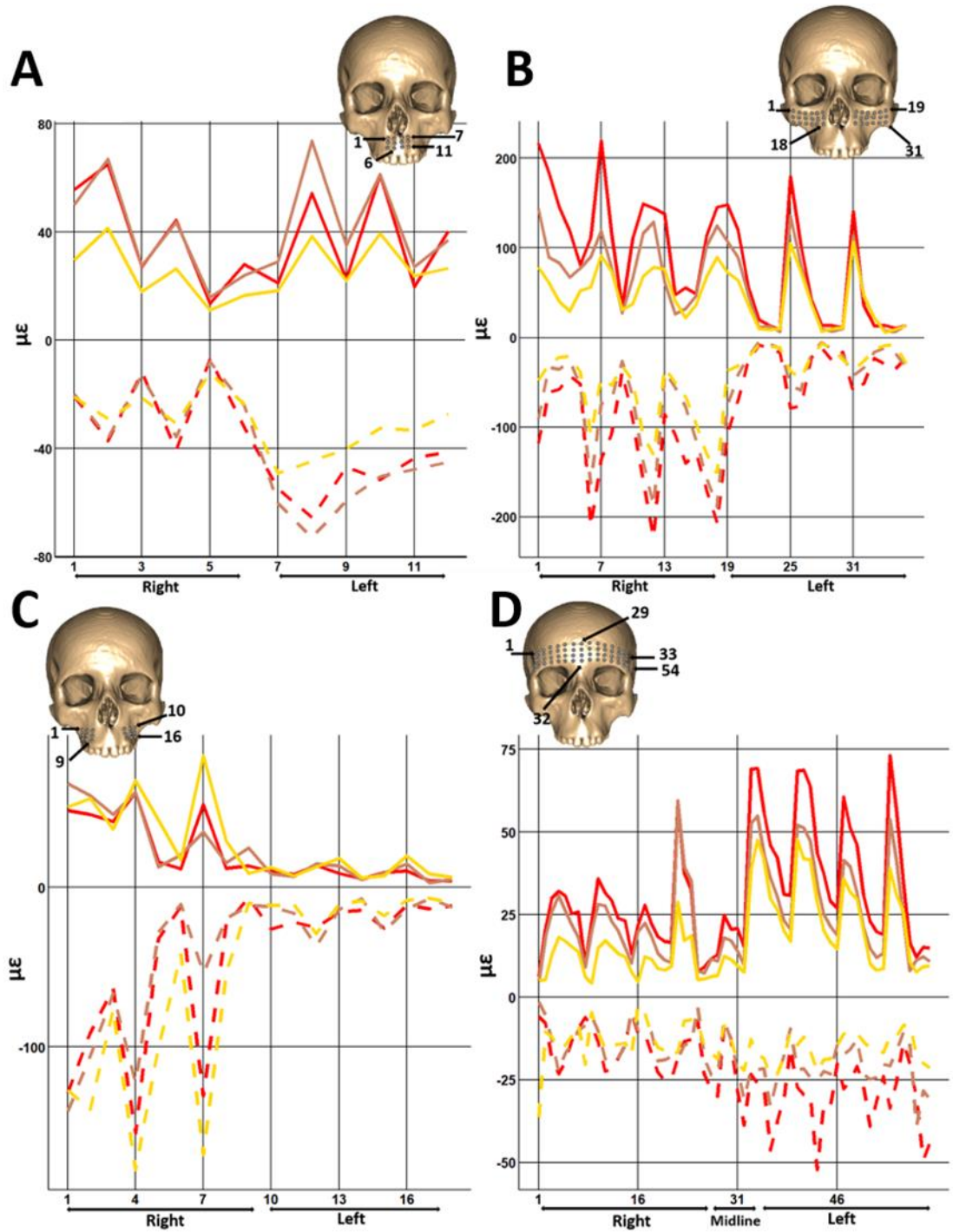


Figure 34. Strains experienced by the modern human (MH) infant (red), juvenile (brown) and adult (yellow) FE models at the 126 sampling points over the face during the RP<sup>2</sup>/RdM<sup>2</sup> biting simulations. The tensile (solid) and compressive (dashed) strains are unscaled. See landmark details in supplementary material Figure 1.

The predicted principal strains at the 126 landmarks (Figures 34-39) from the biting simulations reflect the findings of the previous contour plots (Figures 30 to 31). In Figure 34, from the RP<sup>2</sup>/RdM<sup>2</sup> biting simulation, the pattern of variation of strain magnitudes among landmarks is generally similar between the models representing different ages, although some regions experience greater strains in one model compared to the others. The region just below the nasal aperture presents large tensile ( $\epsilon_1$ ) strains which are greatest in the juvenile, especially on the balancing side (points 7-12, labelled left in the graph, Fig 34A). Figure 34B shows that on the anterior aspect of the maxilla, the infant model experiences greater tensile and compressive strains than the other models, especially on the working side (labelled Right). In Figure 34C, over the region directly above the bite point (point 6), the adult shows the greatest strains with the infant intermediate and the juvenile the smallest tensile ( $\epsilon_1$ ) and compressive ( $\epsilon_3$ ) strains. Moreover, this graph shows considerable asymmetry between the working and balancing sides. Finally, from Figure 34D the modern human infant and juvenile models experience greater tensile and compressive strains in the supraorbital region than the adult. Asymmetry is present between the working and balancing sides with the balancing side (labelled Left) presenting greater strains, especially for the infant and juvenile models in both species.

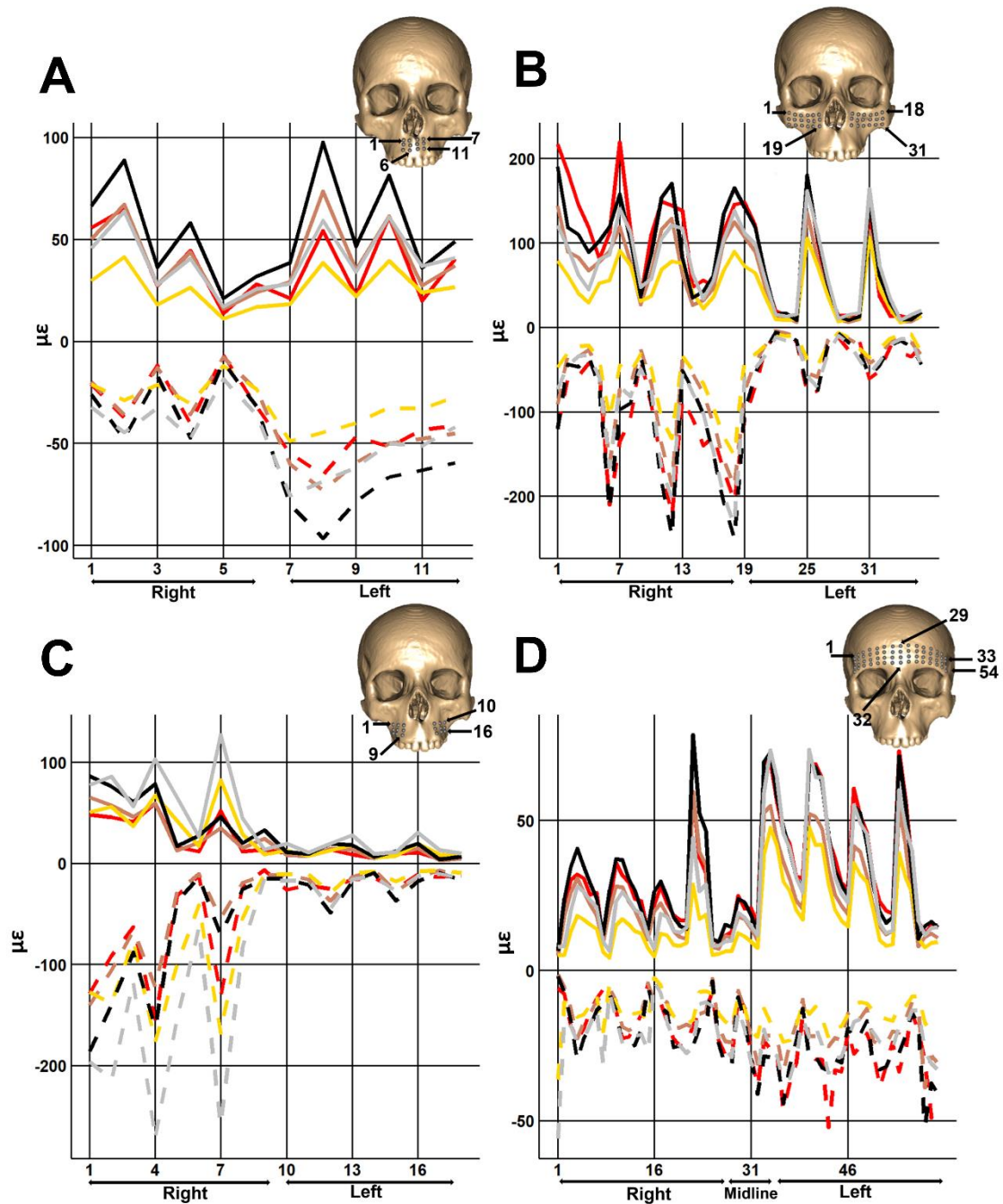
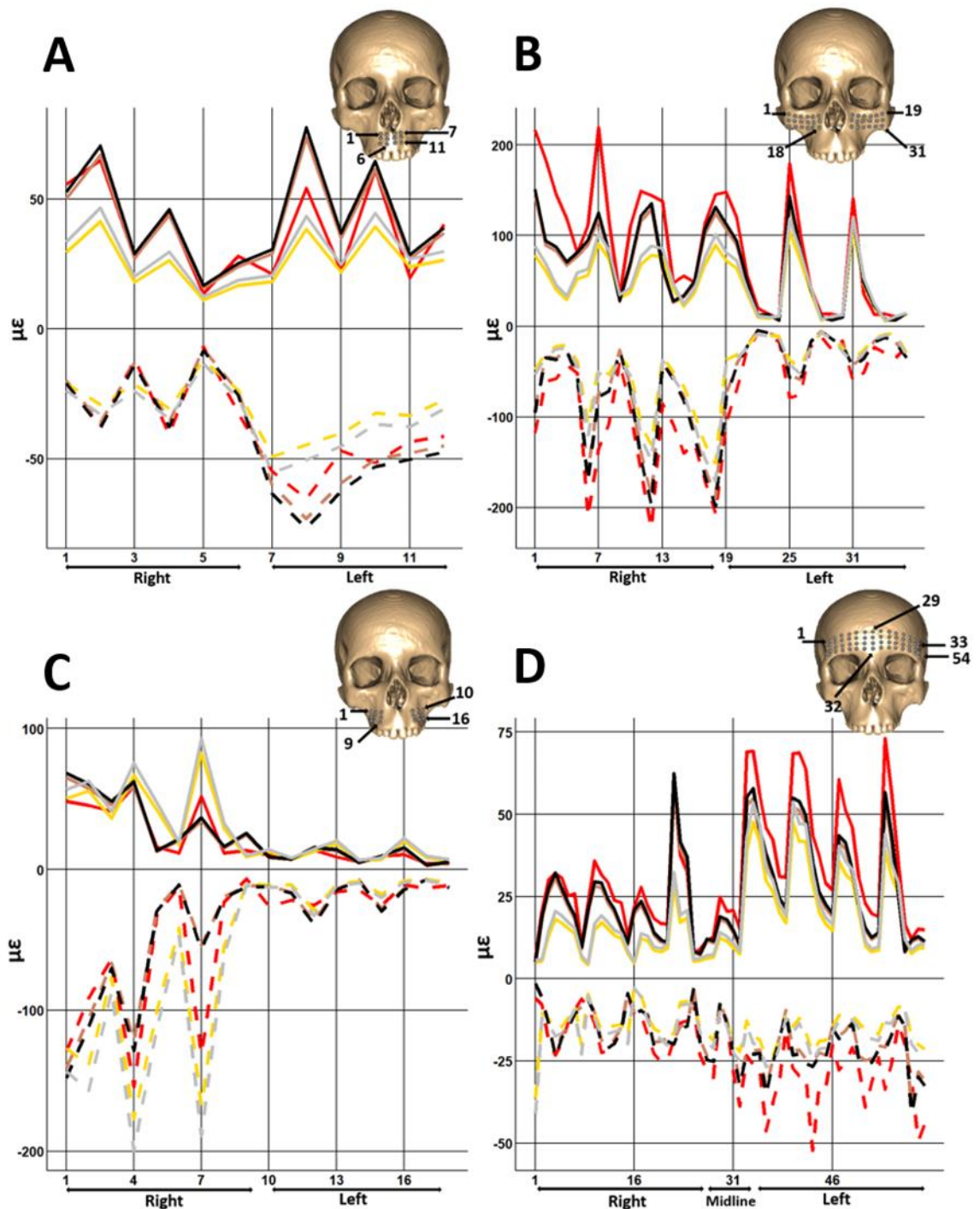


Figure 35. Unscaled and scaled by size strains experienced by the modern human (MH) infant (red), juvenile (brown) and adult (yellow) FE models at the 126 sampling points over the face during the RP<sup>2</sup>/RdM<sup>2</sup> biting simulation. The juvenile (black) and adult (grey) models were scaled according to the infant centroid size (cs). See landmark details in supplementary material Figure 1.

The strain values were then scaled by size (square of centroid size, squared cs) and peak bite force (Table 6) in the adult and juvenile models, using the infant model as a reference (Figure 35 and Figure 36). Figures 35 and Figure 36 show that the scaling by size increases the absolute magnitudes of the strains in both models with the juvenile presenting higher or equivalent tensile and compressive strain magnitudes than the infant

model. Scaling by peak bite forces has little effect because these differ little. It slightly increases strains in the adult and juvenile in  $RP^2/RdM^2$  biting simulations.



*Figure 36.* Unscaled and scaled by peak bite force strains experienced by the modern human (MH) infant (red), juvenile (brown) and adult (yellow) FE models at the 126 sampling points over the face during the  $RP^2/RdM^2$  biting simulation. The juvenile (black) and adult (grey) models were scaled according to the infant peak bite force. See landmark details in supplementary material Figure 1.

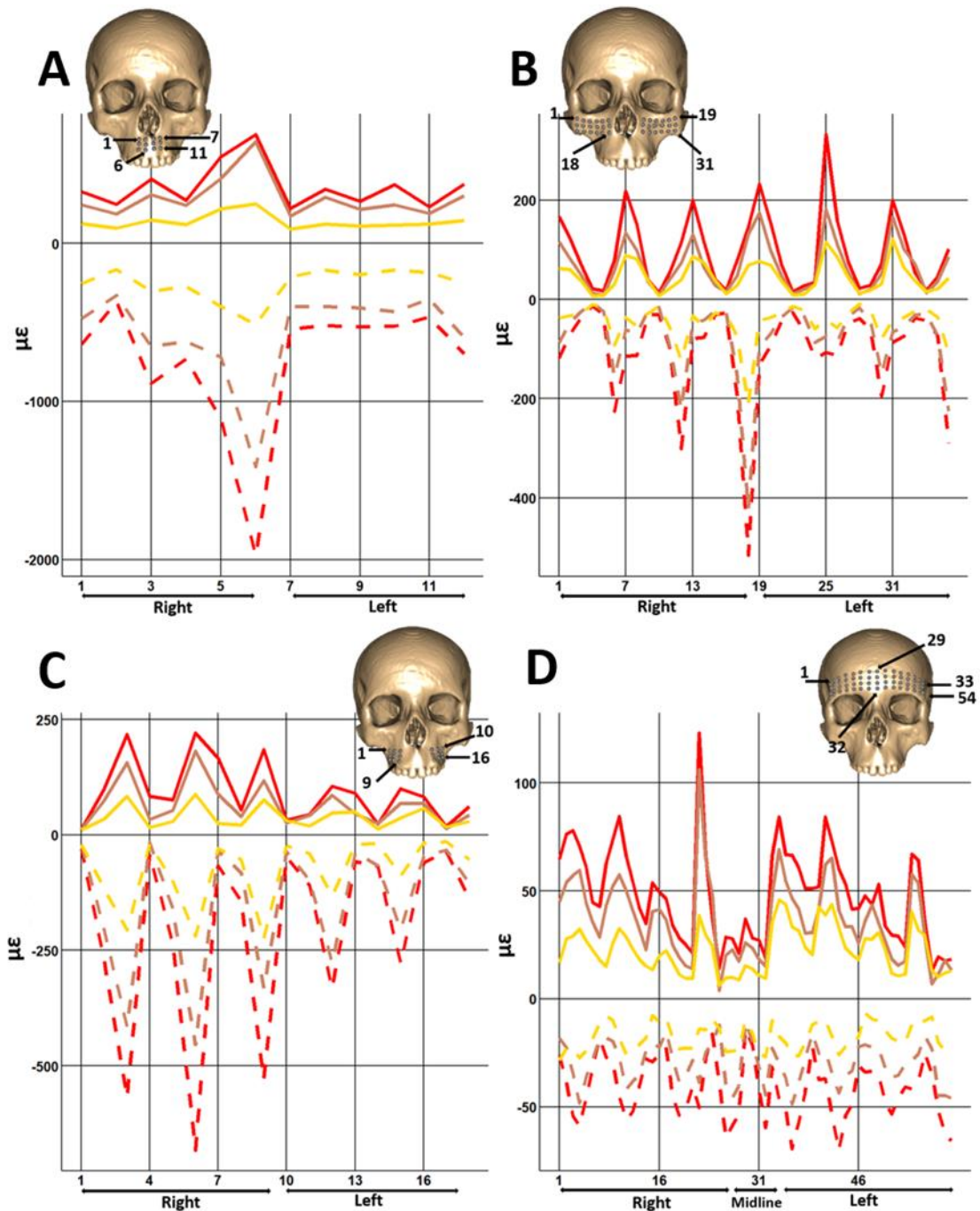


Figure 37. Strains experienced by the modern human (MH) infant (red), juvenile (brown) and adult (yellow) FE models at the 126 sampling points over the face during the RI<sup>1</sup> biting simulation. The tensile (solid) and compressive (dashed) strains are unscaled. See landmark details in supplementary material Figure 1.

Strain magnitudes were extracted at the same 126 landmarks from each model during the simulated right first incisor biting simulation (RI<sup>1</sup>; Figure 37). As for the RP<sup>2</sup>/RdM<sup>2</sup> biting simulation, the pattern of variation among landmarks is similar in all models, although some regions experience greater strains in one age group than others. In all regions where the strains were recorded, the strains decreased from the infant to the

adult model. Strains are generally symmetric between the balancing (left) and working sides (right) except above the bite point (Fig. 37A point 6) where the working side presents greater values in all models.

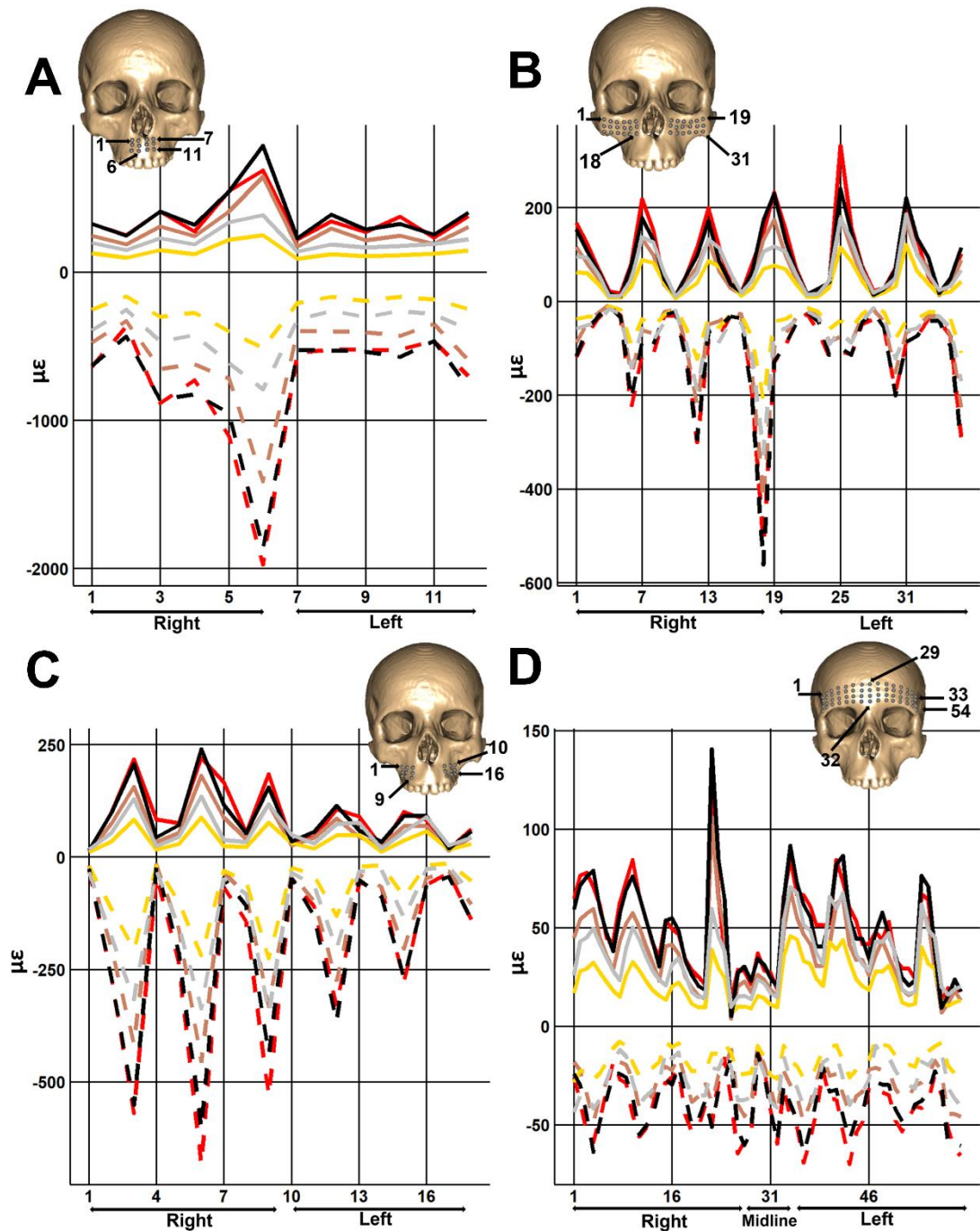


Figure 38. Unscaled and scaled by size strains experienced by the modern human (MH) infant (red), juvenile (brown) and adult (yellow) FE models at the 126 sampling points over the face during the R1<sup>1</sup> biting simulation. The juvenile (black) and adult (grey) models were scaled according to the infant centroid size (cs). See landmark details in supplementary material Figure 1.

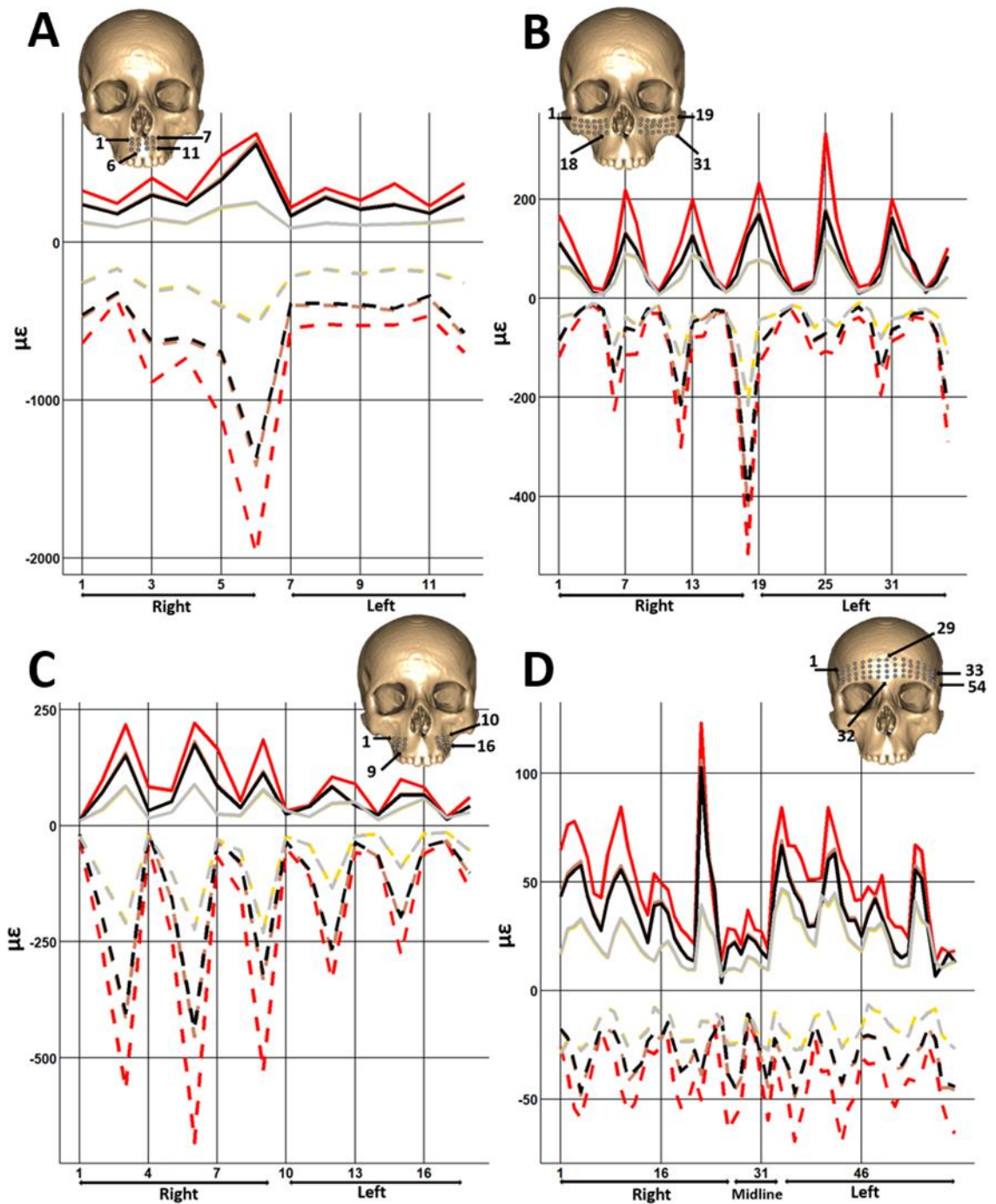


Figure 39. Unscaled and scaled by peak bite force strains experienced by the modern human (MH) infant (red), juvenile (brown) and adult (yellow) FE models at the 126 sampling points over the face during the RI<sup>1</sup> biting simulation. The juvenile (black) and adult (grey) models were scaled according to the infant peak bite force. See landmark details in supplementary material Figure 1.

After scaling by size and peak bite force (Figure 38 and Figure 39) the magnitudes of the strains change as expected from the differences in Table 6, with scaling by squared cs increasing the strain values in the juvenile and adult models (Table 6). Thus, after scaling, the juvenile model presents both tensile and compressive strains with similar

magnitudes to the infant with higher tensile strains adjacent to the bite points (RI<sup>1</sup>; Figure 38A). Scaling by peak bite force (Figure 39) slightly increases both tensile and compressive strains for the adult model but decreases them for the juvenile model, however, because differences in peak bite forces are small the effect of scaling is small.

### 3.4 Discussion

#### 3.4.1 Mechanical advantages, peak bite forces and force production efficiencies

Models of masticatory system function are routinely used in comparative analyses of peak bite force in modern humans as well as fossil hominins (e.g. Eng et al., 2013; Godinho et al., 2018a; O'Connor et al., 2005). The present study compares the mechanical advantages and force production efficiencies between infant, juvenile and adult mean modern humans. The mechanical advantages (MAs) of mean forms show that for RP<sup>2</sup>/RdM<sup>2</sup>, MA decreases from infant to adult, except at the anterior part of the masseter muscle where the infant presents the smallest value and the juvenile the greatest (Table 7 and Table 8). The MA estimations for RI<sup>1</sup> biting show a less clear pattern, the juvenile presents the greatest MAs for the temporalis muscle (anterior, middle and posterior parts) and the three models present similar values for the rest of the masticatory muscles (Tables 7 and 8). These findings reflect the peak bite forces calculated for the mean infant, juvenile and adult models. Thus, in the RP<sup>2</sup>/RdM<sup>2</sup> biting simulation, the mean infant specimen peak bite force (Table 6) is 5% or 11% greater than those for the juvenile and adult models, respectively. In the RI<sup>1</sup> biting simulation, estimated peak bite forces show more similar values among the models, with the juveniles presenting a peak bite force 3% greater than the infant and 5% greater than the adult model and the adult achieving the lowest peak bite force. Mechanical advantages and peak bite force values are reflected in force production efficiency, where the infant presents a greater ratio of peak bite force to net applied muscle force during the RP<sup>2</sup>/RdM<sup>2</sup> biting simulation (Table 9). For the RI<sup>1</sup> biting simulation, the infant presents the lowest ratio and the juvenile and adult, have identical higher values (Table 9). The mechanical advantages, peak bite forces and force production efficiencies calculated for the adult model in this study were compared with those found in *Homo sapiens* adults by Godinho et al., (2018) and O'Connor et al., (2005). The mechanical advantages calculated for the masticatory muscles in the modern human adult model during RI<sup>1</sup> biting (Table 7) are slightly lower than those found for an adult *H. sapiens* specimen during the same bite in Godinho et al., (2018), except for the posterior

part of the temporalis which shows similar values to the adult model in this study. Moreover, the peak bite force and force production efficiency (ratio of peak bite force to net muscle forces applied) calculated during RI<sup>1</sup> biting (Table 7 and Table 9) in this study is lower than that found by Godinho et al., (2018), which is consistent with the differences in mechanical advantages found between this study and Godinho et al., (2018). O'Connor et al., (2005) also reported mechanical advantages (MAs) of 26 *H.sapiens* (11 females and 15 males) for the RI1 bite point. The mechanical advantages calculated for the middle part of the temporalis and on average for the masseter ( $\text{mean}_{\text{anterior+posterior}} = 0.39$  see Table 8) in this study fall within the range of MA values found in O'Connor et al., (2005). Moreover, in both previous studies (Godinho et al., 2018; O'Connor, Franciscus and Holton, 2005), the masseter muscles present the highest MA followed by the medial pterygoid muscles and finally, the temporalis. The same pattern was found in this study for the mean adult model (Table 7).

In this chapter, the results show that the infant model is more efficient at converting muscle force into peak bite force than the juvenile and adult models, especially during RP<sup>2</sup>/RdM<sup>2</sup> biting simulations. This is probably due to the smaller size and shorter face of the infant model, which shortens the bite out-lever relative to the muscle in-lever arms compared to the juvenile and adult models. For the RI<sup>1</sup> bite, the mechanical advantages show more variation among the models and greater peak bite force in the juvenile model. Previous studies calculated and compared predicted peak bite force using a constrained lever model (CLM) and *in vivo* peak bite forces in a modern human ontogenetic series from 6.5 to 29 years (Edmonds and Glowacka, 2020). They show that maximum peak bite force increases throughout ontogeny to reach a peak around 20 years and then decreases as the masticatory complex ages (Edmonds and Glowacka, 2020; Bakke, 2006).

Moreover, peak bite force changes along the tooth row, with the highest occurring at the posterior dentition (Edmonds and Glowacka, 2020). However, previous *in vivo* studies also show that significant inter and intra-individual variation exists in peak bite forces, especially when measured on the molars and incisors of children (Mountain, Wood and Toumba, 2011; Gavião, Raymundo and Rentes, 2007; Edmonds and Glowacka, 2020). These variations have been attributed to several physiological factors such as masticatory muscle strength, sex, dental occlusion and dental condition (Maki et al., 2001; Mountain, Wood and Toumba, 2011). In this study, applied muscle forces are identical in all models because of the lack of information on muscle forces in infants and

juveniles. Previous studies estimated muscle forces, such as that for the temporalis, in modern humans and fossil specimens based on a hypothesised relationship between muscle cross-sectional area and temporal fossa area (Koolstra et al., 1988; Weijjs and Hillen, 1985; O'Connor, Franciscus and Holton, 2005). However, recently it has been shown that those bony proxies do not necessarily lead to reliable estimates of muscle cross-sectional areas (Toro-Ibacache, Zapata Muñoz and O'Higgins, 2015).

Therefore, the comparisons of forces between ages in this study overestimates biting forces in smaller crania relative to larger ones. However, these differences in biting forces among all models still reflect relative differences in the efficacy of the conversion of muscle into biting forces. These differences in efficiency arise because of differences in cranial form and so, in lever arms and muscle force directions (Godinho et al., 2018).

#### 3.4.2 Craniofacial skeletal performance during right first incisor and second premolar/deciduous molar biting

The findings show that even if tensile and compressive strains are generally comparable among infant, juvenile and adult models, the largest strains are found on the working side (right) and in similar anatomical areas (such as directly above the bite point, the zygoma, the right part of the anterior maxilla, around the orbits, and nasal bone), some differences exist in the spatial distributions and magnitudes of strains between the three models.

Overall, the infant model in both biting simulations presents greater tensile and compressive strain magnitudes followed by the juvenile and adult models. The exception is over the inferior aspect of the maxilla and the around the post-canine alveolar process during the RP<sup>2</sup>/RdM<sup>2</sup> biting simulation, where the juvenile and the adult models present greater strains.

The GM size and shape analysis of global magnitudes and modes of deformation (Figures 30 and Figure 31) shows that the three models deform differently, with the infant deforming to a greater degree during both biting simulations. This is consistent with the strain contour plots and graphs (Figures 32 to 39), which show small differences in which regions experience high and low strains.

Thus, the results indicate that the cranium of the infant, in general, deforms more and is more strained during both biting simulations. The predicted higher strain magnitudes in the face of the mean modern human infant arise because of size differences and

because, in reality, the muscle forces in the infant would have been smaller than the applied adult forces. As previously reported (in section 3.2), the crania of the juvenile and adult models are significantly larger than the infant. However, after accounting for differences in centroid size, the infant deforms to a greater degree during both biting simulations. Similarly, when strains were scaled according to cranial size (square of centroid size, squared cs) the discrepancies between models are reduced but not eliminated. In the juvenile and adult models,

No adjustment was made for (unknown differences in) muscle forces. Because muscle forces are not scaled, strain magnitudes were still greater after scaling for size in the infant except at the inferior aspect of the maxilla and the around the post-canine alveolar process during the  $RP^2/RdM^2$  biting simulation, where the juvenile and adult models still present higher strains.

Deformations and strains were also adjusted for differences in peak bite force, calculated from Vox-FE outputs for the two biting simulations (section 3.2.1). This scaling resulted in similar changes in magnitudes of deformation and strains as when adjusting for cranial centroid size. If peak bite forces are constant throughout postnatal ontogeny this scaling might be expected to correct for different input muscle forces, however (Edmonds and Glowacka, 2020) have shown that *in vivo* maximum  $I^1$  and  $P^2/dM^2$  biting forces increase between infancy (8.3N for the  $I^1$  and 67.2N to 97.5N for  $P^2/dp^2$  between 6.5 and 9 years, Edmonds and Glowacka, 2020) and adulthood (69.3N to 158.6 for the  $I^1$  and 130.2N to 424.4N for  $P^2/dp^2$  between 20 to 29 years of age, Edmonds and Glowacka, 2020), so the correction for simulated biting forces does not correct for ontogenetic differences in input muscle forces that occur in reality.

Thus, accounting for size or peak bite force, the juvenile and adult models better resisted masticatory functional loadings, developing generally lower strain magnitudes than the infant. Not reported here, but explored during the study was a combined scaling for centroid size and biting forces, but because biting forces vary little in the models, compared to the real differences found in previous work, the net effect of these two scalings combined was that strain magnitudes remained high in the infant relative to the adult and juvenile.

The scaled results suggest that the infant model is relatively (taking account of size) less stiff than the juvenile and adult models. This might be because of the generally

more robust facial skeletons (differences in shape and size of the facial bones) of the juvenile and adult specimens and aspects of craniofacial architecture that develop later in post-natal ontogeny (White and Folkens, 2011; Sadler, 2003; Schaefer et al., 2009). These include overall the development of a more robust cranial vault, subnasal and peri-orbital regions, the increases in relative size and thickness of the zygomatic arches, the development of relatively bigger alveolar processes and the presence of the larger permanent dentition (Sadler, 2003; Schaefer et al., 2009). However, differences between models might also be due to modelling errors and simplifications. These simplifications, many of which are necessary to work with fragmentary and incomplete fossil material, include how the zygomatic arch is loaded, the absence of sutures, the use of a single material property for all cranial skeletal components and the filling in of paranasal sinuses.

Thus, juvenile and especially infant models present high tensile and compressive strains over the zygomatic bones and the zygomatic arches compared to the adult model. This has been noted before (Ledogar et al., 2016; Hylander, Johnson and Picq, 1991; Hylander and Johnson, 1997; Ross, 2001; Ross et al., 2011) and attributed to the differences in height and breadth of the zygomatic arch. Indeed, based on beam theory, a reduction in the height and/or breadth of the zygomatic arches will weaken them under bending and shear, respectively. However, all of the models in these studies were built without temporal fasciae. A recent study has shown that in macaques, the temporal fasciae act as a stabiliser of the arch, opposing the masseteric contraction forces during mastication (Curtis et al., 2011) and working with them to put the arch into pure compression, rather than bending as a cantilever. The authors show that the high-strain gradients in and around the zygomatic arch are reduced when the temporal fasciae are added to the model (Curtis et al., 2011).

In the same way, sutures are important. Thus, in australopithecines, it has been suggested that the structural strength of the zygomatic body could be adaptively significant in reducing strains in the nearby zygomatico-maxillary suture (Smith et al., 2015a). It has been suggested that among smaller-faced modern human crania, the zygomatico-maxillary suture may be especially prone to experiencing relatively large masticatory stresses (Ledogar et al., 2016; Smith et al., 2015b) and studies on facial fractures have shown that these are often located around the zygomatico-maxillary suture (Ellis, El-Attar and Moos, 1985). In this study, the cranial sutures are missing. However, sutures are thought to be of particular importance in modifying cranial strains during ontogeny, and

are the sites of bone deposition, permitting growth. Moreover, during growth, sutures tend to become more ossified or “fused” (Hall, 2005), and so, stiffer in adults. Previous experimental work has shown that bone strain magnitudes and orientations often vary from one bone to another, across a suture (Moazen et al., 2009; Kupczik et al., 2007). This has led to the hypothesis that sutures act to modify the strain environment of the cranium, possibly to dissipate high stresses generated during feeding or impact (Reed et al., 2011). However, other studies using macaque or *Uromastix hardwickii* lizard skull Finite Element (FE) models have shown that the inclusion of facial sutures impacts overall strain magnitudes but makes little or no difference to the distribution of regions of relatively high and low strains over the cranium when compared with a solid model (Wang et al., 2010; Moazen et al., 2009). Other FE models of macaques built without craniofacial sutures have demonstrated a reasonable correlation with *in vivo* experimental strain data, reporting strain ratios and orientations within the experimentally measured range (Strait et al., 2005; Ross et al., 2005, 2011) while another study on the pig skull has shown that the inclusion of sutures in finite element models affected strain data but do not improve the fit of the model to the experimental data (Bright, 2012). Therefore, it has been suggested that the presence or absence of sutures alone is not the main reason for the differences in model strains, and in this study likely does not explain the differences in strains observed between ontogenetic stages.

For this study, bones are simplified, being modelled as ‘solid’, without a cancellous interior and with the same material properties throughout. Further, the teeth are allocated the same material properties as bone. Prior sensitivity tests conducted on *H. sapiens* crania, using the same modelling tools and procedures as the present study have shown that simplifying the models from three materials (cortical bone, cancellous bone and teeth) to a model with one material with properties of cortical bone has a significant impact on reducing the magnitude of the strains but not on the mode of deformation and so on relative strains and the spatial distribution of strains over the model (Toro-Ibacache et al., 2016; Godinho et al., 2017). Because all models in this study were built with the same material properties, we expect them to be impacted in the same way, however, it is well-known (Dechow et al., 1993) that material properties change with age and the differences observed between age stages do not account for this.

The allocation of cortical bone material to teeth as well as the form of the teeth included in cranial FE models has been noted to slightly impact strain magnitudes (Fitton

et al., 2015; Godinho et al., 2017; Lacruz et al., 2015b). In the present study, teeth had to be applied to the cranial models after creating them by warping and so the effect of using different teeth was investigated. In Appendix 3, the modern human teeth on the mean Neanderthal adult were swapped for Neanderthal adult teeth and the results showed a small impact on strain data.

Another sensitivity test was carried out on the paranasal sinuses (Appendix 2). Indeed, because of a lack of preservation of the sinuses in Neanderthals, it was decided to fill them (with material with the same properties as the rest of the cranium and teeth) in both species for all models. However, the models were also loaded similarly with the sinuses unfilled and the results were compared with those presented in this chapter. The results of the sensitivity test in Appendix 2 reflect those of previous studies (Renders et al., 2011; Toro-Ibacache et al., 2016) in indicating that filling the sinuses mostly reduces the strain magnitudes and much less, the mode of deformation.

#### 3.4.3 Significance of apparent differences between the mean modern human infant, juvenile and adult models

The present study compares the biting performance and resistance of mean modern human infant, juvenile and adult models extracted from a growth model using a specific sample of European modern human crania, so it is necessary to consider sampling errors and inter-population variability before generalising. Thus, the findings, on the mean adult modern human FE model reflect and extend those of other recent studies. Ledogar et al., (2016), conducted an FEA analysis simulating third upper and second molar biting and compared seven recent adult human crania from a wide geographic range. In the same way, Godinho et al., (2018) built a modern human adult FE model and conducted first incisor and first premolar biting simulations. Both found that, despite intraspecific morphological differences, the crania resisted biting similarly. Moreover, the distribution of regions of high and low strain (tensile and compressive) in the Godinho et al., (2018) study was found to be generally consistent with what was found by Ledogar et al., (2016). The strain contour maps arising from premolar and incisor biting simulations in these two studies (Godinho et al., 2018; Ledogar et al., 2016), while not identical, are comparable with those in the mean modern human model of this study. Thus, for a first premolar bite, Ledogar et al., (2016) found among the models, a maximum principal strain ( $\epsilon_1$ ) of approximately  $280 \mu\epsilon$  and a minimum principal strain ( $\epsilon_3$ ) of  $-600 \mu\epsilon$  while Godinho et al., (2018) (who loaded the left first premolar in a human cranium) found a

maximum of 468  $\mu\epsilon$  and a minimum of -302  $\mu\epsilon$ . The values in this study, from the loading (107  $\mu\epsilon$  to -176  $\mu\epsilon$ ) for the RP<sup>2</sup> biting are comparable, but lower in the study by Godinho et al., (2018) and in this study. While these studies did not load the same tooth, the proximity of premolars means that similar strains should be expected. In the same way, for the incisor bite, Godinho et al., (2018) found maximum principal strains of approximately 490  $\mu\epsilon$  and a minimum of -500  $\mu\epsilon$  while in this study, the mean adult model exhibited a maximum  $\epsilon_1$  of 249  $\mu\epsilon$  and a minimum  $\epsilon_3$  of -514  $\mu\epsilon$ .

It is important to be cautious when comparing predicted principal strain magnitudes among models built using different protocols. Indeed, Ledogar et al., (2016) built their models with a wide range of material properties and conducted their biting simulation on the third premolars while in this study and the one from Godinho et al., (2018), the models were built with a single homogenous isotropic material (based on prior validations and sensitivity works (Toro-Ibacache et al., 2016; Godinho et al., 2017) and loaded on the fourth premolar. Further, in Godinho et al., (2018) a single male *H. sapiens* cranium was loaded, while in this study, the model represents the mean of 20 adult specimens.

Toro-Ibacache et al., (2016) performed FEAs, using the same protocol as in the present study, on two crania representing the extremes of shape variation (assessed by PCA) in a sample of 20 adult modern humans of both sexes. The models were loaded using identical peak bite force at the central incisor (350 N) and the first molar and found a similar distribution of strains between the extremes, comparable with other studies in humans such as Ledogar et al., (2016). Peak strains for these same individuals loaded with their real muscle forces (i.e., not necessarily generating identical peak bite force) ranged from, approximately, 400  $\mu\epsilon$  to -450  $\mu\epsilon$  for central incisor bites, and 350  $\mu\epsilon$  to -300  $\mu\epsilon$  for first molar bites (Toro-Ibacache, Zapata Muñoz and O'Higgins, 2016).

Thus, the mean modern human model used in this study seems to show similar behaviour under RI<sup>1</sup> and RP<sup>2</sup> biting simulations in terms of strain distribution and mode of deformation to those from previous studies. The infant and juvenile mean models develop peak tensile and compressive strains that are greater than those found in the mean adult, at the 126 sampling points. As the models were built using the same muscle forces but the infant and juvenile mean crania are smaller than the adult ones, it is expected that the strains will be greater in these models, because of their differences in size. However,

scaling by the ratio of squared centroid sizes affects strain magnitudes especially when comparing the infant and juvenile but the adult still presents generally lower strains than the two other, smaller models. Thus, the adult model presents a craniofacial morphology better adapted than the infant and juvenile models to resist equivalent biting. Thus, size differences alone do not account for these differences. Differences in shape likely also play a significant role in strain development.

The present findings show that modern human infants are more efficient at converting muscle forces into peak bite forces due to their shorter faces. However, they also develop greater strains, similarly distributed to adults indicating less ability to resist masticatory functional loading. This has been previously suggested specifically for *H. sapiens* when compared to other *Homo* species (Antón, 1990; O'Connor, Franciscus and Holton, 2005; Lieberman et al., 2008; Eng et al., 2013), facial reduction in *H. sapiens* increases mechanical efficiency in peak bite force generation due to alteration in relative in and out-lever arm lengths. However, this greater ability to generate high peak bite force results in the *H. sapiens* cranium deforming more and presenting greater strain magnitudes (Godinho et al., 2018; Rak, 1986; Demes, 1987; Lieberman, 2011, 2008; Ledogar et al., 2016). This could also apply to the infant specimens which present a smaller facial skeleton and greater mechanical advantages (Edmonds and Glowacka, 2020). However, differences in tensile and compressive strain magnitude and distribution among the models exist, especially at the inferior aspect of the maxilla in the juvenile model. Thus, the mode of deformation is also different between the three models.

The human cranium shows a degree of integration (Bastir and Rosas, 2005, 2016; Neaux et al., 2019, 2018; Lieberman, 2008), which implies changes in one component of the cranium impact other components (Lieberman, 2011, 2008). This has been studied from an ontogenetic point of view and findings suggest a hierarchy of ontogenetic interactions that impact the development of aspects of facial form such as its vertical development and its orientation (Bastir, Rosas and O'higgins, 2006; Bastir et al., 2008; Lieberman, McBratney and Krovitz, 2002; Neaux et al., 2015). A study on a sample of modern humans from newborn to 6 years old has shown that there is an important interaction between the nasal capsule derivatives and the development of the face (Landi et al., 2021). Little is known about ontogenetic interactions between craniofacial components in older children and how these contribute to the development of adult morphology.

The differences observed between the three models in how strains are developed in response to masticatory loads may reflect both the mechanical consequences of alterations in form and contribute to subsequent, integrated, mechanically adaptive changes in form during post-natal growth and development.

It is also important to take into account the development of masticatory system loading and its interactions with other craniofacial components during post-natal ontogeny, as the muscles of mastication increase in size and thickness, teeth are shed and replaced and the palatal arch changes in dimension etc (Thompson, Biknevičius and German, 2003; Le Révérend, Edelson and Loret, 2014). The development of the masticatory apparatus has an impact on oral food processing during childhood with functional capacity reached at 6 and 8 months of age, for purée and soft solid foods and after 6 years for more solid food (Le Révérend, Edelson and Loret, 2014; Gisel, 1988). However, the consequences of masticatory system loading on the development of craniofacial form are also interesting to consider. Indeed, oral processing of different food consistencies has an impact on children's development, especially on orofacial growth (Larsson, 1998; Castelo et al., 2007; García-Morales et al., 2003; Gavião, Raymundo and Rentes, 2007; Ingervall and Minder, 1997; Julien et al., 1996). Hall in (2010), reported that for the face of a newborn to have a normal morphological appearance, contraction of the muscles involved in mastication and facial expression must occur to stimulate forward bone growth, cartilage growth and facial muscle bulk (Hall, 2010). It has been hypothesised that the development of masticatory muscles could depend on the consistency of children's early diet (Sakashita et al., 1998).

The forward and downward directions of midfacial growth (relative to the cranial base) have been also studied in terms of bone deposition and resorption, especially over the maxilla and zygomatic bone (Enlow and Bang, 1965; Martinez-Maza, Rosas and Nieto-Díaz, 2013; Kurihara and Enlow, 1980; Schuh et al., 2019; Lacruz et al., 2015b; Enlow and Hans, 2008). Indeed, analyses of bone growth remodeling in modern human adults and subadults (Figure 41) have shown that the posterior and superior parts of the maxilla are depository, whereas the anterior subnasal maxilla was predominantly resorptive (Enlow and Bang, 1965; Enlow and Hans, 2008; Martinez-Maza, Rosas and Nieto-Díaz, 2013; Kurihara and Enlow, 1980; Lacruz et al., 2015b).

A recent study on a modern human ontogenetic series ranging from 0 to 12 years confirms these results (Schuh et al., 2019, 2020), with resorptive activity affecting the anterior subnasal maxilla, inferior part of the orbital rim, zygomatic process and the top of the frontal process (around the fronto-maxillary suture) already present at birth. This resorptive activity has been related to modification of the direction of facial growth (Enlow and Bang, 1965; Kurihara and Enlow, 1980; Martinez-Maza, Rosas and Nieto-Díaz, 2013). Indeed, previous studies proposed that as the maxilla increase in size, the resorptive field enlarges from the anterior subnasal maxilla to the zygomatic bone to compensate for forwarding displacements. This forward and downward direction of growth in relation to the resorptive activity seems to result in the characteristic orthognathic face of *Homo sapiens* (Enlow and Hans, 2008; Martinez-Maza, Rosas and Nieto-Díaz, 2013). Moreover, several authors (Freidline et al., 2017; Martinez-Maza, Rosas and Nieto-Díaz, 2013) observed that the anterior maxilla is morphologically and microscopically more variable in *H. sapiens*. It has been suggested that this was due to fewer functional constraints leading to greater plasticity in these regions (Freidline et al., 2017; Martinez-Maza, Rosas and Nieto-Díaz, 2013). Martinez-Maza et al., (2013) discover that the upper face, under less functional constraints, shows more consistently forming fields and higher morphological variability (Martinez-Maza, Rosas and Nieto-Díaz, 2013; Evteev, Anikin and Satanin, 2018), especially in older age groups. This had been mostly related by the authors to sexual dimorphism inducing morphological changes in those areas (Freidline et al., 2017; Holton et al., 2016). However, Schuh et al., (2019) also show frequent switching between bone resorption and formation around the fronto-maxillary, zygomatic-maxillary, inter-maxillary sutures and along the maxillary dental arcade. This could be related to mechanical loadings, in these areas, with the sutures diffusing mechanical loads across the skull (Popowics and Herring, 2007).

The differences in mode and magnitude of deformation observed between the infant and juvenile models might therefore reflect an adaptative response to the differences in mechanical loading that arise during ontogeny as the teeth erupt and become functional and the face grows and develops, triggering differential expressions of osteoclastic and osteoblastic activities (Schuh et al., 2019). Regardless of the size differences between the infant, juvenile and adult models, the juvenile and especially infant show greater mechanical advantages and convert muscle into peak bite force more efficiently, yet they are not better able to resist these forces than the modern human mean adult model. In reality,

muscle forces in infants and juveniles are less than the adults, and full muscle force may not be applied in most contexts. In consequence, strain magnitudes will very likely be less than those predicted by the simulations presented here. Thus, these immature faces do not experience failure, but rather they adapt ontogenetically to the changing distributions and magnitudes of strains they experience as the craniofacial skeleton, teeth and soft tissues grow and develop.

## 4.0 Biting simulations in Neanderthals

### 4.1 Introduction

In this chapter the 3D models representing a Neanderthal infant, juvenile and adult from Chapter 2 are used as in the previous chapter on humans, to estimate the action and mechanical advantages of masticatory muscles that act to load the masticatory system and generate biting forces at the incisors and last premolar (infants) or first molar (juveniles and adults). They are then used as the basis for construction of finite element models simulating these bites. The results of these analyses and biting simulations (biting forces, cranial deformations and resulting strains) are reported and compared between age stages.

The aim of these analyses is to test the third hypothesis of this thesis: that there are no ontogenetic changes in cranial load resistance in Neanderthals. This hypothesis will be tested by qualitatively and quantitatively comparing load resistance (deformations and resulting strains) in finite element models representing different post-natal stages based on the surfaces of infant, juvenile and adult Neanderthal crania derived in Chapter 2. The results of these analyses will later be compared with the results of similar analyses from the previous chapter in modern humans and related to differences in craniofacial growth, development and remodeling.

### 4.2 Material and Methods

#### 4.2.1 Finite element models

##### 4.2.1.1 Model creation

The same protocol was followed for the Neanderthal finite element models as for the modern human ones. The three FE models were created from the three mean surfaces extracted from the growth model to represent Neanderthals at different age states (infant, juvenile and adult; Chapter 2). The same modern human teeth used for the modern human FE models were used in the Neanderthal models (see section 3.1.2.1). It was decided to use modern human teeth because they are of similar size and there is a lack of complete Neanderthal juvenile and infant dentitions (Figure 40). Tooth and bite point correspondence were established in terms of position along the dental arcade. Previous FE studies conducted on another modern human cranium (Godinho et al., 2018) have shown that differences in tooth type affect the magnitude of strains on a loaded model but not the general location of them. A similar sensitivity test was conducted with the Neanderthal adult model to assess the effects of using human teeth. The modern human adult dentition

was swapped for that extracted from the Amud 1 fossil specimen. The same tendency regarding changes in magnitude of strains, but not the mode of deformation was found as that by Godinho et al., (2018) and Toro-Ibacache et al., (2016a) (see Appendix 3). Finally, the models were segmented semiautomatically, with manual filling of the frontal and maxillary sinuses and all contact points between the teeth removed before the model was allocated a single material, with the properties of bone (Toro-Ibacache et al., 2016a; Godinho et al., 2018). The final three surfaces were converted into a volume stack using Avizo 9.0 (FEI Visualization) resampled to a medium resolution and to an isometric voxel size of 0.30 mm for the infant, 0.40 mm for the juvenile and 0.40 mm for the adult. Then, these were converted into a mesh for FEA (voxel-based model-cubic mesh as used by Vox-FE) using the vox3mat software tool.

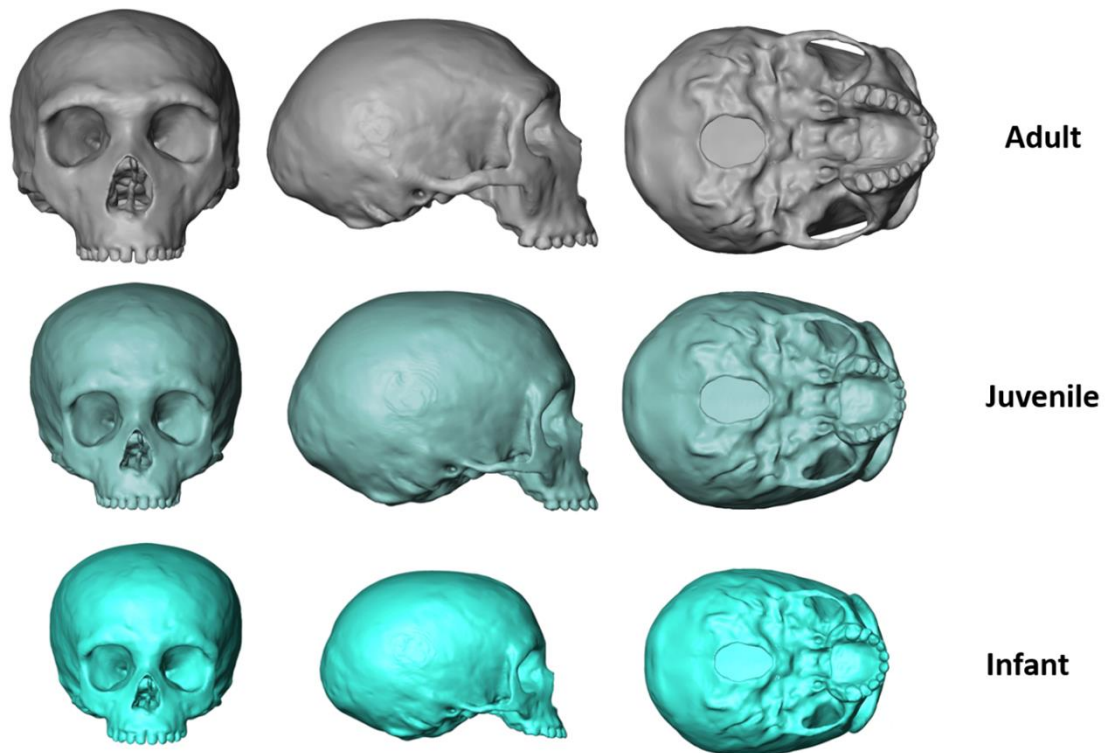


Figure 40. Neanderthal adult, juvenile and infant models with the corresponding human teeth.

#### 4.2.1.2 Finite element parameters

##### 4.2.1.2.1 Muscle loads

Loads were applied to each Neanderthal model in the same way as to the modern human ones (Chapter 3 section 3.2.1.1), directly to the nodes of the voxel elements representing the regions of muscle attachment. The muscles modelled in these experiments are the same as in the modern human of Chapter 3 section 3.2.1.2.1 and are based on those

used in previous FEAs conducted on modern humans and hominins (Godinho, Fitton, et al., 2018; Toro-Ibacache and O’Higgins, 2016). Neanderthals lack reliable ontogenetic data on muscle forces, for this reason, the same values as in adult modern humans (Chapter 3, section 3.2.1.2) were applied to all three models (infant, juvenile and adult). Likely these overestimate forces in the infant and juvenile and possibly underestimate them in adults, but the use of the same forces in all (modern human and Neanderthal models) controls for differences in deformation that might occur simply because of different forces and force ratios between muscles. FEA results were subsequently scaled for peak bite force difference to assess the impact of varying loads. This parallels the procedures used in previous similar studies (Godinho, Fitton, et al., 2018; Toro-Ibacache and O’Higgins, 2016).

The directions of muscle force vectors were estimated by warping adult and juvenile Neanderthal mandibles to fit the adult, juvenile and infant models. Muscle force vectors were then estimated as the mean line of pull of each muscle based on attachment points on the crania and mandibles. The mandibles used for this were the La Chapelle aux Saints and Roc de Marsal mandibles. The Roc de Marsal mandible CT-scans were obtained from the NESPOS database (Neandertal Studies Professional Online Service, [www.nespos.org](http://www.nespos.org)). The La Chapelle aux Saints mandible was obtained using a landmark configuration from the archives of the Department of Archaeology of the University of York (unpublished). This landmark configuration was aligned into the adult FE model using a warped human adult mandible as well, to guide the alignment. The Roc de Marsal mandible was scaled and warped into the juvenile model. Because of the lack of a complete Neanderthal infant mandible in the fossil record, the Roc de Marsal mandible was also scaled and warped for the infant FE models using Avizo 9.0 (FEI Visualization).

#### 4.2.1.2.2 Constraints

The same biting simulations as those carried out in modern humans (RI<sup>1</sup>, RP<sup>2</sup>/RdM<sup>2</sup>) were conducted on the three Neanderthal models. To control the experiments and for comparability of the biting simulations between both species, we used the same constraint parameters as for the modern human models. Thus, constraints were applied at both temporomandibular joints (TMJ). These were constrained in the x, y and z-axes on each model. These constraints are necessary to prevent models from rotating when loaded (Godinho et al., 2018). Other constraints comprising 30 nodes were applied in z direction at the teeth to simulate biting (RP<sup>2</sup>/RdM<sup>2</sup> and RI<sup>1</sup>).

#### 4.2.1.2.3 Material properties

As for the modern human FE models, each model was created as a single material (including teeth, filled sinuses and diploe) with the material properties of bone: Young's modulus of 17 GPa and Poisson's ratio of 0.3 (see section 3.2.1.2.3).

#### 4.2.1.2.4 Scalings

The same scaling approaches used in the mean modern human models were applied to the Neanderthal models (Chapter 3 section 3.2.1.2.4). The overall deformations (size and shape distances) between unloaded and loaded models under both biting simulations were also scaled following the approach used in previous studies (Godinho, Spikins and O'Higgins, 2018; O'Higgins and Milne, 2013) and explained in Chapter 3 section 3.2.1.2.4 which showed that size and shape distances between identically shaped loaded and unloaded models of different size scale inversely with lengths (such as centroid size) and directly with force.

Principal strains ( $\epsilon_1$  and  $\epsilon_3$ ) were scaled by the ratio of squared centroid sizes (squared cs) to account for differences in size between the infant, juvenile and adult models. As described in Chapter 3 section 3.2.1.2.4, squared centroid size (based on the same landmarks and semi-landmarks configuration for each model) was used instead of surface areas to scale principal strains calculated for each model. Arguably it is more consistent that surface areas which can be difficult to obtain especially here for the Neanderthal models which lack internal features due to preservation and the virtual reconstruction approach used.

To compare performance between the mean Neanderthal models, differences in peak biting forces between infant and adult models were also taken into account by scaling both principal strains and deformations by the ratio of peak bite forces generated by each model during the RP<sup>2</sup>/RdM<sup>2</sup> and RI<sup>1</sup> biting simulations. The centroid sizes of the models and the peak bite forces produced by them during each biting simulation are listed in Table 10.

*Table 10.* Centroid sizes (cs) for the Neanderthal infant, juvenile and adult models. Bite reaction forces (Peak bite force) generated by the infant, juvenile and adult models and calculated for the right first incisor (RI<sup>1</sup>) and right second premolar or second deciduous molar (RP<sup>2</sup>/RdM<sup>2</sup>) bite points.

	<b>Neanderthal</b>		
	<b>Centroid size</b>	<b>Peak bite force (RI<sup>1</sup>)</b>	<b>Peak bite force (RP<sup>2</sup>/RdM<sup>2</sup>)</b>
<b>Infant</b>	1145.22	241	357
<b>Juvenile</b>	1352.47	257	330
<b>Adult</b>	1536.99	225	291

#### 4.2.2 Mechanical advantages and peak bite forces

Mechanical advantages (MA: ratio of force out to force in) were calculated for the jaw adductor muscles (temporalis, masseter and medial pterygoid) based on 3D landmarks on the mean Neanderthal infant, juvenile and adult models (see section 3.2.2 and Figure 27). Landmarking of these models was based on their surfaces using Avizo 9.0 (FEI Visualization). To estimate the insertion of the temporalis, masseter and pterygoid muscles in the Neanderthal infant and juvenile models, the Roc de Marsal mandible was scaled to these models to estimate the masseter and medial pterygoid muscle insertions. For the temporalis, another juvenile and infant modern human mandible was scaled to these Neanderthal models to help estimate the temporalis muscle insertion. The same muscle insertions were estimated in the Neanderthal adult model by aligning the adult La Chapelle aux Saints mandible landmark configuration. To estimate and bracket the mechanical advantages of the temporalis and masseter muscles, these were calculated for their most anterior and posterior points of origin. For the temporalis, a third, intermediate, line of action was also defined, approximately in the centre line of the muscle, where it bulges and reaches its most superior point (Godinho et al., 2018). The in-lever arms were calculated as the perpendicular distance from the fulcrum to the respective muscle line of action (Figure 27). The out-lever arms for the right incisor and second premolar or deciduous molar bite were calculated as the perpendicular distance from the fulcrum to the vector of the peak bite force applied (O'Connor, Franciscus and Holton, 2005).

Following the same methods as for the modern human models (see section 3.2.2), maximal peak bite forces were calculated from the reaction forces at the bite points of the finite element models of the Neanderthal infant, juvenile and adult ( $F_b$ ). The maximal peak bite force production efficiency was calculated for each model (ratio of peak bite force and net muscle force,  $F_m$ ;  $F_b/F_m$ ) as was the ratio of reaction force at the glenoid fossa ( $F_c$ ) and net muscle force ( $F_c/F_m$ ). As with the study of the previous chapter, it should be noted that maximal bite forces are estimated by the FEA and that these are referred to simply as ‘peak bite forces’ throughout this chapter for brevity.

#### 4.3 Model solution and data analysis

The three FE models based on the Neanderthal growth model were solved using Vox-FE (Fagan et al., 2007). As with the modern human models, the resulting deformations were then evaluated and compared by visual assessment of contour plots of the compressive and tensile strain magnitudes over the face. The same 126 points, as for modern humans, distributed along the midface and supraorbital were used to quantitatively compare surface strain (tensile and compressive) magnitudes (Figure 41).

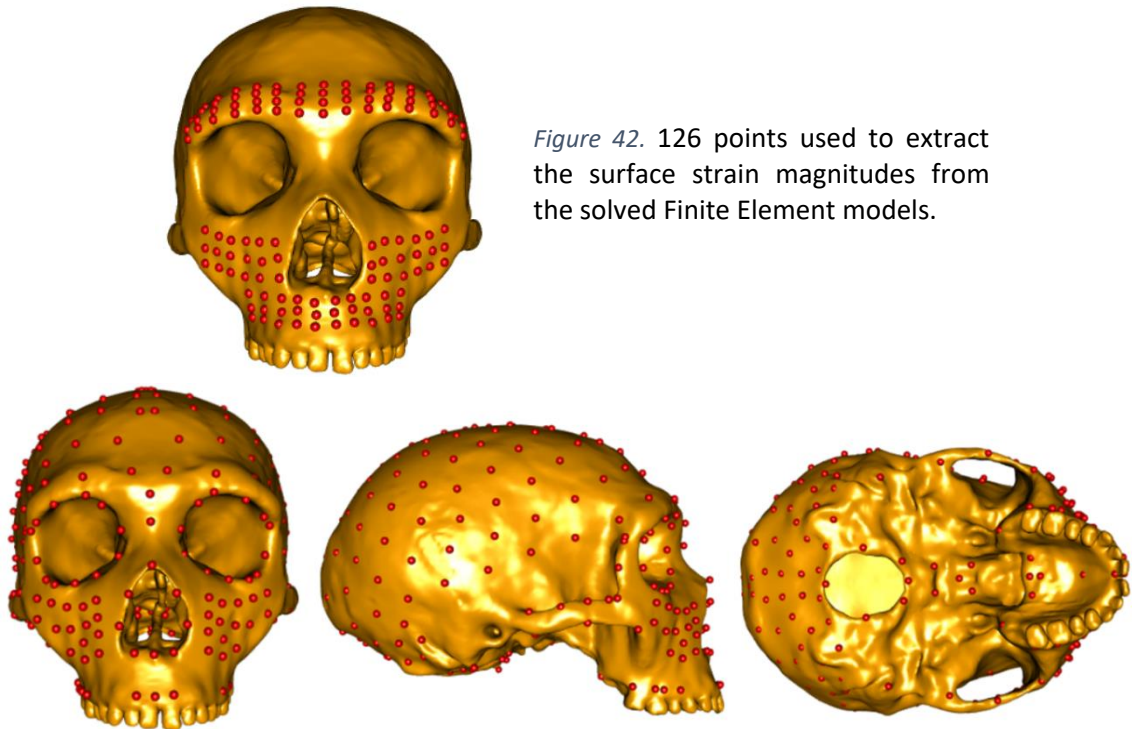


Figure 42. 126 points used to extract the surface strain magnitudes from the solved Finite Element models.

Figure 41. Landmark and semi-landmark configuration used to calculate the deformation of the cranium in each model after loading at the right first incisor ( $RI^1$ ) and right premolar 2 ( $RP^2$ ) or deciduous molar 2 ( $RdM^2$ ). Note: The teeth were added to the cranium after warping to estimate age means, so are not perfectly aligned with the landmarks.

Finally, the modes of global deformation (change in size and shape due to loading) were compared relative to the unloaded grand mean (of the infant, juvenile and adult models) using the same landmark and semi-landmark configuration of 303 points (Figure 42, see section 3.2.1).

#### 4.3.1 Mechanical advantages

Mechanical advantages (MAs) were calculated for the jaw adductor muscles (anterior, middle and posterior temporalis, anterior and posterior masseter and medial pterygoid) using the methods described in section 3.2.2, for the mean Neanderthal infant, juvenile and adult models (Figure 27). The ratios of the mechanical advantages of the main masticatory muscles were also calculated between the three models. Differences in MAs are expected between the Neanderthal models (Table 11 and Table 12) because of their differences in form.

*Table 11.* Mechanical advantages of the main masticatory muscles for the mean Neanderthal infant, juvenile and adult.

			Temporalis (anterior)	Temporalis (middle)	Temporalis (posterior)	Masseter (anterior)	Masseter (posterior)	Medial pterygoid
Neanderthal	Infant	RI <sup>1</sup>	0.39	0.34	0.23	0.28	0.26	0.25
		RdM <sup>2</sup>	0.59	0.51	0.35	0.43	0.39	0.38
	Juvenile	RI <sup>1</sup>	0.37	0.30	0.17	0.37	0.30	0.28
		RP <sup>2</sup>	0.49	0.40	0.23	0.50	0.41	0.37
	Adult	RI <sup>1</sup>	0.31	0.31	0.19	0.36	0.28	0.32
		RP <sup>2</sup>	0.42	0.41	0.25	0.48	0.38	0.42

*Table 12.* Ratios of the Mechanical advantages of the main masticatory muscles for the mean modern human infant, juvenile and adult.

			Temporalis (anterior)	Temporalis (middle)	Temporalis (posterior)	Masseter (anterior)	Masseter (posterior)	Medial pterygoid
Neanderthal	juvenile/infant	RI <sup>1</sup>	0.95	0.90	0.74	1.32	1.19	1.11
		RP <sup>2</sup> /RdM <sup>2</sup>	0.83	0.79	0.65	1.16	1.05	0.97
	adult/infant	RI <sup>1</sup>	0.81	0.91	0.82	1.27	1.12	1.28
		RP <sup>2</sup> /RdM <sup>2</sup>	0.71	0.80	0.71	1.11	0.98	1.12
	adult/juvenile	RI <sup>1</sup>	0.85	1.01	1.11	0.96	0.93	1.15
		RP <sup>2</sup>	0.85	1.01	1.10	0.96	0.93	1.15

At the RI<sup>1</sup> bite point, the mechanical advantages (MAs) of the main muscles of mastication show different patterns of change from infant to adult (Tables 11 and 12). For the anterior and posterior masseter, MAs increase from infant to juvenile, then fall in adults. For the medial pterygoid, the lowest MA value is in the infant model and this rises to the juvenile and then adult models and for the anterior temporalis the MAs decrease from infant to adult. Finally, for the middle and posterior parts of the temporalis MA falls from infant to juvenile, then rises in adult (Table 11).

At the RP<sup>2</sup>/RdM<sup>2</sup> bite point, the mechanical advantages (MAs) for all the models are, as expected, greater than those for the RI<sup>1</sup> bite (Table 11). The mechanical advantages (MAs) show different patterns of change among the three models for the main muscles of mastication (Tables 11 and 12). For the anterior part of the temporalis MAs decrease from infant to adult, which presents the lowest MA, for the middle and posterior temporalis and the medial pterygoid, MA falls between infant and juvenile and then rises in adults and for the anterior and posterior masseter, it rises from infant to juvenile and then falls in adults (Table 11 and Table 12).

*Table 13.* Force Production efficiencies in the RI<sup>1</sup> and RP<sup>2</sup>/RdM<sup>2</sup> biting simulations, calculated from the Finite Element models of a mean Neanderthal infant, juvenile and adult. Fb, peak bite force; Fm, net applied muscle force, Fc, glenoid fossa reaction force.

bite point	Force production efficiencies					
	Fb/Fm			Fc/Fm		
	Infant	Juvenile	Adult	Infant	Juvenile	Adult
RI1	0.36	0.35	0.31	0.64	0.65	0.69
RP2/RdM2	0.51	0.45	0.40	0.49	0.55	0.60

The ratios of peak bite force (Fb) and the condylar constraint (Fc) reaction forces to the net muscle forces (the sum of all reaction forces at the constrained nodes on the teeth and glenoid fossa - Fm) predicted for the Neanderthal models, are presented in Table 13. For the right first incisor (RI<sup>1</sup>) bite point, the infant model presents the highest peak bite force production efficiency (Fb/Fm) followed by the juvenile model and the adult, which presents the lowest. The ratio of the glenoid fossa reaction force to net applied muscle force is larger in the adult model than in the juvenile and infant models which present smaller values. For the right second premolar or deciduous molar (RP<sup>2</sup>/RdM<sup>2</sup>), the infant model presents the greatest peak bite force production efficiency (Fb/Fm) and the lowest ratio of the glenoid fossa reaction force to net applied muscle force (Table 13).

The former progressively increases and the latter decreases between infant, through juvenile to adult models.

#### 4.3.2 Deformations

Size and shape analyses of the global deformation of the three models were conducted for both biting simulations (Figure 43 and Figure 44). To aid visualisation, deformations

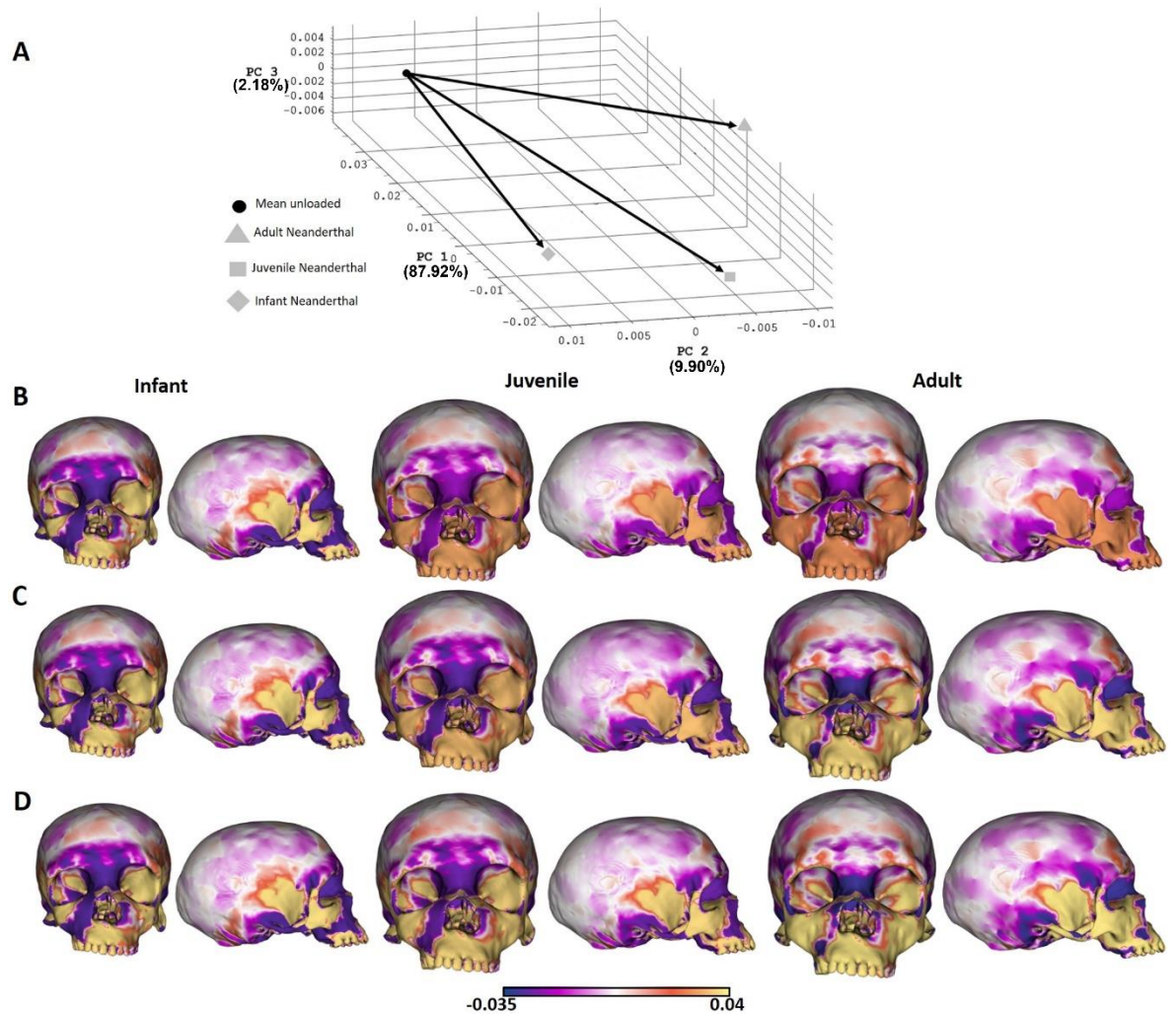


*Figure 43.* Size and shape analysis of modes and magnitudes of deformation of the Neanderthal infant, juvenile and adult models from the RP<sup>2</sup>/RdM<sup>2</sup> biting simulations. A) Size and shape PC 1-3 plot. B-D, warped surfaces between unloaded and loaded models with colourmaps illustrating regions of surface contraction and expansion under RP<sup>2</sup>/RdM<sup>2</sup> biting: B) unscaled, C) scaled by size and D) scaled by peak bite force. The deformations were magnified x1000. Colour scale bars indicate ratios of areas between unloaded and loaded models.

were magnified 500x for RI<sup>1</sup> biting and 1000x for RP<sup>2</sup>/RdM<sup>2</sup> biting using the Evan toolbox v.1.75. Then, using the R package “Arothron” (Profico et al., 2019), the mean unloaded cranium mesh triangle areas were compared with those of the loaded specimens to create colourmaps (Profico et al., 2017) showing regions of the cranial surface where

the triangles in the cranial mesh are reduced in area (in purple) or increased (yellow/orange) as a consequence of the deformations resulting from the biting simulation (Figure

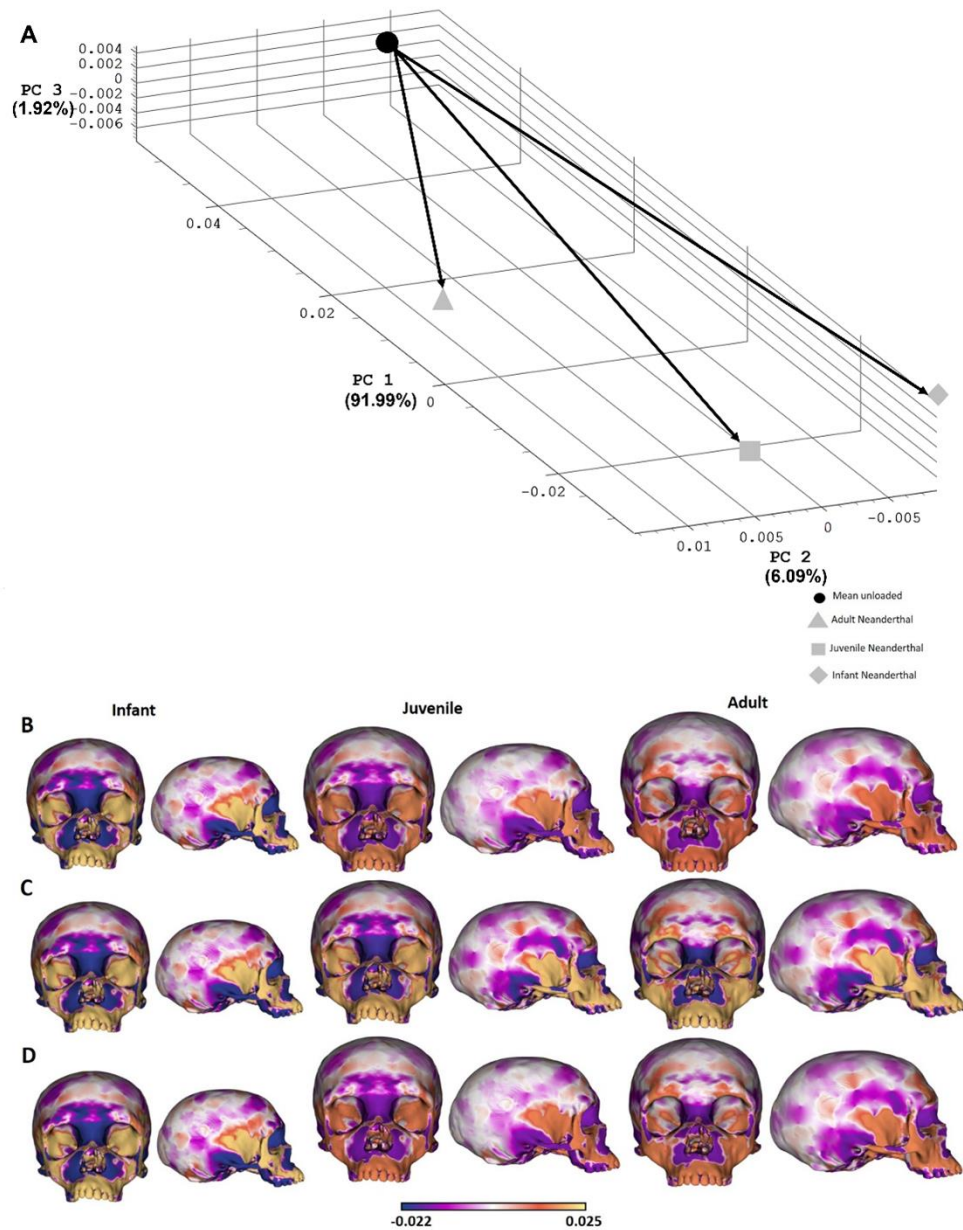


Figure 44. Size and shape analysis of modes and magnitudes of deformation of the Neanderthal infant, juvenile and adult models from the  $RI^1$  biting simulations. A) Size and shape PC1-3 plot. B-D, warped surfaces between unloaded and loaded models with colourmaps illustrating regions of surface contraction and expansion in each Neanderthal relative to the mean unloaded model under  $RI^1$  biting simulations: B) unscaled, C) scaled by size and D) scaled by peak bite force. The deformations were magnified x500. Colour scale bars indicate ratios of areas between unloaded and loaded models.

43B-D and Figure 44B-D). Raw deformations as well as deformations scaled for centroid size and peak bite force with the infant model as a reference were compared among models and biting simulations. To do so, the juvenile and adult loaded surfaces were extracted from their vector between the unloaded surface and the loaded ones, at an increased or

decreased distance from the unloaded mean, in proportion to their ratios of size (cs) and peak bite force with the infant Neanderthal model.

In both biting simulations, the infant, juvenile and adult models present subtle differences in magnitudes and modes of deformation. During the RP<sup>2</sup>/RdM<sup>2</sup> biting simulation, the infant model deforms more than the juvenile one and the adult model deforms the least. During the RI<sup>1</sup> biting simulation the juvenile model deforms the most. In the PC plots, PC1 represents 87.92% of the total variance for the RP<sup>2</sup>/RdM<sup>2</sup> biting simulation and 91.99% for the RI<sup>1</sup> biting simulation (Figure 43A and Figure 44A) indicating greater variance in vectors of deformation among models under RP<sup>2</sup>/RdM<sup>2</sup> biting simulation.

Warping from the unloaded cranium to the loaded crania shows that loading on the RP<sup>2</sup>/RdM<sup>2</sup> causes, in all models, a lateral rotation of the palate, together with the lateral margin of the nose such that the working side (right) is raised. As for the modern human models (see section 3.4.2), this results in an asymmetry of deformation between the working and balancing sides of the cranium. The warped surfaces and their associated colourmaps show that the infant model surface reduces in area over the right anterior maxilla above the bite point, over the supraorbital region, the orbits and around the nasal aperture. Expansion of area is found over the inferior maxilla away from the bite point, and zygomatic arches. The juvenile model surface shows a large degree of contraction of area over the nasal bridge, orbits and around the nasal aperture on both sides of the face. Over the inferior maxilla away from the bite point, zygomatic arches and alveolar process the mesh mostly increases in area (Figure 43B). The adult presents a similar mode of deformation to the juvenile model but with a lower magnitude. The scaling by cs and by bite force increase the magnitude of the deformation in the juvenile and adult models (Figure 43B and Figure 44C), however scaling by bite force has little effect because bite forces vary little and (Table 10), in the biting simulations.

The RI<sup>1</sup> biting simulation causes a relative upward movement of the anterior maxilla as well as a large inferior deflection of the zygomatic arches, especially on the working side of the three models (Figure 44A). The colourmaps showing regions of surface expansion and contraction are similar between the models and are generally symmetric between the working and balancing sides. Contractions of the meshes are observed between the orbits, around the nasal aperture and at the supraorbital, and expansions of the meshes are found at the inferior, anterior maxilla, the alveolar process and the zygomatic

arches. The magnitudes of the deformation and the degree of surface contraction or expansion decrease from the infant to the adult model. As for the RP<sup>2</sup>/RdM<sup>2</sup> biting simulations, scaling by centroid size (Table 10) increases the degree of deformation in juvenile and adult models. Scaling by bite force has little effect because bite forces vary little (Table 10), however, it slightly increases the degree of deformation in the adult but slightly decreases it in the juvenile (Figure 44C and Figure 44D).

#### 4.3.3 Tensile and compressive strains

The present section describes the results obtained from the right second premolar (RP<sup>2</sup>) or right deciduous molar 2 (RdM<sup>2</sup>) and right first incisor 1 (RI<sup>1</sup>) biting simulations in Neanderthal (NEA) infant, juvenile and adult models. Strain contour plots and strain values were used to assess the impact on biting, and resistance of muscle and biting forces, of the morphological differences in cranial form at each age stage. It is expected that differences will be found in; i) ability to resist masticatory loading, ii) magnitudes and modes of deformation experienced by the craniofacial complex.

During the RP<sup>2</sup>/RdM<sup>2</sup> biting simulation, the Neanderthal infant model presents the greatest tensile strains ( $\epsilon_1$ ) and the adult the least even after scaling for size and bite force (Figure 45). In the three models, strains are generally similarly distributed, with the largest strains found on the working side of the cranium (right) and in similar anatomical areas, such as directly above the bite point, the zygoma and the right part of the anterior maxilla and around the orbits. The same is observed for the compressive strains ( $\epsilon_3$ ). When scaled by size (squared cs) or bite force, both compressive and tensile strain magnitudes increase (Table 11; Figure 45). However, scaling by bite force has a very small effect because bite forces differ little among models (Figure 45B, Figure 45C, Figure 45E and Figure 45F).

During the RI<sup>1</sup> biting simulation, strains decrease from infant to adult stages, both when the data are unscaled or scaled for size (squared of centroid size, see chapter 4.2.1.2.4) or bite force (Figure 46). Among models, strain maps are generally comparable, with the largest strains found in similar anatomical areas, such as directly above the bite point at the inferior part of maxilla, around the nasal aperture, at the zygomatic arches, the supraorbital region, the orbits and nasal bones. The strains are relatively symmetric between the working and balancing (left) sides except at the inferior maxilla (from the alveolar process to the nasal aperture), just above the bite point, where they are greater

on the working side. In all models, the maximum tensile strains are found just above the bite point at the inferior maxilla and the zygomatic bone and arches. As previously observed in the RP<sup>2</sup>/RdM<sup>2</sup> biting simulation, when scaled for size (squared cs), both tensile and compressive strain magnitudes increase for the juvenile and adult models. At the RP<sup>2</sup>/RdM<sup>2</sup>, the juvenile model presents slightly higher strains at the anterior maxilla, above the alveolar process and around the nasal aperture for both tensile and compressive strains. When scaled by peak bite force, strains change slightly, increasing in the adult and decreasing in the juvenile (Figure 46B, Figure 46C, Figure 46E and Figure 46F).

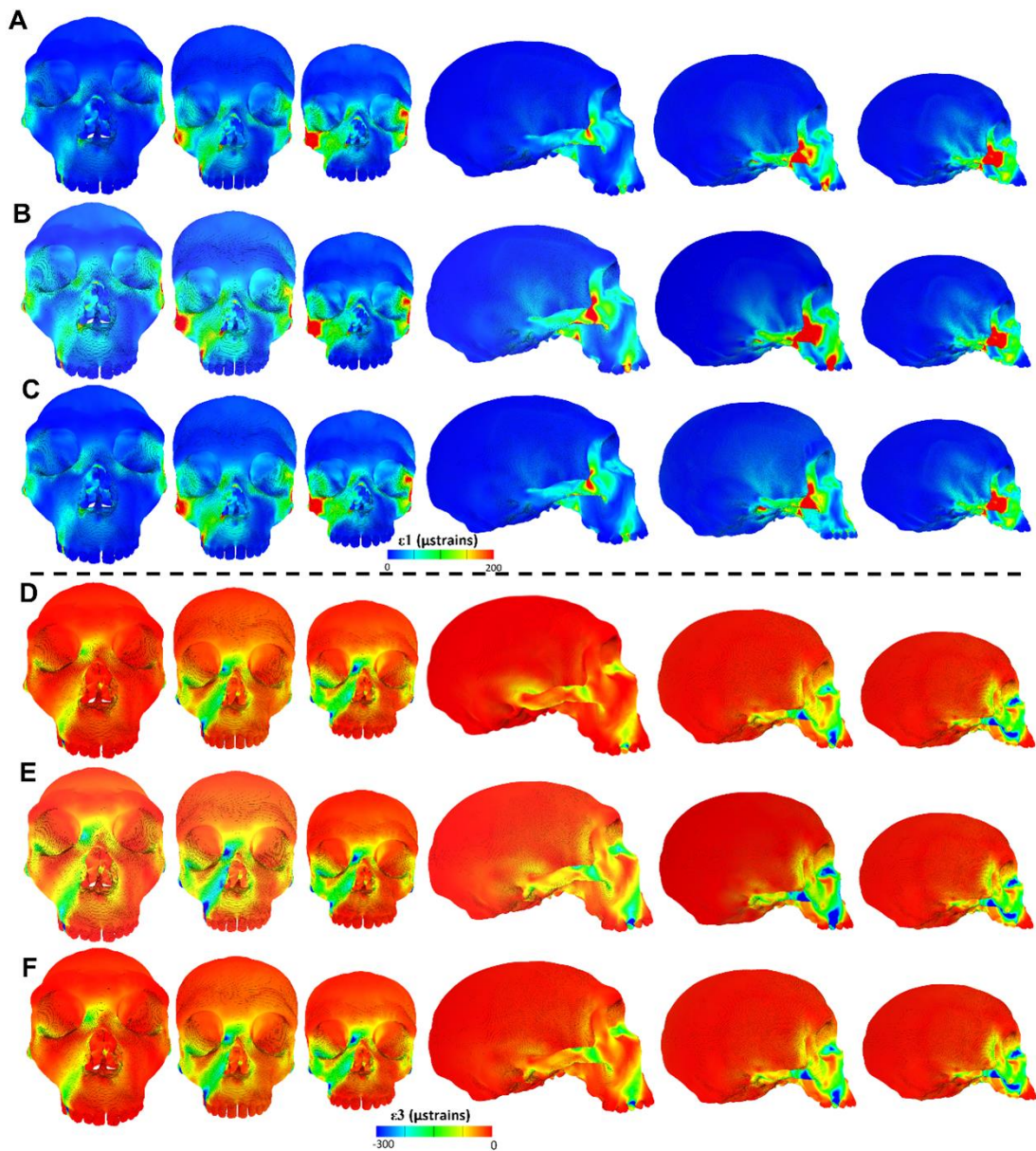


Figure 45. Strain contour plots of the solved Neanderthal infant juvenile and adult FE models (from left to right) under  $RP^2/RdM^2$  biting simulation in frontal and lateral views. Tensile (top) and compressive strains (bottom) are unscaled (A, D), scaled by size (B, E) and scaled by bite force (C, F).

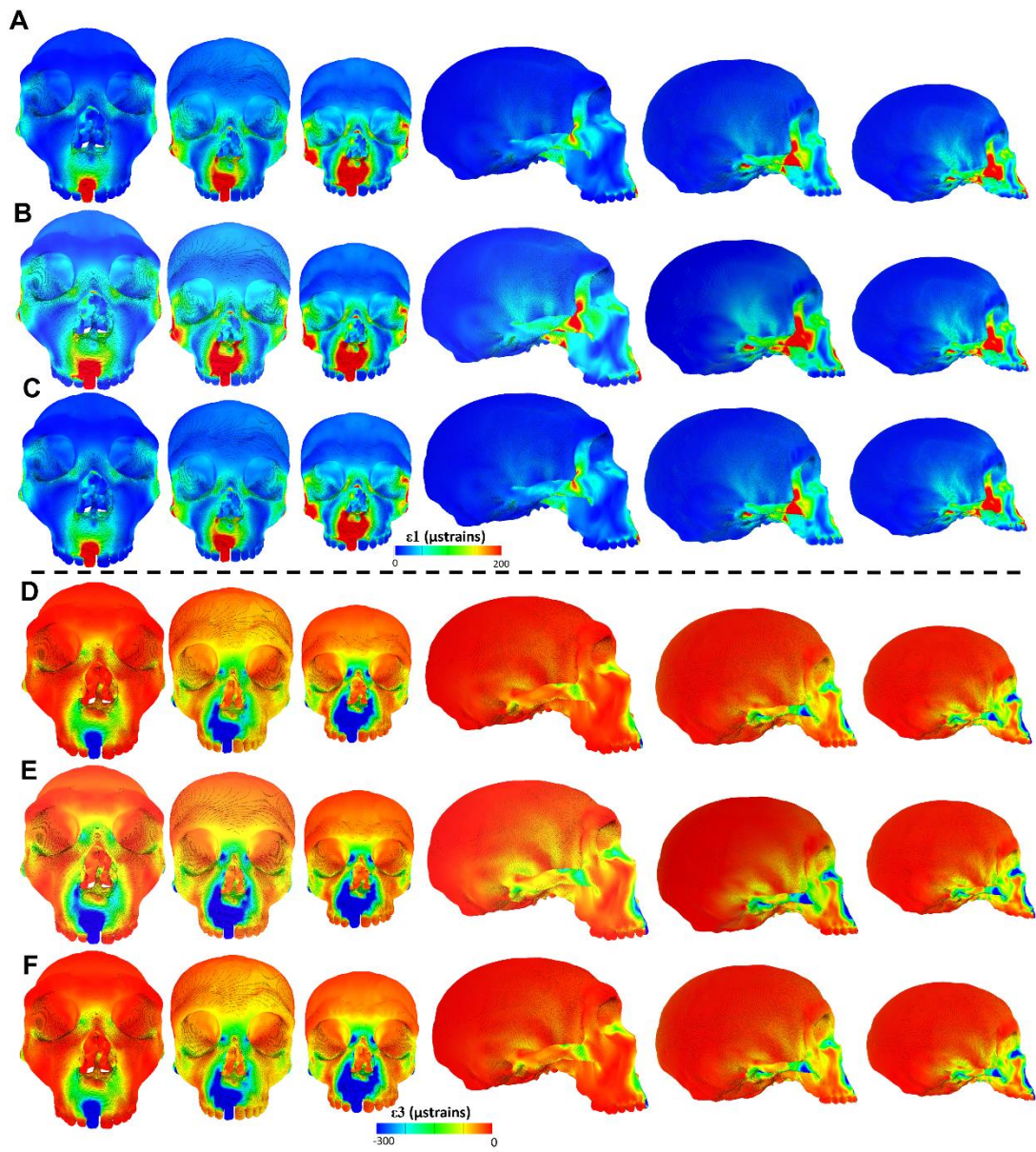


Figure 46. Strain contour plots of the solved Neanderthal infant juvenile and adult FE models (from left to right) under  $RI^1$  biting simulation in frontal and lateral views. Tensile (top) and compressive strains (bottom) are unscaled (A, D), scaled by size (B, E) and scaled by bite force (C, F).

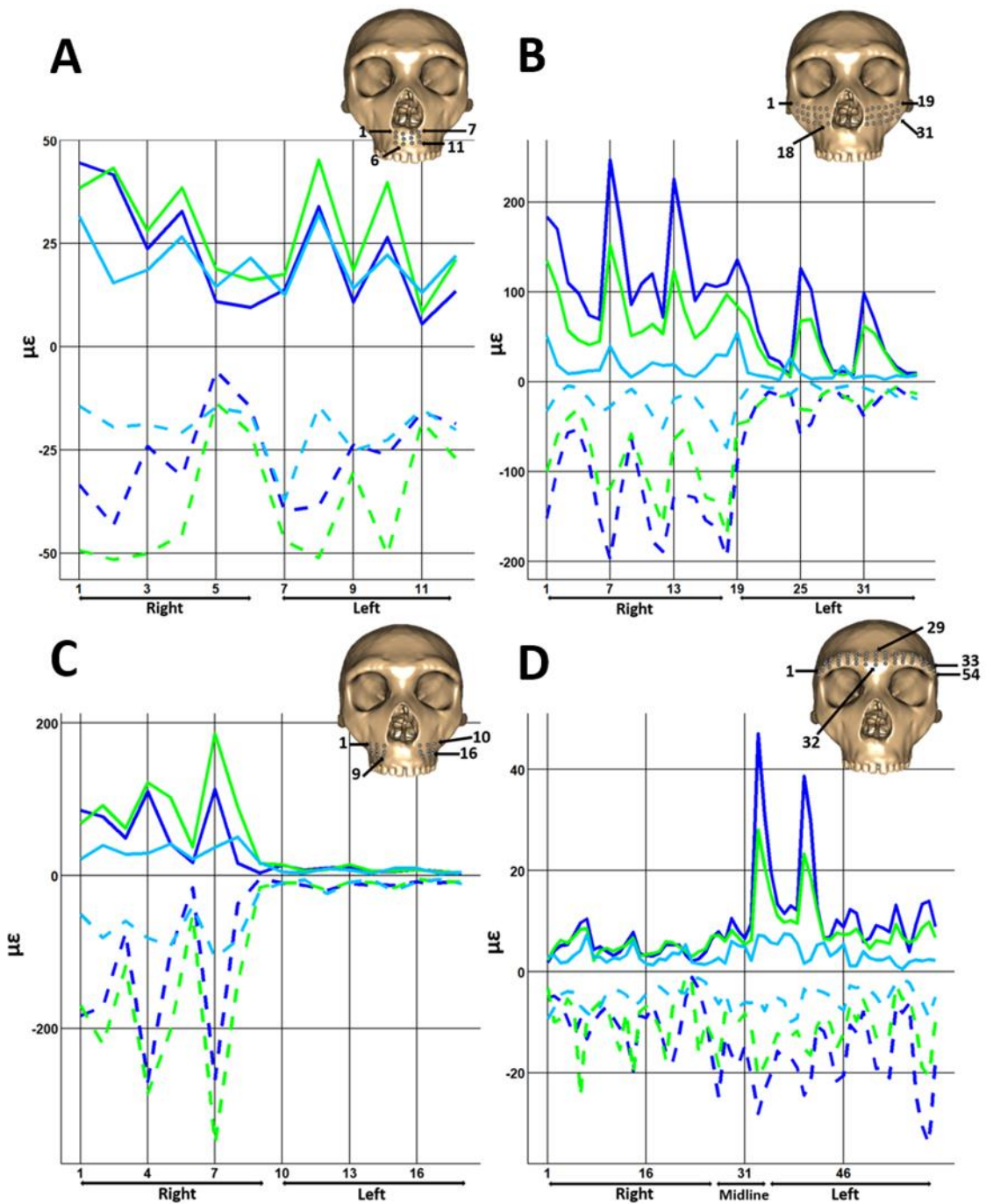


Figure 47. Strains experienced by the Neanderthal (NEA) infant (blue), juvenile (green) and adult (sky blue) FE models at the 126 sampling points distributed over the maxilla and supraorbital ridge during the RP<sup>2</sup>/RdM<sup>2</sup> biting simulations. The tensile (solid) and compressive (dashed) strains are unscaled. See landmark details in supplementary material Figure 1.

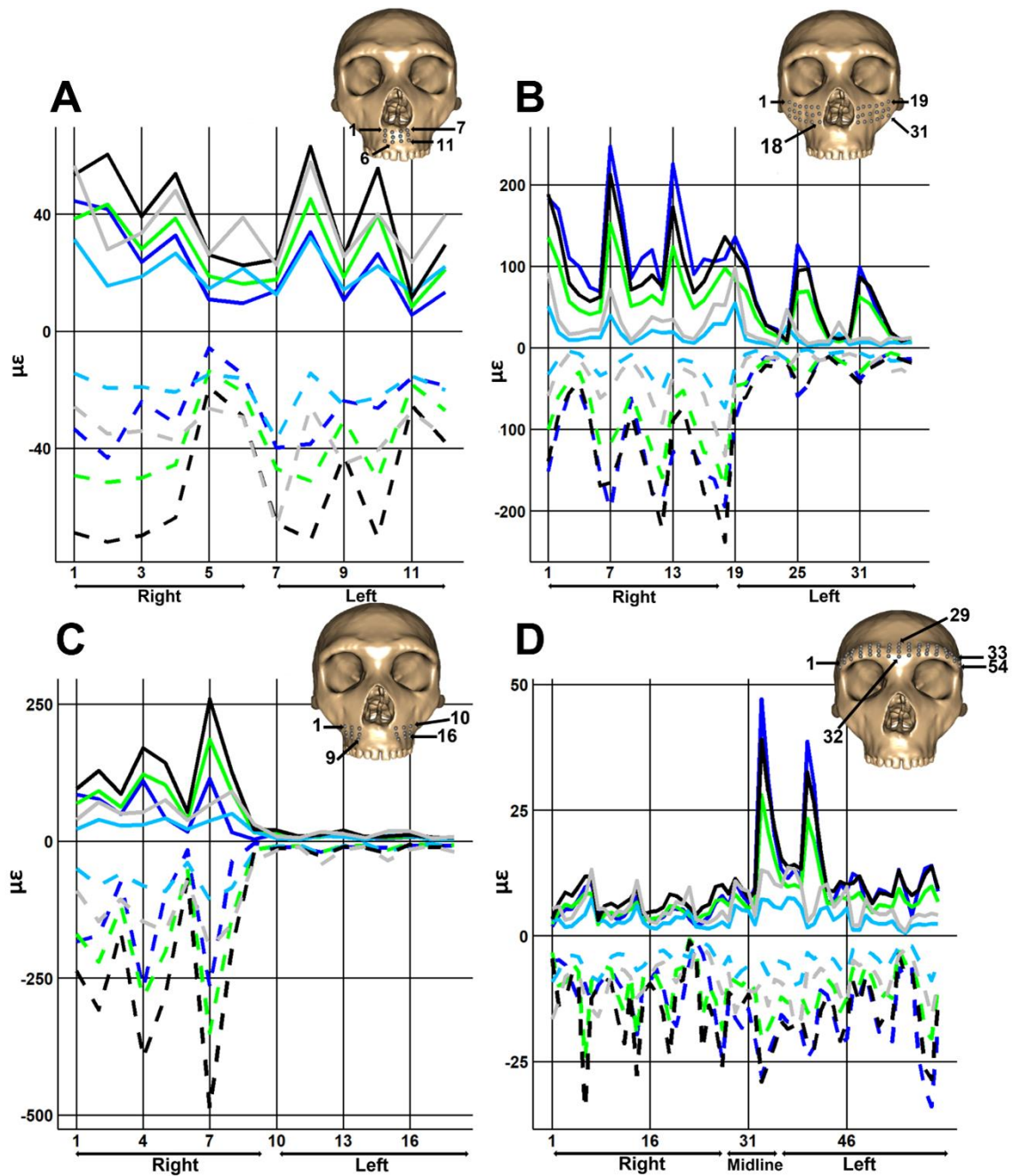


Figure 48. Strains, unscaled and scaled by size, experienced by the Neanderthal (NEA) infant (blue), juvenile (green) and adult (sky blue) FE models at the 126 sampling points distributed over the face during the  $RP^2/RdM^2$  biting simulation. The juvenile (black) and adult (grey) models were scaled according to the infant centroid size (cs). See landmark details in supplementary material Figure 1.

The principal strains recorded at the 126 landmarks (section 4.3) are presented in Figures 47-52 as plots to facilitate comparison between models. Figures 47 and Figure 52 show that, for each biting simulation, the distribution of regions of large and small principal tensile ( $\epsilon_1$ ) and compressive ( $\epsilon_3$ ) strains over the craniofacial surface is generally similar among the models, with only a few local differences. The magnitudes of these strains are the main difference among these models. During the RP<sup>2</sup>/RdM<sup>2</sup> biting simulation, the infant and juvenile models present the greatest tensile and compressive strains with the juvenile exceeding the infant at the inferior maxilla (under the nasal aperture and at the bite point, see Figures 47A from point 2 to 10 and Figure 47C from point 1 to 8). Overall, the adult shows the smallest strains (Figure 47). In each biting simulation, asymmetric variation is observed in both compressive and tensile strains. Thus, in the RP<sup>2</sup>/RdM<sup>2</sup> simulation, directly above the bite points and at the anterior maxilla (Figure 47B and Figure 47C), the working side (labelled Right) exhibits greater strains than the balancing side, especially in the infant and juvenile models. The opposite pattern is observed at the supraorbital where tensile strains are generally greater at the balancing side (labelled Left).

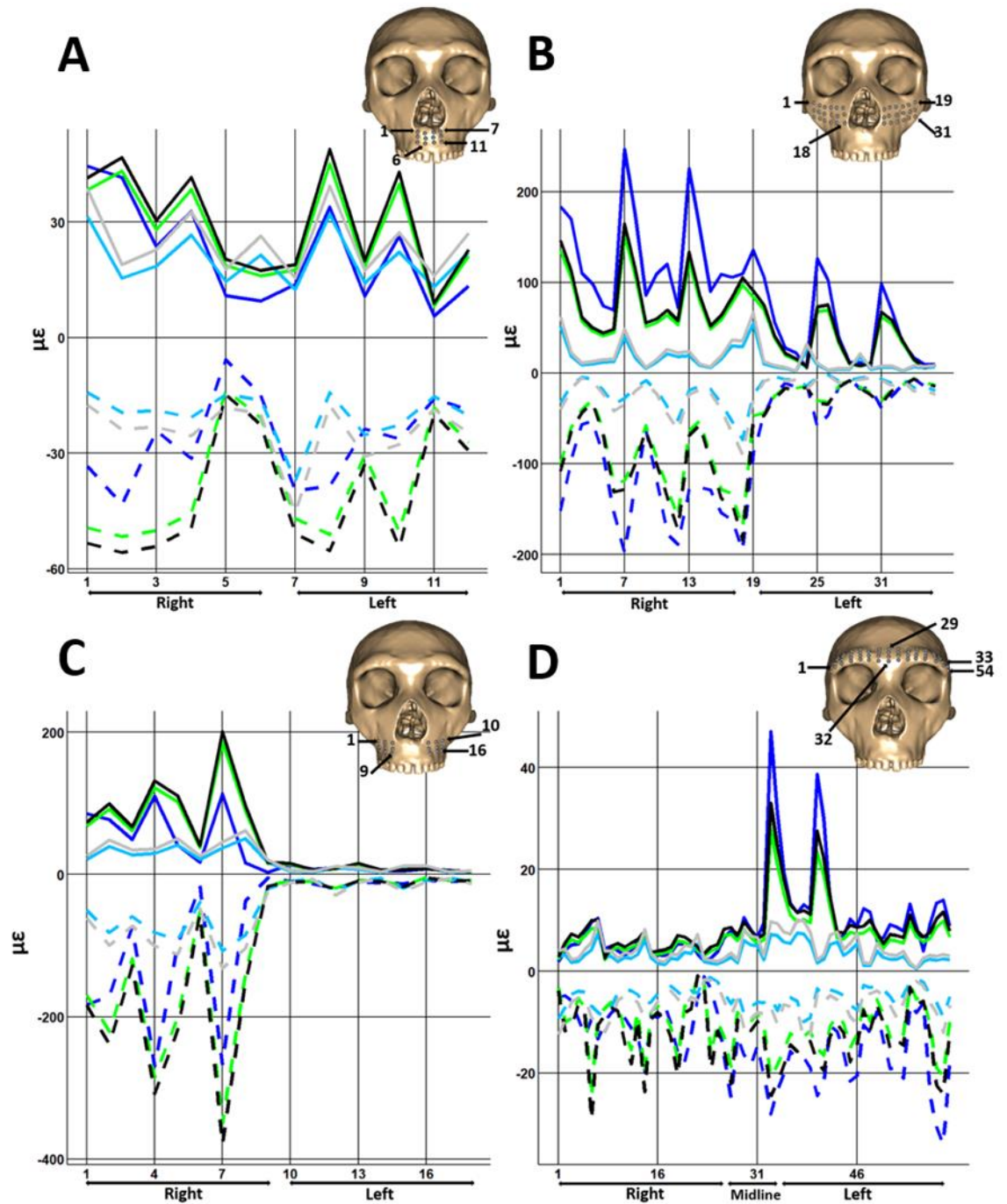


Figure 49. Unscaled and scaled by bite force strains experienced by the Neanderthal (NEA) infant (blue), juvenile (green) and adult (sky blue) FE models at the 126 sampling points distributed over the face during the  $RP^2/RdM^2$  biting simulation. The juvenile (black) and adult (grey) models were scaled according to the infant bite force. See landmark details in supplementary material Figure 1.

During the RI<sup>1</sup> biting simulation, both tensile and compressive strains decrease from infant to adult models (Figure 50). Among models, asymmetric distributions of strains are found at the same locations but are less marked than those observed under the RP<sup>2</sup>/RdM<sup>2</sup> biting simulation.

The principal tensile and compressive strain values were scaled by the square of centroid size (squared cs) and peak bite force. When scaling by squared cs, the distribution of low or high tensile strains changes in the three models for the RP<sup>2</sup>/RdM<sup>2</sup> biting simulations (Figure 48), with the juvenile model presenting higher strains than the infant especially at the inferior maxilla and over the alveolus process above the bite point (Figure 48A and 48C). For the RI<sup>1</sup> biting, scaling by squared cs affect the magnitudes of the strains without changing the ordering of models with respect to which presents the greatest and least tensile and compressive strains in each simulation. Scaling by bite forces has the least effect because these varied little (Table 10). Scaling by bite force for the RI<sup>1</sup> biting simulation slightly increases strains in the adult but decreases them slightly in the juvenile model (Table 10).

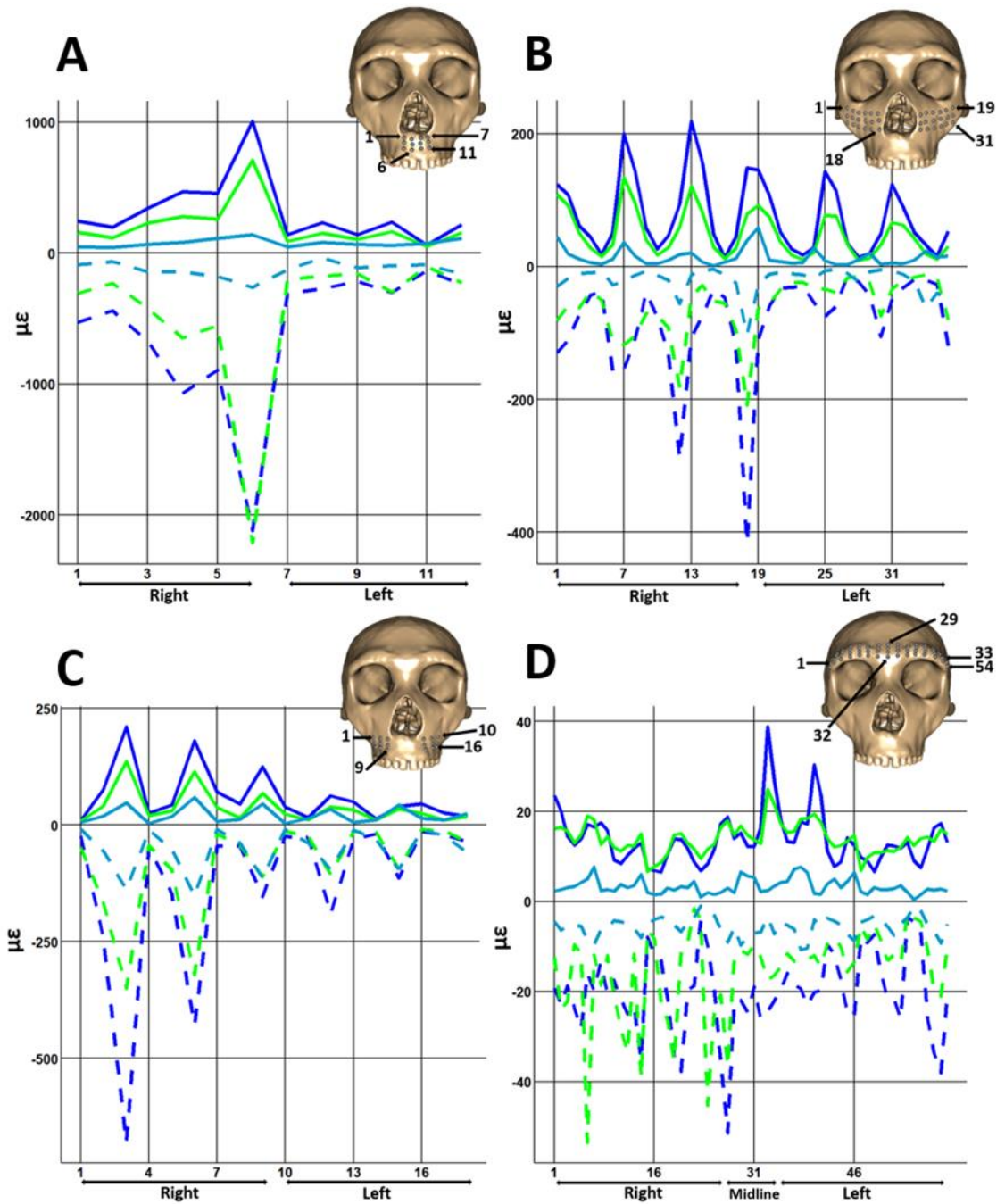


Figure 50. Strains experienced by the Neanderthal (NEA) infant (blue), juvenile (green) and adult (sky blue) FE models at the 126 sampling points distributed over the maxilla and supraorbital ridge during the  $R1^1$  biting simulations. The tensile (solid) and compressive (dashed) strains are unscaled. See landmark details in supplementary material Figure 1.

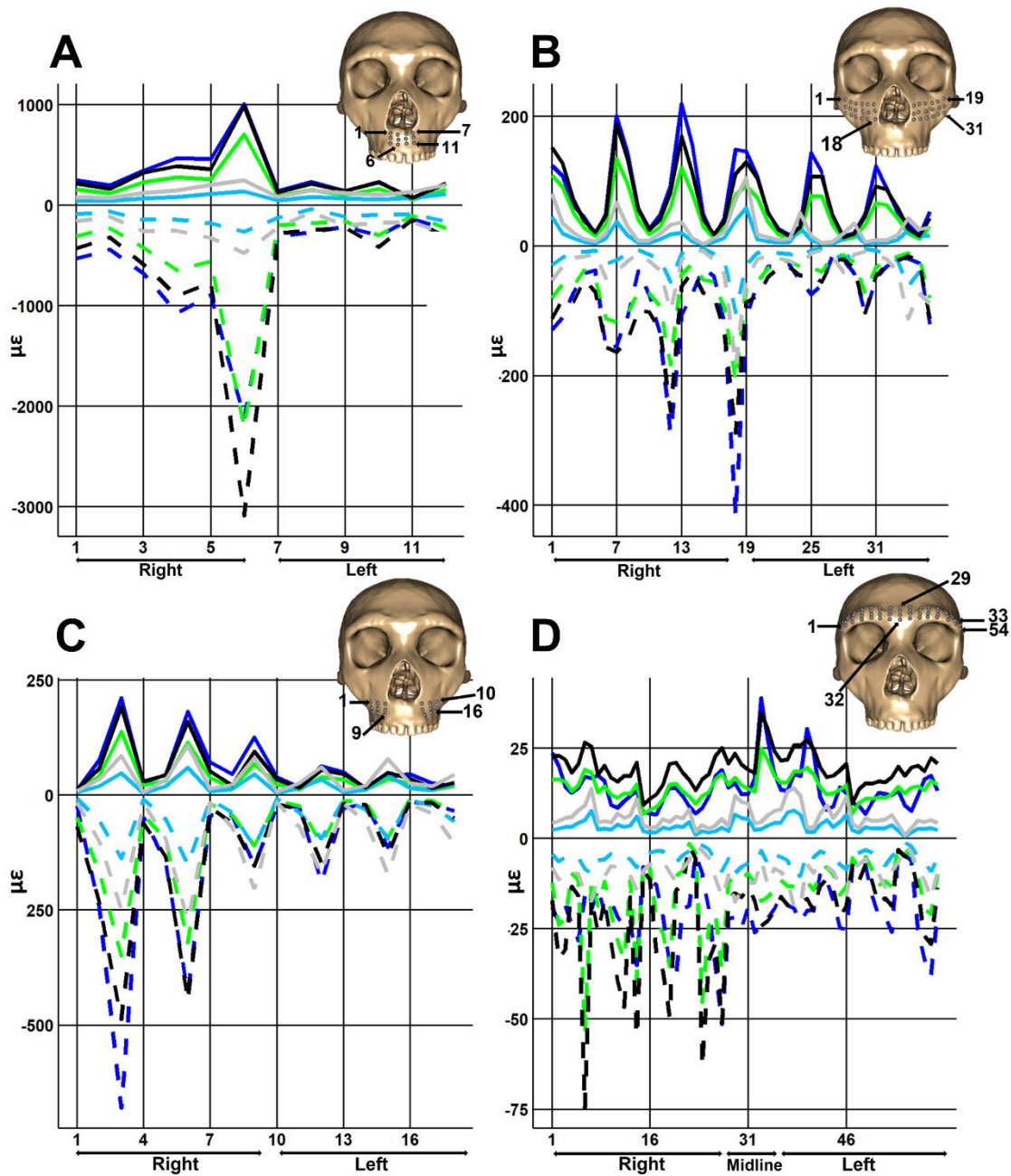


Figure 51. Unscaled and scaled by size strains experienced by the Neanderthal (NEA) infant (blue), juvenile (green) and adult (sky blue) FE models at the 126 sampling points distributed over the face during the  $RI^1$  biting simulation. The juvenile (black) and adult (grey) models were scaled according to the infant centroid size (cs). See landmark details in supplementary material Figure 1.

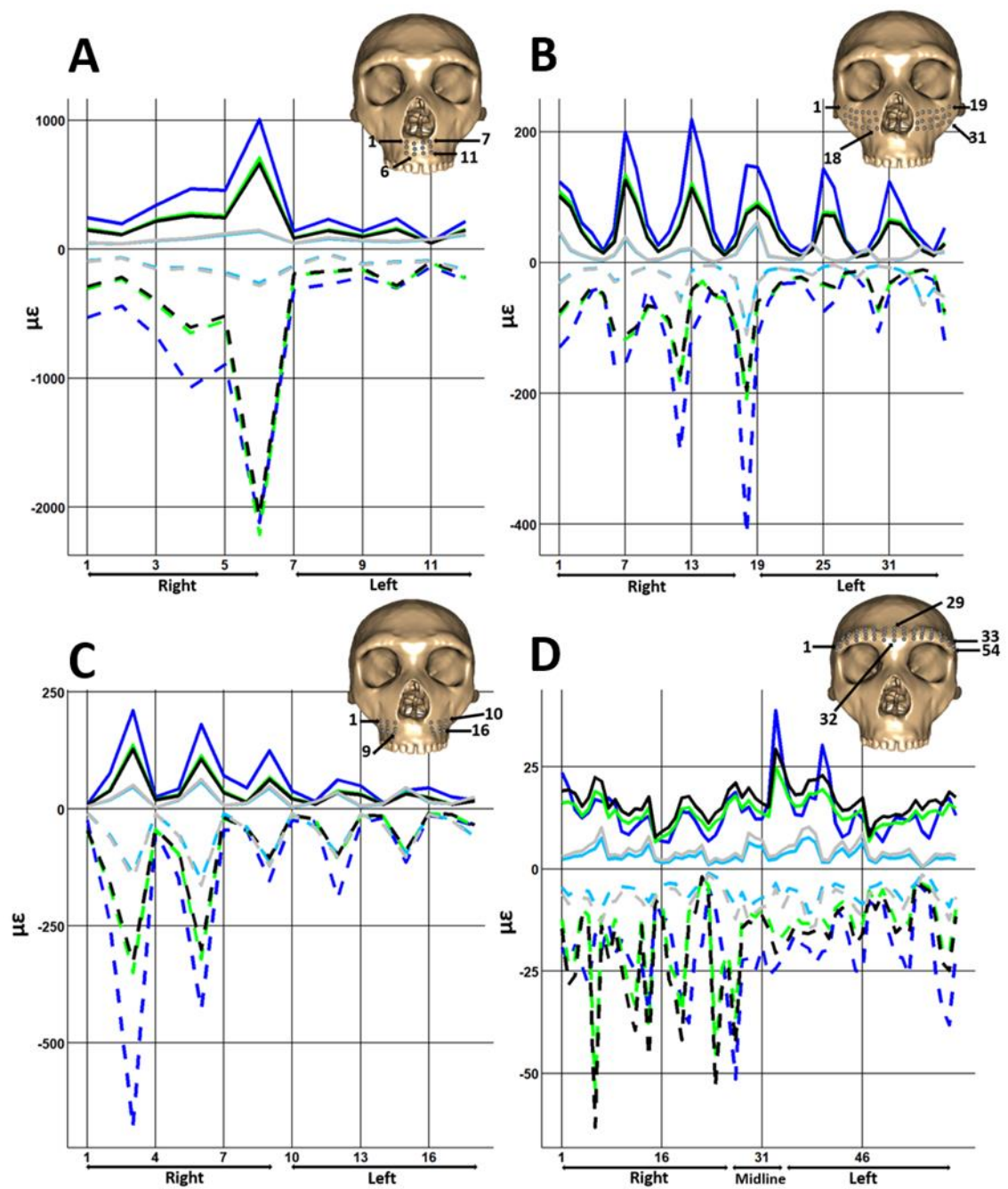


Figure 52. Unscaled and scaled by bite force strains experienced by the Neanderthal (NEA) infant (blue), juvenile (green) and adult (sky blue) FE models at the 126 sampling points distributed over the face during the RI<sup>1</sup> biting simulation. The juvenile (black) and adult (grey) models were scaled according to the infant bite force. See landmark details in supplementary material Figure 1.

## 4.4 Discussion

### 4.4.1 Mechanical advantages, peak bite forces and force production efficiencies

Several studies have investigated the masticatory biomechanics of Neanderthals (Rak, 1986; Trinkaus, 1987a; Demes and Creel, 1988; Antón, 1990; Spencer and Demes, 1993; Antón, 1996; Clement, Hillson and Aiello, 2012; O'Connor, Franciscus and Holton, 2005). One proposal arising from these studies is that Neanderthals were adapted to generate and withstand high and/or repetitive occlusal loads at the anterior dentition (the anterior dental loading hypothesis; Demes and Creel, 1988; Rak, 1986). The present study compares the mechanical advantages and forces production efficiencies between Neanderthal infant, juvenile and adult means.

The results show that for both biting simulations ( $RP^2/RdM^2$  and  $RI^1$ ) the infant presents a greater MA than the juvenile and adult models. For the masseter muscle, the juvenile presents the highest values while at the medial pterygoid, the adult model shows the greatest MAs for both biting simulations (Table 11 and Table 12). The mechanical advantage explains the bite forces calculated for each model (Table 10). For the  $RP^2/RdM^2$  biting simulation, the mean infant specimen bite force (Table 10) is 8% or 20% greater than those for the juvenile and adult models respectively. In the  $RI^1$  biting simulation, estimated bite forces show more similar values among the models, with the juveniles presenting a bite force 6% greater than the infant and 13% greater than the adult model, and the adult having the lowest bite force (Table 10). Between the infant and juvenile models, the MAs of each masticatory muscle vary considerably (Tables 11 and 12). This has also been found in modern humans *in vivo* and based on models (Edmonds and Glowacka, 2020; Mountain, Wood and Toumba, 2011; Gavião, Raymundo and Rentes, 2007). Force production efficiencies were also calculated and show that in both biting simulations, the infant presents the highest ratio of bite force to net applied muscle force (Table 13). Therefore, overall, the infant model seems to be more efficient at converting muscle force into bite force than the juvenile and adult models. This is probably due to the smaller, shorter and less prognathic face of the infant model compared to the adult and juvenile models, which shortens the bite out-lever relative to the muscle in-lever arms of the juvenile and adult model.

The mechanical advantages calculated in this study for the adult Neanderthal model were compared with those obtained by O'Connor et al., (2005) for Amud 1, La Chapelle aux Saints 1 and La Ferrassie 1 in incisor biting. In this study, the mechanical

advantages for the mean Neanderthal adult model fall within the range of values found by O'Connor et al., (2005) except for the medial pterygoid which presents a slightly lower MA (0.30) than that found by O'Connor et al., (2005) in Amud 1 (0.364), La Chapelle aux Saints 1 (0.332) and La Ferrassie 1 (0.344). In both previous studies (Godinho et al., 2018; O'Connor, Franciscus and Holton, 2005), the masseter muscles present the highest MA followed by the medial pterygoid muscles and finally, the temporalis with the lowest MA value. The same pattern was found in this study for the anterior masseter, medial pterygoid and temporalis in the mean adult model for both bites, but this ordering varies among juvenile and infant bites, with infants having higher temporalis MAs (Table 11).

These comparisons do not take into account differences in muscle forces that may have existed from infancy to adulthood. As explained for the modern human models in Chapter 3 section 3.1.2, no data on real muscle forces exist in infant and juvenile modern humans and of course in Neanderthals due to a lack of preservation of soft tissues. So far, studies have used bony proxies to estimate the cross-sectional areas of the masticatory muscles (Koolstra et al., 1988; Antón, 1994; Antón, 1990). However, it has been shown that this is not a reliable method (Toro-Ibacache, Zapata Muñoz and O'higgins, 2015). Therefore, the human muscle forces used here likely impact the resulting estimates of biting force.

The diet of Neanderthals has been widely studied and it appears to show a large degree of variability in terms of food selection and processing (Richards et al., 2000; Bocherens, 2009; Weyrich et al., 2017; Hardy, 2010a; Henry, Brooks and Piperno, 2011; Sistiaga et al., 2014; Hardy et al., 2022). However, little is known about the diet of Neanderthal infants and juveniles, the development of the deciduous teeth and the age of transition from soft to solid food (Hardy et al., 2012; Mahoney et al., 2021; Nava et al., 2020). Indeed, the pace of Neanderthal growth has been heavily debated. Evidence from permanent teeth suggests a course of development that was either similar to modern humans or accelerated. Studies on deciduous teeth from the Krapina Neanderthal have shown that these teeth formed relatively quickly and emergence is advanced relative to the modern human schedule (Mahoney et al., 2021). This suggests that Neanderthals would have started processing a wider range of food types earlier than modern humans. Explanations of this accelerated tooth formation and emergence have been advanced in relation to higher energy demands in Neanderthals during post-natal ontogeny (Ponce De León et al., 2008; Kuzawa et al., 2014). However, this is still debated.

#### 4.4.2 Craniofacial skeletal performance during right first incisor and second premolar/deciduous molar biting

The study findings show that even if tensile and compressive strains are generally comparable among age stages, with the largest strains being found on the working side (right) and in similar anatomical areas (such as directly above the bite point, the zygoma, the right part of the anterior maxilla, around the orbitals, and nasal bone), differences in magnitude and mode of straining exist in some locations. Thus, during both biting simulations, the infant presents generally higher tensile and compressive strains on both sides than the juvenile and adult models except over the inferior maxilla, subnasal region and post-canine alveolar process on the working side during RP<sup>2</sup>/RdM<sup>2</sup> biting where the juvenile presents higher strains. Because of the differences in size and the same muscle forces being applied in all the models, the results were scaled for size (square of centroid size, squared cs) and bite force using the infant as a reference. These scalings show that the higher strains in the mean infant crania are not accounted for by the size of the specimens but clearly show that the infant model deforms more than the other models in response to masticatory system loadings, especially along the anterior maxilla and supraorbital during both unilateral biting simulations. An exception is shown at the inferior maxilla and alveolar process during RP<sup>2</sup>/RdM<sup>2</sup> biting where the juvenile presents higher strains, even when scaled for size and bite force. Thus, even accounting for size or bite force, the juvenile and adult models seem to better resist masticatory loadings than the infant model. However, scaling by bite force does not necessarily account for differences in applied muscle forces, because bite forces vary little (Table 10). Here, the same muscle forces were applied for all the models despite muscles being much smaller in the infant and since bite and muscle forces are unknown it is unclear if (but unlikely that) this scaling actually compensates for the same muscle forces being applied to each age stage.

However, the Neanderthal infant appears to deform more, when bite forces and size are taken into account and this could be because of its less well-developed craniofacial skeleton in comparison to the juvenile and adult models. Indeed, the juvenile and adult models present generally more robust facial skeletal features, that arise during post-natal ontogeny (White and Folkens, 2011; Sadler, 2003; Schaefer et al., 2009). The juvenile and especially infant models present absolutely, and relatively, after scaling, higher tensile and compressive strains over the zygomatic body and zygomatic arches compared to the adult model. Based on beam theory, a reduction in the height and/or breadth of the

zygomatic arches would weaken them under bending and shear, respectively (Ledogar et al., 2016; Hylander, Johnson and Picq, 1991; Hylander and Johnson, 1997; Ross, 2001; Ross et al., 2011) which, given the less well-developed arches in the juvenile and infant models, would result in greater strains.

However, it is also important to bear in mind potential errors in the reconstruction of the fossil material. In particular, reconstructions of the zygomatic arches and bones were based on juvenile and infant modern humans for the infant and juvenile Neanderthal specimens. which could have led to an underestimation of the thicknesses and heights of the temporal and zygomatic process and zygomatic arch curvature. Together, these approximations in the Neanderthal reconstructions could impact the modes and magnitudes of deformation among the models. Moreover, the models in these studies were built without temporal fasciae. A recent study has shown that the temporal fasciae might act as a stabiliser by opposing masseteric contraction forces during mastication (Curtis et al., 2011). The authors show that high-strain gradients in and around the zygomatic arch are reduced when the temporal fasciae are added to a macaque model (Curtis et al., 2011). As for the modern human models (Chapter 3), the Neanderthal mean models were made solid (with cortical bone, trabecular bone and teeth having the same mechanical properties) which has been demonstrated to impact the magnitudes of predicted strains but not their distribution (Toro-Ibacache et al., 2016; Godinho et al., 2017; Lacruz et al., 2015b). In the same way, modern human teeth at different age stages were added to the mean Neanderthal models and studies have shown that these could also impact strain magnitudes. A sensitivity test was conducted to assess the effects of replacing Neanderthal teeth with modern human ones in the Neanderthal adult model. This showed local differences in predicted strains mostly affecting their magnitudes rather than distributions or modes (Appendix 3). As seen in the previous Chapter, the models were also loaded similarly with the sinuses unfilled or filled to investigate the impact on the strain data when the models sinuses are filled with bones (Appendix 2). Results were compared, and the sensitivity test reflects previous studies (Toro-Ibacache et al., 2016; Renders et al., 2011) in indicating that filling of the sinuses mostly reduced strain magnitudes during the loading experiment but did not markedly impact the mode of deformation (Appendix 2).

The GM size and shape analysis of global magnitudes and modes of deformation (Figures 43 and Figure 44) shows that the three models deform differently with the infant deforming to a greater degree during both biting simulations even when accounting for

differences in size and possible differences in bite force. This is consistent with the strain contour plots and graphs (Figures 45 to 46), which show small differences in which regions experience high and low strains.

#### 4.4.3 Significance of apparent differences between the mean Neanderthal infant, juvenile and adult models

The present study compares mean Neanderthal infant, juvenile and adult models extracted from a growth model using a small sample of reconstructed Neanderthal crania, so it is necessary to consider the size of the sample and the impact of reconstructions. Our findings on the mean Neanderthal adult FE model reflect and extend those of other recent studies. Wroe et al., (2018) built composite Neanderthal FE models based on a series of virtual reconstructions of Neanderthal adults (La Chapelle aux Saints 1, La Ferrassie 1 and Gibraltar 1) using a modern *Homo sapiens* surface as a reference. The Von Mises strain contour plots extracted after anterior biting simulation in that study show similar areas of low and high strain distribution to those of the tensile and compressive strains found in the present study (e.g., large strains over the anterior maxilla, around the nasal aperture, around and between the orbits (Wroe et al., 2018). Moreover, Chapter 3 section 3.3 shows that in the modern human adult RI<sup>1</sup> biting simulation, peak  $\epsilon_1$  and  $\epsilon_3$  principal strains are 249  $\mu\epsilon$  and -514  $\mu\epsilon$  while in the adult Neanderthal model, peak  $\epsilon_1$  and  $\epsilon_3$  principal strains are 139  $\mu\epsilon$  to -263  $\mu\epsilon$ . Likewise, the mean Neanderthal adult model presents peak  $\epsilon_1$  and  $\epsilon_3$  strains of 55  $\mu\epsilon$  to -107  $\mu\epsilon$  for the RP<sup>2</sup> biting simulation and the modern human, 107  $\mu\epsilon$  to -176  $\mu\epsilon$ . Therefore, the Neanderthal mean model develops peak  $\epsilon_1$  and  $\epsilon_3$  strains that are approximately 50% of those in the modern human mean adult model (even when size was taken into account). Because the models were built in the same way and have the same applied muscle forces but the Neanderthal adult mean cranium is bigger, we expect the strains to be lower in the Neanderthal. However, when scaling for size (using the ratio of squared centroid sizes) or peak bite force, the adult models still present lower strains. As for the modern human adult model, it could indicate that the adult craniofacial complex in this species is better adapted to sustain loadings due to mastication. Generally, the Neanderthal models seem to respond similarly to models run in previous studies (Wroe et al., 2018; Godinho et al., 2018) and the differences between the three models in load resistance are likely due to differences in form but could also reflect a real difference in functional loading resistance between age stages.

The present findings show that Neanderthal infants, as for modern human ones, are more efficient at converting muscle forces into bite forces due to their shorter faces yet appear to be less well able to resist applied loads. Additionally, differences in tensile and compressive strain magnitudes and distributions exist among the models, especially at the inferior aspect of the maxilla and the alveolar process in the juvenile model consistent with the GM analysis of deformations showing that modes, as well as degrees of deformation, also differ between the three models.

These differences in load resistance between age stages likely interact with and modulate craniofacial growth and development. Such effects might be local, with regions that are strained adapting over time but they might also have more diffuse effects by impacting cranial components that are developmentally integrated with other components. Whether or not Neanderthal craniofacial integration (Bastir and Rosas, 2016) is the same as is found in modern humans is unknown and so it is unclear to what extent the divergent development of these two species can be accounted for by differences in loading interacting with differences in integration.

Moreover, the masticatory system also changes throughout post-natal ontogeny, with more rapid development and eruption of the teeth (Smith et al., 2010a; Mahoney et al., 2021; Boughner and Dean, 2004; Macchiarelli et al., 2006) and development of the mandible (Bastir, O'Higgins and Rosas, 2007) in Neanderthals than humans. Throughout post-natal ontogeny, the Neanderthal mandible presents anteriorward growth resulting in a forward shift of the alveolar process, which is responsible for the typical Neanderthal retromolar space and the sloping symphysis (Bastir, O'Higgins and Rosas, 2007). The retromolar space found in Neanderthals has been associated with a forwardly placed mid-face and nasal aperture coupled with an anteroinferior growth vector of the face which results in a relatively more anterior positioning of prosthion and the tooth row with respect to the maxillary tuberosity (Bastir, O'Higgins and Rosas, 2007). This is associated with bone deposition over the anterior mandible which is extensive from around 5 years; (Lacruz et al., 2015b). This spatial pattern of deposition has been associated with an expansion vertically of the nasal capsule during ontogeny, increasing the rate of bone remodeling of the nasal and oral components of the palate (deposition on the oral lamina of the palate) which likely increases downward and forward drift of this structure, resulting in a large nasopharyngeal airway (Lacruz et al., 2015b). The differences in mode and magnitude of deformation observed between the models could also underlie these

changes, with mechanical loading throughout ontogeny modulating bone growth remodeling. This will be considered further in the next chapters where Neanderthal craniofacial masticatory system loading, resistance and growth are compared with modern humans.

## 5.0 Comparison of modern human and Neanderthal biting performance

In Chapters 3 and 4, the ontogeny of masticatory system mechanical performance in modern humans and Neanderthal infant, juvenile and adult models were assessed. The present chapter compares the results obtained from these earlier chapters and assesses the impact of the morphological differences found between modern humans and Neanderthals at each age stage on their ability to generate and resist biting forces.

Morphological studies of the Neanderthal craniofacial system as well as the results in chapter 2 have shown that the post-natal ontogenetic trajectory in this species diverges from that of modern humans. Analyses of bone modelling of the developing craniofacial complex provide insights into the growth process that the craniofacial complex undergoes during development and inform us about ontogenetic processes that lead to differences in final adult form observed between these two species. In modern humans, maxillary growth is characterised by bone resorption on the anterior subnasal surface, whereas in Neanderthals extensive bone deposition is found in similar areas. Such differences in the pattern of bone remodeling between Neanderthals and modern humans have been hypothesized to be related to genetic signals that differ between these species, or to differences in the forces arising from food processing during post-natal development. While we cannot test the hypothesis that differences in growth remodeling are driven by differences in the genetic regulation of craniofacial growth, this chapter tests the hypothesis that remodeling differences arise from differences in how biting forces are generated and borne by the cranium. Thus, if changes in mechanical forces interact with changes in cranial form during development to drive differences in growth remodeling, differences in strain magnitudes and distributions might be expected to reflect the anatomical locations of differences in growth remodeling. Here, it is expected that differences will be found in; i) biting forces, ii) the ability to resist masticatory system loading, iii) the magnitudes and modes of deformation experienced by the different craniofacial skeletons.

Additionally, different explanations have been raised for the development of the supraorbital region in Neanderthals. It has been shown that within each species, the forces the cranium experiences change over time as diet and paramasticatory behaviour change and differences in these have been suggested to underlie differences in craniofacial morphology. Thus, paramasticatory behaviour as well as heavy anterior loading have been

proposed as a possible explanation for the large supraorbital ridges in Neanderthals. Indeed, several studies have suggested that the supraorbital region develops as an adaptation to withstand high and/or repetitive occlusal loads. However, this hypothesis is contested and other explanations have been proposed such as the “spatial theory”, which posits that variations in the supraorbital region arise as a result of the spatial relationships of different components of the hominin cranium (Zollikofer and Weissmann, 2008; Zollikofer et al., 2008; Nakashige, Smith and Strait, 2011; Smith et al., 2011). This is not tested here, rather the mechanical hypothesis is investigated. It is expected to find differences in the mode of deformation in this region between both species and relatively higher strains in this region in modern human.

The same mean models and the same biting simulations, described in Chapter 3 and Chapter 4, are used ( $RI^1$  and  $RdM^2/ RP^2$ ). Mechanical advantages and force production efficiencies are calculated and compared between the two species at each age stage. This chapter also compares the differences in mode of deformation and the resulting strain distributions and magnitudes between modern human and Neanderthal craniofacial skeletons. The study proceeds by testing the null hypothesis that these will not differ between the two species at each age stage. Raw results are adjusted to account for differences in cranial size and peak bite force (Table 14 and Figure 55) by scaling the deformations and strains in the Neanderthal models relative to the corresponding modern human models within each age stage. The same scaling approaches described in Chapter 3.2.1.2.4 were followed for this chapter. These results are then related to the craniofacial growth differences among these species.

## 5.1 Craniofacial deformations, strains and bone growth remodeling

### 5.1.1 Mechanical advantages

Mechanical advantages (MAs) were calculated for the jaw adductor muscles (anterior, middle and posterior temporalis, anterior and posterior masseter and medial pterygoid) using the methods described in section 3.2.2 for the mean modern human and Neanderthal infant, juvenile and adult models. The results are compared between modern human and Neanderthal mean models and presented in Figure 53 and Figure 54.

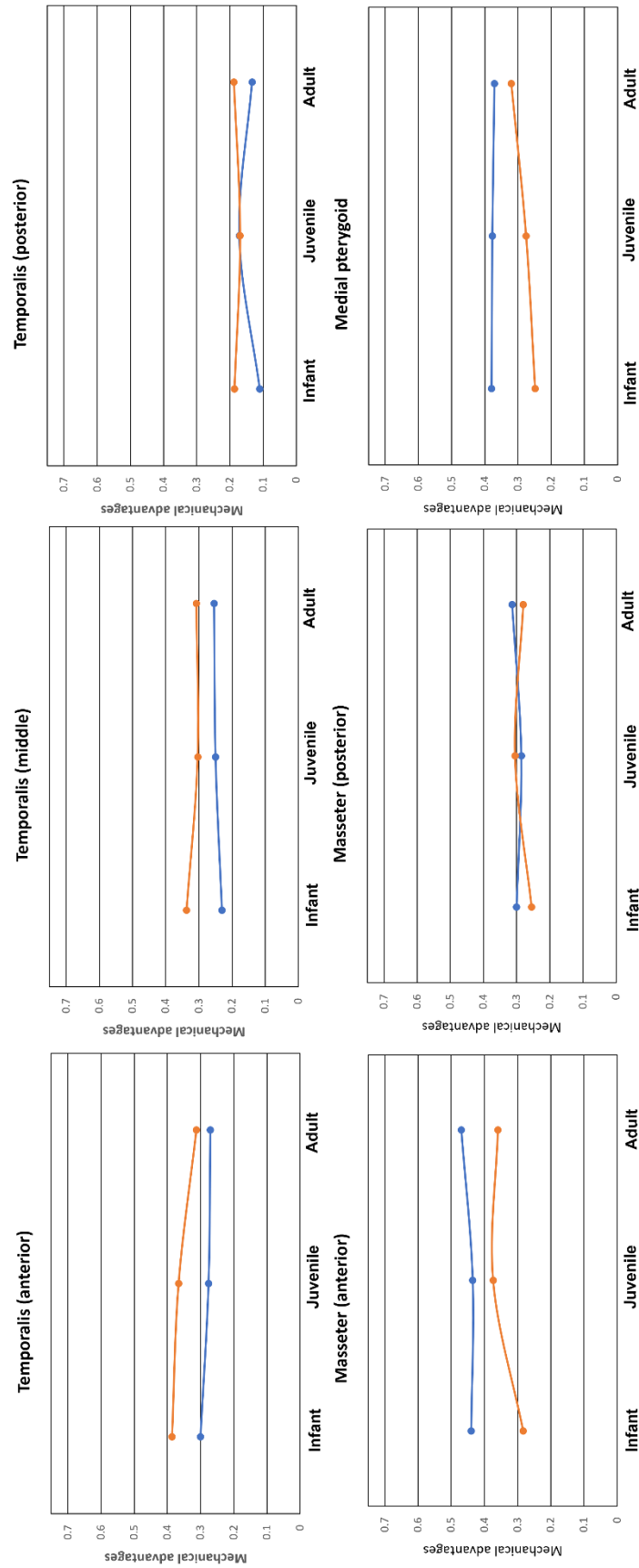


Figure 53. Graphs of mechanical advantages of each muscle in Neanderthals (orange) and modern human (blue) infant, juvenile and adult models at the RI<sup>1</sup> bite point.

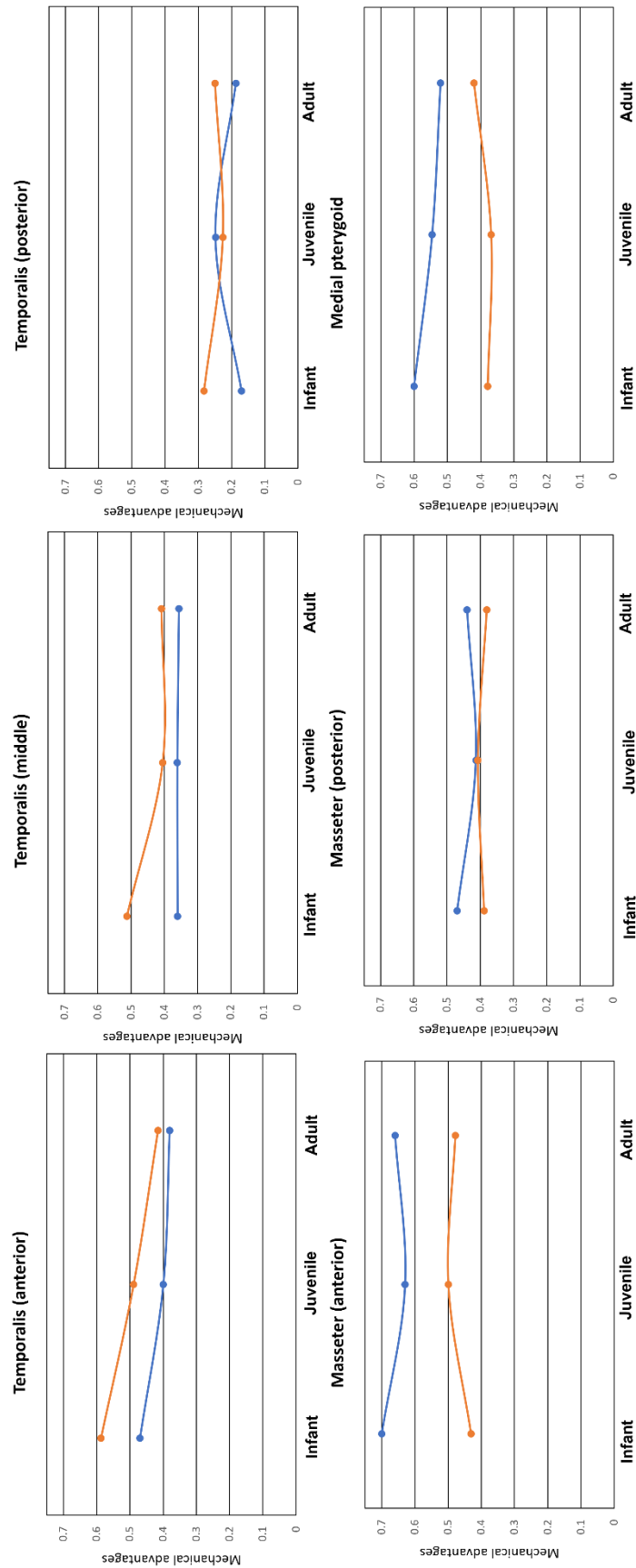


Figure 54. Graphs of mechanical advantages of each muscle in Neanderthals (orange) and modern human (blue) infant, juvenile and adult models at the  $RP^2/RdM^2$  bite point.

For the right first incisor bite ( $RI^1$ , Figure 53), Neanderthal models show higher MAs than the modern human ones for the temporalis muscle except for the juvenile model at the posterior temporalis while the opposite pattern is found for the anterior part of the masseter and medial pterygoid muscles. The MAs increase from infant to adult in the Neanderthals for the medial pterygoid muscle. However, at the anterior part of the temporalis muscle, the MA decreases from infant to adult. For the middle and posterior parts of the temporalis, the MA decrease from infant to juvenile then slightly increases in the adult model (Figure 53) with the infant presenting the maximum value. Finally for the masseter muscle, the MA increase from infant to juvenile then slightly decreases in the adult model (Figure 53) with the juvenile presenting the maximum value. The modern human MAs present the same age trends as the Neanderthal in the anterior part of the temporalis muscle with MAs decreasing from infant to adult. In the middle part of the temporalis, the modern human MAs increase from the infant to the adult model. The infant presents the lowest MA. At the posterior part of the temporalis, the modern human juvenile presents the maximum value of MA, with MA increasing between infant and juvenile and decreasing in the adult model. For the masseter muscle, the modern human MA decreases from the infant to reach its minimum value in the juvenile before becoming greater in the adult model.

With the right second premolar and deciduous molar bites ( $RP^2/RdM^2$ ) the mechanical advantages (MAs) for all the models are, as expected, greater than those for the  $RI^1$  bite (Figures 53 and 54). The modern human models show greater mechanical advantages than Neanderthal models for the masseter, medial pterygoid muscles and for the juvenile model at the posterior temporalis (Figure 54). For the rest of the temporalis muscle, Neanderthal models present higher MAs. The Neanderthal model MAs decrease from infant to juvenile and then increase in the adult model for the middle and posterior parts of the temporalis and medial pterygoid with the adult presenting the highest value. At the anterior part of the temporalis, the MAs for the Neanderthal models decrease from infant to adult. The MAs for the masseter in the Neanderthal models increase from infant to juvenile to decrease again in the adult model, the juvenile shows the greatest MA (Figure 54).

The modern human models present lower MAs but similar patterns of change with age to the Neanderthal models for the anterior and middle parts of the temporalis and medial pterygoid. However, the differences in MAs between species are more marked in

the posterior temporalis and anterior part of the masseter, where the modern human presents an opposite pattern than the Neanderthals. Finally, for the anterior part of the masseter muscle, the modern human models present a decrease in MAs from infant to juvenile, to reach the smallest value and an increase again with the adult model. At the middle part of the temporalis, in the modern human models MA varies little between stages (Figure 54).

*Table 14.* Centroid sizes (cs) and peak bite forces from previous FEAs, for the right first incisor (RI<sup>1</sup>) and right second premolar and second deciduous molar (RP<sup>2</sup>/RdM<sup>2</sup>) bite points in the modern human and Neanderthal infant, juvenile and adult models.

	Modern human			Neanderthal		
	Centroid size	Peak bite force (RI <sup>1</sup> )	Peak bite force (RP <sup>2</sup> -RdM <sup>2</sup> )	Centroid size	Peak bite force (RI <sup>1</sup> )	Peak bite force (RP <sup>2</sup> -RdM <sup>2</sup> )
<b>Infant</b>	1139.63	262	399	1145.22	241	357
<b>Juvenile</b>	1311.38	271	379	1352.47	257	330
<b>Adult</b>	1414.24	256	354	1536.99	225	291

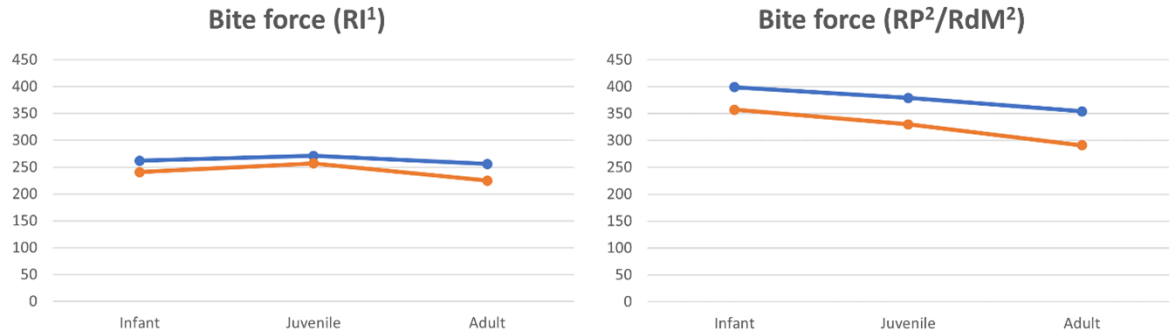


*Figure 55.* Right first incisor (RI<sup>1</sup>) and right second premolar and second deciduous molar (RP<sup>2</sup>/RdM<sup>2</sup>) peak bite forces for the modern human (orange) and Neanderthal (blue) infant, juvenile and adult models.

*Table 15.* Peak bite forces estimated from the mechanical advantages for the right first incisor (RI<sup>1</sup>) and right second premolar and second deciduous molar (RP<sup>2</sup>/RdM<sup>2</sup>) bite points in the modern human and Neanderthal infant, juvenile and adult models. Peak bite force estimation= (in-lever arms for each masticatory muscle part\*(muscle forces/number of masticatory muscle parts))/out-lever arms; Mechanical advantages in modern humans are presented in Table 8 and for Neanderthals in Table 13; muscle forces presented in Table 6.

	Modern human		Neanderthal	
	Peak bite force (RI <sup>1</sup> )	Peak bite force (RP <sup>2</sup> -RdM <sup>2</sup> )	Peak bite force (RI <sup>1</sup> )	Peak bite force (RP <sup>2</sup> -RdM <sup>2</sup> )
<b>Infant</b>	258	409	237	361
<b>Juvenile</b>	263	380	249	332
<b>Adult</b>	265	372	251	334

Table 14 and Figure 55 present the reaction forces at the RI<sup>1</sup> and RP<sup>2</sup>/RdM<sup>2</sup> bite points calculated (with Vox-FE) for the mean modern human and Neanderthal infant, juvenile and adult FE models. For both biting simulations, the modern human models show higher peak bite forces than the Neanderthal ones. Peak bite force, in both species, decreases from infant to adult stages but at the RI<sup>1</sup> bite point, both juvenile models present the highest peak bite force. Table 15 presents the peak bite force estimated using mechanical advantages in order to validate those calculated using Vox-FE. For the modern human models, differences range between 0.3% to 5% between the estimate peak bite forces from Vox-FE and lever mechanics. In the Neanderthal models, differences range between 0.6% to 14%, with the largest difference in the adult model (Tables 14 vs 15).

*Table 16.* Force Production efficiencies at the RI<sup>1</sup> and RP<sup>2</sup>/RdM<sup>2</sup> biting simulations, calculated from the Finite Element models of the mean modern human Neanderthal infant, juvenile and adult models. Fb, peak bite force; Fm, net applied muscle force, Fc, joint (at the glenoid fossa) reaction force.

		Force production efficiencies			
		Fb/Fm		Fc/Fm	
		Modern human	Neanderthal	Modern human	Neanderthal
<b>Infant</b>	<b>RI<sup>1</sup></b>	0.33	0.36	0.67	0.64
	<b>RdM<sup>2</sup></b>	0.50	0.51	0.50	0.49
<b>Juvenile</b>	<b>RI<sup>1</sup></b>	0.35	0.35	0.65	0.65
	<b>RP<sup>2</sup></b>	0.48	0.45	0.52	0.55
<b>Adult</b>	<b>RI<sup>1</sup></b>	0.35	0.31	0.65	0.69
	<b>RP<sup>2</sup></b>	0.48	0.40	0.52	0.60

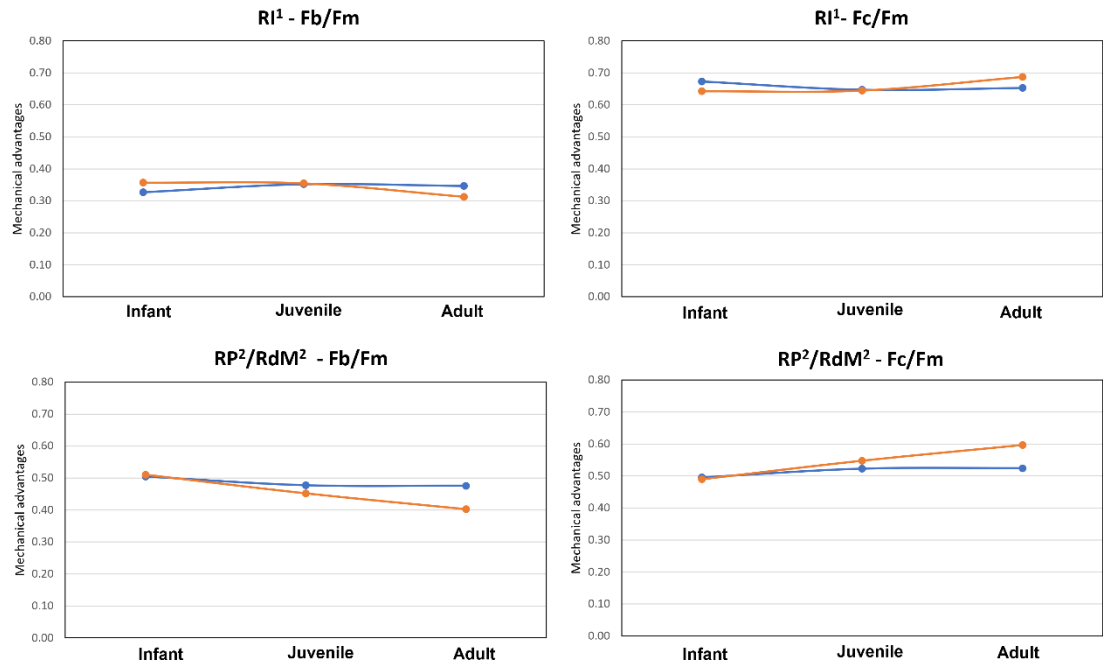
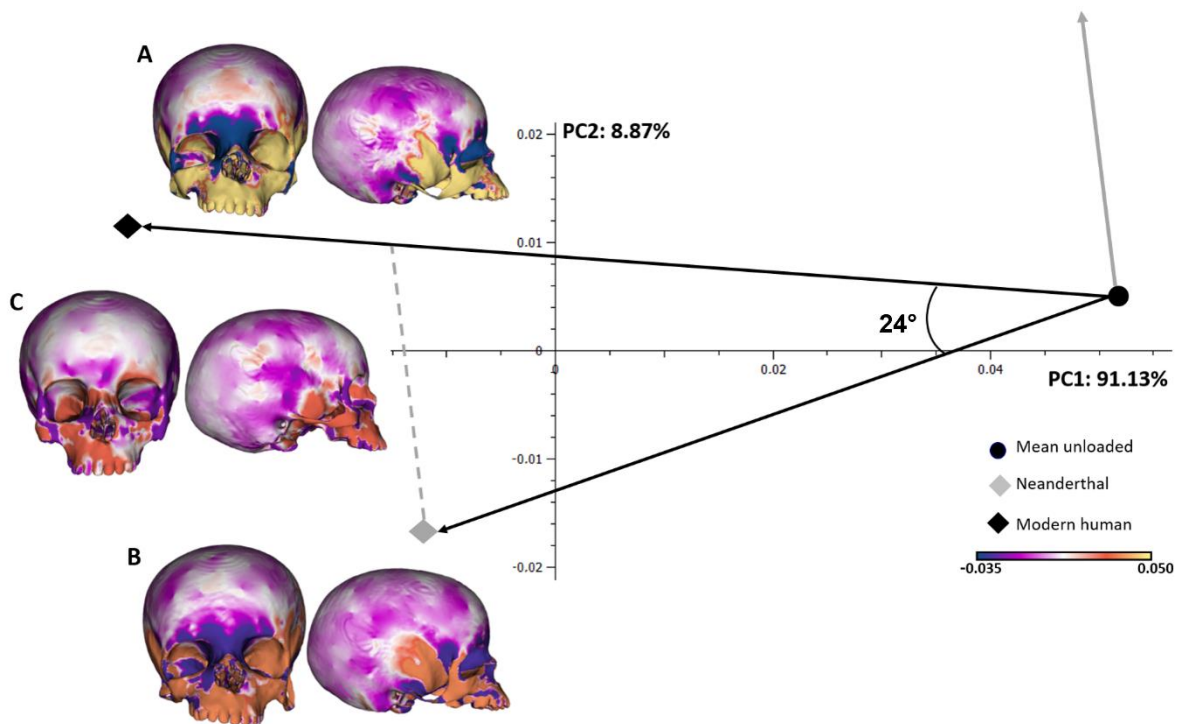


Figure 56. Plots of force production efficiencies in the  $RI^1$  and  $RP^2/RdM^2$  biting simulations comparing the mean modern (blue) human and Neanderthal (orange) infant, juvenile and adult models. Fb, peak bite force; Fm, net applied muscle force, Fc, joint (at the glenoid fossa) reaction force.

Peak bite force production efficiencies (Fb/Fm) vary with age in both modern human and Neanderthal models, in both biting simulations. The ratio of peak bite force to net applied muscle force (Fb/Fm) ranges from 0.31 to 0.51 in Neanderthals while in modern human models the ratio ranges from 0.33 to 0.50. Incisor biting efficiency is greater in Neanderthal infants than in modern humans, but less in adults (Table 16 and Figure 56). The opposite is true for Fc/Fm in incisor biting. In the  $RP^2/RdM^2$  biting simulations, bite force production efficiency is very similar at all ages between modern human and Neanderthal models, with the adult modern human presenting a slightly higher value. Likewise, Fc/Fm is similar, but Neanderthals present a higher value in adults.

In summary, in both biting simulations, muscle mechanical advantages vary between infancy and adulthood, often non-linearly, some muscles have greater MAs in infancy, others in adults and some in modern humans, and others in Neanderthals. These MAs lead to higher peak bite forces in modern humans of all ages.

### 5.1.2 Deformations



*Figure 57.* Size and shape analysis of modes and magnitudes of deformation (changes in size and shape) of the modern human (black diamond) and Neanderthal (grey diamond) infant models for the RP<sup>2</sup>/RdM<sup>2</sup> biting simulation. Surface colourmaps A and B illustrate the deformations between the mean unloaded model (Black circle) and loaded modern human and Neanderthal infant models, respectively. The deformation of the modern human (insets A) is visualised at the same distance (degree of overall deformation) from the unloaded mean as the loaded Neanderthal (Inset B), indicated by the intersection of the dashed grey line with the modern human loading vector. The difference in deformation between these models (Neanderthal as reference, modern human as target) is visualised with the unloaded mean as reference, along the (grey arrow) vector parallel to and the same length as the (dashed grey line) vector between the deformed Neanderthal and modern human (see text). The deformations were magnified x1000.

A size and shape analysis comparing modern human and Neanderthal cranial deformation at each age stage was conducted for both biting simulations (Figures 57 to Figure 62). This section will focus on the mode and not on the magnitude of deformations between the modern human and Neanderthal models, because of the uncertainties in assessing magnitude noted in (Chapter 3.2; Appendix 2 and Appendix 3) Thus, these colourmaps were not scaled for size or peak bite force and are computed at the same distance (degree of overall size and shape change) from the unloaded mean in each species. The resulting tensile and compressive strains will be scaled by size (centroid size, cs) and peak bite force in the next sections to compare them while taking into account these variables.

In Figures 57 to 62, the differences in length of the vectors connecting the mean unloaded and loaded models in each species show that at each age stage and in both biting simulations, the Neanderthal models deform less than the modern human ones.

During  $RP^2/RdM^2$  biting simulations, the angles between vectors in the PC plots (Figures 57-59) are larger for infants and adults than for the juveniles (adult and infant,  $24^\circ$  and  $25^\circ$  respectively; Juvenile  $17^\circ$  in Figure 58). This indicates that modern human and Neanderthal juveniles show a slightly more similar mode of deformation than infants or adults.

The deformations due to the loading of each species are visualised in Figures 57-59 by warping the unloaded mean surface to the landmark and semi-landmark coordinates of the loaded surfaces. To compare the modes of deformation between species (ignoring magnitude), the Neanderthal deformation is visualised at the limit of its loading vector and the human one at the point where the dashed line in each PC plot meets the human deformation vector, which is the same distance along its length as the entire Neanderthal vector (A in Figures 57-59). These deformations are very small, and so to appreciate them, they have been magnified (1000x for the  $RP^2/RdM^2$  biting simulation and 500x for the  $RI^1$  biting simulation).

To compare the modes of deformation between the Neanderthal (reference) and modern humans (target), colourmaps are drawn (C in Figures 57-59; see section 3.2.2) to indicate the degree of expansion (yellow/orange) or contraction (purple) of the surface area of the surface mesh triangles between the loaded, deformed species surface meshes. These differences in deformation are drawn with reference to the undeformed, unloaded mean to focus on them alone (i.e., to visualise them with respect to the undeformed mean surface rather than the deformed Neanderthal one). This is achieved by taking the unloaded mean as the reference at the tail of the solid grey arrow and the target as the tip of this arrow (Figures 57-59) which is parallel to and of the same length as the dashed grey line connecting the points on loading vectors representing the specific deformations that are to be compared.

In all of these loadings, the zygomatic arches deform to a considerable degree, asymmetrically and differently between species. The magnitudes and differences in deformation may simply reflect the difficulties in reconstructing the zygomatic arches in

Neanderthals, and plausibly, the lack of modelling of the temporal fasciae (Curtis et al., 2011). As such, they are not considered further.

The RP<sup>2</sup>/RdM<sup>2</sup> biting simulations all result in asymmetric deformation of the facial skeleton (A and B in Figures 57-59) with the biting side maxilla vertically compressed (raised dental arch at the bite point). This is accompanied by vertical compression of the right (working side) orbit and expansion of the left. The upward deflection of the maxilla in all models in both species results in expansion of the whole surface (yellow/orange colours in A and B in Figures 57-59), except immediately above the bite point and contraction of the inter orbital region, especially on the working side, and to a lesser extent, the upper rim of the orbits (purple in A and B in Figures 57-59).

Comparing deformations, in the infant, Figure 57C presents the difference in deformation in the modern human relative to the deformation in the Neanderthal during simulated RP<sup>2</sup>/RdM<sup>2</sup> biting. Over the vault and lateral aspects of the nasal cavity, there are patches where the human model surface contracts more than the Neanderthal (purples) and in the face where it expands more, especially over the anterior midface on the working (right) side (orange). In the juveniles (Figure 58C) the difference in deformation is similar but the region of expansion of the anterior maxilla is extended, to the balancing (left) side and a region of relatively greater contraction is present over the balancing side anterior and subnasal maxilla. Comparing the adults (Figure 59C) expansion of the anterior maxillary surface in modern humans relative to Neanderthals is no longer marked and bilateral regions of surface contraction relative to the Neanderthal deformation in the human (purple) become evident on either side of the nasal aperture.

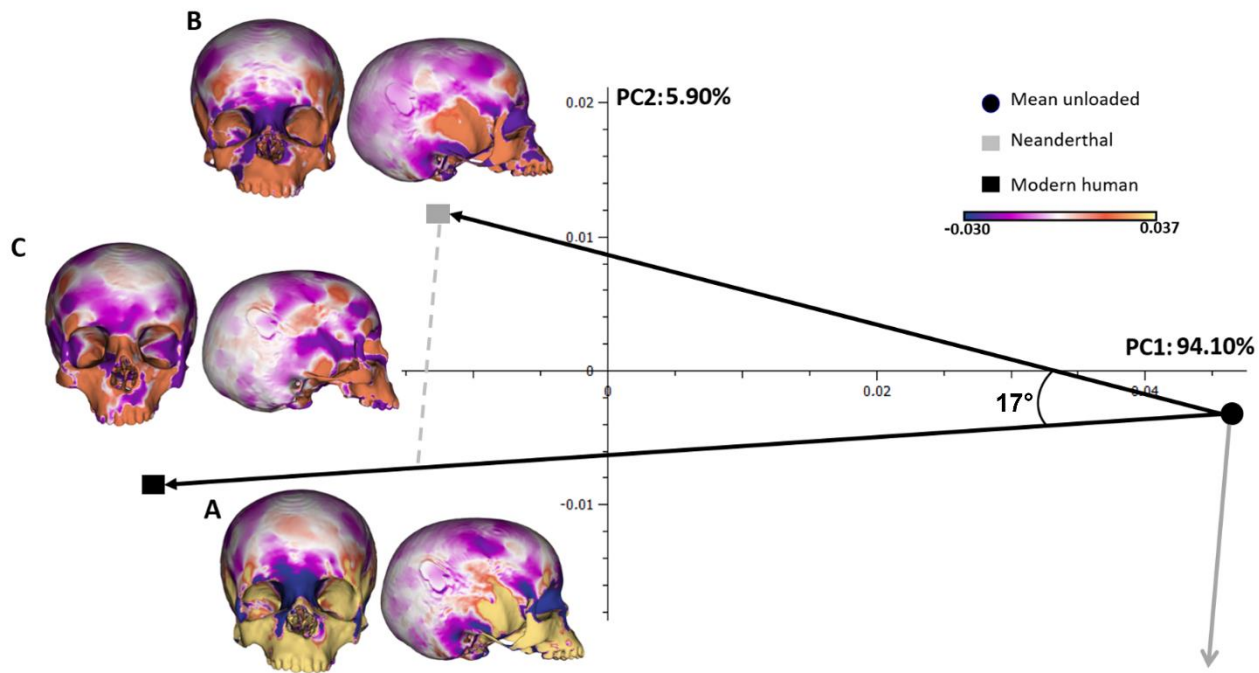
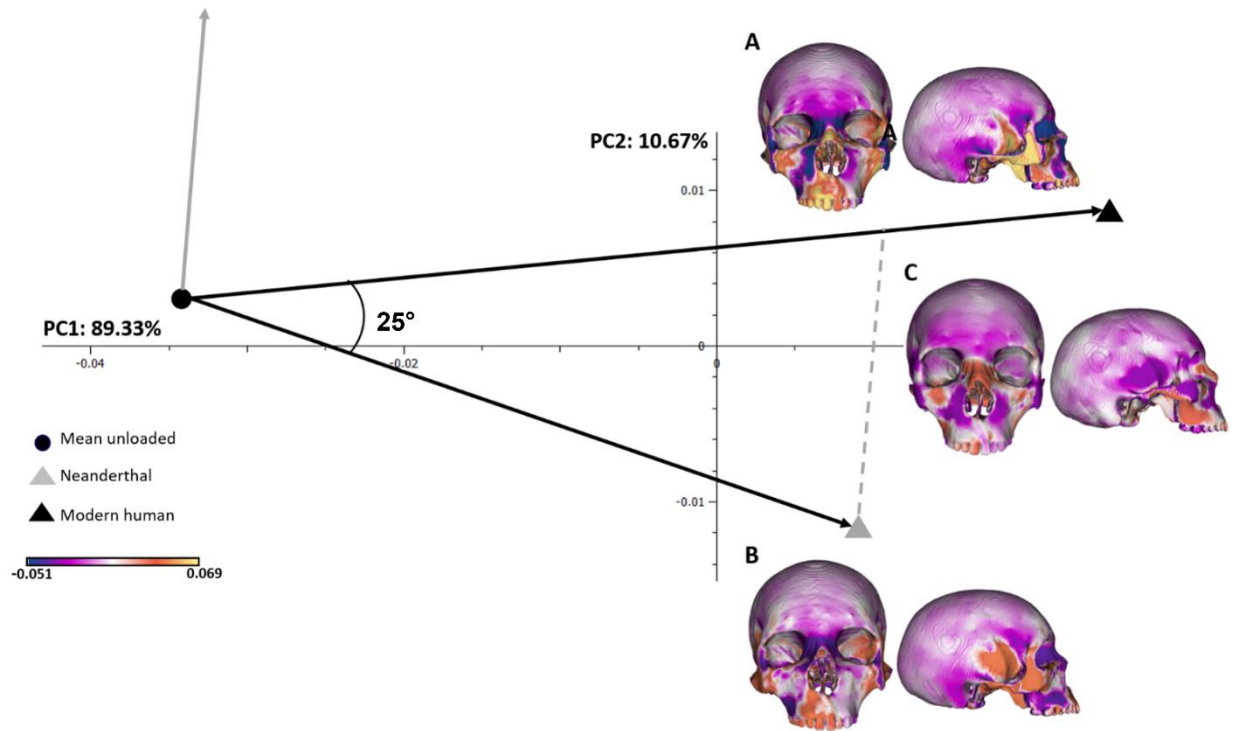


Figure 58. Size and shape analysis of modes and magnitudes of deformation of the modern human (black diamond) and Neanderthal (grey diamond) juvenile models for the  $RP^2/RdM^2$  biting simulation. Surface colourmaps A and B illustrate the deformations between the mean unloaded model (Black circle) and loaded Neanderthal and modern human juvenile models, respectively. The deformation of the modern human (insets A) is visualised at the same distance (degree of overall deformation) from the unloaded mean as the loaded Neanderthal (Inset B), indicated by the intersection of the dashed grey line with the modern human loading vector. The difference in deformation between these models (Neanderthal as reference, modern human as target) is visualised with the unloaded mean as reference, along the (grey arrow) vector parallel to and the same length as the (dashed grey line) vector between the deformed Neanderthal and modern human (see text). The deformations were magnified x1000.

From the  $RI^1$  biting simulations, in the PCA plots (Figures 60-62) the vectors of deformation of the modern human models are longer than those of the Neanderthal models. Additionally, the degree of deformation (distance between the unloaded and loaded models) is greater for the incisor than the  $RP^2/RdM^2$  biting simulations and so it should be noted that the visualisations of deformation in Figures 60-62 ( $RI^1$ ) are magnified 500x rather than 1000x as in Figures 57-59 ( $RP^2/RdM^2$ ).

The vectors of deformation diverge more at the adult and infant stages than at the juvenile, reflected in the angle between unloaded and modern human and Neanderthal models;  $21^\circ$  to  $19^\circ$  for infants and adults in these analyses (Figure 60 and Figure 62) vs. juveniles (Figure 61,  $11^\circ$ ). The warped surfaces from the unloaded mean to the loaded specimen at each age stage, indicate that in both species at all age stages, incisor biting causes an upward deflection of the maxilla, with vertical compression of the nasal and

interorbital regions as well as parts of the orbits and their rims (Purples in A in Figures 60-62). The upward deflection of the anterior maxilla results in expansion of the zygoma, maxillary (yellows/oranges in A in Figures 60-62) and palatal surfaces. These deformations are more symmetrical than those arising from the RP<sup>2</sup>/RdM<sup>2</sup> biting simulations.



*Figure 59.* Size and shape analysis of modes and magnitudes of deformation of the modern human (black diamond) and Neanderthal (grey diamond) adult models for the RP<sup>2</sup>/RdM<sup>2</sup> biting simulation. Surface colourmaps A and B illustrate the deformations between the mean unloaded model (Black circle) and loaded modern human and Neanderthal adult models, respectively. The deformation of the modern human (insets A) is visualised at the same distance (degree of overall deformation) from the unloaded mean as the loaded Neanderthal (Inset B), indicated by the intersection of the dashed grey line with the modern human loading vector. The difference in deformation between these models (Neanderthal as reference, modern human as target) is visualised with the unloaded mean as reference, along the (grey arrow) vector parallel to and the same length as the (dashed grey line) vector between the deformed Neanderthal and modern human (see text). The deformations were magnified x1000.

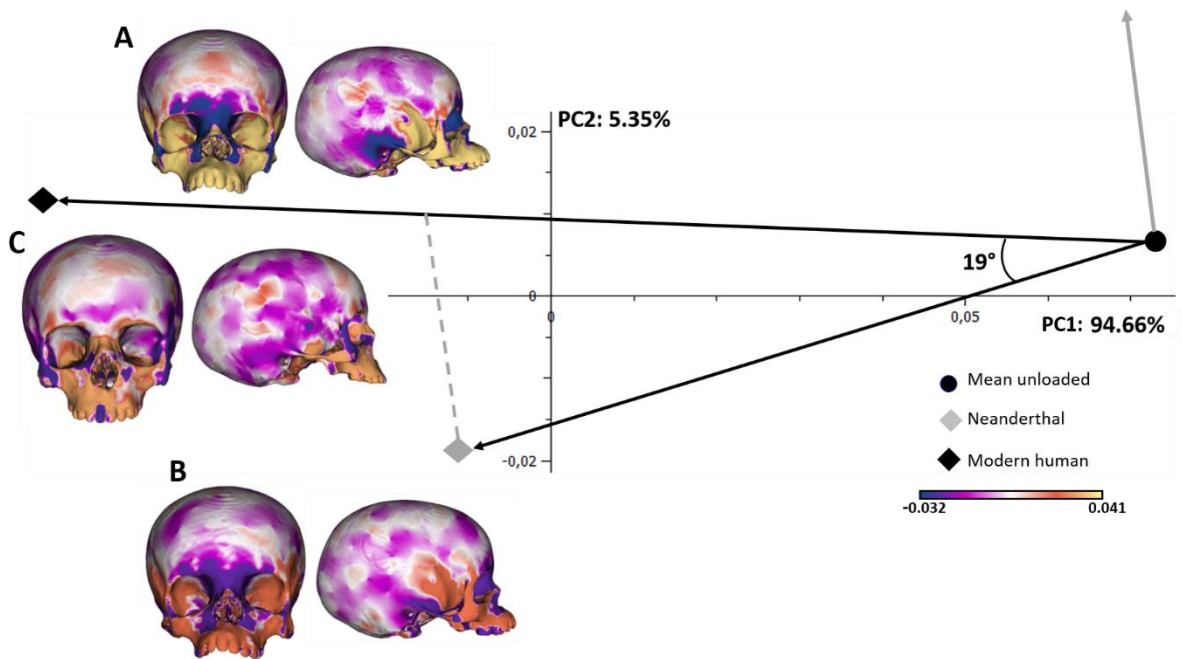
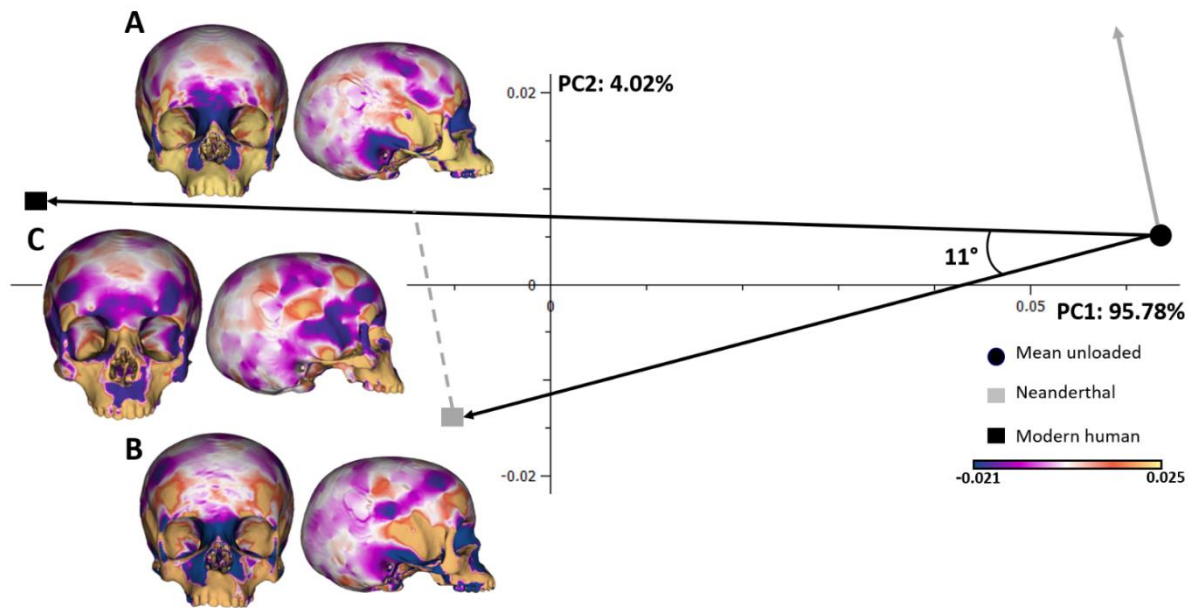


Figure 60. Size and shape analysis of modes and magnitudes of deformation of the modern human (black diamond) and Neanderthal (grey diamond) infant models for the RI<sup>1</sup> biting simulation. Surface colourmaps A and B illustrate the deformations between the mean unloaded model (Black circle) and loaded modern human and Neanderthal infant models, respectively. The deformation of the modern human (insets A) is visualised at the same distance (degree of overall deformation) from the unloaded mean as the loaded Neanderthal (Inset B), indicated by the intersection of the dashed grey line with the modern human loading vector. The difference in deformation between these models (Neanderthal as reference, modern human as target) is visualised with the unloaded mean as reference, along the (grey arrow) vector parallel to and the same length as the (dashed grey line) vector between the deformed Neanderthal and modern human (see text). The deformations were magnified x500.

Comparing deformations between age groups, the deflection and expansion of the right and left maxillary and palatal surfaces is most marked in the infant models (Figure 60 vs. Figure 62) and least in the adults. Further, in both species, the contraction of the surface over the interorbital region and around the nasal aperture (purple) is most marked in the infant and juvenile models (A and B in Figures 60 and 61 vs. Figure 62).

Deformations between species are compared in Figures 60-62C, which are colourmaps (see section 3.3.2) showing the differences in deformations between Neanderthals and modern humans arising from RI<sup>1</sup> loading at different age stages. As noted earlier, the zygomatic region required extensive reconstruction in the Neanderthals and may not have been adequately loaded, lacking the forces potentially arising from the temporalis fascia (Curtis et al., 2011). As such zygomatic arch deformation is not considered

further. As for the previous biting simulation, small regions of differences in surface expansion and contraction are observed in all models over the cranial vault.



*Figure 61.* Size and shape analysis of modes and magnitudes of deformation of the modern human (black diamond) and Neanderthal (grey diamond) juvenile models for the RI<sup>1</sup> biting simulation. Surface colourmaps A and B illustrate the deformations between the mean unloaded model (Black circle) and loaded modern human and Neanderthal juvenile models, respectively. The deformation of the modern human (insets A) is visualised at the same distance (degree of overall deformation) from the unloaded mean as the loaded Neanderthal (Inset B), indicated by the intersection of the dashed grey line with the modern human loading vector. The difference in deformation between these models (Neanderthal as reference, modern human as target) is visualised with the unloaded mean as reference, along the (grey arrow) vector parallel to and the same length as the (dashed grey line) vector between the deformed Neanderthal and modern human (see text). The deformations were magnified x500.

The colourmap illustrating the differences between Neanderthal (reference) and modern human (target) deformations due to RI<sup>1</sup> loading (Figures 60C-62C) in infants (Figure 60) indicates that the modern human shows greater contraction of the alveolar surface directly above the bite point (purple incisor and local alveolar process) and greater expansion of much of the anterior and subnasal maxilla than the Neanderthal (orange). The modern human juvenile presents greater contraction of the anterior subnasal surface of the maxilla (especially on the balancing/left side) than the Neanderthal model (purple; Figure 61C). Further, relative to the Neanderthal, the modern human juvenile presents greater expansion of the right and left anterior maxillae, both zygomas and the nasal bones (yellow/orange in Figure 61C), with greater contraction of the supraorbital region (purple

in Figure 61C). During RI<sup>1</sup> simulated biting the modern human adult shows greater contraction of the surface surrounding the nasal aperture, interorbital and frontal regions (purple Figure 62C) with a small region of greater expansion of the incisor alveolus (orange). The rest of the maxilla shows little difference in local surface areas (white/grey).

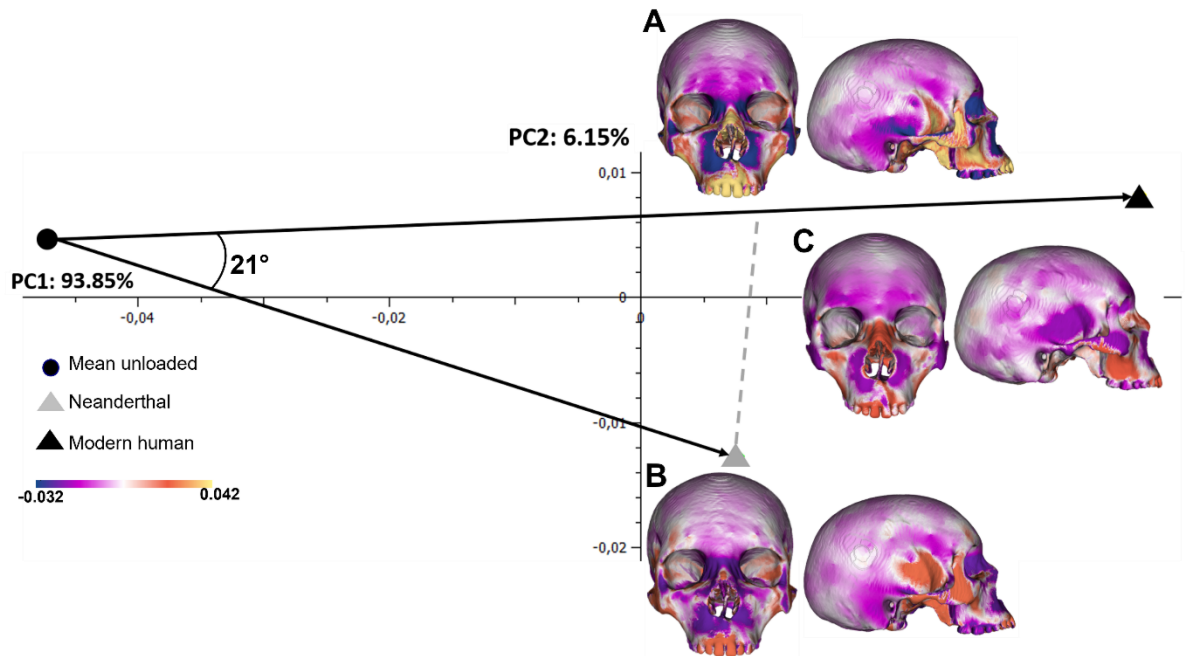


*Figure 62.* Size and shape analysis of modes and magnitudes of deformation of the modern human (black diamond) and Neanderthal (grey diamond) adult models for the RI<sup>1</sup> biting simulation. Surface colourmaps A and B illustrate the deformations between the mean unloaded model (Black circle) and loaded modern human and Neanderthal adult models, respectively. The deformation of the modern human (insets A) is visualised at the same distance (degree of overall deformation) from the unloaded mean as the loaded Neanderthal (Inset B), indicated by the intersection of the dashed grey line with the modern human loading vector. The difference in deformation between these models (Neanderthal as reference, modern human as target) is visualised with the unloaded mean as reference, along the (grey arrow) vector parallel to and the same length as the (dashed grey line) vector between the deformed Neanderthal and modern human (see text). The deformations were magnified x500.

In summary, within both biting simulations, modes of deformation are similar between species and age groups with adults deforming less than infants and Neanderthals less than modern humans. Despite these similarities, there are notable differences in modes and degrees of deformation between biting simulations. Additionally, differences in the degree to which some regions deform relative to others, rather than differences in which regions deform, exist between age stages and between Neanderthals and modern humans. Between modern humans and Neanderthals, differences exist in the degree of deformation of the midfacial skeleton and supraorbital region.

These deformations strain the skeleton and so further analyses focused on mapping and comparison of facial strains between species and age stages.

### 5.1.3 Tensile and compressive strains

Figures 63 and 64 present the principal tensile ( $\epsilon_1$ ) and compressive ( $\epsilon_3$ ) strain contour plots for both species at the three age stages from the RP<sup>2</sup>/RdM<sup>2</sup> biting simulations. Modern human models present generally greater tensile and compressive strains than Neanderthals, reflecting the greater deformation observed in the previous size and shape analyses. In both species, their magnitudes decrease from infant to adult. Tensile strains are generally comparable in their distribution in all models, with the largest being found on the working side (right) and in similar anatomical regions: directly above the bite point, the zygoma, the right anterior maxilla, the inferior aspect of the maxilla (above the alveolar process), in and around the orbits and nasal bones (Figure 63). In both species, the strains decrease from infant to adult. The modern human infant presents greater strains than the Neanderthal over the anterior maxilla.

Figure 63 presents the distribution and magnitudes of compressive strains in all of the models. These show a similar anatomical distribution to the tensile strains in both species (Figure 63). Like the tensile strains, their magnitudes decrease from infant to adult and modern human models present greater strains than the Neanderthal ones.

Adjusting tensile and compressive strains in the Neanderthal to account for size (squared cs) differences between species at each age stage for these biting simulations (Figure 63C and 64C) moderately increases their magnitudes in Neanderthal models, especially over the anterior maxilla, around and in the orbits, nasal bones and the supra-orbital region for the juvenile and adult models. RP<sup>2</sup>/RdM<sup>2</sup> peak bite forces are greater in modern humans (Table 14), therefore scaling of strains by peak bite force (Figures 63D and 64D) increases the magnitudes of strains for the Neanderthal infant, juvenile and adult models. Scaling by size (squared of centroid size, squared cs) or peak bite force does not change their distribution, and so does not affect how this differs between and among the modern human and Neanderthal models prior to scaling.

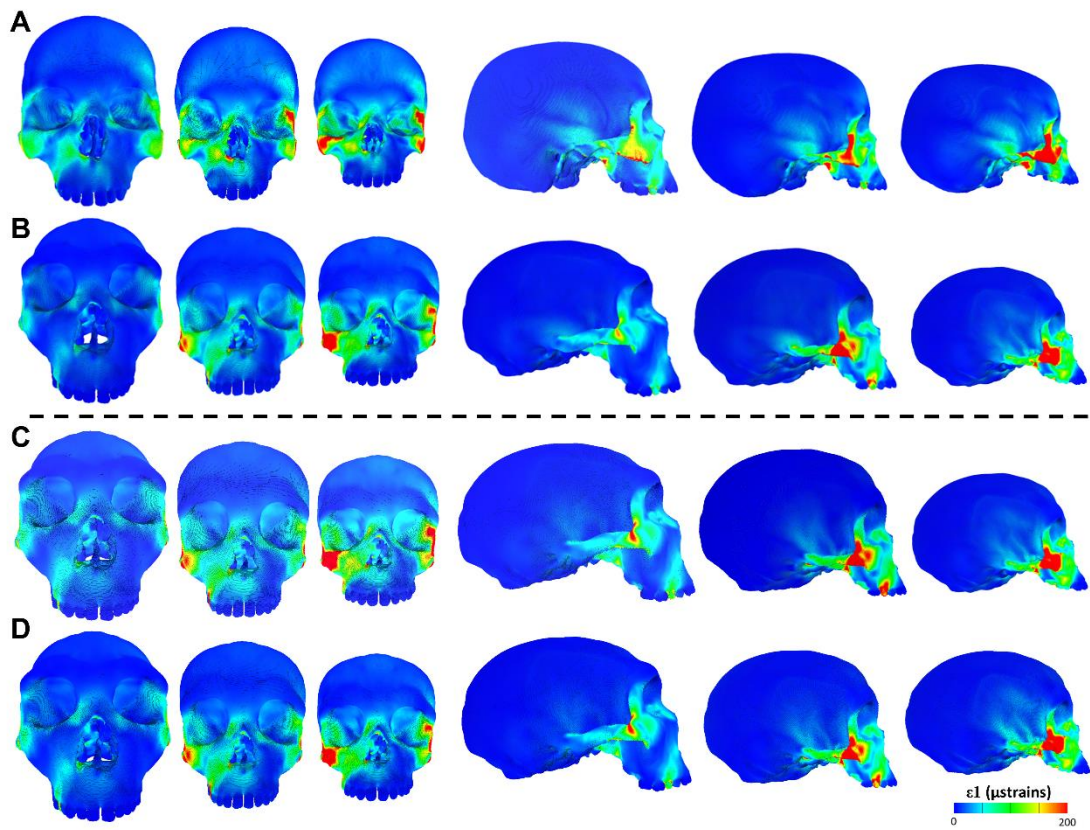


Figure 63. Tensile ( $\epsilon_1$ ) strain contour plots, in frontal and lateral views, of the solved modern human (A) and Neanderthal (B, C, D) infant juvenile and adult FE models (from left to right) under  $RP^2/RdM^2$  biting simulations. Tensile strains are unscaled (A, B), scaled in Neanderthals by size (C) and scaled by peak bite force (D) relative to modern humans per age stage.

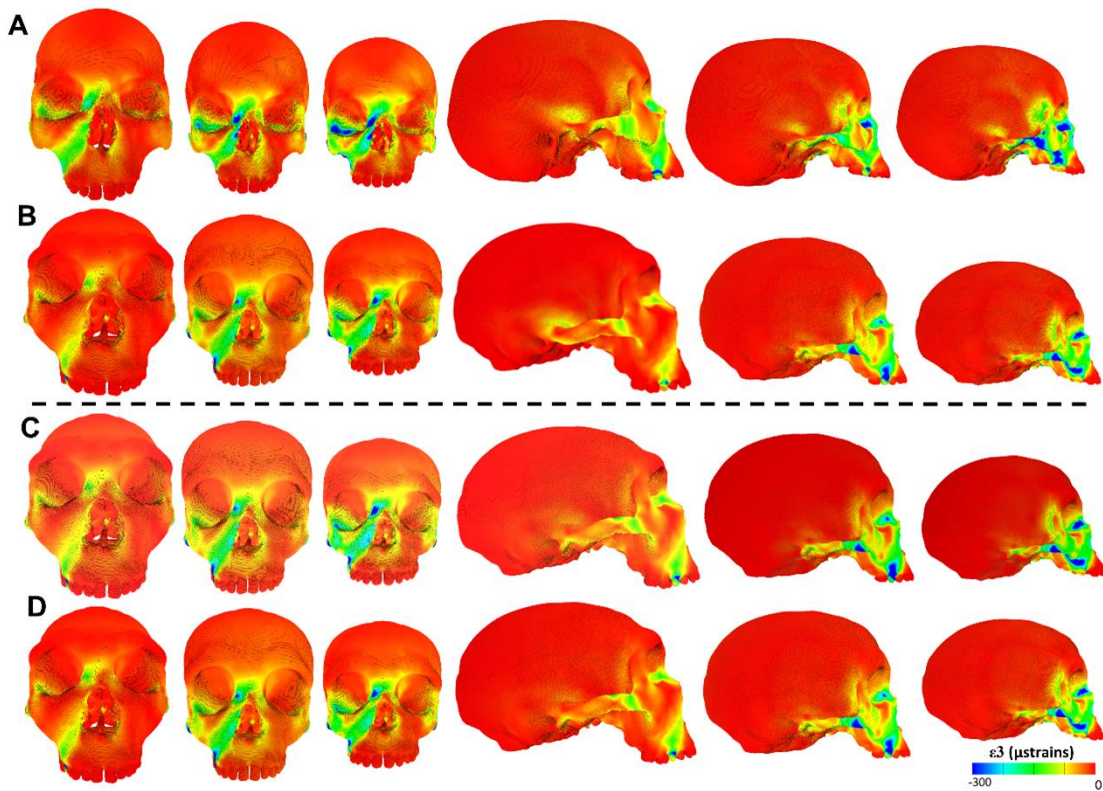


Figure 64. Compressive ( $\epsilon_3$ ) strain contour plots, in frontal and lateral views, of the solved modern human (A) and Neanderthal (B, C, D) infant, juvenile and adult FE models (from left to right) under  $RP^2/RdM^2$  biting simulations. Tensile strains are unscaled (A, B), scaled in Neanderthals by size (C) and scaled by peak bite force (D) relative to modern humans per age stage.

Figures 65 and 66 present the tensile and compressive strain contour plots for the  $RI^1$  biting simulations. The tensile strains (Figure 65) are similarly distributed in all models, being largest directly above the bite point at the inferior aspect of the maxilla, the zygomatic, around and within the orbits. The modern human models present generally greater tensile strains than the Neanderthal ones and, in both species, these decrease from infant to adult. The compressive strains are similarly distributed (Figure 65). As with the previous biting simulations (Figure 63, Figure 64;  $RP^2/RdM^2$ ), adjusting Neanderthal tensile and compressive strains to correct for size (squared cs) differences between species, increases the magnitude of the strains in the adult and juvenile Neanderthal models, but does not affect the distribution of regions of high and low strain. Scaling by peak bite force differences between species (see Table 14), moderately increases the magnitude of strains in the Neanderthal models while preserving the distributions of regions of high and low strain.

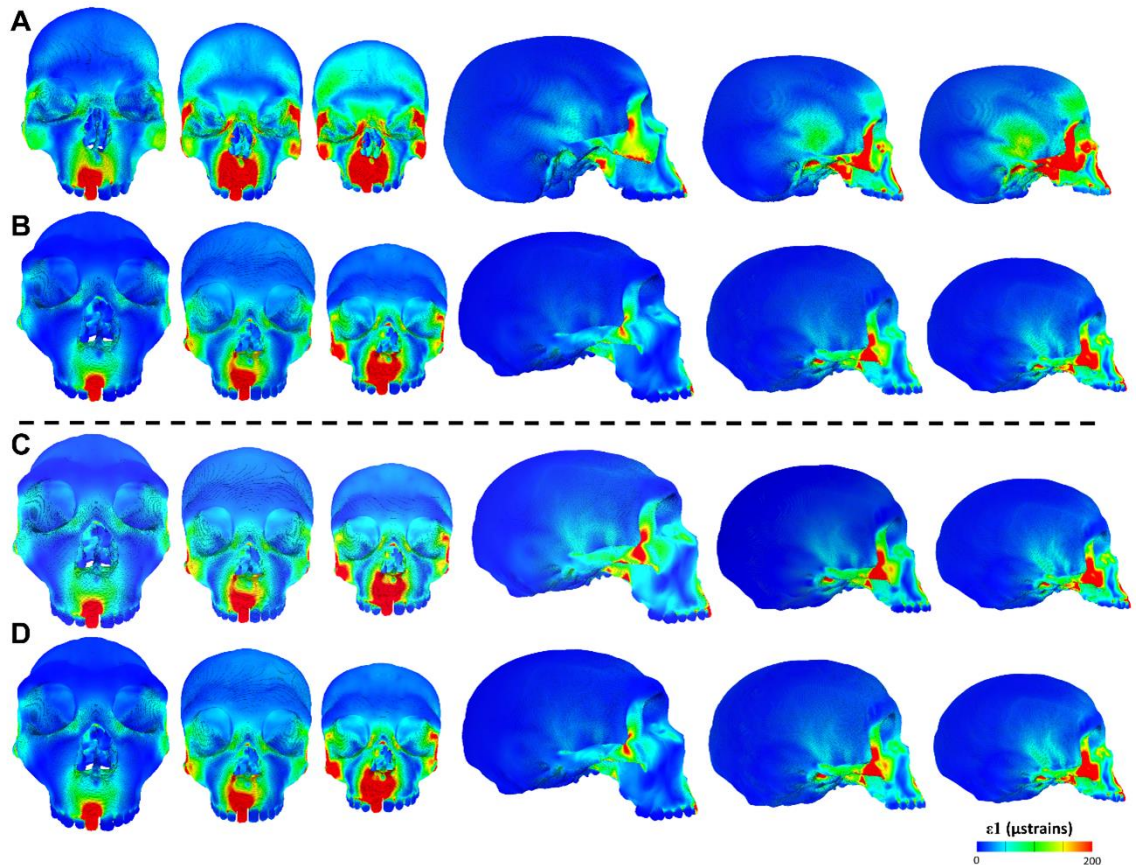


Figure 65. Tensile ( $\epsilon_1$ ) strain contour plots, in frontal and lateral views, of the solved modern human (A) and Neanderthal (B, C, D) infant, juvenile and adult FE models (from left to right) under  $RI^1$  biting simulations. Tensile strains are unscaled (A, B), scaled in Neanderthals by size (C) and scaled by peak bite force (D) relative to modern humans per age stage.

Tensile ( $\epsilon_1$ ) and compressive ( $\epsilon_3$ ) strain values were collected at 126 landmarks to quantify the spatial distributions of strain magnitudes among and between the modern human and Neanderthal models for both biting simulations (Figures 67-72). It should be noted that these strain values arise from loading all models with identical muscle forces, this is unphysiological and is expected to lead to strain magnitudes decreasing with model size, and so age stage. The relative differences in strain among craniofacial regions are, however, unaffected and can be compared directly, or after further scaling to account for size differences or differences in biting force.

During  $RP^2/RdM^2$  biting, the patterns of variation of strain magnitudes among landmarks are generally similar between models, with some exceptions (Figure 67). Over the upper subnasal part of the maxilla (Figure 67A), the modern human models present greater tensile strains than the Neanderthals, with those in the juvenile being greatest, especially on the balancing (left) side. Similarly, compressive strains are largest on the

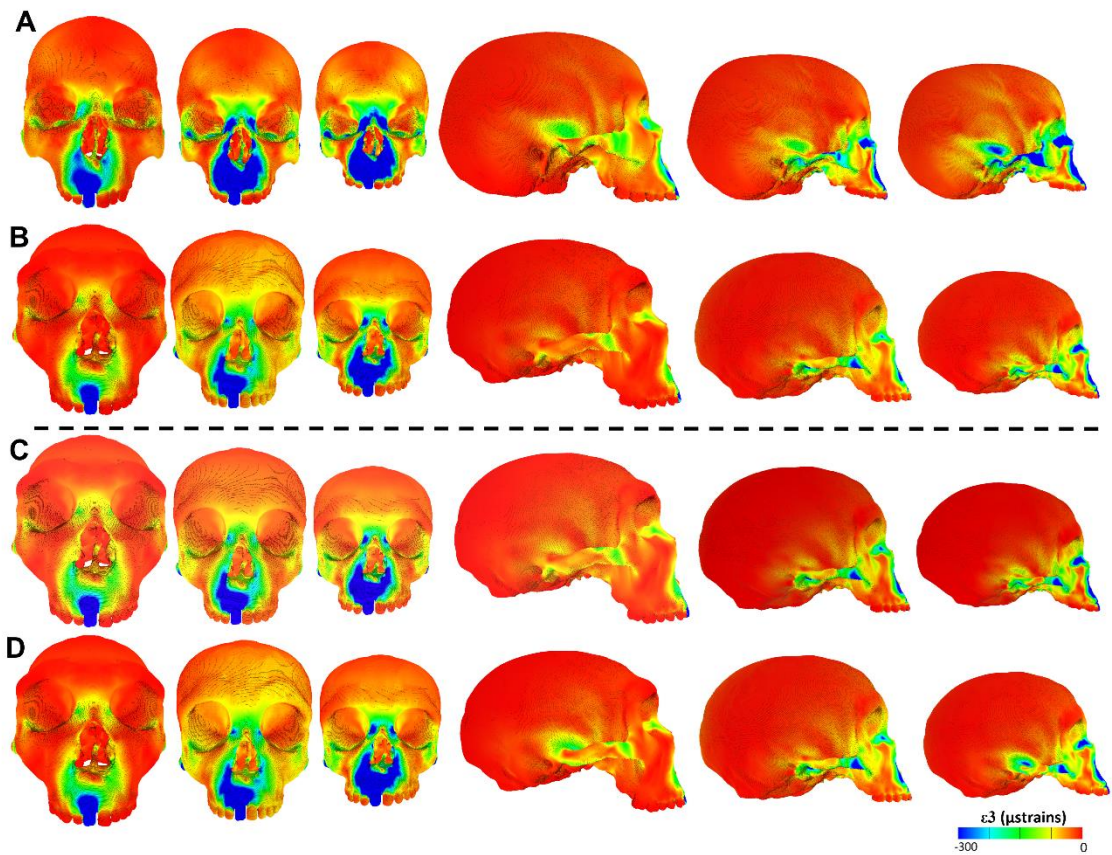


Figure 66. Compressive ( $\epsilon_3$ ) strain contour plots, in frontal and lateral views, of the solved modern human (A) and Neanderthal (B, C, D) infant juvenile and adult FE models (from left to right) under  $RI^1$  biting simulations. Tensile strains are unscaled (A, B), scaled in Neanderthals by size (C) and scaled by peak bite force (D) relative to modern humans per age stage.

balancing (left) side in the modern human over the same region (landmark 6 to 12, Figure 67A). In contrast, the Neanderthal infant and juvenile models experience greater compressive strains than modern humans on the working (right) side (landmarks 1-4, Figure 67A). and less on the balancing (left) side. Figure 67B shows that on the anterior aspect of the maxilla, on the working (right) side, the infant models in both species experience greater tensile and compressive strains than the other models, with those in the infant Neanderthal exceeding those in the infant modern human. However, on the balancing side (left), the infant modern human model presents greater strains than the infant Neanderthal.

The plot of Figure 67C shows marked asymmetry between the working and balancing sides, because the landmarks on the working side, are directly above the bite point. On the working side, directly above the bite point (Figure 67C), the juvenile and infant Neanderthal models present the greatest tensile and compressive strains with the juvenile exceeding the infant. While the modern human models show a similar pattern of strain

variation, strain magnitudes are less than in Neanderthals and the adult model presents the greatest strains.

Finally, modern human models experience generally greater tensile and compressive strains over the supraorbital region in the right  $P^2/dM^2$  biting simulations (Figure 67D). In both species, the tensile and compressive strains decrease from infant to adult, as is expected given size differences and constant muscle forces. Asymmetry is present between the working and balancing sides with the balancing side presenting greater strains, especially for the infant and juvenile models in both species.

Figures 68 and 69, present the strains for this biting simulation scaled in Neanderthals for size (squared cs) and peak bite force (see Table 14) relative to modern humans for each age stage. Scaling tensile and compressive strains by size (squared cs) for this biting simulation slightly increases the magnitudes of the strains in the Neanderthal models (Figures 67-68). When scaled by peak bite force (Table 14), the magnitudes of strains are also slightly increased for all the Neanderthal models (Figures 67-69). Scaling by size or peak bite force does not change the relative differences in strain magnitudes among landmarks.

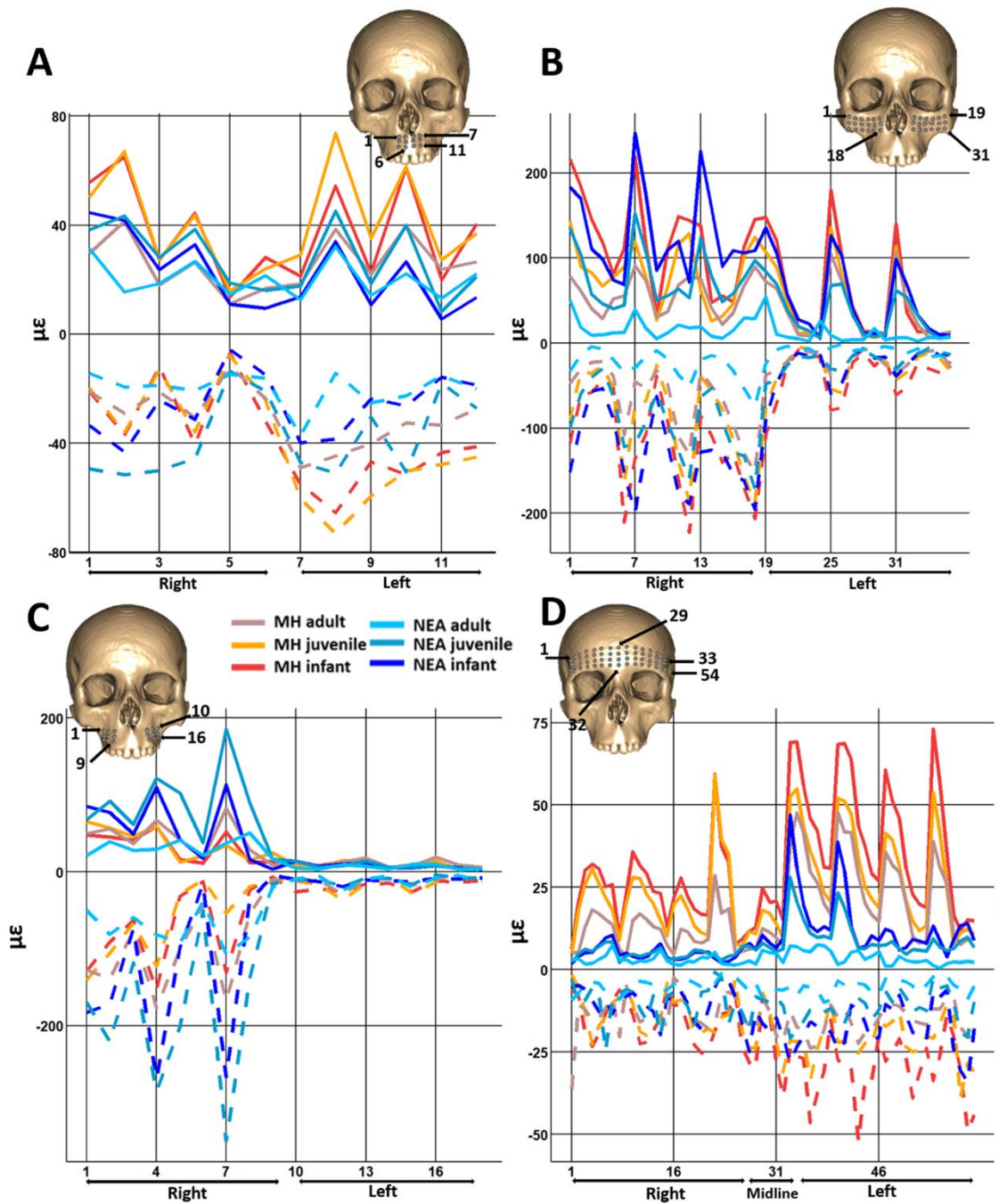


Figure 67. Strains experienced by the Neanderthal (NEA) and modern human (MH) infant, juvenile and adult FE models at the 126 sampling points over the face during the RP<sup>2</sup>/RdM<sup>2</sup> biting simulation. The tensile (solid) and compressive (dashed) strains are unscaled. See landmark details in supplementary material Figure 1.

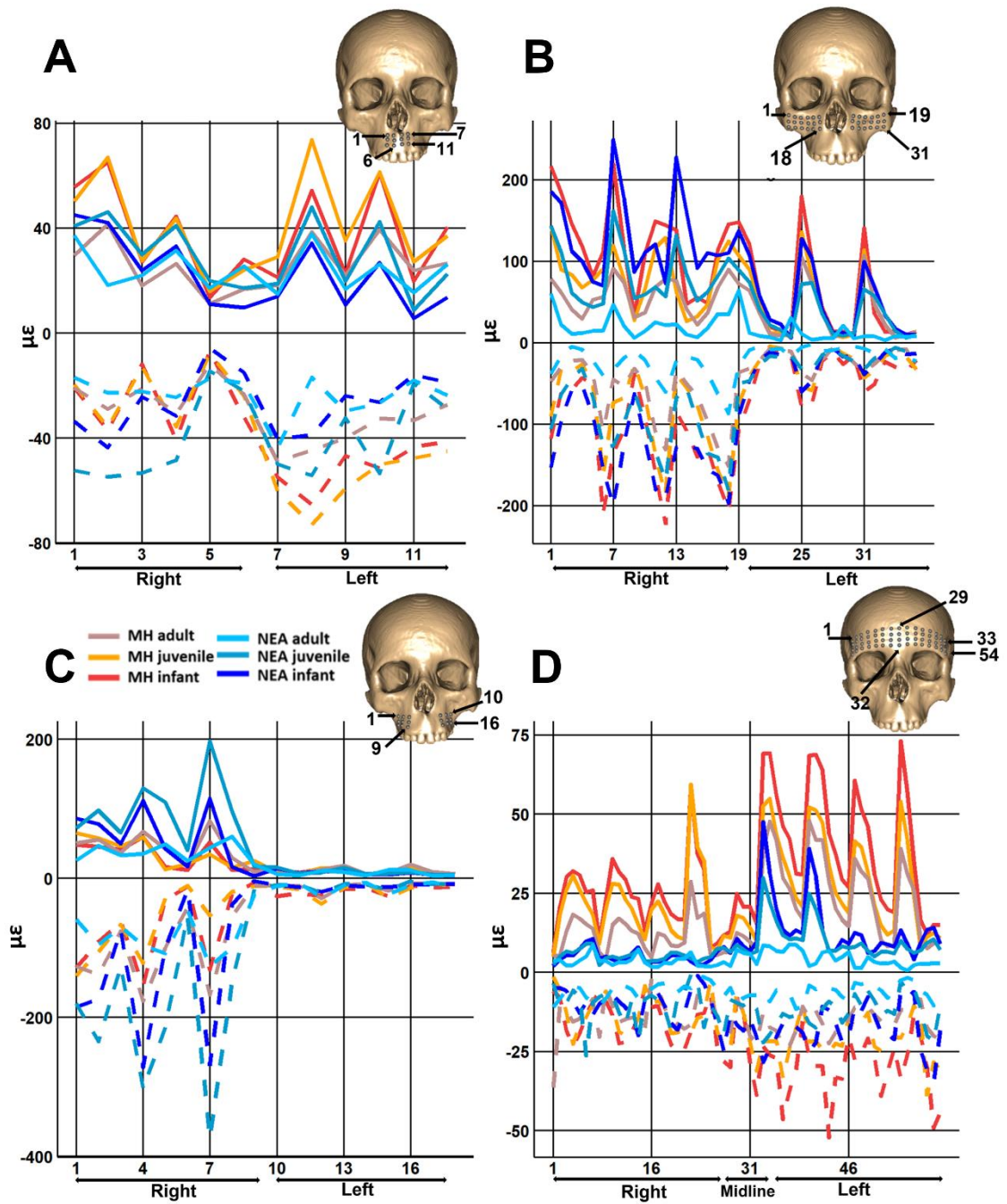


Figure 68. Strains experienced by the Neanderthal (NEA) and modern human (MH) infant, juvenile and adult FE models at the 126 sampling points over the face during the RP<sup>2</sup>/RdM<sup>2</sup> biting simulation. The tensile (solid) and compressive (dashed) strains are scaled in Neanderthals by size relative to humans, per age stage. See landmark details in supplementary material Figure 1.

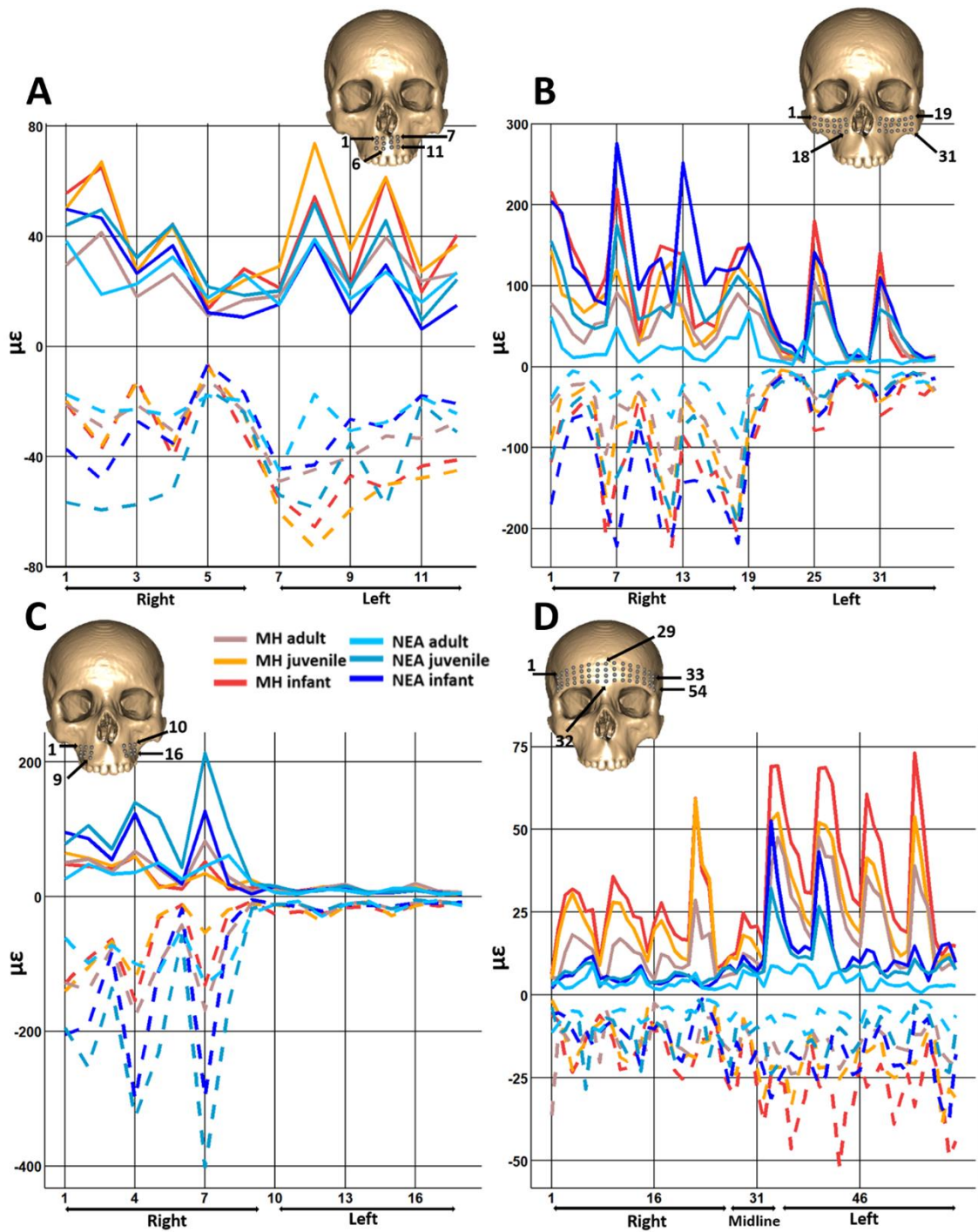


Figure 69. Strains experienced by the Neanderthal (NEA) and modern human (MH) infant, juvenile and adult FE models at the 126 sampling points over the face during the RP<sup>2</sup>/RdM<sup>2</sup> biting simulation. The tensile (solid) and compressive (dashed) strains are scaled in Neanderthals by peak bite force relative to modern humans per age stage. See landmark details in supplementary material Figure 1.

During RI<sup>1</sup> biting, the pattern of variation among landmarks in tensile and compressive strains is similar between species (Figure 70). Asymmetry of strains is evident between working and balancing sides but to a lesser degree than in RP<sup>2</sup>/RdM<sup>2</sup> biting. Consistent with model size differences, within each species, infant models present the greatest tensile and compressive strains, followed by the juvenile and adult models. The Neanderthal infant model presents greater tensile and compressive strains than the other models on the working (right) side immediately above the bite point (alveolar process and inferior part of the maxilla) and the anterior maxilla (Figures 70A and 70B). On the balancing (left) side, the modern human infant model presents the greatest strains (Figures 70A-C). Thus, strains in the Neanderthal infant model on the working side exceed or match those in the modern human, while on the balancing side, the opposite is found.

Over the supraorbital region (Figure 70D), as for the RP<sup>2</sup>/RdM<sup>2</sup> biting simulations, the three modern human models present greater strains than the Neanderthal ones and both the tensile and compressive strains decrease from infant to adult. The Neanderthal models present similar values and patterns of variation of compressive strains to the modern human ones on the working side (right) but lower values than modern human models on the balancing side.

The tensile and compressive strains in each model were scaled for size (square of centroid size, squared cs) and peak bite force (Table 14) in Figures 71 and 72. The scalings slightly increase the magnitudes of the strains in all Neanderthal models but the major differences outlined above remain. Scaling does not affect the pattern of variation of tensile and compressive strain magnitudes between landmarks.

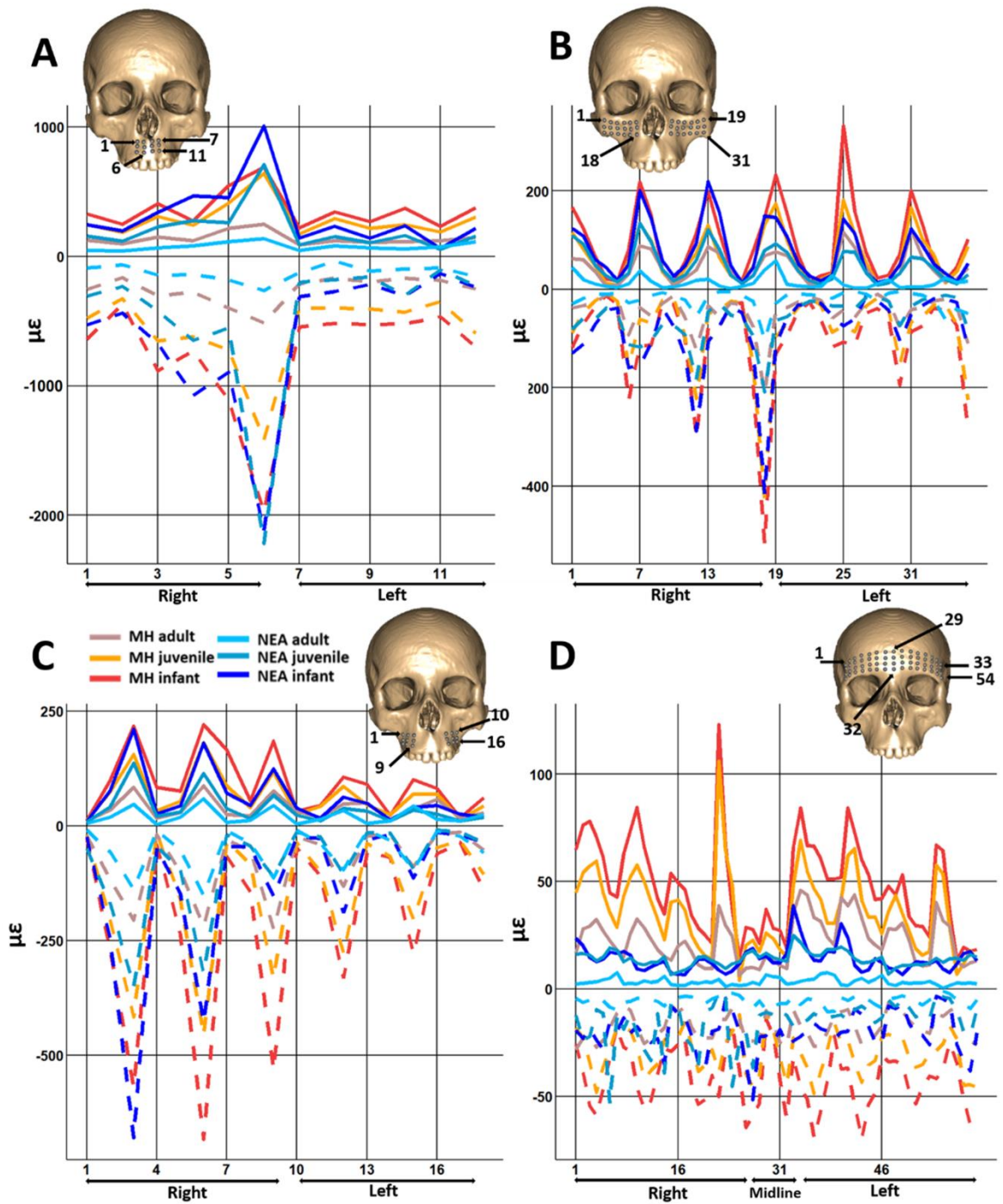


Figure 70. Strains experienced by the Neanderthal (NEA) and modern human (MH) infant, juvenile and adult FE models at the 126 sampling points over the face during the RI<sup>1</sup> biting simulation. The tensile (solid) and compressive (dashed) strains are unscaled. See landmark details in supplementary material Figure 1.

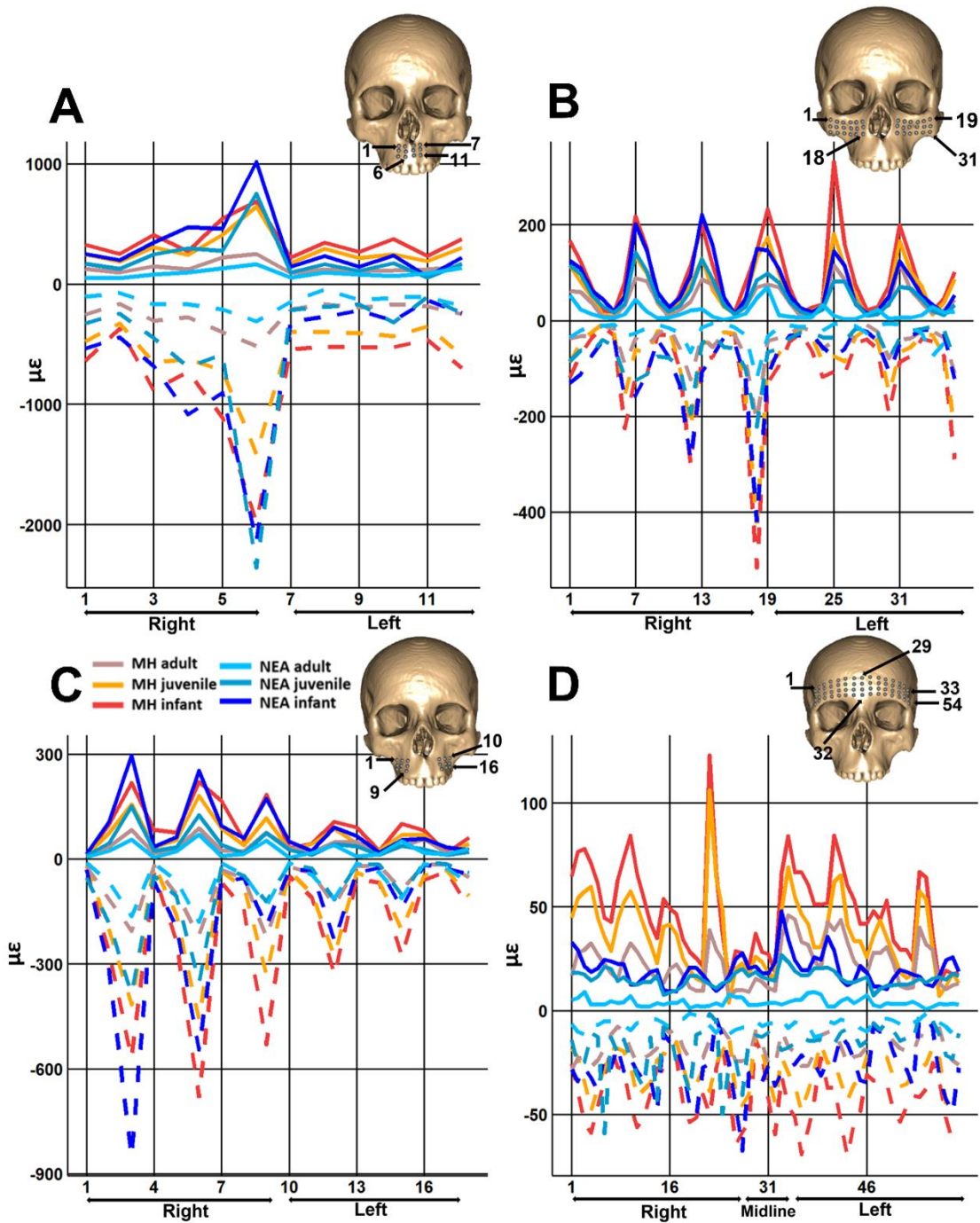


Figure 71. Strains experienced by the Neanderthal (NEA) and modern human (MH) infant, juvenile and adult FE models at the 126 sampling points over the face during the  $R1^1$  biting simulation. The tensile (solid) and compressive (dashed) strains are scaled in Neanderthals by size relative to modern humans per age stage. See landmark details in supplementary material Figure 1.

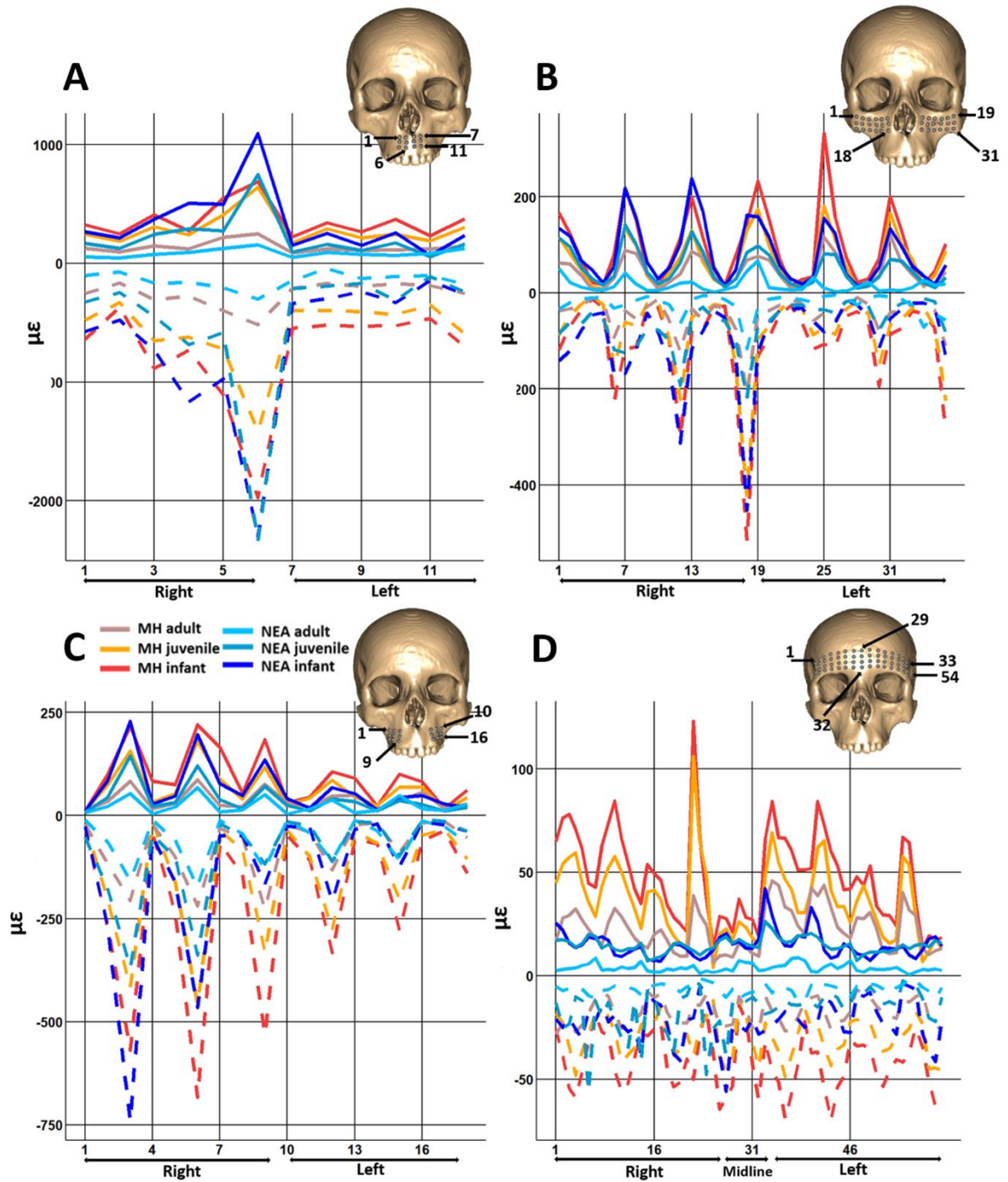


Figure 72. Strains experienced by the Neanderthal (NEA) and modern human (MH) infant, juvenile and adult FE models at the 126 sampling points over the face during the  $R1^1$  biting simulation. The tensile (solid) and compressive (dashed) strains are scaled in Neanderthals by peak bite force relative to modern humans per age stage. See landmark details in supplementary material Figure 1.

#### 5.1.4 Peak strains over both biting simulations

The peak (maximum values of) principal tensile ( $\epsilon_1$ ) and compressive ( $\epsilon_3$ ) strains for both biting simulations (RI<sup>1</sup> and RP<sup>2</sup>/RdM<sup>2</sup>) were used to create contour plots combining the maximum tensile and compressive strains arising during these two-biting simulations. These were plotted for both species at the three age stages (Figure 73).

In both species and for both strain modes, the maximum strains are located in similar areas such as the inferior maxilla, the anterior maxilla, the zygomatic bone and around and between the orbits. The contour plots are more strongly reminiscent of the incisor biting contour plots (Figures 65-66) than the RP<sup>2</sup>/RdM<sup>2</sup> contour plots, reflecting the greater deformations and so, strains experienced in incisor biting. In both species, the maximum tensile and compressive strains decrease from infant to adult. The modern human models present generally greater maximal tensile and compressive strains than the Neanderthal models (Figure 73A vs. Figure 73B). In particular in the subnasal region of the maxilla modern humans present larger regions of high strain than the Neanderthals, which remain larger after scaling strains in Neanderthals. The Neanderthal contour strain plots were adjusted for size (squared of centroid size, squared cs) and peak bite forces (summing the RI<sup>1</sup> and RP<sup>2</sup>/RdM<sup>2</sup> peak bite forces) in each age stage (Figure 73A and Figure 73B). Scalings by size (squared cs) or peak bite force for all models increase the maximal tensile and compressive strains in the Neanderthal models (Figure 73C and Figure 73D) but do not have a notable effect on the differences in maximal strains noted above.

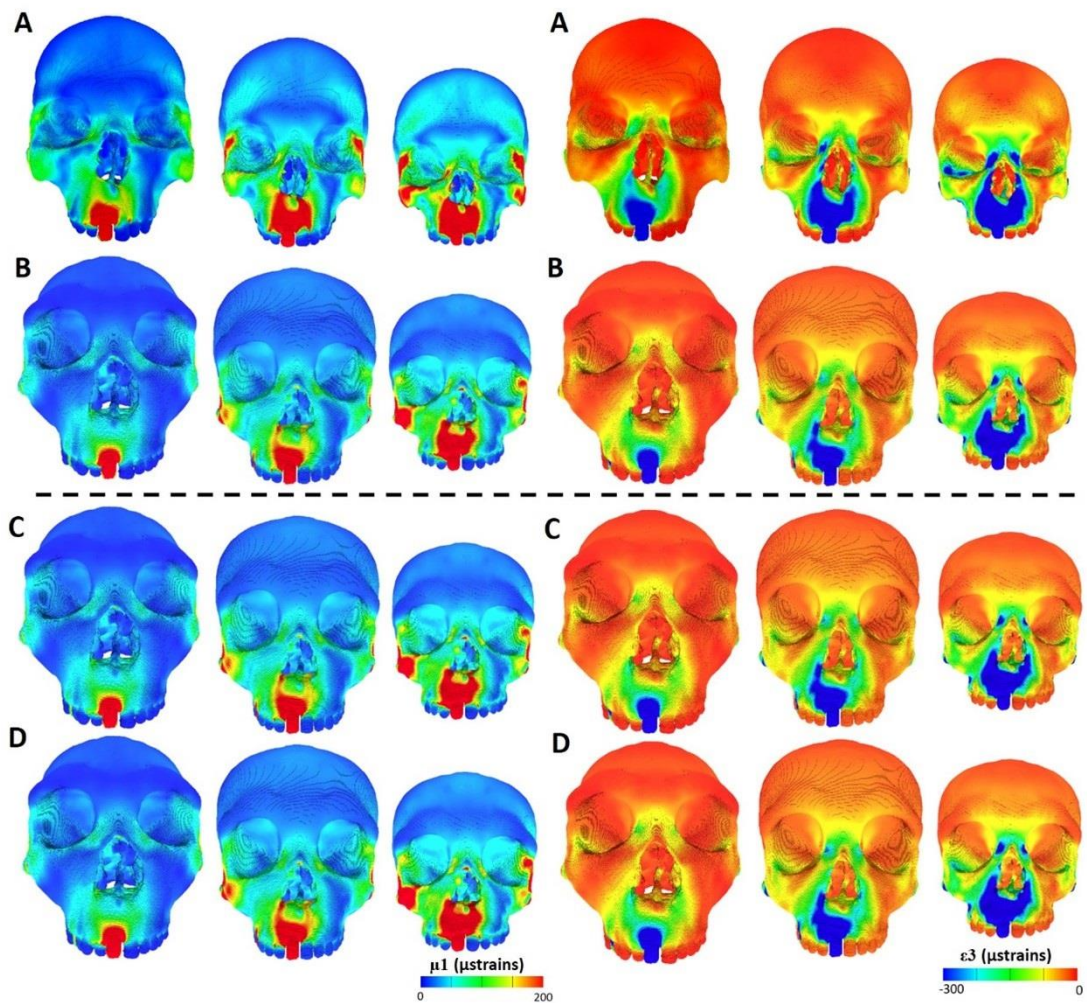


Figure 73. Combined maximum strain contour plots of both RI<sup>1</sup> and RP<sup>2</sup>/RdM<sup>2</sup> biting simulations. Tensile (right) and compressive strains (left) are unscaled (A, modern humans; B, Neanderthals), in Neanderthals these are scaled relative to humans by size per age stage (C) and scaled by peak bite force per age stage (D).

## 5.2 Discussion

### 5.2.1 Mechanical advantages, peak bite forces and force production efficiencies

Neanderthals exhibit unique craniofacial features within the genus *Homo* such as: rounded and laterally projecting parietal bones; a posteriorly projecting occipital bone; sloping squamous portion of the frontal bone with double-arched browridge and midsagittal upper facial projection; a posteriorly and inferiorly orientated temporomandibular joint; reduced mastoid processes; receding zygomatic arches; elongated vertical facial dimensions; total facial and particularly mid-facial prognathism; inflated infra-orbital regions of the maxillae; broad palate and alveolar processes (relative to length); absence of a canine fossa in the maxilla; wide nasal apertures and depressed internal nasal floors; elevated pneumatization in the frontal, nasal and maxillary sinuses robust mandibles with a receding symphysis, a posteriorly positioned mental foramen, high coronoid and/or low condylar processes, large retromolar spaces, and relatively large anterior dentition (Smith, Petersen and Gipe, 1983; Stringer, Hublin and Vandermeersch, 1984; Rak, 1986; Demes, 1987; Trinkaus, 1987a; Smith and Paquette, 1989; Tattersall, 1998; Franciscus, 2003; Nicholson and Harvati, 2006; Rosas et al., 2006; Clement, Hillson and Aiello, 2012).

Explanations of this craniofacial morphology have been debated within the scientific community and these debates have centred around a few key hypotheses. These include: cold adaptation (Coon, 1962), genetic drift (Howell, 1951; Hublin, 2000, 1998), altered growth patterns (Ponce de Léon and Zollikofer, 2001; Smith, 1991) and/or respiratory moisture retention in cold and/or arid climates (Franciscus and Trinkaus, 1988). In recent years, attention has been paid to the masticatory biomechanics of Neanderthals (Rak, 1986; Demes, 1987; Trinkaus, 1987b; Demes and Creel, 1988; Antón, 1990; O'Connor, Franciscus and Holton, 2005; Clement, Hillson and Aiello, 2012). It has been proposed that Neanderthals were adapted to generate and withstand high and/or repetitive occlusal loads, especially at the anterior dentition (the anterior dental loading hypothesis; Rak, 1986; Demes and Creel, 1988; Clement, Hillson and Aiello, 2012). In this study, a comparison of mechanical advantages (MAs), peak bite forces, force production efficiencies and magnitudes and modes of deformation at two bite points were investigated in mean infant, juvenile and adult modern human and Neanderthal models. These aimed to compare and identify differences among the models.

The results show that for both biting simulations ( $RP^2/RdM^2$  and  $RI^1$ ), the Neanderthal models present greater MAs for the temporalis muscles except at the posterior

part in the juvenile, where the modern human model presents a higher value (Figure 51 and Figure 52). For the masseter and medial pterygoid muscles, the modern human models show greater MAs than the Neanderthal models except during RI<sup>1</sup> biting in the juvenile models where the Neanderthal model presents greater MA than the modern human ones (Figure 51). O'Connor et al., (2005) investigated MAs in Neanderthals, including Amud 1, La Chapelle aux Saints 1 and La Ferrassie 1, used in this study, and compare them to MAs calculated at I<sup>1</sup> in 26 adult modern human specimens. In this work, O'Connor et al., (2005) found that, on average, the adult modern human has a greater MA at the masseter, as in this study (Figure 53 and Figure 54), however, for the temporalis and medial pterygoid the results contrast (O'Connor, Franciscus and Holton, 2005).

The MAs reflect the peak bite force calculated for each model in both species. The modern human models present higher peak bite forces at each age stage, with RP<sup>2</sup>/RdM<sup>2</sup> and RI<sup>1</sup> biting simulations in the modern human infant showing 8% and 11% greater peak bite force than the Neanderthal model, respectively. For the juvenile, these are 13% and 5% greater and, for the adult 18% and 12% greater than the Neanderthal model (Table 14). Neanderthal and modern human adult models present greater differences in peak bite force (Table 14). Biting force production efficiencies (ratio of peak bite force over 'net applied muscle forces') were also calculated at each age stage for both species (Table 16 and Figure 56). They indicate that the modern human adult model shows higher force production efficiencies than the Neanderthal for both biting simulations (Table 16). The same pattern is observed for the juvenile model at the RP<sup>2</sup>/RdM<sup>2</sup> bite point while at the RI<sup>1</sup> bite point, both modern human and Neanderthal juvenile models present similar values. For the infant models, in both biting simulations, the Neanderthal shows greater force production efficiencies than the modern human (Table 16).

The results of this study confirm previous ones on Neanderthal masticatory biomechanics (Antón, 1990; Spencer and Demes, 1993; O'Connor, Franciscus and Holton, 2005; Lieberman, 2011). These have shown that *Homo sapiens* are relatively more efficient at generating peak bite forces than Neanderthals. Indeed, Antón (1994) finds that peak bite force magnitude at both incisal and molar bite points was 20 to 22% smaller in Neanderthals than modern humans while O'Connor et al., (2005) found that force-production efficiency is maintained across a considerable range of facial size and robusticity in Neanderthals. Similar results were found in comparing *Homo heidelbergensis* to mod-

ern humans, which, as in the comparison with Neanderthals, appear more efficient at converting muscle forces into peak bite forces (Godinho et al., 2018). Interestingly, in Godinho et al., (2018), the *H. heidelbergensis* adult model (from a reconstruction of Broken Hill) was loaded at the left I<sup>1</sup> bite point and uses similar Finite Element parameters to those in this study for the modern human and Neanderthal adult model. The *H. heidelbergensis* adult model, at that bite point, produces a lower peak bite force than the Neanderthal adult model in this study (Godinho et al., 2018). These findings reflect the lower values of MAs in the *H. heidelbergensis* adult Broken Hill and Petralona fossils reported by Godinho et al., (2018) than are found here in the Neanderthal adult model, with the exception of the medial pterygoid where the opposite pattern is observed. The relatively less robust, less prognathic and smaller craniofacial skeleton of Neanderthals compared to *H. heidelbergensis*, therefore, appears to present greater masticatory muscle MAs.

It has been proposed that the retracted and shorter face and the more anteriorly positioned masticatory muscles in adult *Homo sapiens* underlie greater muscle mechanical advantages and greater ability to generate peak bite force than in adult Neanderthals (Trinkaus, 1987a; Antón, 1990; O'Connor, Franciscus and Holton, 2005; Wroe et al., 2010; Lieberman, 2011; Eng et al., 2013; Ledogar et al., 2016; Godinho and O'Higgins, 2018). From the results of this study, it appears that similarly increased MAs are found among infants and juveniles of these species, and in consequence, modern humans can generate higher peak bite forces from the same applied muscle forces (Table 14). Modern humans are thought to possess masticatory muscles that are generally smaller (Antón, 1990; O'Connor, Franciscus and Holton, 2005) or comparable in cross-sectional area to Pleistocene and recent robust specimens (Eng et al., 2013; O'Connor, Franciscus and Holton, 2005) and therefore muscle forces may well be less or about the same. In interpreting the results of this study, it is important to take into account differences in muscle forces that could have existed between Neanderthals and modern humans at all age stages.

How muscle forces develop in modern humans is not known in detail and predictions of these muscle forces in fossils rely on estimation using cross-sectional areas based on bony proxies (Antón, 1994; Antón, 1990; Koolstra et al., 1988). Recently, it has been shown that those bony proxies do not necessarily lead to reliable estimates of muscle cross-sectional areas (Toro-Ibacache et al., 2016). Therefore, in this study, the same muscle forces used in previous studies from the same laboratory were applied to all the models (Toro-Ibacache et al., 2016; Godinho et al., 2018). While using the same muscle forces

in all models has inevitably led to overestimation of peak bite forces in smaller crania relative to the adult it can be accounted by scaling, until good estimates of cross-sectional areas in Neanderthal adults and subadults become available. For now, comparisons of forces between ages within species overestimate biting forces in smaller crania relative to larger ones. However, comparisons among age groups, between these species may be more reliable, depending on the validity of using modern human adult muscle forces in Neanderthals. In any case, the use of the same muscle forces in all models means that differences in biting forces among them reflect relative differences in the efficacy of conversion of muscle into biting forces. These differences in efficiency arise because of differences in mechanical advantages (Figure 53 and Figure 54 and Godinho et al., 2018).

#### 5.2.2 Craniofacial skeletal performance during right first incisor and second premolar/deciduous molar biting

The findings show that even if tensile and compressive strains are generally comparable among modern human and Neanderthal infant, juvenile and adult models, with the largest strains on the working side (right) and in similar anatomical areas (such as directly above the bite point, the zygoma, the right part of the anterior maxilla, around the orbitals, and nasal bone), there exist some differences and magnitudes of strains between the two species at each age stage. Overall, during both biting simulations, the modern human models develop greater tensile and compressive strains than the Neanderthals except: at the anterior maxilla on the working side where the Neanderthal infant presents slightly higher tensile and compressive strains in both biting simulations, directly above the bite point during the RI<sup>1</sup> biting simulation with the Neanderthal infant again developing greater tensile and compressive strains, and over the alveolar process during RP<sup>2</sup>/RdM<sup>2</sup> biting simulation where both infant and juvenile Neanderthals present higher tensile and compressive strains than the modern human models (Figure 67 to Figure 72). Differences in spatial distribution are also observed between the two species at all age stages, especially in peak tensile and compressive strains when combining both biting simulations (Figure 73). Differences in the spatial distribution of tensile and compressive strains between modern humans and Neanderthals are present, for all models, at the anterior maxilla where modern humans present larger fields of tensile strains at the working side. Between the modern human and Neanderthal juvenile models, differences are seen at the left (balancing side) inferior maxilla with the modern human model showing larger

regions of tensile strain, of greater magnitude. Finally, differences in straining are observed over the supraorbital region, where the modern human models present greater tensile and compressive strains (Figure 73) for both biting simulations.

Similarly, the GM size and shape analysis of global magnitudes and modes of deformation (Figure 57 to Figure 62) shows that at each age stage, the models deform differently with the modern human deforming to a greater degree during both biting simulations. This is consistent with the strain contour plots and graphs, which show small differences in which regions experience high and low strains (Figure 57 to Figure 62).

### 5.2.3 Significance of apparent differences between the mean Neanderthal and modern human infant, juvenile and adult models

The present findings are consistent with previous studies that have compared adult *Homo sapiens* and Neanderthals (Antón, 1990; O'Connor, Franciscus and Holton, 2005; Lieberman, 2008, 2011; Eng et al., 2013). These studies suggested that facial reduction in *H. sapiens* increases mechanical efficiency in peak bite force generation. However, this greater mechanical efficiency is associated with a lesser ability to resist masticatory or paramasticatory, functional loadings (Lieberman, 2011, 2008; Ledogar et al., 2016; Godinho and O'Higgins, 2018; Demes, 1987; Rak, 1986). The present study shows that these differences are also found at each age stage with few exceptions, at specific locations (see above).

The differences in tensile and compressive strain magnitudes and locations are found in regions where differences in bone growth remodeling exist between Neanderthals and modern humans, especially among infants and juveniles. Indeed, Neanderthals show a pattern of maxillary bone growth remodeling characterized by extensive bone deposition while modern humans present mainly resorption in the same area (Figure 81, Chapter 6; Lacruz et al., 2015b; Martinez-Maza, Rosas and Nieto-Díaz, 2013). The depository activity in Neanderthals is present in the remains of Gibraltar 2, a 5-year-old individual, while resorption in modern humans is already found at birth and continues and expands in area throughout infancy (Lacruz et al., 2015b; Schuh et al., 2019). When looking at differences in the modes of deformation between the two species at each age stage, using registration-free colourmaps of local surface area expansion or contraction in area, there appears to be a reasonable correspondence between regions of the bone surface that contract and expand and regions of facial bone resorption and deposition in

Neanderthals and modern human subadults (Lacruz et al., 2015b). This is explored in detail in Chapter 6. The different growth remodeling patterns found in modern humans and Neanderthals are said to impact growth direction differently. Lacruz et al., (2015b) suggested that extensive bone deposition over the maxilla is consistent with a strong forward growth component in the Neanderthal midface; whereas resorption over this region in the modern human face moderates forward displacement. Indeed, the development of large nasal cavities in Neanderthals is combined with a pattern of deposition that displaces the prosthion inferiorly and more anteriorly than in modern humans. As a result of the more anterior location of prosthion in the Neanderthals, the tooth row drifts forward with respect to the maxillary tuberosity, thus generating the retromolar space characteristic of Neanderthals (Martinez-Maza, Rosas and Nieto-Díaz, 2013; Lacruz et al., 2015b). These previous findings combined with the present ones regarding differences in modes of deformation at the infant and juvenile stages between modern humans and Neanderthals suggest that masticatory loadings during development could affect growth and potentially explain differences in a final craniofacial form in both species. Moreover, the low strains observed in the Neanderthal models over the supraorbital region during right first incisor biting are consistent with the anterior dental loading hypothesis, which also posits that the Neanderthal browridge develops as a buttress to resist heavy loadings (Rak, 1986; Demes and Creel, 1988), especially at the anterior dentition. This will be discussed in further detail in Chapter 6.

Changes in facial skeletal morphology in the human lineage have been related to multiple factors such as expansion and development of the brain (Lieberman et al., 2002b; Lieberman, 2011, 2008; Lieberman et al., 2008); increased cranial base angle (Enlow and Hans, 2008; Bastir, O'Higgins and Rosas, 2007), thermoregulation and air conditioning (Coon, 1962; Wolpoff, 1968a; Carey and Steegmann, 1981; Franciscus and Trinkaus, 1988) and preprocessing of food (Carlson, 1976; Carlson and Van Gerven, 1977). Moreover, compared to other hominins, modern humans present smaller masticatory muscles (Antón, 1990; O'Connor, Franciscus and Holton, 2005), a reduction in the size of the dentition (Brace, 1967; Brace and Mahler, 1971; Brace, Rosenberg and Hunt, 1987) and decrease in the proportion of fast twitch muscle fibres (Stedman et al., 2004). Therefore, it is not possible to determine whether facial reduction is an outcome of positive selection or an evolutionary by-product. In the latter scenario increased peak bite force efficiency

would be an incidental consequence of changes in midfacial morphology in our species, a spandrel (Godinho et al., 2018; Gould and Lewontin, 1979).

## 6.0 General discussion and conclusions

The general aim of the thesis is to understand and compare how biting mechanics interact with cranial form during post-natal craniofacial ontogeny in modern humans and Neanderthals. To this end, the thesis investigated differences in loading history between modern humans and Neanderthals by creating and loading infant (2-3 years old), juvenile (8-10 years old) and adult finite element models to compare the resulting deformations and strains between ages and species. The analyses rely on the creation of a craniofacial growth model for each species using GM and multivariate regression analyses.

The thesis is presented in six chapters. The first provides context through a literature review of the core topics approached in the dissertation. The second describes the approaches used to reconstruct the Neanderthal cranial specimens, derive the regression-based growth models of each species and extract 3D cranial surfaces representing the mean form of infants, juveniles and adults in each species. This chapter also provides new findings with regard to the comparison of post-natal ontogenetic trajectories between modern humans and Neanderthals. Chapters three and four present the finite element analyses of modern humans and Neanderthals, while chapter five compares FEA results between these species in the light of, and in relation to, known differences in morphology and morphogenesis. Finally, this chapter draws together and summarizes the key findings while identifying ways in which the study could be improved and extended.

### 6.1 Synthesis of key findings and discussion

In chapter 2, post-natal craniofacial ontogenetic trajectories were estimated and compared between samples of modern humans and Neanderthals ranging in age from infancy to adulthood, through geometric morphometric (GM) analyses of 3D landmarks and semi-landmarks. The analyses of both species indicate non-linear trajectories of development (shape change over time) of the cranium with a change in trajectory between the later juvenile and adult stages. Moreover, the results of a permutation test on the angle between developmental trajectories show that these differ between the two species and indicate differences in the way the midface changes during ontogeny. This result, concerning divergence, supports previous findings that found divergence in the trajectories of mandibular development between the two species (Bastir, O'Higgins and Rosas, 2007), and those of previous studies in indicating that the craniofacial ontogeny of both species

is consistently different at all stages and that post-natal ontogeny contributes to the establishment of differences in their final adult morphologies. However, it should be treated with caution, because of the lack of adequate sampling of especially infant Neanderthals.

Previous studies have investigated differences in growth patterns and rates between *H. sapiens* and Neanderthals (Martínez-Maza and Rosas, 2002; Rosas et al., 2006; Terhune, Ritzman and Robinson, 2018; Bastir, O’Higgins and Rosas, 2007; Macchiarelli et al., 2013; Mahoney et al., 2021; Lieberman, McBratney and Krovitz, 2002; Gunz et al., 2010; Smith et al., 2010a) and differences in developmental integration between cranial components as potential causes of differences (Enlow, 1990; Martínez-Maza and Rosas, 2002; Rosas and Bastir, 2002; Ross and Ravosa, 1993; Lieberman, 2011; Marcucio et al., 2011; Bastir and Rosas, 2016; Ross et al., 2004). Here, functional performance and adaptation to masticatory (or paramasticatory) biomechanics (e.g., the “anterior dental loading hypothesis”; Lieberman, 2011; Rak, 1986; Spencer and Demes, 1993) are investigated as potential factors underlying the development of differences in facial form between modern humans and Neanderthals.

Chapter 3 and Chapter 4 indicated that in modern humans and Neanderthals, infants are more efficient at converting muscle forces into bite forces due to the lever mechanics of their relatively shorter faces. Additionally, differences in tensile and compressive strain magnitudes and distributions exist among the models representing different age stages. In both species, differences are found at the inferior aspect of the maxilla and the alveolar process in the juvenile model, consistent with the GM analysis of deformations showing that modes, as well as degrees of deformation, also differ between the infant, juvenile and adult models. Chapter 5 finds that the modern human models present greater force production efficiency than the Neanderthal, and so develop greater peak bite forces, for the same muscle force input, as well as greater tensile and compressive strains at each age stage. Thus, the findings of this study are consistent with previous ones that show that modern humans are more efficient at converting muscle forces into peak bite forces (probably due to their retracted and orthognathic faces) compared to Neanderthals or *Homo heidelbergensis* (Antón, 1990; O’Connor, Franciscus and Holton, 2005; Lieberman, 2008, 2011; Eng et al., 2013; Godinho et al., 2018). However, this greater mechanical efficiency is associated with a lesser ability to resist masticatory or paramasticatory, functional loadings (Rak, 1986; Demes, 1987; Lieberman, 2008, 2011; Ledogar et al., 2016; Godinho et al., 2018). This study shows that this difference is found at each

age stage. More specifically, the results show differences in strain magnitude and distributions at specific locations in all models, at the anterior and inferior maxilla, and over the supraorbital region.

Interestingly, in this study, modern human models at all stages present higher tensile and compressive strains over the supraorbital region. The underlying causes of the development of large supraorbital tori in many primates and hominins have been debated over the last 50 years. Two different, but not mutually exclusive, models have been hypothesized to explain their presence or absence in different species: the spatial/structural hypothesis (Biegert, 1963, 1957; Enlow and Azuma, 1975; Enlow and Bostwick, 1977; Enlow and Hans, 1996; Enlow and Moyers, 1971; Fenart and Deblock, 1978; Hofer, 1952; Lieberman et al., 2002a; Moss and Young, 1960; Ravosa, 1991b, 1988; Schultz, 1940; Shea, 1985a; Vogel, 1968, 1966; Weidenreich, 1941) and the biomechanical hypothesis (Endo, 1970; Russell et al., 1985; Hilloowala and Trent, 1988b, 1988a; Hylander, Picq and Johnson, 1991; Ravosa et al., 2000; Bernal, Perez and Gonzalez, 2006; Baab et al., 2010; Godinho and O'Higgins, 2018; Witzel, 2011; Oyen and Tsay, 1991).

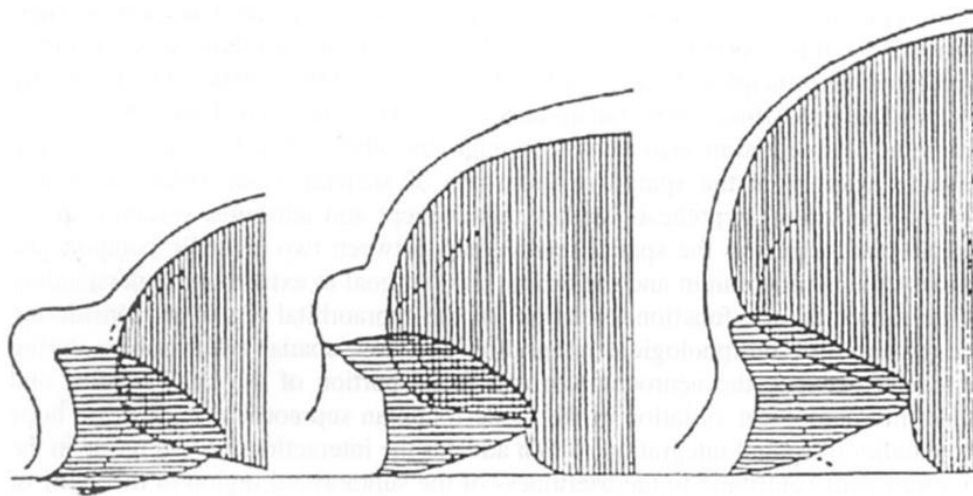


*Figure 74.* Schematic representation of a male chimpanzee (A), a female *Sinantropus* (B) and male modern human skull representing phylogenetic changes leading to the reduction of the neural-orbital disjunction in hominid crania according to the spatial model (Fiscella and Smith, 2006, adaptation from Weidenreich 1941).

The structural/spatial hypothesis posits that the supraorbital torus arises as a result of the spatial relationships of the different components of the hominin cranium (Enlow, 1968; Zollikofer et al., 2008; Zollikofer and Weissmann, 2008; Smith et al., 2010b, 2011).

Thus, previous workers have hypothesised that the development of the marked separation between the orbital and cerebral components of the frontal bone during ontogeny and/or phylogeny (Figure 74) is associated with the development of a supraorbital ridge to maintain the integrity (anatomical continuity) of the skull between these regions in primates and hominins (Weidenreich, 1941; Moss and Young, 1960; Enlow and McNamara, 1973; Shea and Russell, 1986; Shea, 1985a; Nowaczewska, Kuźmiński and Biecek, 2015). Moreover, consistent with this model, other authors have argued that variation in supraorbital ridge form is directly related to overall craniofacial size, being due to the differential growth rates of the upper facial skeleton and braincase (Vinyard and Smith, 1997, 2001). Studies on ontogenetic series of non-primates and *M. fascicularis* crania have supported this, finding that the variation in supraorbital torus size observed between these species is related to variation in craniofacial size (Ravosa, 1988, 1991b; Hylander, Johnson and Picq, 1991). In modern humans, supraorbital ridge variation has been associated with craniofacial size and cranial robustness (Lahr and Wright, 1996; Vinyard and Smith, 2001; but see Hawks et al., 2000). However, Baab et al., (2010) have demonstrated no correlation between cranial size and cranial robustness.

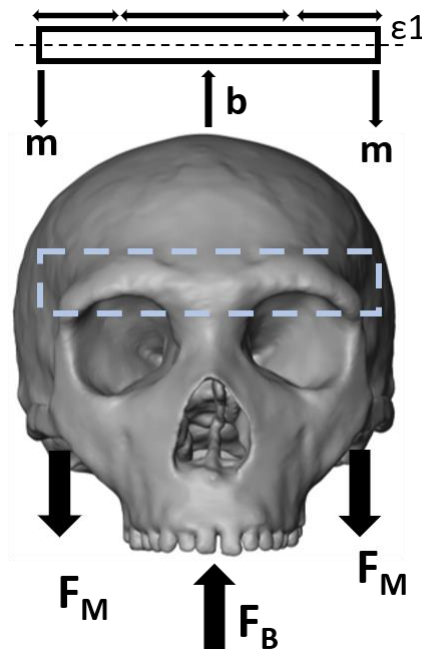


Figure 75. Bending of the supraorbital region in the frontal plane in the Neanderthal adult model. The forces causing bending in the frontal plane are the bite force ( $F_B$ ) pushing upward and the masseter and temporalis muscles ( $F_M$ ) pulling downward. Adaptation of Hylander et al, 1991.

The alternative, mechanical hypothesis, links variation of the supraorbital region to resistance to masticatory system loading (Hilloowala and Trent, 1988b; Russell et al., 1985; Endo, 1970). Indeed, early studies of the supraorbital region suggested that it develops as a buttress against the forces generated by mastication (Endo, 1966; Endo, 1970; Ravosa, 1988, 1991b). It is hypothesised that, particularly during anterior dental loading, the supraorbital torus acts like a beam, with its lateral aspects pulled downward by the action of the masseter and temporalis while the “glabellar” region is pushed upward by the peak bite force (Figure 75). Thus, a larger torus might be expected where bite forces are high.

Fossil hominins present significant variation in supraorbital region size and shape as is the case for the frontal sinus which may extend laterally into the supraorbital tori. These variations have been considered to be of taxonomic relevance, and it has been proposed that generally large supraorbital tori with massive sinuses are one of the distinctive cranial traits of *H. heidelbergensis* (Stringer, 2012; Prossinger et al., 2003). A study on Kabwe 1 using Finite Element (FE) analyses has shown that, under biting simulations, the supraorbital region experiences low strains (with frontal sinus filled or unfilled), compared to the rest of the cranium (Godinho and O’Higgins, 2018). These findings do not support the mechanical hypothesis, and the browridge in this individual is much larger than is needed to accommodate the spatial relationships between the orbits and the brain (Moss and Young, 1960). This led Godinho et al., (2018) to hypothesise that, in *H. heidelbergensis*, the massive supraorbital structures exist to accommodate social signalling, like the paranasal swellings of some papionin monkeys.

Neanderthals also present a prominent supraorbital region and large frontal sinus (but much smaller than in *H. heidelbergensis*). This has been related to particular features in this species such as the lack of the canine fossa (Coon, 1962; Wolpoff, 1999). However, other studies show that Neanderthals do not have large supraorbital and frontal sinuses relative to modern humans when cranial size differences are taken into account (Rae, Koppe and Stringer, 2011). Witzel (2011) virtually synthesised a Neanderthal cranium using FEA to adapt the form of a block of material with only the initial locations of the eyes, nasal cavity, dental arcade and brain defined. He iteratively loaded it to simulate a range of bites, sequentially removing voxels that experienced small or no compressive strains to adapt their form to biting loads. The model predicted sinus, and especially frontal sinus, formation in the Neanderthal cranium as well as a supraorbital torus. This

suggests that sinuses appear in regions that experience low strains. This is supported by the study of Godinho and O’Higgins (2018) who showed that infilling the frontal sinus of *H. heidelbergensis* in a Finite Element model had little or no effect on strains over the face and supraorbital region and that the infilled material experiences very low strains. It also suggests that there is a mechanical role for the torus, but does not exclude structural/spatial influences on supraorbital form. The presence of the low strains over the supraorbital region in adults (Chapter 5 section 5.1.3, Figures 67 and 72) could indicate either that at this stage, this region is adapted to biting loads or that it is not strained by biting at any stage in development.

However, previous studies have hypothesised that Neanderthal craniofacial form is adapted to generate and withstand high and/or repetitive occlusal loads, especially at the anterior dentition (the anterior dental loading hypothesis; Demes and Creel, 1988; Rak, 1986). Trinkaus (1987b) also argues that paramasticatory loading (that is, forces due to tasks outside the normal range required for feeding) at the Neanderthal anterior dentition resulted in elevated levels of mechanical stress in the facial skeleton. Rak (1986) also proposes that several features of the zygomatico-maxillary region were an adaptation to this elevated level of stress. He also agrees with Endo (1966b) who suggested that the mid-facial prognathism and steepness of the nasoalveolar clivus bearing the anterior teeth are advantageous in resisting vertical peak bite forces.

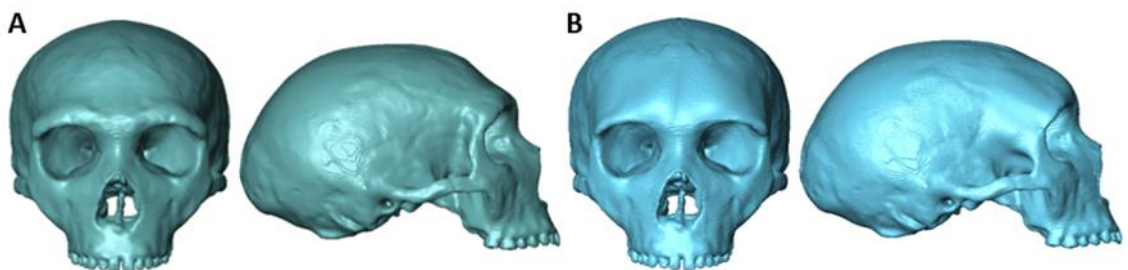
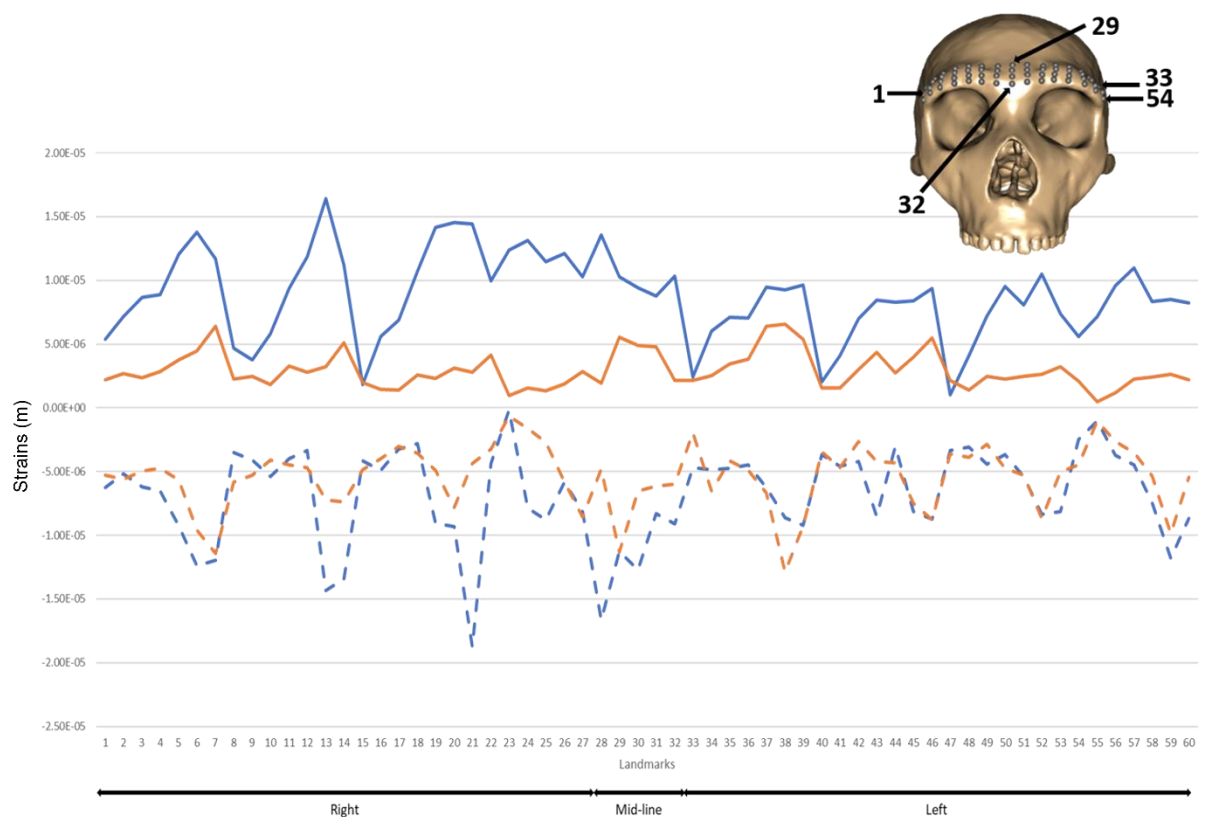


Figure 76. A) Original Neanderthal mean adult model, B) altered supraorbital Neanderthal model.

The present study shows that under unilateral biting simulations, the Neanderthals are more able to resist strains due to masticatory loading than modern humans especially during incisor biting (see section 5.1.1). These results were extended in a parallel study undertaken as an MSc project, co-supervised by me (Ben Mapplebeck, MSc Human Anatomy and Evolution, Hull York Medical School, University of York, 2022). The project aimed to alter the supraorbital region to create a more modern human-like supraorbital region. This involved the creation of a flatter, more vertical forehead with loss of the supraorbital sulcus. To achieve this, the supraorbital region of the original Neanderthal adult mean model surface (Figure 76) was altered using a variety of tools within Geomagic® (Studio 2018).



*Figure 77.* Tensile and compressive strains experienced by the Neanderthal with altered supraorbital (blue) and mean Neanderthal adult FE models at 60 sampling points over the supraorbital during the RI<sup>1</sup> biting simulation. The tensile (solid) and compressive (dashed) strains are unscaled. See landmark details in supplementary material Figure 3.

A similar biting simulation at the right first incisor (see section 4.2.1.2) was conducted in the two models. The tensile and compressive strains at the supraorbital (60 semi-landmark locations) were compared between this modified and the original model by plotting them together (Figure 77). Figure 77 shows that the Neanderthal model with the altered supraorbital presents generally greater tensile and compressive strains than the

original mean Neanderthal adult. Thus, creating a more vertical forehead in the Neanderthal model made it less able to sustain anterior masticatory loading, suggesting that the sloping frontal of Neanderthals is advantageous in anterior dental loading.

Moreover, the results in chapter 4 section 4.3, show that, over the supraorbital region, the Neanderthal mean infant and juvenile models present large tensile and compressive strains on both sides of the cranium for  $RP^2/RdM^2$  and  $RI^1$  biting simulations, while the adult presents smaller strains even after scaling them for centroid size or peak bite force. As noted above, this gradient from high to low strains from the infant to adult stage could reflect ontogenetic adaptation, that is, strains are low in the adult because the morphology is optimized for resisting these loading regimens. In the infant and juvenile models, the higher strains in the same region might stimulate adaptive bone remodeling. By using a Finite element synthesis approach, Witzel (2011) was able to predict the overall shape of a Neanderthal cranium and its sinuses based on loading. These results combined with the results of this thesis support the notion that the supraorbital region in Neanderthals may arise in part from mechanical bone adaptation during growth, and in part because of spatial requirements (Zollikofer et al., 2008; Godinho and O'Higgins, 2018; Witmer, 1997).

Bone remodeling plays an important role in skeletal adaptation to loads. It begins early in development and is a key mechanism, acting to modify the size and shape of the bones of the facial skeleton (Enlow and Hans, 1996; Bromage and Boyde, 2008; Lacruz et al., 2015b). This process occurs by a combination of bone deposition at the sutures and/or at the bone surface affected by highly specialised cells, the osteoblasts; and bone resorption by osteoclasts. The coordinated actions of these cells play a key role in modifying skeletal form during growth. The majority of bone remodeling is completed by skeletal maturity but Haversian bone remodeling (distinct from bone surface growth remodeling) still occurs in adults, modifying bone at the microstructural level to maintain skeletal integrity and repair microdamage (Frost, 1990a, 1990b; Mori and Burr, 1993; Bentolila et al., 1998; Pearson and Lieberman, 2004). Mechanical forces are believed to play a key role in driving the locations, rates and modes of bone remodeling activity during growth and in adults (Bouvier and Hylander, 1996; Pearson and Lieberman, 2004; Ruff, Holt and Trinkaus, 2006) throughout the skeleton.

Facial growth remodeling in non-human primates, *Homo sapiens* and fossil hominins has been actively mapped over the last 50 years through microscopic bone surface analyses (Enlow and Bang, 1965; Enlow, 1966, 1996; Bromage, 1989; Bromage and Boyde, 2008; Lacruz et al., 2013; McCollum, 2008; Rosas and Martinez-Maza, 2010; Martinez-Maza, Rosas and Nieto-Díaz, 2013; Schuh et al., 2019, 2020). In the growing and adult modern human face, bone deposition is present over the upper parts whereas the middle and lower face are commonly dominated by bone resorption beginning sometime after birth and maintained until adulthood (Lacruz et al., 2015b; Schuh et al., 2019; Martinez-Maza, Rosas and Nieto-Díaz, 2013). However, there is notable temporal and spatial variability depending on sampling and approach to mapping of these fields (see Figures 80-82).

A similar distribution of growth remodeling fields is also likely to have characterised *H. antecessor* (Lacruz et al., 2013) and subnasal resorption with an otherwise entirely depository facial surface has been identified in *Paranthropus* (Bromage, 1989). In contrast, bone deposition over the entire anterior facial surface has been associated with specimens with more prognathic faces such as great apes, *Australopithecus africanus* (Bromage, 1989; McCollum, 2008), early African *Homo*, *H. habilis* and *H. erectus* (Bromage and Boyde, 2008; Lacruz et al., 2013) as well as Neanderthals (Lacruz et al., 2015b; Figure 82).

The growth of the craniofacial skeleton is the product of the growth (change in size), development (change in shape) and relative displacements of its constituent elements. Its bony elements become displaced relative to each other (in part because of the growth of soft tissues, e.g. brain, muscles), increase in size and change in shape and undergo coordinated bone growth remodeling (see (Moss and Young, 1960; Björk and Skieller, 1972; Björk, 1969; Enlow and Hans, 1996). Studies of *H. sapiens* midfacial bone growth remodeling and bone displacement have shown that as the face grows, the midfacial region is displaced forward, a resorptive area develops and extends over the anterior aspect of the mid-face from an early age and its action is believed to maintain a vertical, rather than anteriorward growth vector for midface (Enlow, 1963; Enlow and Hans, 2008; Björk and Skieller, 1976; Martinez-Maza, Rosas and Nieto-Díaz, 2013; Lacruz et al., 2015b; Schuh et al., 2019). In Neanderthals, the growth remodeling activity state is mostly depository over the midface and nasal aperture which is more forwardly placed and presents an anteroinferior growth vector (Lacruz et al., 2015b).

It is not known if these differences in remodeling reflect phylogenetic relationships, and so are regulated by genetic systems or whether they reflect genetically mediated differences in facial form and function in earlier stages of development that then impact how loads are borne and resisted and modulate subsequent remodeling via the distribution and magnitudes of resultant strains.

Bone architecture is determined by the action of osteoblasts and osteoclasts, building on the (pre-existing form of) cartilaginous and membranous precursors (Robling, Castillo and Turner, 2006; Turner and Pavalko, 1998). The differentiation of cell activities is said to be influenced by several epigenetic factors and by many genetically encoded signalling molecules, such as growth factors and hormones (Atchley and Hall, 1991; Bidwell and Pavalko, 2010; Duncan and Turner, 1995; Giustina, Mazziotti and Canalis, 2008; Grimston et al., 2008; Judex, Donahue and Rubin, 2002; Ramirez-Yañez et al., 2005; Robling, Bellido and Turner, 2006), suggesting that direct genetic regulation of the locations and activity states of remodeling fields is a possibility.

However, little is known about the regulation of bone remodeling field activity at specific locations in the facial skeleton during post-natal ontogeny, especially in hominins. A recent study of jaw (beak) length in duck and quail found that spatially patterned differences in bone resorption field locations, mediated by neural crest mesenchymal cells and their derivatives (which exert precise control over the expression levels of key transcription factors as well as the timing of skeletal cell differentiation) are important in mediating differences in jaw length (Ealba et al., 2015). This might indicate that genetic mechanisms exist that can specify the timings of onset, locations and activity states of craniofacial remodeling fields, in the fetus at least. These remodeling fields are spatially patterned and generally symmetrical (see Figure 82), however, they occur over developing beaks of different sizes and shapes, which may lead to differences in straining and so, responses to loading during embryonic movements.

The formation of repetitive patterning (such as stripes and spots) has been associated with chemical systems by Turing (1952). In his morphogenesis theory, Turing considered a system where a chemical is diffused and interacts with two or more other chemical species to induce a spatial pattern (Turing, 1952; Maini et al., 2012). In this model, the final patterning is dependent on the size and shape of the tissue in which it occurs, the velocity and quantity of diffusion of each chemical as well as other patterning elements

that might be present. A Turing-like model has been shown to be involved in the formation of other spatially patterned repetitive structures in mammals such as digits (Sheth et al., 2012; Batista et al., 2008; Zeller, López-Ríos and Zuniga, 2009).

Such a model, and alternative as yet unknown molecular mechanisms, could potentially pattern the activity and spatial locations of craniofacial remodeling fields. Alternatively, the differences in the locations and activity states of remodeling fields might be indirectly regulated by the interaction of genetic systems that regulate the sizes and shapes of the precursors of craniofacial skeletal elements with forces arising from muscular action, which occurs even in the fetal stages of development.

Thus, it is currently understood that mechanical stimuli, by inducing bone stresses and strains above a certain threshold result in bone deposition while the same mechanical stimuli below another threshold result in bone resorption (e.g., Carter et al., 1996; Frost, 1990a, 1987; Huiskes et al., n.d.; Lobo et al., 2001). Little is known about these thresholds, however, it is likely that they vary according to age, individual, and location within the skeleton, and that dynamic rather than static loads are important in regulating bone adaptation (Beaupré, Orr and Carter, 1990; Gross et al., 1997; Cowin, 2001; Hsieh et al., 2001; Pearson and Lieberman, 2004; Lanyon and Rubin, 1984). Moreover, infants and juveniles are more susceptible than adult skeletons to changes in the mechanical environment (Bouvier and Hylander, 1996; Carter et al., 1996; Pearson and Lieberman, 2004; Ruff et al., 2006). Thus, high densities of secondary osteons, an indication of bone remodeling, have been found in *M. fascicularis* subadult faces and mandibles in high-strain regions while adults present similar densities in both high- and low-strain regions (Bouvier and Hylander, 1996 but see Kupczik et al., 2009)

One study (Walters and O'Higgins, 1992) has examined changes in facial remodeling in adult *Procolobus verus*, finding that when teeth on the side habitually used for leaf stripping become heavily worn down, the teeth on the opposite side are used, and with this shift, resorptive remodeling fields also switch sides. This supports the notion that the facial skeleton, like the rest of the skeleton, is responsive to loading and accommodates changes in loading through changes in form effected, at least in part, by surface remodeling fields.

Thus, it may be that the cumulative straining of facial skeletal elements, through the action of the masticatory system in varying loading scenarios directly modulates bone

remodeling field activity and location during growth. In this scenario, stresses and strains might interact in analogous ways to Turing's diffusible chemical systems and likewise, the resulting spatial distribution and activity states of facial growth remodeling fields would be dependent on the size and shape of the facial skeleton in which it occurs, and the loads applied.

While molecular control of facial remodeling cannot be assessed using the techniques applied in this thesis, it is possible to consider if deformation and consequent straining of the facial skeleton arising from masticatory system loading could potentially pattern the activity states and locations of remodeling fields. While it is not possible to accurately model how masticatory system loading deforms the facial skeleton (see 6.2 Limitations, below), it is possible to consider if there is any indication of differences in spatial patterning of load resistance (deformations, stresses and strains) from the finite element simulations of biting in modern human and Neanderthals that resemble the differences in spatial patterning of remodeling fields. This would imply that mechanical forces are potentially capable of generating observed remodeling field distributions.

The results of Chapters 3-5 highlight differences from both biting simulations in deformation, strain modes, magnitudes and distributions between the two species at all age stages. Indeed, these differences are clear when looking at differences in principal tensile ( $\epsilon_1$ ) and compressive ( $\epsilon_3$ ) strains during unilateral biting simulations (Chapters 3-5). Figure 73 shows the combined  $RI^1$  and  $RP^2/RdM^2$  strain maps, and these present many subtle differences between modern humans and Neanderthals. The differences are mainly localised along the inferior maxilla, the anterior maxilla, the zygomatic bone and around and between the orbits.

Despite higher principal strains recorded in modern human and Neanderthal models for the  $RI^1$  bite, differences in tensile and compressive strains are more evident between each age stage and the two species in the  $RP^2/RdM^2$  biting simulations. Moreover,

food processing and particularly the chewing cycle, involves mostly the posterior dentition, since the role of incisors is to cut food in order to push it to the back of the mouth. Therefore, in the rest of this discussion, the focus is on differences in principal strains and deformations from the RP<sup>2</sup>/RdM<sup>2</sup> biting simulations.

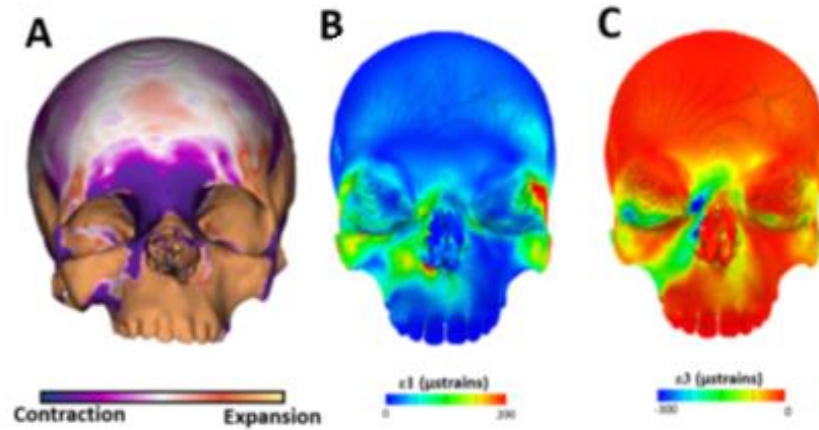


Figure 78. RP<sup>2</sup> biting simulation in the modern human juvenile model. A) Surface colourmap (from Figure 27, Chapter 3) illustrating the surface deformation between the mean unloaded model and the loaded modern human juvenile. B) Tensile ( $\epsilon_1$ ) strain contour plot. C) Compressive ( $\epsilon_3$ ) strain contour plot (both strain maps from Figure 32, Chapter 3).

Figure 78 presents three representations of the results of the simulated RP<sup>2</sup> bite in the modern human juvenile model (from Chapter 3, Figures 32). The surface deformations (Figure 78A) closely reflect the strain contour maps. Regions of high compressive strain (Figure 78B and 78C) are coincident with regions of the surface that are contracted in area, as is expected. Regions of high tensile strain are mostly coincident with those of high compressive strain, but also extend over the anterior maxilla, where surface expansion is evident. The match is reasonable, but not perfect because the colourmaps of area change with loading, describe a different aspect of deformation and use a colour scale that is not the same as either of the strain contour maps.

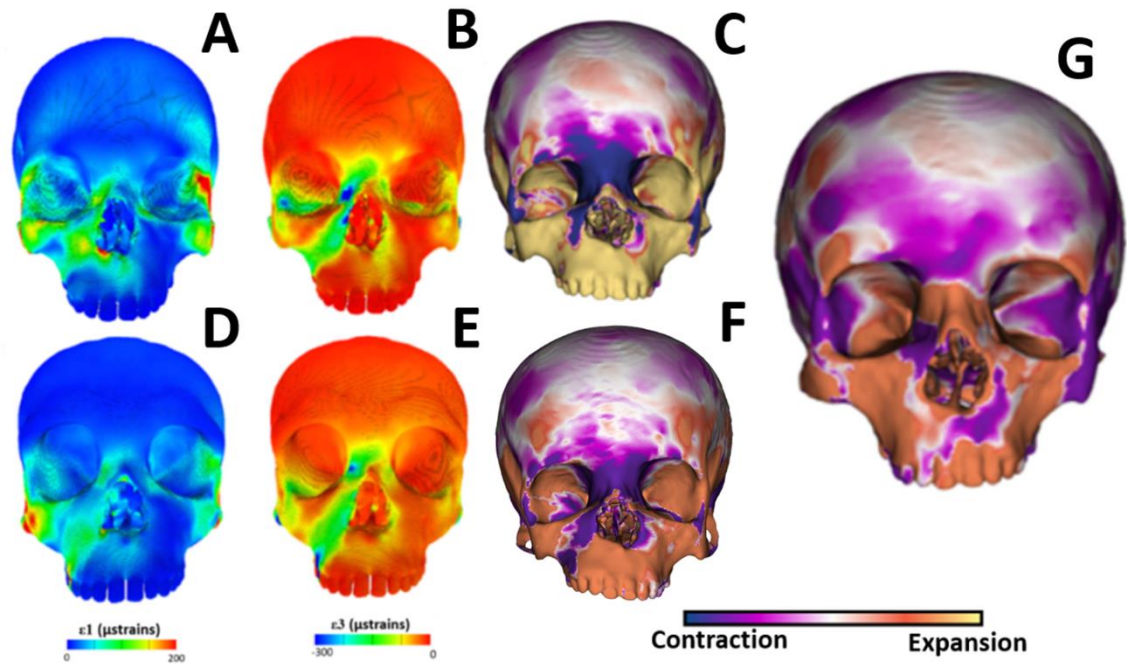


Figure 79. RP<sup>2</sup> biting A), D) Tensile ( $\epsilon_1$ ) strains in the modern human and Neanderthal juveniles, respectively. B), E) Compressive ( $\epsilon_3$ ) strains in the modern human and Neanderthal juveniles, respectively. From Figure 54: C), F) Colourmaps of surface area change (deformation) in the modern human and Neanderthal, respectively and G) colour map of difference in deformation between the Neanderthal (reference) and modern human (target).

The colourmaps of surface area change with biting readily allow differences in deformation to be assessed. Thus, in Figure 79, the colourmaps from the comparison of modern human and Neanderthal RP<sup>2</sup> simulated biting are compared with the strain maps arising from this bite in both species. Contrasting strains in modern humans (Figure 79A, B) with those in Neanderthals (Figure 79D, E) it has already been noted that these are generally greater in modern humans than Neanderthals (Chapter 5) and these differences are reflected in the greater deformation (e.g. more yellow maxilla and deeper purple interorbital region) of the modern human cranial surface than that of the Neanderthal (Figure 79C vs. 79F). The difference colour map (G) shows that the modern human juvenile manifests greater expansion of much of the maxillary surface area (orange) with less expansion (relative contraction, in purple) of a region lateral and inferior to the nasal aperture on the left (balancing side), a strip of relative contraction (purple) on the lateral side of the nasal cavity extending to the orbit on the right (working) side, with a strip of relative expansion (orange) above it and greater contraction of the interorbital area (also purple).

To relate maps of differences between modern humans and Neanderthals in the deformation of the cranial surface to differences in facial bone surface remodeling, the colourmaps of the infant and juvenile surfaces during  $RP^2/RdM^2$  biting were mirrored because biting occurs on both sides. As biting shifts between sides, so will deformation become mirrored. The net deformation experienced by each side of the cranium is likely to be a combination of the deformations mapped for working and balancing sides. Thus, the colourmaps were reflected (for both working and balancing sides, Figures 78-80) to compare them with published bone remodeling maps for modern humans and Neanderthals (Lacruz et al., 2015b; Martinez-Maza, Rosas and Nieto-Díaz, 2013; Schuh et al., 2019).

The colourmaps of Figures 78-82 represent the differences in local surface area expansion or contraction between Neanderthals (reference) and modern humans (target), and they are reflected and superimposed for both sides of the craniofacial skeleton. They indicate where, over an approximately similar number of right and left-sided bites, the surface in modern humans would be differently deformed compared to Neanderthals.

We know nothing of thresholds of mechanical signals (e.g. local net compression or tension, related to surface area changes) required to initiate a remodeling response, but if these are similar in both species, then it is possible that the differences observed in these colourmaps cross those thresholds and so, result in differences in remodeling activity. Thus, in Figure 79, both modern human and Neanderthal juvenile models experience surface area expansion, with contraction above the bite point, in  $RP^2$  biting, but modern humans show more expansion over much of the maxilla (orange) and a small area of relatively less expansion (purple) lateral and inferior to the nasal aperture. If the threshold to initiate resorption lies between the degree of deformation experienced by these two regions, one might predict resorption over much of the maxilla, with deposition lateral to the nasal aperture. This is similar to the approach used by Oxnard (1993, 2004) to predict

the presence or absence of bone based on compression vs. tension, and Witzel (2011) and Witzel and Preuschoft (2005) to predict cranial form based on compressive strains.

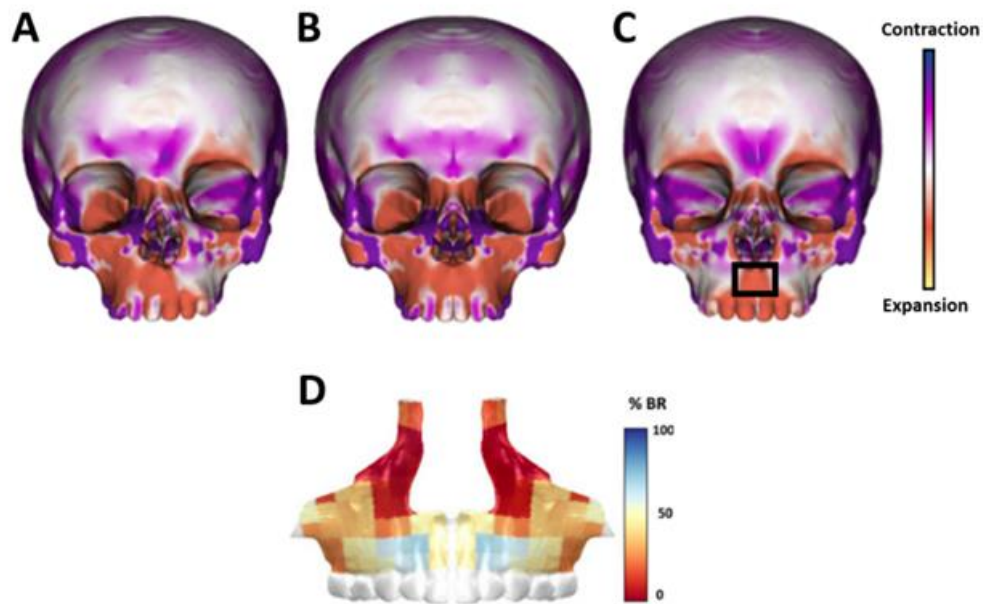


*Figure 80.* Registration-free colourmaps of local surface area expansion or contraction showing differences in mode and magnitude of deformation between the Neanderthal and modern human infant models during the RdM<sup>2</sup> biting simulations. A) original, B) reflected working to balancing sides, C) reflected working to balancing to working sides with black rectangle indicating that the expansion of area at that location is consistent irrespective of biting side, D) Mean bone growth remodeling maps representing the average distribution of remodeling activity for modern humans aged 3 to 6 years old (red= non or low resorption, blue = usually resorptive; Schuh et al, 2019).

Thus, reflected maps of differences in surface deformation between modern human and Neanderthal infants and juveniles are compared here with published facial remodeling maps of these species. Figure 80A presents the between species difference colour map of area changes in the RdM<sup>2</sup> biting simulations. In Figures 80B and 80C working and balancing side maps are reflected. From these, it is evident that an area resembling an inverted triangle below the nose, and extending to the incisors undergoes expansion in RdM<sup>2</sup> biting, irrespective of which side is the working side (see the rectangle in Figure 80C). Further, the anterior maxilla on the working side experiences a degree of surface expansion and nasal margin, compression. These differences show some concordance between regions that experience more expansion in the modern human than the Neanderthal models and regions that are usually resorptive (blue/yellow: Figure 80D) in modern hu-

man infants (and depository in Neanderthals). Likewise, resorption is infrequently observed (i.e., deposition is the common condition, Figure 80D) lateral to the nasal aperture and the difference colourmaps indicate this region experiences relatively less area expansion in modern humans.

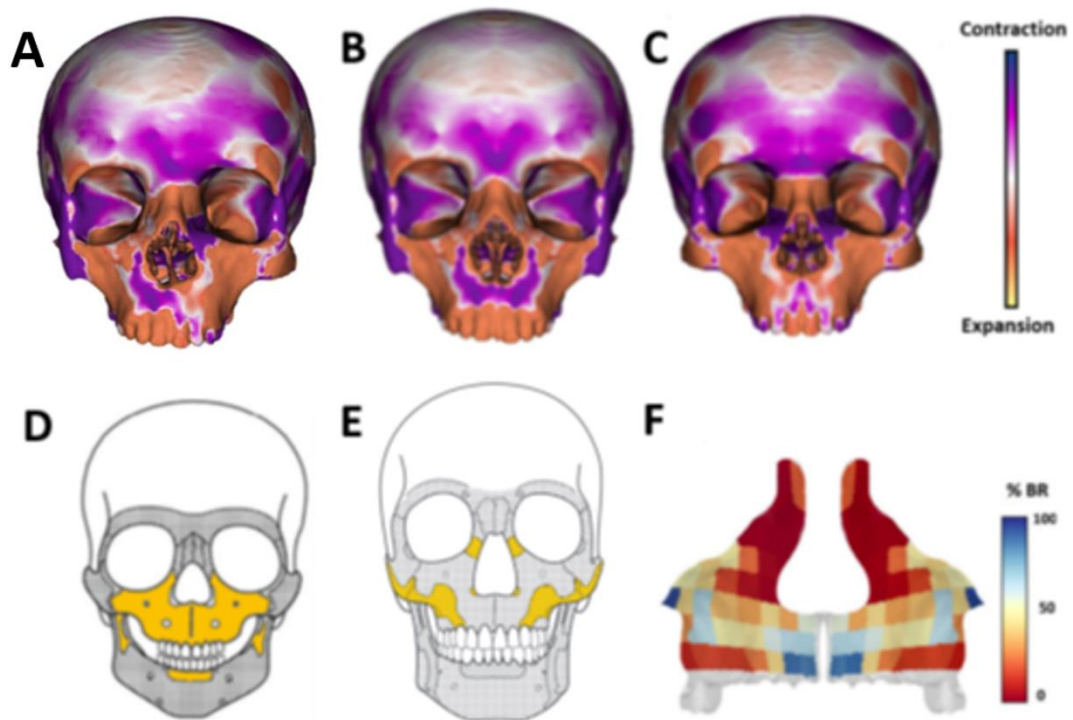


*Figure 81.* Colourmaps of local surface area expansion or contraction showing differences in mode and magnitude of deformation between the Neanderthal and modern human juvenile models during the RP<sup>2</sup> biting simulations. A) original, B) reflected working to balancing side, C) reflected balancing to working side D) Generalized bone growth remodeling patterns for modern humans aged 7 to 17 years and E) for adults (Martinez-Maza et al, 2013), F) Bone growth surface remodeling map representing the average pattern for modern humans aged 7 to 12 years old (Schuh et al, 2019).

Likewise, Figure 81 compares, between modern human and Neanderthal juveniles, surface area changes arising from RP<sup>2</sup> biting. The locations of regions of difference in surface area expansion and contraction once reflected (Figure 81B and Figure 81C), show a spatial distribution somewhat comparable to published bone growth remodeling maps (Figure 81D and 81E, Schuh et al., 2019; Figure 81F, Martinez-Maza, Rosas and Nieto-Díaz, 2013) at different stages of post-natal development. Thus, the modern human juvenile shows a greater expansion than the Neanderthal of surface area over the balancing side maxilla during RdM<sup>2</sup> and RP<sup>2</sup> biting simulations (Figure 81A and 81C), with less expansion lateral and inferior to the nasal aperture on the working side (Figure 81B). Based on the approach of workers such as Oxnard (1993, 2004), Witzel (2011) and Witzel

and Preuschoft (2005) this might be expected to predict resorption over much of the anterior maxilla and deposition lateral and inferior to the nasal aperture. This is not a good match to the juvenile remodeling maps published by Martinez-Maza et al., (2013, Figure

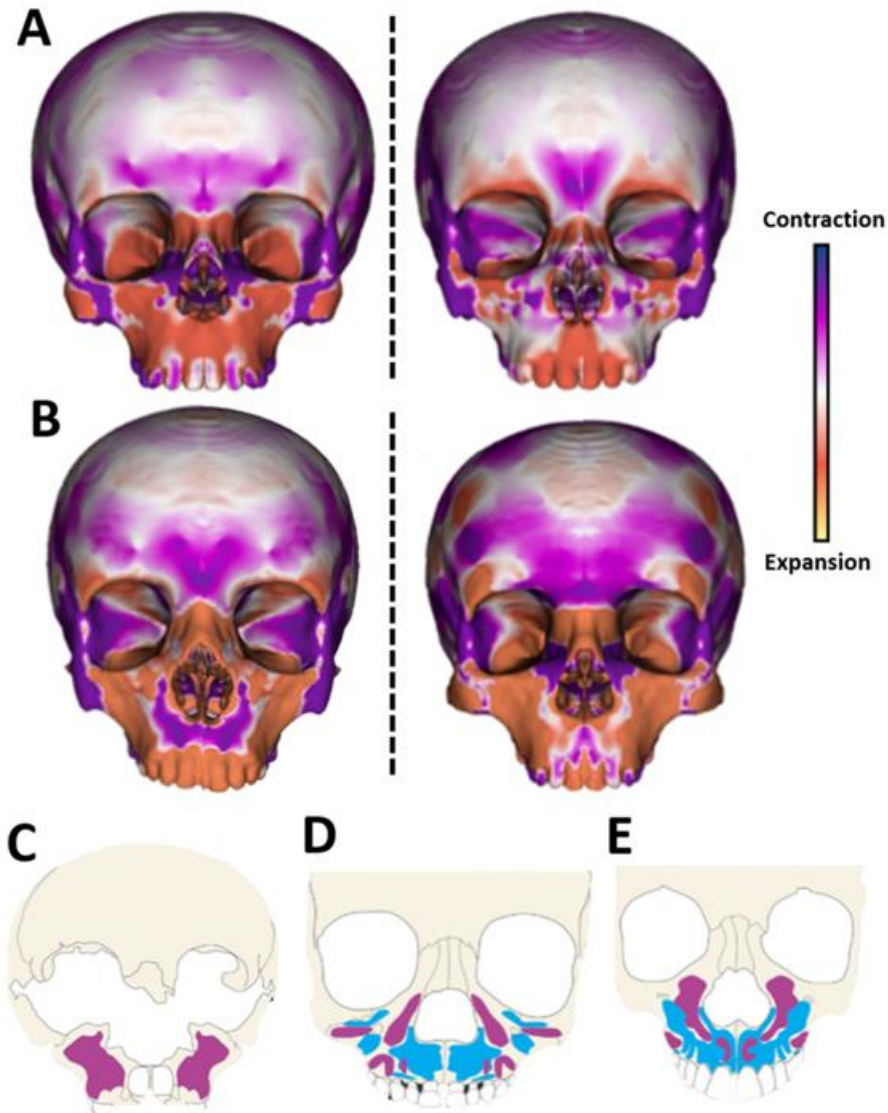


*Figure 82.* Colourmaps of local surface area expansion or contraction showing differences in mode and magnitude of deformation between the Neanderthal and modern human infant (A: top row) and juvenile (B: bottom row) models during the  $RP^2/RdM^2$  biting simulations. Rows A, B Left column, reflected working to balancing sides and rows A, B right column, reflected balancing to working side. Remodeling maps showing bone deposition (in purple) and resorption (in blue) for a 5-year-old Neanderthal (C), 5 year old modern human (D) and a (E) 12 year old modern human (Lacruz et al., 2015b).

81D) or Schuh et al., (2019; Figure 81F). However, it is a reasonable match to the adult remodeling map published by Martinez-Maza et al, (2013; Figure 81E). Additionally, in this adult remodeling map (Figure 81E) a strip of resorption, with deposition above and below, is noted at the upper part of the nasal aperture. This approximates the strips of area

contraction and expansion at the upper part of the nasal aperture and over the nasal bones in the area difference colour map (Figures 81B, 81C).

It should be noted that there is variability among studies and samples in published remodeling maps and that remodeling maps change with age. As such, a perfect match between the results of the present study and published remodeling maps cannot be expected. This is illustrated by the maps of differences in surface area changes and remodeling maps in Figure 82. The maps of differences in surface area come from Figures 80 and 81 and are redrawn in Figure 82 to facilitate comparison with the remodeling maps which come from Lacruz et al., (2015b). These remodeling maps differ in slight details from those shown in Figures 80 and 81, demonstrating variation (in samples, methods, or interpretation). Further, the remodeling map for the juvenile in this study (Figure 80E) more closely matches the colour map of differences in area expansion/contraction among modern human and Neanderthal juveniles (Figure 82B).

While interesting, these similarities do not establish a mechanistic link between resistance to masticatory system loading, facial deformation and remodeling maps, but they demonstrate some association, even in these simplified scenarios. Further, given the lack of knowledge of actual strain magnitudes (because of modelling limitations, see below) and of thresholds for stimulating depository or resorptive growth remodeling activity it is not known if mechanical stimuli such as those raised from masticatory system loading are sufficient to activate osteoclastic and/or osteoblastic activity. It is also not known if the differences in these stimuli between the two species are sufficient to account for the differences in bone remodeling field activity and location. However, the present studies have shown that differences between modern humans and Neanderthals in modes of deformation and so of straining of the facial skeleton during masticatory system loading are consistent, even in these simplified models, with the known differences in facial growth remodeling field activity and location. As such, the results of the present study do not exclude biomechanical modulation of facial growth remodeling.

In summary, the results show that modern humans at each age stage are more efficient in converting muscle forces into peak bite forces. However, during biting, the modern human infant, juvenile and adult crania deform and are strained more than Neanderthals, even after accounting for biting force, indicating that they are less able to resist

high peak bite forces. This was also found when comparing modern human biting performances with that of *H. heidelbergensis* (Godinho et al., 2018). Rather than an adaptation, it has been suggested that modern human peak bite force production efficiency could be a by-product of the retracted and orthognathic face in modern humans which arose for reasons other than biting efficiency (Antón, 1990; O'Connor, Franciscus and Holton, 2005; Lieberman, 2008, 2011; Eng et al., 2013; Neaux et al., 2013, 2015).

Because crania show a degree of integration (Bastir and Rosas, 2005; Lieberman, 2008, 2011; Neaux et al., 2015; Bastir and Rosas, 2016), evolutionary and adaptative changes in one component can impact another. Thus, differences in facial morphology between these two species have been variously attributed to: differences in the development of other craniofacial elements, such as the brain (Lieberman, McBratney and Krovitz, 2002; Lieberman, 2008, 2011; Enlow and Hans, 1996), adaptations of parts of the cranium to thermoregulation and air conditioning (Coon, 1962; Wolpoff, 1968b; Carey and Steegmann, 1981; Franciscus and Trinkaus, 1988; Churchill, 2006), diet and food processing (Carlson, 1976; Carlson and Van Gerven, 1977; Schwartz and Tattersall, 2000; Bocherens, 2009; Hardy, 2010b; Hoffecker, 2009) or differences in the size of the dentition (Brace, 1967; Brace and Mahler, 1971; Brace, Rosenberg and Hunt, 1987). However, this study indicates that modern humans and Neanderthals likely experience different loading and straining histories, especially at the infant and juvenile stages. Differences in deformation show a degree of correspondence with differences in facial remodeling maps found in previous studies (Lacruz et al., 2015b; Schuh et al., 2019, 2020; Martinez-Maza, Rosas and Nieto-Díaz, 2013).

Therefore, in this study, the results do not allow for the rejection of mechanical loading due to mastication as a possible explanation for the differences in bone remodeling patterns and so in at least some aspects of the eventual adult form. It will be of interest to further investigate this by experimenting with more complex biting and other dental loading scenarios. Moreover, it will also be of interest to conduct similar experiments on a wider range of infant and juvenile age stages to detail the ontogeny of differences in modes and magnitudes of deformation during post-natal growth and development.

This study has relied on simple unilateral biting scenarios, yet has provided several novel insights into differences in craniofacial form and function between modern

humans and Neanderthals. In the next section, the limitations of this study are explored to assess its validity and guide future work.

## 6.2 Limitations of the present study and implications

In this study, geometric morphometric and multivariate regression analyses were conducted to create a modern human and Neanderthal craniofacial growth model and extract 3D virtual crania representing the mean adult, juvenile, and infant in both species. Potential issues with this work arise because it is based on morphometric and finite element analyses (FEA) both of which are sensitive to input data. The first limitations arise from the sizes of the samples of both species, with a limited number of infant and juvenile specimens. Small sample sizes likely impact estimation of mean models, especially for the infants and juveniles, from the regression analyses. Indeed, the small samples in both species limit the extent to which the range of ontogenetic and geographic variation can be taken into account. Therefore, the results found in this thesis should be interpreted cautiously, recognising the limitations of sample sizes. It would be of interest in future work to follow the same methodology described in this thesis but with a larger sample for each age stage when this becomes possible (e.g., when more CT data of living and especially fossils specimens become available) to check if similar results are found when ontogenetic and geographic variations are better represented.

For the Neanderthal fossils, damaged and incomplete craniofacial specimens were reconstructed using virtual anthropology toolkits. Virtual reconstruction of damaged skeletal material from CT scans has opened new possibilities in virtual palaeoanthropology and brought new morphological information to light (Amano et al., 2015; Benazzi et al., 2011, 2014; Grine et al., 2010; Gunz et al., 2009; Kranioti et al., 2011; Neubauer et al., 2004; Watson et al., 2011; Zollikofer et al., 2005; Ponce De León and Zollikofer, 1999). However, because reconstructions are to some degree subjective, a few studies have assessed the impact of different methods and approaches (TPS, missing landmarks, semi-landmarks, reflected relabelling, etc) on reconstruction (Arbour and Brown, 2014; Gunz et al., 2009; Neeser, Ackermann and Gain, 2009), but further work is needed to evaluate the impact of reconstruction error and alternative approaches to reconstruction, especially in subadults and so, on post-natal growth models.

While every Neanderthal specimen was reconstructed to some degree (see Appendix 1), depending on their state of preservation, every fossil lacked the nasal septum,

which in the Neanderthal models was reconstructed using a modern human one. Only the part of the vomer that constitutes the posteroinferior part of the nasal septum was reconstructed. The septum, nasal walls and vomer are important in FE modelling of biting. It has been shown that the absence of a septum and the thickness of the nasal walls have an impact on the distribution of the strains extending from the lower to the upper part of the face (Toro-Ibacache et al., 2016). Moreover, the vomer articulates with the viscerocranium through the two maxillae and palatine bones, and with the neurocranium through the sphenoid and ethmoid bones (Netter, 2019). Therefore, the vomer could be important in resisting strains generated during mastication. Indeed, studies investigating the relationship between facial and brain injuries have shown that during various types of facial injuries, the cartilaginous part of the nasal septum deforms and eventually fractures, dissipating the impact energy while the anterior aspect of the vomer diverts stress to the “crumple zone” of air-filled sphenoidal and ethmoidal sinuses, protecting the brain (Tse et al., 2015). Therefore, the vomer plays an important role in the distribution of strains between the face and neurocranium during biting. It would be of interest in future work to assess the impact of different septum reconstruction approaches as well as the absence or presence of the vomer on strain distributions and magnitudes. Finally, the lack of availability of longitudinal ontogenetic data, of living (*H. sapiens*) and inevitably fossil (*H. neanderthalensis*) material, as well as lack of information about those data (exact age and gender), also limit this study. Inevitably this study has used cross-sectional data and heavily reconstructed fossil material, limiting the resolution and reliability of estimates of ontogenetic changes in size and shape to an unknown degree.

Finite Element Analyses (FEA) have been applied extensively, over the last twenty years, to study the craniofacial biomechanics of masticatory system loading in extant and living hominids (Strait et al., 2007, 2009, 2010; O’Higgins et al., 2011; Witzel, 2011; O’Higgins et al., 2012; Smith et al., 2015a; Ledogar et al., 2016; Godinho et al., 2018; Wroe et al., 2018). This engineering approach has enabled a more comprehensive understanding of cranial skeletal performance (Kupczik et al., 2007; Curtis et al., 2011; Fitton et al., 2012; Godinho et al., 2018) during biting however the issue of the validity of the models arises with simulation (Godinho et al., 2017; Toro-Ibacache et al., 2016). Previous validation studies have reported that FE models often fail to accurately reproduce absolute strain magnitudes while relative strain magnitudes among different regions

of the model are consistent with relative strains from experimental loadings of real specimens (Bright and Rayfield, 2011; Kupczik et al., 2007; Strait et al., 2005; Toro-Ibacache et al., 2016). Other validation studies of a human cranium FE model, using simplifications applied in this study, have identified limitations that need to be taken into consideration for this study (Toro-Ibacache et al., 2016; Godinho et al., 2017). Additionally, this study is based on Neanderthal fossil remains and so there are additional issues because of model reconstruction and simplification and the lack of knowledge of important input parameters, such as muscle forces.

The first simplification of these models, necessary because of poor preservation, was to allocate the material properties of cortical bone to teeth and bone (both cortical and trabecular; Young's modulus of 17 GPa and Poisson's ratio of 0.3). This ignores the known differences between cortical and trabecular bone and between these and teeth, as well as the variations in bone material properties that are known to exist throughout the cranium (Peterson and Dechow, 2003). Two validation studies of human cranial models have shown that this simplification in material properties mostly impacts the magnitude of strains but not the general distribution (Godinho et al., 2017; Strait et al., 2005; Toro-Ibacache et al., 2016). Godinho et al., (2017) also found that the absence of periodontal ligaments (PDL) in models impacts their functioning, resulting in discrepancies in magnitude close to the alveolar process, this is less marked with increasing distance from the teeth.

However, improvement in FE model complexity is highly dependent on the technology used to scan and then segment and reconstruct specimens in 3D. In this study, mostly medical CTs were used, with a few micro CTs. The difficulty in imaging soft tissues and limitations of resolution make it difficult or impossible to extract fine and complex structures such as the PDL (Gröning, Fagan and O'Higgins, 2011). This limits the accuracy of predictions of absolute strains from FEA (Godinho et al., 2017). Simplifications of anatomy and material properties inevitably affect the accuracy of strain magnitude prediction. However, as far as possible all models were reconstructed, simplified and loaded in the same ways to limit additional sources of error. Further, prior validation and sensitivity studies, as well as those presented in Appendix 2 and 3, suggest that relative strain magnitudes and the spatial distribution of strains are predictable with sufficient accuracy to identify the main differences in relative straining of regions and between

modern humans and Neanderthals at each age stage (Godinho et al., 2017; Godinho and O'Higgins, 2018; Strait et al., 2005).

Finite Element Analyses of the craniofacial complex predict structural deformations during biting simulations with specified loads and constraints. In this study, the models were constrained at a unique bite point unilaterally and loaded with a representation of the major adductor muscles (masseter, temporalis, and medial pterygoid). However, previous studies have indicated that other anatomical structures, such as the temporal fascia, the craniofacial sutures, and the cranial foramina impact FEA results (Curtis et al., 2010; Witzel, 2011; Bright, 2012; Gröning et al., 2012; Barbeito-Andrés et al., 2020).

The deep temporal fascia originates from the periosteum of the superior temporal line and attaches to the superior border and lateral surface of the zygomatic arch (Eisenberg and Brodie, 1965; Wormald and Alun-Jones, 1991; Oxnard and Franklin, 2008). Recently its potential role in resisting the action of the masseter on the zygomatic arch has been investigated (Curtis et al., 2010). This study showed that, in a macaque cranium, tensing of the temporal fasciae by contraction of the temporalis muscle contributes to the stabilization of the zygomatic arch during biting (Eisenberg and Brodie, 1965; Witzel et al., 2011; Witzel et al., 2004). Thus, finite element analyses on models that include this structure have shown a reduction in peak strains, especially at the zygomatic arch (Curtis et al., 2010). According to these models, the zygomatic arch is stabilized during biting by a synchronized tensioning of the fasciae acting to oppose masseteric contraction forces (Curtis et al., 2010). Because, this is as yet an unconfirmed action in hominins, and because of a lack of detailed knowledge of muscle volumes, forces and fascial attachments in Neanderthals, the temporal fasciae were not included in these models. In this study, these models present a high strain gradient over the zygomatic bone and arches but this should be interpreted in light of the lack of applied temporal fascial forces. Further investigations are needed to assess the potential role of the temporal fasciae in hominins.

The models in this project do not include any craniofacial sutures in any age stage. This decision is mainly due to the low resolution of modern human cranial CT scans used to create the mean infant, juvenile, and adult models and the inevitable limits on the resolution of FE models. The segmentation of fine and complex structures such as sutures

was impossible with this material. Moreover, the Neanderthal models used a reconstruction of Gibraltar1 to obtain a surface mesh, but in this specimen, as with others, the craniofacial sutures were not modelled. Craniofacial sutures change in terms of size, shape, and material properties throughout post-natal ontogeny. Many mammalian, and some human sutures remain patent into at least early adulthood and this has led to the hypothesis that sutures may have a role in relation to cranial mechanical functioning (Herring and Mucci, 1991; Jaslow, 1990; Jaslow and Biewener, 1995). Moreover, *ex vivo* and *in vivo* experiments on several mammalian taxa have shown that strain magnitudes are higher in sutures than in the adjacent bones (Herring and Mucci, 1991; Rafferty and Herring, 1999; Popowics and Herring, 2007; Thomason et al., 2001; Wang et al., 2008). Sutures seem to act to modify the strain environment of the skull, possibly dissipating high stresses generated during feeding or impact and so protecting the adjacent bones (Thomason et al., 2001; Wang et al., 2008; Reed et al., 2011).

The presence or the absence of sutures in FE models and the possible impact of this on model strains has been considered in previous studies. Finite element models of pig crania have shown that the inclusion of sutures does not improve the fit of the model to experimental data (Bright, 2012). Other FE models of macaques built without craniofacial sutures have demonstrated a reasonable correlation with *in vivo* experimental strain data, reporting strain ratios and orientations within the experimentally measured range (Strait et al., 2005; Ross et al., 2005, 2011). Thus, it has been suggested that the presence or absence of sutures alone is not a source of significant inaccuracies in estimating craniofacial strains.

Finally, the models of both species were built without craniofacial foramina and fissures. The foramina and fissures of the skull are narrow openings that allow the passage of different structures such as nerves and blood vessels. These openings vary in size and shape between individuals and throughout post-natal development (Lang, Maier and Schafhauser, 1984; Azab, 2016; Raguž et al., 2021). Because their locations, sizes and shapes are often unclear in the fragmentary Neanderthal material, they were closed and filled with bone in all models. However, to date, no FEA studies have assessed the impact of the inclusion or exclusion of these structures on strains resulting from biting. However, based on previous sensitivity studies of the impact of other structures (discussed above) it seems likely that the presence or absence of these openings will affect strain magnitudes and distribution but only locally. Most of these structures are in the basicranium (except

for the inferior and superior orbital fissures, infraorbital foramina with the incisive foramina, and lesser and greater palatine foramina on the palate) and therefore, likely do not impact the distribution and magnitudes of strains in the face and calvarium, but further sensitivity studies are needed to understand the impact of this simplification.

In the same way, here it is important to take into account errors in the estimation of muscle vectors in the Neanderthal infant and juvenile models using Roc de Marsal Neanderthal mandible (5-6 years old) for both models due to the lack of availability of a complete infant Neanderthal mandible for this study. However, geometric morphometric warping approaches were used to scale the Roc de Marsal mandible to the infant and juvenile Neanderthal models and to guide the estimation of muscle vectors. Isometric scaling partially (ignoring allometry) corrected for the size difference between the infant and juvenile models and the Roc de Marsal mandible and provided a useful approximation of the muscle vectors, but with unknown error. Several prior sensitivity studies have found that varying muscle vectors mainly impact the mode of deformation, albeit in limited ways (Fitton et al., 2012; Bright and Rayfield, 2011; Toro-Ibacache, Zapata Muñoz and O'Higgins, 2016; Toro-Ibacache et al., 2016). As such, strain distributions in the present study are also likely impacted to some degree. Godinho et al., (2018) carried out sensitivity analyses that showed that by varying the lines of action of the three muscles (temporalis, masseter, medial pterygoid) by 5°, the impact on the magnitudes and distributions of strains is low to negligible (Godinho et al., 2018). It would have been of interest to assess the extent to which errors in the estimation of muscle vectors impact the results in this study, however, time limited the number and range of sensitivity studies that could be carried out.

In this study, the infant, juvenile, and adult mean models of modern humans and Neanderthals were created to represent similar age stages in each species (see Chapter 2). However, it is important to understand that the age stage was estimated and bracketed to 8-10 years old for the juvenile and 2-3 years old for the infant model. The limited sample in both species did not allow for more precise age estimations for each model. Moreover, previous studies on Neanderthal permanent teeth have suggested that the course of development in this species was either similar to modern humans or accelerated. Studies on deciduous teeth from the Krapina Neanderthals have shown that these teeth formed relatively quickly and emergence is advanced relative to the modern human schedule (Mahoney et al., 2021). Therefore, the modern human and Neanderthal infant and juvenile

models could represent slightly different stages of growth and development. However, the accelerated development of the craniofacial complex in Neanderthals is still a source of debate, and therefore, the approximate age estimations used in this study were deemed appropriate. Further sensitivity analyses could provide more insight into this issue, by conducting FEAs over a wider range of infant and juvenile age stages to track in more detail the differences in modes and magnitudes of deformation that arise during post-natal development between modern humans and Neanderthals.

In this study, tooth and bite point correspondence between the six models was established in terms of position along the dental arcade. We conducted FE analyses on a limited range of biting scenarios, involving unilateral bite points at the right first incisor and right second premolar or second deciduous molar. These do not represent the complexity of loading of the masticatory system and are in fact a gross simplification of the range of loading scenarios likely encountered in reality. Given this, it will be of great interest in future studies to explore a wide range of biting scenarios involving different bite points as well as different degrees of gapes and peak bite force at the bite points. Additionally, teeth are loaded in many directions during mastication and the anterior dentition encounters varying loading scenarios during food acquisition and in paramasticatory scenarios, such as when teeth are used as tools. In this study, the biting simulations were kept simple for reasons of practicality and time, however, future studies should explore a wider range of scenarios in relation to craniofacial development and adult form.

## Supplementary materials

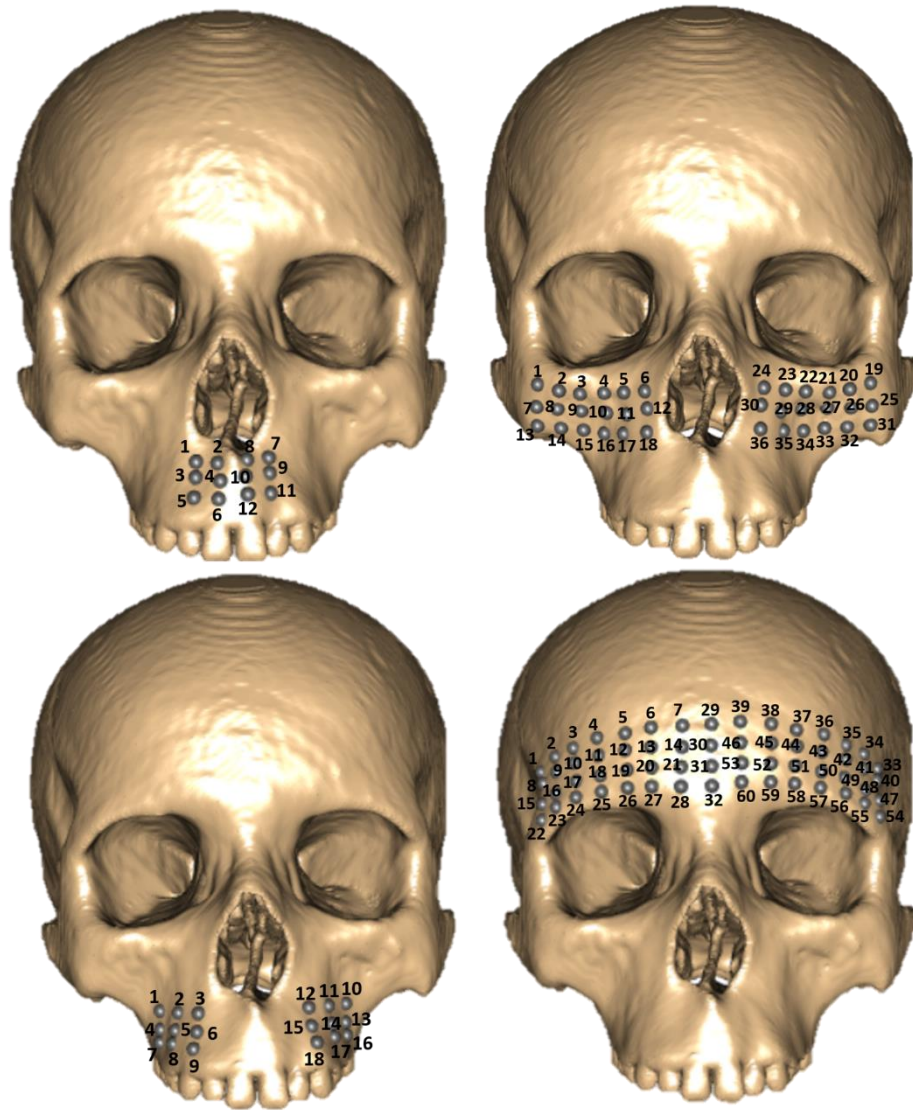


*Figure 1.* Details of the 126 points used to extract the surface strain magnitudes from the solved Finite Element models.

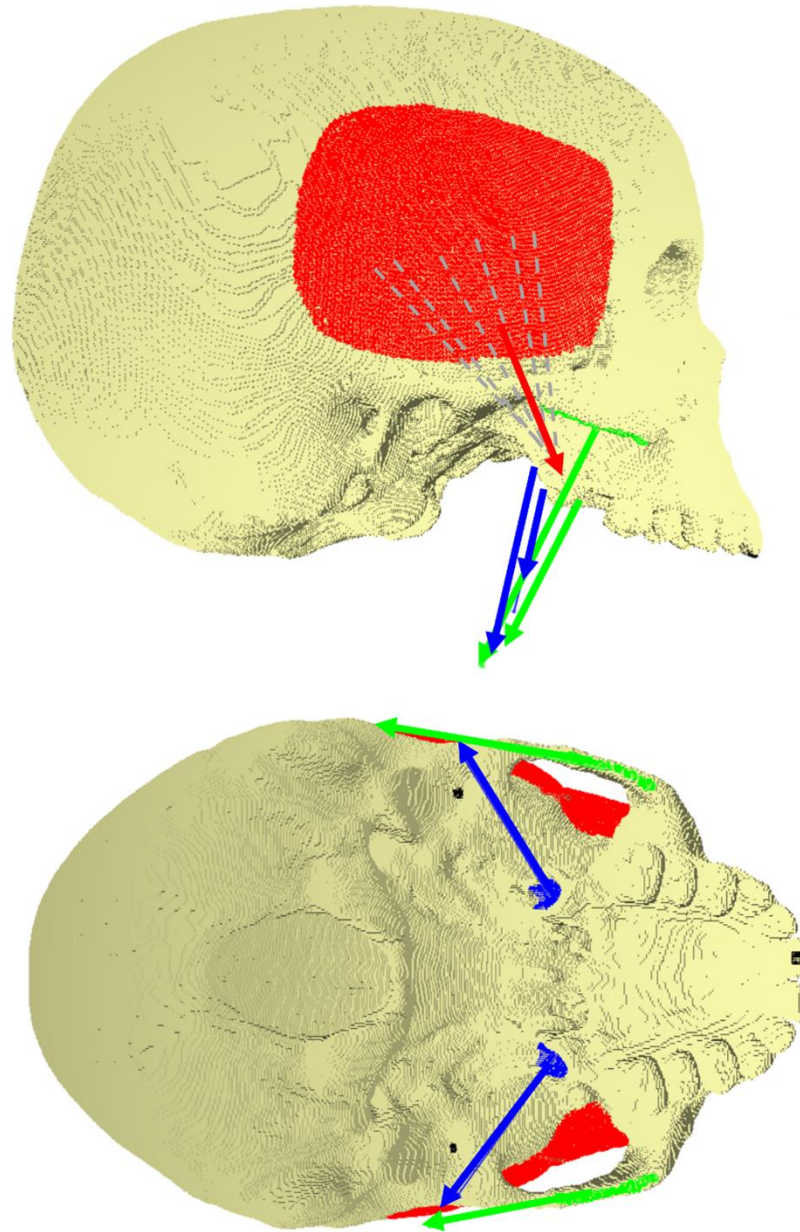


*Figure 2.* Modern human adult model in Vox-FE. The nodes of the voxels underlying the attachments of Temporalis (red), masseter (green) and medial pterygoid (blue) muscle attachments areas were painted using the Node Selection tools of Vox-FE. The black nodes represent the kinematic constraint on the glenoid fossa and the constraint at the bite point (here on the first incisor). The orientations of the Parallel muscle forces (coloured arrows) were defined between with origin which is the mean coordinate of all the nodes selected and the end point, which is the centre of the muscle insertion on the mandible.

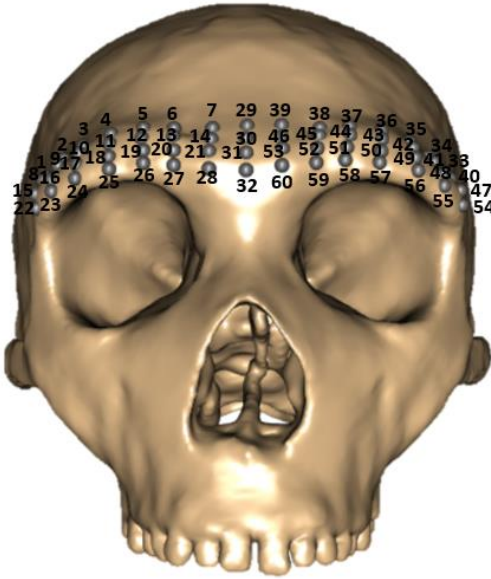


*Figure 3.* Details of the 60 points used to extract the surface strain magnitudes over the supraorbital region from the modified adult Neanderthal solved Finite Element model. Strain magnitudes can be found in Figure 77.

## Literature cited

- Ackermann, R. R. and Krovitz, G. E. (2002). Common patterns of facial ontogeny in the hominid lineage. *Anatomical Record*, 269 (3), pp.142–147. [Online]. Available at: doi:10.1002/ar.10119.
- Adeeb, N. et al. (2012). The cranial dura mater: A review of its history, embryology, and anatomy. *Child's Nervous System*, 28 (6), pp.827–837. [Online]. Available at: doi:10.1007/s00381-012-1744-6.
- Aiello, L. and Dean, C. (1990). *An Introduction to Human Evolutionary Anatomy*. [Online]. Available at: doi:10.2307/2804064 [Accessed 19 May 2022].
- Alfaqeeh, S. A., Gaete, M. and Tucker, A. S. (2013). Interactions of the Tooth and Bone during Development. *Journal of Dental Research*, 92 (12), pp.1129–1135. [Online]. Available at: doi:10.1177/0022034513510321.
- Alomar, X. et al. (2007). Anatomy of the Temporomandibular Joint. *Seminars in Ultrasound, CT and MRI*, 28 (3), pp.170–183. [Online]. Available at: doi:10.1053/j.sult.2007.02.002 [Accessed 29 July 2022].
- AlQahtani, S. J., Hector, M. P. and Liversidge, H. M. (2010). Brief communication: The London atlas of human tooth development and eruption. *American Journal of Physical Anthropology*, 142 (3), pp.481–490. [Online]. Available at: doi:10.1002/ajpa.21258.
- Amano, H. et al. (2015). Virtual reconstruction of the Neanderthal Amud 1 cranium. *American Journal of Physical Anthropology*, 158 (2), pp.185–197. [Online]. Available at: doi:10.1002/ajpa.22777.
- Ammann, P. and Rizzoli, R. (2003). Bone strength and its determinants. *Osteoporosis international*, 14 (3), pp.13–18. [Online]. Available at: doi:10.1007/s00198-002-1345-4.
- Anapol, F., Shahnoor, N. and Ross, C. F. (2008). Scaling of Reduced Physiologic Cross-Sectional Area in Primate Muscles of Mastication. In: *Primate Craniofacial Function and Biology*. pp.201–216. [Online]. Available at: doi:10.1007/978-0-387-76585-3\_10 [Accessed 19 May 2022].
- Antón, S. C. (1990). Neandertals and the anterior dental loading hypothesis: a biomechanical evaluation of bite force production. *Kroeber Anthropological Society Papers*, 71 (72), pp.67–76. [Online]. Available at:

[https://digitalassets.lib.berkeley.edu/anthpubs/ucb/text/kas071\\_072-009.pdf](https://digitalassets.lib.berkeley.edu/anthpubs/ucb/text/kas071_072-009.pdf) [Accessed 25 April 2022].

Antón, S. C. (1994). Biomechanical and other perspectives on the Neanderthal face. In: *Integrative Paths to the Past*. pp.677–695. [Online]. Available at: <https://nyuscholars.nyu.edu/en/publications/chapter-29-biomechanical-and-other-perspectives-on-the-neandertal> [Accessed 24 October 2022].

Antón, S. C. (1996). Tendon-associated bone features of the masticatory system in Neandertals. *Journal of Human Evolution*, 31 (5), pp.391–408. [Online]. Available at: doi:10.1006/jhev.1996.0068 [Accessed 26 April 2022].

Antón, S. C. (1999). Macaque masseter muscle: Internal architecture, fiber length and cross-sectional area. *International Journal of Primatology*, 20 (3), pp.441–462. [Online]. Available at: doi:10.1023/A:1020509006259.

Antón, S. C. (2000). Macaque pterygoid muscles: Internal architecture, fiber length, and cross-sectional area. *International Journal of Primatology*, 21 (1), pp.131–156. [Online]. Available at: doi:10.1023/A:1005431831444.

Antón, S. C. and Howell, F. C. (1994). Masticatory muscle architecture and bone morphology in primates. *Anthropology*, PhD. [Online]. Available at: <https://search.proquest.com/openview/1fecf7b4ef82712857ce7a2e57948c42/1?pq-origsite=gscholar&cbl=18750&diss=y> [Accessed 26 April 2022].

Arambourg, C. R. (1955). Sur l'attitude en station verticale des Neanderthaliens. *C. R. Acad. Sci. Paris*, 240, pp.804–806. [Online]. Available at: [https://scholar.google.com/scholar?hl=en&as\\_sdt=0%2C5&q=Sur+1%27attitude+en+station+verticale+des+Neandcrthalicns&btnG=](https://scholar.google.com/scholar?hl=en&as_sdt=0%2C5&q=Sur+1%27attitude+en+station+verticale+des+Neandcrthalicns&btnG=) [Accessed 19 September 2022].

Arbour, J. H. and Brown, C. M. (2014). Incomplete specimens in geometric morphometric analyses. *Methods in Ecology and Evolution*, 5 (1), pp.16–26. [Online]. Available at: doi:10.1111/2041-210X.12128 [Accessed 5 November 2022].

Atchley, W. R. and Hall, B. K. (1991). A model for development and evolution of complex morphological structures. *Biological Reviews of the Cambridge Philosophical Society*, 66 (2), pp.101–157. [Online]. Available at: doi:10.1111/j.1469-185X.1991.tb01138.x [Accessed 5 November 2022].

- Azab, W. A. (2016). Normal development of the skull and brain. In: *Common Neurosurgical Conditions in the Pediatric Practice: Recognition and Management*. Springer New York. pp.3–9. [Online]. Available at: doi:10.1007/978-1-4939-3807-0\_1.
- Baab, K. L. et al. (2010). Relationship of cranial robusticity to cranial form, geography and climate in *Homo sapiens*. *American Journal of Physical Anthropology*, 141 (1), pp.97–115. [Online]. Available at: doi:10.1002/ajpa.21120 [Accessed 25 April 2022].
- Bakke, M. et al. (1990). Unilateral, isometric bite force in 8-68-year-old women and men related to occlusal factors. *European Journal of Oral Sciences*, 98 (2), pp.149–158. [Online]. Available at: doi:10.1111/j.1600-0722.1990.tb00954.x.
- Bakke, M. (2006). Bite Force and Occlusion. *Seminars in Orthodontics*, 12 (2), pp.120–126. [Online]. Available at: doi:10.1053/j.sodo.2006.01.005.
- Barbeito-Andrés, J. et al. (2015). Developmental covariation of human vault and base throughout postnatal ontogeny. *Annals of Anatomy*, 197, pp.59–66. [Online]. Available at: doi:10.1016/j.aanat.2014.10.002 [Accessed 30 August 2022].
- Barbeito-Andrés, J. et al. (2016). Morphological Integration of the Orbital Region in a Human Ontogenetic Sample. *Anatomical Record*, 299 (1), pp.70–80. [Online]. Available at: doi:10.1002/ar.23282.
- Barbeito-Andrés, J. et al. (2020). Modeling the effect of brain growth on cranial bones using finite-element analysis and geometric morphometrics. *Surgical and Radiologic Anatomy*, 42 (7), pp.741–748. [Online]. Available at: doi:10.1007/s00276-020-02466-y [Accessed 5 August 2022].
- Bastir, M. et al. (2008). Middle cranial fossa anatomy and the origin of modern humans. *Anatomical Record*, 291 (2), pp.130–140. [Online]. Available at: doi:10.1002/ar.20636 [Accessed 22 April 2022].
- Bastir, M., Godoy, P. and Rosas, A. (2011). Common features of sexual dimorphism in the cranial airways of different human populations. *American Journal of Physical Anthropology*, 146 (3), pp.414–422. [Online]. Available at: doi:10.1002/ajpa.21596.
- Bastir, M., O’Higgins, P. and Rosas, A. (2007). Facial ontogeny in Neanderthals and modern humans. *Proceedings of the Royal Society B: Biological Sciences*, 274 (1614), pp.1125–1132. [Online]. Available at: doi:10.1098/rspb.2006.0448.

- Bastir, M. and Rosas, A. (2004). Facial heights: Evolutionary relevance of postnatal ontogeny for facial orientation and skull morphology in humans and chimpanzees. *Journal of Human Evolution*, 47 (5), pp.359–381. [Online]. Available at: doi:10.1016/j.jhevol.2004.08.009 [Accessed 20 April 2022].
- Bastir, M. and Rosas, A. (2005). Hierarchical nature of morphological integration and modularity in the human posterior face. *American Journal of Physical Anthropology*, 128 (1), pp.26–34. [Online]. Available at: doi:10.1002/ajpa.20191 [Accessed 22 April 2022].
- Bastir, M. and Rosas, A. (2013). Cranial airways and the integration between the inner and outer facial skeleton in humans. *American Journal of Physical Anthropology*, 152 (2), pp.287–293. [Online]. Available at: doi:10.1002/ajpa.22359 [Accessed 22 April 2022].
- Bastir, M. and Rosas, A. (2016). Cranial base topology and basic trends in the facial evolution of Homo. *Journal of Human Evolution*, 91, pp.26–35. [Online]. Available at: doi:10.1016/j.jhevol.2015.11.001.
- Bastir, M., Rosas, A. and O’higgins, P. (2006). Craniofacial levels and the morphological maturation of the human skull. *Journal of Anatomy*, 209 (5), pp.637–654. [Online]. Available at: doi:10.1111/j.1469-7580.2006.00644.x [Accessed 22 April 2022].
- Bastir, M., Rosas, A. and Sheets, H. D. (2006). The Morphological Integration of the Hominoid Skull: A Partial Least Squares and PC Analysis with Implications for European Middle Pleistocene Mandibular Variation. In: *Modern Morphometrics in Physical Anthropology*. pp.265–284. [Online]. Available at: doi:10.1007/0-387-27614-9\_12 [Accessed 22 April 2022].
- Batista, R. et al. (2008). Microarray analyses reveal that plant mutagenesis may induce more transcriptomic changes than transgene insertion. *Proceedings of the National Academy of Sciences of the United States of America*, 105 (9), pp.3640–3645. [Online]. Available at: doi:10.1073/pnas.0707881105.
- Baxter, D. J. G. and Shroff, M. M. (2011). Developmental Maxillofacial Anomalies. *Seminars in Ultrasound, CT and MRI*, 32 (6), pp.555–568. [Online]. Available at: doi:10.1053/j.sult.2011.06.004.
- Beaupré, G. S., Orr, T. E. and Carter, D. R. (1990). An approach for time-dependent bone modeling and remodeling—theoretical development. *Journal of Orthopaedic Research*,

8 (5), pp.651–661. [Online]. Available at: doi:10.1002/jor.1100080506.

Benazzi, S. et al. (2011). A new OH5 reconstruction with an assessment of its uncertainty. *Journal of Human Evolution*, 61 (1), pp.75–88. [Online]. Available at: doi:10.1016/j.jhevol.2011.02.005.

Benazzi, S. et al. (2014). Technical Note: Virtual reconstruction of KNM-ER 1813 Homo habilis cranium. *American Journal of Physical Anthropology*, 153 (1), pp.154–160. [Online]. Available at: doi:10.1002/ajpa.22376.

Benninghoff, A. (1925). Form und Bau der Gelenkknorpel in ihren Beziehungen zur Funktion - Zweiter Teil: Der Aufbau des Gelenkknorpels in seinen Beziehungen zur Funktion. *Zeitschrift für Zellforschung und Mikroskopische Anatomie*, 2 (5), pp.783–862. [Online]. Available at: doi:10.1007/BF00583443.

Bentolila, V. et al. (1998). Intracortical remodeling in adult rat long bones after fatigue loading. *Bone*, 23 (3), pp.275–281. [Online]. Available at: doi:10.1016/S8756-3282(98)00104-5 [Accessed 3 November 2022].

Bernal, V., Perez, S. I. and Gonzalez, P. N. (2006). Variation and causal factors of craniofacial robusticity in Patagonian hunter-gatherers from the late Holocene. *American Journal of Human Biology*, 18 (6), pp.748–765. [Online]. Available at: doi:10.1002/ajhb.20546.

Bidwell, J. P. and Pavalko, F. M. (2010). The load-bearing mechanosome revisited. *Clinical Reviews in Bone and Mineral Metabolism*, 8 (4), pp.213–223. [Online]. Available at: doi:10.1007/s12018-010-9075-1.

Biegert, J. (1957). Der Formwandel des Primatenschädels, und seine Beziehungen zur ontogenetischen Entwicklung und den phylogenetischen Spezialisierungen der Kopforgane. *Gegenb Morph Jahrb*, 98, pp.77–199. [Online]. Available at: <https://ci.nii.ac.jp/naid/10015027767/> [Accessed 20 April 2022].

Biegert, J. (1963). The evaluation of characteristics of the skull, hands, and feet for primate taxonomy. In: *Classification and Human Evolution*. Routledge. pp.116–145. [Online]. Available at: doi:10.4324/9781315018010.

Biga, L. et al. (2017). Anatomy & Physiology. University, O. & O. S. (Ed). *Anatomy & Physiology*. [Online]. Available at: doi:10.5399/osu/1116 [Accessed 20 May 2022].

Biga, L. et al. (2020). *Anatomy & physiology*. University, O. S. (Ed). [Online]. Available at: <https://openlibrary-repo.ecampusontario.ca/jspui/handle/123456789/834> [Accessed 6 November 2022].

van der Bilt, A. et al. (2006). Oral physiology and mastication. *Physiology and Behavior*, 89 (1), pp.22–27. [Online]. Available at: doi:10.1016/j.physbeh.2006.01.025 [Accessed 1 August 2022].

Bird, J. and Ross, C. (2014). *Mechanical Engineering Principles*. Routledge. [Online]. Available at: doi:10.4324/9781315769806.

Björk, A. (1969). Prediction of mandibular growth rotation. *American journal of orthodontics*, 55 (6), pp.585–599. [Online]. Available at: doi:10.13076/1300-3550-2-1-73 [Accessed 5 November 2022].

Björk, A. and Skieller, V. (1972). Facial development and tooth eruption. An implant study at the age of puberty. *American Journal of Orthodontics*, 62 (4), pp.339–383. [Online]. Available at: doi:10.1016/S0002-9416(72)90277-1 [Accessed 5 November 2022].

Björk, A. and Skieller, V. (1976). Postnatal growth of the maxillary complex. In: *Center for Human Growth and Development, Ann Arbor, Michigan*. [Online]. Available at: [https://scholar.google.com/scholar?hl=en&as\\_sdt=0%2C5&as\\_ylo=1976&as\\_yhi=1976&q=Postnatal+growth+of+the+maxillary+complex&btnG=](https://scholar.google.com/scholar?hl=en&as_sdt=0%2C5&as_ylo=1976&as_yhi=1976&q=Postnatal+growth+of+the+maxillary+complex&btnG=) [Accessed 5 November 2022].

Blanc, A. C. (1938). Il giacimento musteriano di Saccopastore nel quadro del Pleistocene laziale. *Istituto Italiano Di Antropologia*. [Online]. Available at: [https://scholar.google.com/scholar?hl=en&as\\_sdt=0,5&q=IL+giacimento+musteriano+di+Saccopastore+ncl+quadro+del+pleistocene+laziale](https://scholar.google.com/scholar?hl=en&as_sdt=0,5&q=IL+giacimento+musteriano+di+Saccopastore+ncl+quadro+del+pleistocene+laziale) [Accessed 19 September 2022].

Blanc, A. C. (1961). Social life of early man: Some evidence for the ideologies of early man. In: *Social Life of Early Man*. pp.119–136. [Online]. Available at: doi:10.4324/9781315017761 [Accessed 19 September 2022].

Bluntschli, H. (1926). *Hintermann, Heinr. Unter Indianern und Riesenschlangen*. [Online]. Available at: <https://search.proquest.com/openview/4dad386bb65ef28714737f6e381e32da/1?pq-origsite=gscholar&cbl=1817762> [Accessed 27 April 2022].

- Bocherens, H. (2009). Neanderthal Dietary Habits: Review of the Isotopic Evidence. In: *Vertebrate Paleobiology and Paleoanthropology*. (9781402096983). pp.241–250. [Online]. Available at: doi:10.1007/978-1-4020-9699-0\_19 [Accessed 16 September 2022].
- Bonucci, E. (2009). The osteocyte: The underestimated conductor of the bone orchestra. *Rendiconti Lincei*, 20 (3), pp.237–254. [Online]. Available at: doi:10.1007/s12210-009-0051-y.
- Bookstein, F. et al. (1999). Comparing frontal cranial profiles in archaic and modern homo by morphometric analysis. *Anatomical Record*, 257 (6), pp.217–224. [Online]. Available at: doi:10.1002/(SICI)1097-0185(19991215)257:6<217::AID-AR7>3.0.CO;2-W.
- Bookstein, F. L. (1982). Foundations of morphometrics. *Annual review of ecology and systematics*. Volume 13, 13, pp.451–470. [Online]. Available at: doi:10.1146/annurev.es.13.110182.002315 [Accessed 22 April 2022].
- Bookstein, F. L. (1984). A statistical method for biological shape comparisons. *Journal of Theoretical Biology*, 107 (3), pp.475–520. [Online]. Available at: doi:10.1016/S0022-5193(84)80104-6 [Accessed 26 April 2022].
- Bookstein, F. L. (1991). Thin-Plate splines and the atlas problem for biomedical images. In: *Lecture Notes in Computer Science (including subseries Lecture Notes in Artificial Intelligence and Lecture Notes in Bioinformatics)*. 511 LNCS. 1991. Springer Verlag. pp.326–342. [Online]. Available at: doi:10.1007/BFb0033763.
- Bookstein, F. L. (1996a). Biometrics, biomathematics and the morphometric synthesis. *Bulletin of Mathematical Biology*, 58 (2), pp.313–365. [Online]. Available at: doi:10.1007/BF02458311.
- Bookstein, F. L. (1996b). Combining the Tools of Geometric Morphometrics. In: *Advances in Morphometrics*. Springer US. pp.131–151. [Online]. Available at: doi:10.1007/978-1-4757-9083-2\_12.
- Bookstein, F. L. (1996c). Standard Formula for the Uniform Shape Component in Landmark Data. *Advances in Morphometrics*, pp.153–168. [Online]. Available at: doi:10.1007/978-1-4757-9083-2\_13.

- Bookstein, F. L. (1997). Landmark methods for forms without landmarks: Morphometrics of group differences in outline shape. *Medical Image Analysis*, 1 (3), pp.225–243. [Online]. Available at: doi:10.1016/S1361-8415(97)85012-8 [Accessed 25 May 2022].
- Bordes, F. and Lafille, J. (1962). Paleontologie humaine-découverte d'un squelette d'enfant Mousterien dans le gisement du Roc de Marsal, commune de campagne-du-Bugue (Dordogne). *Comptes rendus hebdomadaires des séances de l'académie des sciences*, 254 (4), p.714. [Online]. Available at: [https://scholar.google.com/scholar?hl=en&as\\_sdt=0%2C5&q=Bordes+and+Lafille%2C+1962&btnG=](https://scholar.google.com/scholar?hl=en&as_sdt=0%2C5&q=Bordes+and+Lafille%2C+1962&btnG=) [Accessed 19 September 2022].
- Boughner, J. C. and Dean, M. C. (2004). Does space in the jaw influence the timing of molar crown initiation? A model using baboons (*Papio anubis*) and great apes (*Pan troglodytes*, *Pan paniscus*). *Journal of Human Evolution*, 46 (3), pp.253–275. [Online]. Available at: doi:10.1016/j.jhevol.2003.11.007 [Accessed 1 November 2022].
- Bourgon, M. (1957). *Les industries mousteriennes et pre-mousteriennes du Périgord*.
- Bouvier, M. and Hylander, W. L. (1996). The mechanical or metabolic function of secondary osteonal bone in the monkey *Macaca fascicularis*. *Archives of Oral Biology*, 41 (10), pp.941–950. [Online]. Available at: doi:10.1016/S0003-9969(96)00047-7 [Accessed 17 May 2022].
- Bouxsein, M. L. and Karasik, D. (2006). Bone geometry and skeletal fragility. *Current Osteoporosis Reports*, 4 (2), pp.49–56. [Online]. Available at: doi:10.1007/S11914-006-0002-9.
- Brace, C. L. (1967). *The Stages of Human Evolution*. [Online]. Available at: doi:10.2307/2799277 [Accessed 20 May 2022].
- Brace, C.L., 1995. Biocultural interaction and the mechanism of mosaic evolution in the emergence of “modern” morphology. *American Anthropologist*, 97(4), pp.711-721.
- Brace, C. L. and Mahler, P. E. (1971). Post-Pleistocene changes in the human dentition. *American Journal of Physical Anthropology*, 34 (2), pp.191–203. [Online]. Available at: doi:10.1002/ajpa.1330340205.
- Brace, C. L., Rosenberg, K. R. and Hunt, K. D. (1987). Gradual change in human tooth size in the Late Pleistocene and post-Pleistocene. *Evolution*, 41 (4), pp.705–720. [Online].

Available at: doi:10.1111/j.1558-5646.1987.tb05847.x [Accessed 25 April 2022].

Brachetta-Aporta, N., Gonzalez, P. N. and Bernal, V. (2018). A quantitative approach for analysing bone modelling patterns from craniofacial surfaces in hominins. *Journal of Anatomy*, 232 (1), pp.3–14. [Online]. Available at: doi:10.1111/joa.12716.

Brachetta-Aporta, N., Gonzalez, P. N. and Bernal, V. (2019). Integrating data on bone modeling and morphological ontogenetic changes of the maxilla in modern humans. *Annals of Anatomy*, 222, pp.12–20. [Online]. Available at: doi:10.1016/j.aanat.2018.10.008.

Brachetta Aporta, N. et al. (2014). Bone modeling patterns and morphometric craniofacial variation in individuals from two prehistoric human populations from Argentina. *Anatomical Record*, 297 (10), pp.1829–1838. [Online]. Available at: doi:10.1002/ar.22999 [Accessed 25 April 2022].

Bright, J. A. (2012). The importance of craniofacial sutures in biomechanical finite element models of the domestic pig. *PLoS ONE*, 7 (2). [Online]. Available at: doi:10.1371/journal.pone.0031769.

Bright, J. A. and Rayfield, E. J. (2011). Sensitivity and ex vivo validation of finite element models of the domestic pig cranium. *Journal of Anatomy*, 219 (4), pp.456–471. [Online]. Available at: doi:10.1111/j.1469-7580.2011.01408.x [Accessed 19 April 2022].

Bromage, T. G. (1989). Ontogeny of the early hominid face. *Journal of Human Evolution*, 18 (8), pp.751–773. [Online]. Available at: doi:10.1016/0047-2484(89)90088-2 [Accessed 25 April 2022].

Bromage, T. G. and Boyde, A. (2008). Bone growth remodeling of the early human face. In: *Essentials of Facial Growth*. pp.319–342. [Online]. Available at: <https://nyuscholars.nyu.edu/en/publications/bone-growth-remodeling-of-the-early-human-face> [Accessed 3 November 2022].

Bromage, T. G. and Dean, M. C. (1985). Re-evaluation of the age at death of immature fossil hominids. *Nature*, 317 (6037), pp.525–527. [Online]. Available at: doi:10.1038/317525a0 [Accessed 20 April 2022].

Brothwell, D. (1975). Adaptive growth rate changes as a possible explanation for the

distinctiveness of the Neanderthals. *Journal of Archaeological Science*, 2 (2), pp.161–163. [Online]. Available at: doi:10.1016/0305-4403(75)90036-9 [Accessed 1 November 2022].

Butaric, L. N. and Maddux, S. D. (2016). Morphological Covariation between the Maxillary Sinus and Midfacial Skeleton among Sub-Saharan and Circumpolar Modern Humans. *American Journal of Physical Anthropology*, 160 (3), pp.483–497. [Online]. Available at: doi:10.1002/ajpa.22986.

Cachel, S. (1984). Growth and allometry in primate masticatory muscles. *Archives of Oral Biology*, 29 (4), pp.287–293. [Online]. Available at: doi:10.1016/0003-9969(84)90102-X [Accessed 19 May 2022].

Capitan, L. and Peyrony, D. (1909). Deux squelettes humains au milieu de foyers de l'époque moustérienne. *Comptes-rendus des séances de l'année - Académie des inscriptions et belles-lettres*, 53 (11), pp.797–806. [Online]. Available at: doi:10.3406/crai.1909.72388 [Accessed 19 September 2022].

Carey, J. W. J. W. and Steegmann, A. T. (1981). Human nasal protrusion, latitude, and climate. *American Journal of Physical Anthropology*, 56 (3), pp.313–319. [Online]. Available at: doi:10.1002/ajpa.1330560312 [Accessed 25 April 2022].

Carlson, D. S. (1976). Temporal variation in prehistoric Nubian crania. *American Journal of Physical Anthropology*, 45 (3), pp.467–484. [Online]. Available at: doi:10.1002/ajpa.1330450308.

Carlson, D. S. (1983). Growth of the masseter muscle in rhesus monkeys (*Macaca mulatta*). *American Journal of Physical Anthropology*, 60 (3), pp.401–410. [Online]. Available at: doi:10.1002/ajpa.1330600310 [Accessed 19 May 2022].

Carlson, D. S. and Van Gerven, D. P. (1977). Masticatory function and post-pleistocene evolution in Nubia. *American Journal of Physical Anthropology*, 46 (3), pp.495–506. [Online]. Available at: doi:10.1002/AJPA.1330460316.

Carlson, D. S. and Schneiderman, E. D. (1983). Cephalometric analysis of adaptations after lengthening of the masseter muscle in adult rhesus monkeys, *Macaca mulatta*. *Archives of Oral Biology*, 28 (7), pp.627–637. [Online]. Available at: doi:10.1016/0003-9969(83)90011-0 [Accessed 19 May 2022].

- Carlson, K. B. et al. (2016). Developmental simulation of the adult cranial morphology of australopithecus sediba. *South African Journal of Science*, 112 (7–8), pp.1–9. [Online]. Available at: doi:10.17159/sajs.2016/20160012 [Accessed 29 April 2022].
- Carlson, K. J. (2005). Investigating the form-function interface in African apes: Relationships between principal moments of area and positional behaviors in femoral and humeral diaphyses. *American Journal of Physical Anthropology*, 127 (3), pp.312–334. [Online]. Available at: doi:10.1002/ajpa.20124.
- Carr, L. M. (1962). Eruption ages of permanent teeth. *Australian Dental Journal*, 7 (5), pp.367–373. [Online]. Available at: doi:10.1111/j.1834-7819.1962.tb04884.x.
- Carter, D. R., van der Meulen, M. C. H. and Beaupré, G. S. (2008). Skeletal Development: Mechanical Consequences of Growth, Aging, and Disease. In: *Osteoporosis, Two-Volume Set*. pp.563–580. [Online]. Available at: doi:10.1016/B978-012370544-0.50023-9 [Accessed 5 November 2022].
- Cartmill, M. (1974). Rethinking primate origins. *Science*, 184 (4135), pp.436–443. [Online]. Available at: doi:10.1126/science.184.4135.436.
- Castelo, P. M. et al. (2007). Masticatory muscle thickness, bite force, and occlusal contacts in young children with unilateral posterior crossbite. *European Journal of Orthodontics*, 29 (2), pp.149–156. [Online]. Available at: doi:10.1093/ejo/cjl089 [Accessed 31 October 2022].
- Cheverud, J. M. (1982). Relationships among ontogenetic, static, and evolutionary allometry. *American Journal of Physical Anthropology*, 59 (2), pp.139–149. [Online]. Available at: doi:10.1002/ajpa.1330590204.
- Cheverud, J. M. et al. (1999). Epistasis and the evolution of additive genetic variance in populations that pass through a bottleneck. *Evolution*, 53 (4), pp.1009–1018. [Online]. Available at: doi:10.1111/j.1558-5646.1999.tb04516.x.
- Cheverud, J. M. and Routman, E. J. (1995). Its Contribution. *Genetics*.
- Churchill, S. E. (2006). Bioenergetic perspectives on Neanderthal thermoregulatory and activity budgets. In: *Vertebrate Paleobiology and Paleoanthropology*. Springer. pp.113–133. [Online]. Available at: doi:10.1007/978-1-4020-5121-0\_7.
- Clement, A. F., Hillson, S. W. and Aiello, L. C. (2012). Tooth wear, Neanderthal facial

morphology and the anterior dental loading hypothesis. *Journal of Human Evolution*, 62 (3), pp.367–376. [Online]. Available at: doi:10.1016/j.jhevol.2011.11.014 [Accessed 26 April 2022].

Cobb, S. N. and O’Higgins, P. (2004). Hominins do not share a common postnatal facial ontogenetic shape trajectory. *Journal of Experimental Zoology Part B: Molecular and Developmental Evolution*, 302 (3), pp.302–321. [Online]. Available at: doi:10.1002/jez.b.21005.

Cohen, M. M. (1993). Sutural biology and the correlates of craniosynostosis. *American Journal of Medical Genetics*, 47 (5), pp.581–616. [Online]. Available at: doi:10.1002/ajmg.1320470507.

Cooke, K. M., Mahoney, P. and Miskiewicz, J. J. (2021). Secondary osteon variants and remodeling in human bone. *Anatomical Record*, (September 2020), pp.1299–1315. [Online]. Available at: doi:10.1002/ar.24646 [Accessed 20 May 2022].

Coon, C. (1962). *The origin of races*. [Online]. Available at: <https://psycnet.apa.org/record/1962-35039-000> [Accessed 20 May 2022].

Couly, G. et al. (2002). Interactions between Hox-negative cephalic neural crest cells and the foregut endoderm in patterning the facial skeleton in the vertebrate head. *Development*, 129 (4), pp.1061–1073. [Online]. Available at: doi:10.1242/dev.129.4.1061.

Couly, G. and Hureau, J. (1976). The oto-meniscal relationship of temporo-mandibular joint in the new-born man. *Arch Anat Histol Embryol*, 59, pp.143–150. [Online]. Available at: <https://europepmc.org/article/med/801315> [Accessed 27 April 2022].

Cowin, S. C. (2001). *Bone Mechanics Handbook*. CRC Press. [Online]. Available at: doi:10.1201/b14263.

Cowin, S. C. (2007). The significance of bone microstructure in mechanotransduction. *Journal of Biomechanics*, 40 (SUPPL. 1). [Online]. Available at: doi:10.1016/j.jbiomech.2007.02.012 [Accessed 20 May 2022].

Cryer, M. H. (1916). The internal anatomy of the face. *International Journal of Orthodontia*, 3 (9), pp.561–562. [Online]. Available at: doi:10.1016/S1072-3471(17)90226-3 [Accessed 27 April 2022].

- Currey, J. D. (2002). The structure of bone tissue. In: *Bones: Structure and mechanics*. p.3r26. [Online]. Available at: [https://scholar.google.com/scholar?hl=en&as\\_sdt=0%2C5&q=Currey+JD.+2002.+Bone+s%3A+structure+and+mechanics.&btnG=](https://scholar.google.com/scholar?hl=en&as_sdt=0%2C5&q=Currey+JD.+2002.+Bone+s%3A+structure+and+mechanics.&btnG=) [Accessed 11 December 2022].
- Currey, J. D. (2003). The many adaptations of bone. *Journal of Biomechanics*, 36 (10), pp.1487–1495. [Online]. Available at: doi:10.1016/S0021-9290(03)00124-6 [Accessed 20 May 2022].
- Currey, J. D. (2006). *Bones: Structure and mechanics*. [Online]. Available at: doi:10.1016/s0021-9290(03)00033-2 [Accessed 17 May 2022].
- Curtis, N. et al. (2010). Comparison between in vivo and theoretical bite performance: Using multi-body modelling to predict muscle and bite forces in a reptile skull. *Journal of Biomechanics*, 43 (14), pp.2804–2809. [Online]. Available at: doi:10.1016/j.jbiomech.2010.05.037.
- Curtis, N. et al. (2011). The mechanical significance of the temporal fasciae in macaca fascicularis: An investigation using finite element analysis. *Anatomical Record*, 294 (7), pp.1178–1190. [Online]. Available at: doi:10.1002/ar.21415.
- Daegling, D. J. et al. (2013). Viewpoints: Feeding mechanics, diet, and dietary adaptations in early hominins. *American Journal of Physical Anthropology*, 151 (3), pp.356–371. [Online]. Available at: doi:10.1002/ajpa.22281.
- Dalgorf, D. and Higgins, K. (2008). Reconstruction of the midface and maxilla. *Current Opinion in Otolaryngology and Head and Neck Surgery*, 16 (4), pp.303–311. [Online]. Available at: doi:10.1097/MOO.0B013E328304B426 [Accessed 19 May 2022].
- Al Dayeh, A. A. et al. (2013). Real-time monitoring of the growth of the nasal septal cartilage and the nasofrontal suture. *American Journal of Orthodontics and Dentofacial Orthopedics*, 143 (6), pp.773–783. [Online]. Available at: doi:10.1016/j.ajodo.2013.01.012 [Accessed 31 October 2022].
- Dean, M., Stringer, C. and Bromage, T. (1986). Age at death of the Neanderthal child from Devil's Tower, Gibraltar and the implications for studies of general growth and development in Neanderthals. *American Journal of Physical Anthropology*, 70 (3), pp.301–309. [Online]. Available at: doi:10.1002/AJPA.1330700305.

- Dechow, P. C. et al. (1993). Elastic properties of human supraorbital and mandibular bone. *American Journal of Physical Anthropology*, 90 (3), pp.291–306. [Online]. Available at: doi:10.1002/ajpa.1330900304.
- Dechow, P. C., Chung, D. H. and Bolouri, M. (2008). Relationship Between Three-Dimensional Microstructure and Elastic Properties of Cortical Bone in the Human Mandible and Femur. In: *Primate Craniofacial Function and Biology*. Springer US. pp.265–292. [Online]. Available at: doi:10.1007/978-0-387-76585-3\_13.
- Demes, B. (1982). The resistance of primate skulls against mechanical stresses. *Journal of Human Evolution*, 11 (8), pp.687–691. [Online]. Available at: doi:10.1016/S0047-2484(82)80056-0 [Accessed 6 November 2022].
- Demes, B. (1987). Another look at an old face: biomechanics of the neandertal facial skeleton reconsidered. *Journal of Human Evolution*, 16 (3), pp.297–303. [Online]. Available at: doi:10.1016/0047-2484(87)90005-4 [Accessed 25 April 2022].
- Demes, B. and Creel, N. (1988). Bite force, diet, and cranial morphology of fossil hominids. *Journal of Human Evolution*, 17 (7), pp.657–670. [Online]. Available at: doi:10.1016/0047-2484(88)90023-1.
- Dickinson, E., Fitton, L. C. and Kupczik, K. (2018). Ontogenetic changes to muscle architectural properties within the jaw-adductor musculature of *Macaca fascicularis*. *American Journal of Physical Anthropology*, 167 (2), pp.291–310. [Online]. Available at: doi:10.1002/ajpa.23628 [Accessed 20 April 2022].
- Dixon, A. D., Hoyte, D. A. N. and Rönning, O. (2017). *Fundamentals of craniofacial growth*. [Online]. Available at: doi:10.1201/9780203755327 [Accessed 19 April 2022].
- Donald, Enlow h, H. M. G. (1996). Overview of Craniofacial growth and Development. In: *Essentials of facial growth*. pp.1–17. [Online]. Available at: <https://ci.nii.ac.jp/naid/10021294587/> [Accessed 25 April 2022].
- Drake, A. G. and Klingenberg, C. P. (2008). The pace of morphological change: Historical transformation of skull shape in St Bernard dogs. *Proceedings of the Royal Society B: Biological Sciences*, 275 (1630), pp.71–76. [Online]. Available at: doi:10.1098/rspb.2007.1169.
- Dryden, I. L. and Mardia, K. V. (1993). Multivariate shape analysis. *Sankhyā: The Indian*

*Journal of Statistics*, 55 (3), pp.460–480. [Online]. Available at: [https://www.jstor.org/stable/25050954?casa\\_token=\\_VPTWXsRhzoAAAAA:WA\\_f1RoINbbv6Gh7bnMoRLRvOMIy4R1TR8aDapZW-adgHt5E3PnduL32joTQOsFOA-5UPWS-gmCErteWi4i\\_VV9-Jt1MXelcUhHrYYRffF4dQzwRxf8u](https://www.jstor.org/stable/25050954?casa_token=_VPTWXsRhzoAAAAA:WA_f1RoINbbv6Gh7bnMoRLRvOMIy4R1TR8aDapZW-adgHt5E3PnduL32joTQOsFOA-5UPWS-gmCErteWi4i_VV9-Jt1MXelcUhHrYYRffF4dQzwRxf8u) [Accessed 26 April 2022].

Dumont, E. R., Grosse, I. R. and Slater, G. J. (2009). Requirements for comparing the performance of finite element models of biological structures. *Journal of Theoretical Biology*, 256 (1), pp.96–103. [Online]. Available at: doi:10.1016/j.jtbi.2008.08.017 [Accessed 12 September 2022].

Duncan, R. L. and Turner, C. H. (1995). Mechanotransduction and the functional response of bone to mechanical strain. *Calcified Tissue International*, 57 (5), pp.344–358. [Online]. Available at: doi:10.1007/BF00302070 [Accessed 5 November 2022].

Ealba, E. L. et al. (2015). Neural crest-mediated bone resorption is a determinant of species-specific jaw length. *Developmental Biology*, 408 (1), pp.151–163. [Online]. Available at: doi:10.1016/j.ydbio.2015.10.001.

Edmonds, H. M. and Glowacka, H. (2020). The ontogeny of maximum bite force in humans. *Journal of Anatomy*, 237 (3), pp.529–542. [Online]. Available at: doi:10.1111/joa.13218.

Eisenberg, N. A. and Brodie, A. G. (1965). Antagonism of temporal fascia to masseteric contraction. *The Anatomical Record*, 152 (2), pp.185–192. [Online]. Available at: doi:10.1002/ar.1091520209.

Ellis, I. E., El-Attar, A. and Moos, K. F. (1985). An analysis of 2,067 cases of zygomatico-orbital fracture. *Journal of Oral and Maxillofacial Surgery*, 43 (6), pp.417–428. [Online]. Available at: <https://www.sciencedirect.com/science/article/pii/S0278239185800495> [Accessed 31 October 2022].

Endo, B. (1965). Distribution of stress and strain produced by the masticatory force. *The Journal of the Anthropological Society of Tokyo*, 73, pp.123–136. [Online]. Available at: [https://www.jstage.jst.go.jp/article/ase1911/73/4/73\\_4\\_123/\\_pdf/-char/en](https://www.jstage.jst.go.jp/article/ase1911/73/4/73_4_123/_pdf/-char/en).

Endo, B. (1966a). A Biomechanical Study of the Human Facial Skeleton by Means of Strain-Sensitive Lacquer. *Okajimas Folia Anatomica Japonica*, 42 (4), pp.205–217. [Online]. Available at: doi:10.2535/ofaj1936.42.4\_205 [Accessed 26 April 2022].

Endo, B. (1966b). Experimental Studies on the Mechanical Significance of the Form of the Human Facial Skeleton. *J Fac Sci Univ of Tokyo, Sec. 5*, 3 (1), pp.1–106. [Online]. Available at: <https://ci.nii.ac.jp/naid/40018672862/> [Accessed 26 April 2022].

Endo, B. (1970). Analysis of Stresses around the Orbit Due to Masseter and Temporalis Muscles Respectively. *Journal of the Anthropological Society of Nippon*, 78 (4), pp.251–266. [Online]. Available at: doi:10.1537/ase1911.78.251.

Endo, B. (1973). Stress analysis on the facial skeleton of gorilla by means of the wire strain gauge method. *Primates*, 14 (1), pp.37–45. [Online]. Available at: doi:10.1007/BF01730514.

Endo, B. and Adachi, K. (1988). Biomechanical Simulation Study on the Forms of the Frontal Bone and Facial Bones of the Recent Human Facial Skeleton by using a Two-dimensional Frame Model with Stepwise Variable Cross-section Members. *Okajimas Folia Anatomica Japonica*, 64 (6), pp.335–349. [Online]. Available at: doi:10.2535/ofaj1936.64.6\_335 [Accessed 25 April 2022].

Eng, C. M. et al. (2009). The morphology of the masticatory apparatus facilitates muscle force production at wide jaw gapes in tree-gouging common marmosets (*Callithrix jacchus*). *Journal of Experimental Biology*, 212 (24), pp.4040–4055. [Online]. Available at: doi:10.1242/jeb.029983 [Accessed 19 May 2022].

Eng, C. M. et al. (2013). Bite force and occlusal stress production in hominin evolution. *American Journal of Physical Anthropology*, 151 (4), pp.544–557. [Online]. Available at: doi:10.1002/ajpa.22296.

Enlow, D. (1996). The Nasomaxillary complex. In: *Essentials of Facial Growth*. pp.79–98. [Online]. Available at: <https://ci.nii.ac.jp/naid/10014985185/> [Accessed 25 April 2022].

Enlow, D. H. (1963). *Principles of bone remodeling: an account of post-natal growth and remodeling processes in long bones and the mandible*. In: Thomas (Ed). p.531. [Online]. Available at: [https://scholar.google.com/scholar?q=Enlow%2C+1963&hl=en&as\\_sdt=0%2C5&as\\_ylo=&as\\_yhi=](https://scholar.google.com/scholar?q=Enlow%2C+1963&hl=en&as_sdt=0%2C5&as_ylo=&as_yhi=) [Accessed 5 November 2022].

Enlow, D. H. (1966). A morphogenetic analysis of facial growth. *American Journal of Orthodontics*, 52 (4), pp.283–299. [Online]. Available at: doi:10.1016/0002-

9416(66)90169-2 [Accessed 3 November 2022].

Enlow, D. H. (1968). *The Human Face. An account of the postnatal growth and development of the craniofacial skeleton.* [Online]. Available at: <https://ci.nii.ac.jp/naid/10022002725/> [Accessed 3 November 2022].

Enlow, D. H. (1979). Facial growth and development. *International Journal of Oral Myology*, 5 (4), pp.7–10. [Online]. Available at: doi:10.52010/ijom.1979.5.4.3 [Accessed 1 August 2022].

Enlow, D. H. (1990). *Facial growth.* [Online]. Available at: doi:10.1097/00006534-199107000-00033 [Accessed 3 November 2022].

Enlow, D. H. and Azuma, M. (1975). Functional growth boundaries in the human and mammalian face. *Birth Defects: Original Article Series*, 11 (7), pp.217–230. [Online]. Available at: <https://europepmc.org/article/med/1212506> [Accessed 3 November 2022].

Enlow, D. H. and Bang, S. (1965). Growth and remodeling of the human maxilla. *American Journal of Orthodontics*, 51 (6), pp.446–464. [Online]. Available at: doi:10.1016/0002-9416(65)90242-3.

Enlow, D. H. and Bostwick, J. (1977). Handbook of facial growth. *Plastic and Reconstructive Surgery*, 59 (1), pp.116–117. [Online]. Available at: doi:10.1097/00006534-197701000-00025 [Accessed 3 November 2022].

Enlow, D. H. and Hans, M. G. (1996). Essentials of facial growth. In: *WB Saunders Company.* [Online]. Available at: [https://scholar.google.com/scholar?hl=en&as\\_sdt=0%2C5&q=enlow+and+hans+1996&oq=Enlow+and+Hans+](https://scholar.google.com/scholar?hl=en&as_sdt=0%2C5&q=enlow+and+hans+1996&oq=Enlow+and+Hans+) [Accessed 3 November 2022].

Enlow, D. H. and Hans, M. G. (2008). Essentials of facial growth. In: *Ann Arbor, Mich, MI: Needham Press.* [Online]. Available at: [https://scholar.google.com/scholar?hl=en&as\\_sdt=0%2C5&q=Essentials+of+facial+growth+Enlow+and+Hans%2C+2008&btnG=](https://scholar.google.com/scholar?hl=en&as_sdt=0%2C5&q=Essentials+of+facial+growth+Enlow+and+Hans%2C+2008&btnG=) [Accessed 31 October 2022].

Enlow, D. H. and McNamara, J. A. (1973). The neurocranial basis for facial form and pattern. *Angle Orthodontist*, 43 (3), pp.256–270. [Online]. Available at: [https://media.dent.umich.edu/labs/mcnamara/files/The neurocranial basis for facial form and pattern.pdf](https://media.dent.umich.edu/labs/mcnamara/files/The%20neurocranial%20basis%20for%20facial%20form%20and%20pattern.pdf) [Accessed 3 November 2022].

Enlow, D. H. and Moyers, R. E. (1971). Growth and architecture of the face. *Journal of the American Dental Association (1939)*, 82 (4), pp.763–774. [Online]. Available at: doi:10.14219/jada.archive.1971.0144 [Accessed 3 November 2022].

Erickson, G. M., Lappin, A. K. and Vliet, K. A. (2003). The ontogeny of bite-force performance in American alligator (*Alligator mississippiensis*). *Journal of Zoology*, 260 (3), pp.317–327. [Online]. Available at: doi:10.1017/S0952836903003819 [Accessed 20 May 2022].

Estalrich, A. and Marín-Arroyo, A.B., 2021. Evidence of habitual behavior from non-alimentary dental wear on deciduous teeth from the Middle and Upper Paleolithic Cantabrian region, Northern Spain. *Journal of Human Evolution*, 158, p.103047.

Ethier, C. and Simmons, C. (2007). Introductory biomechanics: from cells to organisms. *Choice Reviews Online*, 45 (03), pp.45-1476-45–1476. [Online]. Available at: doi:10.5860/choice.45-1476 [Accessed 17 May 2022].

Evteev, A., Anikin, A. and Satanin, L. (2018). Midfacial growth patterns in males from newborn to 5 years old based on computed tomography. *American Journal of Human Biology*, 30 (4). [Online]. Available at: doi:10.1002/ajhb.23132.

Fagan, M. J. et al. (2007). Voxel-based finite element analysis-Working directly with microCT scan data. *Journal of Morphology*, 268 (12), p.1071. [Online]. Available at: <https://scholar.google.com/scholar?cluster=7122342700348473753&hl=en&oi=scholar> [Accessed 29 April 2022].

Fenart, R. and Deblock, R. (1978). [Ontogenic development of the surface of craniofacial sagittal angular sectors in man and chimpanzee]. *Bulletin de l'Association des anatomistes*, 62 (176), pp.85–88. [Online]. Available at: <https://europepmc.org/article/med/728633> [Accessed 3 November 2022].

Fenart, R. and Empereur-Buisson, R. (1970). Application de la méthode ‘vestibulaire’ d’orientation aux crânes du Pech de l’Azé et comparaison avec d’autres crânes néanderthaliens. *Archives de l'institut de Paléontologie Mémoires Humains*, 33, pp.89–148. [Online]. Available at: [https://scholar.google.com/scholar?hl=en&as\\_sdt=0,5&q=Application+de+la+methode+Vestibulaire+d%27orientation+au+cranes+ncandcr-thalicsn](https://scholar.google.com/scholar?hl=en&as_sdt=0,5&q=Application+de+la+methode+Vestibulaire+d%27orientation+au+cranes+ncandcr-thalicsn). [Accessed 19 September 2022].

Ferrario, V. F. et al. (2004). Maximal bite forces in healthy young adults as predicted by surface electromyography. *Journal of Dentistry*, 32 (6), pp.451–457. [Online]. Available at: doi:10.1016/j.jdent.2004.02.009 [Accessed 26 April 2022].

Fiorenza, L., Benazzi, S., Kullmer, O., Zampirolo, G., Mazurier, A., Zanolli, C. and Macchiarelli, R., 2019. Dental macrowear and cortical bone distribution of the Neanderthal mandible from Regourdou (Dordogne, Southwestern France). *Journal of Human Evolution*, 132, pp.174-188.

Fiscella, G. (2004). *Ontogeny, structure, and integration in the supraorbital region of modern humans: a longitudinal study*. [Online]. Available at: <http://commons.lib.niu.edu/handle/10843/13971> [Accessed 20 May 2022].

Fiscella, G. N. and Smith, F. H. (2006). Ontogenetic study of the supraorbital region in modern humans: a longitudinal test of the spatial model. *Anthropologischer Anzeiger; Bericht über die biologisch-anthropologische Literatur*, 64 (2), pp.147–160. [Online]. Available at: doi:10.1127/anthranz/64/2006/147.

Fitton, L. C. et al. (2012). Masticatory loadings and cranial deformation in *Macaca fascicularis*: A finite element analysis sensitivity study. *Journal of Anatomy*, 221 (1), pp.55–68. [Online]. Available at: doi:10.1111/j.1469-7580.2012.01516.x.

Fitton, L. C. et al. (2015). The Impact of Simplifications on the Performance of a Finite Element Model of a *Macaca fascicularis* Cranium. *Anatomical Record*, 298 (1), pp.107–121. [Online]. Available at: doi:10.1002/ar.23075.

Franciscus, R. G. (1999). Neandertal nasal structures and upper respiratory tract ‘specialization’. *Proceedings of the National Academy of Sciences of the United States of America*, 96 (4), pp.1805–1809. [Online]. Available at: doi:10.1073/pnas.96.4.1805.

Franciscus, R. G. (2003). Internal nasal floor configuration in Homo with special reference to the evolution of Neandertal facial form. *Journal of Human Evolution*, 44 (6), pp.701–729. [Online]. Available at: doi:10.1016/S0047-2484(03)00062-9 [Accessed 1 November 2022].

Franciscus, R. G. and Churchill, S. E. (2002). The coastal skeleton of Shanidar 3 and a reappraisal of Neandertal thoracic morphology. *Journal of Human Evolution*, 42 (3), pp.303–356. [Online]. Available at: doi:10.1006/jhev.2001.0528 [Accessed 1 August 2022].

Franciscus, R. G. and Trinkaus, E. (1988). Nasal morphology and the emergence of Homo erectus. *American Journal of Physical Anthropology*, 75 (4), pp.517–527. [Online]. Available at: doi:10.1002/ajpa.1330750409 [Accessed 25 April 2022].

Franciscus, R. G. and Trinkaus, E. (1995). Determinants of retromolar space presence in Pleistocene Homo mandibles. *Journal of Human Evolution*, 28 (6), pp.577–595. [Online]. Available at: doi:10.1006/jhev.1995.1043 [Accessed 22 April 2022].

Freidline, S. E. et al. (2017). Exploring modern human facial growth at the micro- and macroscopic levels. In: *Building Bones: Bone Formation and Development in Anthropology*. pp.104–127. [Online]. Available at: doi:10.1017/9781316388907.006 [Accessed 25 April 2022].

Friedman, A. W. (2006). Important determinants of bone strength: Beyond bone mineral density. *Journal of Clinical Rheumatology*, 12 (2), pp.70–77. [Online]. Available at: doi:10.1353/psg.2006.0122 [Accessed 20 May 2022].

Frost, H. M. (1973). The spinal osteoporoses. Mechanisms of pathogenesis and pathophysiology. *Clinics in Endocrinology and Metabolism*, 2 (2), pp.257–275. [Online]. Available at: doi:10.1016/S0300-595X(73)80043-X [Accessed 12 September 2022].

Frost, H. M. (1987). Bone “mass” and the “mechanostat”: A proposal. *The Anatomical Record*, 219 (1), pp.1–9. [Online]. Available at: doi:10.1002/ar.1092190104.

Frost, H. M. (1990a). Skeletal structural adaptations to mechanical usage (SATMU): 1. Redefining Wolff’s Law: The bone modeling problem. *The Anatomical Record*, 226 (4), pp.403–413. [Online]. Available at: doi:10.1002/ar.1092260402 [Accessed 3 November 2022].

Frost, H. M. (1990b). Skeletal structural adaptations to mechanical usage (SATMU): 2. Redefining Wolff’s Law: The remodeling problem. *The Anatomical Record*, 226 (4), pp.414–422. [Online]. Available at: doi:10.1002/AR.1092260403 [Accessed 3 November 2022].

Frost, H. M. (2003). Bone’s Mechanostat: A 2003 Update. *Anatomical Record - Part A Discoveries in Molecular, Cellular, and Evolutionary Biology*, 275 (2), Wiley-Liss Inc., pp.1081–1101. [Online]. Available at: doi:10.1002/ar.a.10119 [Accessed 20 May 2022].

García-Morales, P. et al. (2003). Maximum bite force, muscle efficiency and mechanical

advantage in children with vertical growth patterns. *European Journal of Orthodontics*, 25 (3), pp.265–272. [Online]. Available at: doi:10.1093/ejo/25.3.265 [Accessed 31 October 2022].

Garrod, D. A. E. et al. (1928). Excavation of a Mousterian Rock-Shelter at Devil's Tower, Gibraltar. *Journal of the Royal Anthropological institute of Great Britain and Ireland*, 58, pp.33–110. [Online]. Available at: <https://www.jstor.org/stable/4619528> [Accessed 19 September 2022].

Gavião, M. B. D., Raymundo, V. G. and Rentes, A. M. (2007). Masticatory performance and bite force in children with primary dentition. *Brazilian Oral Research*, 21 (2), pp.146–152. [Online]. Available at: doi:10.1590/s1806-83242007000200009 [Accessed 31 October 2022].

Gisel, E. G. (1988). Chewing cycles in 2- to 8-year-old normal children: a developmental profile. *The American journal of occupational therapy. : official publication of the American Occupational Therapy Association*, 42 (1), pp.40–46. [Online]. Available at: doi:10.5014/ajot.42.1.40 [Accessed 31 October 2022].

Giustina, A., Mazziotti, G. and Canalis, E. (2008). Growth hormone, insulin-like growth factors, and the skeleton. *Endocrine Reviews*, 29 (5), pp.535–559. [Online]. Available at: doi:10.1210/er.2007-0036 [Accessed 5 November 2022].

Glorieux, F. (2003). *Pediatric bone: biology & diseases*. [Online]. Available at: [https://books.google.com/books?hl=en&lr=&id=mfidZBqeXccC&oi=fnd&pg=PP1&ots=WhVA4SVMkB&sig=-2xMEoXA3bWZwofqu9E7Y16\\_CY](https://books.google.com/books?hl=en&lr=&id=mfidZBqeXccC&oi=fnd&pg=PP1&ots=WhVA4SVMkB&sig=-2xMEoXA3bWZwofqu9E7Y16_CY) [Accessed 29 July 2022].

Godinho, R. M. (2016). Bone biomechanical function and adaptation. *Cadernos do Geevh*, 5 (1), pp.51–63. [Online]. Available at: [https://www.academia.edu/download/47729016/Godinho\\_2016.pdf](https://www.academia.edu/download/47729016/Godinho_2016.pdf) [Accessed 20 May 2022].

Godinho, R. M. et al. (2017). Analyse par éléments finis du crâne : validité, sensibilité et directions futures. In: *Comptes Rendus - Palevol*. 16 (5–6). 1 August 2017. Elsevier Masson SAS. pp.600–612. [Online]. Available at: doi:10.1016/j.crvp.2016.11.002.

Godinho, R. M. et al. (2018). The biting performance of *Homo sapiens* and *Homo heidelbergensis*. *Journal of Human Evolution*, 118, pp.56–71. [Online]. Available at: doi:10.1016/j.jhevol.2018.02.010.

- Godinho, R. M. and O’Higgins, P. (2018). The biomechanical significance of the frontal sinus in Kabwe 1 (*Homo heidelbergensis*). *Journal of Human Evolution*, 114, pp.141–153. [Online]. Available at: doi:10.1016/j.jhevol.2017.10.007.
- Godinho, R. M., Spikins, P. and O’Higgins, P. (2018). Supraorbital morphology and social dynamics in human evolution. *Nature Ecology and Evolution*, 2 (6), pp.956–961. [Online]. Available at: doi:10.1038/s41559-018-0528-0.
- Goergen, M. J., Holton, N. E. and Grünheid, T. (2017). Morphological interaction between the nasal septum and nasofacial skeleton during human ontogeny. *Journal of Anatomy*, 230 (5), pp.689–700. [Online]. Available at: doi:10.1111/joa.12596 [Accessed 31 October 2022].
- Gokhin, D. S. et al. (2009). Reduced thin filament length in nebulin-knockout skeletal muscle alters isometric contractile properties. *American Journal of Physiology - Cell Physiology*, 296 (5). [Online]. Available at: doi:10.1152/ajpcell.00503.2008.
- Golovanova, L. V. et al. (1999). Mezmaiskaya cave: A neanderthal occupation in the northern caucasus. *Current Anthropology*, 40 (1), pp.77–86. [Online]. Available at: doi:10.1086/515805.
- Gonzalez, P. N., Perez, S. I. and Bernal, V. (2010). Ontogeny of robusticity of craniofacial traits in modern humans: A study of South American populations. *American Journal of Physical Anthropology*, 142 (3), pp.367–379. [Online]. Available at: doi:10.1002/ajpa.21231.
- Goodall, C. (1991). Procrustes Methods in the Statistical Analysis of Shape. *Journal of the Royal Statistical Society: Series B (Methodological)*, 53 (2), pp.285–321. [Online]. Available at: doi:10.1111/j.2517-6161.1991.tb01825.x.
- Goodall, C. (1991). Procrustes Methods in the Statistical Analysis of Shape. *Journal of the Royal Statistical Society: Series B (Methodological)*, 53 (2), pp.285–321. [Online]. Available at: doi:10.1111/J.2517-6161.1991.TB01825.X.
- Goodship, A. E. et al. (1998). Bone loss during long term space flight is prevented by the application of a short term impulsive mechanical stimulus. *Acta Astronautica*, 43 (3–6), pp.65–75. [Online]. Available at: doi:10.1016/S0094-5765(98)00144-1 [Accessed 20 May 2022].

Görke, O. (1904). Beitrag zur funktionellen Gestaltung des Schädels bei den Anthropomorphen und Menschen durch Untersuchung mit Röntgenstrahlen. *Arch. Anthropol.*, 1, pp.91–108. [Online]. Available at: [https://scholar.google.com/scholar?hl=en&as\\_sdt=0%2C5&q=Görke+1904&btnG=](https://scholar.google.com/scholar?hl=en&as_sdt=0%2C5&q=Görke+1904&btnG=) [Accessed 26 April 2022].

Gosman, J. H. et al. (2013). Development of Cortical Bone Geometry in the Human Femoral and Tibial Diaphysis. *Anatomical Record*, 296 (5), pp.774–787. [Online]. Available at: doi:10.1002/ar.22688 [Accessed 19 May 2022].

Gould, S. J. and Lewontin, R. C. (1979). The spandrels of San Marco and the Panglossian paradigm: a critique of the adaptationist programme. *Proceedings of the Royal Society of London - Biological Sciences*, 205 (1161), pp.581–598. [Online]. Available at: doi:10.1098/rspb.1979.0086 [Accessed 26 April 2022].

Gould, S. J. and Lewontin, R. C. (2020). The spandrels of San Marco and the Panglossian paradigm: a critique of the adaptationist programme. In: *Shaping Entrepreneurship Research*. Routledge. pp.204–221. [Online]. Available at: doi:10.1098/rspb.1979.0086.

Gower, J. C. (1975). Generalized procrustes analysis. *Psychometrika*, 40 (1), pp.33–51. [Online]. Available at: doi:10.1007/BF02291478.

Greaves, W. S. (1985). The mammalian postorbital bar as a torsion-resisting helical strut. *Journal of Zoology*, 207 (1), pp.125–136. [Online]. Available at: doi:10.1111/j.1469-7998.1985.tb04918.x.

Greaves, W. S. (1995). Functional predictions from theoretical models of the skull and jaws in reptiles and mammals. *Functional morphology in Vertebrate Paleontology*, pp.99–115. [Online]. Available at: <https://ci.nii.ac.jp/naid/10019806157/> [Accessed 20 May 2022].

Grimston, S. K. et al. (2008). Attenuated response to in vivo mechanical loading in mice with conditional osteoblast ablation of the connexin43 gene (*Gja1*). *Journal of Bone and Mineral Research*, 23 (6), pp.879–886. [Online]. Available at: doi:10.1359/jbmr.080222 [Accessed 5 November 2022].

Grine, F. E. et al. (2010). Craniofacial biomechanics and functional and dietary inferences in hominin paleontology. *Journal of Human Evolution*, 58 (4), pp.293–308. [Online]. Available at: doi:10.1016/j.jhevol.2009.12.001.

Gröning, F., Fagan, M. J. and O'Higgins, P. (2011). The effects of the periodontal ligament on mandibular stiffness: A study combining finite element analysis and geometric morphometrics. *Journal of Biomechanics*, 44 (7), pp.1304–1312. [Online]. Available at: doi:10.1016/j.jbiomech.2011.01.008.

Gröning, F., Bright, J.A., Fagan, M.J. and O'Higgins, P., 2012. Improving the validation of finite element models with quantitative full-field strain comparisons. *Journal of biomechanics*, 45(8), pp.1498-1506.

Gröning, F., Fagan, M. and O'higgins, P. (2013). Comparing the Distribution of Strains with the Distribution of Bone Tissue in a Human Mandible: A Finite Element Study. *Anatomical Record*, 296 (1), pp.9–18. [Online]. Available at: doi:10.1002/ar.22597.

Gross, T. S. et al. (1997). Strain gradients correlate with sites of periosteal bone formation. *Journal of Bone and Mineral Research*, 12 (6), pp.982–988. [Online]. Available at: doi:10.1359/jbmr.1997.12.6.982.

Grün, R. and Stringer, C. B. (1991). Electron spin resonance dating and the evolution of modern humans. *Archaeometry*, 33 (2), pp.153–199. [Online]. Available at: doi:10.1111/j.1475-4754.1991.tb00696.x [Accessed 19 September 2022].

Guatelli-Steinberg, D. et al. (2005). Anterior tooth growth periods in Neandertals were comparable to those of modern humans. *Proceedings of the National Academy of Sciences of the United States of America*, 102 (40), pp.14197–14202. [Online]. Available at: doi:10.1073/pnas.0503108102 [Accessed 25 April 2022].

Gunz, P. et al. (2009). Principles for the virtual reconstruction of hominin crania. *Journal of Human Evolution*, 57 (1), pp.48–62. [Online]. Available at: doi:10.1016/j.jhevol.2009.04.004 [Accessed 25 May 2022].

Gunz, P. et al. (2010). Brain development after birth differs between Neanderthals and modern humans. *Current Biology*, 20 (21), Cell Press., pp.R921–R922. [Online]. Available at: doi:10.1016/j.cub.2010.10.018.

Gunz, P. et al. (2012). A uniquely modern human pattern of endocranial development. Insights from a new cranial reconstruction of the Neandertal newborn from Mezmaiskaya. *Journal of Human Evolution*, 62 (2), pp.300–313. [Online]. Available at: doi:10.1016/j.jhevol.2011.11.013.

Gunz, P. and Mitteroecker, P. (2013). Semilandmarks: A method for quantifying curves and surfaces. *Hystrix*, 24 (1). [Online]. Available at: doi:10.4404/hystrix-24.1-6292 [Accessed 29 April 2022].

Gunz, P., Mitteroecker, P. and Bookstein, F. L. (2005). Semilandmarks in Three Dimensions. In: *Modern Morphometrics in Physical Anthropology*. pp.73–98. [Online]. Available at: doi:10.1007/0-387-27614-9\_3 [Accessed 29 April 2022].

Guo, X. E. (2001). Mechanical properties of cortical bone and cancellous bone tissue. In: *Bone Mechanics Handbook, Second Edition*. pp.10-1-10–24. [Online]. Available at: <https://ci.nii.ac.jp/naid/10011970255/> [Accessed 20 May 2022].

Hall, B. K. (2005). *Bones and Cartilage: Developmental and Evolutionary Skeletal Biology*. [Online]. Available at: doi:10.1016/B978-0-12-319060-4.X5000-3 [Accessed 17 May 2022].

Hall, B. K. and Precious, D. S. (2013). Cleft lip, nose, and palate: The nasal septum as the pacemaker for midfacial growth. *Oral Surgery, Oral Medicine, Oral Pathology and Oral Radiology*, 115 (4), pp.442–447. [Online]. Available at: doi:10.1016/j.oooo.2012.05.005 [Accessed 31 October 2022].

Hall, J. G. (2010). Importance of muscle movement for normal craniofacial development. *Journal of Craniofacial Surgery*, 21 (5), pp.1336–1338. [Online]. Available at: doi:10.1097/SCS.0b013e3181ebcd4f [Accessed 10 December 2022].

Hardy, B. L. (2010a). Climatic variability and plant food distribution in Pleistocene Europe: Implications for Neanderthal diet and subsistence. *Quaternary Science Reviews*, 29 (5–6), pp.662–679. [Online]. Available at: doi:10.1016/j.quascirev.2009.11.016 [Accessed 16 September 2022].

Hardy, K. et al. (2012). Neanderthal medics? Evidence for food, cooking, and medicinal plants entrapped in dental calculus. *Naturwissenschaften*, 99 (8), pp.617–626. [Online]. Available at: doi:10.1007/s00114-012-0942-0.

Hardy, K. et al. (2022). Reconstructing Neanderthal diet: The case for carbohydrates. *Journal of Human Evolution*, 162. [Online]. Available at: doi:10.1016/j.jhevol.2021.103105 [Accessed 16 September 2022].

Hardy, R. W. (2010b). Utilization of plant proteins in fish diets: Effects of global demand

and supplies of fishmeal. *Aquaculture Research*, 41 (5), pp.770–776. [Online]. Available at: doi:10.1111/j.1365-2109.2009.02349.x.

Hart, N. H. et al. (2017). Mechanical basis of bone strength: Influence of bone material, bone structure and muscle action. *Journal of Musculoskeletal Neuronal Interactions*, 17 (3), pp.114–139. [Online]. Available at: <https://www.ncbi.nlm.nih.gov/pmc/articles/pmc5601257/> [Accessed 20 May 2022].

Hartstone-Rose, A. et al. (2018). Dietary Correlates of Primate Masticatory Muscle Fiber Architecture. *Anatomical Record*, 301 (2), pp.311–324. [Online]. Available at: doi:10.1002/ar.23715 [Accessed 19 May 2022].

Hauser, C. (1909). Notes on the geography of palestine. *Palestine Exploration Quarterly*, 41 (4), pp.275–279. [Online]. Available at: doi:10.1179/PEQ.1909.41.4.275.

Hawks, J. et al. (2000). Population bottlenecks and Pleistocene human evolution. *Molecular Biology and Evolution*, 17 (1), pp.2–22. [Online]. Available at: doi:10.1093/oxfordjournals.molbev.a026233 [Accessed 25 April 2022].

Hay, E. D. (2005). The mesenchymal cell, its role in the embryo, and the remarkable signaling mechanisms that create it. *Developmental Dynamics*, 233 (3), pp.706–720. [Online]. Available at: doi:10.1002/DVDY.20345 [Accessed 29 July 2022].

Heim, J. L. (1974). Les hommes fossiles de la Ferrassie (Dordogne) et le problème de la définition des Neandertaliens classiques. *Anthropologie*, 78 (2), pp.321–378. [Online]. Available at: <https://pascal-francis.inist.fr/vibad/index.php?action=getRecordDetail&idt=PASCALGEODEBRGM7520011419> [Accessed 19 September 2022].

Henri-Martin, G. (1964). La dernière occupation moustérienne de La Quina (Charente) datation par le radiocarbone. *Comptes rendus hebdomadaires des séances de l'académie des sciences*, 258 (13), p.3533. [Online]. Available at: [https://scholar.google.com/scholar?hl=en&as\\_sdt=0%2C5&q=La+derniere+occupation+mousterienne+de+La+Quina+%28Charcnte%29.&btnG=](https://scholar.google.com/scholar?hl=en&as_sdt=0%2C5&q=La+derniere+occupation+mousterienne+de+La+Quina+%28Charcnte%29.&btnG=) [Accessed 19 September 2022].

Henry, A. G., Brooks, A. S. and Piperno, D. R. (2011). Microfossils in calculus demonstrate consumption of plants and cooked foods in Neanderthal diets (Shanidar III, Iraq; Spy I and II, Belgium). *Proceedings of the National Academy of Sciences of the*

*United States of America*, 108 (2), pp.486–491. [Online]. Available at: doi:10.1073/pnas.1016868108.

Herrel, A. and O'Reilly, J. C. (2006). Ontogenetic scaling of bite force in lizards and turtles. In: *Physiological and Biochemical Zoology*. 79 (1). January 2006. pp.31–42. [Online]. Available at: doi:10.1086/498193.

Herring, S. W. and Mucci, R. J. (1991). In vivo strain in cranial sutures: The zygomatic arch. *Journal of Morphology*, 207 (3), pp.225–239. [Online]. Available at: doi:10.1002/jmor.1052070302.

Hesse, H. and Ullrich, H. (1966). *Schädel des "Homo mousteriensis Hauseri"*. [Online]. Available at: [https://scholar.google.com/scholar?hl=en&as\\_sdt=0%2C5&q=Schadel+der+%22Homo+mousteriensis+Hauseri%22+wiedergefunden+1966+Hesse&btnG=](https://scholar.google.com/scholar?hl=en&as_sdt=0%2C5&q=Schadel+der+%22Homo+mousteriensis+Hauseri%22+wiedergefunden+1966+Hesse&btnG=) [Accessed 19 September 2022].

Hilloowala, R. A. and Trent, R. B. (1988a). Supraorbital ridge and masticatory apparatus I: Primates. *Human Evolution*, 3 (5), pp.343–350. [Online]. Available at: doi:10.1007/BF02447216.

Hilloowala, R. A. and Trent, R. B. (1988b). Supraorbital ridge and masticatory apparatus II: Humans (Eskimos). *Human Evolution*, 3 (5), pp.351–356. [Online]. Available at: doi:10.1007/BF02447217.

Hofer, H. E. L. M. J. T. (1952). Der Gestaltwandel des Schädels der Säugetiere und Vögel. mit besonderer Berücksichtigung der Knickungstypen und der Schädelbasis. *Verh Anat Ges*, 99, pp.102–126. [Online]. Available at: [https://scholar.google.com/scholar?hl=en&as\\_sdt=0%2C5&q=Der+Gestaltwandels+des+Schadels+der+Saugetiere+und+Vogel%2C+mit+besonderer+Knickungstypen+und+der+SchadelbasikBerucksichtigung+der&btnG=](https://scholar.google.com/scholar?hl=en&as_sdt=0%2C5&q=Der+Gestaltwandels+des+Schadels+der+Saugetiere+und+Vogel%2C+mit+besonderer+Knickungstypen+und+der+SchadelbasikBerucksichtigung+der&btnG=) [Accessed 3 November 2022].

Hoffecker, J. F. (2009). Neanderthal and Modern Human Diet in Eastern Europe. In: *Vertebrate Paleobiology and Paleoanthropology*. Springer. pp.87–98. [Online]. Available at: doi:10.1007/978-1-4020-9699-0\_6.

Holly Smith, B., Crummett, T. L. and Brandt, K. L. (1994). Ages of eruption of primate teeth: A compendium for aging individuals and comparing life histories. *American Journal of Physical Anthropology*, 37 (19 S), pp.177–231. [Online]. Available at:

doi:10.1002/AJPA.1330370608.

Holton, N. E. et al. (2011). Nasal Septal and Premaxillary Developmental Integration: Implications for Facial Reduction in Homo. *Anatomical Record*, 294 (1), pp.68–78. [Online]. Available at: doi:10.1002/ar.21288 [Accessed 31 October 2022].

Holton, N. E. et al. (2016). The ontogeny of nasal shape: An analysis of sexual dimorphism in a longitudinal sample. *American Journal of Physical Anthropology*, 160 (1), pp.52–61. [Online]. Available at: doi:10.1002/ajpa.22941.

Holton, N. E., Yokley, T. R. and Figueroa, A. (2012). Nasal septal and craniofacial form in European- and African-derived populations. *Journal of Anatomy*, 221 (3), pp.263–274. [Online]. Available at: doi:10.1111/j.1469-7580.2012.01533.x [Accessed 31 October 2022].

Howell, F. C. (1951). The place of Neanderthal man in human evolution. *American Journal of Physical Anthropology*, 9 (4), pp.379–416. [Online]. Available at: doi:10.1002/ajpa.1330090402.

Hsieh, Y. F. et al. (2001). Mechanical loading of diaphyseal bone in vivo: The strain threshold for an osteogenic response varies with location. *Journal of Bone and Mineral Research*, 16 (12), pp.2291–2297. [Online]. Available at: doi:10.1359/jbmr.2001.16.12.2291 [Accessed 5 November 2022].

Hublin, J.-J. (1998). Climatic Changes, Paleogeography, and the Evolution of the Neandertals. In: *Neandertals and Modern Humans in Western Asia*. Kluwer Academic Publishers. pp.295–310. [Online]. Available at: doi:10.1007/0-306-47153-1\_18.

Hublin, J. J. (2000). Modern-nonmodern hominid interactions: a Mediterranean perspective. In: *The geography of Neandertals and modern humans in Europe and the greater Mediterranean*. pp.157–182. [Online]. Available at: <https://ci.nii.ac.jp/naid/10029566860/> [Accessed 1 November 2022].

Huiskes, R. et al. Adaptive bone-remodeling theory applied to prosthetic-design analysis. *Elsevier*. [Online]. Available at: <https://www.sciencedirect.com/science/article/pii/0021929087900303> [Accessed 5 November 2022].

Humphrey, J. D. and Delange, S. . (2004). *An Introduction to Biomechanics*. Springer

(Ed). [Online]. Available at: doi:10.1302/0301-620x.50b1.242 [Accessed 20 May 2022].

Hylander, W. L. (1977). Morphological changes in human teeth and jaws in a high-attrition environment. In: *Orofacial Growth and Development*. pp.301–330. [Online]. Available at: doi:10.1515/9783110807554.301 [Accessed 6 November 2022].

Hylander, W. L. and Johnson, K. R. (1997). In vivo bone strain patterns in the zygomatic arch of macaques and the significance of these patterns for functional interpretations of craniofacial form. *American Journal of Physical Anthropology*, 102 (2), pp.203–232. [Online]. Available at: doi:10.1002/(SICI)1096-8644(199702)102:2<203::AID-AJPA5>3.0.CO;2-Z.

Hylander, W. L., Johnson, K. R. and Picq, P. G. (1991). Masticatory-stress hypotheses and the supraorbital region of primates. *American Journal of Physical Anthropology*, 86 (1), pp.1–36. [Online]. Available at: doi:10.1002/ajpa.1330860102.

Hylander, W. L., Picq, P. G. and Johnson, K. R. (1991). Function of the supraorbital region of primates. *Archives of Oral Biology*, 36 (4), pp.273–281. [Online]. Available at: doi:10.1016/0003-9969(91)90097-E [Accessed 25 April 2022].

Ingervall, B. and Minder, C. (1997). Correlation between maximum bite force and facial morphology in children. *Angle Orthodontist*, 67 (6), pp.415–424. [Online]. Available at: <https://meridian.allenpress.com/angle-orthodontist/article-abstract/67/6/415/56667> [Accessed 27 April 2022].

Jaslow, C. R. (1990). Mechanical properties of cranial sutures. *Journal of Biomechanics*, 23 (4), pp.313–321. [Online]. Available at: doi:10.1016/0021-9290(90)90059-C [Accessed 5 November 2022].

Jaslow, C. R. and Biewener, A. A. (1995). Strain patterns in the horncores, cranial bones and sutures of goats (*Capra hircus*) during impact loading. *Journal of Zoology*, 235 (2), pp.193–210. [Online]. Available at: doi:10.1111/j.1469-7998.1995.tb05137.x.

Jin, S.W., Sim, K.B. and Kim, S.D., 2016. Development and growth of the normal cranial vault: an embryologic review. *Journal of Korean Neurosurgical Society*, 59(3), pp.192-196.

Judex, S. et al. (2007). Low-magnitude mechanical signals that stimulate bone formation in the ovariectomized rat are dependent on the applied frequency but not on the strain

magnitude. *Journal of Biomechanics*, 40 (6), pp.1333–1339. [Online]. Available at: doi:10.1016/j.jbiomech.2006.05.014 [Accessed 20 May 2022].

Judex, S., Donahue, L. R. and Rubin, C. (2002). Genetic predisposition to low bone mass is paralleled by an enhanced sensitivity to signals anabolic to the skeleton. *The FASEB journal*, 16 (10), pp.1280–1282. [Online]. Available at: doi:10.1096/fj.01-0913fje [Accessed 20 October 2022].

Julien, K. C. et al. (1996). Normal masticatory performance in young adults and children. *Archives of Oral Biology*, 41 (1), pp.69–75. [Online]. Available at: doi:10.1016/0003-9969(95)00098-4 [Accessed 31 October 2022].

Kamegai, T. et al. (2005). A determination of bite force in northern Japanese children. *European Journal of Orthodontics*, 27 (1), pp.53–57. [Online]. Available at: doi:10.1093/ejo/cjh090 [Accessed 27 April 2022].

Katz, J. L. et al. (2008). Mechanics of hard tissue. In: *Biomechanics: Principles and Practices*. pp.1-1–26. [Online]. Available at: doi:10.1201/b15575 [Accessed 20 May 2022].

Keaveny, T. M. et al. (2001). Biomechanics of trabecular bone. *Annual Review of Biomedical Engineering*, 3, pp.307–333. [Online]. Available at: doi:10.1146/annurev.bioeng.3.1.307.

Kelley, J. and Schwartz, G. T. (2010). Dental development and life history in living African and Asian apes. *Proceedings of the National Academy of Sciences of the United States of America*, 107 (3), pp.1035–1040. [Online]. Available at: doi:10.1073/PNAS.0906206107.

Kendall, D. G. (1977). The diffusion of shape. *Advances in Applied Probability*, 9 (3), pp.428–430. [Online]. Available at: doi:10.2307/1426091 [Accessed 26 April 2022].

Kendall, D. G. (1984). Shape manifolds, procrustean metrics, and complex projective spaces. *Bulletin of the London Mathematical Society*, 16 (2), pp.81–121. [Online]. Available at: doi:10.1112/blms/16.2.81.

Kenkre, J. S. and Bassett, J. H. D. (2018). The bone remodeling cycle. *Annals of Clinical Biochemistry*, 55 (3), pp.308–327. [Online]. Available at: doi:10.1177/0004563218759371 [Accessed 17 May 2022].

- Kent, J. T., Tyler, D. E. and Vardi, Y. (1994). A curious likelihood identity for the multivariate t-distribution. *Communications in Statistics - Simulation and Computation*, 23 (2), pp.441–453. [Online]. Available at: doi:10.1080/03610919408813180.
- Klein-Nulend, J. and Bonewald, L. F. (2019). The osteocyte. In: *Principles of Bone Biology*. pp.133–162. [Online]. Available at: doi:10.1016/B978-0-12-814841-9.00006-3 [Accessed 17 May 2022].
- Klingenberg, C. P. (2013). Cranial integration and modularity: Insights into evolution and development from morphometric data. *Hystrix*, 24 (1), pp.43–58. [Online]. Available at: doi:10.4404/hystrix-24.1-6367 [Accessed 29 April 2022].
- Klingenberg, C. P. and Marugán-Lobón, J. (2013). Evolutionary covariation in geometric morphometric data: Analyzing integration, modularity, and allometry in a phylogenetic context. *Systematic Biology*, 62 (4), pp.591–610. [Online]. Available at: doi:10.1093/sysbio/syt025 [Accessed 29 April 2022].
- Klingenberg, C. P. and McIntyre, G. S. (1998). Geometric morphometrics of developmental instability: Analyzing patterns of fluctuating asymmetry with procrustes methods. *Evolution*, 52 (5), pp.1363–1375. [Online]. Available at: doi:10.1111/j.1558-5646.1998.tb02018.x.
- Klingenberg, C. P., McIntyre, G. S. and Zaklan, S. D. (1998). Left-right asymmetry of fly wings and the evolution of body axes. *Proceedings of the Royal Society B: Biological Sciences*, 265 (1402), pp.1255–1259. [Online]. Available at: doi:10.1098/rspb.1998.0427.
- Koolstra, J. H. et al. (1988). A three-dimensional mathematical model of the human masticatory system predicting maximum possible bite forces. *Journal of Biomechanics*, 21 (7), pp.563–576. [Online]. Available at: doi:10.1016/0021-9290(88)90219-9 [Accessed 31 October 2022].
- Kranioti, E. F. et al. (2009). Remodeling patterns of occipital growth: A preliminary report. *Anatomical Record*, 292 (11), pp.1764–1770. [Online]. Available at: doi:10.1002/ar.20997 [Accessed 25 April 2022].
- Kranioti, E. F. et al. (2011). Virtual assessment of the endocranial morphology of the early modern European fossil calvaria from Cioclovina, Romania. *Anatomical Record*, 294 (7), pp.1083–1092. [Online]. Available at: doi:10.1002/ar.21420 [Accessed 5

November 2022].

Krantz, G. S. (1973). Cranial Hair and Brow Ridges. *The Australian Journal of Anthropology*, 9 (2), pp.109–111. [Online]. Available at: doi:10.1111/j.1835-9310.1973.tb01381.x [Accessed 25 April 2022].

Krimmel, M. et al. (2015). Three-dimensional normal facial growth from birth to the age of 7 Years. *Plastic and Reconstructive Surgery*, 136 (4), pp.490e-501e. [Online]. Available at: doi:10.1097/PRS.0000000000001612 [Accessed 19 April 2022].

Krovitz, G. E., Thompson, J. L. and Nelson, A. J. (2009). *Hominid growth and development from australopithecines to Middle Pleistocene Homo*. [Online]. Available at: doi:10.1017/cbo9780511542565.011 [Accessed 22 April 2022].

Krueger, K.L., Willman, J.C., Matthews, G.J., Hublin, J.J. and Pérez-Pérez, A., 2019. Anterior tooth-use behaviors among early modern humans and Neandertals. *Plos one*, 14(11), p.e0224573.

Kular, J. et al. (2012). An overview of the regulation of bone remodelling at the cellular level. *Clinical Biochemistry*, 45 (12), pp.863–873. [Online]. Available at: doi:10.1016/j.clinbiochem.2012.03.021 [Accessed 17 May 2022].

Kupczik, K. et al. (2007). Assessing mechanical function of the zygomatic region in macaques: Validation and sensitivity testing of finite element models. *Journal of Anatomy*, 210 (1), pp.41–53. [Online]. Available at: doi:10.1111/j.1469-7580.2006.00662.x [Accessed 25 April 2022].

Kupczik, K. et al. (2009). Masticatory loading and bone adaptation in the supraorbital torus of developing macaques. *American Journal of Physical Anthropology*, 139 (2), pp.193–203. [Online]. Available at: doi:10.1002/ajpa.20972.

Kurihara, S. and Enlow, D. H. (1980). An electron microscopic study of attachments between periodontal fibers and bone during alveolar remodeling. *American Journal of Orthodontics*, 77 (5), pp.516–531. [Online]. Available at: doi:10.1016/0002-9416(80)90131-1 [Accessed 25 April 2022].

Kuzawa, C. W. et al. (2014). Metabolic costs and evolutionary implications of human brain development. *Proceedings of the National Academy of Sciences of the United States of America*, 111 (36), pp.13010–13015. [Online]. Available at:

- doi:10.1073/pnas.1323099111 [Accessed 16 September 2022].
- Lacruz, R. S. et al. (2013). Facial Morphogenesis of the Earliest Europeans. *PLoS ONE*, 8 (6). [Online]. Available at: doi:10.1371/journal.pone.0065199.
- Lacruz, R. S. et al. (2015a). Distinct growth of the nasomaxillary complex in Au. sediba. *Scientific Reports*, 5. [Online]. Available at: doi:10.1038/srep15175.
- Lacruz, R. S. et al. (2015b). Ontogeny of the maxilla in Neanderthals and their ancestors. *Nature Communications*, 6. [Online]. Available at: doi:10.1038/ncomms9996.
- Lacruz, R. S. et al. (2019). The evolutionary history of the human face. *Nature Ecology and Evolution*, 3 (5), pp.726–736. [Online]. Available at: doi:10.1038/s41559-019-0865-7.
- Lahr, M. M. and Wright, R. V. S. (1996). The question of robusticity and the relationship between cranial size and shape in Homo sapiens. *Journal of Human Evolution*, 31 (2), pp.157–191. [Online]. Available at: doi:10.1006/jhev.1996.0056 [Accessed 3 November 2022].
- Landi, F. and O’Higgins, P., 2019. Applying geometric morphometrics to digital reconstruction and anatomical investigation. *Biomedical Visualisation: Volume 4*, pp.55-71.
- Landi, F. (2020). *Craniofacial growth and development in modern humans and Neanderthals*. PhD diss., University of Hull and the University of York. [Online]. Available at: <https://ethos.bl.uk/OrderDetails.do?uin=uk.bl.ethos.824857> [Accessed 12 December 2022].
- Landi, F. et al. (2021). The role of the nasal region in craniofacial growth: An investigation using path analysis. *Anatomical Record*, (April), pp.1–18. [Online]. Available at: doi:10.1002/ar.24719.
- Lang, J., Maier, R. and Schafhauser, O. (1984). Über die postnatale vergrößerung der foramina rotundum, ovale et spinosum und deren lageveränderungen. *Anatomischer Anzeiger*, 156 (5), pp.351–387. [Online]. Available at: <https://europepmc.org/article/med/6486466> [Accessed 30 September 2022].
- Lanyon, L. E. (1987). Functional strain in bone tissue as an objective, and controlling stimulus for adaptive bone remodeling. *Journal of Biomechanics*, 20 (11–12), pp.1083–1093. [Online]. Available at: doi:10.1016/0021-9290(87)90026-1 [Accessed 1 August

2022].

Lanyon, L. E. and Rubin, C. T. (1984). Static vs dynamic loads as an influence on bone remodelling. *Journal of Biomechanics*, 12 (17), pp.897–905. [Online]. Available at: doi:10.1016/0021-9290(85)90028-4 [Accessed 20 May 2022].

Larsson, E. (1998). Orthodontic aspects on feeding of young children: 1. A comparison between Swedish and Norwegian-Sami children. *Swedish Dental Journal*, 22 (3), pp.117–121. [Online]. Available at: <https://europepmc.org/article/med/9768459> [Accessed 31 October 2022].

Ledogar, J. A. et al. (2016). Human feeding biomechanics: Performance, variation, and functional constraints. *PeerJ*, 2016 (7). [Online]. Available at: doi:10.7717/peerj.2242.

Lieberman, D. E. et al. (2003). Optimization of bone growth and remodeling in response to loading in tapered mammalian limbs. *Journal of Experimental Biology*, 206 (18), pp.3125–3138. [Online]. Available at: doi:10.1242/jeb.00514.

Lieberman, D. E. et al. (2004). Effects of food processing on masticatory strain and craniofacial growth in a retrognathic face. *Journal of Human Evolution*, 46 (6), pp.655–677. [Online]. Available at: doi:10.1016/j.jhevol.2004.03.005 [Accessed 19 May 2022].

Lieberman, D. E. et al. (2008). Spatial packing, cranial base angulation, and craniofacial shape variation in the mammalian skull: Testing a new model using mice. *Journal of Anatomy*, 212 (6), pp.720–735. [Online]. Available at: doi:10.1111/j.1469-7580.2008.00900.x [Accessed 20 April 2022].

Lieberman, D. E. (2008). Speculations about the selective basis for modern human craniofacial form. *Evolutionary Anthropology*, 17 (1), pp.55–68. [Online]. Available at: doi:10.1002/evan.20154 [Accessed 31 October 2022].

Lieberman, D. E. (2011). *The Evolution of the Human Head*. [Online]. Available at: doi:10.4159/9780674059443 [Accessed 20 April 2022].

Lieberman, D. E., Mcbratney, B. M. and Krovitz, G. (2002). The evolution and development of cranial form in *Homo sapiens*. *Proceedings of the National Academy of Sciences of the United States of America*, 99 (3), pp.1134–1139. [Online]. Available at: doi:10.1073/pnas.022440799 [Accessed 22 April 2022].

Lieberman, D. E., McBratney, B. M. and Krovitz, G. (2002). The evolution and

development of cranial form in *Homo sapiens*. *Proceedings of the National Academy of Sciences of the United States of America*, 99 (3), pp.1134–1139. [Online]. Available at: doi:10.1073/pnas.022440799.

Lieberman, D. E. and McCarthy, R. C. (1999). The ontogeny of cranial base angulation in humans and chimpanzees and its implications for reconstructing pharyngeal dimensions. *Journal of Human Evolution*, 36 (5), pp.487–517. [Online]. Available at: doi:10.1006/jhev.1998.0287 [Accessed 20 April 2022].

Lieberman, D. E., Pearson, O. M. and Mowbray, K. M. (2000). Basicranial influence on overall cranial shape. *Journal of Human Evolution*, 38 (2), pp.291–315. [Online]. Available at: doi:10.1006/jhev.1999.0335.

Lieberman, D. E., Ross, C. F. and Ravosa, M. J. (2000). The primate cranial base: Ontogeny, function, and integration. *American Journal of Physical Anthropology*, 113 (S31), pp.117–169. [Online]. Available at: doi:10.1002/1096-8644(2000)43:31+<117::aid-ajpa5>3.3.co;2-9.

Lindsay, D. T. (1996). *Functional Human Anatomy*. Inc, M.--Y. B. (Ed). [Online]. Available at: [https://scholar.google.com/scholar?hl=en&as\\_sdt=0%2C5&as\\_ylo=1996&as\\_yhi=1996&q=Functional+Human+Anatomy+Lindsay&btnG=](https://scholar.google.com/scholar?hl=en&as_sdt=0%2C5&as_ylo=1996&as_yhi=1996&q=Functional+Human+Anatomy+Lindsay&btnG=) [Accessed 20 May 2022].

Lipphaus, A. and Witzel, U. (2019). Biomechanical Study of the Development of Long Bones: Finite Element Structure Synthesis of the Human Second Proximal Phalanx Under Growth Conditions. *Anatomical Record*, 302 (8), pp.1389–1398. [Online]. Available at: doi:10.1002/ar.24006 [Accessed 10 December 2022].

Liu, J. et al. (2012). The application of muscle wrapping to voxel-based finite element models of skeletal structures. *Biomechanics and Modeling in Mechanobiology*, 11 (1–2), pp.35–47. [Online]. Available at: doi:10.1007/s10237-011-0291-5 [Accessed 24 November 2022].

Liversidge, H. M. (1994). Accuracy of age estimation from developing teeth of a population of known age (0–5.4 years). *International Journal of Osteoarchaeology*, 4 (1), pp.37–45. [Online]. Available at: doi:10.1002/oa.1390040107.

Loboa, E. G., Beaupré, G. S. and Carter, D. R. (2001). Mechanobiology of initial pseudarthrosis formation with oblique fractures. *Journal of Orthopaedic Research*, 19

(6), pp.1067–1072. [Online]. Available at: doi:10.1016/S0736-0266(01)00028-6 [Accessed 5 November 2022].

Logan, D. L. (2016). A first course in the finite element method. *Finite Elements in Analysis and Design*, 3 (2), pp.162–163. [Online]. Available at: doi:10.1016/0168-874x(87)90008-4 [Accessed 20 April 2022].

Macchiarelli, R. et al. (2006). How Neanderthal molar teeth grew. *Nature*, 444 (7120), pp.748–751. [Online]. Available at: doi:10.1038/nature05314 [Accessed 1 November 2022].

Macchiarelli, R. et al. (2013). From outer to inner structural morphology in dental anthropology: integration of the third dimension in the visualization and quantitative analysis of fossil remains. In: *Anthropological Perspectives on Tooth Morphology*. pp.250–277. [Online]. Available at: doi:10.1017/cbo9780511984464.011 [Accessed 12 September 2022].

Machanda, Z. et al. (2015). Dental eruption in East African wild chimpanzees. *Journal of Human Evolution*, 82, pp.137–144. [Online]. Available at: doi:10.1016/j.jhevol.2015.02.010 [Accessed 20 April 2022].

Madre-Dupouy, M. (1992). *L'enfant du Roc de Marsal: étude analytique et comparative*. [Online]. Available at: [https://scholar.google.com/scholar?hl=en&as\\_sdt=0%2C5&q=Madre-Dupouy%2C+1992&btnG=](https://scholar.google.com/scholar?hl=en&as_sdt=0%2C5&q=Madre-Dupouy%2C+1992&btnG=) [Accessed 19 September 2022].

Mahoney, P. et al. (2021). Growth of Neanderthal infants from Krapina (120-130 ka), Croatia. *Proceedings of the Royal Society B: Biological Sciences*, 288 (1963). [Online]. Available at: doi:10.1098/rspb.2021.2079 [Accessed 18 August 2022].

Maini, P. K. et al. (2012). Turing's model for biological pattern formation and the robustness problem. *Interface Focus*, 2 (4), pp.487–496. [Online]. Available at: doi:10.1098/rsfs.2011.0113.

Maki, K. et al. (2001). A study on the measurement of occlusal force and masticatory efficiency in school age Japanese children. *International Journal of Paediatric Dentistry*, 11 (4), pp.281–285. [Online]. Available at: doi:10.1046/j.1365-263X.2001.00298.x.

Manolagas, S. C. and Almeida, M. S. (2018). Gonadal steroids. In: *Primer on the*

*Metabolic Bone Diseases and Disorders of Mineral Metabolism*. pp.194–204. [Online]. Available at: doi:10.1002/9781119266594.ch26 [Accessed 17 May 2022].

Mansoor, A. et al. (2015). Segmentation and image analysis of abnormal lungs at CT: Current approaches, challenges, and future trends. *Radiographics*, 35 (4), pp.1056–1076. [Online]. Available at: doi:10.1148/rg.2015140232 [Accessed 12 September 2022].

Marcucio, R. et al. (2011). Mechanisms that underlie co-variation of the brain and face. *genesis*, 49 (4), pp.177–189. [Online]. Available at: doi:10.1002/dvg.20710 [Accessed 3 November 2022].

Marcus, L. F. and Corti, M. (1996). Overview of the New, or Geometric Morphometrics. In: *Advances in Morphometrics*. Springer US. pp.1–13. [Online]. Available at: doi:10.1007/978-1-4757-9083-2\_1.

Mardia, K. V., Bookstein, F. L. and Moreton, I. J. (2005). Statistical assessment of bilateral symmetry of shapes. *Biometrika*, 92 (1), pp.249–250. [Online]. Available at: doi:10.1093/biomet/92.1.249-a [Accessed 25 May 2022].

Martin, R. M. and Correa, P. H. S. (2010). Bone quality and osteoporosis therapy. *Arquivos Brasileiros de Endocrinologia & Metabologia*, 54 (2), pp.186–199. [Online]. Available at: doi:10.1590/s0004-27302010000200015 [Accessed 20 May 2022].

Martinez-Maza, C. et al. (2011). Bone remodeling in Neanderthal mandibles from the El Sidrón site (Asturias, Spain). *Biology Letters*, 7 (4), pp.593–596. [Online]. Available at: doi:10.1098/rsbl.2010.1188.

Martinez-Maza, C. et al. (2016). Bone Growth Dynamics of the Facial Skeleton and Mandible in Gorilla gorilla and Pan troglodytes. *Evolutionary Biology*, 43 (1), pp.60–80. [Online]. Available at: doi:10.1007/s11692-015-9350-7 [Accessed 25 April 2022].

Martínez-Maza, C. and Rosas, A. (2002). Bone remodeling in the Atapuerca-SH mandibles. Implications for growth patterns in middle pleistocene hominids. *Am. J. Phys. Anthropol.*, (115), pp.107–108. [Online]. Available at: [https://scholar.google.com/scholar?hl=en&as\\_sdt=0%2C5&q=Bone+remodeling+in+the+Atapuerca-SH+mandibles.+Implications+for+growth+patterns+in+middle+pleistocene+hominids.&btnG=](https://scholar.google.com/scholar?hl=en&as_sdt=0%2C5&q=Bone+remodeling+in+the+Atapuerca-SH+mandibles.+Implications+for+growth+patterns+in+middle+pleistocene+hominids.&btnG=) [Accessed 3 November 2022].

- Martinez-Maza, C., Rosas, A. and Nieto-Díaz, M. (2013). Postnatal changes in the growth dynamics of the human face revealed from bone modelling patterns. *Journal of Anatomy*, 223 (3), pp.228–241. [Online]. Available at: doi:10.1111/joa.12075 [Accessed 25 April 2022].
- Mazza, D. et al. (2009). Anatomic examination of the upper head of the lateral pterygoid muscle using magnetic resonance imaging and clinical data. *Journal of Craniofacial Surgery*, 20 (5), pp.1508–1511. [Online]. Available at: doi:10.1097/SCS.0b013e3181b09c32 [Accessed 6 November 2022].
- McCollum, M. A. (1999). The robust australopithecine face: A morphogenetic perspective. *Science*, 284 (5412), pp.301–305. [Online]. Available at: doi:10.1126/science.284.5412.301 [Accessed 25 April 2022].
- McCollum, M. A. (2008). Nasomaxillary remodeling and facial form in robust *Australopithecus*: a reassessment. *Journal of Human Evolution*, 54 (1), pp.2–14. [Online]. Available at: doi:10.1016/j.jhevol.2007.05.013 [Accessed 25 April 2022].
- Mellars, P. (1996). *The Neanderthal legacy: An archaeological perspective from western Europe*. [Online]. Available at: doi:10.5860/choice.34-1013 [Accessed 19 September 2022].
- Milne, N. and O’Higgins, P. (2012). Scaling of form and function in the xenarthran femur: A 100-fold increase in body mass is mitigated by repositioning of the third trochanter. *Proceedings of the Royal Society B: Biological Sciences*, 279 (1742), pp.3449–3456. [Online]. Available at: doi:10.1098/rspb.2012.0593 [Accessed 27 April 2022].
- Mitteroecker, P. et al. (2004). Comparison of cranial ontogenetic trajectories among great apes and humans. *Journal of Human Evolution*, 46 (6), pp.679–698. [Online]. Available at: doi:10.1016/j.jhevol.2004.03.006.
- Mitteroecker, P. et al. (2013). A brief review of shape, form, and allometry in geometric morphometrics, with applications to human facial morphology. *Hystrix*, 24 (1), pp.1–8. [Online]. Available at: doi:10.4404/hystrix-24.1-6369.
- Mitteroecker, P. and Gunz, P. (2009). Advances in Geometric morphometrics. *Evolutionary Biology*, 36 (2), pp.235–247. [Online]. Available at: doi:10.1007/s11692-009-9055-x.

- Mitteroecker, P., Gunz, P. and Bookstein, F. L. (2005). Heterochrony and geometric morphometrics: A comparison of cranial growth in *Pan paniscus* versus *Pan troglodytes*. *Evolution and Development*, 7 (3), pp.244–258. [Online]. Available at: doi:10.1111/j.1525-142X.2005.05027.x [Accessed 29 April 2022].
- Moazen, M. et al. (2009). Assessment of the role of sutures in a lizard skull: A computer modelling study. *Proceedings of the Royal Society B: Biological Sciences*, 276 (1654), pp.39–46. [Online]. Available at: doi:10.1098/rspb.2008.0863.
- Moore, K., Persaud, T. and Torchia, M. (2018). *The developing human-e-book: clinically oriented embryology*. [Online]. Available at: <https://books.google.com/books?hl=en&lr=&id=OTaBDwAAQBAJ&oi=fnd&pg=PP1&dq=The+Developing+Human+&ots=GoBKvfmm1x&sig=5nQcQ0yeF6xYH54H0w3AGv-hi3w> [Accessed 29 July 2022].
- Mori, S. and Burr, D. B. (1993). Increased intracortical remodeling following fatigue damage. *Bone*, 14 (2), pp.103–109. [Online]. Available at: doi:10.1016/8756-3282(93)90235-3 [Accessed 3 November 2022].
- Mosley, J. R. and Lanyon, L. E. (1998). Strain rate as a controlling influence on adaptive modeling in response to dynamic loading of the ulna in growing male rats. *Bone*, 23 (4), pp.313–318. [Online]. Available at: doi:10.1016/S8756-3282(98)00113-6 [Accessed 20 May 2022].
- Moss, M. L. (1997a). The functional matrix hypothesis revisited. 2. The role of an osseous connected cellular network. *American journal of orthodontics and dentofacial orthopedics : official publication of the American Association of Orthodontists, its constituent societies, and the American Board of Orthodontics*, 112 (2), pp.221–226. [Online]. Available at: doi:10.1016/S0889-5406(97)70249-X [Accessed 17 May 2022].
- Moss, M. L. (1997b). The functional matrix hypothesis revisited. 4. The epigenetic antithesis and the resolving synthesis. *American journal of orthodontics and dentofacial orthopedics : official publication of the American Association of Orthodontists, its constituent societies, and the American Board of Orthodontics*, 112 (4), pp.410–417. [Online]. Available at: doi:10.1016/S0889-5406(97)70049-0 [Accessed 17 May 2022].
- Moss, M. L. and Young, R. W. (1960). A functional approach to craniology. *American Journal of Physical Anthropology*, 18 (4), pp.281–292. [Online]. Available at:

doi:10.1002/ajpa.1330180406 [Accessed 19 April 2022].

Mountain, G., Wood, D. and Toumba, J. (2011). Bite force measurement in children with primary dentition. *International Journal of Paediatric Dentistry*, 21 (2), pp.112–118. [Online]. Available at: doi:10.1111/j.1365-263X.2010.01098.x [Accessed 30 August 2022].

Mowbray, K. (2005). Surface bone histology of the occipital bone in humans and chimpanzees. *Anatomical Record - Part B New Anatomist*, 283 (1), pp.14–22. [Online]. Available at: doi:10.1002/ar.b.20055 [Accessed 25 April 2022].

Ms, P. D. L. and Cpe, Z. (2001). Neanderthal cranial ontogeny and its implications for late hominid diversity. *Nature*, 412 (August), pp.534–538.

Nakashige, M., Smith, A. L. and Strait, D. S. (2011). Biomechanics of the macaque postorbital septum investigated using finite element analysis: Implications for anthropoid evolution. *Journal of Anatomy*, 218 (1), pp.142–150. [Online]. Available at: doi:10.1111/j.1469-7580.2010.01316.x.

Napier, S. S. and Ullah, R. M. (2017). Nasal cavities and paranasal sinuses. In: *Histopathology Specimens: Clinical, Pathological and Laboratory Aspects: Third Edition*. pp.149–156. [Online]. Available at: doi:10.1007/978-3-319-57360-1\_13 [Accessed 20 April 2022].

Nava, A. et al. (2020). Early life of Neanderthals. *Proceedings of the National Academy of Sciences of the United States of America*, 117 (46), pp.28719–28726. [Online]. Available at: doi:10.1073/pnas.2011765117.

Neaux, D. et al. (2013). Facial Orientation and Facial Shape in Extant Great Apes: A Geometric Morphometric Analysis of Covariation. *PLoS ONE*, 8 (2). [Online]. Available at: doi:10.1371/journal.pone.0057026.

Neaux, D. et al. (2015). Implications of the Relationship Between Basicranial Flexion and Facial Orientation for the Evolution of Hominid Craniofacial Structures. *International Journal of Primatology*, 36 (6), pp.1120–1131. [Online]. Available at: doi:10.1007/s10764-015-9886-5 [Accessed 31 October 2022].

Neaux, D. et al. (2018). Basicranium and face: Assessing the impact of morphological integration on primate evolution. *Journal of Human Evolution*, 118 (March), pp.43–55.

[Online]. Available at: doi:10.1016/j.jhevol.2018.02.007.

Neaux, D. et al. (2019). Morphological integration affects the evolution of midline cranial base, lateral basicranium, and face across primates. *American Journal of Physical Anthropology*, 170 (1), pp.37–47. [Online]. Available at: doi:10.1002/ajpa.23899.

Neeser, R., Ackermann, R. R. and Gain, J. (2009). Comparing the accuracy and precision of three techniques used for estimating missing landmarks when reconstructing fossil hominin crania. *American Journal of Physical Anthropology*, 140 (1), pp.1–18. [Online]. Available at: doi:10.1002/ajpa.21023.

Nelson, A. J., Krovitz, G. E. and Thompson, J. L. (2009). Hominid growth and development in Upper Pleistocene Homo . In: *Patterns of Growth and Development in the Genus Homo* . pp.412–435. [Online]. Available at: doi:10.1017/cbo9780511542565.017 [Accessed 22 April 2022].

Netter, F. and Scott, J. (2019). *Atlas d'anatomie humaine*. [Online]. Available at: [https://books.google.com/books?hl=en&lr=&id=XKegDwAAQBAJ&oi=fnd&pg=PP1&dq=Netter,+2019&ots=e0tPKgjI\\_6&sig=nrGZNazISDcZGv0IJRHs4zcdE20](https://books.google.com/books?hl=en&lr=&id=XKegDwAAQBAJ&oi=fnd&pg=PP1&dq=Netter,+2019&ots=e0tPKgjI_6&sig=nrGZNazISDcZGv0IJRHs4zcdE20) [Accessed 1 August 2022].

Neubauer, S. et al. (2004). Three-dimensional digital imaging of the partial *Australopithecus africanus* endocranium MLD 37/38. In: *Canadian Association of Radiologists Journal*. 55 (4). 2004. pp.271–278. [Online]. Available at: [https://www.researchgate.net/profile/Philipp-Gunz/publication/8352943\\_Three-dimensional\\_digital\\_imaging\\_of\\_the\\_partial\\_Australopithecus\\_africanus\\_endocranium\\_MLD\\_3738/links/5f05a8484585155050948600/Three-dimensional-digital-imaging-of-the-partial-Australo](https://www.researchgate.net/profile/Philipp-Gunz/publication/8352943_Three-dimensional_digital_imaging_of_the_partial_Australopithecus_africanus_endocranium_MLD_3738/links/5f05a8484585155050948600/Three-dimensional-digital-imaging-of-the-partial-Australo) [Accessed 5 November 2022].

Neubauer, S., Gunz, P. and Hublin, J. J. (2009). The pattern of endocranial ontogenetic shape changes in humans. *Journal of Anatomy*, 215 (3), pp.240–255. [Online]. Available at: doi:10.1111/j.1469-7580.2009.01106.x [Accessed 29 April 2022].

Nicholson, E. and Harvati, K. (2006). Quantitative analysis of human mandibular shape using three-dimensional geometric morphometrics. *American Journal of Physical Anthropology*, 131 (3), pp.368–383. [Online]. Available at: doi:10.1002/ajpa.20425.

Nordström, P. et al. (1996). High bone mass and altered relationships between bone mass, muscle strength, and body constitution in adolescent boys on a high level of physical

activity. *Bone*, 19 (2), pp.189–195. [Online]. Available at: doi:10.1016/8756-3282(96)00163-9 [Accessed 20 May 2022].

Nowaczewska, W., Kuźmiński, Ł. and Biecek, P. (2015). Morphological relationship between the cranial and supraorbital regions in homo sapiens. *American Journal of Physical Anthropology*, 156 (1), pp.110–124. [Online]. Available at: doi:10.1002/ajpa.22632.

O'Connor, C. F., Franciscus, R. G. and Holton, N. E. (2005). Bite force production capability and efficiency in neandertals and modern humans. *American Journal of Physical Anthropology*, 127 (2), pp.129–151. [Online]. Available at: doi:10.1002/ajpa.20025 [Accessed 25 April 2022].

O'Connor, J. A., Lanyon, L. E. and MacFie, H. (1982). The influence of strain rate on adaptive bone remodeling. *Journal of Biomechanics*, 15 (10), pp.767–781. [Online]. Available at: doi:10.1016/0021-9290(82)90092-6 [Accessed 1 August 2022].

O'Higgins, P. et al. (2007). Modelling the mechanical modulation of bone remodeling fields in the cercopithecine face. *Journal of Anatomy*, 210 (6), pp.772–773. [Online]. Available at: [https://pure.mpg.de/pubman/faces/ViewItemOverviewPage.jsp?itemId=item\\_1554843](https://pure.mpg.de/pubman/faces/ViewItemOverviewPage.jsp?itemId=item_1554843) [Accessed 25 April 2022].

O'Higgins, P. et al. (2011). Combining geometric morphometrics and functional simulation: An emerging toolkit for virtual functional analyses. *Journal of Anatomy*, 218 (1), pp.3–15. [Online]. Available at: doi:10.1111/j.1469-7580.2010.01301.x.

O'Higgins, P. et al. (2012). Virtual Functional Morphology: Novel Approaches to the Study of Craniofacial Form and Function. *Evolutionary Biology*, 39 (4), Springer Verlag., pp.521–535. [Online]. Available at: doi:10.1007/s11692-012-9173-8.

O'Higgins, P., Bastir, M. and Kupczik, K. (2006). Shaping the human face. *International Congress Series*, 1296, pp.55–73. [Online]. Available at: doi:10.1016/j.ics.2006.03.036.

O'Higgins, P., Chadfield, P. and Jones, N. (2001). Facial growth and the ontogeny of morphological variation within and between the primates *Cebus apella* and *Cercocebus torquatus*. *Journal of Zoology*, 254 (3), pp.337–357. [Online]. Available at: doi:10.1017/S095283690100084X [Accessed 25 April 2022].

O'Higgins, P. and Dryden, I. L. (1992). Studies of craniofacial development and evolution. *Archaeology in Oceania*, 27 (3), pp.105–112. [Online]. Available at: doi:10.1002/j.1834-4453.1992.tb00293.x.

O'Higgins, P., Fitton, L. C. and Godinho, R. M. (2019). Geometric morphometrics and finite elements analysis: Assessing the functional implications of differences in craniofacial form in the hominin fossil record. *Journal of Archaeological Science*, 101, pp.159–168. [Online]. Available at: doi:10.1016/j.jas.2017.09.011.

O'Higgins, P. and Jones, N. (1998). Facial growth in *Cercocebus torquatus*: an application of three-dimensional geometric morphometric techniques to the study of morphological variation. *Journal of Anatomy*, 193 (2), pp.251–272. [Online]. Available at: doi:10.1046/j.1469-7580.1998.19320251.x.

O'Higgins, P. and Milne, N. (2013). Applying geometric morphometrics to compare changes in size and shape arising from finite elements analyses. *Hystrix*, 24 (1). [Online]. Available at: doi:10.4404/hystrix-24.1-6284 [Accessed 23 May 2022].

Okay, D. J. et al. (2001). Prosthodontic guidelines for surgical reconstruction of the maxilla. *the Journal of Prosthetic Dentistry*, 86 (4), pp.352–363.

Opperman, L. A. (2000). Cranial sutures as intramembranous bone growth sites. *Developmental Dynamics*, 219 (4), pp.472–485. [Online]. Available at: doi:10.1002/1097-0177(2000)9999:9999<::AID-DVDY1073>3.0.CO;2-F.

Ortner, D. J. (2003). *Identification of Pathological Conditions in Human Skeletal Remains*. [Online]. Available at: doi:10.1016/B978-0-12-528628-2.X5037-6 [Accessed 20 May 2022].

Oxnard, C. E. (1993). Bone and bones, architecture and stress, fossils and osteoporosis. *Journal of Biomechanics*, 26 (SUPPL. 1), pp.63–79. [Online]. Available at: doi:10.1016/0021-9290(93)90080-X.

Oxnard, C. E. (2004). Thoughts on bone biomechanics. *Folia Primatologica*, 75 (4), pp.189–201. [Online]. Available at: doi:10.1159/000078934 [Accessed 7 December 2022].

Oxnard, C. E. and Franklin, D. (2008). Ghosts of the past I: Some muscles and fasciae in the head domain. *Folia Primatologica*, 79 (6), pp.429–440. [Online]. Available at:

doi:10.1159/000151356 [Accessed 5 November 2022].

Oxnard, C., Lannigan, F. and O'Higgins, P. (1995). The mechanism of bone adaptation: tension and resorption in the human incus. *Bone Structure and Remodeling*, (World Scientific Publishing), pp.105–125.

Oyen, O. J., Rice, R. W. and Samuel Cannon, M. (1979). Browridge structure and function in extant primates and Neanderthals. *American Journal of Physical Anthropology*, 51 (1), pp.83–95. [Online]. Available at: doi:10.1002/ajpa.1330510111.

Oyen, O. J. and Tsay, T. P. (1991). A biomechanical analysis of craniofacial form and bite force. *American Journal of Orthodontics and Dentofacial Orthopedics*, 99 (4), pp.298–309. [Online]. Available at: doi:10.1016/0889-5406(91)70012-L [Accessed 3 November 2022].

Paphangkorakit, J. and Osborn, J. W. (1997a). Effect of jaw opening on the direction and magnitude of human incisal bite forces. *Journal of Dental Research*, 76 (1), pp.561–567. [Online]. Available at: doi:10.1177/00220345970760010601 [Accessed 18 April 2022].

Paphangkorakit, J. and Osborn, J. W. (1997b). The effect of pressure on a maximum incisal bite force in man. *Archives of Oral Biology*, 42 (1), pp.11–17. [Online]. Available at: doi:10.1016/S0003-9969(96)00106-9 [Accessed 18 April 2022].

Parkinson, I. H. and Fazzalari, N. L. (2013). Characterisation of Trabecular Bone Structure. In: *Studies in Mechanobiology, Tissue Engineering and Biomaterials*. 5. Springer. pp.31–51. [Online]. Available at: doi:10.1007/8415\_2011\_113 [Accessed 20 May 2022].

Parr, L. A., Waller, B. M. and Vick, S. J. (2007). New developments in understanding emotional facial signals in chimpanzees. *Current Directions in Psychological Science*, 16 (3), pp.117–122. [Online]. Available at: doi:10.1111/J.1467-8721.2007.00487.X.

Patte, E. (1957). *L'enfant Néanderthalien du Pech de L'Azé*. p.248. [Online]. Available at: <https://pascal-francis.inist.fr/vibad/index.php?action=getRecordDetail&idt=GEODEBRGMFR2019132> [Accessed 19 September 2022].

Pearson, O. M. (1997). Postcranial Morphology and the Origin of Modern Humans. *Vasa*, (December), p.1146. [Online]. Available at:

<https://search.proquest.com/openview/8256636494d929e657eb4983828a7425/1?pq-origsite=gscholar&cbl=18750&diss=y> [Accessed 19 May 2022].

Pearson, O. M. and Lieberman, D. E. (2004). The aging of Wolff's 'law': Ontogeny and responses to mechanical loading in cortical bone. *Yearbook of Physical Anthropology*, 47, pp.63–99. [Online]. Available at: doi:10.1002/ajpa.20155.

Perez, S. I., Bernal, V. and Gonzalez, P. N. (2006). Differences between sliding semi-landmark methods in geometric morphometrics , with an application to human craniofacial and dental variation. *Journal of anatomy*, 208 (6), pp.769–784. [Online]. Available at: doi:10.1111/J.1469-7580.2006.00576.X.

Perry, J. M. G. et al. (2014). Anatomy and adaptations of the chewing muscles in Daubentonia (Lemuriformes). *Anatomical Record*, 297 (2), pp.308–316. [Online]. Available at: doi:10.1002/ar.22844 [Accessed 19 May 2022].

Perry, J. M. G., Hartstone-Rose, A. and Logan, R. L. (2011). The Jaw Adductor Resultant and Estimated Bite Force in Primates. *Anatomy Research International*, 2011 (Figure 1), pp.1–11. [Online]. Available at: doi:10.1155/2011/929848.

Peterson, J. and Dechow, P. C. (2003). Material properties of the human cranial vault and zygoma. *Anatomical Record - Part A Discoveries in Molecular, Cellular, and Evolutionary Biology*, 274 (1), pp.785–797. [Online]. Available at: doi:10.1002/ar.a.10096 [Accessed 5 November 2022].

Picq, P. G. and Hylander, W. L. (1989). Endo's stress analysis of the primate skull and the functional significance of the supraorbital region. *American Journal of Physical Anthropology*, 79 (3), pp.393–398. [Online]. Available at: doi:10.1002/ajpa.1330790315.

Piperno, M., Segre, A. and Ronen, A. (1982). The transition from Lower to Middle Palaeolithic in Central Italy: an example from latium. In: *The Transition from Lower to Middle Palaeolithic and the origin of modern man*. pp.203–221. [Online]. Available at: [https://scholar.google.com/scholar?hl=en&as\\_sdt=0%2C5&q=Piperno+and+Segre%2C+1982&btnG=](https://scholar.google.com/scholar?hl=en&as_sdt=0%2C5&q=Piperno+and+Segre%2C+1982&btnG=) [Accessed 19 September 2022].

Ponce De León, M. S. et al. (2008). Neanderthal brain size at birth provides insights into the evolution of human life history. *Proceedings of the National Academy of Sciences of the United States of America*, 105 (37), pp.13764–13768. [Online]. Available at: doi:10.1073/pnas.0803917105 [Accessed 25 April 2022].

Ponce De Leon, M. S. and Zollikofer, C. P. E. (1999). New evidence from Le Moustier 1: Computer-assisted reconstruction and morphometry of the skull. *The Anatomical Record*, 254 (4), pp.474–489. [Online]. Available at: doi:10.1002/(sici)1097-0185(19990401)254:4<474::aid-ar3>3.0.co;2-3 [Accessed 5 November 2022].

Ponce de León, M. S. and Zollikofer, C. P. E. (2001a). Neanderthal cranial ontogeny and its implications for late hominid diversity. *Nature*, 412 (6846), pp.534–538. [Online]. Available at: doi:10.1038/35087573 [Accessed 22 April 2022].

Ponce de León, M. S. and Zollikofer, C. P. E. (2001b). The Brain and its Case: Computer-based Case Studies on the Relation Between Software and Hardware in Living and Fossil Hominid Skulls. *The Brain and its Case: Computer-based Case Studies on the Relation Between Software and Hardware in Living and Fossil Hominid Skulls*, pp.379–384. [Online]. Available at: <https://www.torrossa.com/gs/resourceProxy?an=2254828&publisher=FF3888> [Accessed 22 April 2022].

Popowics, T. E. and Herring, S. W. (2007). Load transmission in the nasofrontal suture of the pig, *Sus scrofa*. *Journal of Biomechanics*, 40 (4), pp.837–844. [Online]. Available at: doi:10.1016/j.jbiomech.2006.03.011 [Accessed 31 October 2022].

Preuschoft, H. et al. (1986). *The biomechanical principles realised in the upper jaw of long-snouted primates*. Cambridge (Ed). [Online]. Available at: [https://scholar.google.com/scholar?start=10&q=Preuschoft+et+al,+1986&hl=en&as\\_sdt=0,5](https://scholar.google.com/scholar?start=10&q=Preuschoft+et+al,+1986&hl=en&as_sdt=0,5) [Accessed 6 November 2022].

Profico, A. et al. (2017). The evolution of cranial base and face in Cercopithecoidea and Hominoidea: Modularity and morphological integration. *American Journal of Primatology*, 79 (12). [Online]. Available at: doi:10.1002/ajp.22721.

Profico, A. et al. (2019). A New Tool for Digital Alignment in Virtual Anthropology. *Anatomical Record*, 302 (7), pp.1104–1115. [Online]. Available at: doi:10.1002/ar.24077.

Profico, A. et al. (2021). Arothron: An R package for geometric morphometric methods and virtual anthropology applications. *American Journal of Physical Anthropology*, 176 (1), pp.144–151. [Online]. Available at: doi:10.1002/AJPA.24340 [Accessed 29 April 2022].

- Prossinger, H. et al. (2003). Electronic removal of encrustations inside the steinheim cranium reveals paranasal sinus features and deformations, and provides a revised endocranial volume estimate. *Anatomical Record - Part B New Anatomist*, 273 (1), Wiley-Liss Inc., pp.132–142. [Online]. Available at: doi:10.1002/ar.b.10022 [Accessed 3 November 2022].
- Pun, T. (1980). A new method for grey-level picture thresholding using the entropy of the histogram. *Signal Processing*, 2 (3), pp.223–237. [Online]. Available at: doi:https://doi.org/10.1016/0165-1684(80)90020-1.
- Radlanski, R. J. and Renz, H. (2006). Genes, forces, and forms: Mechanical aspects of prenatal craniofacial development. *Developmental Dynamics*, 235 (5), pp.1219–1229. [Online]. Available at: doi:10.1002/dvdy.20704.
- Rae, T. C. and Koppe, T. (2004). Holes in the head: Evolutionary interpretations of the paranasal sinuses in catarrhines. *Evolutionary Anthropology*, 13 (6), pp.211–223. [Online]. Available at: doi:10.1002/evan.20036.
- Rae, T. C. and Koppe, T. (2008). Independence of biomechanical forces and craniofacial pneumatization in *Cebus*. *Anatomical Record*, 291 (11), pp.1414–1419. [Online]. Available at: doi:10.1002/ar.20786 [Accessed 1 August 2022].
- Rae, T. C., Koppe, T. and Stringer, C. B. (2011). The Neanderthal face is not cold adapted. *Journal of Human Evolution*, 60 (2), pp.234–239. [Online]. Available at: doi:10.1016/j.jhevol.2010.10.003 [Accessed 26 April 2022].
- Rafferty, K. L. and Herring, S. W. (1999). Craniofacial sutures: Morphology, growth, and in vivo masticatory strains. *Journal of Morphology*, 242 (2), pp.167–179. [Online]. Available at: doi:10.1002/(SICI)1097-4687(199911)242:2<167::AID-JMOR8>3.0.CO;2-1 [Accessed 5 November 2022].
- Raguž, M. et al. (2021). FORAMEN OVALE AND FORAMEN ROTUNDUM: CHARACTERIZATION OF POSTNATAL DEVELOPMENT. *Acta Clinica Croatica*, 60 (3), pp.415–422. [Online]. Available at: doi:10.20471/acc.2021.60.03.11.
- Rak, Y. (1983). The Australopithecine Face. *American Anthropologist*, 86 (4), pp.1033–1034. [Online]. Available at: doi:10.1525/aa.1984.86.4.02a00450 [Accessed 25 April 2022].

- Rak, Y. (1986). The Neanderthal: A new look at an old face. *Journal of Human Evolution*, 15 (3), pp.151–164. [Online]. Available at: doi:10.1016/S0047-2484(86)80042-2.
- Ramirez-Yañez, G. O. et al. (2005). Influence of growth hormone on the craniofacial complex of transgenic mice. *The European Journal of Orthodontics*, 27 (5), pp.494–500. [Online]. Available at: [https://scholar.google.com/scholar?hl=en&as\\_sdt=0%2C5&q=Ramirez%2C+Smid%2C+Young%2C+%26+Waters%2C+2005&btnG=](https://scholar.google.com/scholar?hl=en&as_sdt=0%2C5&q=Ramirez%2C+Smid%2C+Young%2C+%26+Waters%2C+2005&btnG=) [Accessed 5 November 2022].
- Ramirez Rozzi, F. V. and Bermudez De Castro, J. M. (2004). Surprisingly rapid growth in Neanderthals. *Nature*, 428 (6986), pp.936–939. [Online]. Available at: doi:10.1038/nature02428 [Accessed 25 April 2022].
- Ravosa, M. J. (1988). Browridge development in cercopithecidae: A test of two models. *American Journal of Physical Anthropology*, 76 (4), pp.535–555. [Online]. Available at: doi:10.1002/ajpa.1330760413 [Accessed 20 May 2022].
- Ravosa, M. J. (1991a). Interspecific perspective on mechanical and nonmechanical models of primate circumorbital morphology. *American Journal of Physical Anthropology*, 86 (3), pp.369–396. [Online]. Available at: doi:10.1002/ajpa.1330860305 [Accessed 25 April 2022].
- Ravosa, M. J. (1991b). Ontogenetic perspective on mechanical and nonmechanical models of primate circumorbital morphology. *American Journal of Physical Anthropology*, 85 (1), pp.95–112. [Online]. Available at: doi:10.1002/AJPA.1330850111.
- Ravosa, M. J. (1991c). The ontogeny of cranial sexual dimorphism in two old world monkeys: *Macaca fascicularis* (Cercopithecinae) and *Nasalis larvatus* (Colobinae). *International Journal of Primatology*, 12 (4), pp.403–426. [Online]. Available at: doi:10.1007/BF02547620 [Accessed 25 April 2022].
- Ravosa, M. J. et al. (2000). Masticatory stress, orbital orientation and the evolution of the primate postorbital bar. *Journal of Human Evolution*, 38 (5), pp.667–693. [Online]. Available at: doi:10.1006/jhev.1999.0380 [Accessed 20 May 2022].
- Reed, D. A. et al. (2011). The impact of bone and suture material properties on mandibular function in *Alligator mississippiensis*: Testing theoretical phenotypes with finite element analysis. *Journal of Anatomy*, 218 (1), pp.59–74. [Online]. Available at:

doi:10.1111/j.1469-7580.2010.01319.x [Accessed 31 October 2022].

Reina, J. M. et al. (2007). Numerical estimation of bone density and elastic constants distribution in a human mandible. *Journal of Biomechanics*, 40 (4), pp.828–836. [Online]. Available at: doi:10.1016/j.jbiomech.2006.03.007 [Accessed 11 December 2022].

Renders, G. A. P. et al. (2011). Mineral heterogeneity affects predictions of intratrabecular stress and strain. *Journal of Biomechanics*, 44 (3), pp.402–407. [Online]. Available at: doi:10.1016/j.jbiomech.2010.10.004 [Accessed 19 September 2022].

Le Révérend, B. J. D., Edelson, L. R. and Loret, C. (2014). Anatomical, functional, physiological and behavioural aspects of the development of mastication in early childhood. *British Journal of Nutrition*, 111 (3), pp.403–414. [Online]. Available at: doi:10.1017/S0007114513002699.

Rho, J. Y. et al. (1999). Elastic properties of microstructural components of human bone tissue as measured by nanoindentation. *Journal of Biomedical Materials Research*, 45 (1), pp.48–54. [Online]. Available at: doi:10.1002/(SICI)1097-4636(199904)45:1<48::AID-JBM7>3.0.CO;2-5.

Richards, M. P. et al. (2000). Neanderthal diet at Vindija and Neanderthal predation: The evidence from stable isotopes. *Proceedings of the National Academy of Sciences of the United States of America*, 97 (13), pp.7663–7666. [Online]. Available at: doi:10.1073/pnas.120178997.

Richter, E. (1920). Grundlinien der Wortstellungslehre. *Zeitschrift für Romanische Philologie*, 40 (1), pp.9–61. [Online]. Available at: doi:10.1515/zrph.1920.40.1.9.

Richtsmeier, J. T. and DeLeon, V. B. (2009). Morphological integration of the skull in craniofacial anomalies. *Orthodontics and Craniofacial Research*, 12 (3), pp.149–158. [Online]. Available at: doi:10.1111/j.1601-6343.2009.01448.x [Accessed 30 August 2022].

Rink, W. J. et al. (2001). Electron Spin Resonance (ESR) and Thermal Ionization Mass Spectrometric (TIMS) <sup>230</sup>Th/<sup>234</sup>U Dating of Teeth in Middle Paleolithic Layers at Amud Cave, Israel. *Geoarchaeology - An International Journal*, 16 (6), pp.701–717. [Online]. Available at: doi:10.1002/gea.1017.

Roberts, D. and Tattersall, I. (1974). Skull Form and the Mechanics of Mandibular

Elevation in Mammals. *American Museum Novitates*, 2536, pp.1–10. [Online]. Available at: <https://digitallibrary.amnh.org/handle/2246/2739> [Accessed 26 April 2022].

Robling, A. G., Bellido, T. and Turner, C. H. (2006). Mechanical stimulation in vivo reduces osteocyte expression of sclerostin. *Journal of Musculoskeletal Neuronal Interactions*, 6 (4), p.354. [Online]. Available at: <http://www.ismni.org/jmni/pdf/download.php?file=26/19ROBLING.pdf> [Accessed 17 May 2022].

Robling, A. G., Castillo, A. B. and Turner, C. H. (2006). Biomechanical and molecular regulation of bone remodeling. *Annual Review of Biomedical Engineering*, 8, pp.455–498. [Online]. Available at: doi:10.1146/annurev.bioeng.8.061505.095721 [Accessed 17 May 2022].

Rodeck, C. and Whittle, M. (2019). *Fetal Medicine: Basic Science and Clinical Practice*. [Online]. Available at: doi:10.1016/B978-0-7020-6956-7.01001-0 [Accessed 1 August 2022].

Rohlf, F. J. (1990). Rotational fit (Procrustes) methods. In: *Proceedings of the Michigan Morphometrics Workshop. Special Publication Number 2*. 1990. pp.227-236. [Online]. Available at: [https://www.researchgate.net/profile/F-Rohlf/publication/30850286\\_Proceedings\\_of\\_the\\_Michigan\\_Morphometric\\_Workshop/links/5566227508aefcb861d1971b/Proceedings-of-the-Michigan-Morphometric-Workshop.pdf#page=237](https://www.researchgate.net/profile/F-Rohlf/publication/30850286_Proceedings_of_the_Michigan_Morphometric_Workshop/links/5566227508aefcb861d1971b/Proceedings-of-the-Michigan-Morphometric-Workshop.pdf#page=237) [Accessed 22 April 2022].

Rohlf, F. J. and Slice, D. (1990). Extensions of the procrustes method for the optimal superimposition of landmarks. *Systematic Zoology*, 39 (1), pp.40–59. [Online]. Available at: doi:10.2307/2992207 [Accessed 22 April 2022].

Rosas, A. et al. (2006). Inquiries into Neanderthal craniofacial development and evolution: “accretion” versus “organismic” models. In: *Vertebrate Paleobiology and Paleoanthropology*. (9781402051203). Springer. pp.37–69. [Online]. Available at: doi:10.1007/978-1-4020-5121-0\_4.

Rosas, A. and Bastir, M. (2002). Thin-plate spline analysis of allometry and sexual dimorphism in the human craniofacial complex. *American Journal of Physical Anthropology*, 117 (3), pp.236–245. [Online]. Available at: doi:10.1002/ajpa.10023.

Rosas, A. and Bastir, M. (2004). Geometric morphometric analysis of allometric variation

in the mandibular morphology of the hominids of Atapuerca, Sima de los Huesos site. *Anatomical Record - Part A Discoveries in Molecular, Cellular, and Evolutionary Biology*, 278 (2), pp.551–560. [Online]. Available at: doi:10.1002/ar.a.20049 [Accessed 22 April 2022].

Rosas, A. and Martinez-Maza, C. (2010). Bone remodeling of the *Homo heidelbergensis* mandible; the Atapuerca-SH sample. *Journal of Human Evolution*, 58 (2), pp.127–137. [Online]. Available at: doi:10.1016/j.jhevol.2009.10.002 [Accessed 25 April 2022].

Ross, C. F. (2001). In vivo function of the craniofacial haft: The interorbital ‘pillar’. *American Journal of Physical Anthropology*, 116 (2), pp.108–139. [Online]. Available at: doi:10.1002/ajpa.1106.

Ross, C. F. et al. (2004). Curvilinear, geometric and phylogenetic modeling of basicranial flexion: Is it adaptive, is it constrained? *Journal of Human Evolution*, 46 (2), pp.185–213. [Online]. Available at: doi:10.1016/j.jhevol.2003.11.001 [Accessed 3 November 2022].

Ross, C. F. (2005). Finite element analysis in vertebrate biomechanics. In: *Anatomical Record - Part A Discoveries in Molecular, Cellular, and Evolutionary Biology*. 283 (2). 2005. pp.253–258. [Online]. Available at: doi:10.1002/ar.a.20177.

Ross, C. F. et al. (2005). Modeling masticatory muscle force in finite element analysis: Sensitivity analysis using principal coordinates analysis. In: *Anatomical Record - Part A Discoveries in Molecular, Cellular, and Evolutionary Biology*. 283 (2). April 2005. pp.288–299. [Online]. Available at: doi:10.1002/ar.a.20170 [Accessed 20 April 2022].

Ross, C. F. (2008). Does the Primate Face Torque? In: *Primate Craniofacial Function and Biology*. pp.63–81. [Online]. Available at: doi:10.1007/978-0-387-76585-3\_4 [Accessed 20 May 2022].

Ross, C. F. et al. (2011). In vivo bone strain and finite-element modeling of the craniofacial haft in catarrhine primates. *Journal of Anatomy*, 218 (1), pp.112–141. [Online]. Available at: doi:10.1111/j.1469-7580.2010.01322.x [Accessed 20 April 2022].

Ross, C. F. and Hylander, W. L. (1996). In vivo and in vitro bone strain in the owl monkey circumorbital region and the function of the postorbital septum. *American Journal of Physical Anthropology*, 101 (2), pp.183–215. [Online]. Available at: doi:10.1002/(SICI)1096-8644(199610)101:2<183::AID-AJPA6>3.0.CO;2-3 [Accessed 20 May 2022].

- Ross, C. F. and Ravosa, M. J. (1993). Basicranial flexion, relative brain size, and facial kyphosis in nonhuman primates. *American Journal of Physical Anthropology*, 91 (3), pp.305–324. [Online]. Available at: doi:10.1002/AJPA.1330910306.
- Rubin, C. T. and Lanyon, L. E. (1985). Regulation of bone mass by mechanical strain magnitude. *Calcified Tissue International*, 37 (4), pp.411–417. [Online]. Available at: doi:10.1007/BF02553711.
- Ruff, C., Holt, B. and Trinkaus, E. (2006). Who’s afraid of the big bad Wolff?: ‘Wolff’s law’ and bone functional adaptation. *American Journal of Physical Anthropology*, 129 (4), pp.484–498. [Online]. Available at: doi:10.1002/ajpa.20371.
- Russell, M. D. et al. (1985). The Supraorbital Torus: ‘A Most Remarkable Peculiarity’ [and Comments and Replies]. *Current Anthropology*, 26 (3), pp.337–360. [Online]. Available at: doi:10.1086/203279.
- Sadler, T. W. (2003). *Langman’s Medical Embryology*. [Online]. Available at: doi:10.1097/00006534-198801000-00024 [Accessed 17 May 2022].
- Sadler, T. W. (2018). *Langman’s medical embryology*. Wilkins, L. W. & (Ed). [Online]. Available at: [https://books.google.com/books?hl=en&lr=&id=izltDwAAQBAJ&oi=fnd&pg=PT26&dq=Sadler,+2018&ots=4\\_NVtmhz13&sig=3v-h4StOxrTC404uoA683-iQqAw](https://books.google.com/books?hl=en&lr=&id=izltDwAAQBAJ&oi=fnd&pg=PT26&dq=Sadler,+2018&ots=4_NVtmhz13&sig=3v-h4StOxrTC404uoA683-iQqAw) [Accessed 1 August 2022].
- Sadrameli, M. and Mupparapu, M. (2018). Oral and Maxillofacial Anatomy. *Radiologic Clinics of North America*, 56 (1), pp.13–29. [Online]. Available at: doi:10.1016/j.rcl.2017.08.002 [Accessed 19 May 2022].
- Saffar, J. L., Lasfargues, J.-J. and Cherruau, M. (1997). Alveolar bone and the alveolar process: The socket that is never stable. *Periodontology 2000*, 13 (1), pp.76–90. [Online]. Available at: doi:10.1111/j.1600-0757.1997.tb00096.x.
- Sakashita, R. et al. (1998). Electromyographic evidence for sufficient and insufficient developmental space in juvenile jaws. *Orthodontic waves (Journal of Japanese Orthodontic Society)*, 57 (6), pp.409–416. [Online]. Available at: <https://ci.nii.ac.jp/naid/110004015548/> [Accessed 31 October 2022].
- Schaefer, M. et al. (2009). *Juvenile Osteology*. [Online]. Available at: doi:10.1016/b978-

0-12-374635-1.x0001-x [Accessed 29 April 2022].

Schlager, S. (2017). Morpho and Rvcg - Shape Analysis in R: R-Packages for Geometric Morphometrics, Shape Analysis and Surface Manipulations. In: *Statistical Shape and Deformation Analysis: Methods, Implementation and Applications*. Academic Press. pp.217–256. [Online]. Available at: doi:10.1016/B978-0-12-810493-4.00011-0 [Accessed 29 April 2022].

Schmerling, P. C. (1833). *Recherches sur les ossemens fossiles découverts dans les cavernes de la province de Liège*. [Online]. Available at: doi:10.5962/bhl.title.77328 [Accessed 19 September 2022].

Schuh, A. et al. (2019). Ontogeny of the human maxilla: a study of intra-population variability combining surface bone histology and geometric morphometrics. *Journal of Anatomy*, 235 (2), pp.233–245. [Online]. Available at: doi:10.1111/joa.13002.

Schuh, A. et al. (2020). Intraspecific variability in human maxillary bone modeling patterns during ontogeny. *American Journal of Physical Anthropology*, 173 (4), pp.655–670. [Online]. Available at: doi:10.1002/ajpa.24153.

Schultz, A. H. (1940). The size of the orbit and of the eye in primates. *American Journal of Physical Anthropology*, 26 (1), pp.389–408. [Online]. Available at: doi:10.1002/ajpa.1330260138.

Schwarcz, H. P. et al. (1991). On the Reexamination of Grotta Guattari: Uranium-Series and Electron-Spin-Resonance Dates. *Current Anthropology*, 32 (3), pp.313–316. [Online]. Available at: doi:10.1086/203959.

Schwarcz, H. P. and Blackwell, B. (1983).  $^{230}\text{Th}/^{234}\text{U}$  age of a Mousterian site in France. *Nature*, 301 (5897), pp.236–237. [Online]. Available at: doi:10.1038/301236a0 [Accessed 19 September 2022].

Schwartz-Dabney, C. L. and Dechow, P. C. (2003). Variations in cortical material properties throughout the human dentate mandible. *American Journal of Physical Anthropology*, 120 (3), pp.252–277. [Online]. Available at: doi:10.1002/ajpa.10121.

Schwartz, G. T. (2012). Growth, development, and life history throughout the evolution of Homo. *Current Anthropology*, 53 (SUPPL. 6). [Online]. Available at: doi:10.1086/667591.

Schwartz, J. H. and Tattersall, I. (2000). The human chin revisited: What is it and who has it? *Journal of Human Evolution*, 38 (3), pp.367–409. [Online]. Available at: doi:10.1006/jhev.1999.0339 [Accessed 5 November 2022].

Schwartz, J. H. and Tattersall, I. (2003). *The Human Fossil Record. Volume Two: Cranio-dental Morphology of Genus Homo (Africa and Asia)*. [Online]. Available at: [https://scholar.google.com/scholar?hl=en&as\\_sdt=0%2C5&q=he+Human+Fossil+Record+%2C+Volume+Two+%3A+Craniodental+Morphology+The+Human+Fossil+Record+%2C+Volume+Three+%3A+Craniodental+Morphology&btnG=](https://scholar.google.com/scholar?hl=en&as_sdt=0%2C5&q=he+Human+Fossil+Record+%2C+Volume+Two+%3A+Craniodental+Morphology+The+Human+Fossil+Record+%2C+Volume+Three+%3A+Craniodental+Morphology&btnG=) [Accessed 19 September 2022].

Sella-Tunis, T. et al. (2018). Human mandibular shape is associated with masticatory muscle force. *Scientific Reports*, 8 (1). [Online]. Available at: doi:10.1038/s41598-018-24293-3.

Shea, B. T. (1985a). On aspects of skull form in African apes and orangutans, with implications for hominoid evolution. *American Journal of Physical Anthropology*, 68 (3), pp.329–342. [Online]. Available at: doi:10.1002/ajpa.1330680304 [Accessed 20 April 2022].

Shea, B. T. (1985b). Ontogenetic Allometry and Scaling. In: *Size and Scaling in Primate Biology*. Springer US. pp.175–205. [Online]. Available at: doi:10.1007/978-1-4899-3647-9\_9 [Accessed 20 April 2022].

Shea, B. T. and Russell, M. D. (1986). On Skull Form and the Supraorbital Torus in Primates. *Current Anthropology*, 27 (3), pp.257–260. [Online]. Available at: doi:10.1086/203427.

Sheth, R. et al. (2012). Hox genes regulate digit patterning by controlling the wavelength of a turing-type mechanism. *Science*, 338 (6113), pp.1476–1480. [Online]. Available at: doi:10.1126/science.1226804.

Sicher, H. and Tandler, J. (1928). Anatomie für zahnärzte. *J. Springer*. [Online]. Available at: [https://scholar.google.com/scholar?hl=en&as\\_sdt=0%2C5&as\\_ylo=1928&as\\_yhi=1928&q=Sicher+and+Tandler%2C+1928&btnG=](https://scholar.google.com/scholar?hl=en&as_sdt=0%2C5&as_ylo=1928&as_yhi=1928&q=Sicher+and+Tandler%2C+1928&btnG=) [Accessed 27 April 2022].

Singh, N. et al. (2012). Morphological evolution through integration: A quantitative study of cranial integration in Homo, Pan, Gorilla and Pongo. *Journal of Human Evolution*, 62

(1), pp.155–164. [Online]. Available at: doi:10.1016/j.jhevol.2011.11.006 [Accessed 30 August 2022].

Singleton, M. (2015). Functional Geometric Morphometric Analysis of Masticatory System Ontogeny in Papionin Primates. *Anatomical Record*, 298 (1), pp.48–63. [Online]. Available at: doi:10.1002/ar.23068.

Sinn, D. P., De Assis, E. A. and Throckmorton, G. S. (1996). Mandibular excursions and maximum bite forces in patients with temporomandibular joint disorders. *Journal of Oral and Maxillofacial Surgery*, 54 (6), pp.671–679. [Online]. Available at: doi:10.1016/S0278-2391(96)90678-3.

Sirianni, J. E. and Swindler, D. R. (1985). *Growth and Development of the Pigtailed Macaque*. [Online]. Available at: [https://scholar.google.com/scholar?hl=en&as\\_sdt=0%2C5&q=Sirianni+and+Swindler%2C+1985&btnG=](https://scholar.google.com/scholar?hl=en&as_sdt=0%2C5&q=Sirianni+and+Swindler%2C+1985&btnG=) [Accessed 25 April 2022].

Sistiaga, A. et al. (2014). The Neanderthal meal: A new perspective using faecal biomarkers. *PLoS ONE*, 9 (6). [Online]. Available at: doi:10.1371/journal.pone.0101045.

Skerry, T. (2000). *And Development*. [Online]. Available at: <https://books.google.com/books?hl=en&lr=&id=yXHv6MaB7gQC&oi=fnd&pg=PA29&dq=Skerry,+2000&ots=xAdrIgSjad&sig=CJETTDUNAnOshRES62vYlpM7ZJQ> [Accessed 20 May 2022].

Smith, A. L. et al. (2015a). The Feeding Biomechanics and Dietary Ecology of *Paranthropus boisei*. *Anatomical Record*, 298 (1), pp.145–167. [Online]. Available at: doi:10.1002/ar.23073 [Accessed 20 April 2022].

Smith, A. L. et al. (2015b). The Feeding Biomechanics and Dietary Ecology of *Paranthropus boisei*. *Anatomical Record*, 298 (1), pp.145–167. [Online]. Available at: doi:10.1002/ar.23073 [Accessed 24 November 2022].

Smith, B. H. (1986). Dental development in *Australopithecus* and early *Homo*. *Nature*, 323 (6086), pp.327–330. [Online]. Available at: doi:10.1038/323327A0.

Smith, B. H. (1991). Standards of Human Tooth Formation. In: *Advances in Dental Anthropology*. pp.143–168. [Online]. Available at: [https://deepblue.lib.umich.edu/bitstream/handle/2027.42/90867/Holly\\_Smith\\_Chapter](https://deepblue.lib.umich.edu/bitstream/handle/2027.42/90867/Holly_Smith_Chapter)

1991 Standards of Human Tooth.pdf?sequence=1 [Accessed 20 April 2022].

Smith, B. H. (1994). Sequence of emergence of the permanent teeth in *Macaca*, *Pan*, *Homo*, and *Australopithecus*: Its evolutionary significance. *American Journal of Human Biology*, 6 (1), pp.61–76. [Online]. Available at: doi:10.1002/ajhb.1310060110.

Smith, F.H. and Paquette, S.P., 1989. The adaptive basis of Neandertal facial form, with some thoughts on the nature of modern human origins. *The Emergence of Modern Humans: Biocultural Adaptations in the Later Pleistocene*. Cambridge University Press, Cambridge, pp.181-210.

Smith, R. J., Petersen, C. E. and Gipe, D. P. (1983). Size and shape of the mandibular condyle in primates. *Journal of Morphology*, 177 (1), pp.59–68. [Online]. Available at: doi:10.1002/jmor.1051770106.

Smith, T. D. et al. (2011). Comparative microcomputed tomography and histological study of maxillary pneumatization in four species of new world monkeys: The perinatal period. *American Journal of Physical Anthropology*, 144 (3), pp.392–410. [Online]. Available at: doi:10.1002/ajpa.21421.

Smith, T. D. et al. (2014). Mapping bone cell distributions to assess ontogenetic origin of primate midfacial form. *American Journal of Physical Anthropology*, 154 (3), pp.424–435. [Online]. Available at: doi:10.1002/ajpa.22540.

Smith, T. M. et al. (2007a). Molar development in common chimpanzees (*Pan troglodytes*). *Journal of Human Evolution*, 52 (2), pp.201–216. [Online]. Available at: doi:10.1016/j.jhevol.2006.09.004.

Smith, T. M. et al. (2007b). Rapid dental development in a Middle Paleolithic Belgian Neanderthal. *Proceedings of the National Academy of Sciences of the United States of America*, 104 (51), pp.20220–20225. [Online]. Available at: doi:10.1073/pnas.0707051104.

Smith, T. M. et al. (2010a). Dental evidence for ontogenetic differences between modern humans and Neanderthals. *Proceedings of the National Academy of Sciences of the United States of America*, 107 (49), pp.20923–20928. [Online]. Available at: doi:10.1073/pnas.1010906107.

Smith, T. M. et al. (2010b). Dental evidence for ontogenetic differences between modern

humans and Neanderthals. *Proceedings of the National Academy of Sciences of the United States of America*, 107 (49), pp.20923–20928. [Online]. Available at: doi:10.1073/pnas.1010906107 [Accessed 25 April 2022].

Sneath, P. H. A. (1967). Some Statistical Problems in Numerical Taxonomy. *The Statistician*, 17 (1), p.1. [Online]. Available at: doi:10.2307/2987198 [Accessed 26 April 2022].

Soboļeva, U., Lauriņa, L. and Slaidiņa, A. (2005). The masticatory system--an overview. *Stomatologija*, 7 (3), pp.77–80. [Online]. Available at: <https://sbdmj.lsmuni.lt/053/053-03.pdf> [Accessed 19 May 2022].

Spencer, M. A. and Demes, B. (1993). Biomechanical analysis of masticatory system configuration in Neandertals and Inuits. *American Journal of Physical Anthropology*, 91 (1), pp.1–20. [Online]. Available at: doi:10.1002/AJPA.1330910102.

Sperber, G., Sperber, S. and Guttman, G. (2010). *Craniofacial embryogenetics and development*. PMPH-USA (Ed). [Online]. Available at: <https://books.google.com/books?hl=en&lr=&id=OvM0jkob9GgC&oi=fnd&pg=PP7&dq=Sperber+et+al,+2010&ots=LwcdVHv8Rg&sig=txbsprcizCMz1Y6E6f4oNUenLTU> [Accessed 19 May 2022].

Standring, S. ed. (2021). *Gray's anatomy e-book: the anatomical basis of clinical practice*. [Online]. Available at: doi:10.1001/jama.2009.594 [Accessed 6 November 2022].

Stedman, H. H. et al. (2004). Myosin gene mutation correlates with anatomical changes in the human lineage. *Nature*, 428 (6981), pp.415–418. [Online]. Available at: doi:10.1038/nature02358 [Accessed 1 November 2022].

Stewart, S. A. and German, R. Z. (1999). Sexual dimorphism and ontogenetic allometry of soft tissues in *Rattus norvegicus*. *Journal of Morphology*, 242 (1), pp.57–66. [Online]. Available at: doi:10.1002/(SICI)1097-4687(199910)242:1<57::AID-JMOR4>3.0.CO;2-5 [Accessed 19 May 2022].

Stool, S. E. (2001). Prenatal and Postnatal Craniofacial Development. *Handbook of Genetic Communicative Disorders*, pp.31–67. [Online]. Available at: doi:10.1016/B978-012280605-6/50005-6.

Strait, D. S. et al. (2005). Modeling elastic properties in finite-element analysis: How much precision is needed to produce an accurate model? In: *Anatomical Record - Part A Discoveries in Molecular, Cellular, and Evolutionary Biology*. 283 (2). April 2005. pp.275–287. [Online]. Available at: doi:10.1002/ar.a.20172 [Accessed 20 April 2022].

Strait, D. S. et al. (2007). Masticatory biomechanics and its relevance to early hominid phylogeny: An examination of palatal thickness using finite-element analysis. *Journal of Human Evolution*, 52 (5), pp.585–599. [Online]. Available at: doi:10.1016/j.jhevol.2006.11.019.

Strait, D. S. et al. (2009). The feeding biomechanics and dietary ecology of *Australopithecus africanus*. *Proceedings of the National Academy of Sciences of the United States of America*, 106 (7), pp.2124–2129. [Online]. Available at: doi:10.1073/pnas.0808730106.

Strait, D. S. et al. (2010). The structural rigidity of the cranium of *Australopithecus africanus*: Implications for diet, dietary adaptations, and the allometry of feeding biomechanics. *Anatomical Record*, 293 (4), pp.583–593. [Online]. Available at: doi:10.1002/ar.21122.

Stringer, C. (1990). On the emergence of modern humans. *Scientific American*, 103 (3), pp.358–385. [Online]. Available at: doi:10.1016/j.cognition.2006.04.002 [Accessed 25 April 2022].

Stringer, C. (2002). Modern human origins: Progress and prospects. *Philosophical Transactions of the Royal Society B: Biological Sciences*, 357 (1420), pp.563–579. [Online]. Available at: doi:10.1098/rstb.2001.1057.

Stringer, C. (2012). The status of *Homo heidelbergensis* (Schoetensack 1908). *Evolutionary Anthropology*, 21 (3), pp.101–107. [Online]. Available at: doi:10.1002/evan.21311.

Stringer, C. B., Hublin, J. J. and Vandermeersch, B. (1984). The origin of anatomically modern humans in Western Europe. In: *The origins of modern humans: a world survey of the fossil evidence*. pp.51–135. [Online]. Available at: [https://www.academia.edu/download/32141337/Stringer\\_\\_1984b.pdf](https://www.academia.edu/download/32141337/Stringer__1984b.pdf) [Accessed 1 November 2022].

Sugiyama, T. et al. (2012). Bones' adaptive response to mechanical loading is essentially

linear between the low strains associated with disuse and the high strains associated with the lamellar/woven bone transition. *Journal of Bone and Mineral Research*, 27 (8), pp.1784–1793. [Online]. Available at: doi:10.1002/jbmr.1599.

Sugiyama, T., Price, J. S. and Lanyon, L. E. (2010). Functional adaptation to mechanical loading in both cortical and cancellous bone is controlled locally and is confined to the loaded bones. *Bone*, 46 (2), pp.314–321. [Online]. Available at: doi:10.1016/j.bone.2009.08.054 [Accessed 1 August 2022].

Suzuki, H. (1970). *The skull of the Amud man*. [Online]. Available at: <https://ci.nii.ac.jp/naid/10030340580/> [Accessed 19 September 2022].

Tallman, M. (2016). Shape ontogeny of the distal femur in the hominidae with implications for the evolution of bipedality. *PLoS ONE*, 11 (2). [Online]. Available at: doi:10.1371/journal.pone.0148371.

Tappen, N. C. (1973). Structure of bone in the skulls of Neanderthal fossils. *American Journal of Physical Anthropology*, 38 (1), pp.93–97. [Online]. Available at: doi:10.1002/ajpa.1330380123.

Tappen, N. C. (1978). The vermiculate surface pattern of brow ridges in Neanderthal and modern crania. *American Journal of Physical Anthropology*, 49 (1), pp.1–10. [Online]. Available at: doi:10.1002/AJPA.1330490102.

Tarala, M., Janssen, D. and Verdonchot, N. (2011). Balancing incompatible endoprosthetic design goals: A combined ingrowth and bone remodeling simulation. *Medical Engineering and Physics*, 33 (3), pp.374–380. [Online]. Available at: doi:10.1016/j.medengphy.2010.11.005 [Accessed 11 December 2022].

Taschini, M. (1979). L'industrie lithique de Grotta Guattari au Monte Circé (Latium) définition culturelle, typologique et chronologique du Pontinien. *Quaternaria*, 21, pp.179–247. [Online]. Available at: <https://pascal-francis.inist.fr/vibad/index.php?action=getRecordDetail&idt=12588308> [Accessed 19 September 2022].

Tattersall, I. (1998). Morphology, paleoanthropology, and Neanderthals. *Anatomical Record*, 253 (4), pp.113–117. [Online]. Available at: doi:10.1002/(SICI)1097-0185(199808)253:4<113::AID-AR6>3.0.CO;2-U [Accessed 1 November 2022].

- Taylor, A. B. and Vinyard, C. J. (2009). Jaw-muscle fiber architecture in tufted capuchins favors generating relatively large muscle forces without compromising jaw gape. *Journal of Human Evolution*, 57 (6), pp.710–720. [Online]. Available at: doi:10.1016/j.jhevol.2009.06.001 [Accessed 19 May 2022].
- Terhune, C. E., Ritzman, T. B. and Robinson, C. A. (2018). Mandibular ramus shape variation and ontogeny in *Homo sapiens* and *Homo neanderthalensis*. *Journal of Human Evolution*, 121, pp.55–71. [Online]. Available at: doi:10.1016/j.jhevol.2018.03.009.
- Thomason, J. J. et al. (2001). In vivo surface strain and stereology of the frontal and maxillary bones of sheep: Implications for the structural design of the mammalian skull. *Anatomical Record*, 264 (4), pp.325–338. [Online]. Available at: doi:10.1002/ar.10025 [Accessed 5 November 2022].
- Thompson, E. N., Biknevicius, A. R. and German, R. Z. (2003). Ontogeny of feeding function in the gray short-tailed opossum *Monodelphis domestica*: Empirical support for the constrained model of jaw biomechanics. *Journal of Experimental Biology*, 206 (5), pp.923–932. [Online]. Available at: doi:10.1242/jeb.00181 [Accessed 20 May 2022].
- Tillier, A. M. (1983). Le crâne d'enfant d'Engis 2: un exemple de distribution des caractères juvéniles, primitifs et néanderthaliens. *Bulletin de la Société Royale Belge d'Anthropologie et de Préhistoire Bruxelles*, (94), pp.51–75. [Online]. Available at: [https://biblio.naturalsciences.be/associated\\_publications/anthropologica-prehistorica/bulletin-de-la-societe-royale-belge-d-anthropologie-et-de-prehistoire/ap-094-1983/ap94\\_51-75.pdf](https://biblio.naturalsciences.be/associated_publications/anthropologica-prehistorica/bulletin-de-la-societe-royale-belge-d-anthropologie-et-de-prehistoire/ap-094-1983/ap94_51-75.pdf) [Accessed 19 September 2022].
- Toro-Ibacache, V. et al. (2016). Validity and sensitivity of a human cranial finite element model: Implications for comparative studies of biting performance. *Journal of Anatomy*, 228 (1), pp.70–84. [Online]. Available at: doi:10.1111/joa.12384.
- Toro-Ibacache, V. and O'Higgins, P. (2016). The Effect of Varying Jaw-elevator Muscle Forces on a Finite Element Model of a Human Cranium. *Anatomical Record*, 299 (7), pp.828–839. [Online]. Available at: doi:10.1002/ar.23358.
- Toro-Ibacache, V., Zapata Muñoz, V. and O'higgins, P. (2015). The Predictability from Skull Morphology of Temporalis and Masseter Muscle Cross-Sectional Areas in Humans. *Anatomical Record*, 298 (7), pp.1261–1270. [Online]. Available at: doi:10.1002/ar.23156.

Toro-Ibacache, V., Zapata Muñoz, V. and O'Higgins, P. (2016). The relationship between skull morphology, masticatory muscle force and cranial skeletal deformation during biting. *Annals of Anatomy*, 203, pp.59–68. [Online]. Available at: doi:10.1016/j.aanat.2015.03.002.

Trevizan, M. and Consolaro, A. (2017). Premaxilla: An independent bone that can base therapeutics for middle third growth! *Dental Press Journal of Orthodontics*, 22 (2), pp.21–26. [Online]. Available at: doi:10.1590/2177-6709.22.2.021-026.oin.

Trinkaus, E., 1983. *The shanidar neandertals*. Academic Press.

Trinkaus, E. (1987a). The Neandertal face: evolutionary and functional perspectives on a recent hominid face. *Journal of Human Evolution*, 16 (5), pp.429–443. [Online]. Available at: doi:10.1016/0047-2484(87)90071-6 [Accessed 26 April 2022].

Trinkaus, E. (1987b). The Neandertal face: evolutionary and functional perspectives on a recent hominid face. *Journal of Human Evolution*, 16 (5), pp.429–443. [Online]. Available at: doi:10.1016/0047-2484(87)90071-6 [Accessed 6 November 2022].

Trinkaus, E. (2003). Neandertal faces were not long; modern human faces are short. *Proceedings of the National Academy of Sciences of the United States of America*, 100 (14), pp.8142–8145. [Online]. Available at: doi:10.1073/pnas.1433023100 [Accessed 22 April 2022].

Trinkaus, E. (2005). Early modern humans. *Annual Review of Anthropology*, 34, pp.207–230. [Online]. Available at: doi:10.1146/annurev.anthro.34.030905.154913 [Accessed 25 April 2022].

Tse, K.M., Tan, L.B., Lee, S.J., Lim, S.P. and Lee, H.P., 2015. Investigation of the relationship between facial injuries and traumatic brain injuries using a realistic subject-specific finite element head model. *Accident Analysis & Prevention*, 79, pp.13-32.

Tubbs, R. S., Bosmia, A. N. and Cohen-Gadol, A. A. (2012). The human calvaria: A review of embryology, anatomy, pathology, and molecular development. *Child's Nervous System*, 28 (1), pp.23–31. [Online]. Available at: doi:10.1007/s00381-011-1637-0.

Turing, A. (1952). The Chemical Basis of Morphogenesis. In: *B Jack Copeland*. p.519. [Online]. Available at: doi:10.1400/281797 [Accessed 5 November 2022].

Turner, C. H. and Pavalko, F. M. (1998). Mechanotransduction and functional response

of the skeleton to physical stress: The mechanisms and mechanics of bone adaptation. In: *Journal of Orthopaedic Science*. 3 (6). 1998. Springer Japan. pp.346–355. [Online]. Available at: doi:10.1007/s007760050064.

Turner, R. T. et al. (1998). Programmed administration of parathyroid hormone increases bone formation and reduces bone loss in hindlimb-unloaded ovariectomized rats. *Endocrinology*, 139 (10), pp.4086–4091. [Online]. Available at: doi:10.1210/endo.139.10.6227 [Accessed 20 May 2022].

Turq, A. (1979). *L'évolution du Moustérien du type Quina au Roc de Marsal et en Périgord: modifications de l'équilibre technique et typologie*. [Online]. Available at: [https://scholar.google.com/scholar?hl=en&as\\_sdt=0%2C5&q=L%27evolution+du+Mousterien+du+type+Quina+au+Roc+de+Marsal+et+en+Perigord&btnG=](https://scholar.google.com/scholar?hl=en&as_sdt=0%2C5&q=L%27evolution+du+Mousterien+du+type+Quina+au+Roc+de+Marsal+et+en+Perigord&btnG=) [Accessed 19 September 2022].

Usui, T. et al. (2007). Change in maximum occlusal force in association with maxillofacial growth. *Orthodontics and Craniofacial Research*, 10 (4), pp.226–234. [Online]. Available at: doi:10.1111/j.1601-6343.2007.00405.x.

Valladas, H. et al. (1986). Thermoluminescence dating of Le Moustier (Dordogne, France). *Nature*, 322 (6078), pp.452–454. [Online]. Available at: doi:10.1038/322452a0 [Accessed 19 September 2022].

Valladas, H. et al. (1999). TL dates for the Neanderthal site of the Amud Cave, Israel. *Journal of Archaeological Science*, 26 (3), pp.259–268. [Online]. Available at: doi:10.1006/jasc.1998.0334 [Accessed 19 September 2022].

Vatsa, A. et al. (2008). Osteocyte morphology in fibula and calvaria - Is there a role for mechanosensing? *Bone*, 43 (3), pp.452–458. [Online]. Available at: doi:10.1016/j.bone.2008.01.030 [Accessed 20 May 2022].

Verhaegen, M. (2013). The Aquatic Ape Evolves: Common Misconceptions and Unproven Assumptions About the So-Called Aquatic Ape Hypothesis. *Human evolution*, 28 (3–4), pp.237–266. [Online]. Available at: [https://www.researchgate.net/profile/Marc-Verhaegen-2/post/Will\\_Chimps\\_Pan\\_troglodytes\\_and\\_P\\_paniscus\\_eventually\\_evolve\\_into\\_a\\_Hom\\_o-like\\_being/attachment/59d62da079197b807798be1a/AS%3A351016529743872%4014](https://www.researchgate.net/profile/Marc-Verhaegen-2/post/Will_Chimps_Pan_troglodytes_and_P_paniscus_eventually_evolve_into_a_Hom_o-like_being/attachment/59d62da079197b807798be1a/AS%3A351016529743872%4014)

60700270474/download/HE%2713.pdf [Accessed 25 April 2022].

Verwoerd, C. D. A. and Verwoerd-Verhoef, H. L. (2007). Rhinosurgery in children: Basic concepts. *Facial Plastic Surgery*, 23 (4), pp.219–230. [Online]. Available at: doi:10.1055/s-2007-995814.

Vidarsdóttir, U. S. and Cobb, S. (2004). Inter- and intra-specific variation in the ontogeny of the hominoid facial skeleton: Testing assumptions of ontogenetic variability. *Annals of Anatomy*, 186 (5–6), pp.423–428. [Online]. Available at: doi:10.1016/S0940-9602(04)80076-1.

Vinyard, C. J. and Smith, F. H. (1997). Morphometric relationships between the supraorbital region and frontal sinus in Melanesian crania. *HOMO- Journal of Comparative Human Biology*, 48 (1), pp.1–21. [Online]. Available at: [https://scholar.google.com/scholar?hl=en&as\\_sdt=0%2C5&q=Vinyard+and+Smith%2C+1997&btnG=](https://scholar.google.com/scholar?hl=en&as_sdt=0%2C5&q=Vinyard+and+Smith%2C+1997&btnG=) [Accessed 25 April 2022].

Vinyard, C. J. and Smith, F. H. (2001). Morphometric testing of structural hypotheses of the supraorbital region in modern humans. *Zeitschrift für Morphologie und Anthropologie*, 83 (1), pp.23–41. [Online]. Available at: doi:10.1127/zma/83/2001/23.

Vioarsdóttir, U. S., O’Higgins, P. and Stringer, C. (2002). A geometric morphometric study of regional differences in the ontogeny of the modern human facial skeleton. *Journal of Anatomy*, 201 (3), pp.211–229. [Online]. Available at: doi:10.1046/j.1469-7580.2002.00092.x.

Vogel, C. (1966). Morphologische Studien am Gesichtsschädel catarrhiner Primaten. *Bibl. Primatol.*, 4, pp.1–226. [Online]. Available at: <https://ci.nii.ac.jp/naid/10006684694/> [Accessed 3 November 2022].

Vogel, C. (1968). The phylogenetical evaluation of some characters and some morphological trends in the evolution of the skull in catarrhine primates. In: *Taxonomy and Phylogeny of Old World Primates with References to the Origin of Man*. pp.21–55. [Online]. Available at: <https://ci.nii.ac.jp/naid/10006684695/> [Accessed 3 November 2022].

Volpato, V. et al. (2012). Hand to mouth in a Neandertal: Right-handedness in Regourdou 1. *PLoS ONE*, 7 (8). [Online]. Available at: doi:10.1371/journal.pone.0043949.

Walters, M. and O'Higgins, P. (1992). Factors influencing craniofacial growth: a scanning electron microscope study of high resolution facial replicas. *Proc Australas Soc Hum Biol*, 5, pp.391–403.

Wang, Q. et al. (2008). Primate Craniofacial Function and Biology. *Primate Craniofacial Function and Biology*, pp.149–150. [Online]. Available at: doi:10.1007/978-0-387-76585-3.

Wang, Q. et al. (2010). Mechanical impact of incisor loading on the primate midfacial skeleton and its relevance to human evolution. *Anatomical Record*, 293 (4), pp.607–617. [Online]. Available at: doi:10.1002/ar.21123 [Accessed 26 April 2022].

Watson, P. J. et al. (2011). Validation of a morphometric reconstruction technique applied to a juvenile pelvis. *Proceedings of the Institution of Mechanical Engineers, Part H: Journal of Engineering in Medicine*, 225 (1), pp.48–57. [Online]. Available at: doi:10.1243/09544119JEIM810 [Accessed 5 November 2022].

Weaver, T. D. (2009). The meaning of Neandertal skeletal morphology. *Proceedings of the National Academy of Sciences of the United States of America*, 106 (38), pp.16028–16033. [Online]. Available at: doi:10.1073/pnas.0903864106.

Weaver, T. D., Roseman, C. C. and Stringer, C. B. (2007). Were neandertal and modern human cranial differences produced by natural selection or genetic drift? *Journal of Human Evolution*, 53 (2), pp.135–145. [Online]. Available at: doi:10.1016/j.jhevol.2007.03.001.

Weber, G. W. and Bookstein, F. L. (2011). *Virtual anthropology: a guide to a new interdisciplinary field*. [Online]. Available at: <https://link.springer.com/book/9783211486474> [Accessed 24 November 2022].

Weidenreich, F. (1941). The Brain and its Role in the Phylogenetic Transformation of the Human Skull. *Transactions of the American Philosophical Society*, 31 (5), p.320. [Online]. Available at: doi:10.2307/1005610 [Accessed 3 November 2022].

Weijs, W. A. and Hillen, B. (1985). Physiological cross-section of the human jaw muscles. *Acta Anatomica*, 121 (1), pp.31–35. [Online]. Available at: doi:10.1159/000145938 [Accessed 31 October 2022].

Weyrich, L. S. et al. (2017). Neanderthal behaviour, diet, and disease inferred from

ancient DNA in dental calculus. *Nature*, 544 (7650), pp.357–361. [Online]. Available at: doi:10.1038/nature21674 [Accessed 16 September 2022].

White, T. D. and Folkens, P. A. (2011). *Human osteology*. 2000. 05 (Anth 411), pp.161–164. [Online]. Available at: <https://books.google.com/books?hl=en&lr=&id=oCSG2mYID90C&oi=fnd&pg=PP1&dq=human+osteology+white&ots=VolMgMKCYD&sig=eZjCGDZIGo0QvfT1ro6mnRCiXbc> [Accessed 1 August 2022].

White, T. and Folkens, P. (2005). *The Human Bone Manual*. [Online]. Available at: doi:10.1016/C2009-0-00102-0 [Accessed 20 May 2022].

Wilderman, A. et al. (2018). High-Resolution Epigenomic Atlas of Human Embryonic Craniofacial Development Resource High-Resolution Epigenomic Atlas of Human Embryonic Craniofacial Development. *CellReports*, 23 (5), pp.1581–1597. [Online]. Available at: doi:10.1016/j.celrep.2018.03.129.

Witmer, L. M. (1997). The evolution of the antorbital cavity of archosaurs: A study in soft-tissue reconstruction in the fossil record with an analysis of the function of Pneumaticity. *Journal of Vertebrate Paleontology*, 17, pp.1–76. [Online]. Available at: doi:10.1080/02724634.1997.10011027 [Accessed 3 November 2022].

Witzel, U. (2011). Virtual synthesis of the skull in neanderthals by FESS. In: *Vertebrate Paleobiology and Paleoanthropology*. (9789400704916). Springer. pp.203–211. [Online]. Available at: doi:10.1007/978-94-007-0492-3\_18.

Witzel, U. and Preuschoft, H. (2002). Function-dependent shape characteristics of the human skull. *Anthropologischer Anzeiger Jahrg*, 2 (Juni 2002), pp.113–135. [Online]. Available at: doi:10.1127/anthranz/60/2002/113 [Accessed 20 May 2022].

Witzel, U. and Preuschoft, H. (2005). Finite-element model construction for the virtual synthesis of the skulls in vertebrates: Case study of Diplodocus. In: *Anatomical Record - Part A Discoveries in Molecular, Cellular, and Evolutionary Biology*. 283 (2). April 2005. pp.391–401. [Online]. Available at: doi:10.1002/ar.a.20174 [Accessed 20 May 2022].

Witzel, U., Preuschoft, H. and Sick, H. (2004). The role of the zygomatic arch in the statics of the skull and its adaptive shape. *Folia Primatologica*, 75 (4), pp.202–218. [Online]. Available at: doi:10.1159/000078935.

Wolpoff, M. H. (1968a). Climatic influence on the skeletal nasal aperture. *American Journal of Physical Anthropology*, 29 (3), pp.405–423. [Online]. Available at: doi:10.1002/ajpa.1330290315.

Wolpoff, M. H. (1968b). ‘Telanthropus’ and the Single Species Hypothesis. *American Anthropologist*, 70 (3), pp.477–493. [Online]. Available at: doi:10.1525/AA.1968.70.3.02A00020.

Wolpoff, M. H. (1999). Paleoanthropology: Controversy without end or an end without controversy? *Reviews in Anthropology*, 28 (3), pp.267–288. [Online]. Available at: doi:10.1080/00988157.1999.9978235 [Accessed 3 November 2022].

Wong, K. K., Filatov, S. and Kibblewhite, D. J. (2010). Septoplasty retards midfacial growth in a rabbit model. *Laryngoscope*, 120 (3), pp.450–453. [Online]. Available at: doi:10.1002/lary.20769.

Wood, S. A. et al. (2011). The effects of modeling simplifications on craniofacial finite element models: The alveoli (tooth sockets) and periodontal ligaments. *Journal of Biomechanics*, 44 (10), pp.1831–1838. [Online]. Available at: doi:10.1016/j.jbiomech.2011.03.022 [Accessed 20 April 2022].

Wormald, P. J. and Alun-Jones, T. (1991). Anatomy of the temporalis fascia. *The Journal of Laryngology & Otology*, 105 (7), pp.522–524. [Online]. Available at: doi:10.1017/S0022215100116500 [Accessed 5 November 2022].

Wroe, S. et al. (2010). The craniomandibular mechanics of being human. *Proceedings of the Royal Society B: Biological Sciences*, 277 (1700), pp.3579–3586. [Online]. Available at: doi:10.1098/rspb.2010.0509.

Wroe, S. et al. (2018). Computer simulations show that Neanderthal facial morphology represents adaptation to cold and high energy demands, but not heavy biting. *Proceedings of the Royal Society B: Biological Sciences*, 285 (1876). [Online]. Available at: doi:10.1098/rspb.2018.0085.

Zelditch, M. and Moscarella, R. (2004). *Form, function, and life history*. [Online]. Available at: [https://books.google.com/books?hl=en&lr=&id=tarmCwAAQBAJ&oi=fnd&pg=PA274&dq=Zeldich+et+al,+2004+principal+component&ots=qiHJZ0rUnT&sig=-CbR9sGkHgHVY\\_rh2M9z5K-VaB4](https://books.google.com/books?hl=en&lr=&id=tarmCwAAQBAJ&oi=fnd&pg=PA274&dq=Zeldich+et+al,+2004+principal+component&ots=qiHJZ0rUnT&sig=-CbR9sGkHgHVY_rh2M9z5K-VaB4) [Accessed 12 September 2022].

- Zeller, R., López-Ríos, J. and Zuniga, A. (2009). Vertebrate limb bud development: Moving towards integrative analysis of organogenesis. *Nature Reviews Genetics*, 10 (12), pp.845–858. [Online]. Available at: doi:10.1038/nrg2681 [Accessed 5 November 2022].
- Zink, K. D. and Lieberman, D. E. (2016). Impact of meat and Lower Palaeolithic food processing techniques on chewing in humans. *Nature*, 531 (7595), pp.500–503. [Online]. Available at: doi:10.1038/nature16990 [Accessed 25 April 2022].
- Zink, K. D., Lieberman, D. E. and Lucas, P. W. (2014). Food material properties and early hominin processing techniques. *Journal of Human Evolution*, 77, pp.155–166. [Online]. Available at: doi:10.1016/j.jhevol.2014.06.012 [Accessed 25 April 2022].
- Zollikofer, C. P. E. et al. (1995). Neanderthal computer skulls. *Nature*, 375 (6529), pp.283–285. [Online]. Available at: doi:10.1038/375283b0 [Accessed 19 September 2022].
- Zollikofer, C. P. E. et al. (2005). Virtual cranial reconstruction of Sahelanthropus tchadensis. *Nature*, 434 (7034), pp.755–759. [Online]. Available at: doi:10.1038/nature03397 [Accessed 5 November 2022].
- Zollikofer, C. P. E. et al. (2008). New insights into mid-late pleistocene fossil hominin paranasal sinus morphology. *Anatomical Record*, 291 (11), pp.1506–1516. [Online]. Available at: doi:10.1002/ar.20779 [Accessed 3 November 2022].
- Zollikofer, C. P. E. (2012). *Evolution of hominin cranial ontogeny*. 1st ed. Elsevier B.V. [Online]. Available at: doi:10.1016/B978-0-444-53860-4.00013-1.
- Zollikofer, C. P. E., Bienvenu, T. and Ponce de León, M. S. (2017). Effects of cranial integration on hominid endocranial shape. *Journal of Anatomy*, 230 (1), pp.85–105. [Online]. Available at: doi:10.1111/joa.12531.
- Zollikofer, C. P. E. and de León, M. S. P. (2001). Computer-assisted morphometry of hominoid fossils: the role of morphometric maps. In: *Hominoid Evolution and Climatic Change in Europe: Volume 2. Phylogeny*. pp.50–59. [Online]. Available at: doi:10.1017/cbo9780511600449.003 [Accessed 22 April 2022].
- Zollikofer, C. P. E. and Ponce De León, M. S. (2004). Kinematics of cranial ontogeny: Heterotopy, heterochrony, and geometric morphometric analysis of growth models. *Journal of Experimental Zoology Part B: Molecular and Developmental Evolution*, 302

(3), pp.322–340. [Online]. Available at: doi:10.1002/jez.b.21006 [Accessed 22 April 2022].

Zollikofer, C. P. E., Ponce de León, M. S. and Martin, R. D. (1998). Computer-assisted paleoanthropology. *Evolutionary Anthropology: Issues, News, and Reviews*, 6 (2), pp.41–54. [Online]. Available at: [https://onlinelibrary.wiley.com/doi/abs/10.1002/\(SICI\)1520-6505\(1998\)6:2%3C41::AID-EVAN2%3E3.0.CO;2-Z?casa\\_token=vqELhO1dDNEAAAAA:VaQVGrnUayBs6pAd6RXPxR9kDmVe\\_mPfBqSIHYboExh\\_yhcqDK57oLk52mDuR5E2Gdue7bY2mynkpYU](https://onlinelibrary.wiley.com/doi/abs/10.1002/(SICI)1520-6505(1998)6:2%3C41::AID-EVAN2%3E3.0.CO;2-Z?casa_token=vqELhO1dDNEAAAAA:VaQVGrnUayBs6pAd6RXPxR9kDmVe_mPfBqSIHYboExh_yhcqDK57oLk52mDuR5E2Gdue7bY2mynkpYU) [Accessed 19 September 2022].

Zollikofer, C. P. E. and Weissmann, J. D. (2008). A morphogenetic model of cranial pneumatization based on the invasive tissue hypothesis. *Anatomical Record*, 291 (11), pp.1446–1454. [Online]. Available at: doi:10.1002/ar.20784 [Accessed 3 November 2022].

## Appendix 1: Neanderthal reconstructions

### **Amud 1**

The Amud 1 (Figure 1) adult male cranium was found in the Amud Cave, near the Amud Gorge (Wadi el ‘Amud) just northwest of lake Tiberias (Sea of Galilee, Israel). The remains were dated between 50,000-70,000 years ago (Valladas et al., 1999; Rink et al., 2001). The cranium is filled with matrix and lacks the basicranium and palate. The right side was also slightly compressed during fossilisation. An initial manual reconstruction was conducted by Suzuki, (1970) using plaster and Shanidar 1 fossil and this was used as a reference.

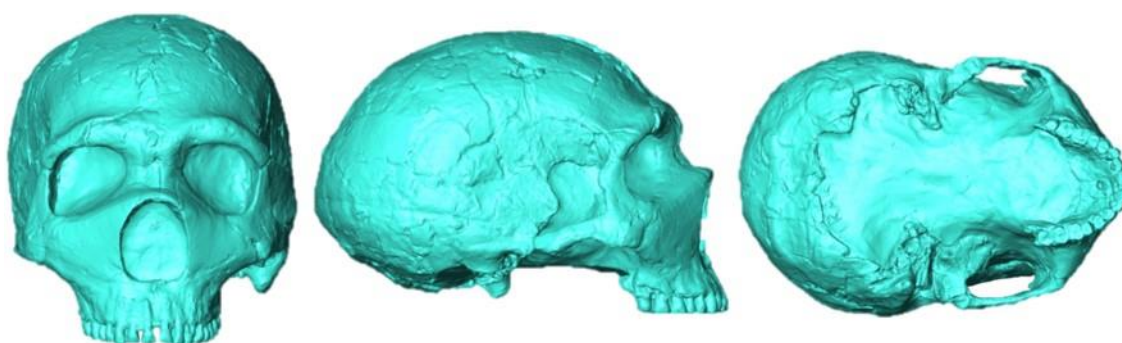


*Figure 1.* Amud 1 cranium remain.

A first warping was conducted using 24 landmarks. Then a second affine rigid warping was conducted using the same landmarks and 185 semi-landmarks located on the cranial vault, maxilla and zygomatics to align and scale Saccopastore 1 cranium (see below). Then, the basicranium and palate from the warped Saccopastore 1 specimen were extracted and merged using Geomagic® (Studio 2018). Finally, the external surface was then extracted using R and the “Arothron” package for R (Profico et al., 2019). The final mesh was then cleaned and remeshed (Figure 2).

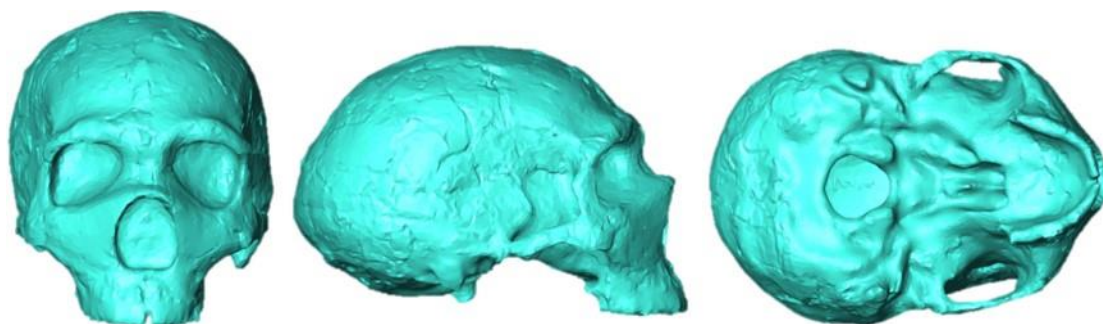


*Figure 2.* Final reconstruction of Amud 1 external surface.

### **La Chapelle aux Saints 1:**

La Chapelle aux Saints 1 (Figure 3) adult cranium was found in the Bouffa Bonneval Cave, in the Sourdoire River Valley near the village of La-Chapelle aux Saints (40km from Brive-la-Gaillarde, Corrèze, France). This skull was dated using mammal teeth found in the cave and is estimated to have lived between 47 +/- 3 and 56 +/- 4 ka ago (Grün and Stringer, 1991). The skull is well preserved, especially the maxilla and frontal bone as well as the orbitals. However, the skull is missing nasal bones, orbital cones, almost all the sphenoidal region, part of the left parietal, and regions of jugular foramina (Arambourg, 1955; Schwartz and Tattersall, 2003).

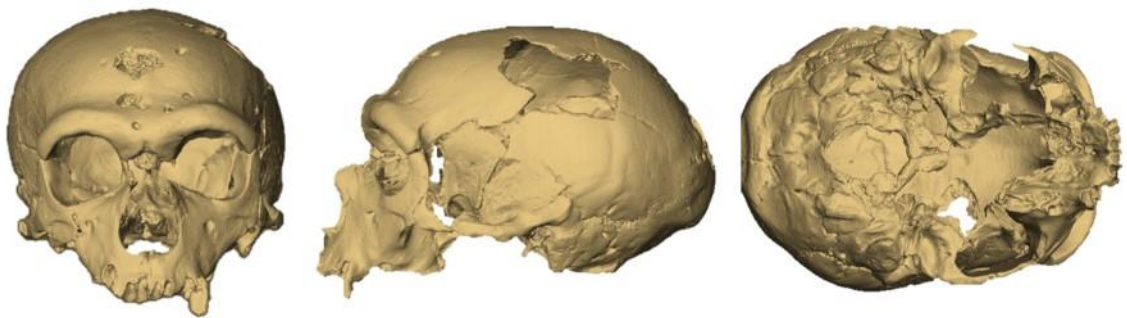


*Figure 3.* La Chapelle-aux-Saints 1 cranium remain.

First, the cranium was segmented and the reflected relabelling approach was used based on 13 paired landmarks in order to reconstruct the left parietal and temporal bones, and part of the zygomatic arches. Then, Geomagic® (Studio 2018) was used to clean the mesh using the “point warp retriangulation” and “mesh doctor” tools and to consolidate the zygomatic arches (Figure 4).

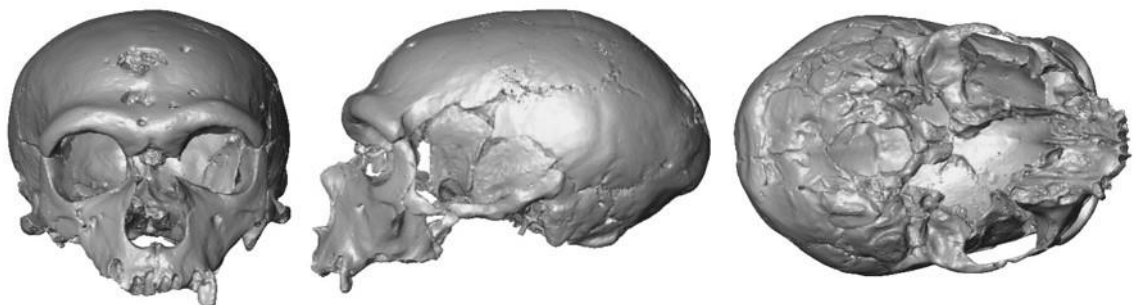


*Figure 4.* La Chapelle-aux-Saints 1 reconstructed using reflected relabeling approach.

A retro-deformed version of Saccopastore was then warped to fit the surface using Avizo 9.0 (FEI Visualization) and R (Schlager, 2017) in order to reconstruct the missing parts of the sphenoidal region, the inferior part of the right malar and dental arcades, orbital floor, cones of the orbits and nasal bones), part of the basicranium and the posterior part of the palate. The Saccopastore specimen was used here because it is well-preserved. A total of 37 fixed landmarks and 150 approximately equidistant semi-landmarks on the cranial vault and 120 on the face (maxilla, orbits, supraorbital) were used to control the warping. The missing parts were then extracted from the warped Saccopastore specimen using Geomagic® (Studio 2018) Studio and merged into the La Chapelle aux Saints mesh. The external surface was then extracted using the R package “Arothron” (Profico et al, 2019). The final mesh of La Chapelle aux Saints 1 was then cleaned (holes filled and remeshed) to obtain a complete external surface (Figure 5).

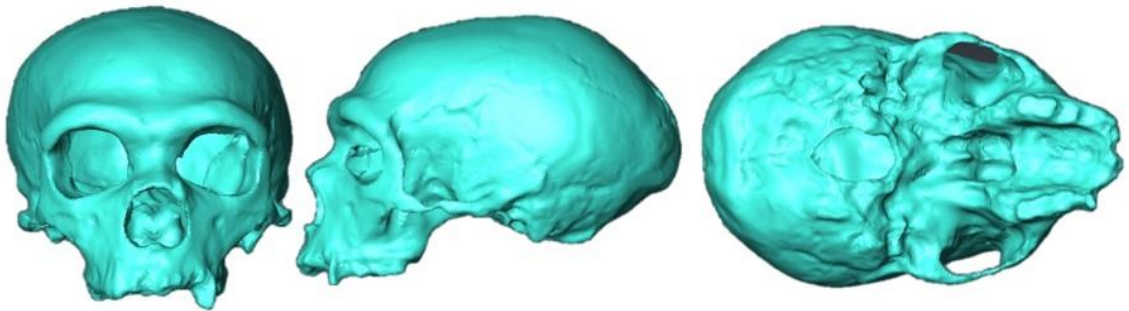
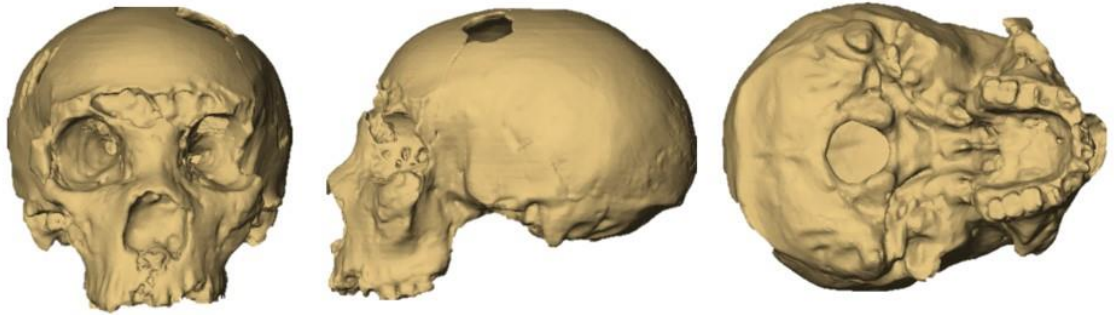


Figure 5. Final reconstruction of La-Chapelle-aux-Saints 1 external surface.

### **Saccopastore 1:**

The Saccopastore 1 adult specimen (Figure 6) was discovered in a Gravel pit (now gone), in the suburbs of Rome, within a meander of the Aniene river, a tributary of the Tiber, Italy (Blanc, 1938; Piperno, Segre and Ronen, 1982). Saccopastore 1 is a fairly complete cranium but lacks the supraorbital and glabellar regions, both of the zygomatic arches and parts of the left frontal and right parietal bones (Schwartz and Tattersall, 2003).



*Figure 6.* Saccopastore 1 cranium remain.

The first step was to reconstruct the supraorbital ridge using the Gibraltar 1 specimen. We used a total of 15 fixed landmarks and 160 semi-landmarks to scale and warp Gibraltar 1 onto the Saccopastore 1 cranium using Avizo 9.0 (FEI Visualization). The supraorbital ridge and the superior part of the orbits were then extracted from the warped mesh and merged with Saccopastore 1 using Geomagic® (Studio 2018). The mesh was then cleaned and remeshed in Geomagic® using the “mesh doctor” and “remeshed” tools. Then, the reconstructed version of La-Chapelle aux Saints 1 was scaled and warped to Saccopastore using 18 fixed landmarks in order to repair the inferior part of the maxilla, the zygomatic arches and lateral orbitals. Finally, the parts of interest were extracted and merged into the Saccopastore mesh using Geomagic® (Studio 2018). The external surface was then extracted using R and the “Arothron” package for R (Profico et al, 2019). The final mesh was then cleaned and remeshed to obtain a good external surface (Figure 7).

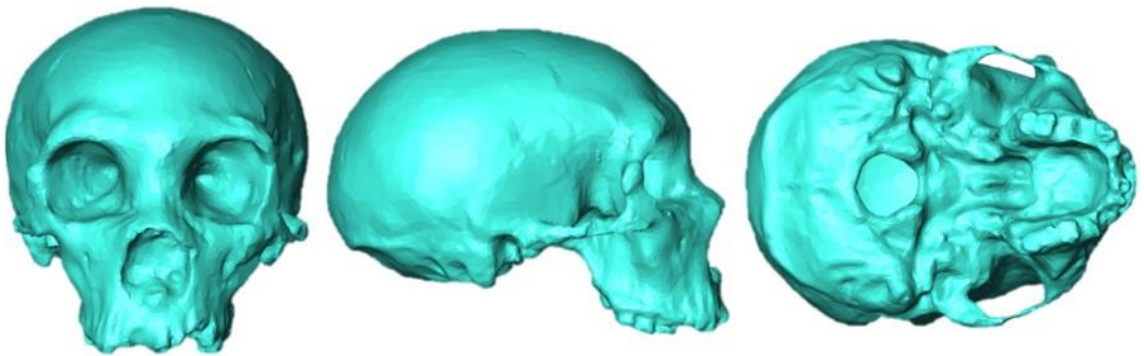


*Figure 7.* Final reconstruction of Saccopastore 1 external surface.

## Guattari:

The Guattari 1 adult cranium (Figure 8) was found in the Grotta Guattari located near the village of San Felice on the eastern flank of Monte Morrone, the eastern spur of Monte Circeo in Italy (Taschini, 1979; Blanc, 1961). The surface of the cave (where the fossil was found) was dated using U-series on the earliest calcite coating of surface bones and this estimated it to be dated from 51 +/- 3 ka. Moreover, dating using mammalian fauna has given dates of 44.0 +/- 5 ka to 62.6 +/- 6 ka (Schwarcz et al., 1991). This cranium is lacking a large portion of the base, the right sphenoorbito-maxillary region, the right zygomatic arch and nasal bones. Some of the external surfaces are damaged (Schwartz and Tattersall, 2003).



*Figure 8.* Guattari 1 cranium.

In this specimen, first, reflected relabelling was used to reconstruct the right sphenoorbito-maxillary region and zygomatic arch using the R package “Arothron” with 14 paired landmarks. Then, the basicranium was reconstructed using the la Chapelle aux Saints 1 Neanderthal. This was scaled and warped to Guattari 1 with Avizo 9.0 (FEI Visualization) using a total of 16 fixed landmarks and 134 semi-landmarks (vault and anterior maxilla bone) to control the warping. The basicranium was then extracted from the warped La Chapelle aux Saints 1 and merged to the Guattari 1 mesh in Geomagic® (Studio 2018). The external surface (Figure 9) was then extracted using the R package “Arothron” and the final mesh was cleaned and remeshed in Geomagic® (Studio 2018).

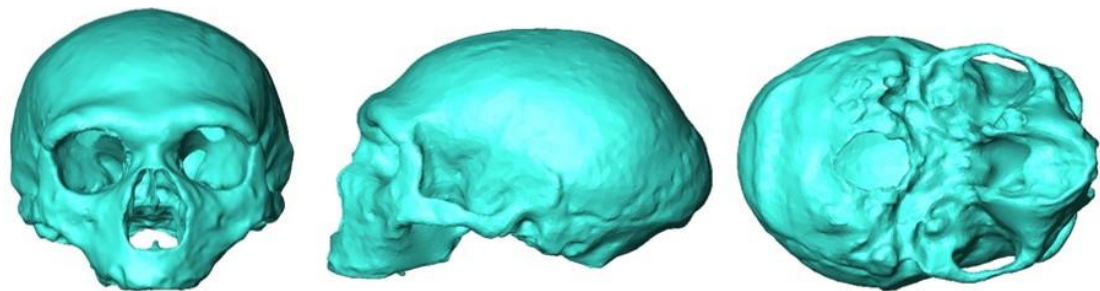


*Figure 9.* Final reconstruction of the Guattari 1 external surface

### **La Ferrassie 1:**

The La Ferrassie 1 adult cranium (Figure 10) was discovered in a rock shelter near Savignac du Bugue in Dordogne, France (Capitan and Peyrony, 1909; Bourgon, 1957). The stratigraphy of the rock shelter and associated fauna place the Ferrassie 1 site within the Mousterian at around 70 ka (Mellars, 1996). The fossils have been suggested to be somewhat younger than this (Heim, 1974). The fossil presents quite a large and complete cranium that lacks nasal bones, medial orbital walls, sphenoid and alisphenoid regions, as well as part of the right and left petrosals (Schwartz and Tattersall, 2003).



*Figure 10.* La Ferrassie 1.

This fossil is largely preserved. In order to reconstruct the nasal bones, a crack in the supraorbital torus, a small posterior part of the palate and the anterior basicranium, the reconstructed skull of La Chapelle aux Saints 1 was warped (in R) onto La Ferrassie 1 using 33 fixed landmarks, patches of semi-landmarks on the supraorbital torus (50), face and zygomatic bone (120), neurocranium (200) and palate (30) as well as curve semi-landmarks around the orbits (20), nasal cavity (20) and foramen magnum (20).

The anatomical parts to replace the missing ones were extracted from the warped mesh and merged in R (“Morpho” package) retriangulated in Avizo 9.0 (FEI Visualization) and cleaned up in Geomagic® (Studio 2018). Finally, the external surface was isolated and the mesh was cleaned and remeshed in Geomagic® (Studio 2018) (Figure 11).

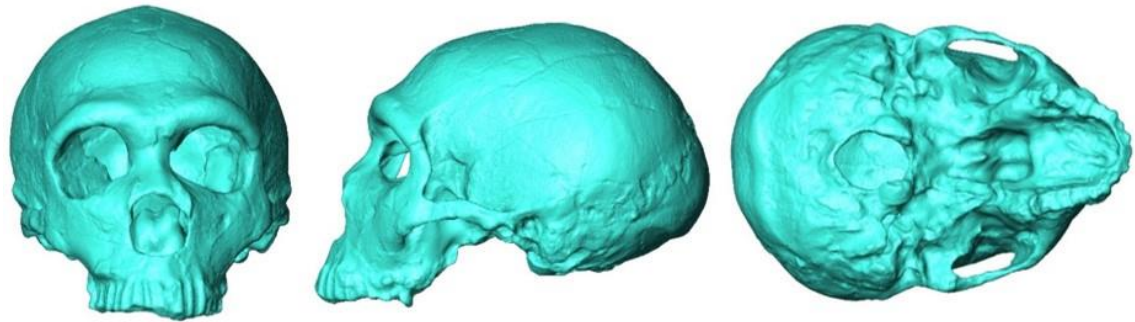


Figure 11. Final reconstruction of La Ferrassie 1 external surface.

### **Pech de l'Azé:**

The infant Pech de l'Azé partial cranium (Figure 12) was found in a cavity near Carsac in the Dordogne, France (Capitan and Peyrony, 1909). The fossil was dated using mammal teeth and by reference to the lithic industry. It is estimated to have lived around 45 to 55 ka (Grün and Stringer, 1991; Schwarcz and Blackwell, 1983). The infant cranium age is estimated to be around 3 to 4 years, based on osteological and dental criteria (Patte, 1957). This partial cranium is missing parts of the parietals, occipital, basicranium, and all of the sphenoid and internal facial structures (Schwartz and Tattersall, 2003).

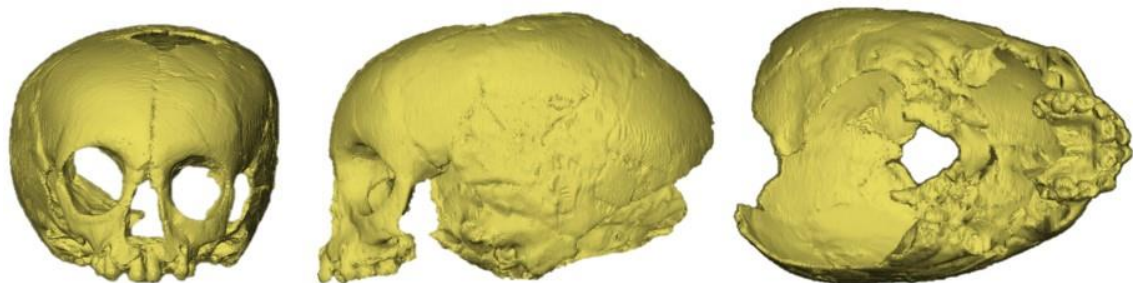


Figure 12. Pech de l'Azé.

The basicranium, sphenoid and occipital bones of this specimen were reconstructed using the Engis 2 specimen. Engis 2 was aligned and scaled to Pech de l'Azé 1 using an affine warping approach in Avizo 9.0 (FEI Visualization) with 12 fixed landmarks. A non-affine warp using 12 fixed landmarks and 90 semi-landmarks (maxilla bone) was used to finalise the warping of Engis 2 to Pech de l'Azé. The basicranium, sphenoid, and part of the occipital bone were extracted and merged with the Pech de l'Azé mesh in Geomagic® (Studio 2018). Small holes in the cranial vault were manually filled using Geomagic® (Studio 2018) tools. A juvenile modern human (Bosma 14 ≤ 5 years

old) was used as the basis for repair of the zygomatic arches. Bosma 14 was first aligned and scaled to Pech de l’Azé using the Avizo 9.0 (FEI Visualization) an affine warping approach and 22 landmarks. Then, Bosma 14 was warped (Bookstein approach) to Pech de l’Azé using 120 semi-landmarks (on the cranial vault and maxilla bone). The zygomatic arches were extracted and merged with the Pech de l’Azé mesh in Geomagic® (Studio 2018). Finally, the external surface was isolated using the “Arothron” package in R. The final mesh was cleaned and remeshed using the “remeshed” and “mesh doctor” Geomagic® (Studio 2018) tools (Figure 13).

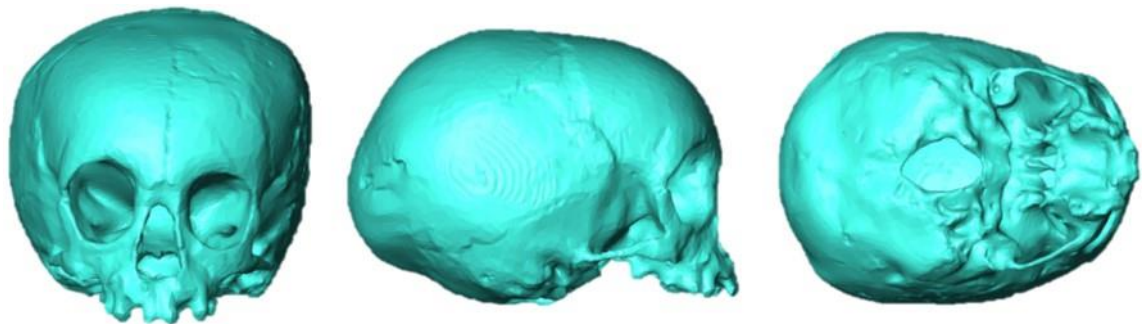


Figure 13. Final reconstruction of Pech de l’Azé 1 external surface.

### **Roc de Marsal:**

The Roc de Marsal infant cranium was found in stratified cave entrance deposits in a side valley of the Vezère river at Campagne-du-Bugue in Dordogne, France (Bordes and Lafille, 1962). The fossil was dated, based on associated fauna and the lithic industry, as around 50 ka (Turq, 1979; Schwartz and Tattersall, 2003). The partial cranium presents

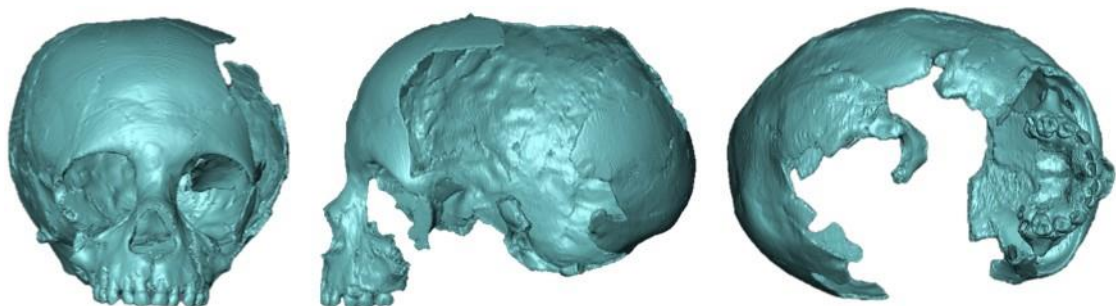
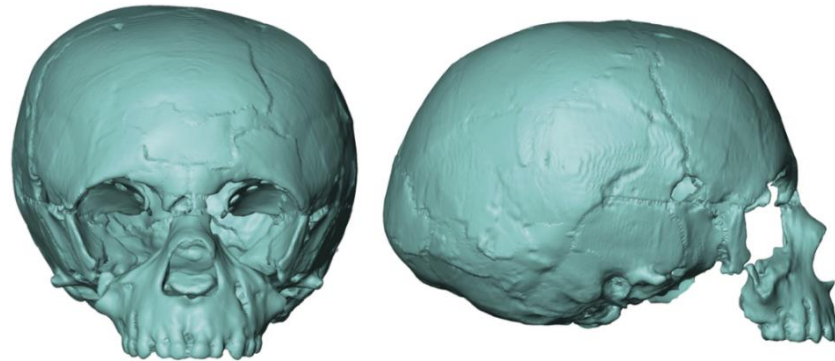


Figure 14. Roc de Marsal.

most of the face, a part of the left parietal, part of the squamous region of the right temporal, and part of the occiput including the basiocciput (Figure 14). This specimen is probably around 4 to 5 years old based on osteological and dental criteria (Madre-Dupouy, 1992; Schwartz and Tattersall, 2003).

This specimen has been previously reconstructed using plaster infill between bones. However, there remain some irregularities in the position and alignment of bones (especially at the cranial vault). Using the provided CT scans, a segmentation of the



*Figure 15.* Roc de Marsal reconstructed after alignment of the bones, mirroring and first round of warping with Engis 2.

specimen was conducted and the occipital and temporal bones were repositioned. Insufficient paired landmarks were identifiable on preserved parts as to conduct symmetrisation through reflected relabeling. Therefore, a series of mirroring and manual alignments were required to reconstruct the occipital (using the left side to reconstruct the right side), the frontal, right sphenoid and right temporal bones (mirrored along a plane that runs through along the crista galli). The original left orbit was not aligned with the mirrored right orbit after mirroring the frontal bone to reconstruct missing areas on the left. Since the left orbit was attached to the frontal with plaster this is likely due to errors in the original reconstruction. In order to use as many original parts as possible, the left orbit (including the partial zygomatic process) was cut from the frontal through the plaster and then aligned with the orbit mirrored right orbit and frontal. The newly repositioned left orbit was then mirrored to the right side and registered to the frontal to reconstruct the right orbital roof. Finally, the face was re-aligned manually (requiring a very slight rotation to preserve the overall position of the face relative to the neurocranium according to the original reconstruction). The midline of the nasal aperture and the central incisors were aligned with the midline of the nasal bones on the external surface and the crista galli on the interior. In the inferior view, the face was then slightly rotated to better align the dental arcade with the neurocranium (Figure 15).

The Engis 2 reconstruction (cranial vault) was used to repair the rest of the cranial vault using warping approaches (in R, with the packages “Morpho” (Schlager, 2017) and “Arothron”) (Figure 15). The first warping of Engis 2 on Roc de Marsal was conducted

using 17 fixed landmarks, 100 surface semi-landmarks on the right parietal, 20 on the partial left parietal, 100 semi-landmarks on occipital, 20 semi-landmarks on each temporal, and 100 semi-landmarks on the frontal. The second warping of Engis 2 was performed using the same semi-landmark configuration and 19 fixed landmarks. Then, the original basioccipital and right inferior part of the occipital were aligned with those of the warped Engis neurocranium using Geomagic® (Studio 2018) to replace these parts in the Roc de Marsal cranium. The right (mirrored) part of the occipital squama was deleted because it did not fit well with the right parietal. Then, the basicranium, zygomatic arches, posterior part of the palate as well as the anterior part of the maxilla were reconstructed using the reconstructed version of Pech de l’Azé 1, a modern human juvenile Bosma 11 (around 5 years old) and a juvenile mean mesh extracted from a single linear regression analysis based on the other Neanderthal specimens in order to check the consistency reconstruction and smooth it. First, Pech de l’Azé 1 was aligned and scaled using Avizo 9.0 (FEI Visualization) and 14 fixed landmarks. Then, the scaled Pech de l’Azé 1 mesh was warped to Roc de Marsal using 12 landmarks and 88 semi-landmarks. The basicranium and posterior part of the palate were extracted and merged with Roc de Marsal in Geomagic® (Studio 2018). Small bony defects were corrected manually in Geomagic® (Studio 2018). Then, the same protocol was followed to warp Bosma 11 using 12 landmarks and 88 semi-landmarks to reconstruct the zygomatic arches. Finally, the external surface was extracted as for the other specimens and the final mesh was cleaned and remeshed in Geomagic® (Studio 2018) (Figure 16).

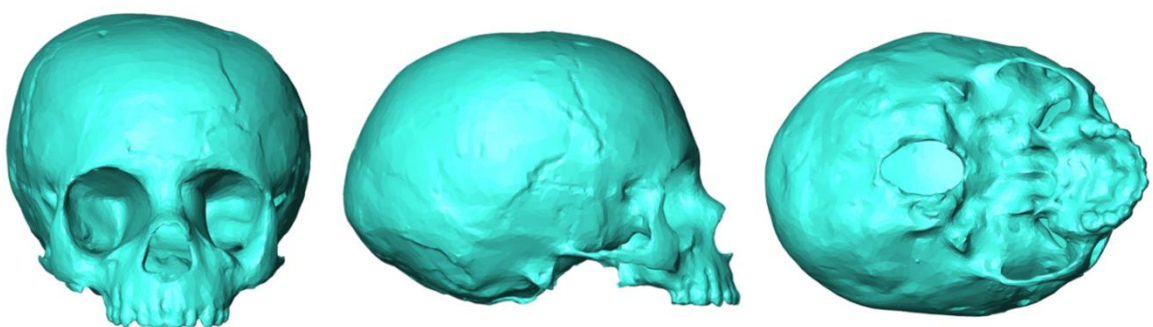


*Figure 16.* Final reconstruction of Roc de Marsal external surface.

## **Gibraltar 2:**

The Gibraltar 2 partial cranium was found in a limestone rock shelter at the western end of North Front, Gibraltar (Garrod et al., 1928). The fossil was dated by extrapolation from charcoal with a similar archaeological context at the nearby Gorham's Cave. It was estimated to have lived 50 ka (Figure 17). Based on dental criteria, the fossil was aged at around 5 years old (Garrod et al., 1928; Zollikofer et al., 1995). The frontal bone, right hemi-maxilla with teeth, left parietal, and right temporal bones are preserved, as well as a partial mandible with erupted left deciduous molars 1 and 2. Some steps were



*Figure 17.* Gibraltar 2 partial cranium remains.

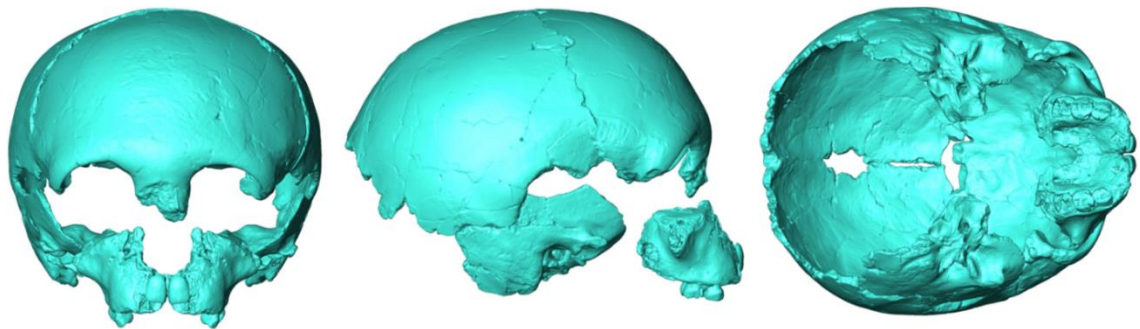


*Figure 18.* Gibraltar 2 juvenile specimen after alignment of the bones and reflected relabeling.

followed of those outlined by Zollikofer et al. (Zollikofer, Ponce de León and Martin, 1998) and the photos of their reconstruction were referred to in order to align the disarticulated bones and reconstruct the cranium using mirror imaging. We used the partial mandible to reconstruct the cranium and align the bones (Schwartz and Tattersall, 2003). The partial mandible was mirrored and aligned with the original to reconstruct the teeth on the right side. We used Geomagic® (Studio 2018) to auto-align the fragments, resulting in a large overlap between the original and mirrored models. The right hemi-maxilla was manually aligned to the reconstructed mandible using maxillary teeth and

reconstructed mandibular teeth on the right side. To guide this, the following parameters were assessed: proper occlusion, anatomically reasonable positioning of the central upper incisor relative to the mandibular symphysis, and similarity with the Zollikofer reconstruction (they used 3D printed models which would have allowed for a better alignment of the teeth since they could feel the relief). A copy of the hemimaxilla was mirrored onto the left side of the mandible. The only points of contact are between the frontal (complete) and left parietal (complete), along the coronal suture which is mostly very well preserved. These bones were fitted together manually in Geomagic® (Studio 2018). A mirrored model of the right temporal bone was then aligned manually to the left parietal bone using the squamosal suture. The left parietal and left temporal were mirrored to the right side using a sagittal plane, aligned with the sagittal frontal crest, the projected lambda and the sagittal suture. Their positions were then slightly adjusted manually to better fit the curve of the coronal suture. There is overlap along the sagittal suture between the original and reconstructed parietals, which could be due to natural asymmetry. The fit is good along the coronal suture, the midline (reconstructed sagittal suture) is well aligned to the frontal crest, and vault symmetry is good, as was symmetry of the length of the fronto-sphenoidal suture. The mandible and temporarily aligned maxilla were then aligned with the reconstructed vault using the mandibular condyles and the condylar fossae of the temporal bones. The fit between the mandible and the cranium, and between the two temporal fossae was used to assess the quality of reconstruction. The positions of the hemi-maxillae were adjusted manually checking for: good occlusion between the cheek teeth, continuity between the locations of the nasal bones, the still patent suture between the frontal bones, the partially preserved outline of the nasal fossa, and the orientation of the central incisors relative to the mandibular symphysis. The mandible was, then, removed (Figure 18).

In order to reconstruct the missing parts of the vault, the cranial vault of the Engis 2 Neandertal juvenile was warped to it, which was itself reconstructed, but to a much lesser extent since bones are better preserved and articulated. We used a total of 28 fixed landmarks and 250 surface semi-landmarks (200 on the cranial vault and 50 on each of the temporal bones) to warp the missing area of the cranial vault, including part of the sphenoid and occipital to Gibraltar 2 using Avizo 9.0 (FEI Visualization). The remaining areas of the malar, zygomatic arches, nose, sphenoid, nasal aperture and basioccipital (anterior margin of the foramen magnum) were also reconstructed by warping these from

the modern human juvenile Bosma 11 (which is of similar age, using a total of 168 fixed landmarks and semi-landmarks). The parts of interest were then extracted and merged to Gibraltar 2 using Geomagic® (Studio 2018). Finally, the mesh was cleaned using Mesh Doctor (ref) and the external surface was isolated before cleaning remeshing in Geomagic® (Studio 2018) (Figure 19).

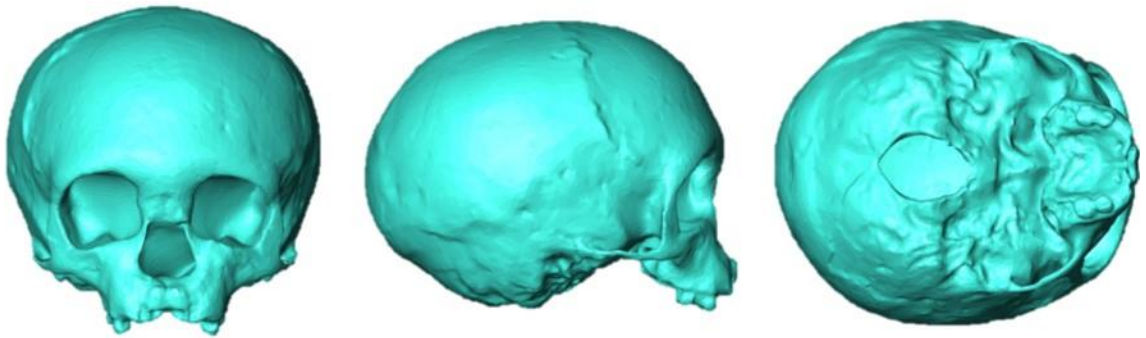


*Figure 19.* Final reconstruction of Gibraltar 2 external surface.

### **Engis 2:**

The juvenile Engis 2 partial cranium (Figure 20) was found in the cave site of Awirs (which no longer exists), near Engis village in Belgium (Schmerling, 1833; Tillier, 1983; Fenart and Empeur-Buisson, 1970). The Engis 2 fossil was associated with the Mousterian level 3 “upper ossiferous layer” and is now dated to 34.5 to 36 ka. The cranium is a juvenile aged around 3 to 5 years based on auditory and mastoid characters. It consists of a partial cranium with a separated maxilla, plus some isolated upper and lower teeth. It is missing most of the left side of the skull (from the orbit to the parietal region), nasal bones, posterior nasal cavity, ethmoid, sphenoid, and parts of occipital and

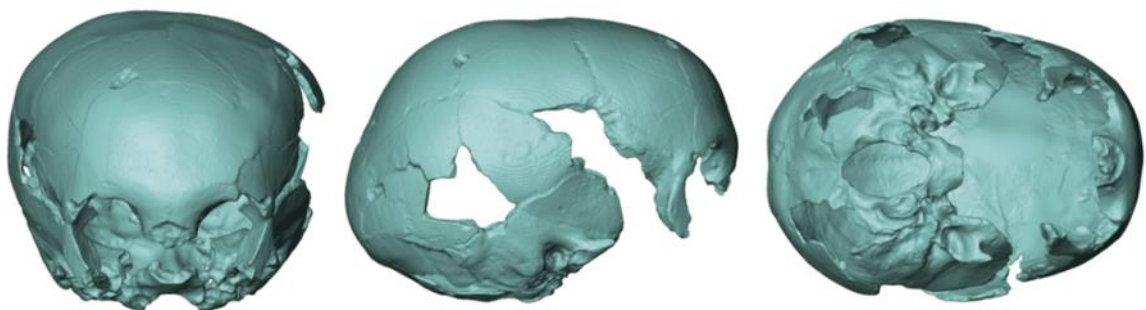


*Figure 20.* Engis 2 partial cranium.

right parietal and temporal bones. The maxilla was not used in this study because of the difficulty of reconstruction (Schwartz and Tattersall, 2003).

The first step of the reconstruction used mirroring and reflected relabeling approaches to reconstruct the cranial vault. The partial cranium was mirrored to reconstruct the occipital region. Then, a reflected relabelling was applied to the mirrored partial cranium using 39 paired landmarks and the R package (“Morpho” and “Arothron”), to symmetrise it. Next, the right temporal and part of the frontal were extracted and reflected to complete the left side of the cranial vault. The fit between the coronal suture and reconstructed part of the frontal, as well as the fit between the reconstructed temporal and the preserved parts of the temporal on the left side (external meatus, mastoid process), was checked and accepted. The mesh was then cleaned (by filling small holes) and retriangulated using Geomagic® (Studio 2018). The second round of reflected relabelling was then carried out using 158 fixed landmarks and semi-landmarks (cranial vault and paired landmarks from the first round) to reconstruct the left parietal bone. The left parietal bone was then extracted and merged to the Engis 2 mesh using Geomagic® (Studio 2018). Finally, to reconstruct the missing part of the cranial vault (part of the sphenoid bones and occipital bone), another Neanderthal specimen, the reconstructed version of La Chapelle aux Saints was warped to Engis 2 using 350 landmarks and semi-landmarks (cranial vault). This resulted in an accurate fit, which was not the case using other Neanderthal juvenile and infant specimens. Then, a modern human juvenile (Bosma 11) was used to reconstruct the missing parts of the basicranium, the rest of the facial skeleton and the zygomatic arches. The surface was aligned and scaled on Engis 2 using 18 landmarks and 150 semi-landmarks (cranial vault) in Avizo 9.0 (FEI Visualization). The parts of interest were extracted and merged using Geomagic® (Studio 2018). However, the alignment and form of the maxilla and zygomatic bones were not a good fit for this reconstruction. Therefore, this reconstruction was only used for the next step.

The last step of the reconstruction was to estimate the form of the maxillae and the zygomatic arches. For this, the estimated mean mesh for the size of Roc de Marsal was extracted from an initial regression-based (shape regressed on size) allometry model, using the other juveniles in the sample. The surface was aligned and scaled on Engis 2-Bosma 11 using 38 landmarks and 225 semi-landmarks in Avizo 9.0 (FEI Visualization). The maxillae and zygomatic arches were extracted using Geomagic® (Studio 2018) and merged with the Engis 2 mesh. The mesh was then cleaned using Geomagic® (Studio 2018). Finally, the external surface mesh was isolated using the R package “Arothron” (Profico et al., 2019) and cleaned/remeshed using Geomagic® (Studio 2018) Studio tools (Figure 21).

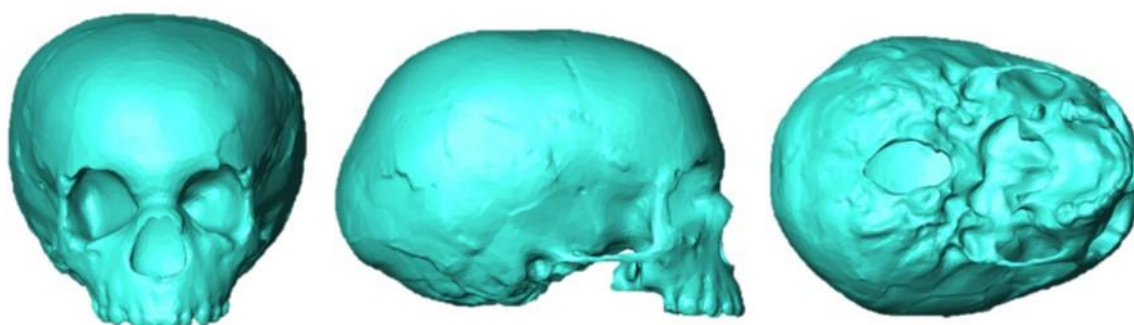


Figure 21. Final reconstruction of Engis 2 external surface.

### **La Quina H18:**

The La Quina H18 infant partial cranium was found in a rock shelter complex near Villebois-Lavalette, Charente, France (Henri-Martin, 1964). The fossil was dated using faunal remains and archaeological association and is estimated to date from 65 ka (Mellars, 1996). The age of this specimen is estimated to be 8 to 11 years. The partial

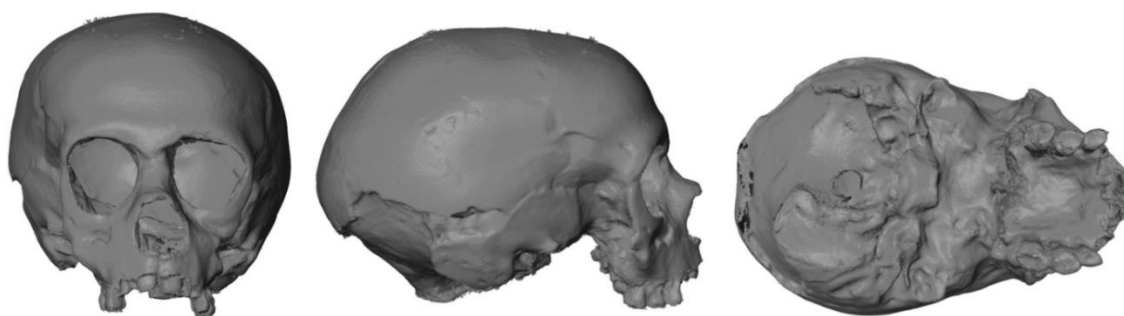
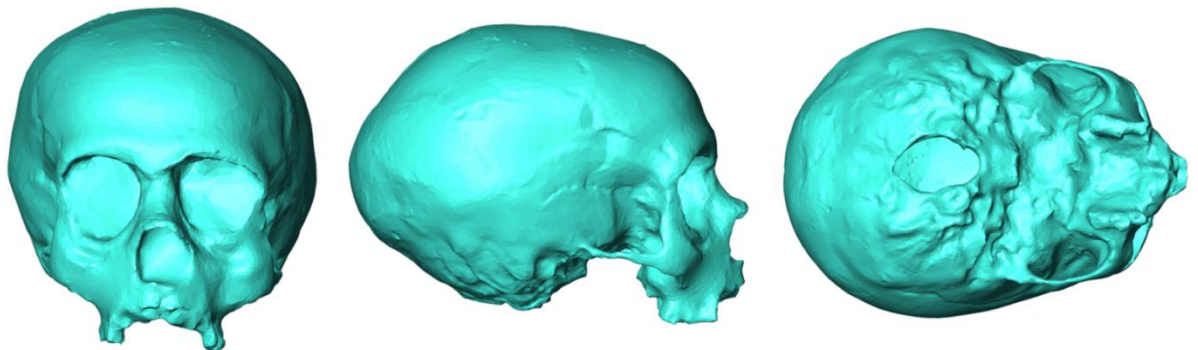


Figure 22. La Quina H18 cranium remains.

cranium is fairly complete and is heavily reconstructed. However, it presents some taphonomic deformations that were partially corrected during the initial reconstruction. It

is missing the sphenoid, ethmoid, most of the orbital cones, nasal cavity structures, and most of the occiput (Figure 22). An external surface mesh was made available for this specimen (Schwartz and Tattersall, 2003), and forms the basis of the reconstruction

The reconstructed Engis 2 specimen was used to reconstruct the occipital bone, basicranium and left zygoma and zygomatic arch. Engis 2 was first, aligned and scaled to La Quina H18 using the Avizo 9.0 (FEI Visualization) affine warping tool and 34 landmarks. Then, another, non-affine warping was conducted of the scaled Engis 2 to La Quina H18 using 35 landmarks and 160 semi-landmarks over the anterior maxilla and cranial vault. The basicranium, occipital bone, left zygomatic arch and zygoma were extracted from the warped mesh and merged with La Quina H18. To reconstruct the right zygomatic arch and zygoma a reflected relabelling mirroring was conducted using 16 paired landmarks. The structures needed to reconstruct the missing parts were then extracted from the mirrored surface and merged with the La Quina H18 mesh. Finally, the final external surface was cleaned and remeshed in Geomagic® (Studio 2018) Studio (Figure 23).



*Figure 23.* Final reconstruction of La Quina H18 external surface.

### **Mezmaiskaya (MCZ) – Le Moustier 2:**

The Le Moustier 2 infant partial skull was found in Le Moustier village in the Dordogne, France (Hauser, 1909; Hesse and Ullrich, 1966). The fossil was dated based on analyses of associated burned flint (Valladas et al., 1986) and is estimated to date from 4.3 +/- 2.6 ka. The partial cranium consists of a largely complete frontal, most of the left temporal with adjacent pieces of the left parietal, occipital and alisphenoid, most of the right parietal, a fragment of the basiocciput and the adjacent right occipital, a fragment of the sphenoid and partial palate (Schwartz and Tattersall, 2003).

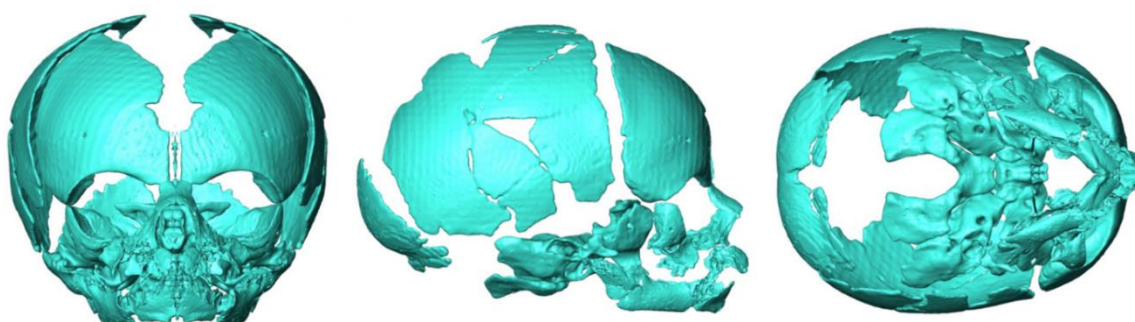


*Figure 24.* The Mezmaiskaya-Le Moustier 2 reconstruction by Gunz et al., 2012.

The Mezmaiskaya infant cranium remains were found in Mezmaiskaya cave in the Northern Caucasus. It was dated based on faunal remains and is estimated to date from 63 -73 ka (Golovanova et al., 1999; Ponce De León et al., 2008). The infant cranium comprises most of the cranial vault, part of the basicranium, and subnasal parts of the maxilla. In this study, we based our reconstruction on one previously made by Ponce De León et al in 2008 using the Mezmaiskaya fossil alone, and on one made Gunz et al. (2012) in which this fossil was reconstructed using parts of Le Moustier 2 (Gunz et al., 2012; Figure 24).

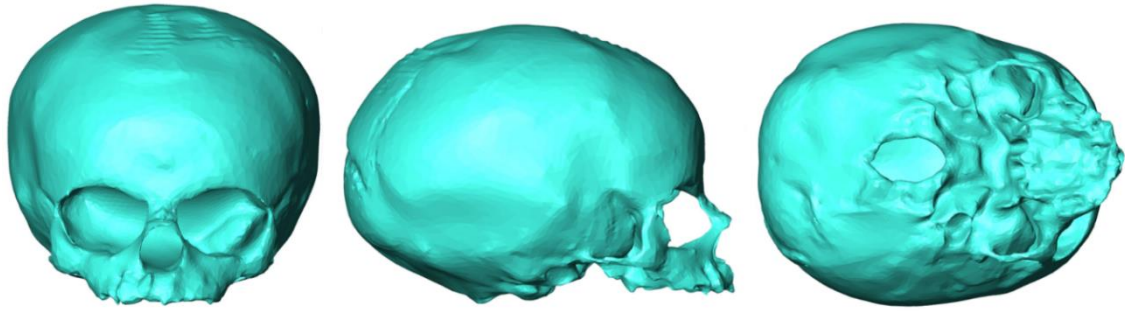


*Figure 25.* Final reconstruction of the Mezmaiskaya-Le Moustier 2 external surface.

Nasal and other missing portions of the Mezmaiskaya-Le Moustier reconstruction by Gunz et al, 2012 were reconstructed using the modern human infant BOSMA 7 (which is around one year old) and the Neanderthal allometric mean infant surface predicted for its size, extracted from a preliminary regression-based model of allometry based on the other subadult Neanderthal specimens in this study and using the reconstructed version of Roc de Marsal as a reference surface. The mean Neanderthal infant surface was aligned and scaled to fit Mezmaiskaya-Le Moustier 2 in Avizo 9.0 (FEI Visualization) using 17 landmarks. A Bookstein warping of the scaled mean Neanderthal infant mesh to Mezmaiskaya-Le Moustier 2 was conducted using 17 landmarks and 89 semi-landmarks over the cranial vault, maxilla and orbitals. The basicranium, maxilla and posterior part of the palate were extracted from the warped surface and merged with Mezmaiskaya-Le Moustier 2 using Geomagic® (Studio 2018). A modern human infant (BOSMA 7) was used to reconstruct the zygomatic arches after being aligned and scaled to Mezmaiskaya-Le Moustier 2 using Avizo 9.0 (FEI Visualization) and 17 landmarks. This was then warped to fit using 17 landmarks and 77 semi-landmarks and the zygomatic arches were extracted from the warped surface and merged with Mezmaiskaya-Le Moustier 2 using Geomagic® (Studio 2018). Finally, the external surface of the reconstructed specimen was extracted using R and “Arothron” package, and the final mesh was cleaned and remeshed in Geomagic® (Studio 2018) Studio (Figure 25).

## Appendix 2: Sensitivity test of the effect of filling in of frontal and maxillary sinuses

In this study, the finite element (FE) modern human and Neanderthal models were segmented as a single material (eventually allocated the material properties of bone, see below) and the frontal and maxillary sinuses were filled for both species and with the same material. In addition, the ethmoid sinuses were also filled in the same way in modern human models but not in Neanderthal ones as these areas were already solid due to the fossils conservation state and the reconstruction. In fossils the sinus is not easily segmented and prior studies have indicated that the filling of the sinuses has little effect on how the cranium resists strains (Toro-Ibacache et al., 2016). Sensitivity tests were conducted here to evaluate the impact on strains of having filled frontal and maxillary sinuses with bone in the infant, juvenile and adult models of both species. Therefore, the biting simulations on the right first incisor (RI<sup>1</sup>) and second premolar or deciduous molar 2 (RP<sup>2</sup>/RdM<sup>2</sup>) were conducted with unfilled sinus models. The same finite element parameters were applied for the FE analyses in the thesis that use sinus-filled models. Tensile ( $\epsilon_1$ ) and compressive ( $\epsilon_3$ ) strain contour plots and strain values at 126 landmark locations were produced and compared with those from filled sinus models (see section 3.2.1).

Figure 1 and Figure 2 show that the unfilled and filled sinuses models present similar distributions of tensile and compressive strains along the midface. However, the magnitude of these strains is different between these two models, especially for the RP<sup>2</sup>/RdM<sup>2</sup> biting simulation. Indeed, the unfilled sinuses models present higher tensile and compressive strain magnitudes than the stiffer models. Finally, the tensile and compressive strain values at 126 sampling points were plotted in Figures 3 to 6. These present similar patterns of spatial variation of strains as were noted in the strain contour plots and confirm that, in general, both tensile and compressive strain magnitudes are reduced in the sinus filled model during both biting simulations. However, the spatial distribution of regions of high and low strain is similar during RI<sup>1</sup> and RP<sup>2</sup>/RdM<sup>2</sup> biting simulations (Figure 3 to Figure 6).

These findings reflect those of Fitton et al., (2015), Toro-Ibacache et al., (2016) and Renders et al., (2011), who show that a stiffer model (here and in Fitton et al., (2015), with sinuses filled and treated as bone material) experiences a reduction of strains during loading experiments. Moreover, Fitton et al., (2015) compare direct measurements of

strains from a dry *Macaca fascicularis* cranium under incisor biting with those from solid FE models (sinuses filled and treated like cortical bone material) and found that even if the magnitude of strains is impacted, the mode of deformation is relatively constant (Fitton et al., 2015). These findings are of particular relevance when working with fossil material such as the Neanderthal skulls examined in this thesis because the internal structures of these specimens are not well preserved and the sinuses are often missing. By filling the locations of the sinuses in the Neanderthal skull, FE the mode of deformation remains similar to what has been already observed during *in vitro* strain measurements (Fitton et al., 2015; Toro-Ibacache et al., 2016; Renders et al., 2011).

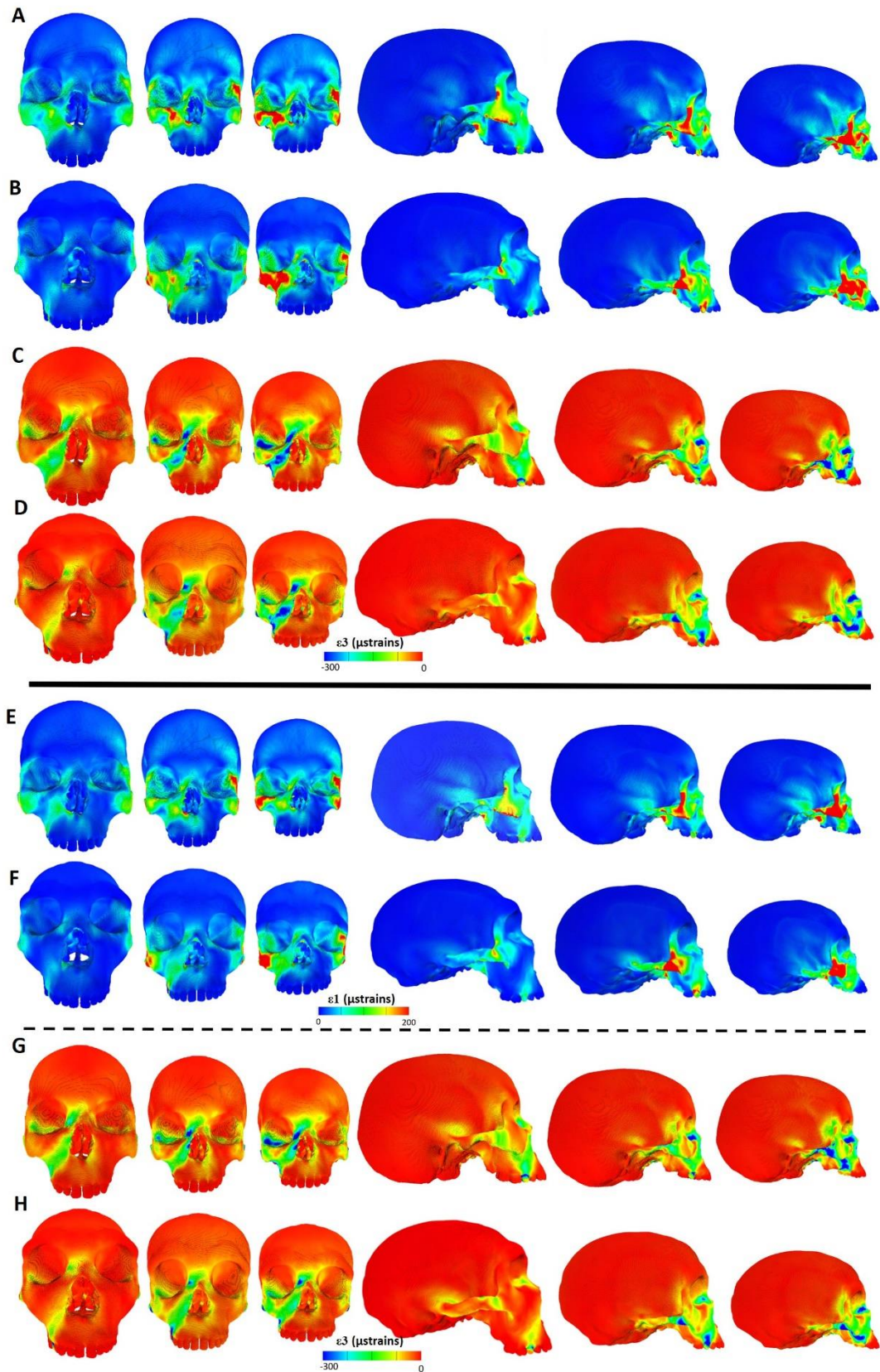


*Figure 1.* Strain contour plot of the solved modern human (A, C, E, F) and Neanderthal (B, D, G, H) infant, juvenile and adult FE models (from left to right) under RP<sup>2</sup>/RdM<sup>2</sup> biting simulation in front and lateral views. The first four rows show the FE models with unfilled sinuses and the last four rows are the FE models with the sinuses filled. Tensile (A, B, E, F) and compressive strains (C, D, G, H) are unscaled.

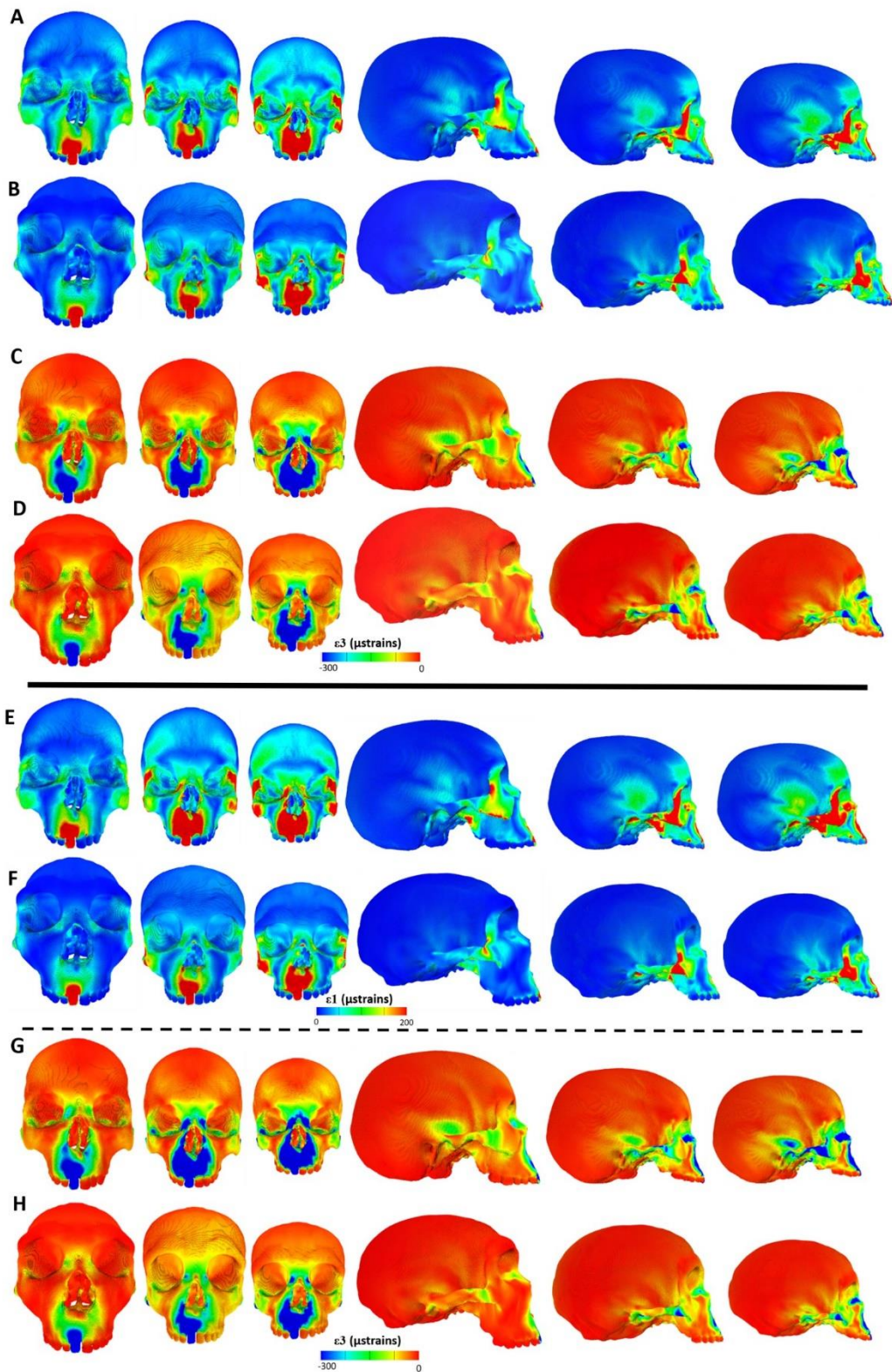


Figure 2. Strain contour plot of the solved modern human (A, C, E, F) and Neanderthal (B, D, G, H) infant, juvenile and adult FE models (from left to right) under  $RI^1$  biting simulation in front and lateral views. The first four rows (A-D) show the FE models with unfilled sinuses and the last four rows (E-H) are the FE models with the sinuses filled. Tensile (A, B, E, F) and compressive strains (C, D, G, H) are unscaled.

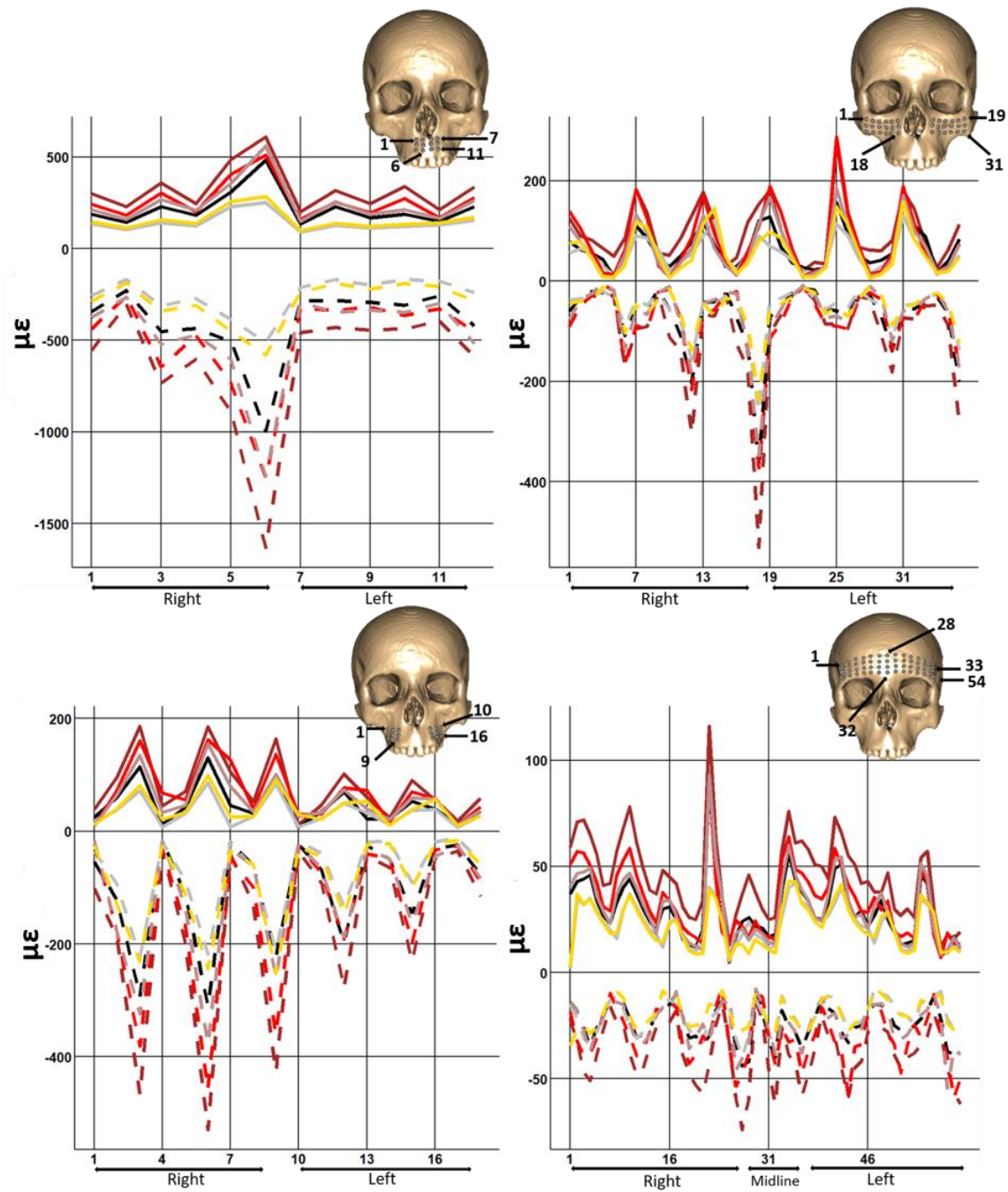


Figure 3. Tensile and compressive strains experienced by the unfilled modern human FE infant (rouge), juvenile (brown) and adult (yellow) filled sinus modern human FE infant (brown), juvenile (black) and adult (grey) at the 126 sampling points collected on the midface and supra-orbital ridge during the RI<sup>1</sup> biting simulation.

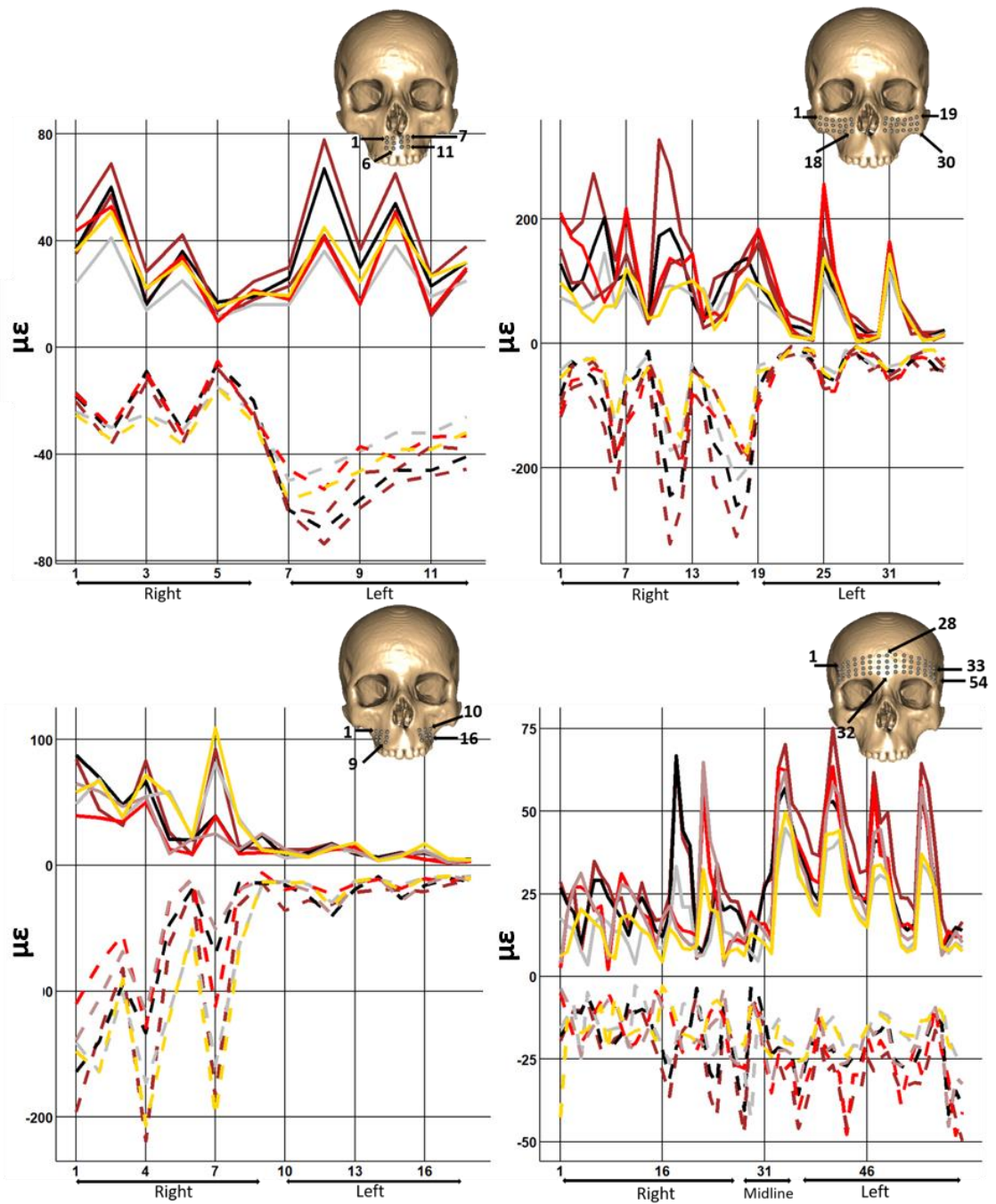


Figure 4. Tensile and compressive strains experienced by the unfilled modern human FE infant (rouge), juvenile (brown) and adult (yellow) filled sinus modern human FE infant (brown), juvenile (black) and adult (grey) at the 126 sampling points collected on the midface and supraorbital ridge during the RP<sup>2</sup>/RdM<sup>2</sup> biting simulation.

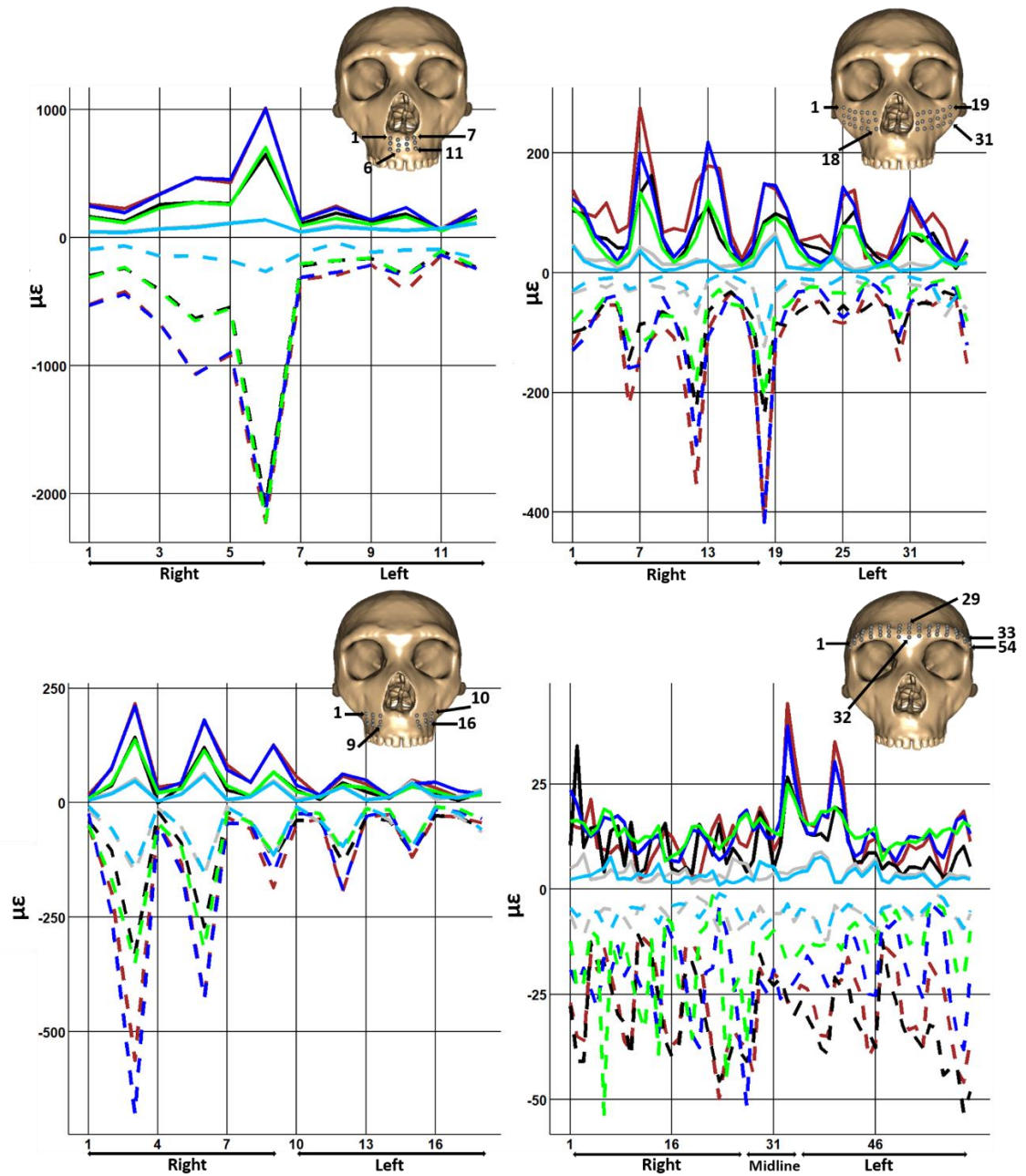


Figure 5. Tensile and compressive strains experienced by the unfilled Neanderthal FE infant (blue), juvenile (green) and adult (deepskyblue) filled sinus Neanderthal FE infant (brown), juvenile (black) and adult (grey) at the 126 sampling points collected on the midface and supra-orbital ridge during the RI<sup>1</sup> biting simulation.

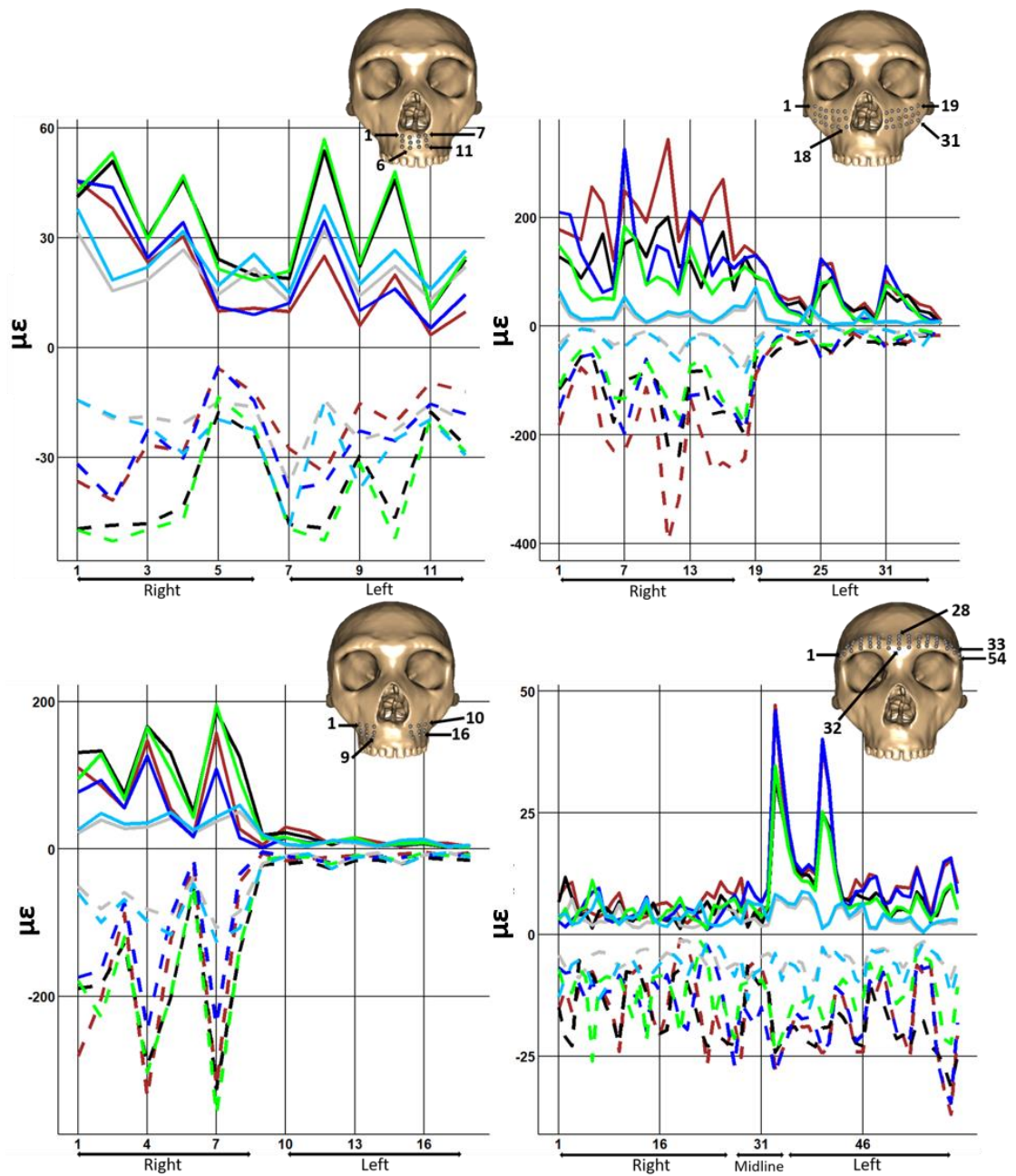
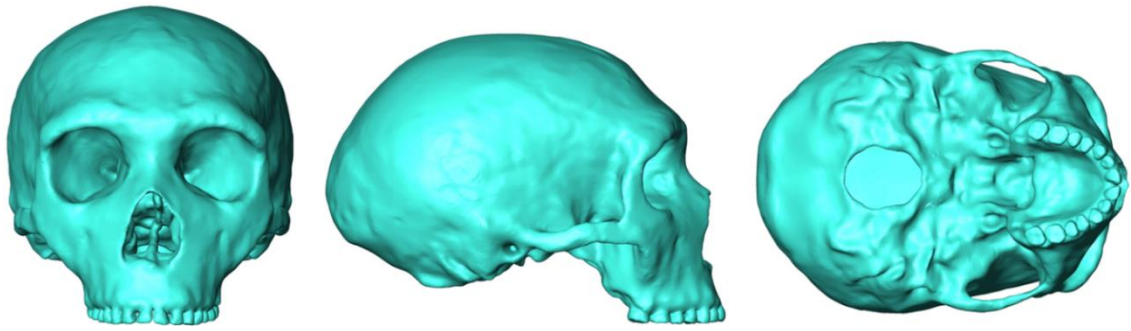


Figure 6. Tensile and compressive strains experienced by the unfilled Neanderthal FE infant (blue), juvenile (green) and adult (deepskyblue) filled sinus modern human FE infant (brown), juvenile (black) and adult (grey) at the 126 sampling points collected on the midface and supraorbital ridge during the RP<sup>2</sup>/RdM<sup>2</sup> biting simulation.

### Appendix 3: Sensitivity test on the effects of different teeth

We conducted a sensitivity test in order to test the effect on craniofacial strains of using a modern human set of teeth in Neanderthal FE models. A Neanderthal set of teeth from Amud 1 was warped onto the mean adult Neanderthal FE model. First, these were segmented from the Amud 1 cranium using Avizo 9.0 (FEI Visualization) v 9.0. Then, using Geomagic Studio, the left side of the tooth set was mirrored to produce identical teeth for the right side. Finally, the complete dentition was warped onto the Neanderthal adult mean model using Avizo 9.0 (FEI Visualization) using 6 fixed landmarks. The warped dentition was, then, merged into the mean model and the final surface was cleaned and remeshed in Geomagic Studio (Figure 1).



*Figure 1.* Neanderthal adult mean model with Neanderthal adult (Amud 1) teeth set.

The new Neanderthal adult mean model was then constrained at the right first incisor (RI<sup>1</sup>) and second premolar (RP<sup>2</sup>) following the same finite element parameters presented in section 4.1.2. The resulting deformations of this model and the model used in the thesis with modern human dentition were then compared by visual assessment of contour plots of the compressive and tensile strain magnitudes over the face (maxilla, nasal, and zygomatic bones). The surface strain (tensile and compressive) magnitudes at 126 points (see section 4.2.1) distributed along the midface and supraorbital were also plotted and compared (Figure 3 and Figure 4).

The results confirm those found in previous studies (Godinho et al., 2017; Toro-Ibacache et al., 2016); the strain contour plots show that changing the dentition mostly affects the magnitudes of tensile ( $\mu 1$ ) and compressive ( $\mu 3$ ) strains rather than the distribution of regions of low and high strain (mode of deformation: see Figure 2). The tensile and compressive strain values plotted from the face are similar to the findings observed in the strain contour plots but the magnitudes of strains in the supraorbital region do change (Figures 3 and 4).

There is a lack of dentition suitable for the Neanderthal juvenile and infant specimens and for this reason modern human teeth were used throughout. It is important for the interpretation of the results in this study, to take into account that a change of shape and/or the size of the teeth seem to have an impact on the magnitudes of the strains rather than their distributions, but that supraorbital strain magnitudes may be reduced to a greater degree.

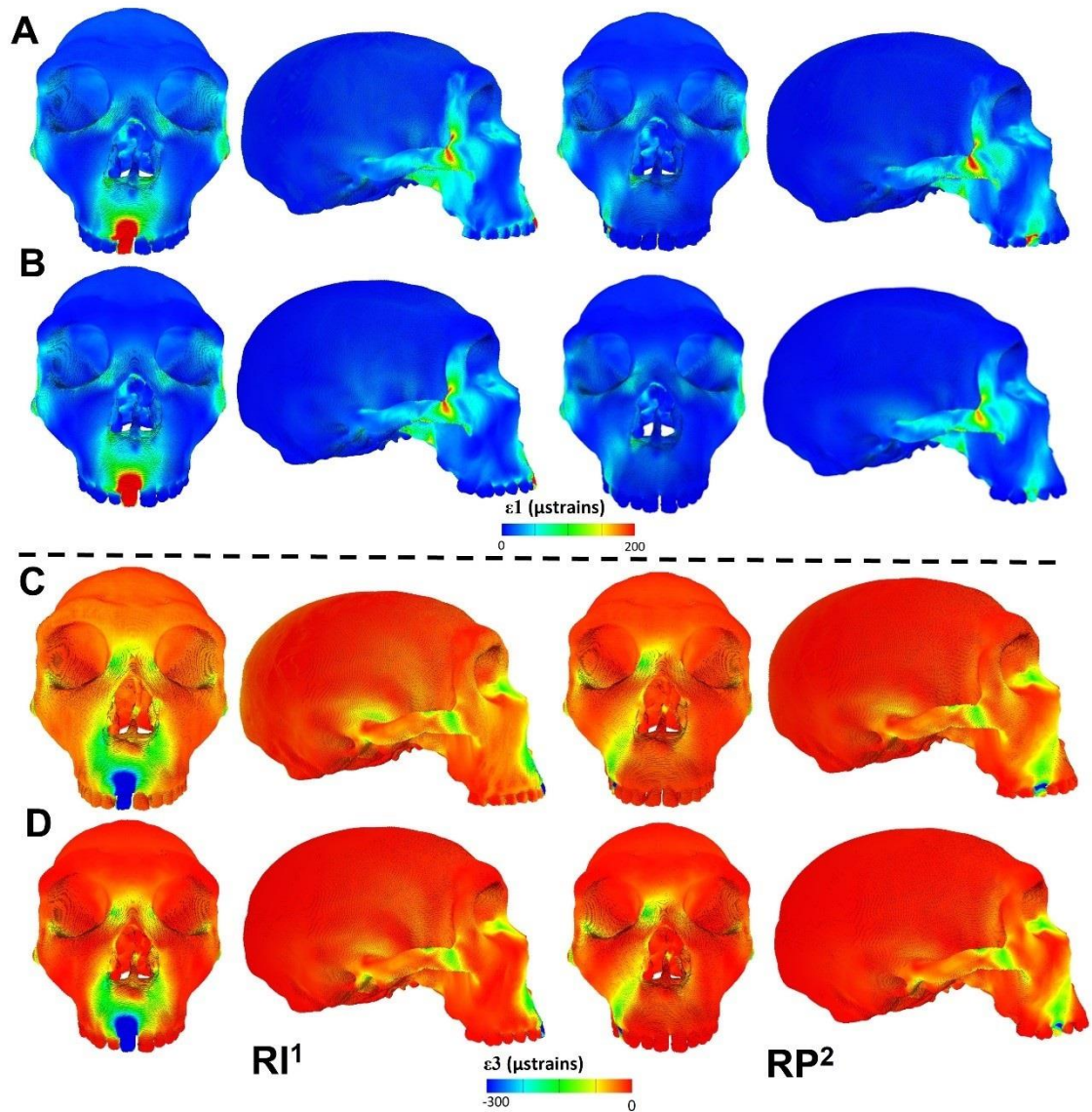


Figure 2. Strain contour plot of the solved Neanderthal with Amud teeth (A, C) and Neanderthal with adult modern human teeth (B, D) adult FE models under RI<sup>1</sup> and RP<sup>2</sup> biting simulation in front and lateral views.

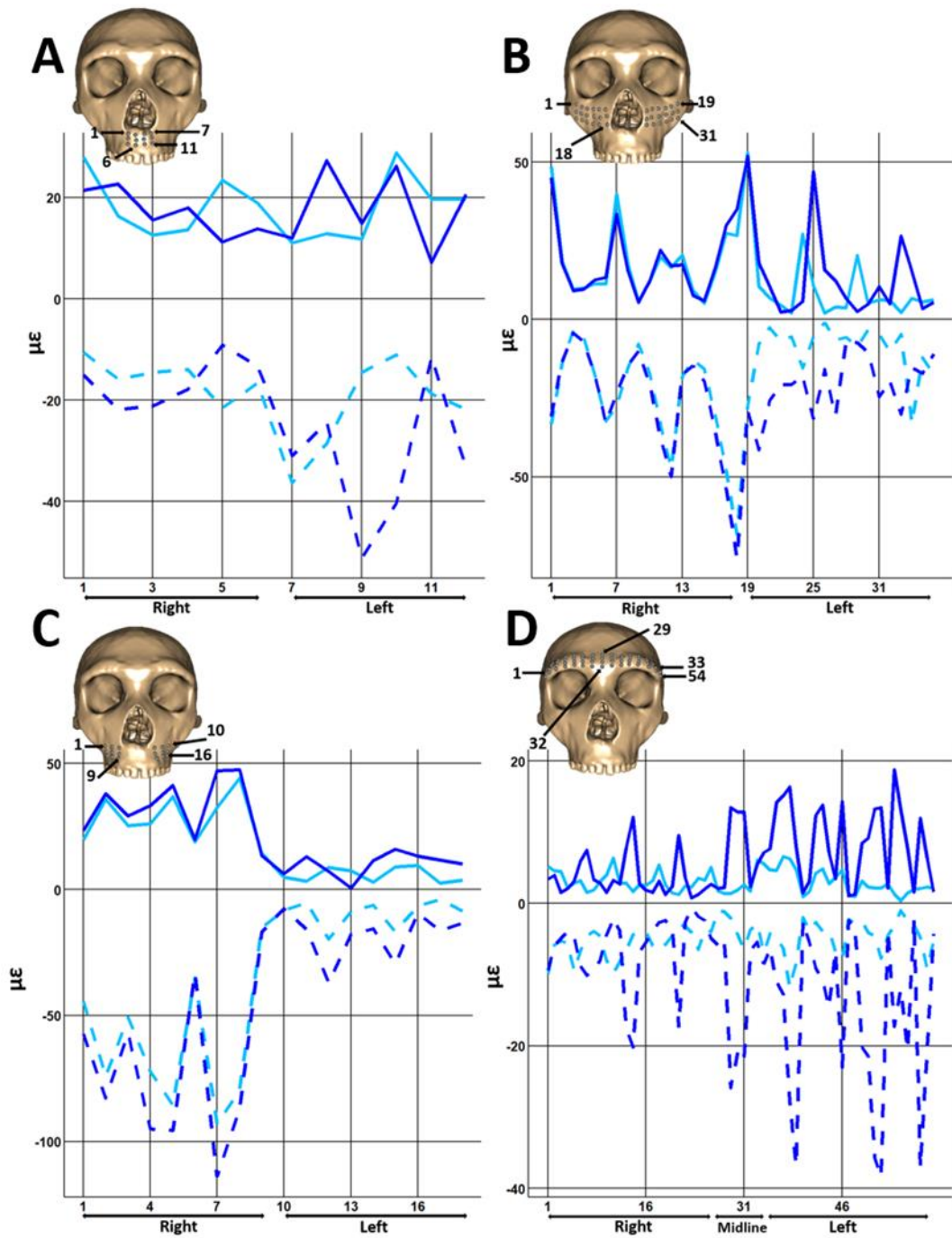


Figure 3. Strains experienced by the Neanderthal FE models with modern human teeth (in light blue) and Neanderthal teeth (in dark blue) at the 126 sampling points collected on the maxilla and supraorbital ridge during the  $RP^2$  biting. The tensile (solid) and compressive (dashed) strains are unscaled.

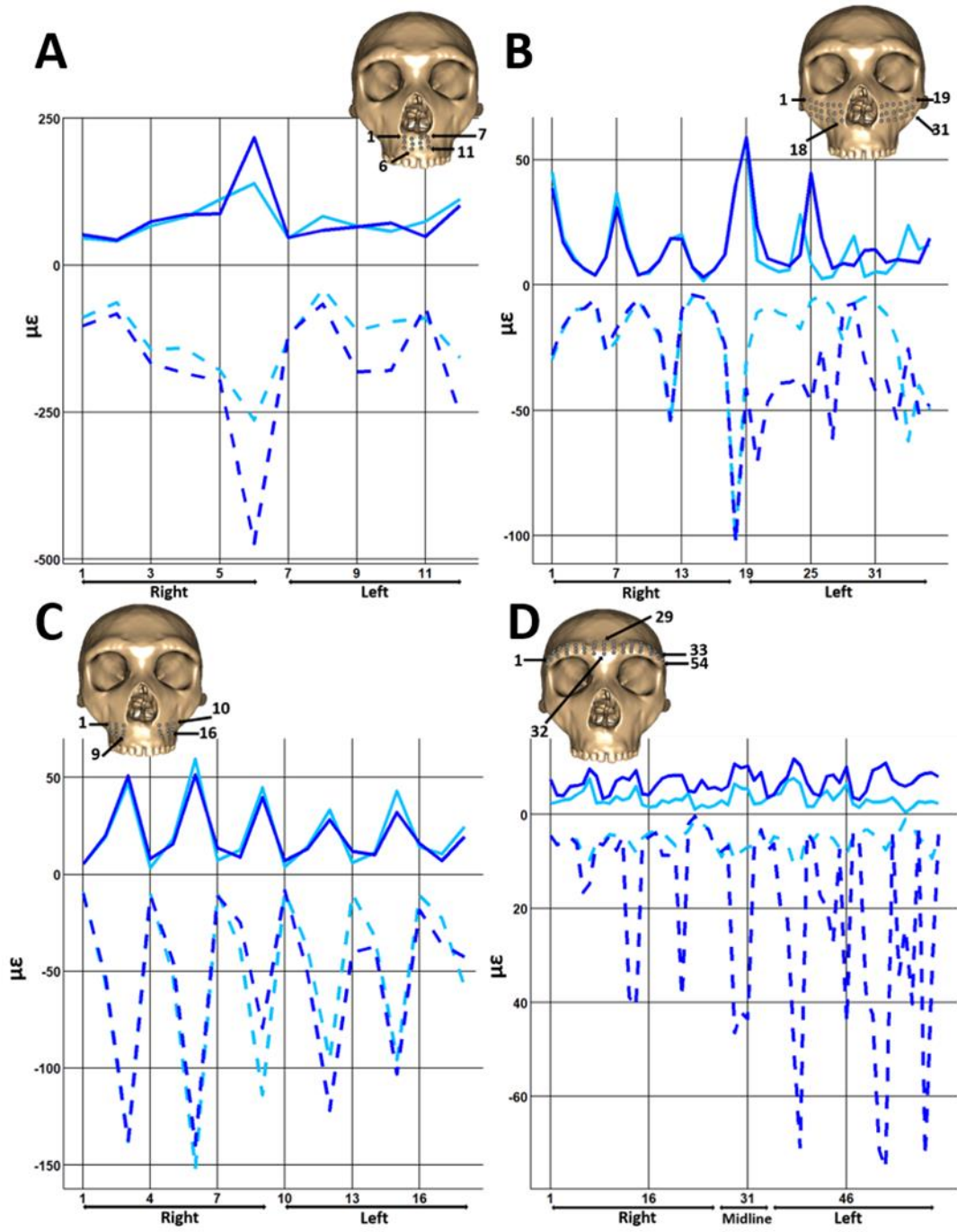


Figure 4. Strains experienced by the Neanderthal FE models with modern human teeth (in light blue) and Neanderthal teeth (in dark blue) at the 126 sampling points collected on the maxilla and supraorbital ridge during the R1<sup>1</sup> biting simulation. The tensile (solid) and compressive (dashed) strains are unscaled.